

AD A108354

LEVEL //



Rockwell International

DTIC FILE COPY

DTIC  
ELECTE  
DEC 10 1981  
S D D

DISTRIBUTION STATEMENT A

Approved for public release;  
Distribution Unlimited

81103007 1

File No. \_\_\_\_\_

**LEVEL**Report No. NR81H-50

Accession For

NTIS GRA&I ☒DTIC TAB ☐Unannounced ☐

Justification \_\_\_\_\_

**Rockwell International**By Per Ltr. on File

Distribution/

Availability Codes

Dist Avail and/or  
SpecialA**SUMMARY REPORT****XFV-12A DIAGNOSTIC****AND DEVELOPMENT****PROGRAM****CONTRACT NO. N00019-73-C-0053****NOVEMBER 1981**

North American Aircraft Division

4300 East Fifth Avenue

PO Box 1259

Columbus, Ohio 43216

**PREPARED BY** V/STOL AerodynamicsP. M. Bevilaqua  
ManagerAero/Test & DevelopmentC. P. Combs  
Manager**APPROVED BY**C. G. Cline  
XFV-12A Project MgrP. L. Marshall  
Director, Adv Systems

No. of Pages \_\_\_\_\_

**REVISIONS**

Date \_\_\_\_\_

DATE	REV BY	PAGES AFFECTED	REMARKS

**DISTRIBUTION STATEMENT A**Approved for public release;  
Distribution Unlimited**DTIC  
ELECTE  
DEC 10 1981****D**



ABSTRACT

This report summarizes the diagnostic and development program of the XFV-12A thrust augmented wing technology prototype conducted during the period of January 1979 through May 1981 and is presented in compliance with Item 0014 of Contract No. N00019-73-C-0053.



## TABLE OF CONTENTS

<u>SECTION</u>	<u>TITLE</u>	<u>PAGE</u>
	ABSTRACT	1
	TABLE OF CONTENTS	ii
	LIST OF FIGURES	v
	LIST OF TABLES	xiii
	LIST OF ABBREVIATIONS AND SYMBOLS	xiv
	REFERENCES	xix
1.0	INTRODUCTION	1-1
2.0	BACKGROUND	2-1
	2.1 GENERAL	2-1
	2.2 AIRCRAFT DESCRIPTION	2-6
	2.3 XFV-12A AIRCRAFT DEVELOPMENT	2-19
	2.3.1 Static and Dynamic Tethered Hover Tests	2-19
	2.3.1.1 Facility	2-19
	2.3.1.2 Test Program	2-23
	2.3.1.3 Results of the Tethered Hover Testing	2-23
	2.3.2 Diagnostic Testing	2-25
	2.3.2.1 Diagnostic Test Results	2-27
	2.4 SUMMARY	2-27
3.0	DEVELOPMENT PROGRAM	3-1
	3.1 DEVELOPMENT LOGIC	3-1
	3.2 SUMMARY	3-6
4.0	DESIGN STUDIES SUMMARY	4-1
	4.1 INTRODUCTION	4-1
	4.2 COANDA SHAPE DEVELOPMENT	4-1
	4.3 CENTERBODY DEVELOPMENT	4-5
	4.3.1 Hypermixing Nozzle	4-5
	4.3.2 Asymmetric Nozzle	4-9
	4.3.3 Symmetric Nozzle	4-10
	4.4 CONFIGURATION EVOLUTION	4-12
	4.4.1 Wide Throat	4-12
	4.4.2 Blended Wing	4-17
	4.4.3 Rectangular Augmenter Study	4-31
	4.5 SUMMARY	4-42
5.0	MODELING	5-1
	5.1 GENERAL	5-1
	5.2 NUMERICAL MODELS	5-1
	5.2.1 JET MIXING ANALYSIS	5-1
	5.2.2 EJECTOR POTENTIAL FLOW ANALYSIS	5-4
	5.3 EJECTOR SCALING LAWS	5-6
	5.4 APPARATUS	5-10
	5.5 AUGMENTER MODELS	5-16
	5.6 INSTRUMENTATION ACCURACY	5-29





## TABLE OF CONTENTS (CONTINUED)

<u>SECTION</u>	<u>TITLE</u>	<u>PAGE</u>
5.7	TEST PROCEDURES AND METHODS	5-31
5.7.1	Short Time Repeatability	5-31
5.7.2	Long Time Repeatability	5-31
5.7.3	Rig 1 to Rig 5 Data Comparison/ Repeatability	5-31
5.8	SUMMARY	5-34
6.0	COANDA DEVELOPMENT	6-1
6.1	INTRODUCTION	6-1
6.2	SCALE COANDA EVALUATION	6-1
6.3	INTERNAL RADIUS EVALUATION	6-5
6.3.1	Phase I	6-5
6.3.2	Phase II	6-16
6.4	COANDA SEGMENT MODEL	6-21
6.4.1	Introduction	6-21
6.4.2	Test Program	6-21
6.4.3	Model	6-22
6.4.4	Baseline Performance	6-22
6.4.5	Location of Feed Duct	6-28
6.4.6	Effect of Inlet Mach Number	6-28
6.4.7	External Coanda Shape Evaluation	6-37
6.4.8	Phase III - Internal Radius Evaluation	6-40
6.4.8.1	General	6-40
6.4.8.2	Turning Efficiency and Jet Growth	6-40
6.4.8.3	Flow and Velocity Coefficients	6-55
6.4.9	Summary	6-55
7.0	CENTERBODY NOZZLE DEVELOPMENT	7-1
7.1	GENERAL	7-1
7.2	HYPERMIXING NOZZLES	7-1
7.2.1	Analytical Improvements	7-5
7.3	ASYMMETRIC NOZZLES	7-14
7.3.1	Introduction	7-14
7.3.2	14 Element Asymmetric Centerbody Nozzle	7-16
7.3.3	14 Element Mod 2 Asymmetric Nozzle	7-20
7.3.4	14 Element Mod 3 Asymmetric Nozzle	7-20
7.3.5	18 Element Asymmetric Nozzle	7-27
7.4	SYMMETRIC CENTERBODY NOZZLE	7-29
7.4.1	Introduction	7-29
7.4.2	Bowtie Ratio Effects	7-31
7.4.3	Span Slot Aspect Ratio Effects	7-39
7.4.4	Cross Slot Aspect Ratio	7-42
7.4.5	Effect of Span-Slot/Cross-Slot Flow Split	7-42
7.4.6	Effect of Number of Elements	7-58
7.4.7	Jet Angle Study	7-60
7.5	SUMMARY	7-70



## TABLE OF CONTENTS (CONTINUED)

<u>SECTION</u>	<u>TITLE</u>	<u>PAGE</u>
8.0	SHROUD STUDY	8-1
8.1	GENERAL	8-1
8.2	EFFECT OF FLAP LENGTH	8-2
8.3	FLAP LENGTH ASYMMETRIES	8-5
8.4	LOCAL SEPARATION EFFECTS (BUBBLES)	8-10
8.5	INVISCID ANALYSIS OF SHROUD	8-13
8.6	FLAPERONS	8-20
8.7	BOATTAIL ANGLE EFFECTS	8-23
8.8	SUMMARY	8-24
9.0	FULL SCALE COMPONENTS	9-1
9.1	INTRODUCTION	9-1
9.2	PROTO NO. 1	9-1
9.2.1	Diffuser	9-1
9.2.2	Elevon	9-14
9.2.3	Isolated Wing Endwall Blowing	
	Nozzle Tests	9-24
9.2.3.1	Outboard Endwall Blowing Tests	9-24
9.2.3.2	Inboard Endwall Blowing Tests	9-27
9.3	IMPROVED ELEVON	9-33
9.3.1	Test Article	9-33
9.3.2	Test Results	9-38
9.4	SUMMARY	9-53
10.0	TEST FACILITIES	10-1
10.1	GENERAL	10-1
10.2	WHIRL-RIG TEST FACILITY	10-1
10.2.1	Instrumentation and Data Acquisition	10-6
10.2.2	Engine Instrumentation	10-6
10.2.3	Instrumentation Van	10-11
10.2.4	Model Instrumentation	10-11
10.2.5	Traversing Probe	10-16
10.3	THERMODYNAMICS LABORATORY	10-16
10.3.1	Air Compressor	10-16
10.3.2	Control and Distribution System	10-16
10.4	TEST FACILITY - WPAFB	10-21
10.4.1	General	10-21
10.4.2	Test Enclosure	10-21
10.4.3	Operations Trailer	10-25
10.4.4	Instrumentation and Data	10-25
11.0	AIRCRAFT PRESERVATION	11-1
11.1	GENERAL	11-1
11.2	INSPECTION/PRESERVATION SUMMARY	11-1
12.0	CONCLUSIONS AND RECOMMENDATIONS	12-1



## LIST OF FIGURES

<u>FIGURE NO.</u>	<u>TITLE</u>	<u>PAGE</u>
2-1	V/STOL Prototypes	2-2
2-2	Lift System Footprint (At Exit)	2-3
2-3	Fighter/Attack Useful Load Comparison	2-4
2-4	Lift Control Conversion	2-5
2-5	XFV-12A Airplane Three View	2-7
2-6	XFV-12A Inboard Profile	2-9
2-7	Engine Air Induction and Distribution System	2-13
2-8	Prototype Structure	2-14
2-9	Diverter Valve Design	2-15
2-10	Lift and Control	2-17
2-11	Conversion to Conventional Flight	2-18
2-12	Test Site - Impact Dynamics Research Facility at Langley	2-20
2-13	Z-System	2-21
2-14	Static Load System	2-22
2-15	Augmenter Performance	2-26
3-1	Summary of Expected Test Mission Performance	3-2
3-2	Wing Development Program	3-3
3-3	Geometric Relationship of the Wing and Canard Thrust Vectors	3-4
3-4	Wing $\emptyset$ Versus Canard $\emptyset$	3-5
4-1	Comparison of Xfv-12A Proto #1 Elevon and Original Full Scale Whirl Rig Elevon Nozzle Shapes	4-2
4-2	Spiral Definition	4-3
4-3	Example of Various Spirals With Identical Thickness	4-3
4-4	Initial Radius $R_0$ Versus K	4-4
4-5	Minimum K Versus Y/t	4-4
4-6	Running Length from Nozzle to Throat Versus K	4-4
4-7	Empirical Coanda Selection Criteria	4-6
4-8	Comparison of Coanda Shapes	4-7
4-9	Centerbody Shape Comparison	4-7
4-10	Hypermixing Nozzle	4-8
4-11	Typical Cross-Section of the Centerbody Nozzle	4-8
4-12	Asymmetric Centerbody Nozzle	4-9
4-13	Closeout System On the Upper Surface	4-9
4-14	Symmetric Centerbody Nozzle	4-10
4-15	Nozzle Configuration	4-11
4-16	Nozzle Parameters	4-11
4-17	Wedge Versus Launch Angle	4-12
4-18	Wing Cross-Section with Improved Centerbody Nozzle	4-13
4-19	Flexibility In Wing Augmenter Design	4-14
4-20	Wing Wide Throat Planform	4-15
4-21	Co-Planar Wing and Canard Configuration	4-18
4-22	Augmenter Performance Tapered Versus Rectangular	4-19
4-23	Blended Wing Concept	4-21



## LIST OF FIGURES (CONTINUED)

<u>FIGURE NO.</u>	<u>TITLE</u>	<u>PAGE</u>
4-24	Forward Augmenter Cross-Sections	4-23
4-25	Aft Augmenter Cross-Sections	4-24
4-26	Aft Augmenter Cross-Section	4-26
4-27	Ducting System	4-27
4-28	Ducting System	4-28
4-29	Wing Structure	4-29
4-30	Fuselage Structure	4-30
4-31	Summary of Expected Test Mission Performance	4-32
4-32	Rectangular Augmenters	4-33
4-33	Wing Augmenter Cross-Sections	4-34
4-34	Canard Augmenter Cross-Sections	4-35
4-35	Ducting System	4-37
4-36	Ducting System	4-38
4-37	Wing Structure	4-39
4-38	Fuselage Structure	4-40
4-39	Summary of Expected Test Mission Performance XfV-12C	4-41
5-1	Computational Grid for Cross Slot - Span Slot Centerbody Configuration	5-5
5-2	Mathematical Model of Ejector Wing	5-7
5-3	Reynolds No. Variation With Temperature	5-8
5-4	Temperature Effect	5-9
5-5	Scale and Full Size Ejectors	5-11
5-6	Air Supply System	5-12
5-7	Plan View of Rig #1	5-13
5-8	Section Blowups of Modifications to Rig #1	5-14
5-9	Overall View of Test Stand No. 1	5-15
5-10	Augmenter Geometry	5-18
5-11	Augmenter Model Construction Details	5-19
5-12	Model Flap Pressure Tap Locations	5-21
5-13	Model Flap Pressure Tap Locations	5-22
5-14	Model Flap Pressure Tap Locations	5-23
5-15	Surface Static Press Tap Location - Rig 5, Test 307	5-24
5-16	Effect of Internal Screening On Jet Turbulence Intensity	5-25
5-17	VEE/FLAT Screen $\phi$ Comparison SCBT15-1 Centerbody	5-26
5-18	Endwall Blower Locations	5-27
5-19	Augmenter Endwall Construction Details	5-28
5-20	Data Repeatability - Short Term $\phi$ Versus NPR	5-32
5-21	Data Repeatability - Long Term $\phi$ Versus $A_3/A_2$	5-33
5-22	Rig 1/Rig 5 Comparison	5-35
6-1	Coanda Spiral - Definition and Packaging	6-3
6-2	Photo - 20-Inch Span Coanda Segment Model	6-6
6-3	Photo - Cross Section of 20-inch Coanda Segment Model	6-7
6-4	Sketch of Cross Section Test Hardware and Effect of Internal Radius On Nozzle Approach $M_N$	6-9



## LIST OF FIGURES (CONTINUED)

<u>FIGURE NO.</u>	<u>TITLE</u>	<u>PAGE</u>
6-5	CTE Versus $X/t$ for $R_1/t = 2, 3, 4$ , and 5	6-10
6-6	$w/t$ Versus $S/t$ for $R_1/t = 2, 3, 4, 5$ , and 6.9	6-11
6-7	Surface Static Pressure Distributions for $R_1/t = 2, 3$ , and 5	6-12
6-8	$P_{Tpeak}/P_{Tnozzle}$ Versus Distance ( $s/t$ )	6-13
6-9	$w/t$ Versus $s/t$ , $R_1/t = 2, 0^\circ$ and 10° Convergence	6-14
6-10	Surface Static Pressure Distribution for $R_1/t = 2, 0^\circ$ and 10° Lip Convergence	6-15
6-11	Photo - Test Hardware Installed At WPAFB Facility	6-17
6-12	Photo - Test Hardware Installed at WPAFB Facility	6-18
6-13	Component $C_v$ and Nozzle $C_D$ Versus NPR, $R_1/t = 3, 5^\circ$ Lip Convergence Angle	6-20
6-14	Coanda Segment Model Test Summary	6-23
6-15	Full-Scale Elevon Coanda Segment Model	6-24
6-16	Feed Duct Positions	6-25
6-17	Dump Door	6-26
6-18	Coanda Shape Comparison	6-27
6-19	Nozzle Total Pressure Distribution Comparison	6-29
6-20	Flow Visualization-Elevon In Thermo Lab	6-30
6-21	Flow Visualization-Coanda Segment Model Run 34	6-31
6-22	Nozzle Total Pressure Distribution Versus Span	6-32
6-23	Nozzle Total Pressure Distribution Versus Span	6-33
6-24	Flow and Velocity Coefficients	6-34
6-25	Jet Width Versus Chord 16-inch Span Station	6-35
6-26	Nozzle Total Pressure Distribution Versus Span	6-36
6-27	Flow and Velocity Coefficients Comparison- WPAFB Coanda Segment Model	6-38
6-28	Jet Growth Versus Chord Distance Comparison- Span Sta 16	6-39
6-29	Turning Efficiency Versus Span-K = 1.17 and Proto #1 Simulation	6-41
6-30	Turning Efficiency Versus Span-K = 1.3 and Proto 1 Simulation	6-42
6-31	Nozzle Total Pressure Distribution Versus Span	6-43
6-32	Dedicated Nozzle Vanes - Single Vane	6-44
6-33	Dedicated Nozzle Vanes - Double Vane	6-45
6-34	Dedicated Nozzle Vanes - 3 Vane Cascade	6-46
6-35	Nozzle Total Pressure Distribution Versus Span	6-47
6-36	Primary Nozzle Vane	6-48
6-37	Sketch of Internal Radius Variations	6-49
6-38	Turning Efficiency Versus Span	6-50
6-39	Jet Growth Versus Chord Distance	6-51
6-40	Comparison of Turning Efficiency for $R_1/t = 3$ and $R_1/t = 4$	6-52



## LIST OF FIGURES (CONTINUED)

<u>FIGURE NO.</u>	<u>TITLE</u>	<u>PAGE</u>
6-41	Jet Growth Comparison - $R_1/t = 3.0$ and $R_1/t = 4.0$ Configuration	6-53
6-42	Flow Visualization	6-54
6-43	Flow and Velocity Coefficients	6-56
7-1	Hypermixing Nozzle Exit	7-1
7-2	Effect of Jet Parameter Variations on Thrust Augmentation	7-2
7-3	Computed Effect of Hypermixing Aspect Ratio on the Jet Mixing	7-3
7-4	Effect of Hypermixing Nozzle Aspect Ratio on Thrust Augmentation At Deflection = $23^\circ$	7-4
7-5	Comparison of Computed and Measured Effect of Hypermixing Angle	7-5
7-6	Comparison of Hypermixing Velocity Distributions at Ejector Exit	7-6
7-7	Hypermixing Nozzle Survey Stations	7-7
7-8	Measured Inlet Velocities	7-7
7-9	Dynamic Pressures and Angularity of Inlet Secondary Flow, $15^\circ$ Hypermixing Angle and $A_2/A_0 = 15.2$	7-8
7-10	$22.5^\circ$ Hypermixing Jet Velocity Distribution with Original Values of $C_k$ and $C_e$	
7-11	$22.5^\circ$ Hypermixing Jet Velocity Distribution with $C_k = 4. \times C_{k,ref}$	7-10
7-12	$22.5^\circ$ Hypermixing Jet Velocity Distribution with $C_e = C_{e,ref}/16$	7-11
7-13	Comparison of Measured and Computed Augmentation	7-12
7-14	Effect of Swirl on Analytical Prediction	7-13
7-15	Asymmetric Centerbody Packaging Concept	7-15
7-16	14 Element Asymmetric Nozzle	7-17
7-17	Isolated Centerbody Nozzle Efficiency ( $C_T$ )	7-18
7-18	14 Element Asymmetric Versus $15^\circ$ Hypermix Centerbody Nozzle $A_3/A_2$ Comparison	7-18
7-19	14 Element Asymmetric Throat Width Comparison	7-19
7-20	14 Element Asymmetric Mod No. 1	7-21
7-21	14 Element Asymmetric and 14 Element Asymmetric Mod No. 1 Comparison	7-22
7-22	14 Element Asymmetric Mod No. 2	7-23
7-23	Isolated Nozzle Efficiency	7-24
7-24	14 Element Asymmetric and 14 Element Asymmetric Mod No. 2 Comparison	7-24
7-25	14 Element Asymmetric Mod No. 3	7-25
7-26	Isolated Nozzle Efficiency ( $C_T$ )	7-26
7-27	14 Element Asymmetric Mod 2 and Mod 3 Comparison	7-27
7-28	18 Element Asymmetric Nozzle	7-28
7-29	14 Element Mod 2 and 18 Element Asymmetric, Comparison Isolated Nozzle Efficiency ( $C_T$ )	7-29



## LIST OF FIGURES (CONTINUED)

<u>FIGURE NO.</u>	<u>TITLE</u>	<u>PAGE</u>
7-30	14 Element Mod 2 Asymmetric and 18 Element Asymmetric $\phi$ versus $A_3/A_2$ Comparison	7-30
7-31	Symmetric Cross-Slot Nozzle (BT-3)	7-31
7-32	Symmetric Cross-Slot Nozzle Thrust Augmentation versus Diffuser Area Ratio	7-32
7-33	Reduced Width Symmetric Cross-Slot Nozzle	7-33
7-34	Variation of Jet Flow Angle for Various Nozzle Bowtie Ratios	7-34
7-35	Effect of Bowtie Ratio on Thrust Augmentation	7-34
7-36	Effect of Nozzle Bowtie Ratio on Nozzle Thrust Coefficient	7-35
7-37	Bowtie Ratio 1 Nozzle	7-36
7-38	Bowtie Ratio 2 Nozzle	7-37
7-39	Bowtie Ratio 3 Nozzle	7-38
7-40	Simulation of Vortex Structure Produced by Cross-Slot Nozzle	7-39
7-41	Axial Velocity Profiles at Augmenter Throat	7-40
7-42	Axial Velocity Profiles At Augmenter Exit	7-41
7-43	Effect of Span Slot Aspect Ratio on Thrust Augmentation	7-42
7-44	Span Slot Aspect Ratio 1 Nozzle	7-43
7-45	Span Slot Aspect Ratio 9 Nozzle	7-44
7-46	Span Slot Aspect Ratio 12 Nozzle	7-45
7-47	Span Slot Aspect Ratio 17.5 Nozzle	7-46
7-48	Effect of Cross Slot Aspect Ratio on Thrust Augmentation	7-47
7-49	Spanwise Variation of Exit Massflow	7-48
7-50	Spanwise Variation of Exit Velocity Profile Shape Factor, $\beta$	7-49
7-51	Effect of Flow Split on Thrust Augmentation	7-51
7-52	0% Flow Split Nozzle	7-52
7-53	60% Flow Split Nozzle	7-53
7-54	80% Flow Split Nozzle	7-54
7-55	Effect of Flow Split on Spanwise Variation of Exit Massflow	7-55
7-56	Effect of Flow Split on Spanwise Variation of Exit Velocity Profile Shape Factor	7-55
7-57	Comparison of Exit Axial Velocity Profiles for 36 Percent and 65 Percent Flow Split Nozzles	7-56
7-58	Comparison of Exit Axial Velocity Profiles for 0 Percent and 36 Percent Flow Split Nozzles	7-57
7-59	Variation of Thrust Augmentation with Number of Elements ( $C_T$ = Constant)	7-58
7-60	Variation of Nozzle Aspect Ratio with Element Spacing	7-59
7-61	Variation of Thrust Augmentation with Number of Elements (Adjusted for $C_T$ Effects)	7-60
7-62	Nozzle Test Matrix for Jet Angle Study	7-61
7-63	Measured Cross-Slot Nozzle Exit Flow Angles	7-62



## LIST OF FIGURES (CONTINUED)

<u>FIGURE NO.</u>	<u>TITLE</u>	<u>PAGE</u>
7-64	Assumed Angle Distribution at Initial Data Plane	7-63
7-65	Effect of Constant and Linearly Varying Cross-Slot Jet Flow Angles on Thrust Augmentation	7-64
7-66	Zero Degree Jet Angle Nozzle	7-65
7-67	Linear Jet Angle Nozzle (0 to 28 Degrees)	7-66
7-68	Constant Jet Angle Nozzle (21 Degrees)	7-67
7-69	Cross Slot-Span Slot Nozzle with a Linearly Varying Exit Profile	7-68
7-70	Measured Flow Angles for Linearly Varying Slot Nozzle Configuration	7-69
7-71	Effect of Linear Jet Angle Distribution on Thrust Augmentation	7-70
8-1	Streamlines of the Flow Induced by a Free Jet	8-1
8-2	Entrainment by the Primary Jet Induces a Secondary Flow	8-2
8-3	Effect of Flap Length on Thrust Augmentation Ratio	8-3
8-4	Effect of Flap Length on Surface Pressure Distribution	8-4
8-5	Effect of Flap Length on Section Mass Flow	8-6
8-6	Effect of Flap Length on Velocity Profile Shape Factor	8-7
8-7	Inclination of the Thrust Vector Limits the Augmentation	8-8
8-8	Effect of Asymmetric Flap Length on $\phi$	8-9
8-9	Effect of Cross-Slot Width on Thrust Augmentation Ratio	8-10
8-10	Forward Flap Surface Pressures for Narrow and Wide Nozzles	8-11
8-11	Variation of Surface Pressure with Diffuser Area Ratio	8-12
8-12	Effect of Roughness on Coanda Surface Pressures	8-13
8-13	Entrainment by the Primary Jet Induces a Secondary Flow	8-15
8-14	Comparison of Experimental and Theoretical Velocities at the Throat Plane	8-16
8-15	Comparison of Experimental and Theoretical Velocities at a Nozzle Plane	8-17
8-16	Comparison of Experimental and Theoretical Flow Angles at the Inlet Plane	8-18
8-17	Comparison of Experimental and Theoretical Surface Pressures	8-19
8-18	Comparison of Predicted and Experimental Shroud Pressure Distributions	8-20
8-19	Sketch of the Flaperon Configuration	8-21
8-20	Comparison of Thrust Augmentation for the Straight Flap and Flaperon Configuration	8-22





## LIST OF FIGURES (CONTINUED)

<u>FIGURE NO.</u>	<u>TITLE</u>	<u>PAGE</u>
8-21	Comparison of Throat Velocity for the Straight Flap and Flaperon Configuration	8-23
8-22	Effect of Boattail Angle on Thrust Augmentation	8-24
9-1	Sketch of XfV-12A Wing Component Test in Thermo Lab	9-2
9-2	Diffuser Nozzle Total Pressure Survey Nominal NPR 1.8:1	9-4
9-3	Pressure Profile Locations, Proto 1 L/H Wing Diffuser	9-5
9-4	Proto 1 L/H Diffuser Jet Profiles Downstream 10t	9-6
9-5	Proto 1 L/H Wing Diffuser, Coanda Turning Efficiency versus Span	9-7
9-6	Flow Visualization	9-8
9-7	Flow Visualization	9-9
9-8	Nozzle Expansion "Pots" - Installation on Wing Diffuser	9-10
9-9	Nozzle Gap Expansion, Proto 1 L/H Wing Diffuser	9-11
9-10	Nozzle Gap versus Span Station, Proto 1 L/H Wing Diffuser	9-12
9-11	XfV-12A L/H Wing Forward Diffuser Surface, Test Nozzle Area Coefficients	9-13
9-12	Elevon Nozzle Total Pressure Survey Nominal NPR 1.7:1	9-15
9-13	Pressure Profile Locations - Proto 1 L/H Wing Elevon	9-16
9-14	Proto 1 L/H Elevon Jet Profiles at Nozzle Exit Nominal NPR 1.6:1	9-17
9-15	Proto 1 L/H Wing Elevon Jet Profiles Downstream 10t Nominal NPR 1.6:1	9-18
9-16	Coanda Turning Efficiency vs Span, Proto 1 L/H Wing Elevon Nominal NPR 1.6:1	9-19
9-17	Flow Visualization	9-20
9-18	Flow Visualization	9-21
9-19	Nozzle Gap Expansion Proto 1 L/H Wing Elevon	9-22
9-20	Nozzle Gap versus Span Station, Proto 1 L/H Wing Elevon	9-23
9-21	XfV-12A L/H Wing Elevon Surface Test Nozzle Coefficients	9-25
9-22	Outboard Endwall Nozzle Dimensions	9-26
9-23	Simulated Extended Elevon Corner Nozzle and Auxiliary Slot Blower	9-28
9-24	Pressure Profiles, Outboard Endwall Blowing, XfV-12A Wing	9-29
9-25	Inboard Endwall Flow Visualization	9-30
9-26	Nozzle System Close Up	9-31
9-27	Traversing Rake Surveys, $P_T$ vs Span, NPR = 1.9:1	9-32



## LIST OF FIGURES (CONTINUED)

<u>FIGURE NO.</u>	<u>TITLE</u>	<u>PAGE</u>
9-28	Comparison of Coanda Shapes	9-35
9-29	Elevon Feed	9-36
9-30	Elevon Installation in Test Stand	9-37
9-31	Nozzle Gap Measurements	9-39
9-32	Gap at Nozzle Lip After Pressurization	9-40
9-33	Nozzle Gap Expansion	9-41
9-34	Primary Nozzle Survey Comparison - Inboard	9-42
9-35	Primary Nozzle Survey Comparison - Midspan	9-43
9-36	Primary Nozzle Survey Comparison - Outboard	9-44
9-37	Dedicated Nozzle Survey Comparison	9-45
9-38	$C_D$ and $C_Y$ vs NPR - Improved Elevon	9-46
9-39	$C_D$ and $C_Y$ vs NPR - Existing Elevon	9-47
9-40	Turning Efficiency vs Span - 10t	9-48
9-41	Turning Efficiency vs Span - 20t	9-49
9-42	Turning Efficiency vs Span - 50t	9-50
9-43	Flow Visualization Comparison at 1 and 4 Inches	9-51
9-44	Flow Visualization Comparison at 8 and 14 Inches	9-52
10-1	Schematic - Whirl Rig with Model Installed	10-2
10-2	F401 Whirl Rig with Model Installed	10-3
10-3	F401 Engine Installation	10-4
10-4	F401 Engine Installation	10-5
10-5	Whirl Rig- Wing Model Instrumentation	10-7
10-6	Outboard End of Boom with Model Installed	10-8
10-7	Outboard End of Boom with Model Installed	10-9
10-8	Wing Center Ejector Instrumentation	10-12
10-9	Wing Forward Diffuser Instrumentation	10-13
10-10	Wing Augmenter Throat $P_s$ Probes	10-15
10-11	Traversing Probe Installation	10-17
10-12	Traversing Rake Instrumentation for Center Ejector Jet Growth	10-18
10-13	Schematic - Thermo Lab Process Air System	10-19
10-14	Columbus Division Laboratory Compressor Operating Characteristics	10-20
10-15	Test Site Unmodified	10-22
10-16	Test Facilities	10-23
10-17	Test Facility - Noise Measurements	10-24
11-1	XFV-12A at NASA Langley - General View	11-2



## LIST OF TABLES

<u>TABLE NO.</u>	<u>TITLE</u>	<u>PAGE</u>
2-1	Aircraft Dimensional Data	2-11
4-1	Wing Augmenter Parameters	4-17
4-2	Design Criteria	4-22
4-3	XFV-12B Augmenter Parameters	4-25
4-4	XFV-12C Augmenter Parameters	4-36
6-1	Physical Parameters of Nozzles Tested	6-4
6-2	Spiral Shapes Tested	6-4
9-1	Design Parameters	9-34
10-1	Major Test Facilities	10-1
10-2	Whirl Rig Instrumentation Parameters	10-10
10-3	Instrumentation Parameters	10-26
11-1	Long Term Indoor Ventilated Storage Type A Modified Ref NAVAIR 15-01-500	11-3



## LIST OF ABBREVIATIONS AND SYMBOLS

A	Area
$A_2/A_0$	Ejector Inlet Area Ratio
$A_3/A_2$	Ejector Diffuser Area Ratio
AR	Aspect Ratio
Asym	Asymmetric
B	Base Angle
BTR	Bow Tie Ratio
C	Dissipation Constant
$C_1, C_2, \text{ and } C$	Turbulence Constants
$C_D$	Flow Coefficient $C_D = \frac{\text{Measured Weight Flow}}{\text{Ideal Weight Flow}}$
$C_E$	Nozzle Pressure Expansion Factor
$C_P$	Pressure Coefficient
$C_T$	Thrust Coefficient $C_T = C_D \times C_V$
$C_V$	Velocity Coefficient $C_V = \frac{\text{Measured Thrust}}{\text{Isentropic Thrust}}$
$C_k$	Energy Constant
$C_{ref}$	Reference Chord Length
C-D	Converging-Diverging
CIVV	Compressor Inlet Variable Vane
CS	Cross Slot
CTA	Coanda Turning Angle
CTE	Coanda Turning Efficiency $(P_{t_{peak}}/P_{t_{nozzle exit}})$
DAR	Diffuser Area Ratio
DLI	Deck Launched Interceptor



## LIST OF ABBREVIATIONS AND SYMBOLS (Continued)

FTIT	Fan Turbine Inlet Temperature
G	Rate of Generation of Turbulence Kinetic Energy
H	Enthalphy
I	Entrainment Index
K	Log Spiral Constant
L	Launch Angle
L	Lift
L/H	Left Hand
L/W or L/D	Ejector Length to Throat Width Ratio
l	Nozzle Width
$l/t$	Nozzle Aspect Ratio
M	Mach Number
MFR	Mass Flow Ratio
Mod	Modified
$N_1$	Engine Low Rotor Speed
$N_2$	Engine High Rotor Speed
NPR	Nozzle Pressure Ratio ( $P_{t \text{ nozzle exit}} / P_{\text{amb}}$ )
P	Pressure
$P_r$	Prandtl Number
$P_s$	Static Pressure
$P_T$	Total Pressure
P&W	Pratt and Whitney Aircraft
R	Coanda Local Radius of Curvature
R	Gas Constant
$R_T$	Empirical Constant



## LIST OF ABBREVIATIONS AND SYMBOLS (Continued)

$R_i$	Internal Coanda Radius
$R_o$	Initial Coanda Radius
RCVV	Rear Compressor Variable Vane
RPM	Revolutions Per Minute
S	Coanda Running Length
S	Spacing
$S_{throat}$	Coanda Running Length to Augmenter Throat
T	Temperature
TAW	Thrust Augmented Wing
$U_j$	Jet Velocity Initial
U, V, and W	Time Averaged Velocity Components
Unmod	Unmodified
V	Velocity
$V_p$	Local Peak Jet Velocity
$V_o$	Nozzle Exit Velocity
V/STOL	Vertical/Short Takeoff and Landing
VTOW	Vertical Takeoff Gross Weight
VTOL	Vertical Takeoff and Landing
W	Local Jet Width
W	Wedge Angle
X	Internal Nozzle Envelope
Y	External Coanda Shape Envelope
a	Speed of Sound
e	Base of Napierian Logarithms (2.71828)



## LIST OF ABBREVIATIONS AND SYMBOLS (Continued)

$k$	Turbulence Kinetic Energy
$\dot{m}$	Mass Flow
$t$	Jet Width Initial
$t$	Nozzle Gap
$\rho$	Fluid Density
$\gamma$	Ratio or Specific Heats
$\sigma$	Source Strength
$\epsilon$	Turbulence Rate of Dissipation
$\gamma$	Vortex Strength
$\phi$	Augmentation Ratio (Lift/Isentropic Thrust)
$\delta$	Hypermixing Angle
$\sigma_\epsilon$	Turbulent Prandtl Number for $\epsilon$
$\sigma_k$	Turbulent Prandtl Number for $k$
$\beta$	Velocity Profile Shape Factor
$\mu_t$	Turbulent Viscosity



## LIST OF ABBREVIATIONS AND SYMBOLS (Continued)

SUBSCRIPTS

avg	Average
bt	Boat Tail
C	Cross Slot
Cn	Coanda Nozzle
e	Entrainment
H	Hypermixing
isent	isentropic
L	Lift
P	Primary
Pn	Primary Nozzle
S	Span Slot
Sec	Secondary
0	At Primary Nozzle
1	At Ejector Inlet
2	At Ejector Throat
3	At Ejector Exit





## REFERENCES

- | <u>REFERENCE NO.</u> | <u>TITLE</u>  |
|----------------------|---|
| (1)                  | Bevilaqua, P. M. and DeJoode, A. D., "Viscid/Inviscid Interaction Analysis of Thrust Augmenting Ejectors," Report ONR-CR212-249-1, February 28, 1978  |
| (2)                  | "High Speed Wind Tunnel Tests of a 0.03 Scale Model of the XFV-12A Aircraft," 73CL 2976, dated 11 July 1973.  |
| (3)                  | "High Speed Wind Tunnel Tests of a 0.03 Scale Model of the XFV-12A Data Report," 73CL 2655, dated 6 March 1973.   |
| (4)                  | "Low Speed Wind Tunnel Test of a 0.20 Scale Powered Model of the XFV-12A Data Report," 75CL 2104, dated 29 February 1975.   |
| (5)                  | "XFV-12A NASA Langley Static and Dynamic Hover Tests Summary Report," NR78H-111.  |
| (6)                  | "XFV-12A Wing Augmenter System and Component Diagnostic Testing Summary Report," NR78H-1.   |
| (7)                  | Patankar, S. V. and Spalding, D. B., "A Calculation Procedure for Heat, Mass and Momentum Transfer in Three-Dimensional Parabolic Flows," Int. J. Heat Mass Transfer, Vol. 15, pp. 1787-1806. |
| (8)                  | Schlichting, H., "Boundary Layer Theory," 6th Ed., McGraw-Hill Book Co., 1968.  |
| (9)                  | Lauder, B. E. and Spalding, D. B., "The Numerical Computation of Turbulent Flows," Computer Methods in Applied Mechanics and Engineering, Vol. 3, No. 2, March 1974, pp. 269-289.             |
| (10)                 | DeJoode, A. D. and Patankar, S. V., "Prediction of Three-Dimensional Turbulent Mixing in an Ejector," AIAA Journal, Vol. 16, No. 2, February 1978, pp. 145-150.                               |
| (11)                 | Tennekes, H. and Lumley, J. L., A First Course in Turbulence," The MIT Press, 1972.   |
| (12)                 | Mefferd, L. A. and Bevilaqua, P. M., "Computer Aided Design Study of Hypermixing Nozzles," NR78H-91, NASC Contract N00019-77-C-0527, July 1978.   |
| (13)                 | Long, K. A., "Automatic Generation of Computational Grid for P3DFLOW (TKE) Code", Rockwell International Internal Letter, IL 514-13-81, February 1981.  |
| (14)                 | Bevilaqua, P. M., Woan, C. J., and Schum, E. F., "Viscid/Inviscid Interaction Analysis of Ejector Wings," Report Being Reviewed, NASA Contract NAS2-1068, April 1981.                         |
| (15)                 | "Static Test Rig Coandas", Drawing LH-391, Sheet 2.   |
| (16)                 | "Wing Centerbody-Hypermix Rectangular - .20 Scale", Drawing 356-01042, Sheet 2.   |
| (17)                 | Seiler, M. R., "Flow Measurements on Model Coandas," Rockwell International Internal Letter, IL 512-51-78, November 1978.   |
| (18)                 | Smdel, S. J., "Flow Measurements on Model Coandas," Rockwell International Internal Letter, IL 512-59-79, June 1979.  |



## REFERENCES (CONTINUED)

- | <u>REFERENCE NO.</u> | <u>TITLE</u>   |
|----------------------|--|
| (19)                 | Seiler, M. R., "Selection Criteria for Log Spirals," Rockwell International Internal Letter, IL 512-49-79, March 1979.   |
| (20)                 | DeLany, J. T., Jusko, R. L., et.al., "Summary Report, XFV-12A Wing Elevon Segment Model Testing at Wright-Patterson Air Force Base May-September 1979," NR80H-12, NASC Contract N00019-73-C-0053, February 1980.                 |
| (21)                 | Combs, C. P., "Coanda Nozzle Internal Radius of Approach Study," NR80H-19.   |
| (22)                 | Mefferd, L. A.; Alden, R. E.; and Bevilaqua, P. M., "Design and Test of a Prototype Scale Ejector Wing," Workshop on Thrust Augmenting Ejectors, NASA CP-2093, September 1979.   |
| (23)                 | Quinn, B. P., "Compact Ejector Thrust Augmentation," Journal of Aircraft, Vol. 10, No. 8, August 1973, pp. 481-486.  |
| (24)                 | Bevilaqua, P. M., "Evaluation of Hypermixing for Thrust Augmenting Ejectors," ARL 75-0063, Journal of Aircraft, Vol. 11, No. 6, pp. 348-354, June 1974.  |
| (25)                 | Salter, "Mass Entrainment by Hypermixing Jets," ARL TR 75-0132, June 1975.   |
| (26)                 | Mefferd, L. A.; Alden, R. E.; and Bevilaqua, P. M., "Design and Test of a Prototype Scale Ejector Wing," Workshop on Thrust Augmenting Ejectors, NASA CP-2093, September 1979.   |
| (27)                 | "Analytical Evaluation of the Effect of Cross-Slot Nozzle Aspect Ratio for a Symmetrical Cruciform Nozzle," Rockwell International Internal Letter IL 514-25-80.   |
| (28)                 | "Analysis of Performance Increment Accessible Through Variation of the Number of Cross-Slot Elements," Rockwell International Internal Letter, IL 514-19-80.   |
| (29)                 | "Design of Linear Angle Variation Symmetric Cruciform Centerbody," Rockwell International Internal Letter IL 514-13-80.  |
| (30)                 | "Effect of the Flap Length Ratio (L/D) and the Throat Area Ratio ( $A_2/A_0$ ) on Thrust Augmentation - Part I: The Effect of L/D at $A_2/A_0 = 12$ (TPA 261, Task 0001)," Rockwell International Internal Letter, IL 511-71-76. |
| (31)                 | Seiler, M. R. and Schum, E. F., "An Analytical and Experimental Investigation of Diffusers for VSTOL Thrust Augmenting Ejectors," AIAA Paper 78-1509, 1978.  |
| (32)                 | Morrel, Jean-Pierri and Lissaman, Peter B. S., "The Jet Flap Diffuser: A New Thrust Augmenting Device," AIAA Paper 69-777, 1969.   |
| (33)                 | "Results of Laboratory Cold Flow Testing of Isolated XFV-12A Wing Components," NR78H-116, 30 November 1978.  |
| (34)                 | "Summary Report, XFV-12A Existing Wing Elevon Testing at Wright-Patterson Air Force Base," NR80H-17, 21 February 1980.   |



Rockwell International

NR81H-50

REFERENCES (CONTINUED)

REFERENCE NO.

TITLE

- |      |   |
|------|---|
| (35) | "Results of Cold Flow Testing the XFV-12A Improved Wing Elevon at Wright-Patterson Air Force Base," NR80H-55, 21 August 1980. |
| (36) | "Elevon Assembly-Wing (Modification)," Drawing 356-181402.  |



## 1.0 INTRODUCTION

The purpose of this report is to document the activity during the XFV-12A thrust augments development program conducted from May 1979 to June 1981. This phase of the XFV-12A program was initiated subsequent to the tethered hover testing of the XFV-12A conducted at NASA Langley Research Center and immediately following a series of wing augments diagnostic investigations. During the diagnostic investigations, it was confirmed that the established goal performance levels of  $\phi = 1.50$  for the wing augments and  $\phi = 1.30$  for the canard augments system were not achieved during the tethered hover test program.

The diagnostic tests also indicated that a major source of performance deficiency could be attributed to feed duct/augments component interface problems rather than the basic augments configuration. The interface problems seriously affected both the isolated performance and flow quality of the primary augments nozzles resulting in significantly lower levels of augmentation than originally expected.

After an extensive review of both the tethered hover tests and the wing diagnostic investigations by both Navy and Rockwell International personnel, a remedial program which is the subject of this report was initiated. The primary objective of this program was to systematically improve the performance of the XFV-12A aircraft's thrust augments lift systems. Major emphasis was placed not only on correcting the flow deficiencies identified during the wing augments diagnostic investigations, but to identify and incorporate any improvements in the augments design which would increase its performance potential. The basic rationale for this redevelopment program was established by a series of specific guidelines which are listed below:

- The thrust augments development was to proceed in a serial fashion beginning with the development and demonstration of the wing augments performance, to be followed by a similar program for the canard augments system. Finally, assuming adequate performance levels were demonstrated, the XFV-12A aircraft would be reassembled with the improved augments configurations for VTOL hover evaluation.
- An existing analytical method utilized for thrust augments performance studies was to be improved and correlated with experimental data.
- Model scale and full scale isolated component testing would be employed to correct the feed duct/augments component flow deficiencies identified during the wing diagnostic investigations.
- Scale models representative of aircraft augments designs would be utilized to develop and demonstrate desired performance goals.
- Continuous aircraft/augments design studies would be conducted to assure that candidate augments configurations were compatible with aircraft packaging constraints.



Since its inception in May of 1979, this development effort has been progressing in a promising manner. To date, a number of the program's objectives have been successfully completed. The completed objectives include:

- Redevelopment and demonstration of adequate performance and flow quality on full scale aircraft augmentor components as discussed in Sections 6.0 and 9.0 of this report.
- Utilizing both analytical and experimental methods basic augmentor and nozzle design improvements were developed which increased the performance of a 0.20 scale aircraft representative wing augmentor from  $\phi = 1.46$  to  $\phi = 1.64$ . This effort is fully discussed in Sections 7.0 and 8.0 of this report.
- Design studies were successful in not only integrating candidate augmentor configurations in the basic XFV-12A aircraft, but were integral in the evolution of the basic aircraft design as described in Section 4.0.

Unfortunately, the redevelopment effort was terminated in June 1981 prior to successful completion of all of the stated program objectives.

The subsequent sections of this report will present a detailed discussion of the XFV-12A augmentor remedial program and its current status. A more detailed description of the XFV-12A aircraft and a discussion of the significant events leading to the development effort will be presented. This will be followed by a discussion of the augmentor design studies and the evolution of the aircraft design. The ensuing sections will then describe the actual remedial development effort, its philosophy, the facilities and methods utilized, and a presentation of significant results. Finally, in the last section, a series of recommendations for further development of the thrust augmentor/V/STOL aircraft technology will be discussed.



## 2.0 BACKGROUND

### 2.1 GENERAL

On November 15, 1971, the Naval Material Command issued a "letter type" request for proposal to develop and test a V/STOL (Vertical/Short Takeoff and Landing) Technology Demonstrator Aircraft. Proposal guidelines specified that the V/STOL configurations address either a subsonic multipurpose mission or a supersonic fighter attack mission for air superiority or offensive fleet actions. The proposed V/STOL demonstrator aircraft should also be compatible with operations on the new smaller Sea Control Ship carrier concept. Additionally, the technology demonstrator concepts would incorporate imaginative ideas and be directed toward technology development rather than being restricted by established full scale engineering development constraints. Rockwell International responded to this request by submitting two proposals for aircraft utilizing the Rockwell thrust augmented wing concept (see Figure 2-1).

In October 1972, the Navy selected Rockwell International as the winner of this competition and contracted with Rockwell to develop a supersonic V/STOL fighter/attack aircraft employing the thrust augmented wing concept. This aircraft was later officially designated the XFV-12A.

The thrust augments wing concept (TAW) possesses several unique characteristics which identify it as a viable V/STOL aircraft lift system highly compatible with naval shipboard operations.

The low temperature and pressure footprint of the TAW concept is an obvious advantage when compared to other candidate V/STOL lift systems as shown in Figure 2-2. By virtue of entraining and mixing secondary ambient airflow in quantities several times the aircraft's propulsion system primary flow, both the exhaust pressure and temperature at the augmentor exit plane are reduced to 320 psi and 275°F, respectively. At these conditions, support personnel can operate effectively and safely near the aircraft during V/STOL operations.

The propulsion match between the augmentor and conventional mission requirements also tends to reduce the penalties normally associated with V/STOL aircraft propulsion systems. The net effect of the thrust augmentation including duct losses and control allowances allows the use of a smaller thrust engine than would be required for a deflected thrust concept. This results in a better subsonic thrust-to-weight cruise efficiency for the TAW concept. Figure 2-3 compares TAW with other V/STOL propulsion system concepts in a study conducted at the David Taylor Naval Ship Research and Development Center (DTNSRDC) for an aircraft sized to 35,000 pounds Vertical Takeoff Gross Weight (VTOGW) Deck Launched Intercept (DLI) mission. The comparison of percent useful load versus thrust/weight uninstalled shows the potential propulsion system benefits associated with the TAW concept.

The TAW concept also provides a positive circulation lift effect during conversion from vertical to conventional flight modes. As shown in Figure 2-4, this circulation lift provides increased total aircraft lift during this critical flight transition mode. This advantage is inherent to the

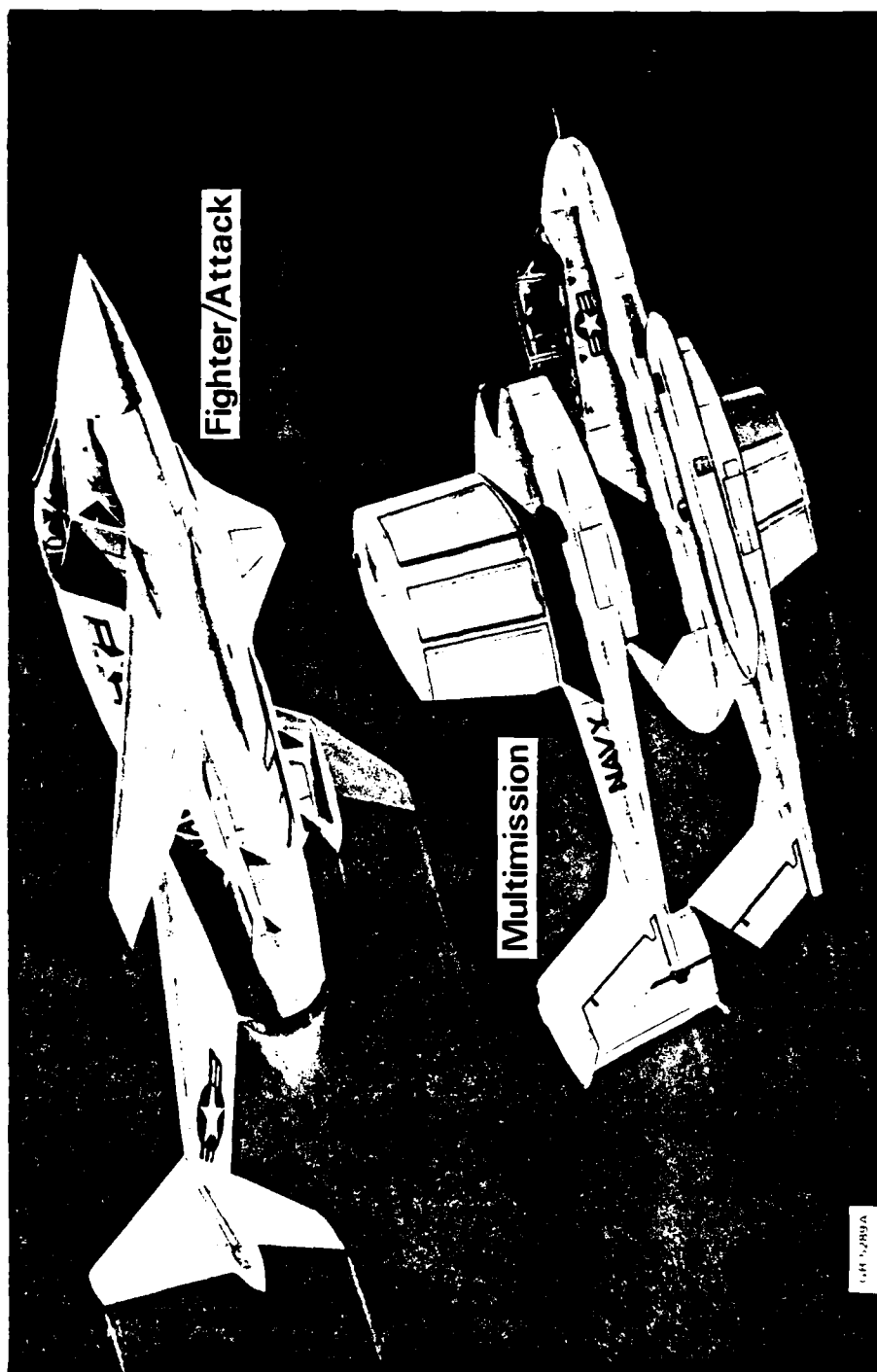
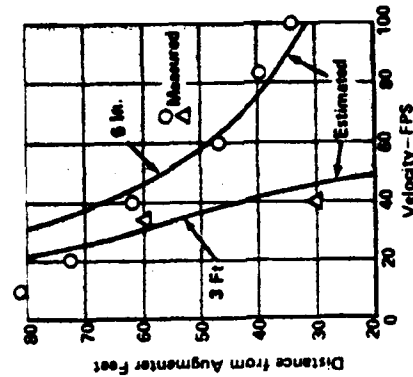
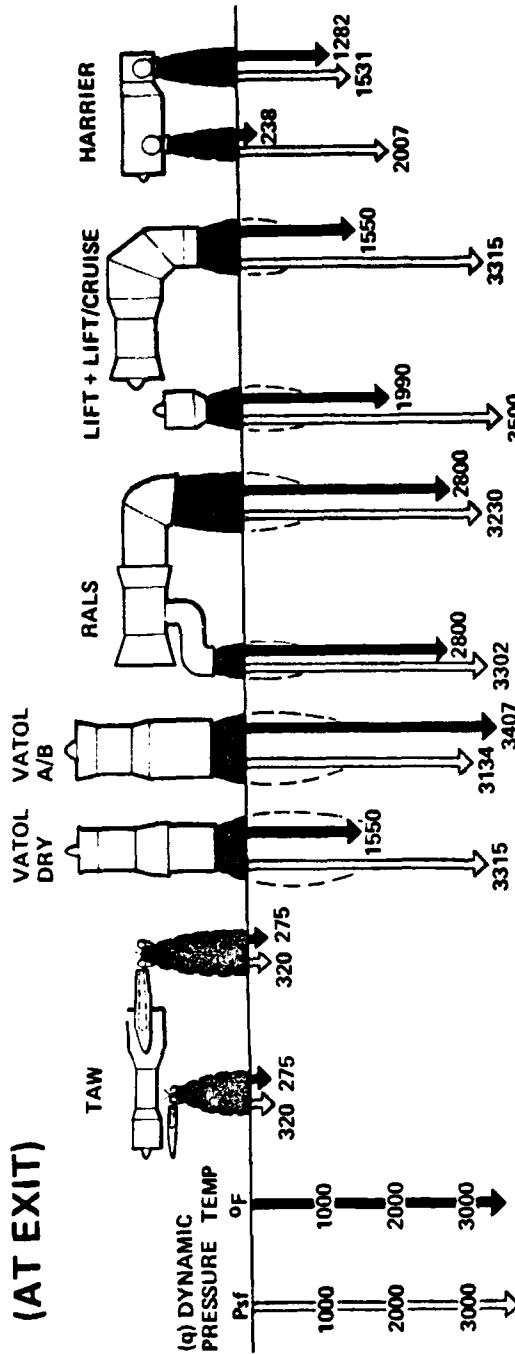


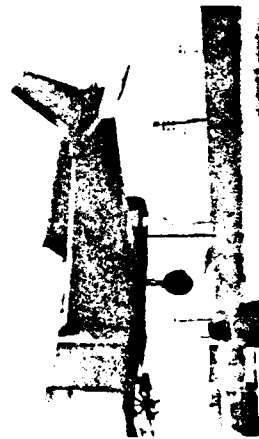
Figure 2-1 V/STOL Prototypes



# LIFT SYSTEM FOOTPRINT (AT EXIT)



Comparison of Measured  
Theoretical and  
Ground Velocities



CAD 1033/A

Figure 2-2 Lift System Footprint (At Exit)





## FIGHTER/ATTACK USEFUL LOAD COMPARISON

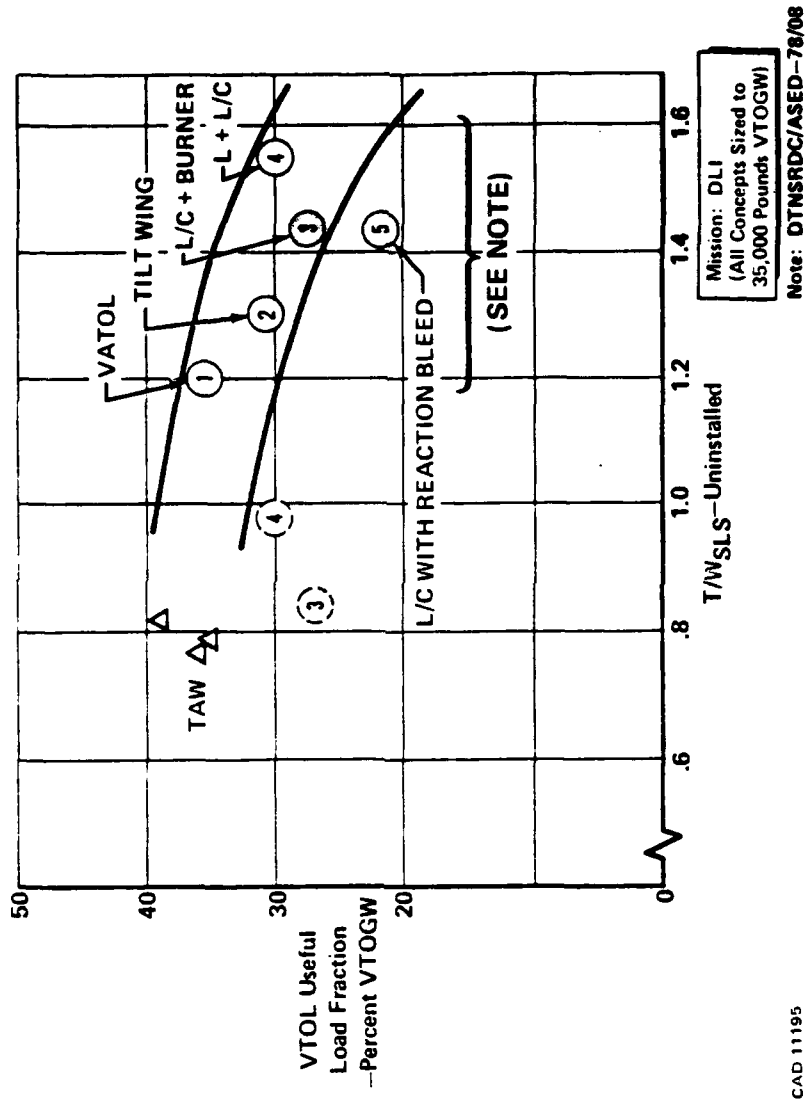


Figure 2-3 Fighter/Attack Useful Load Comparison



# LIFT CONTROL Conversion

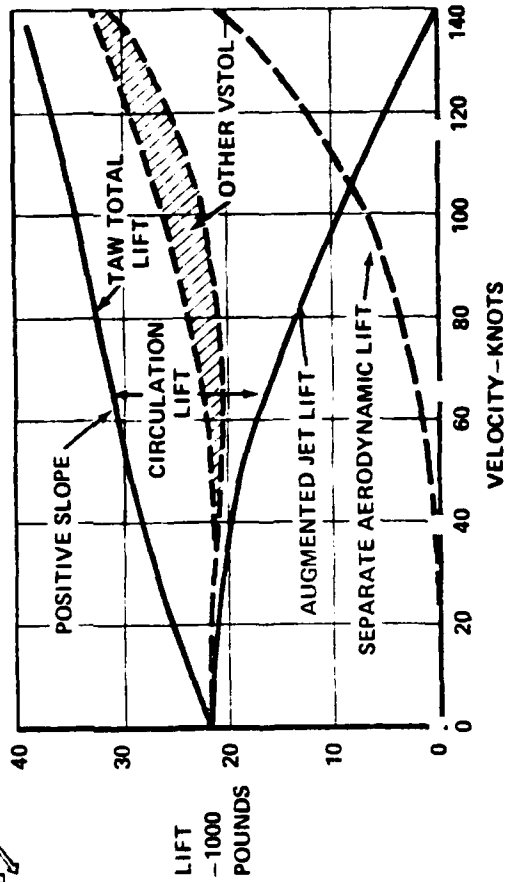
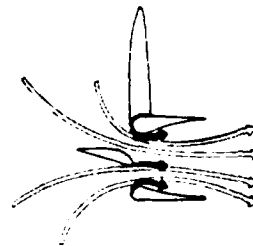
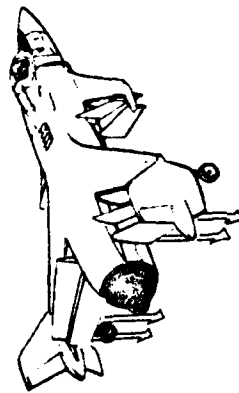
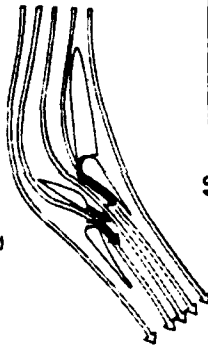
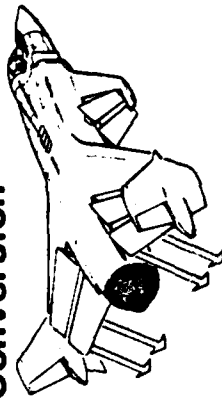
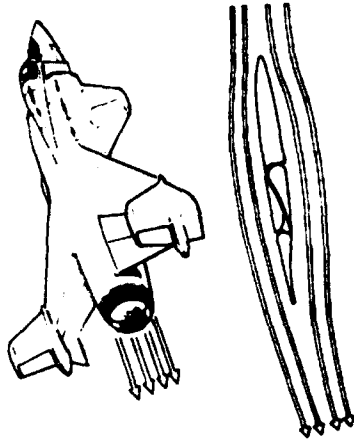


Figure 2-4 Lift Control Conversion

CAD 2282C



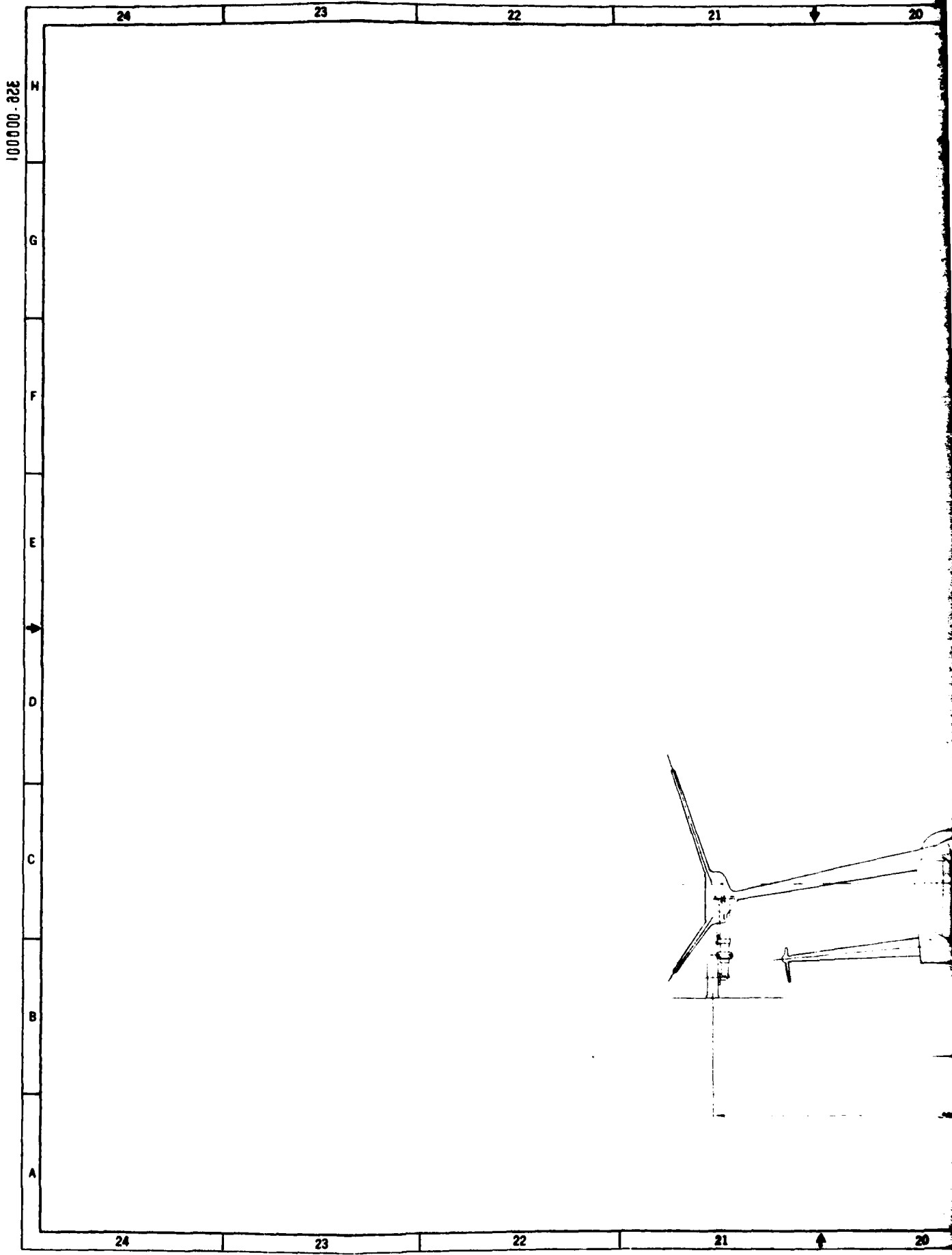
TAW concept because of its unique application of the aircraft (augmenter) flaps as a portion of the aircraft's propulsion/control system.

## 2.2 AIRCRAFT DESCRIPTION

The XFV-12A Technology Prototype airplane is a single-place, single-engine configuration that features the thrust augmented wing concept to achieve vertical lift. The XFV-12A external configuration and arrangement are shown in Figures 2-5 and 2-6. Aircraft dimensional data are presented in Table 2-1. The configuration employs a low-canard, high-wing arrangement with wing tip mounted vertical tails. The use of a canard reduces the wing area required for maneuverability since both surfaces are always lifting and makes feasible the use of wing tip mounted vertical tails. The wing tip vertical tails serve a triple function of providing significant increases in longitudinal stability and effective wing aspect ratio as well as providing the basic directional stability and control for the aircraft. The increases in longitudinal stability and effective wing aspect ratio allows reductions to be made in wing span further compacting the overall aircraft configuration. The multiple interactions of the canard and vertical tails with each other as well as with the wing also allow significant configuration aerodynamic refinement through minor modifications to the basic aircraft arrangement. The primary engine inlets are located on each side of the forward fuselage. An auxiliary air inlet located in the upper forward fuselage aft of the cockpit provides additional air during the V/STOL mode of operation (see Figure 2-7). Every effort was made to reduce aircraft development costs through the extensive use of assets from existing aircraft designs (see Figure 2-8).

Propulsion is provided by a Pratt & Whitney Aircraft YF401-PW-400 gas turbine engine. In the XFV-12A aircraft, this engine is equipped with a translating plug nozzle, shroud, and diverter door system (see Figure 2-9). This diverter unit replaces the conventional aircraft tailpipe and provides three basic modes of operation, an engine divert mode (vertical), a forward thrust mode (conventional) and a transition mode. The engine divert mode of operation directs the entire engine gas flow output through a series of diverter openings into the aircraft's ducting system where it is delivered to the augmenter system nozzles. The engine's forward thrust mode of operation directs the engine gas flow output aft through a translating shroud plug nozzle. In this mode, the engine operates conventionally as a fixed tailpipe area engine. The transition mode of operation schedules the engine gas flow through the diverter openings and plug nozzle as required to maintain essentially constant and uniform back pressure to the engine. This mode is utilized to provide a smooth conversion from the vertical mode to the conventional flight mode and return to the vertical model.

The aircraft augmenter ducting system is comprised of a series of thin gage, complex shaped ducts formed from high temperature titanium alloys



20

19

18

17

16

15

FWS AUXILIARY INLET DOOR

229.32  
18.61 FE.CAMRD DIFFUSER  
HINGE LINECENT  
HINGE

PILOT EYE

F.S. 111.42  
NP 20.5WING PLANE REFERENCE PLANE  
VERTICAL REFERENCE124.50 IN (10.37 FE.)  
OVERALL STATIC HEIGHTCOMP 16-28.07  
STATIC 16-27.07  
LATE 16-32F.S. 111.42 (COMP)  
F.S. 111.42 (STATIC)  
F.S. 111.42 (EXTENDED)

356-000001

A

19

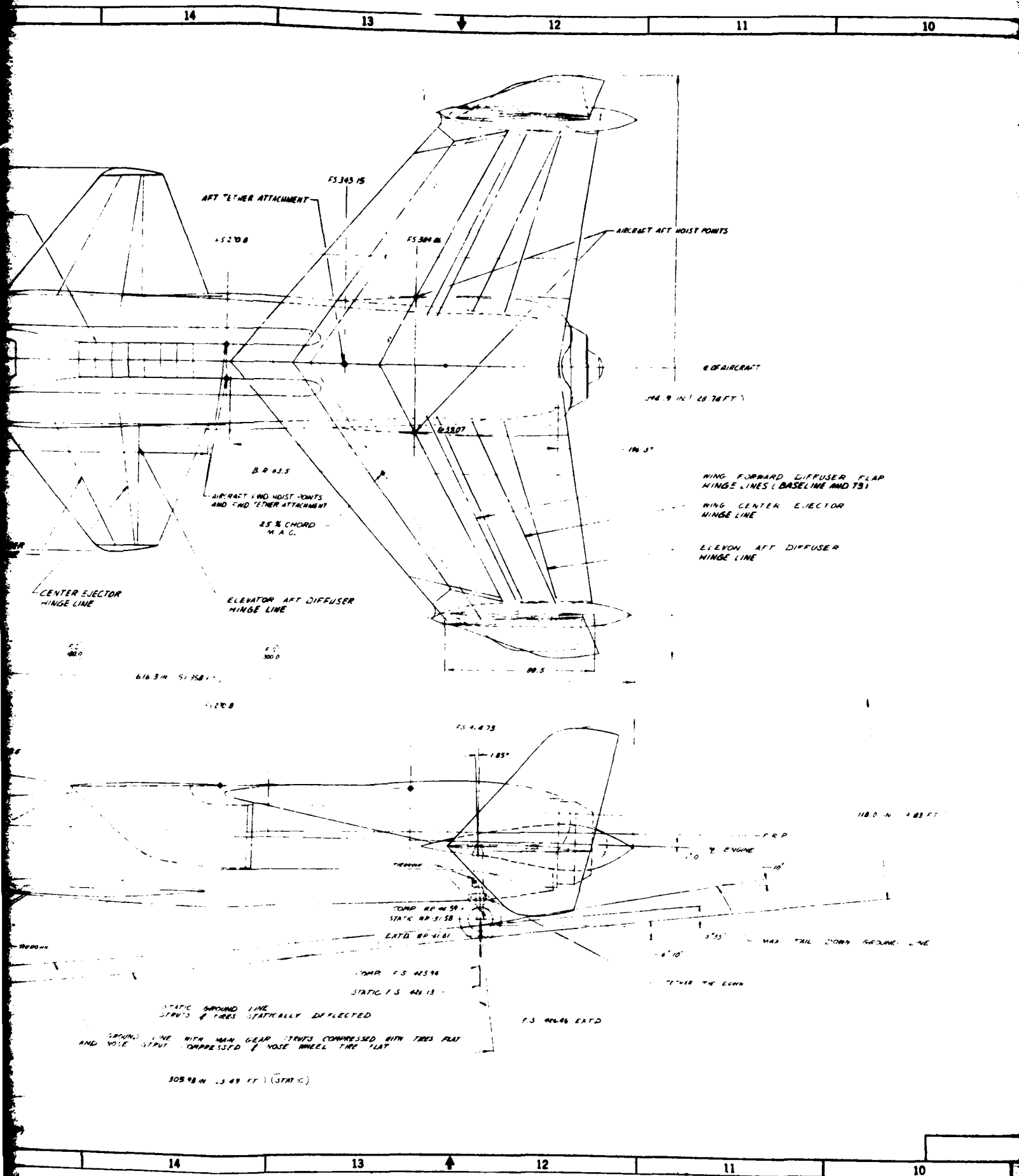
18

17

16

15

2



1-1  
 1-2  
 1-3

NOTE  
 TABULATED AIRCRAFT DIMENSIONAL DATA CAN BE FOUND  
 IN REPORT NR-72M-330-1 SECTION 3.0

356-000001

A

4

--2

NR81H-50

REVISIONS		
REV. NO.	DESCRIPTION	DATE APPROVED
1	1 MAY 58 REWORKED 2 LAMINAR BY REWORKED	
2	2 SECOND CHANGE 4 NEW SHIP PUNCTURE	
3	3 PARTS BUILT ON	
4	4 3 PER REDRAWN 8 NEW	1958 5-7
5	5 100% 100% 100%	
6	6 REDRAWN & REDESIGNED	J. ADAPTING 7-7-58

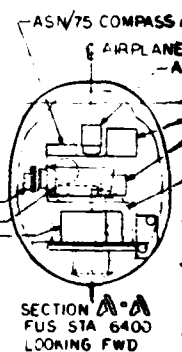
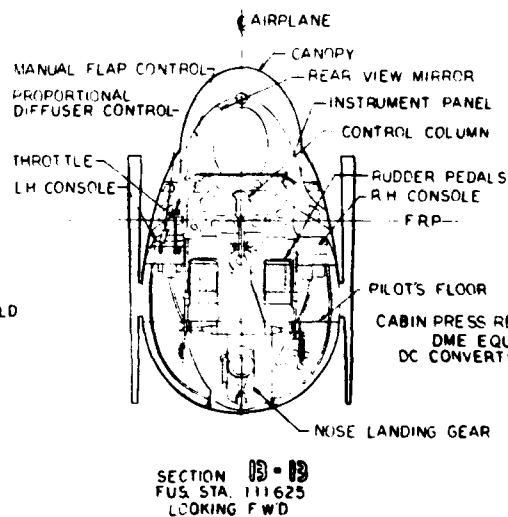
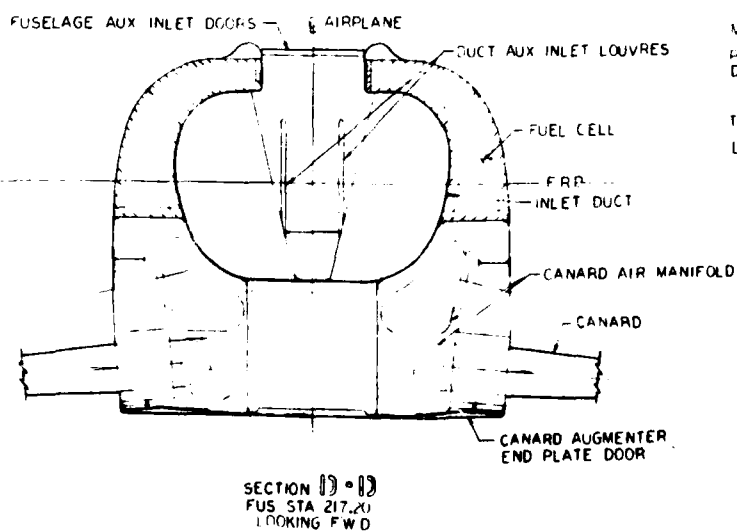
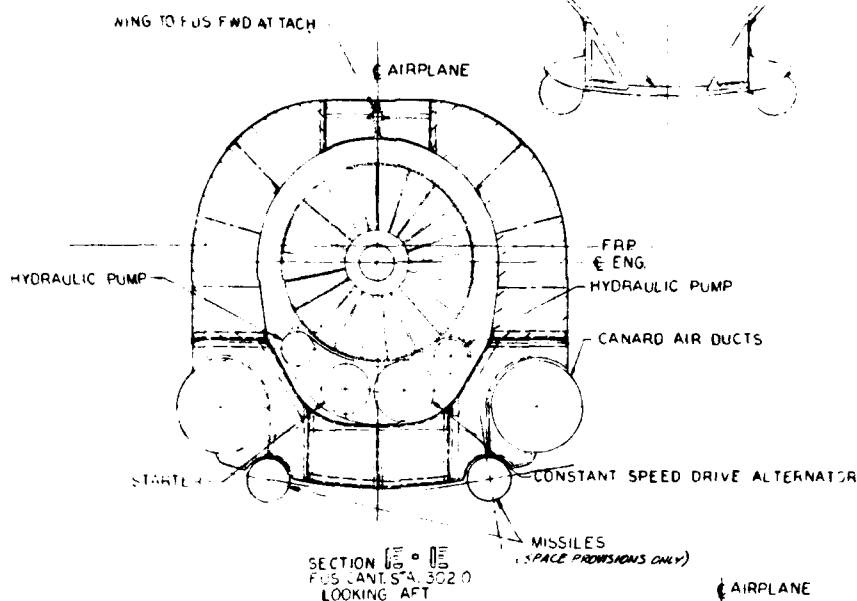
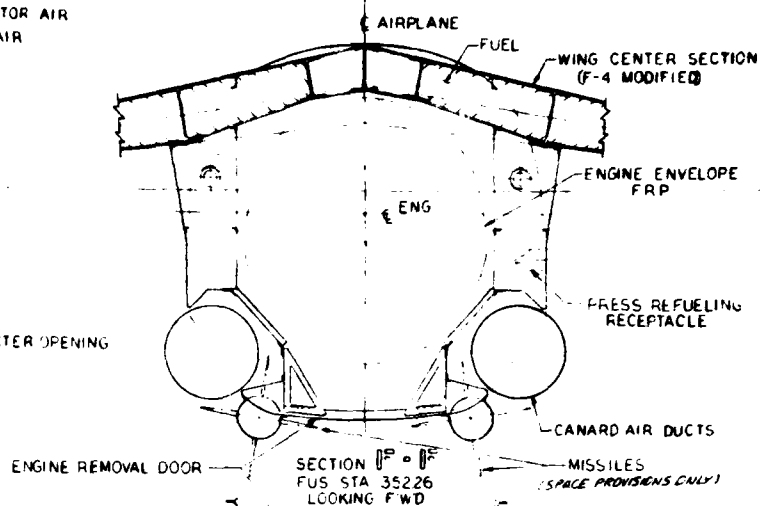
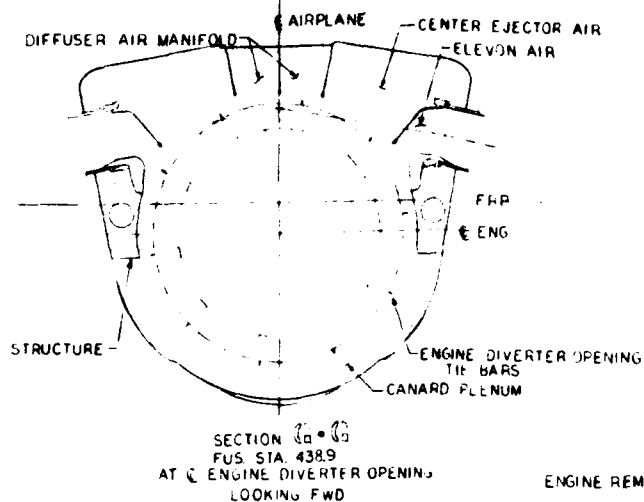
# XFV-12A AIRPLANE THREE VIEW FIGURE 2-5

037	
036	
035	
034	
033	
032	
031	
030	
029	
028	
027	
026	
025	
024	
023	
022	
021	
020	
019	
018	
017	
016	
015	
014	
013	
012	
011	
010	
009	
008	
007	
006	
005	
004	
003	
002	
001	

ITEM OR PART NO.	QUANTITY REQUIRED	CODE IDENT	PART OR IDENTIFYING NUMBER	NOMENCLATURE	MATERIAL	THICKNESS (INCHES)	FINISH	DRAWING OR SPECIFICATION NUMBER	7
									0
PARTS LIST									
UNLESS OTHERWISE SPECIFIED				CONTRACT NO. 356-000001					
DIMENSIONS ARE IN INCHES				COLUMBIAN DIVISION					
UNLESS OTHERWISE SPECIFIED				North American Rockwell					
XX ROUGHENED				GENERAL ARRANGEMENT					
XXX COARSE				THREE VIEW					
XXX FINISH				NR 356					
XXX NOTED				J. ADAPTING					
XXX NOTED				356-000001					
XXX NOTED				SCALE					
XXX NOTED				1					
XXX NOTED				1					
XXX NOTED				1					
XXX NOTED				1					
XXX NOTED				1					
XXX NOTED				1					
XXX NOTED				1					
XXX NOTED				1					
XXX NOTED				1					
XXX NOTED				1					
XXX NOTED				1					
XXX NOTED				1					
XXX NOTED				1					
XXX NOTED				1					
XXX NOTED				1					
XXX NOTED				1					
XXX NOTED				1					
XXX NOTED				1					
XXX NOTED				1					
XXX NOTED				1					
XXX NOTED				1					
XXX NOTED				1					
XXX NOTED				1					
XXX NOTED				1					
XXX NOTED				1					
XXX NOTED				1					
XXX NOTED				1					
XXX NOTED				1					
XXX NOTED				1					
XXX NOTED				1					
XXX NOTED				1					
XXX NOTED				1					
XXX NOTED				1					
XXX NOTED				1					
XXX NOTED				1					
XXX NOTED				1					
XXX NOTED				1					
XXX NOTED				1					
XXX NOTED				1					
XXX NOTED				1					
XXX NOTED				1					
XXX NOTED				1					
XXX NOTED				1					
XXX NOTED				1					
XXX NOTED				1					
XXX NOTED				1					
XXX NOTED				1					
XXX NOTED				1					
XXX NOTED				1					
XXX NOTED				1					
XXX NOTED				1					
XXX NOTED				1					
XXX NOTED				1					
XXX NOTED				1					
XXX NOTED				1					
XXX NOTED				1					
XXX NOTED				1					
XXX NOTED				1					
XXX NOTED				1					
XXX NOTED				1					
XXX NOTED				1					
XXX NOTED				1					
XXX NOTED				1					
XXX NOTED				1					
XXX NOTED				1					
XXX NOTED				1					
XXX NOTED				1					
XXX NOTED				1					
XXX NOTED				1					
XXX NOTED				1					
XXX NOTED				1					
XXX NOTED				1					
XXX NOTED				1					
XXX NOTED				1					
XXX NOTED				1					
XXX NOTED				1					
XXX NOTED				1					
XXX NOTED				1					
XXX NOTED				1					
XXX NOTED				1					
XXX NOTED				1					
XXX NOTED				1					
XXX NOTED				1					
XXX NOTED				1					
XXX NOTED				1					
XXX NOTED				1					
XXX NOTED				1					
XXX NOTED				1					
XXX NOTED				1					
XXX NOTED				1					
XXX NOTED				1					
XXX NOTED				1					
XXX NOTED				1					
XXX NOTED				1					
XXX NOTED				1					
XXX NOTED				1					
XXX NOTED				1					
XXX NOTED				1					
XXX NOTED				1					
XXX NOTED				1					
XXX NOTED				1					
XXX NOTED				1					
XXX NOTED				1					
XXX NOTED				1					
XXX NOTED				1					
XXX NOTED				1					
XXX NOTED				1					
XXX NOTED				1					
XXX NOTED				1					
XXX NOTED				1					
XXX NOTED				1					
XXX NOTED				1					
XXX NOTED				1					
XXX NOTED				1					
XXX NOTED				1					
XXX NOTED				1					
XXX NOTED				1					
XXX NOTED				1					
XXX NOTED				1					
XXX NOTED				1					
XXX NOTED				1					
XXX NOTED				1					
XXX NOTED				1					
XXX NOTED				1					
XXX NOTED				1					
XXX NOTED				1					
XXX NOTED				1					
XXX NOTED				1					
XXX NOTED				1					
XXX NOTED				1					
XXX NOTED				1					
XXX NOTED				1					
XXX NOTED				1					
XXX NOTED				1					
XXX NOTED				1					
XXX NOTED				1					
XXX NOTED				1					
XXX NOTED				1					
XXX NOTED				1					
XXX NOTED				1					
XXX NOTED				1					
XXX NOTED				1					
XXX NOTED				1					
XXX NOTED				1					
XXX NOTED				1					
XXX NOTED				1					
XXX NOTED				1					
XXX NOTED				1					
XXX NOTED				1					
XXX NOTED				1					
XXX NOTED				1					
XXX NOTED				1					
XXX NOTED				1					
XXX NOTED				1					
XXX NOTED				1					
XXX NOTED				1					
XXX NOTED				1					
XXX NOTED				1					
XXX NOTED				1					
XXX NOTED				1					
XXX NOTED				1					
XXX NOTED				1					
XXX NOTED				1					
XXX NOTED				1					
XXX NOTED				1					
XXX NOTED				1					
XXX NOTED				1					
XXX NOTED				1					
XXX NOTED				1					
XXX NOTED				1					
XXX NOTED				1					
XXX NOTED				1					
XXX NOTED				1					
XXX NOTED				1					
XXX NOTED				1					
XXX NOTED				1					
XXX NOTED				1					
XXX NOTED				1					
XXX NOTED				1					
XXX NOTED				1					
XXX NOTED				1					
XXX NOTED				1					
XXX NOTED				1					
XXX NOTED				1					
XXX NOTED				1					
XXX NOTED				1					
XXX NOTED				1					
XXX NOTED				1					
XXX NOTED				1					
XXX NOTED				1					
XXX NOTED				1					
XXX NOTED				1					
XXX NOTED				1					
XXX NOTED				1					
XXX NOTED				1					
XXX NOTED				1					
XXX NOTED				1					



328-000003



WING  
ORIGIN  
4000  
INCID  
DIBED  
S-100  
S-100  
AR-100  
C-1  
C-1

35.20

62.30

31.8  
AR-100  
339  
AIRFOIL

1700

5400

# WING SHOWN IN FUSELAGE REF SYSTEM

## WING DATA

ORIGIN-FUS STA 27354 WP+22061 & FUS STA 4000, WP+1875

INCIDENCE  $P^30$   
 DIHEDRAL  $-10^\circ$   
 $S_{PLAN}$  293789 FT<sup>2</sup>  
 $S_{ACT}$  298323 FT<sup>2</sup>  
 $AR_{PLAN}$  2.085  
 $C_R$  196.370 IN  
 $C_T$  88516 IN

FRP

H REAR SPAR  
ON WRP

H FRONT SPAR  
ON WRP

E CENTER EJECTOR AXIS

E DIFFUSER AXIS

E ELEVON AXIS

LIFT CTR

BP 648957 E=149248

BP 14552 ORIGIN LWR VERT  
 BP 14852 THEO WING TIP  
 BP 15187 ORIGIN UPPR VERT

$S_{UPPER}$  31.2 FT<sup>2</sup>  
 $AR_{UPPER}$  3.39

AIRFOIL NACA 64-004 (MOD)

RUDDER HINGE  
55 C

INCIDENCE  $3^\circ 30'$

19° CANT

WING REF PLANE

BP BP  
1455 1518

$S_{LWR}$  927 FT<sup>2</sup>  
 $AR_{LWR}$  2.771  
 AIRFOIL NACA 64-004

THEO WING SECT  
 BP 1518  
 POINT A  
 FS 419.65  
 WP 22.83  
 BP 153.75

OVERBOARD FUEL VENT  
 LH SIDE

ASN/75 COMPASS AMPL

AIRPLANE

ASN/75 DIR GYRO

FRP

AIR SPEED UNIT (LOW SPEED V/STOL)

RADAR SET ADAPTER

MB-5A LOX CONVERTER (5 LITER)

SECTION A-A  
 IS STA 6400  
 BOWING FWD

356-000003

H

2

14

13

12

11

10

FIRE DETECTION CONTROL  
FUEL FLOW POWER SUPPLYCONTROL SYSTEM  
(RATIO CHANGERS  
MASTER ACTUATORS &  
MIXER ASSEMBLY)

ASN/75 DIR GYRO

EXTERNAL POWER  
RECEPTACLE

AIR SPEED UNIT (LOW SPEED V/STOL)

AIRPLANE

MB-5A LOX CONVERTER

RADAR ALTIMETER APN-94

ASN/75 COMPASS AMPL

BRAKE RESERVOIR

A4C FWD FUS SECTION  
(TO FS 180.00)VOR ANTENNA  
ECS PRESS REG CONTROL  
PRESS RATIO TRANSMITTERF4 INLET  
(MODIFIED)

DIFFUSER AXIS

ELEVATOR  
CENTER EJECTOR

LIFT CTR

C-906

## CANARD DATA

ORIGIN=C-8 WP=3500, BP 3750 &amp; LE &amp; FS 13300

INCIDENCE = 0°

DIHEDRAL = -5°

S<sub>REF</sub> = 82.7 FT<sup>2</sup> ACT = 82.385 FT<sup>2</sup> PROJ

AR = 1.7654 ACT 1.7587 PROJ

B/2<sub>ACT</sub> = 72.50 INC<sub>L</sub> = 0.2800 INC<sub>D</sub> = 0.3626 INA<sub>LE</sub> TRUE = 35°46'

AIRFOIL = NACA 66-008375 (MOD)

DOUGLAS ESCAPAC I-AI  
ESCAPE SYSTEM  
(ZERO ZERO CAPABILITY)PILOTS EYE POSITION --  
FUS STA 111625, WP=20.50

BRAKE SYSTEM RESERVOIR

AIR TRAFFIC CONTROL ANTENNA

AIR TRAFFIC CONTROL ANTENNA

AIR TRAFFIC CONTROL ANTENNA

ASN/75 COMPASS AMPL

AIRSPEED UNIT (LOW

SPEED V/STOL)

FRP

ASN/75 COMPASS

XMITR

INSTRUMENTATION  
BOOMRADAR ALTIMETER ANTENNAS  
RADAR ALTIMETER APN-94  
CABIN PRESS REG  
DC CONVERTER

DME ANTENNA

THRU RH SIDE  
WHEEL WELL  
(CURRENT TRANSFORMERS 3)  
GENERATOR CONTROL UNIT  
LINE CONTACTOR  
AC/DC POWER DISTRIBUTION PANEL

EXTERNAL POWER RECEPTACLE

A4C NOSE LANDING GEAR

M1A1 20 MM GUN  
PAC 1000000000CONTROL SYSTEM  
(RATIO CHANGERS  
MASTER ACTUATORS &  
MIXER ASSEMBLY)

STATIC DEC

POINT B  
FS 467.01  
WP 23.27  
BP 152.98

14

13

12

11

10

3

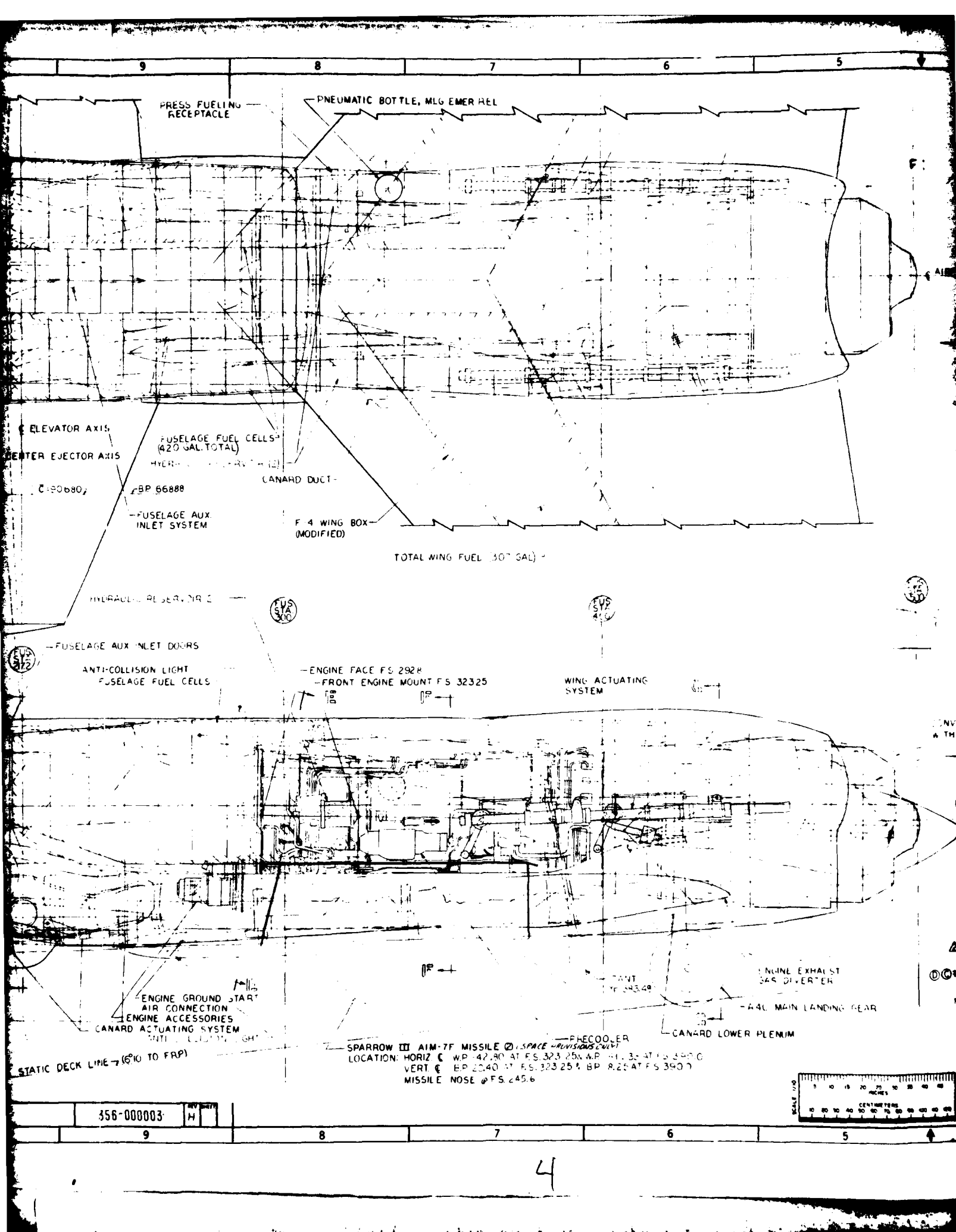






Table 2-1 Aircraft Dimensional Data

WING		CONSOLE (Both Sides)	
$S_{ref}$	Area (Reference)	$S_{ref}$	Area, Exposed, Projected
$S_{ref}^{exp}$	Area, Exposed	$b_c$	Span, Exposed, Projected
$b_w$	Span, Equivalent	$AR_c$	Aspect Ratio, Exposed
$b_{w,theo}$	Span, Theoretical	$\Lambda$	Taper Ratio, Exposed
$b_{w,exp}$	Span, Exposed	$\Gamma_c$	Dihedral Angle
$AR_w$	Aspect Ratio	$c_{ref}$	Root Chord
$AR_c^{exp}$	Aspect Ratio, Exposed	$c_{eq}$	Equivalent Tip Chord
$\Lambda_w$	Taper Ratio	$\tau_c$	Mean Aerodynamic Chord
$\Lambda_c^{exp}$	Taper Ratio, Exposed	$\Lambda_c$	Sweep Angle (Leading Edge)
$\Gamma_w$	Dihedral Angle	$\Lambda_c^{25}$	Sweep Angle (25° Chord)
$c_{ref}$	Root Chord	$i_c$	Incidence Angle
$c_{eq}^{exp}$	Equivalent Tip Chord	$\alpha_c$	Rate of Taper
$\tau_w$	Mean Aerodynamic Chord	$l_c/\sqrt{c_w}$	Chord Length
$\Lambda_w$	Sweep Angle (Leading Edge)	$\sqrt{c_w}/\sqrt{b_w}$	Chord Area/Wing Area
$\Lambda_w^{25}$	Sweep Angle (25° Chord)	ELEVATOR (One Side)	
$i_w$	Incidence Angle	$S_e$	Area, Actual
$\alpha_w$	Rate of Taper	$S_e^{proj}$	Area, Projected
$l_w/\sqrt{c_w}$	Wing Length	$b_e$	Span, Actual
$\theta_w$	Aerodynamic Twist	$b_e^{proj}$	Span, Projected
		$c_{ef}$	Root Chord
		$c_{ef}^{proj}$	Equivalent Tip Chord
		$\tau_e$	Mean Aerodynamic Chord
		$\Lambda_e$	Elevator Area/Chord Area (Projected)
		$\Gamma_e$	Elevator Chord/Chord Area
		$\Lambda_e^{act}$	Area Moment, Actual
		$\alpha_e$	Rate of Taper, Actual
		$\alpha_e^{proj}$	Rate of Taper, Projected

ELEVATOR	
$S_e$	Area, Actual
$S_e^{proj}$	Area, Projected
$b_e$	Span, Actual
$b_e^{proj}$	Span, Projected
$c_{ef}$	Root Chord
$c_{ef}^{proj}$	Tip Chord
$\tau_e$	Mean Aerodynamic Chord
$c_{ef}/l_w$	Chord of Elevator/Chord of Wing
$S_e \cdot \tau_e$	Area Moment, Actual
$\alpha_e$	Rate of Taper, Actual
$\alpha_e^{proj}$	Rate of Taper, Projected



Table 2-1 Aircraft Dimensional Data (Continued)

RUDDER (One Side)		VERTICAL TAIL (One Side)	
$S_r$	Area, Actual	$S_{vu}$	Area, Projected (upper)
$S_{r \text{ proj}}$	Area, Projected	$S_{vl}$	Area, Projected (lower)
$b_r$	Span, Actual	$S_v$	Area (tot l)
$b_{r \text{ proj}}$	Span, Projected	$b_{vu}$	Span, Projected (upper)
$c_{r \text{ tot}}$	Root Chord	$b_{vl}$	Span, Projected (lower)
$c_{r \text{ tip}}$	Tip Chord	$b_v$	Span, Projected (tot l)
$c_{r \text{ mean}}$	Mean Aerodynamic Chord	$AR_v$	Aspect Ratio, Projected
$c_{r \text{ rudder}}$	Rudder Area/Total Vertical Area (one side)	$AR_{vu}$	Taper Ratio (upper)
$c_{r \text{ rudder}}$	Rudder Chord/Vertical Chord	$AR_{vl}$	Taper Ratio (lower)
$c_{r \text{ mean}}$	Area Moment, Actual	$C_{ru}$	Root Chord (upper and lower)
$Q_r$	Rate of Taper, Actual	$C_{ru}$	Equivalent Tip Chord (upper)
$Q_{r \text{ proj}}$	Rate of Taper, Projected	$C_{ru}$	Equivalent Tip Chord (lower)
		$C_{ru}$	Mean Aerodynamic Chord (upper)
		$C_{ru}$	Mean Aerodynamic Chord (lower)
		$C_{ru}$	Leading Edge Sweep Angle (upper)
		$C_{ru}$	Leading Edge Sweep Angle (lower)
		$C_{ru}$	Area Moment (upper)
		$C_{ru}$	Area Moment (lower)
		$C_{ru}$	Vertical Area/Wing Area (verticals)
		$C_{ru}$	Vertical length (upper)
		$C_{ru}$	Vertical length (lower)
		$C_{ru}$	Rate of Taper (upper)
		$C_{ru}$	Rate of Taper (lower)
		$C_{ru}$	Cant Angle (upper)
		$C_{ru}$	Cant Angle (lower)
		$C_{ru}$	Incidence Angle (upper)
		$C_{ru}$	Incidence Angle (lower)

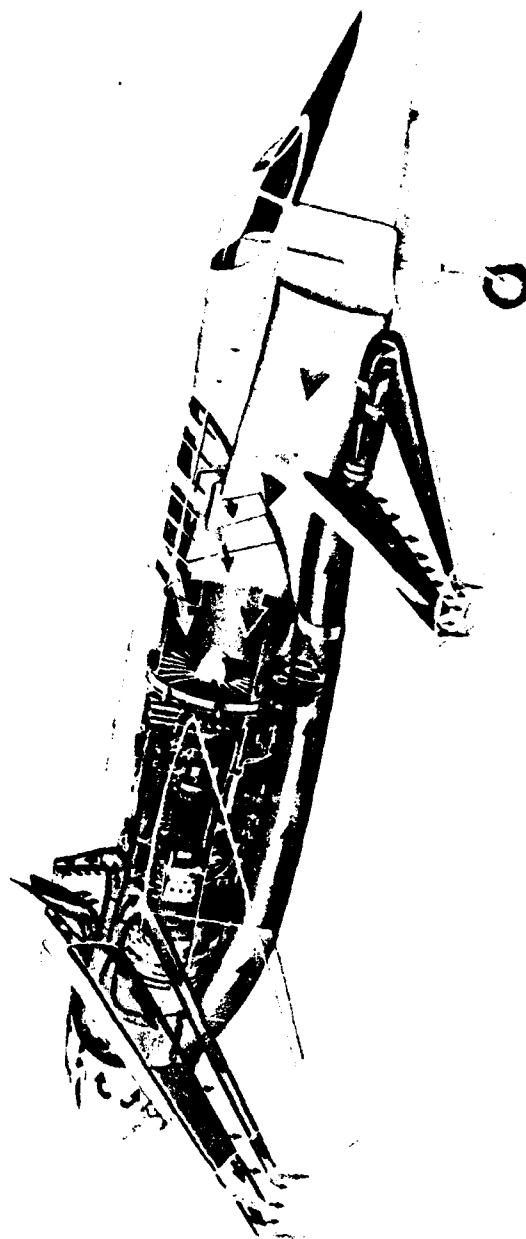
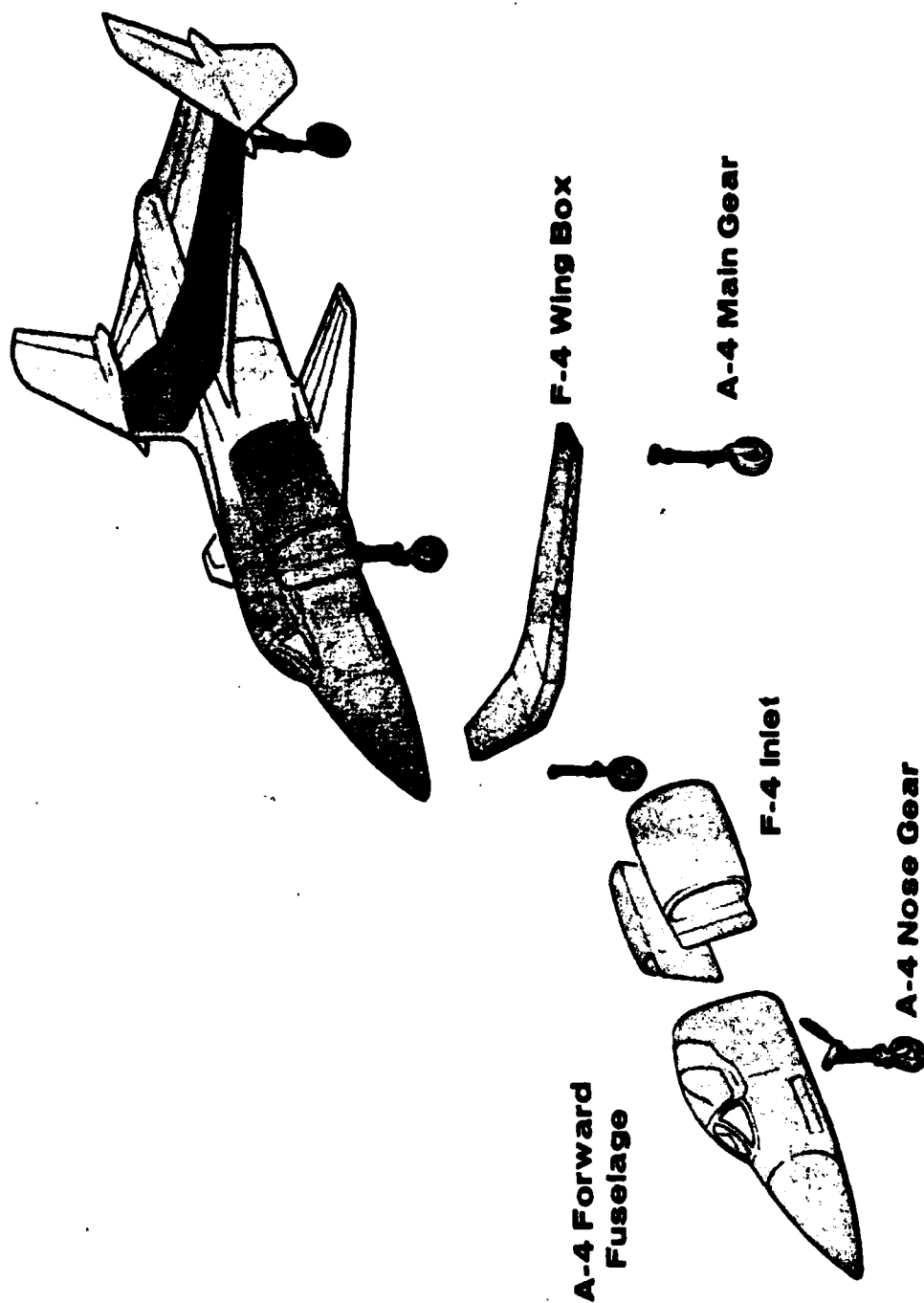


Figure 2-7 Engine Air Induction and Distribution System





# Prototype Structure

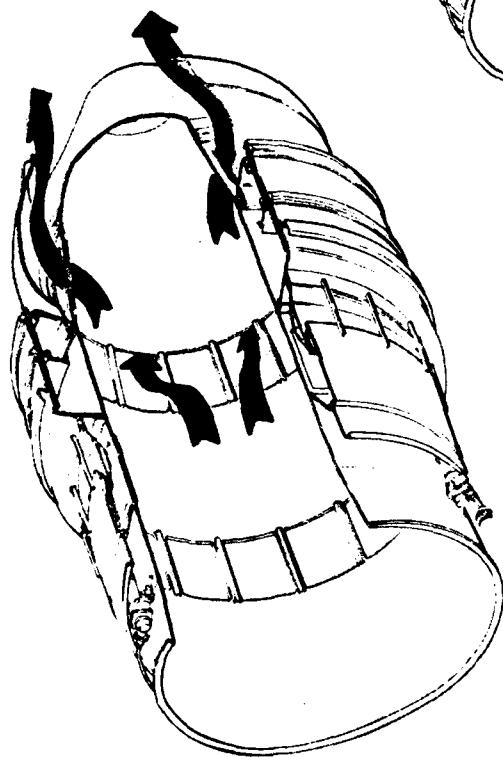


GR 4172D

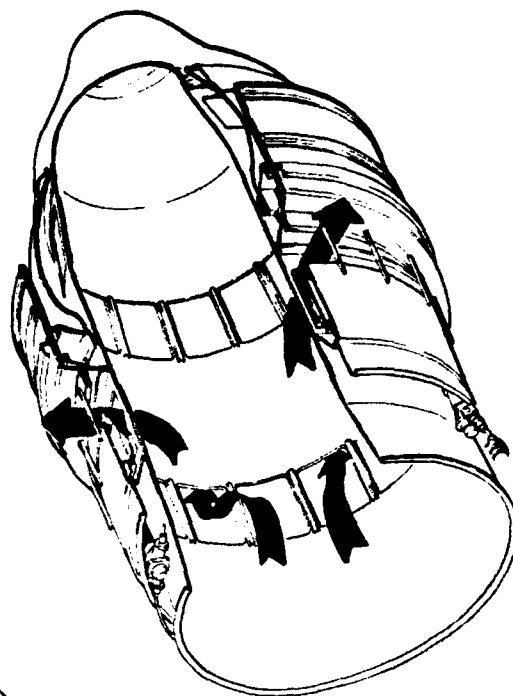
Figure 2-8 Prototype Structure



## DIVERTER VALVE DESIGN



Horizontal Mode



Vertical Mode

Figure 2-9 Diverter Valve Design

GR 1005.3



with a minimum number of joints to reduce system weight. Conventional hot forming techniques could not be employed to produce the complex shapes of the ducting system without placing significant constraints on configuration design options. Therefore, a superplastic forming process utilizing a hot form chamber and low cost ceramic dies was developed. This technique utilizes a unique temperature control process and radiation shielding during the forming cycle permitting close tolerance fabrication of complex shapes not possible with other fabrication methods.

The thrust required for the vertical operation is provided by the thrust augmenting ejectors located in the aircraft's wing and canard surfaces. Each ejector consists of a shroud formed by a pair of Coanda nozzle flap components and a central plenum nozzle assembly as shown in Figure 2-10. Entrainment by the primary exhaust jets is used to pump a large quantity of air through the ejector shroud. By Newton's Law of Action and Reaction, the ejector experiences a force which is equal but opposite to the momentum change of the entrained air. A more complete description of this process is given in Reference (1).

The lift generated by each augments can be simply modulated without changing engine RPM by varying the exit area of the augments as depicted in Figure 2-10. Height control is achieved by collectively controlling the lift from all four augments. Pitch control is achieved by differential lift generated by the canard and wing augments, and roll control is achieved by differential lift generated by the wing augments. Yaw control is achieved by differential control of left and right wing augments mean angle.

Conversion to conventional flight as depicted in Figure 2-11 is accomplished by gradual rotation of the augments flaps toward the closed positions. The horizontal component of the rotated thrust vector provides the force for the initial forward acceleration. During transition from the vertical to the conventional flight mode, additional aircraft lift is contributed by the very strong jet flap "supercirculation lift" effect inherent to the TAW concept. During this transition mode, engine airflow is rescheduled from the augments as a function of augments flap position. When the augments are fully closed, the primary engine flow is completely redirected through the cruise nozzle tailpipe.

In conventional flight, the augments flaps are retracted to form a standard airfoil section and the aft augments flap on both the wing and canard operates as an aerodynamic control device. Aft flaps on both the wing and canard are used for pitch control and wing flaps are used differentially for roll control. The fore and aft wing augments flaps are used together as speed brakes, as depicted in Figure 2-10. Yaw control in conventional flight is provided by left and right rudders.

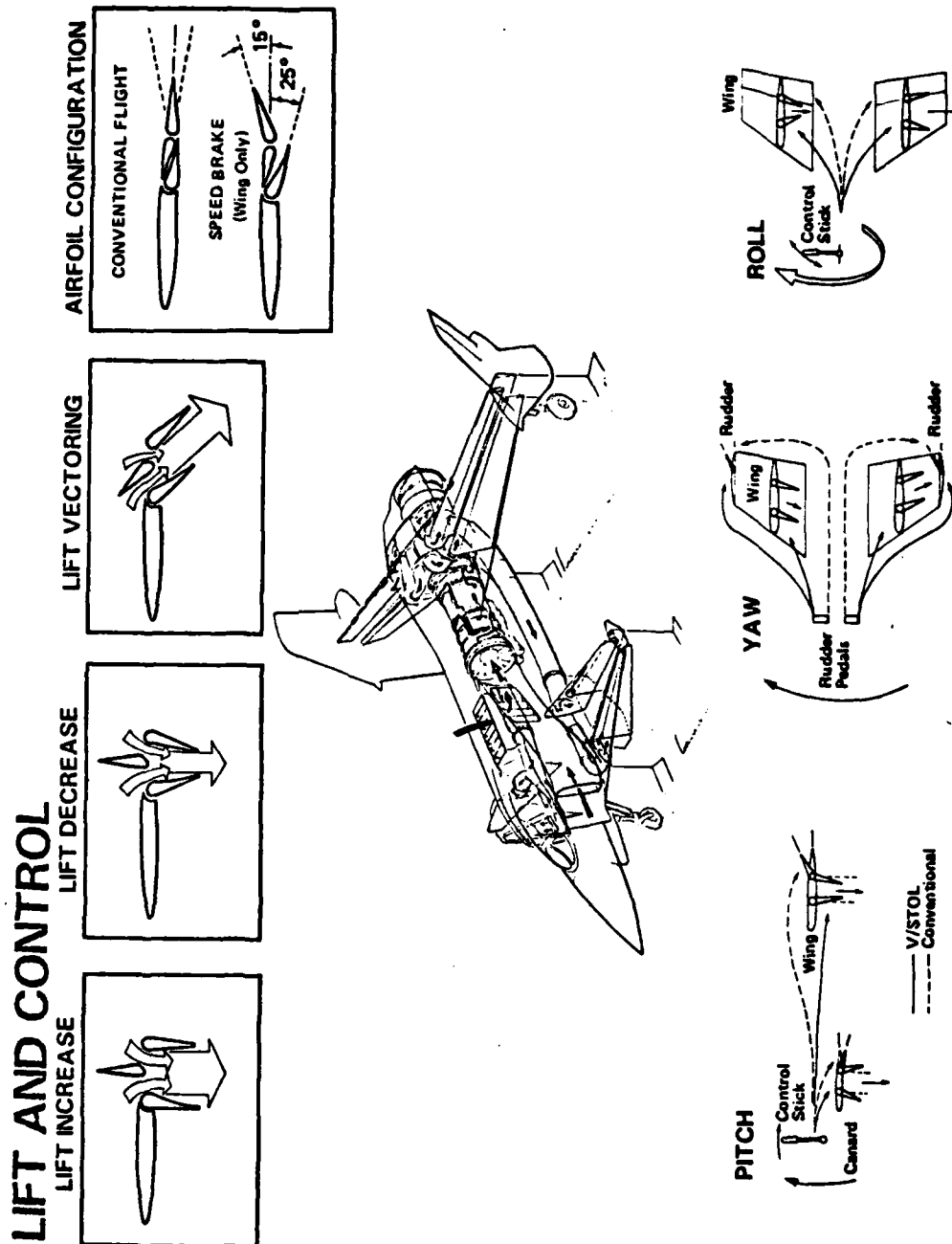


Figure 2-10 Lift and Control

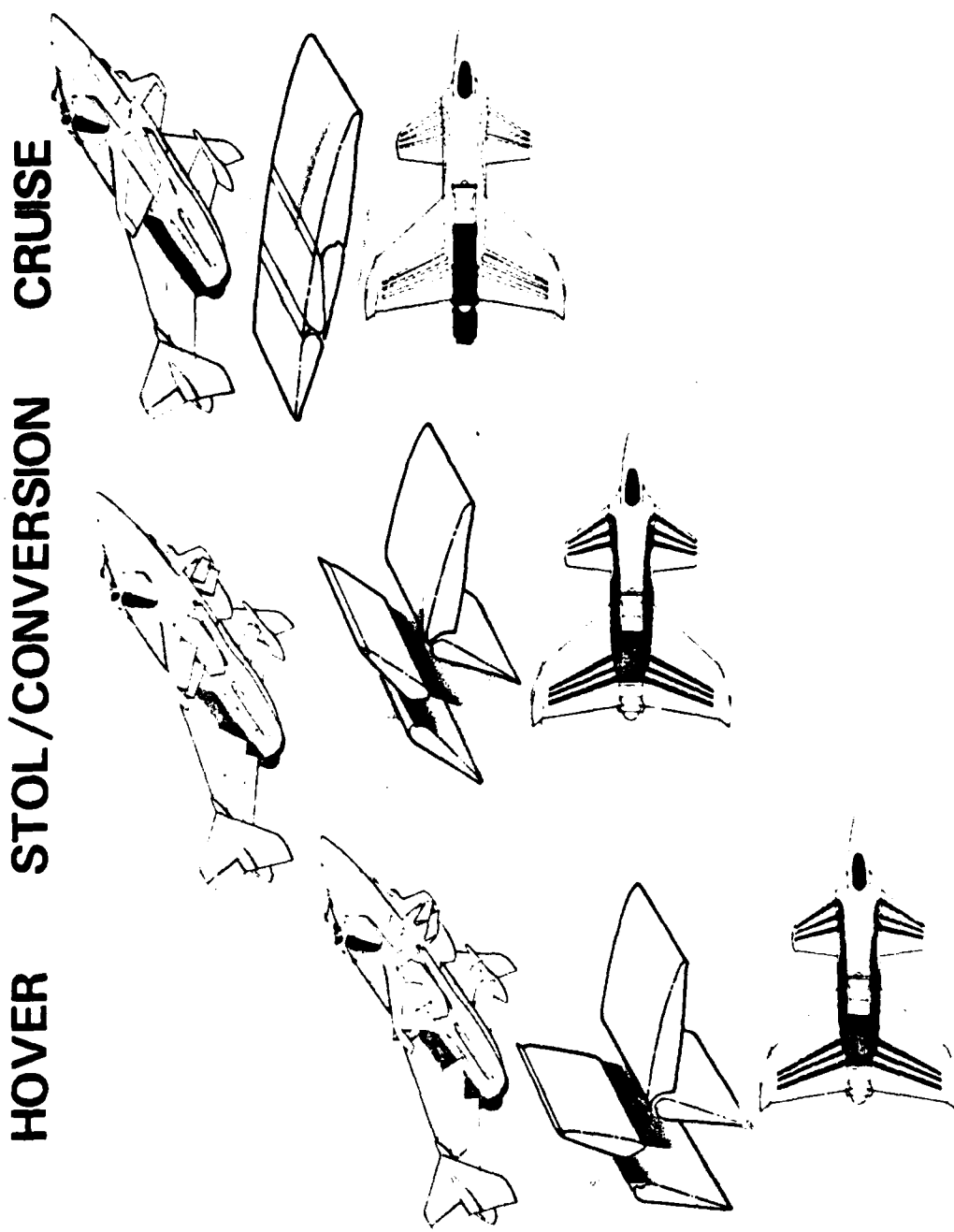


Figure 2-11 Conversion to Conventional Flight

GR 143308



## 2.3 XFV-12A AIRCRAFT DEVELOPMENT

The XFV-12A Technology Demonstrator Aircraft Program utilized both scale models and full scale hardware testing to develop the aircraft and associated systems configurations. Due to the unusual conceptual nature of this aircraft, five key areas of technical uncertainties were identified:

1. Flying qualities of the low canard, high wing configuration
2. Stability and control characteristics during the vertical and transition modes of operation
3. Compatibility of the exhaust diverter system with the P&W YF401 gas turbine engine
4. Efficient ducting of engine efflux to the thrust augmenter systems located in the wing and canard surfaces
5. Development of sufficient augmentation ratio by the thrust augmenter systems for effective VTOL operation

The issues of low canard/high wing flying qualities and stability and control characteristics were satisfied in the aircraft development phase and are fully reported in References (2) to (4). While the remaining technical issues were investigated during the development phase through the use of scale model testing, they could not completely be satisfied until the full scale aircraft could be tested, as discussed in the following sections.

### 2.3.1 Static and Dynamic Tethered Hover Tests

In 1977, the initial development and fabrication of the XFV-12A Technology Demonstrator Aircraft was completed. A series of functional and structural ground tests were performed at Rockwell's Columbus plant to validate the aircraft systems' operation and integrity. Following the ground testing, the aircraft was shipped to NASA Langley for the static and dynamic tethered hover test program. This program is documented in detail in Reference (5).

#### 2.3.1.1 Facility

The tethered hover testing utilized the Impact Dynamics Research Facility located at the NASA Langley Research Center in Hampton, Virginia. The Impact Dynamics Facility's 250 foot high "A" frame gantry provided structural support for the aircraft tether system (see Figure 2-12). The tether system was made up of a one-inch diameter cable, shock absorber, position sensor and a 50,000-pound capacity load cell. This assembly was suspended from a high line which was located on a platform on the gantry bridge. Figure 2-13 shows a schematic of the aircraft tether system. For static testing, the tether system was utilized in combination with a seven cable restraint load cell system, shown in Figure 2-14, to resolve

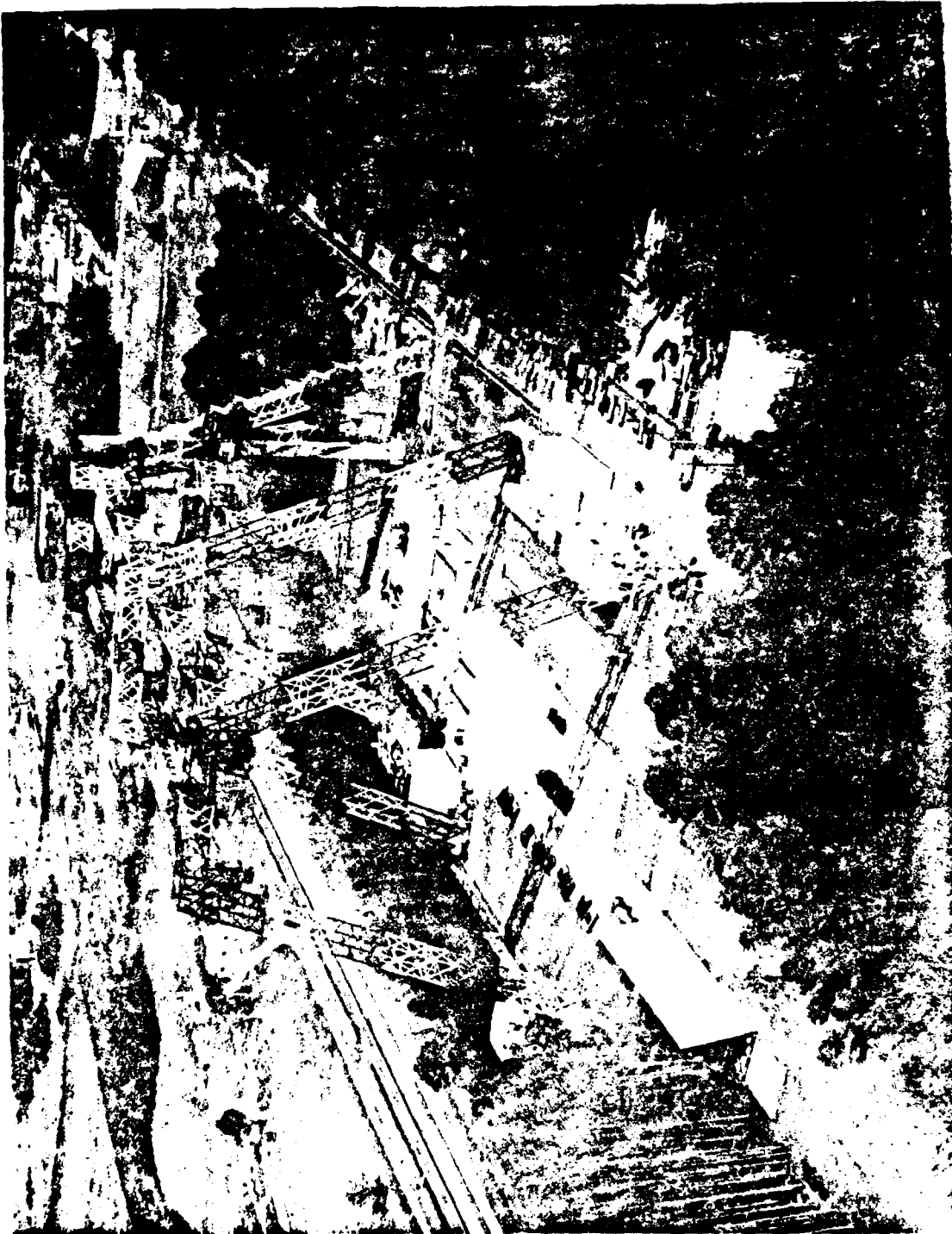


Figure 2-12 Test Site - Impact Dynamics Research Facility at Langley

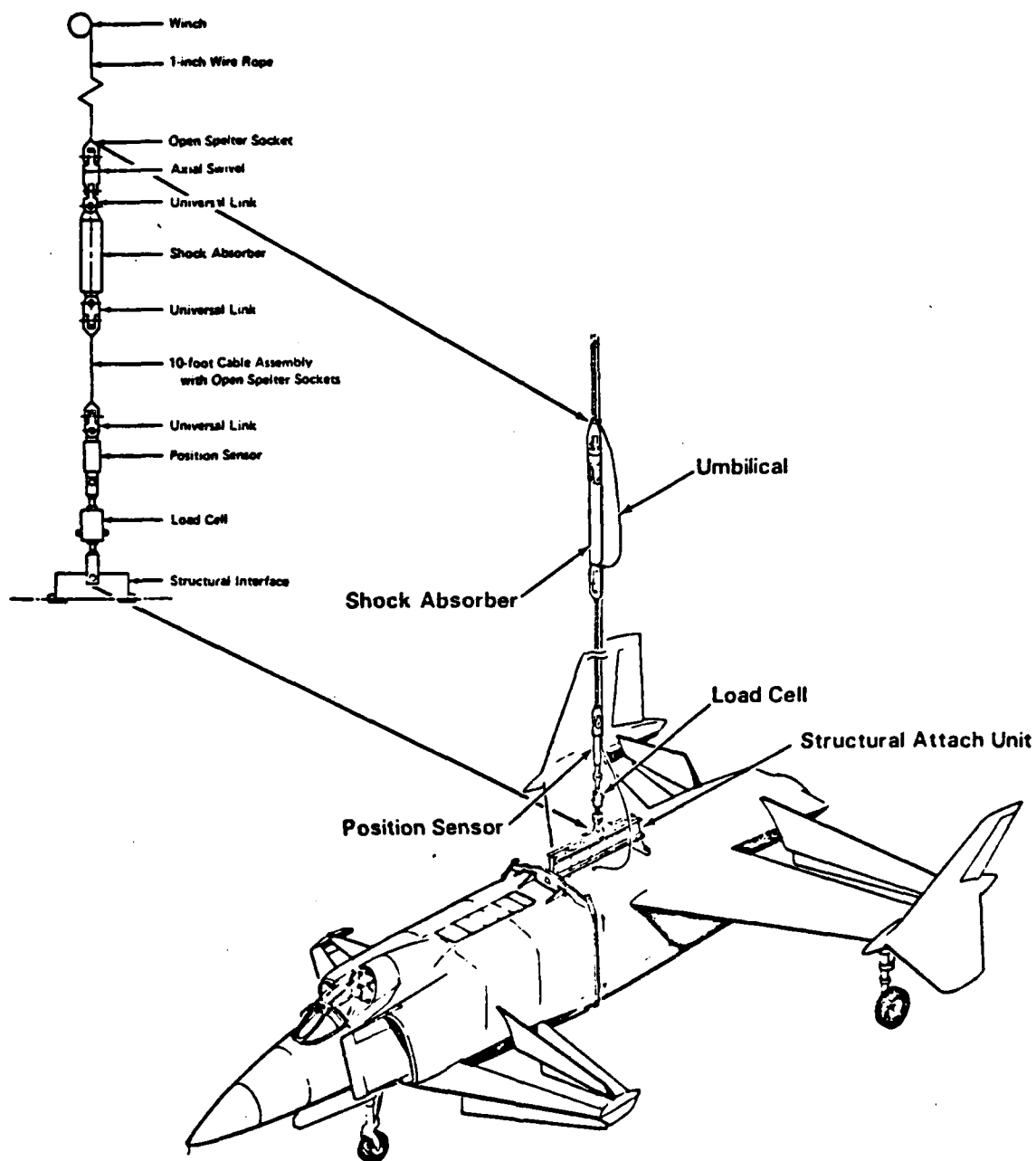


Figure 2-13 Z-System



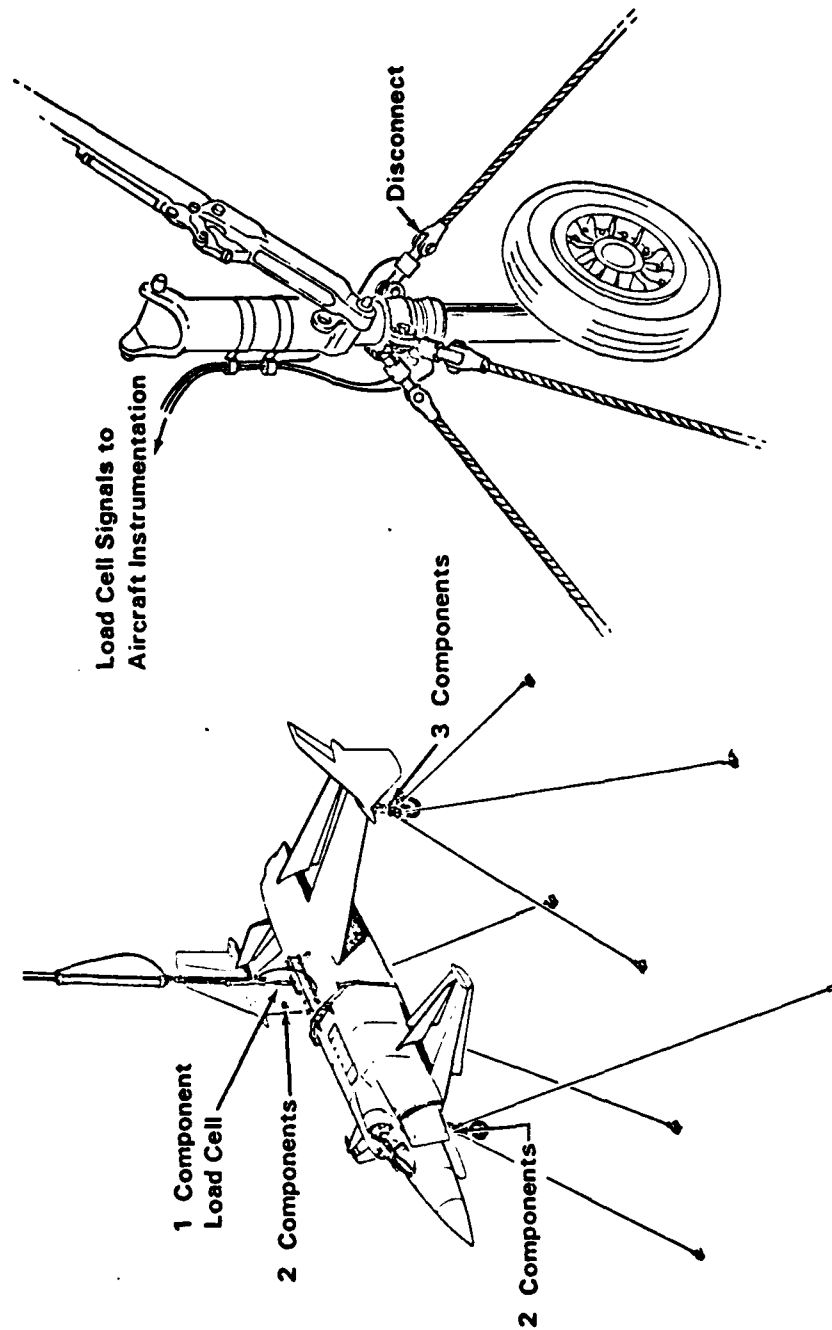


Figure 2-14 Static Load System



aircraft forces and moments. During dynamic testing, the aircraft was suspended on the gantry by the tether system. Prior to testing, the engine was started and the aircraft was positioned at a selected ground height by the high line winch assembly.

#### 2.3.1.2 Test Program

The objectives of the tethered hover test program were to confirm the lift control and moment characteristics of the XfV-12A aircraft. The test program was broken into two distinct phases beginning with the static testing in order to isolate the force and moment characteristics followed by the dynamic test phase to demonstrate the aircraft's hover and control characteristics. Unfortunately, early in the static test program, it became apparent that the total measured lift of the aircraft was lower than was anticipated. Based on this information, the original test plan was modified to include several additional objectives.

- Complete as much of the originally scheduled test as possible based on the limitations placed on the aircraft by insufficient lift for hover operations.
- Utilizing available diagnostic instrumentation, identify and investigate causes for the reduced level of augmentor performance.
- Based on the available diagnostic information, improve the performance of the thrust augmentor systems.

In order to accomplish these objectives, the test period was extended from the originally planned twelve weeks to a program of twenty-six weeks. During this period, a total of 83 static and dynamic test runs were completed. A complete listing of the test operations during the tethered hover test program can be found in Reference (5).

#### 2.3.1.3 Results of the Tethered Hover Testing

The data obtained during the tethered hover testing provided a great deal of information concerning aircraft systems performance and integrity as well as satisfying a number of the original technical uncertainties. The following list summarizes the pertinent conclusions resulting from the tethered hover test program.

##### . Propulsion System

The Pratt & Whitney YF401-PW-400 turbofan engine operated for a total of 28.77 hours (5.36 hours at intermediate power) during which no test time was lost due to engine related problems.

No problems were identified with the exhaust diverter system either during engine trim or test operation.

Inlet recovery data obtained during test operations indicated that the trifurcated inlet system achieved a 97.5 percent pressure recovery with relatively low pressure profile distortion.



The exhaust diverter/flow ducting system pressure drops and leakage rates compared well with pre-test estimates. Total thrust loss was measured at 12.9 percent with 9.9 percent of this due to total pressure loss and three percent associated with system leakage losses.

In summary, the XfV-12A technology demonstrator propulsion system from the trifurcated inlets to the ducting augmentor interface locations was very efficient. Collectively, these findings address and satisfy the technical uncertainties associated with the compatibility of the YF401 turbofan with the exhaust diverter system and the efficiency of the exhaust diverter flow ducting system.

. Aircraft Hover Control

Test data obtained during the static test phase indicated that control sensitivity and force gradients compared well with both pre-test piloted simulations and the NAVAIR simultaneous power requirements. Based on these correlations, the aircraft handling qualities were considered satisfactory for dynamic hover testing.

Pilot workload during dynamic hover testing in and out of ground effect was considered quite acceptable by the test pilots.

In general, the control system proved to be highly responsive, thereby, partially addressing the technical uncertainties concerned with the stability and control characteristics in the hover mode.

. Aircraft Footprint

Augmentor exhaust temperatures were on the order of 250°F.

Augmentor exhaust velocities along the ground 50 ft. from the aircraft were approximately 60 to 100 ft./sec.

These findings as well as the qualitative impressions of test personnel around the aircraft during hover operations indicate that the aircraft does possess a benign pressure-temperature footprint, compatible with shipboard or confined area operations.

. Ground Effects

Variation of lift in ground effect correlated well with previous scale model data indicating positive ground effect characteristics at all heights measured.



- Reingestion

Several techniques were investigated which minimized the reingestion of thrust augments efflux. These techniques provide a means of controlling exhaust reingestion and indicate that no significant performance penalty will be realized due to efflux reingestion under operational conditions.

- Aircraft Structures

During the entire aircraft tethered test program, only minor structural problems were noted. None of the problems compromised the basic structural integrity of the affected parts nor was there any damage to primary aircraft structure.

- Thrust Augmenter Systems

Static lift (load cell) measurements obtained during the first phase of the tethered hover tests indicated that the performance of the thrust augmenter systems was significantly below the anticipated goal levels. As shown in Figure 2-15, the wing performance goal was  $\phi = 1.50$ , however, a  $\phi = 1.26$  was achieved. The canard performance goal was  $\phi = 1.30$  while a  $\phi = 1.11$  was obtained.

Based on these results, a thorough investigation of the thrust augmenters appeared to be the next logical step in an effort to identify the cause for the inadequate thrust augmenters performance.

### 2.3.2 Diagnostic Testing

The primary objective of the diagnostic test program was to identify the causes of the inadequate levels of thrust augmenters performance during the tethered hover test program. The decision was made to proceed first with an investigation of the left hand wing augmenters system. The diagnostic tests of this system included the following investigations:

Testing of the left hand wing augmenters on the whirl rig test facility. These tests utilized aircraft augmenters and ducting hardware, in combination with simulated diverter, fuselage and wing leading edge components.

Cold flow isolated component testing in the Thermodynamics Laboratory of

- Forward diffuser (forward Coanda diffuser flap component)
- Elevon (aft Coanda diffuser flap component)
- Seven degree hypermixing centerbody segment model
- Inboard and outboard endwall blowing nozzle assemblies

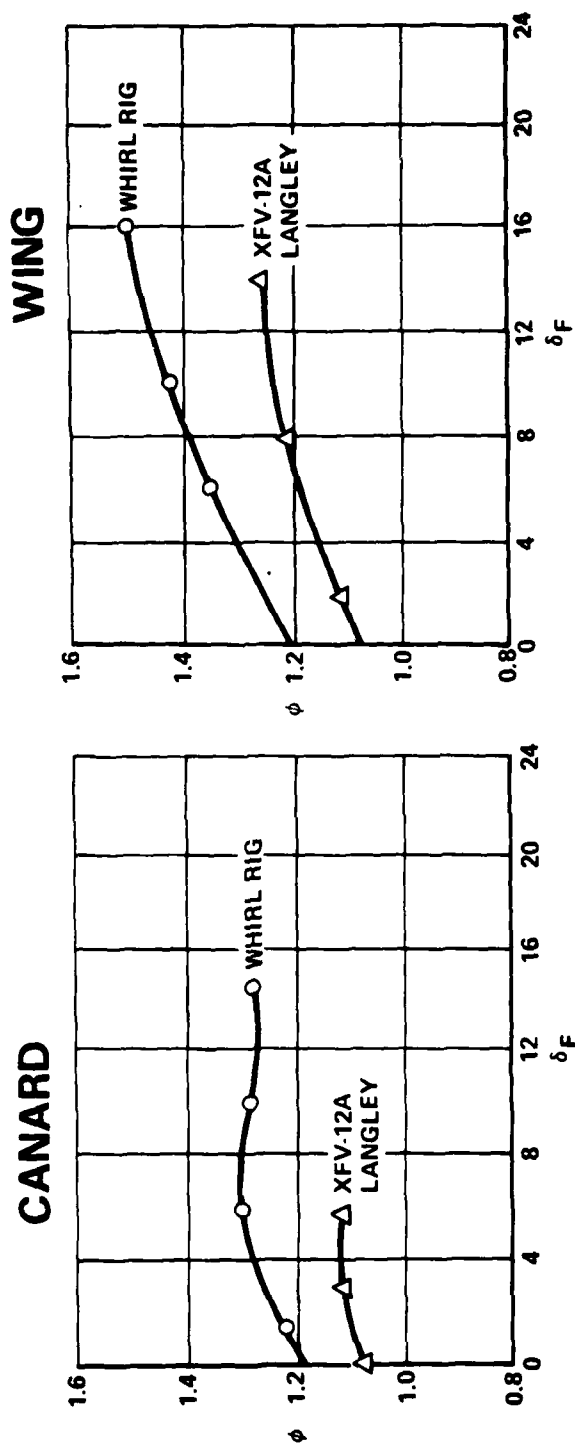


Figure 2-15 Augmenter Performance

Hot flow component testing on the whirl rig facility of the

- Forward diffuser flap (forward diffuser)
- Aft diffuser (elevon)
- Centerbody (Seven degree hypermixing nozzle and plenum assembly)

### 2.3 2.1 Diagnostic Test Results

A complete discussion of the diagnostics tests can be found in Reference (6) Pertinent results are summarized below:

1. Test results of the full wing augmentor on the whirl rig correlated reasonably well with the performance levels obtained during the tethered hover testing indicating a maximum augmentation ratio of  $\phi = 1.26$  for the wing augmentor system.
2. Isolated component testing identified numerous problems associated with each of the primary augmentor components.
  - Aft diffuser flap (elevon)
    - High degree of spanwise flow angularity
    - Irregular spanwise nozzle exit pressure distribution
    - Low component thrust coefficient
  - Forward diffuser flap (forward diffuser)
    - Irregular spanwise pressure distributions
    - Nozzle gapping under pressure and temperature
  - Centerbody Nozzle
    - Irregular spanwise nozzle exit pressure distributions
    - High degree of flow angularity/flow not directed uniformly over endwall
  - Endwall Blowing Nozzle
    - Irregular nozzle exit pressure distributions
    - High degree of flow angularity/flow misdirected.

### 2.4 Summary

The diagnostic tests confirmed that the goal performance levels of the wing augmentor system were not realized during the tethered hover testing. The primary cause of the inadequate performance was identified to be related to the flow quality and isolated performance of each of the primary components of the augmentor system rather than inherent to the basic augmentor configuration. These flow related problems did not exist on the wing development hardware and appear to be related to modifications incorporated in the aircraft augmentor components. These modifications

were necessary to integrate the augmentor system within the aircraft's contours. The major difference resulting from these modifications was the interface of the primary flow feed ducts with the individual augmentor components. These differences seriously affected both the isolated performance and flow quality of the primary augmentor nozzles. When these inferior components were collectively operated as an augmentor, they combined to significantly reduce the performance potential of the system.

After extensive analysis and review of both the tethered hover test and diagnostic test data, a remedial thrust augmentor development program was initiated. The primary objectives of this program were to develop in a serial fashion the wing and canard augmentor systems performance allowing a follow-on tethered aircraft hover test program.



## 3.0 DEVELOPMENT PROGRAM

3.1 DEVELOPMENT LOGIC

Results of the diagnostic tests conducted on the XFV-12A Prototype No. 1 left-hand wing augmentor components identified the problems associated with each component of the wing augmentor system. For each of the defective components, an improvement rationale and method was identified. This program would rework all of the components and demonstrate on the whirl rig the initial desired performance, i.e.,  $\phi_{wing} = 1.50$  and  $\phi_{canard} = 1.30$ . This would allow more than ample test time for VTOL evaluation as shown by the lift summary in Figure 3-1.

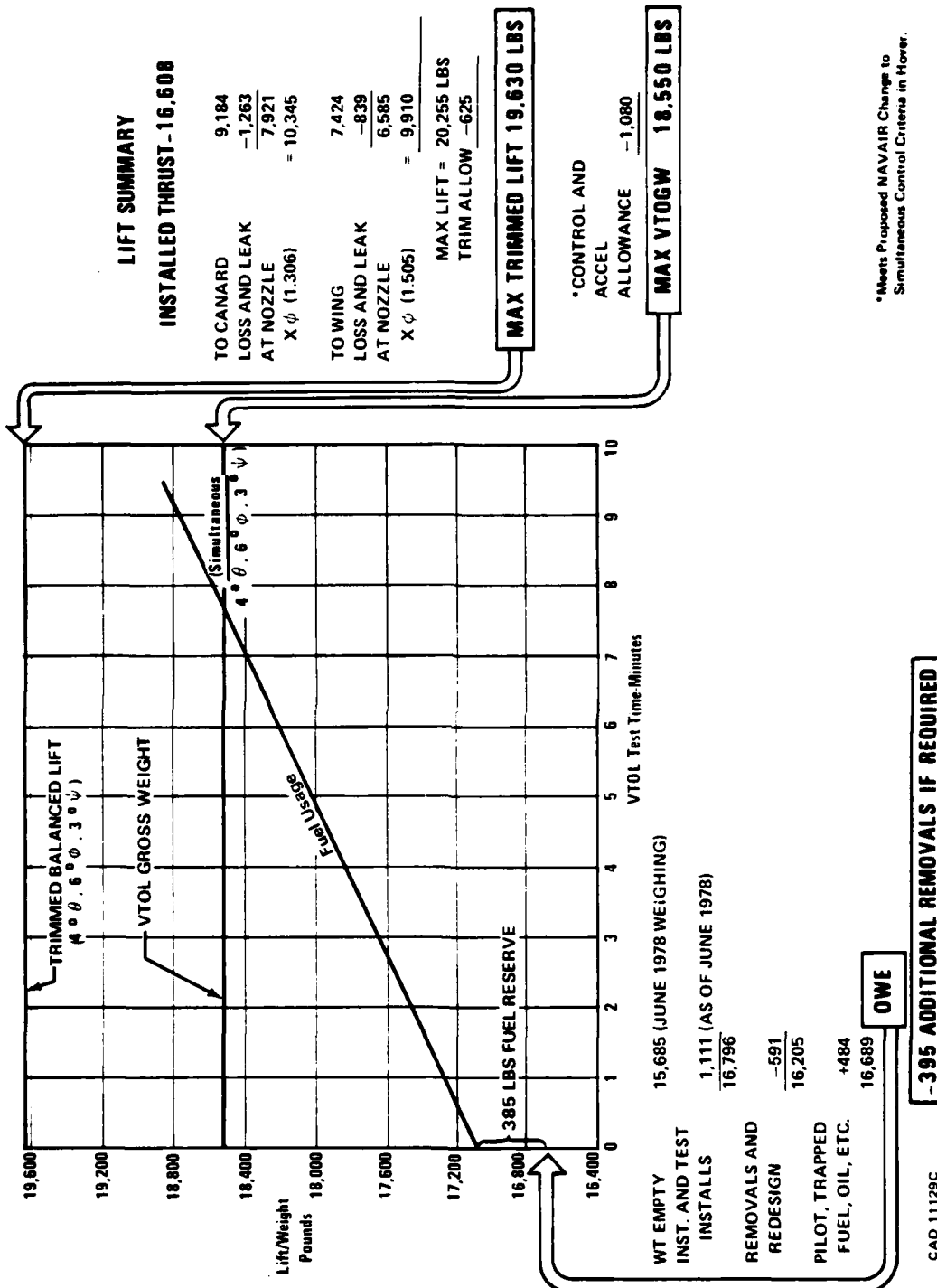
A very detailed task oriented program was developed utilizing an analytical computational fluid dynamics program (developed using discretionary funds), reduced scale experimental testing, full scale component tests, and design studies of aircraft configuration constraints. Figure 3-2 shows the program as developed and the sequentially interlocked tasks. This program was organized in two phases. The first phase was oriented toward modifying the existing components to correct their individual discrepancies and demonstrate the original goal performance level. The objective of the second phase was to develop an advanced centerbody configuration and the necessary modifications to the augmentor geometry to demonstrate increased performance. Subsequently, the phase two performance level was accentuated in order to provide for a more comprehensive evaluation of the thrust augmented wing technology. Additional control capability (over that specified by MIL-F-8300) was desired during hover in order to assure adequate control response for aircraft evaluations in high gust level conditions representative of operations in the vicinity of small ships in high sea states.

This desire to obtain increased performance initiated an evaluation of hover characteristics and the performance requirements of the wing and canard configuration. This evaluation was based upon the configuration, as identified by ongoing design studies, which were required to incorporate an improved wing and a new canard augmentor. A new canard configuration had been identified with an estimated performance capability of  $\phi = 1.40$  for full scale hardware as installed on the XFV-12A. To obtain a wing  $\phi$  that would support this higher canard  $\phi$ , it was necessary to evaluate the geometric relationships of the wing and canard as well as the vertical takeoff gross weight. To provide for test flexibility in the augmentor nozzles and a substantial fabrication time and cost savings, corrosion resistant steel material was substituted for titanium material in the weight evaluation. An additional fuel reserve was carried in the weight estimate to provide for a heat sink in the fuselage fuel sump tank. This vertical takeoff gross weight (VTOGW) summarized to 19,003 pounds with five minutes of fuel at intermediate engine power.





## SUMMARY OF EXPECTED TEST MISSION PERFORMANCE



\*Meets Proposed NAVAIR Change to Simultaneous Control Criteria in Hover.

Figure 3-1 Summary of Expected Test Mission Performance

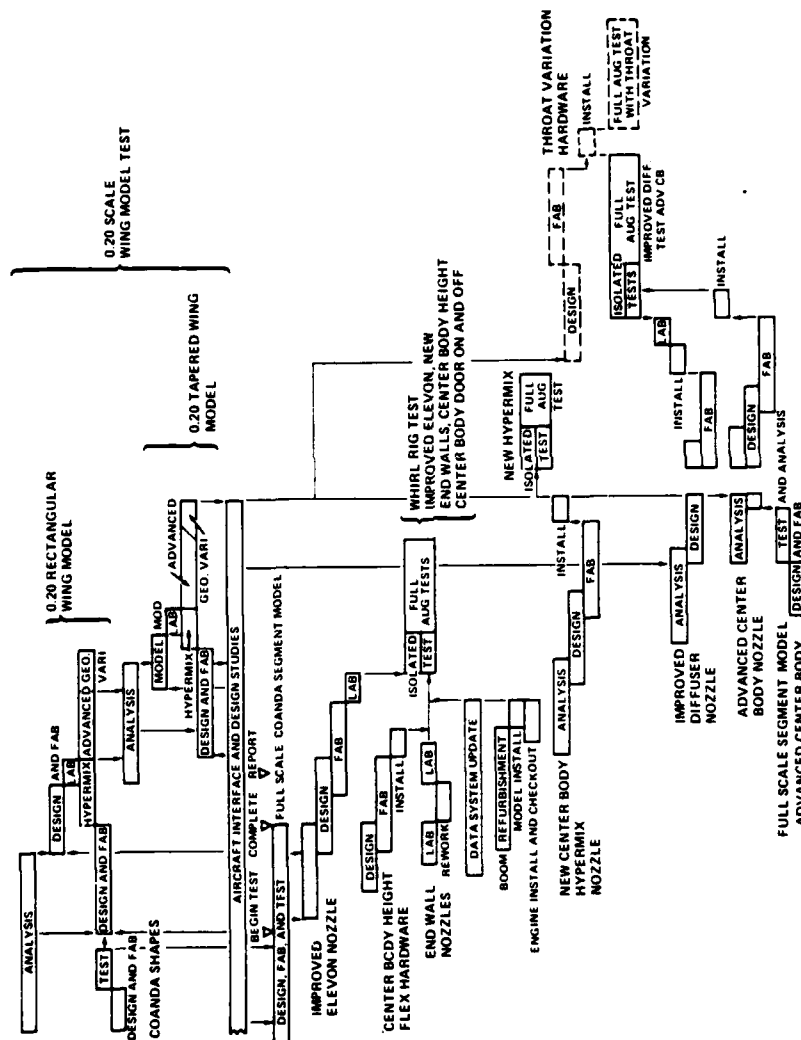


Figure 3-2 Wing Development Program



For the geometric relationships of the wing and canard thrust vectors, Figure 3-3, and the total nozzle thrust of 14,520 pounds (engine thrust of 16,608 less internal duct losses and leakage of 2088 pounds) a plot of

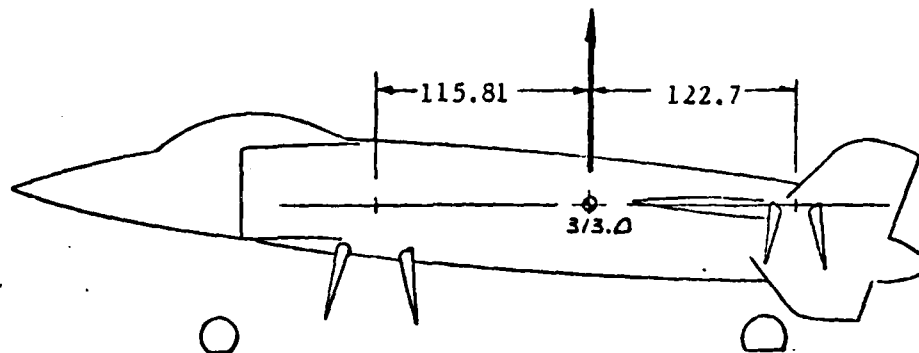


Figure 3-3 Geometric Relationships of the Wing and Canard Thrust Vectors

wing  $\phi$  versus canard  $\phi$  is shown in Figure 3-4. For each condition of maximum trimmed lift and maximum trimmed lift with simultaneous control, the numerical relationships of the canard and wing performance can be evaluated. A wing  $\phi$  of 1.60 is seen to be required to support a canard  $\phi$  of 1.40 and provide full simultaneous control about all three axes during hover.

Historically, data from previous tests indicate a 0.05 decrement of  $\phi$  when converting a rectangular model to a tapered and swept model provided the taper ratio was 0.60 or greater. This 0.05 delta  $\phi$  was added to the full scale hardware requirement of  $\phi_{\text{wing}} = 1.60$  (assumes no scale or temperature effects) to establish the 0.20 scale rectangular model requirement of  $\phi_{\text{wing}} = 1.65$ .

This increase in the wing performance requirement from  $\phi_{\text{wing}} = 1.50$  (full scale tapered hardware) eliminated Phase I of the development program. Phase II was reoriented toward developing the higher performance augmentor configuration. This redirected effort was organized in five separate tasks.

The first task was to improve the Coanda/flap isolated performance through the use of 0.20 scale rectangular models, full scale segment models, and the full scale Coanda/flap article. Coanda/flap surface development was concentrated on the wing aft augmentor flap (elevon) since this surface was common to any tapered throat configuration (see Section 4.0). This hardware development is presented in Sections 6.0 and 9.0.

The second task was to improve the centerbody nozzle configuration through the use of an analytical computer code, 0.20 scale rectangular models,

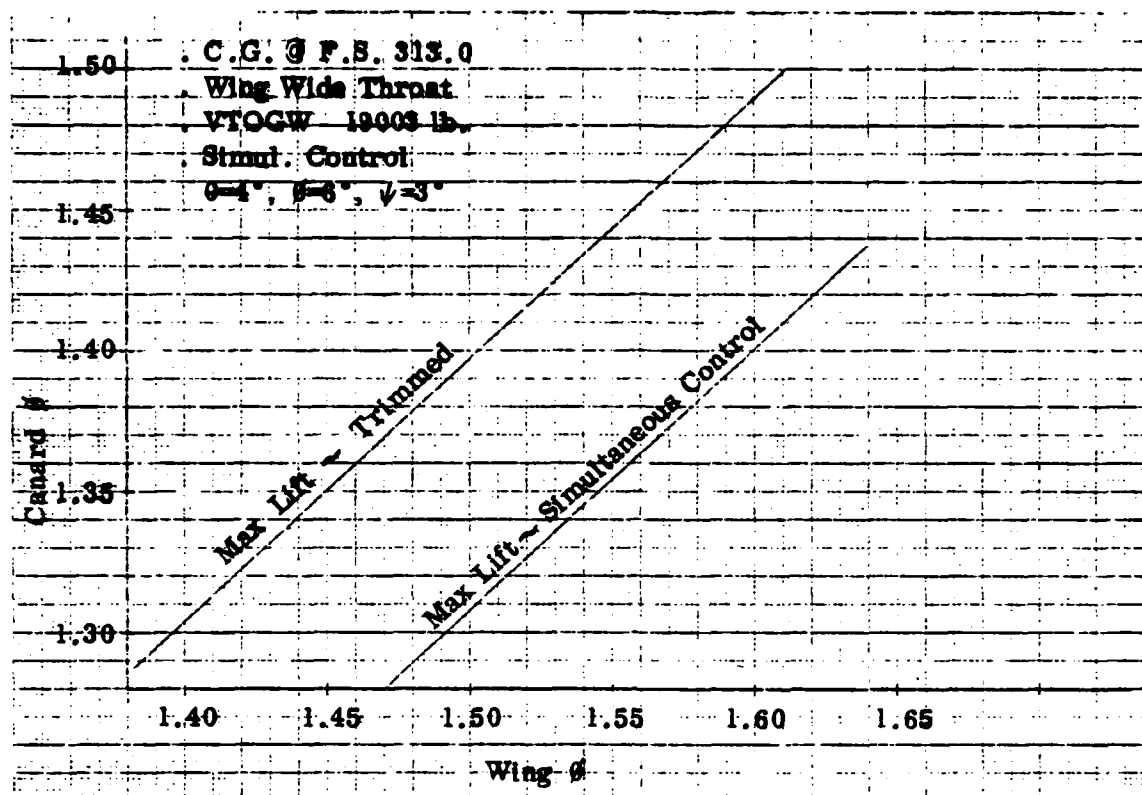


Figure 3-4 Wing Ø Versus Canard Ø

reduced scale segment models, and the full scale centerbody article. The analytical and 0.20 scale rectangular development is presented in Section 7.0.

The third task involved using the improved Coanda/flap and centerbody surfaces to determine the optimum performance configuration for the augmentor (inlet area ratio, diffuser flap length, end wall treatment, and inlet configuration) that could be integrated into the XFV-12A wing airfoil. Because the augmentor configuration is highly dependent on the centerbody nozzle configuration, the second and third tasks were conducted simultaneously and the development results are presented in Section 7.0.

The fourth task was to configure a 0.20 scale tapered model of the full scale configuration using the 0.20 scale rectangular model as the mid-span section cut of the tapered model.

The fifth task was to design and fabricate flight-weight full scale hardware for a full scale, hot, demonstration of the augmentor configuration.

### 3.2 SUMMARY

In an effort to improve the performance of the XFV-12A thrust augmenters, a two-phase remedial development program was initiated. The primary objective of Phase I was to correct deficiencies of the aircraft's augmentor components and demonstrate the original goal performance levels of  $\phi_{wing} = 1.50$  and  $\phi_{canard} = 1.40$ . The objective of Phase II was to develop an improved centerbody nozzle along with necessary modifications to the augmentor shroud to increase augmentor performance. Initially, no specific performance goals were stated, however, subsequent operational studies indicated augmentation levels of  $\phi_{wing} = 1.60$  and  $\phi_{canard} = 1.40$  were necessary to assure adequate control response for the aircraft in high gust level conditions.

Due to this increased goal performance level, the Phase I development effort was terminated and Phase II was directed at achieving a  $\phi_{wing} = 1.65$  on the scale model development augmentor. The Phase II program was then composed of five basic tasks.

1. Develop Coanda flap components compatible with the higher goal augmentation ratios.
2. Develop new centerbody nozzles to maximize augmentor performance.
3. Optimize augmentor geometry with new Coandas and centerbody nozzles.
4. Design, fabricate, and test a .2 scale augmentor model representative of the full scale aircraft augmentor design.
5. Fabricate and test full scale L/H wing flight hardware and demonstrate  $\phi_{wing} = 1.60$ .

To date, tasks 1, 2, and 3 have been initiated and their current status is discussed in the remainder of this report. Unfortunately, the contract effort was terminated before all tasks in the development program could be successfully completed.



#### 4.0 DESIGN STUDIES SUMMARY

##### 4.1 INTRODUCTION

Diagnostic tests, conducted on the XFV-12A Prototype #1 wing augmentor hardware following the hover tests, identified various flow deficiencies on the augmentor components. These diagnostic tests concluded that component modifications to improve the flow qualities would be necessary to obtain the performance previously achieved on the original full scale hardware tested on the whirl rig. Design studies were utilized to identify and control the modifications made to each component to assure compatibility within the aircraft moldline constraints. These studies were used to evaluate configurations, fabrication methods, weight, and cost. To assure that component improvements did not create unacceptable changes in the augmentor parameters, a mid-span cross-section cut of the tapered wing augmentor was utilized to control and/or maintain the augmentor parameters. This augmentor cross-section was also used as the representative cross-section to establish the 0.20 scale augmentor model utilized in the experimental test program.

Concurrent with the effort to remedy the flow quality problems, a desire for increased performance was imposed upon each component.

This section will address the design requirements for the Coanda shape, centerbody nozzle, and the configuration evolution studies.

##### 4.2 COANDA SHAPE DEVELOPMENT

Data from the isolated tests of Reference (6) on the aft flap (wing elevon) demonstrated highly outboard angular flow in the inboard region in addition to poor nozzle total pressure distribution. A comparison of the elevon surfaces from the XFV-12A Prototype #1 and the original full scale whirl rig hardware reveals a large difference between the feed duct location relative to the nozzle exit, Figure 4-1. This nozzle/feed duct configuration from the XFV-12A elevon did not allow adequate distance for the flow to turn effectively and, therefore, exhibited outboard angularity as demonstrated during the isolated tests of the wing elevon.

Derivation of a Coanda shape has until recently been challenging because of the limited airfoil thickness available in a supersonic airfoil. The requirements of large initial radius ( $R_0$ ) and maximum running length to the augmentor throat ( $s_{throat}$ ) were not compatible with supersonic airfoil thicknesses. Articulated concepts were utilized on the XFV-12A canard; however, the penalties of weight, fabrication requirements, and operation under load presented valid arguments for alternate concepts. A convenient shape which was easily definable mathematically and allows a large  $R_0$  at the nozzle exit with a gradual increasing curvature is the log spiral.

The mathematical equations for a log spiral shape are shown in Figure 4-2.

After reserving space for the internal nozzle shaping (dimension X), the remaining width (dimension Y), shown in Figure 4-2, is available for the external shape of the Coanda. Since a number of shapes with various

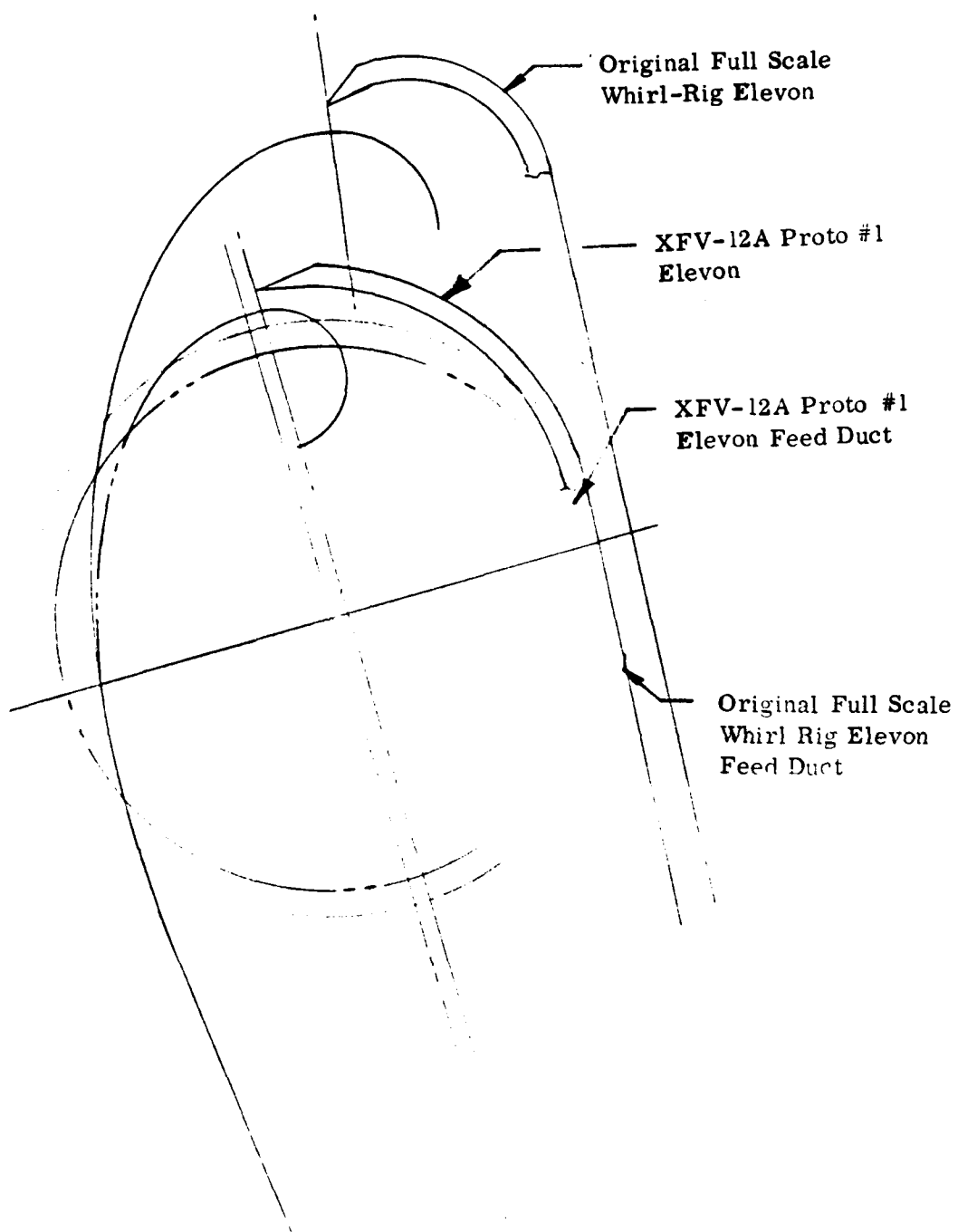


Figure 4-1 Comparison of XfV-12A Proto #1 Elevon and Original Full Scale Whirl Rig Elevon Nozzle Shapes

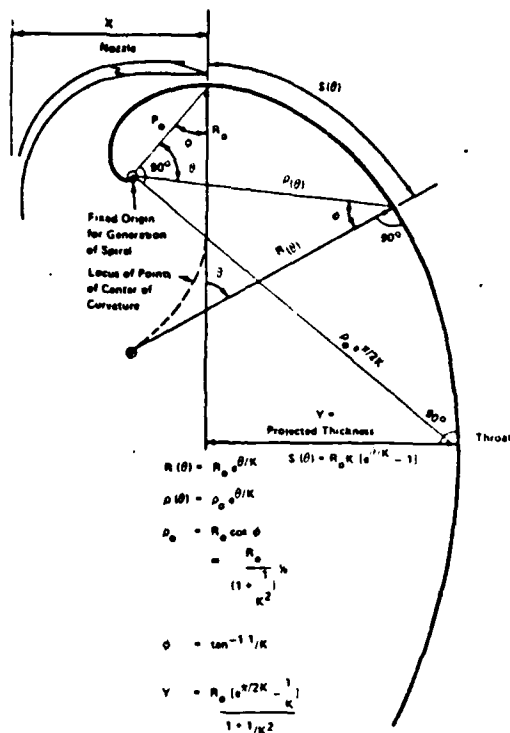


Figure 4-2 Spiral Definition

combinations of spiral constant ( $K$ ) and initial radius ( $R_0$ ) can be configured as shown in Figure 4-3, a method of determining the optimum shape was required.

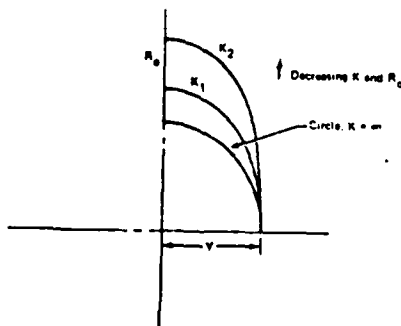


Figure 4-3 Example of Various Spirals with Identical Thickness





From experimental separation criteria, universal jet growth laws, and the geometric relationships of initial radius ( $R_0$ ), running length to the throat ( $S_{throat}$ ), nozzle gap ( $t$ ), and projected Coanda width ( $Y$ ) (Figures 4-4 through 4-6), a carpet plot of jet growth, spiral K factor,

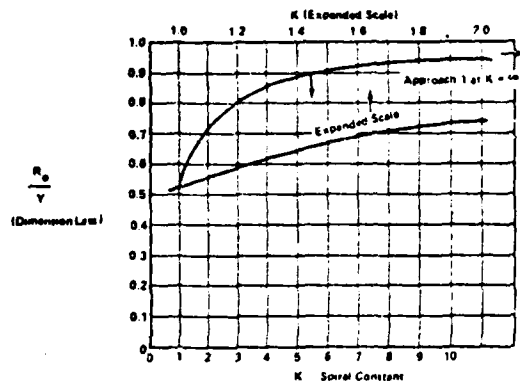


Figure 4-4 Initial Radius  $R_0$  Versus K

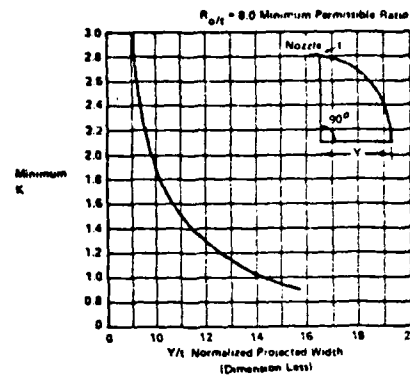


Figure 4-5 Minimum K Versus  $Y/t$

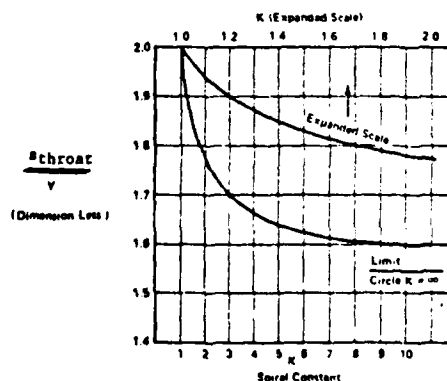


Figure 4-6 Running Length from Nozzle to Throat Versus K



and projected width is shown in Figure 4-7. The boxed areas are the packaging regimes for the XfV-12A wing and canard augmenters utilizing the moldline constraints of the existing airfoils.

As shown in Figure 4-7, the spiral constant (K) for the wing Coandas could vary from a  $K = 1.17$  to a  $K = 1.50$ . To determine the optimum K factor, an experimental test program was developed to quantify performance increments of the revised shape and, as noted earlier, resolve the flow angularity problem of the XfV-12A elevon. This test program concluded that a log spiral shape with a K factor of 1.30 did improve the isolated performance, and simultaneously relocated the nozzle further from the feed duct as shown in Figure 4-8. For details of this test program see Section 6.0. Figure 4-8 compares the improved aft flap nozzle shape and the XfV-12A Proto #1 aft flap nozzle shape.

#### 4.3 CENTERBODY DEVELOPMENT

Data from the isolated test of Reference (6) on the XfV-12A Prototype #1 centerbody demonstrated reduced chordwise spreading when installed in the augmentor, but isolated tests of the same centerbody nozzle showed normal spreading characteristics. A comparison of the centerbody nozzle shapes from the original full scale whirl rig hardware and the XfV-12A prototype nozzle, Figure 4-9, reveals a more blunt base on the XfV-12A prototype centerbody due to the addition of an upper surface close-out door. Hypotheses of probable causes of the reduced spreading included the influence of the poor end flow conditions existing on the prototype augmentor and possible separation off the centerbody's blunt base. Since the XfV-12A Prototype centerbody was also installed at a lower position in the augmentor than the original full scale whirl rig hardware, the influence of the Coanda jets could have contributed to the reduced spreading. Resolution of the above problems were to be addressed in the development of an improved centerbody nozzle configuration.

Three types of centerbody nozzles were investigated for packaging requirements and are identified as; hypermixing, asymmetric and symmetric.

##### 4.3.1 Hypermixing Nozzle

The hypermixing nozzle features alternating jets that create streamwise vortices, Figure 4-10, which accelerate the turbulent mixing and thus increase the entrainment. The amount of hypermixing angle was evaluated experimentally and analytically to optimize the performance potential in the wing augmentor. Results of this experimental and analytical program are presented in Section 7.0. Packaging restraints did not restrict this investigation as shown in Figure 4-11. Figure 4-11 presents a typical cross-section of the centerbody nozzle showing the existing centerbody hypermixing nozzle of the XfV-12A and the highest hypermixing angle possible without affecting the upper panel closeout door.

Because of the limited potential performance of this nozzle configuration, development of this concept was terminated in favor of configurations with higher performance potential.

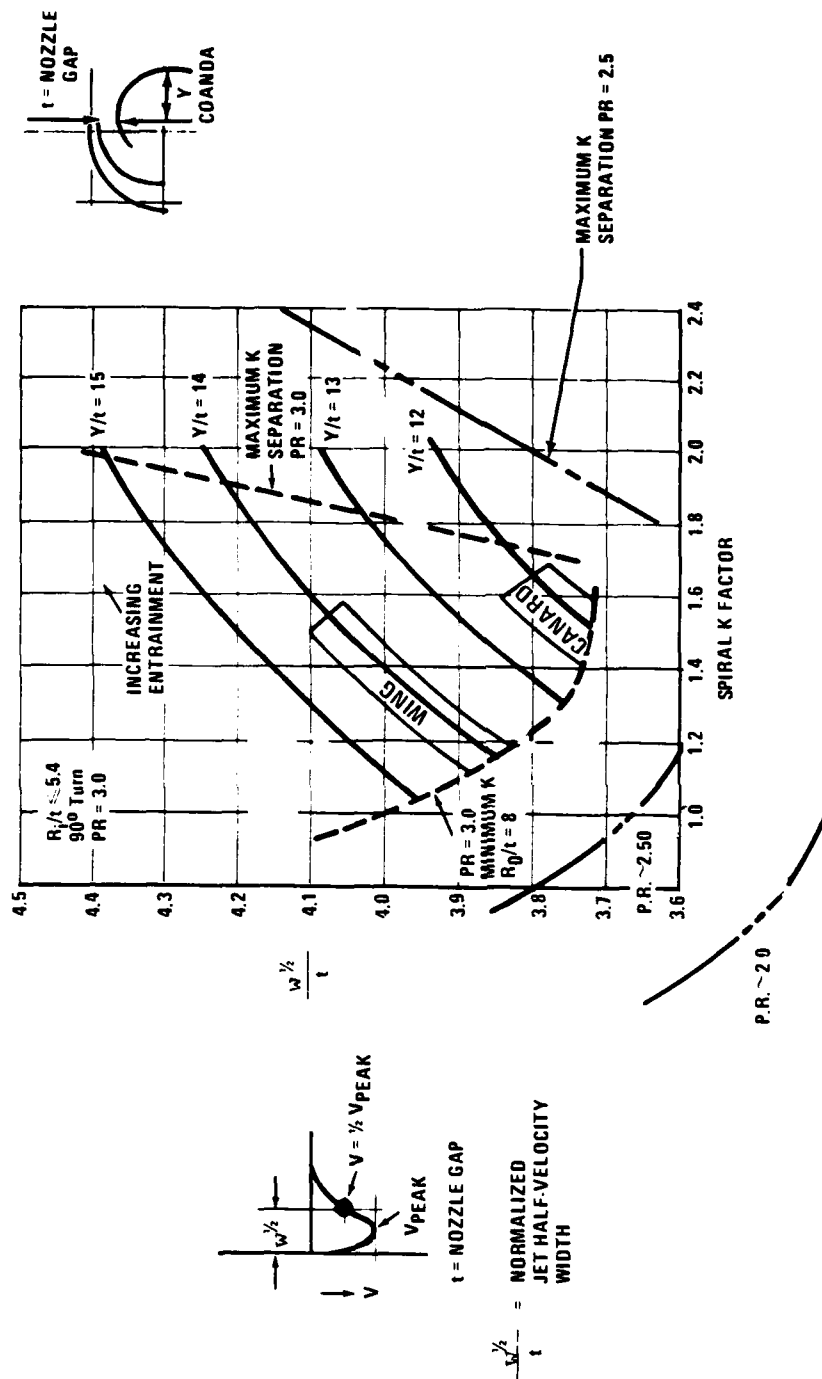


**Figure 4-7 Empirical Coanda Selection Criteria**

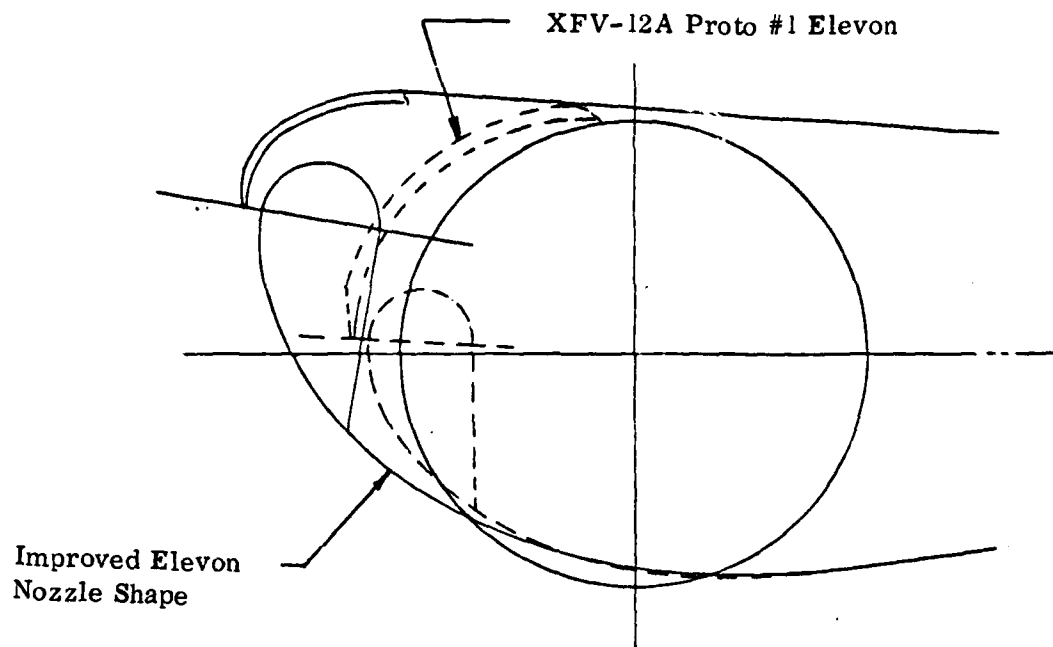


Figure 4-8 Comparison of Coanda Shapes

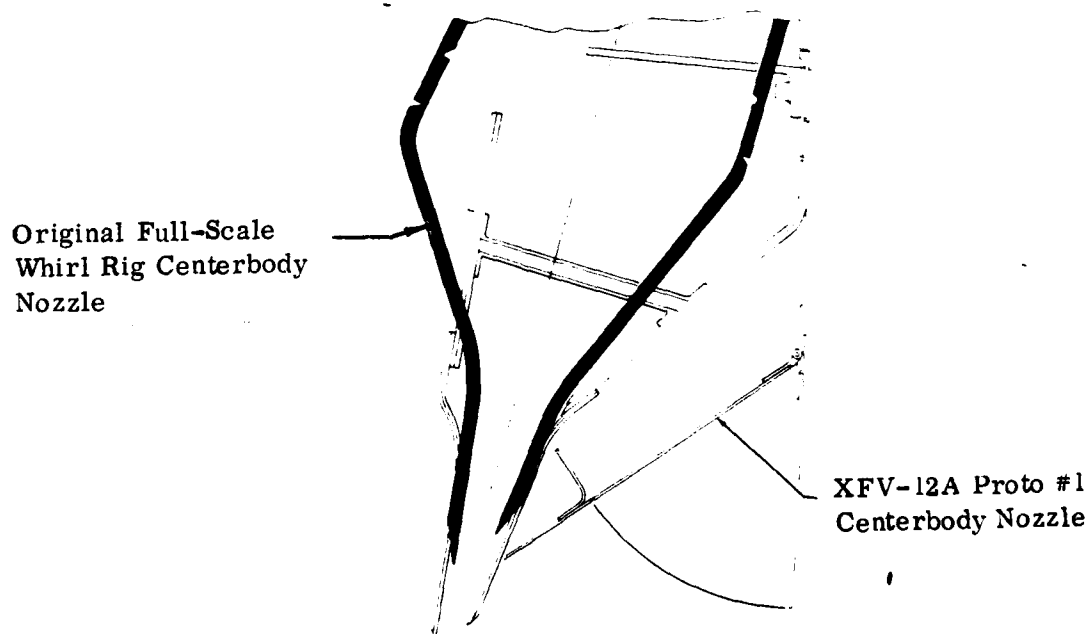


Figure 4-9 Centerbody Shape Comparison

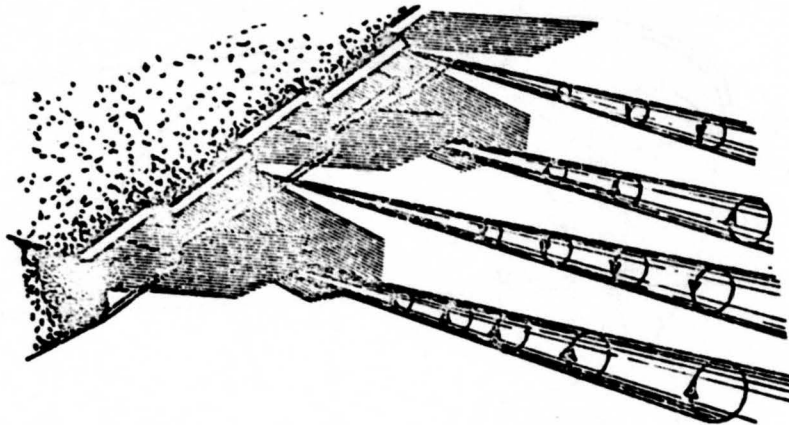


Figure 4-10 Hypermixing Nozzle

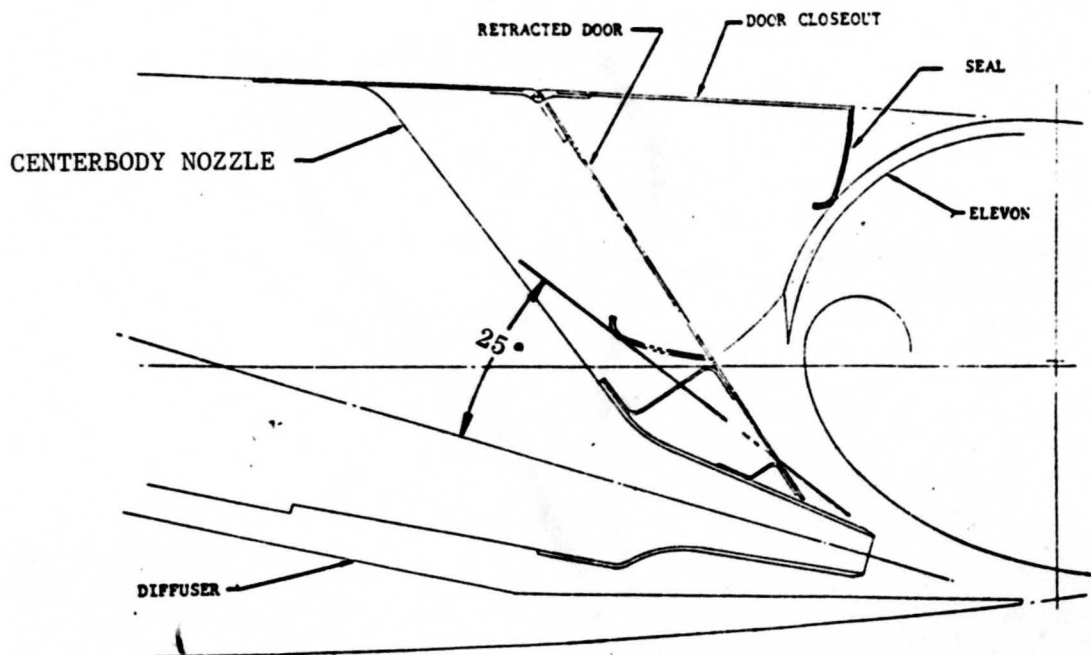


Figure 4-11 Typical Cross-Section of the Centerbody Nozzle



#### 4.3.2 Asymmetric Nozzle

Previous experimental testing had identified a centerbody nozzle configuration that combined a series of aft facing spanwise slots with alternating series of cross-slots on the forward side, shown in Figure 4-12, that would produce increased mixing capability. This concept was advantageous from a packaging viewpoint since it provides its own closeout system on the upper surface as shown in Figure 4-13.

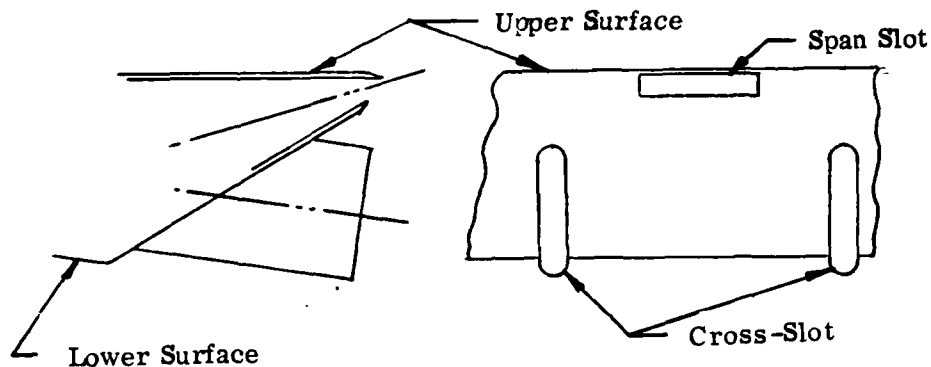


Figure 4-12 Asymmetric Centerbody Nozzle

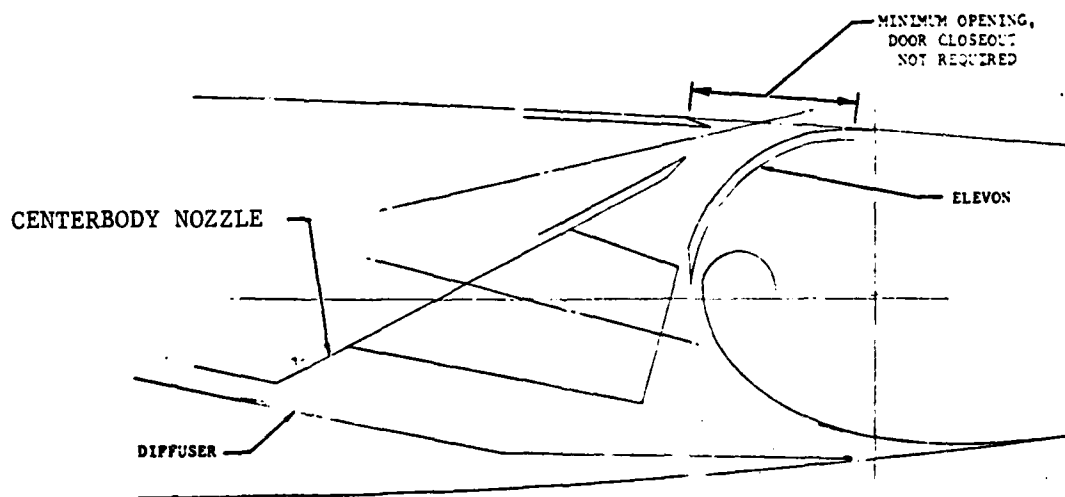


Figure 4-13 Closeout System on the Upper Surface



Packaging constraints only dictated the total width as shown in Figure 4-13 and did not impair the investigation into the number of cross-slots, flow split between the span slots versus the cross-slots, or the launch angle of the nozzles. When the initial performance values from the experimental test model utilizing this nozzle configuration were lower than expected, this nozzle configuration and the development tasks associated with this configuration were terminated prior to completion. The experimental and analytical results of this nozzle configuration are presented in Section 7.0.

#### 4.3.3 Symmetric Nozzle

The symmetric multi-lobed nozzle, shown in Figure 4-14, consists of a series of symmetric cross slots equally spaced along the span. This

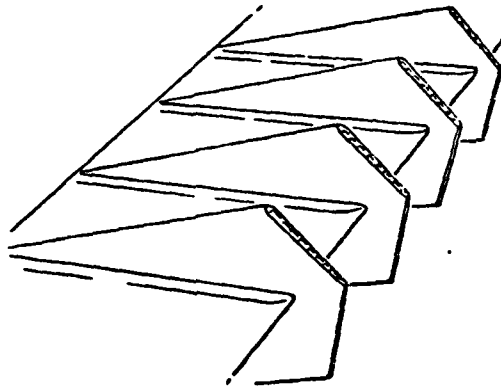


Figure 4-14 Symmetric Centerbody Nozzle

configuration provides increased chordwise jet launching thereby increasing the turbulent mixing capability. The primary disadvantage to this centerbody nozzle configuration is the unsuccessful effort to date to provide a closeout system on the upper surface of the wing airfoil.

Packaging considerations were restricted by the overall width of the nozzle, but being symmetric around the nozzle centerline the realistic restraint is the proximity of the forward flap surface. The nozzle configuration could vary between the boundaries shown in Figure 4-15 with various combinations of nozzle parameters. These parameters are identified by Figure 4-16. All of the parameters are independent of each other except the wedge and launch angle and must maintain the relationship as shown in Figure 4-17.

Since the program was terminated by funding constraints prior to completion, only the recommended nozzle configuration (based upon experimental and analytical trends) can be presented. This nozzle

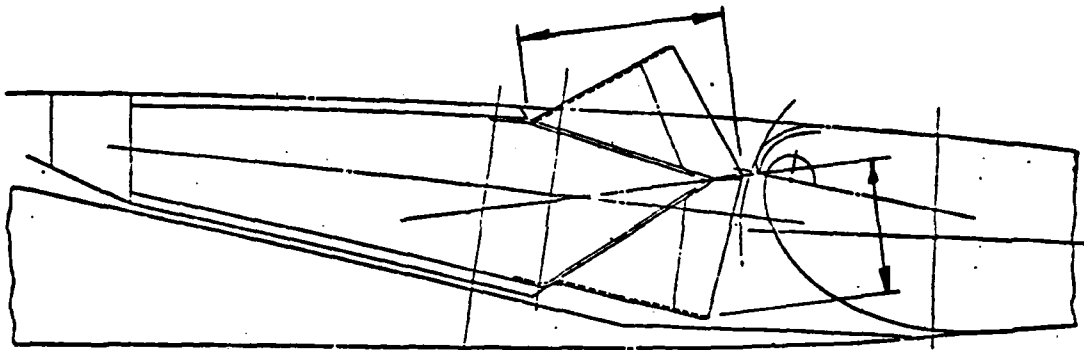
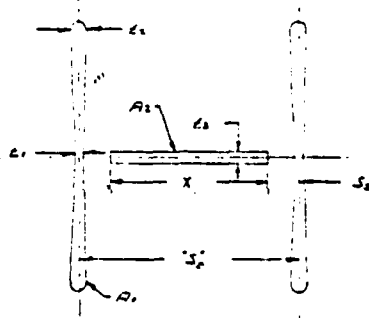
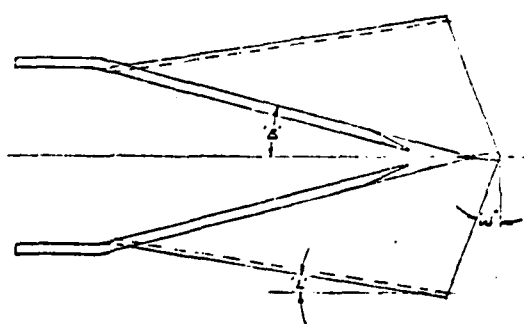


Figure 4-15 Nozzle Configuration



PARAMETER
WEDGE $\angle$ - "W"
LAUNCH $\angle$ - "L"
BASE $\angle$ - "B"
BOW-TIE RATIO $L_2/L_1$
ASPECT RATIO $X/L_2$
SPACING - $S_2/S_1$
CONVERGENCE - $L_2/L_1$

Figure 4-16 Nozzle Parameters



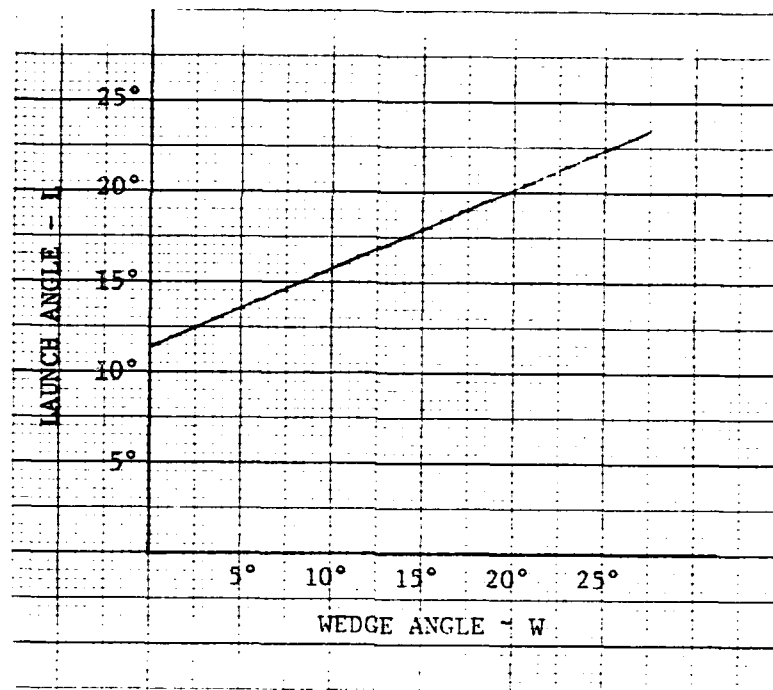


Figure 4-17 Wedge Versus Launch Angle

configuration contains a 25° base angle, 21° launch angle, with a linearly varying wedge angle, 15 element cruciform with a two to one bow-tie ratio on the cross-slots. Figure 4-18 presents the recommended nozzle configuration packaged in the wing cross-section.

#### 4.4 CONFIGURATION EVOLUTION

##### 4.4.1 Wide Throat

Experimental testing of a 0.20 scale rectangular model in the laboratory indicated that a throat width increase (inlet area ratio  $A_2/A_0$ ) was required in the wing augments to fully utilize the higher entraining potential of either the asymmetric or symmetric centerbody nozzles. The XFV-12A prototype hardware had the flexibility initially incorporated in the wing for a throat width increase by revising the forward flap hinge line and modifying the centerbody rotation as shown in Figure 4-19. The narrow throat (XFV-12A prototype hardware) or the wide throat utilizes identical surfaces and the flexibility is accomplished by hinge line location relative to the surfaces. Because of this design flexibility, packaging of increased throat width could be combined with improved Coanda/flap surfaces and an improved centerbody nozzle. Figure 4-20 shows a planform and three section cuts of the wing wide throat. The mid-span cross-section cut is the control section mentioned earlier. This configuration established the model configurations for experimental and analytical studies. If the tapered and swept augments studies had continued, this configuration would have established the control lines for

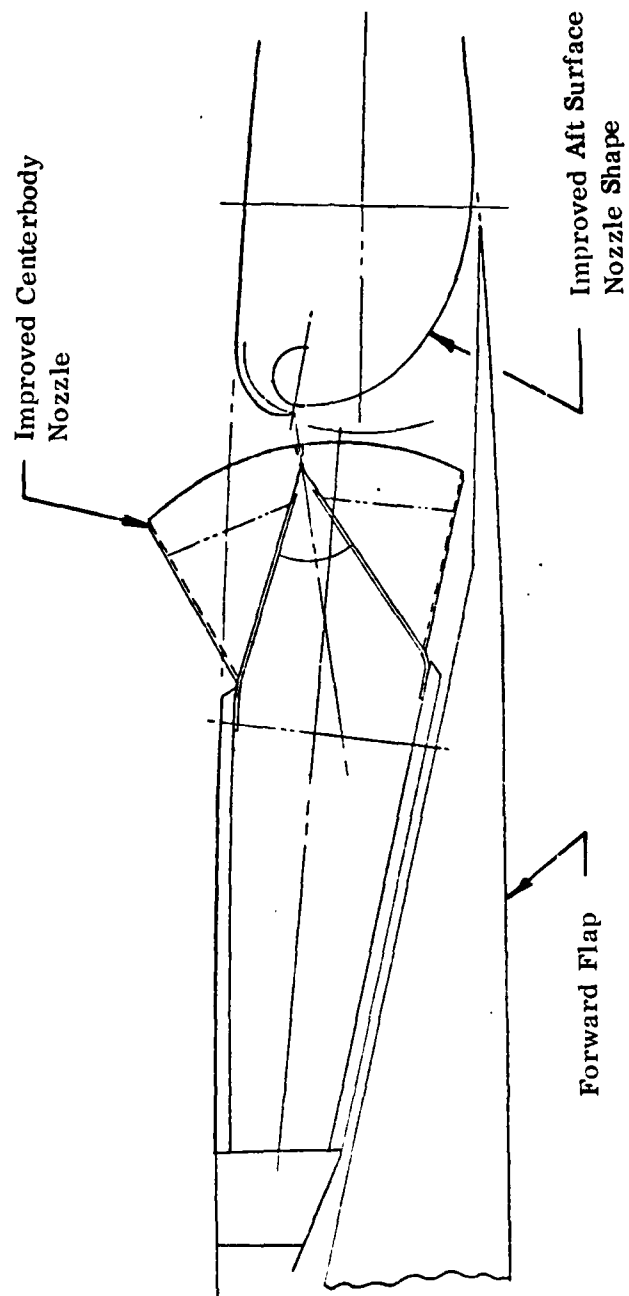


Figure 4-18. Wing Cross-Section with Improved Centerbody Nozzle

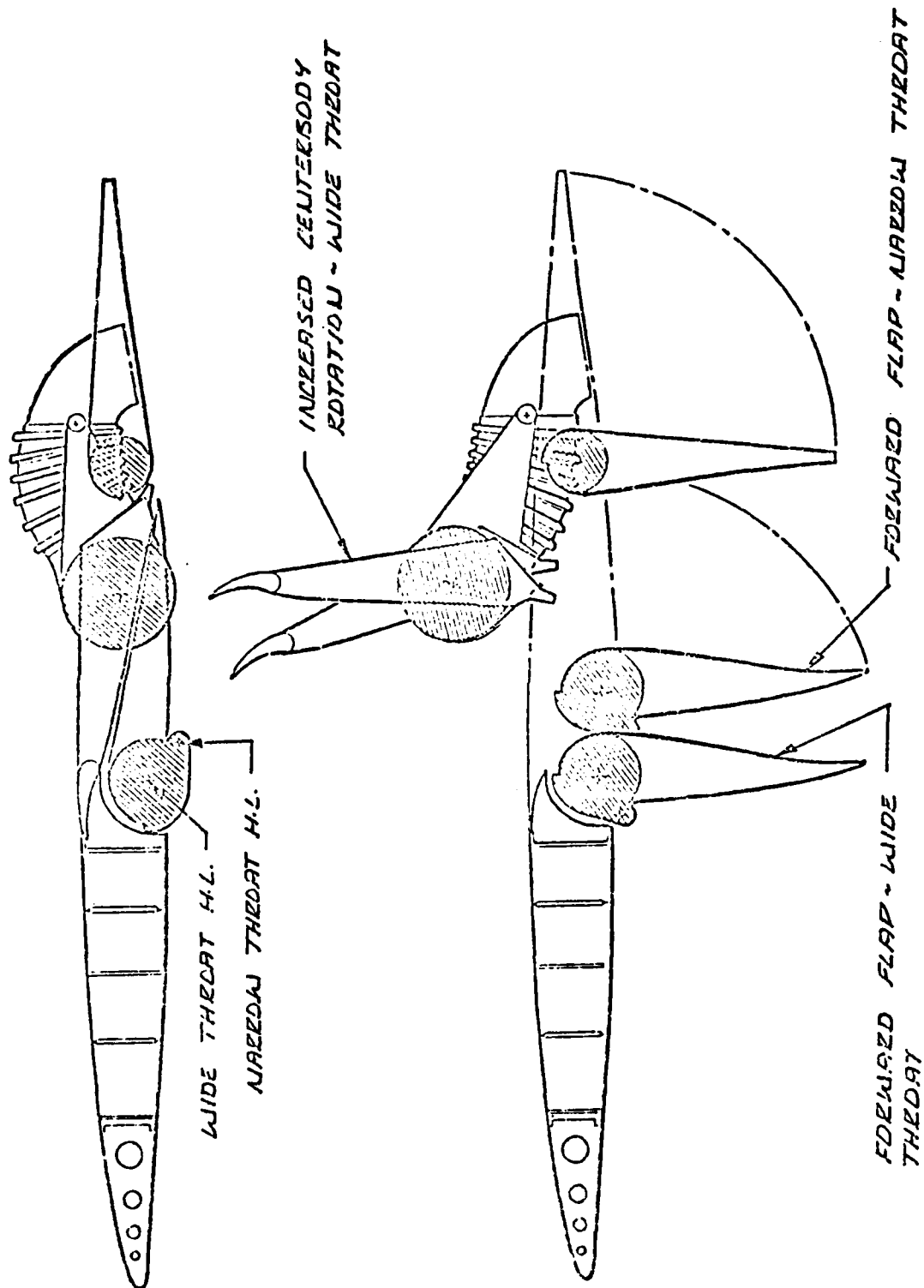


Figure 4-19 Flexibility in Wing Augmenter Design

202810-225

H  
G  
F  
E  
D  
C  
B  
A

22

21

20

TE YWOP O  
YWOP E O

YWOP Z O

TE YWOP O  
YWOP E O

EJECTOR PRIMARY HINGE

ELEVON HINGE

TE ZWOP

TE ZWOP O  
TR DIFF HINGE

ZWOP Z O, ZWOP D, ZWOP E O

TE ZWOP O

DIFFUSER HINGE  
BAL 1

89.5°

16.6°  
16.6°

CUT "13", YWOP Z 85.8321 = YWOP Z O  
VIEW ROTATED INTO PLANE OF PAPER

YWOP E O

TE YWOP

TE ZWOP

TR DIFF HINGE

E THRU OUT

EJECTOR PRIMARY

ELEVON HINGE

MID-SPRALL - XWOP 37.8963  
VIEW ROTATED INTO PLANE OF PAPER

24

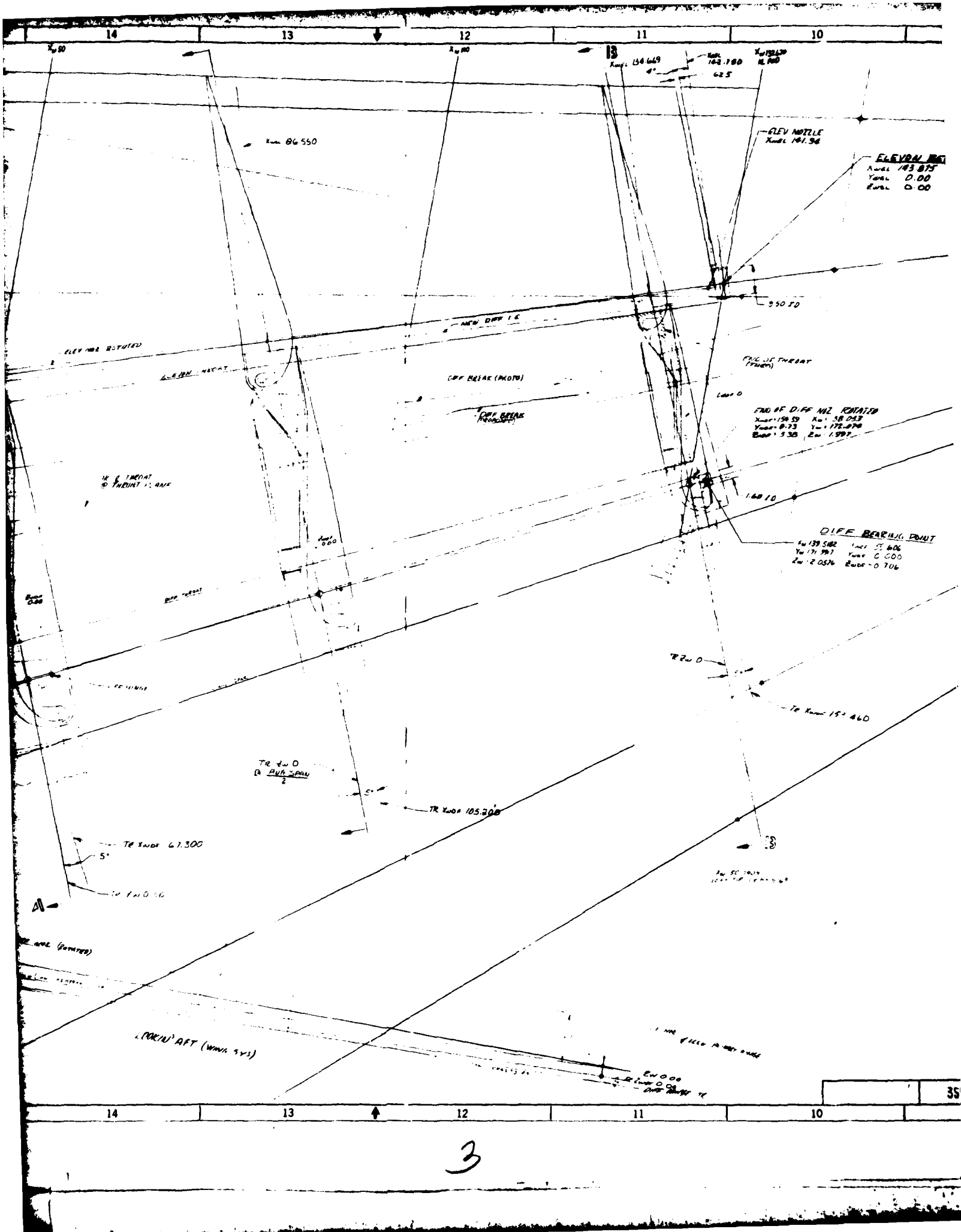
23

22

21

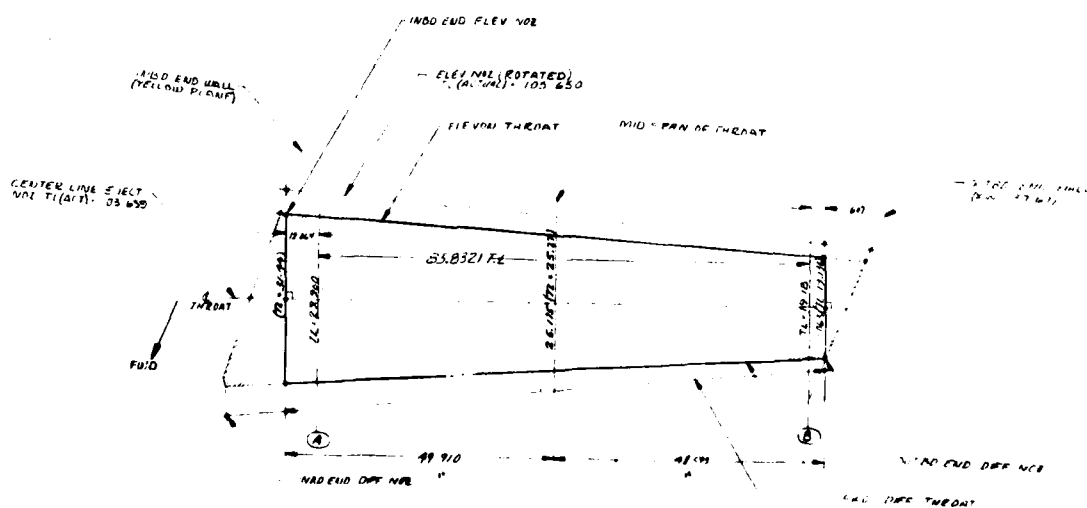
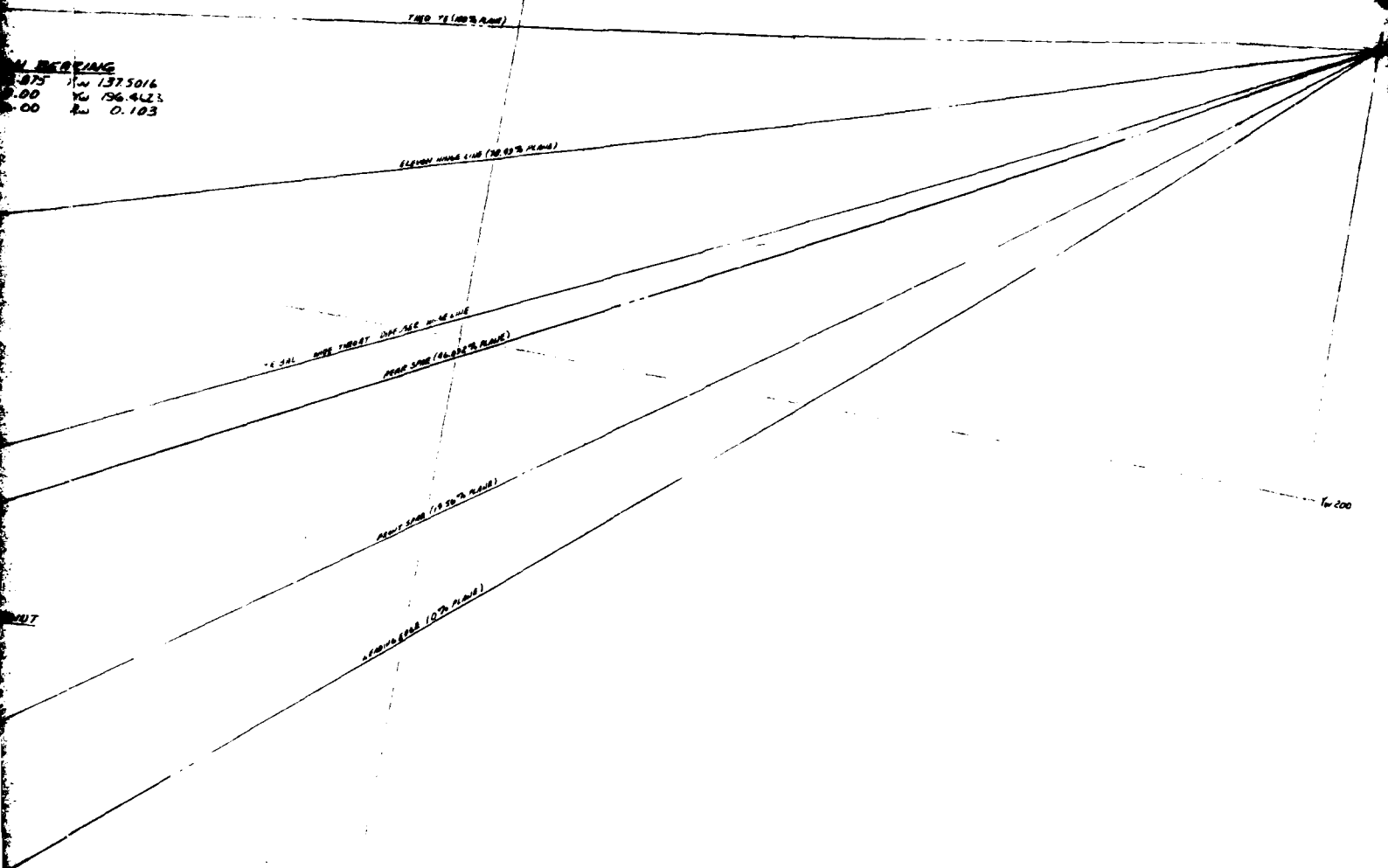
20





W. BEARING

0.75	W	137.5016
0.00	W	196.4123
0.00	W	0.103



WING THROAT TAPER DIAGRAM  
(LOOKING NORMAL TO WING REF PLANE)  
NO SCALE

358-919509

NR81H-50

REVISIONS		DATE	BY
1	REVISED TO 2 CARRY IN REVISIONS		
2	REVISED TO 4 ADD SHOP PRACTICE		
3	REVISED TO 1 ADD BASE ON		

PARAMETER WIDE THROAT DESIGN

THROAT DIAMETER (Dr) 34.00 IN  
 THROAT HEIGHT (Dt) 20.10 IN  
 TAPER RATIO ANG (A) .609  
 SPAN ANG (B) 108.80 IN  
 THROAT AREA (A<sub>1</sub>) 2707 IN<sup>2</sup>  
 NOZZLE EXIT AREA (A<sub>0</sub>)  
 A<sub>1</sub>/A<sub>0</sub> ANG  
 EXIT AREA (A<sub>2</sub>) 4560 IN<sup>2</sup>  
 A<sub>1</sub>/D ANG  
 THROAT EXIT ANG (L)  
 L/D ANG  
 CHANDLER ANG  
 ELEVATION R<sub>1</sub> 3.285 - 1.444  
 R<sub>2</sub> 1.05 - .52  
 K<sub>1</sub> 1.3  
 FWD DIFF R<sub>2</sub> 3.008 - 1.223  
 K<sub>2</sub> 1.080 - .539  
 K<sub>3</sub> 1.3  
 ASPECT RATIO  $\frac{R_1}{R_2}$  4.37  
 A<sub>1</sub> DISTRIBUTION DIFF  
 CB  
 ELEV  
 EWB<sub>1</sub>  
 EWB<sub>2</sub>

NOZZLE SPAN & T DIFF 09.39 IN  
 CB 13.639 IN  
 ELEV 15.650 IN  
 EWB<sub>1</sub>  
 EWB<sub>2</sub>

CORRY ABOVE TWTM  
 FEED DIST @ CB EL 2147.5717, 2147.

FIGURE 4-2D WIDE THROAT PLATFORM

NOTES UNLESS OTHERWISE NOTED

ITEM NO.	DESCRIPTION	USED ON	DATE	BY	THRU
1	APPLICAT ON				
2	EFFECT VTY				

FOR PARTS LIST SEE PL		WORKWELL International Corporation Columbus Aircraft Division	
UNLESS OTHERWISE SPECIFIED DIMENSIONS ARE IN INCHES MFG TOLERANCES ON FRACTIONS DECIMALS ANGLES HOLE LOCATED BY DIMENSIONS HOLE LOCATED BY DIMENSIONS HOLE LOCATED BY DIMENSIONS		DRAWN BY: RALPH J. HEN CHECKED BY: J. HEN DATE: 11/15/59	
TITLE: WIDE THROAT PLATFORM J 89372		356-918509	
SCALE: 1" = 1'-0"		SHEET: 1 OF 1	

356-918509

B

A

4-15 / 4-16

5





hardware development. A comparison of the wing augmentor parameters for the XfV-12A prototype hardware and the wide throat configuration are shown in Table 4-1. Because the same surfaces are utilized with either the wide throat configuration or the XfV-12A prototype hardware, an increase in the throat width produces a decrease in the augmentor parameter L/W.

Table 4-1 Wing Augmentor Parameters

<u>PARAMETER</u>	<u>WIDE THROAT</u>	<u>XfV-12A PROTO 1</u>
$A_2/A_0$	22.304	15.488
$A_0$ Total	121.365 In <sup>2</sup>	121,911 In <sup>2</sup>
$A_0$ Distribution	16.6-58.3-19.4	21.3-48.6-23.1
$A_2$	2702 In <sup>2</sup>	1888.33 In <sup>2</sup>
Span	108.80 In.	101.62 In
$A_2$ Local	25.20 In	23.52 In.
L/W	1.25	1.95
$R_0/t$	Diff 10.39 Elev 10.46	Diff 11.58 Elev 8.08
Spiral K	1.30	-
Duct Area		
. Diffuser	50.27 In <sup>2</sup>	50.27 In <sup>2</sup>
. CB	140.6 In <sup>2</sup>	140.6 In <sup>2</sup>
. Elevon	50.64 In <sup>2</sup>	50.64 In <sup>2</sup>

#### 4.4.2 Blended Wing Study

Concurrent with augmentor development, studies were being conducted on operational configurations and their mission performance evaluated. From these studies evolved a co-planar wing and canard configuration shown in Figure 4-21. This configuration contains an upper inlet and fuselage mounted landing gear as opposed to the side inlets and wing tip mounted landing gear of the XfV-12A. These features, along with the blended wing, result in a supersonic wave drag reduction and, therefore, increased mission performance. This blended wing configuration also permits the use of rectangular augmentors in lieu of swept and tapered augmentors typical of the XfV-12A configuration. This latter advantage allows increased vertical lift and performance. Swept and tapered augmentors investigated to date are lower in performance, as shown in Figure 4-22, because of spanwise flow problems associated with the tapered flap length.

A design study was initiated to investigate the feasibility of incorporating the blended wing concept on the XfV-12A prototype fuselage for a low speed and vertical hover demonstrator.

This configuration, designated the XfV-12B, would utilize hardware assets of the XfV-12A program to the maximum extent possible.

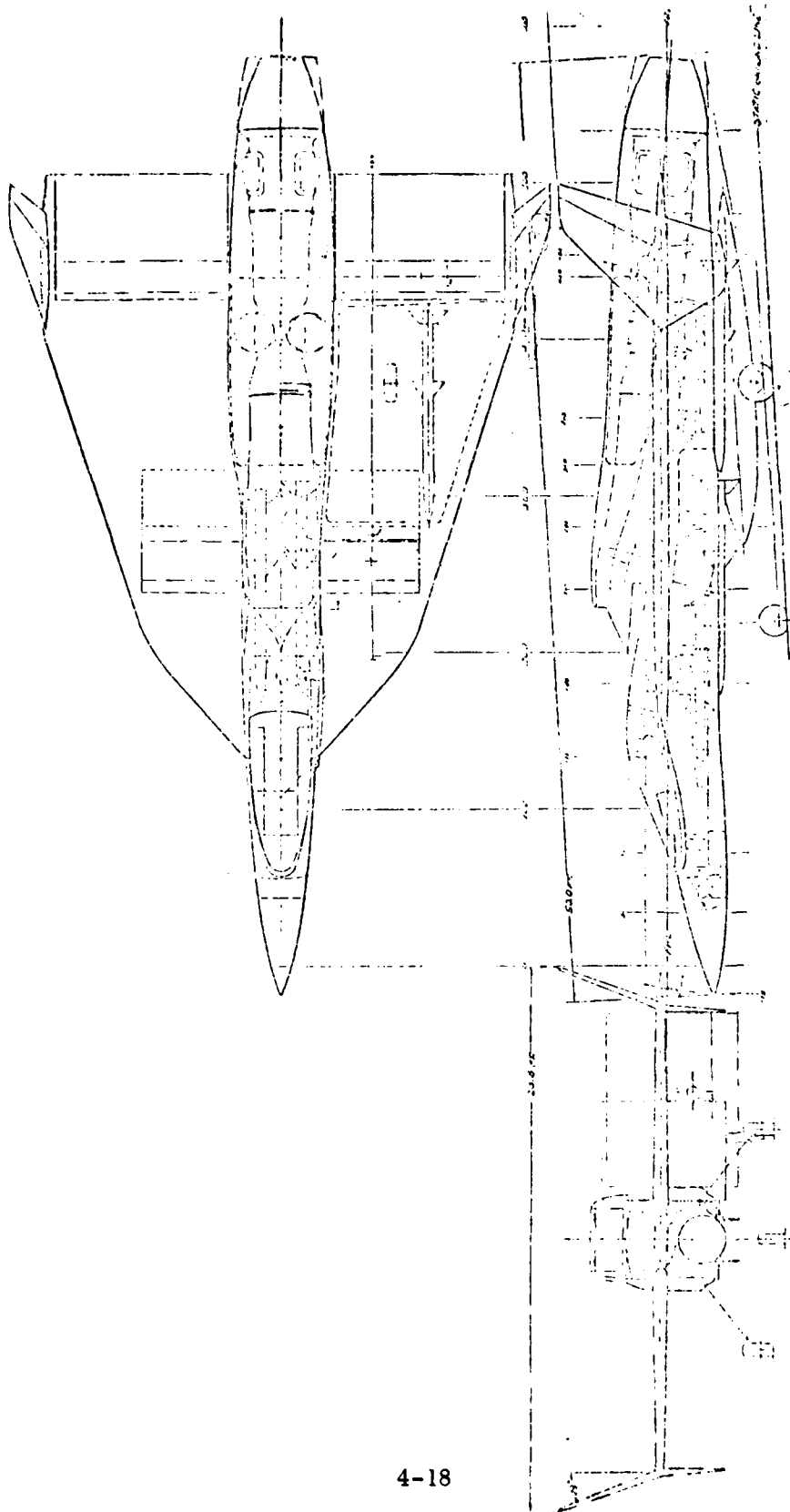


Figure 4-21. Co-Planar Wing and Canard Configuration

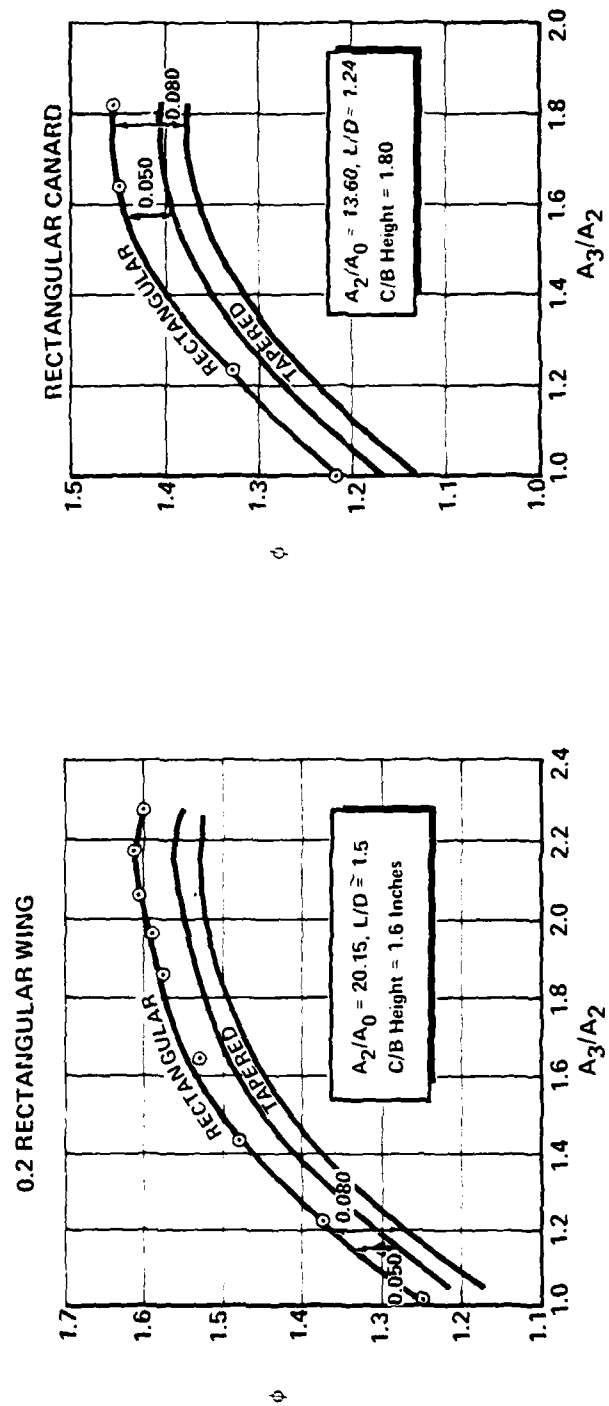


Figure 4-22. Augmenter Performance Tapered vs. Rectangular



The wing location was predicated on maintaining the existing wing-fuselage attach structure which permitted the forward wing area to be above the existing side inlets. The aft wing area span increase was necessary to satisfy longitudinal stability requirements and, to retain the existing fuselage bending moment capability, the main gear trunnion was relocated inboard of the pod area onto the wing main box structure. This gear movement resulted in a reduction of the wing anhedral by 2.0 degrees. Figure 4-23 compares the XfV-12B configuration with the existing XfV-12A prototype.

A set of design criteria, Table 4-2, was established to permit estimates to be formulated for the design and fabrication of a demonstrator prototype.

Packaging of a rectangular augmentor in the blended airfoil is shown in Figures 4-24 and 4-25. The outboard section was determined by the augmentor requirements, i.e., Coanda  $R_0/t$ , nozzle gap thickness, Coanda spiral shape and throat width. This constant section was projected inboard with the increased airfoil thickness utilized for centerbody plenum area and aft diffuser flap feed capability. In both sections, the augmentor itself is a constant, i.e., constant nozzle gap, flap length, constant Coanda shapes, constant throat, and constant centerbody nozzle. The asymmetric centerbody provides its own upper surface closeout door, as shown in Figures 4-24 and 4-25, creating a lighter installation than the symmetric nozzles. Table 4-3 compares the parameters of the forward augmentor with that of an improved rectangular canard that demonstrated 0 performance at model scale of 1.45. These parameters are essentially identical except for diffuser length. This increase in diffuser length on the blended wing version became available with the forward augmentor located above the inlet and will provide slightly higher performance values. Table 4-3 also compares the parameters of the aft augmentor with that of the wide throat tapered wing described earlier. These parameters are also the same except for the diffuser length and span length. A trade study was conducted on the aft augmentor to evaluate fabrication costs and simplicity of internally fed diffuser flaps versus externally fed flaps from dedicated ducts, as shown by Figure 4-26. Although the latter simplifies the diffuser flap structure, an additional control surface is required with actuation mechanisms. Therefore, no apparent reduction in weight or simplicity is obtained. The ducting system utilizes the existing diverter of the XfV-12A. The wing and canard systems are shown in Figure 4-27 with the aircraft installation shown in Figure 4-28. This ducting arrangement has been greatly simplified in comparison to the XfV-12A prototype in that all ducts are circular where possible and are, therefore, lighter and less expensive to fabricate. The wing structural diagram is shown in Figure 4-29 and the fuselage structural arrangement shown in Figure 4-30. Existing assets are noted where they are re-used.

Using the design criteria of Table 4-2, measured weights of existing components, and the estimating techniques generated for the XfV-12A prototype, an operational weight empty of 17,087 pounds was derived. This Operational Weight Empty (OWE) and a reserve of 400 pounds sump fuel were



The image contains two hand-drawn architectural sketches of a building, oriented vertically. The sketches are drawn with dashed lines on a grid background.

**Top Sketch (Side View):** This sketch shows the side profile of a building. It features a series of vertical lines representing walls and a curved line indicating a roof or a specific architectural feature. Annotations include "SIDE VIEW" and "20 X 40".

**Bottom Sketch (Front View):** This sketch shows the front elevation of the building. It includes a central entrance area with a small porch or overhang. Annotations include "FRONT VIEW" and "20 X 40".

Both sketches are accompanied by various dimension lines and numerical values, such as "500", "400", "300", "200", "100", and "50", which likely represent measurements in feet or meters. The sketches are oriented vertically, with the side view at the top and the front view at the bottom.

**Figure 4-23 Blended Wing Concept**

COL 20933A



**$V_{IAS}$  ~ 300 Knots or 0.6MN Whichever Is Less**  
**Sink Speed ~ 15 Feet/Second Maximum**  
**Symmetrical Pull-up ~ -1.0 to 3.0 G's**  
**Rolling Pull-out ~ 1.0 to 2.4 G's with Maximum Roll Rate ~ 100°/Second**  
**Gusts ~ 50 Feet/Second**  
**Altitude ~ 0 to 25,000 Feet**  
**50-Hour Maximum Engine Power**  
**CTOL Flying Qualities Per MIL-F-8785**  
**Transition and Conversion Flying Qualities Per MIL-F-83300**  
**Augmenter Components**

- 900° F
- 25 PSI Limit Internal
- 500-Hour Hot Life

COL 20934

Table 4-2. Design Criteria

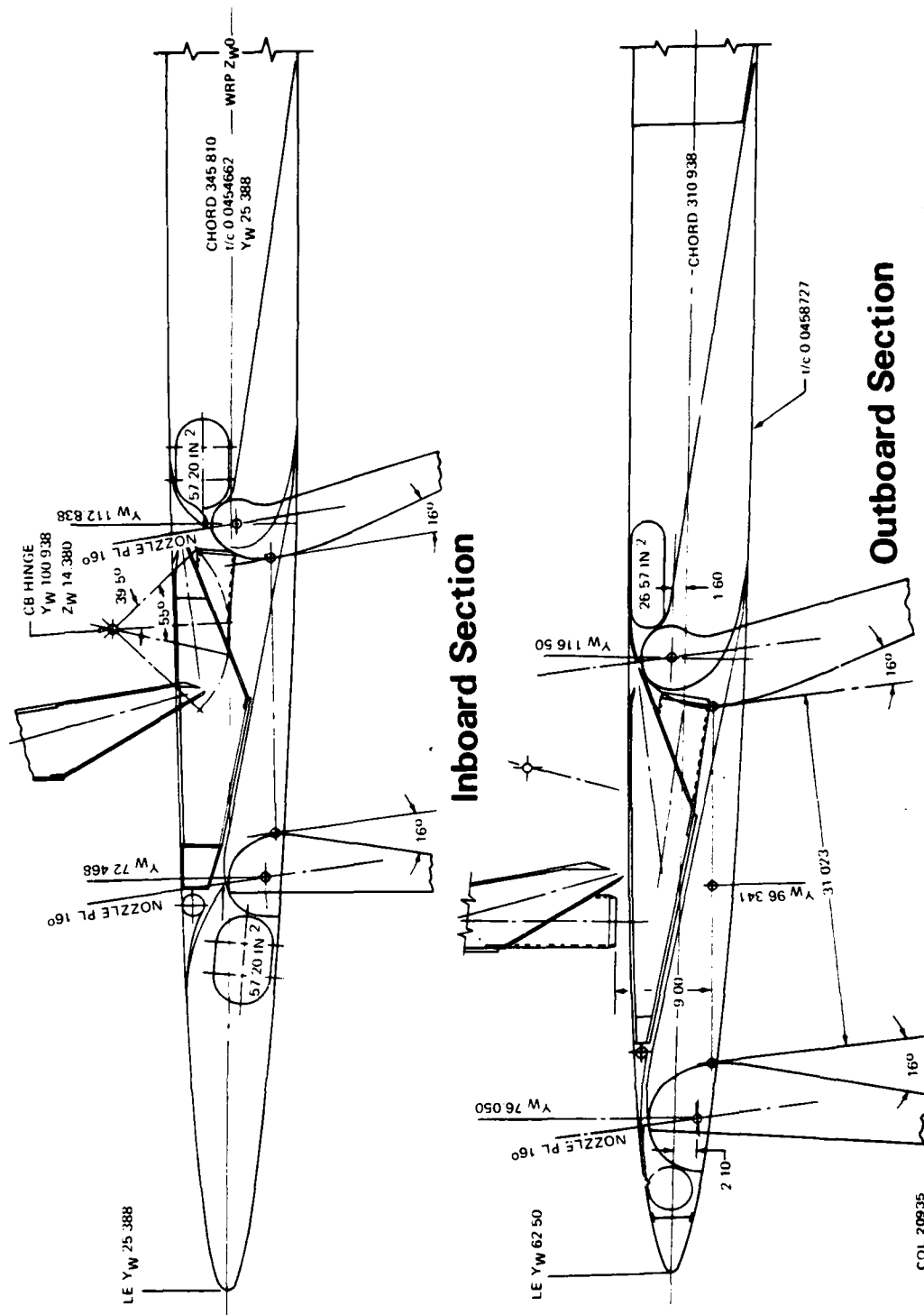


Figure 4-24. Forward Augmenter Cross-Sections

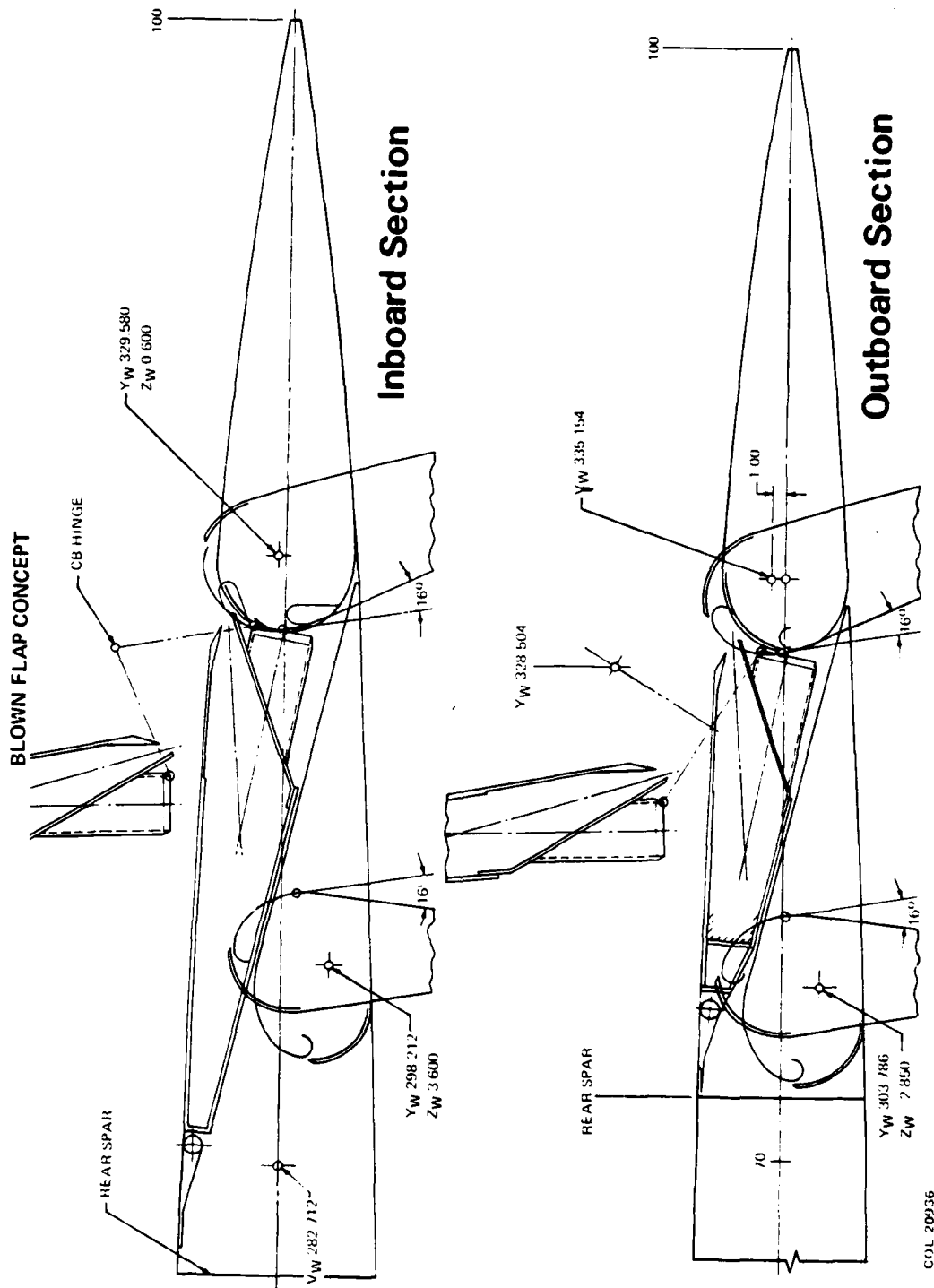


Figure 4-25. Aft Augmenter Cross-Sections





PARAMETER	BLENDED	CONTRACT
$A_2/A_0$	20.50	22.304
$A_0$ TOTAL	121.80 IN. <sup>2</sup>	121.37 IN. <sup>2</sup>
$A_0$ DISTRIBUTION	18-60-18	16.6-58.3-19.4
$A_2$	2497 IN. <sup>2</sup>	2707 IN. <sup>2</sup>
SPAN	123.997 IN.	108.80 IN.
$A_2$ LOCAL	20.137 IN.	25.20 IN.
L/D	1.69	1.25
Ro/t	12.00	DIFF 10.39 ELEV 12.075
SPIRAL-K	1.30	1.30
DUCT AREA:	---	---
• DIFFUSER	70.05 IN. <sup>2</sup>	50.27 IN. <sup>2</sup>
• C.B.	146.16 IN. <sup>2</sup>	140.6 IN. <sup>2</sup>
• ELEVON	70.05 IN. <sup>2</sup>	50.64 IN. <sup>2</sup>

Aft Augmenter

PARAMETER	BLENDED	TPA 175
$A_2/A_0$	13.80	13.600
$A_0$ TOTAL	145.0 IN. <sup>2</sup>	153.38 IN. <sup>2</sup>
$A_0$ DISTRIBUTION	18-60-18	15.5-63-15.5
$A_2$	2001 IN. <sup>2</sup>	2086 IN. <sup>2</sup>
SPAN	64.50 IN.	70.00 IN.
$A_2$ LOCAL	31.023 IN.	29.80 IN.
L/D	1.512	1.240
Ro/t	8.00	8.00
SPIRAL-K	1.60	DIFF 1.80 ELEV 1.20
DUCT AREA:	---	---
DIFFUSER	52.20 IN. <sup>2</sup>	90.00 IN. <sup>2</sup>
C.B.	174.0 IN. <sup>2</sup>	165.0 IN. <sup>2</sup>
ELEVON	58.0 IN. <sup>2</sup>	63.62 IN. <sup>2</sup>

Forward Augmenter

Table 4-3. XFFV-12B Augmenter Parameters



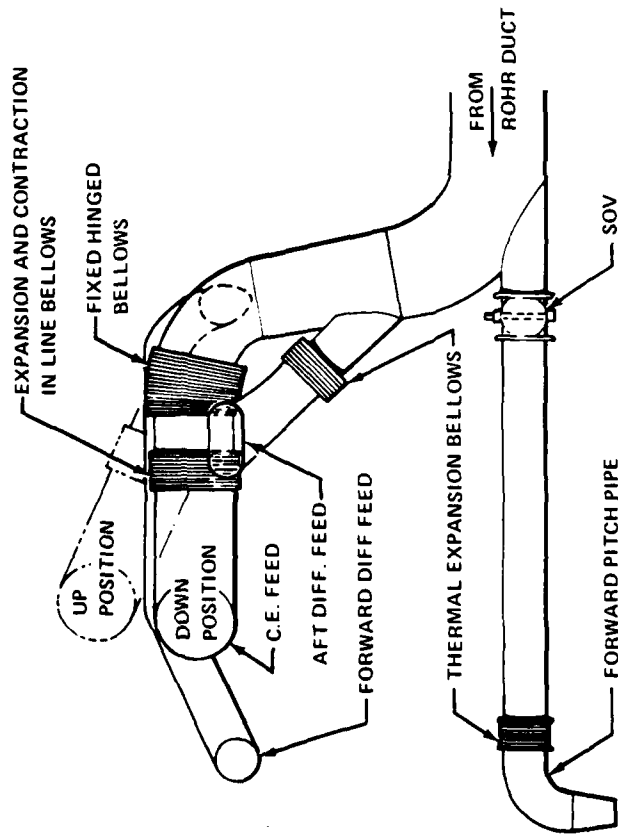
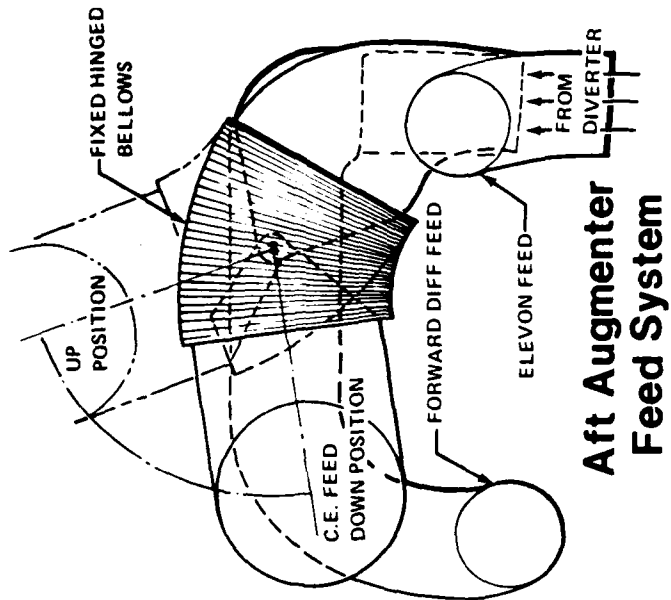


Figure 4-27 Ducting System

COL 20928

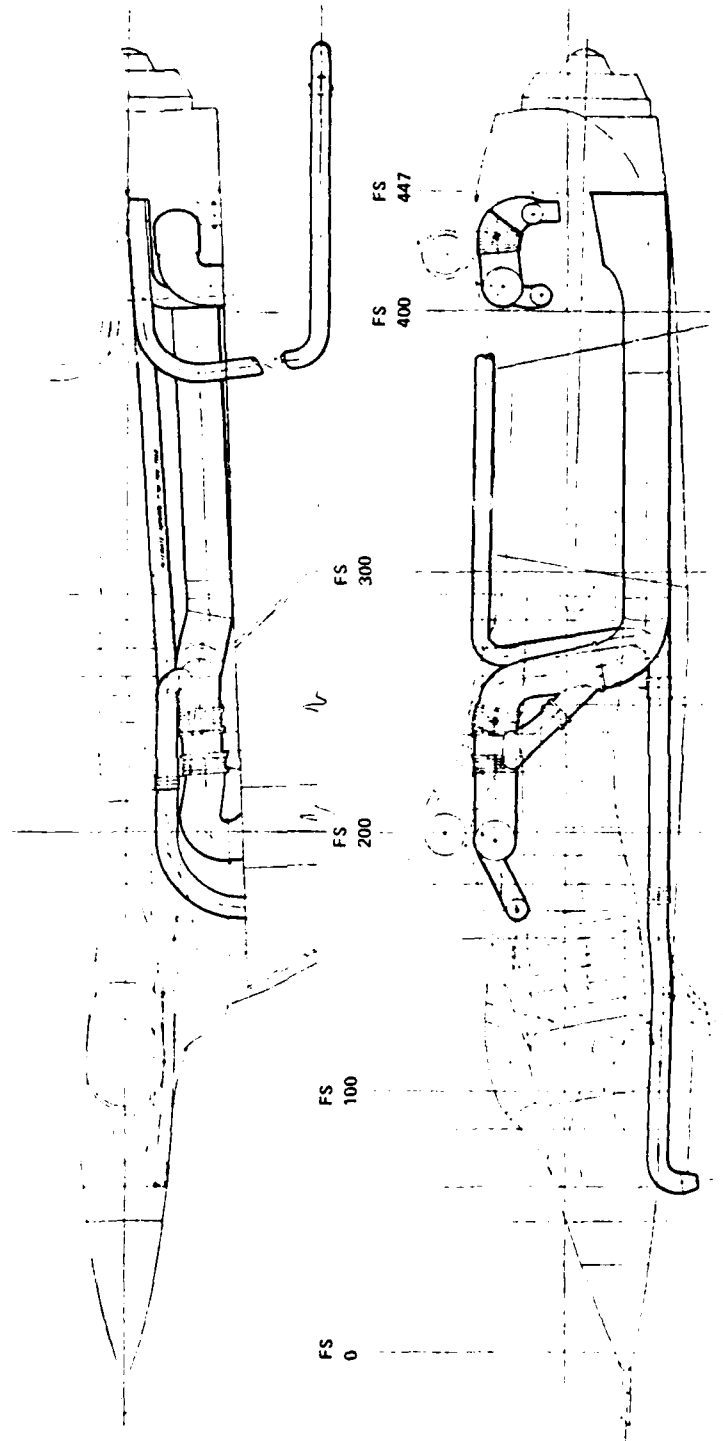


Figure 4-28 Ducting System

601 20940

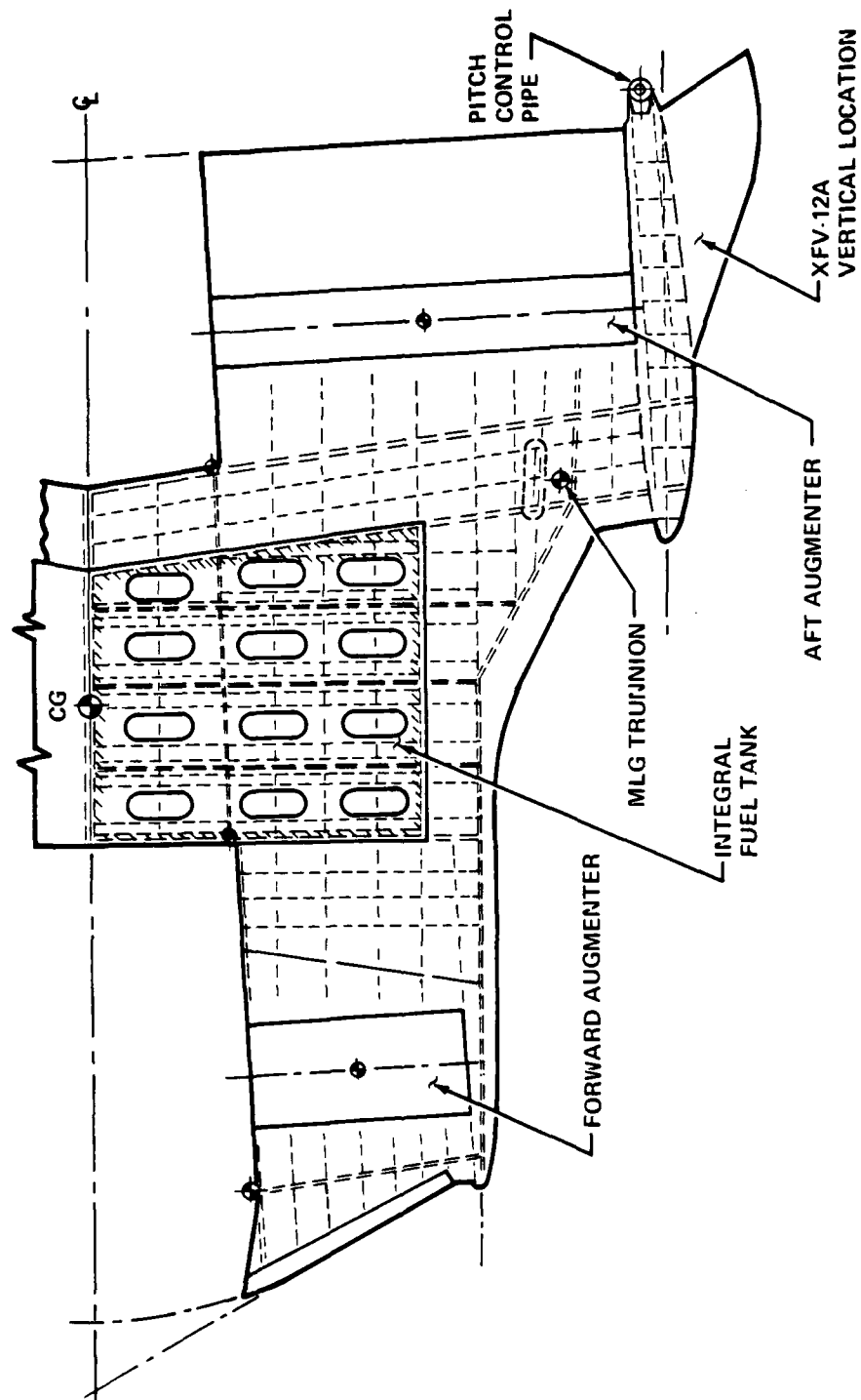


Figure 4-29 Wing Structure

COL 20926A

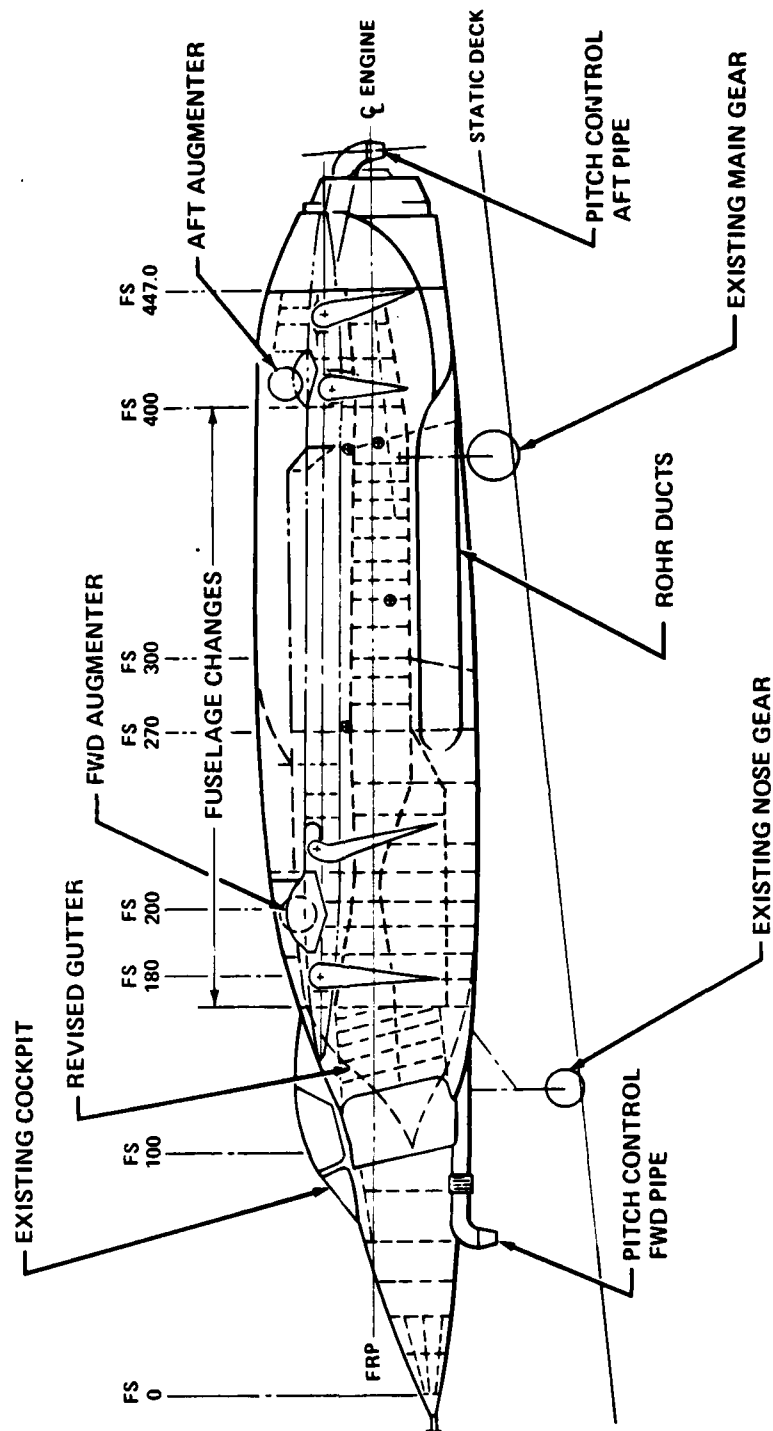


Figure 4-30 Fuselage Structure

COL 20931A

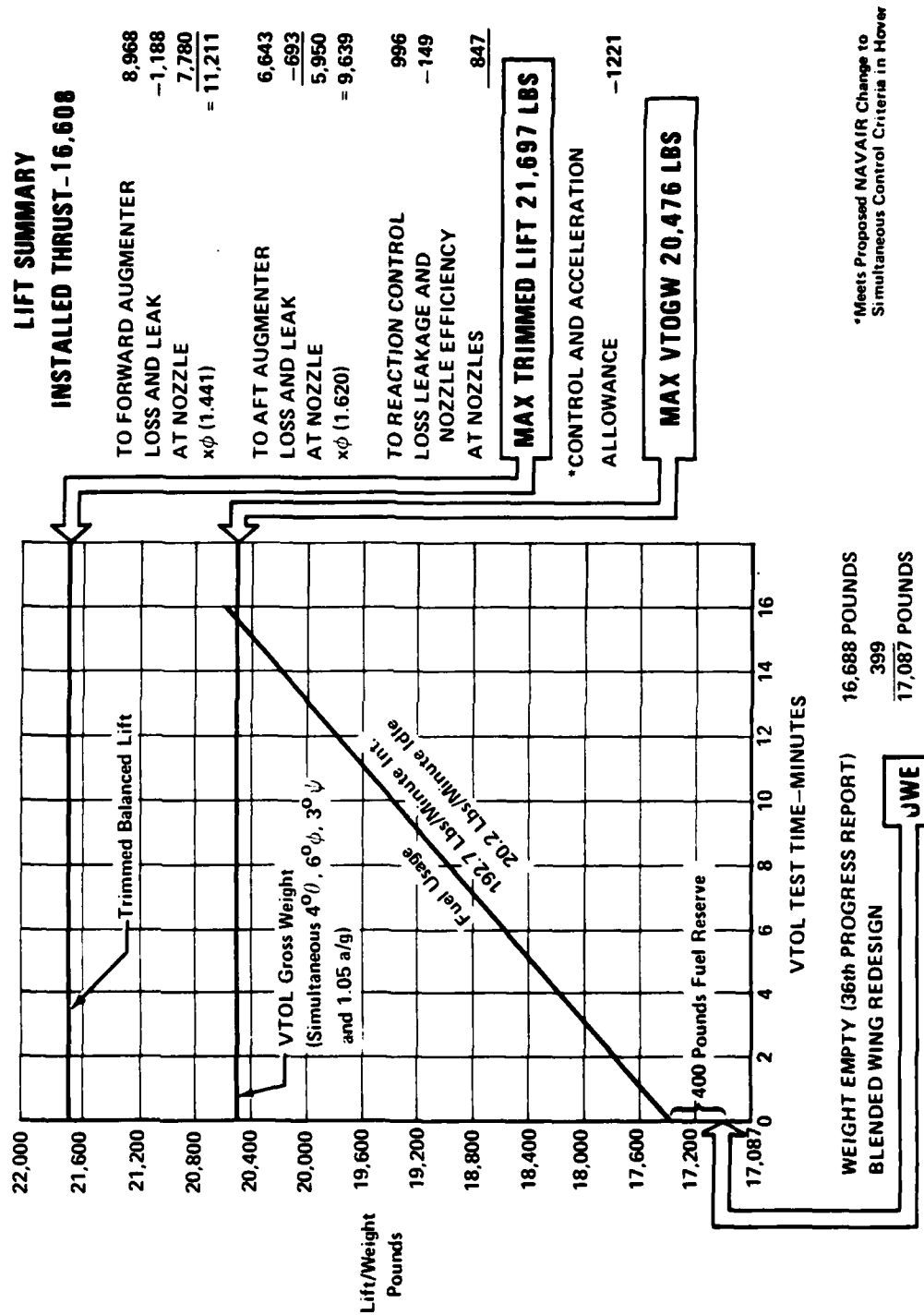


used to evaluate vertical hover time. Figure 4-31 summarizes the XFV-12B test aircraft lift using the duct loss techniques derived from the XFV-12A prototype Langley tests. A lift reserve of 1221 pounds is allocated for simultaneous control and vertical acceleration of 1.05 a/g. The resulting vertical takeoff gross weight of 20,476 pounds provides more than fifteen minutes of vertical hover time at intermediate engine power on a standard day, which is twice the test time originally predicted for the XFV-12A prototype.

#### 4.4.3 Rectangular Augmenter Study

A review of the estimated cost through full scale tests together with the Navy's concern for the level of transition performance of the blended wing configuration, precipitated a design study of incorporating rectangular augmenters in a configuration which maintained the current wing and canard surface locations. This configuration, designated the XFV-12C, was developed using the criteria of Table 4-2 and the design philosophy of the XFV-12B. To balance the canard area increase, an increase in the wing span was required to maintain longitudinal stability. The main gears were relocated inboard on the wing box to retain the wing-fuselage attach structure, reducing the wing anhedral angle to 8.8 degrees. A comparison of the XFV-12C configuration with the XFV-12A prototype configuration is presented in Figure 4-32. Packaging of the rectangular augmenters was approached with the same philosophy as described earlier. Figures 4-33 and 4-34 show the inboard and outboard sections of the resultant wing and canard augmenters. A symmetric centerbody nozzle was incorporated into this study for comparison and to obtain the highest vertical lift possible. A comparison of the augmentor parameters is shown in Table 4-4.

The ducting system shown in Figures 4-35 and 4-36 is very similar to the XFV-12B system except for the canard ducting. Installation of the canard ducting required the canard augmentor to be located outboard of the XFV-12A position. The structural arrangement of the wing and fuselage are shown in Figures 4-37 and 4-38. Modifications to the fuselage are less extensive than with the XFV-12B study but more complex in the canard attachment. Using the weight estimating procedure described earlier, an operational weight empty of 16,963 pounds was derived. The weight and 400 pounds of fuel reserve were used to evaluate vertical hover time of the XFV-12C. Figure 4-39 itemizes the XFV-12C test aircraft lift using the duct loss techniques derived from the XFV-12A test program. Because of the geometric relationships of the canard and wing augmenters, less wing lift is required to balance the same canard lift of the XFV-12B study; therefore, less total aircraft lift is developed. This geometric relationship also requires a higher lift allowance for simultaneous control and vertical acceleration for approximately the same weight. A comparison of the vertical hover time, with and without a reaction control system, is shown to confirm that the additional 1000 pounds of useable lift more than offsets the 300 pounds of additional weight (included in the OWE of 16,963) and system complexity.

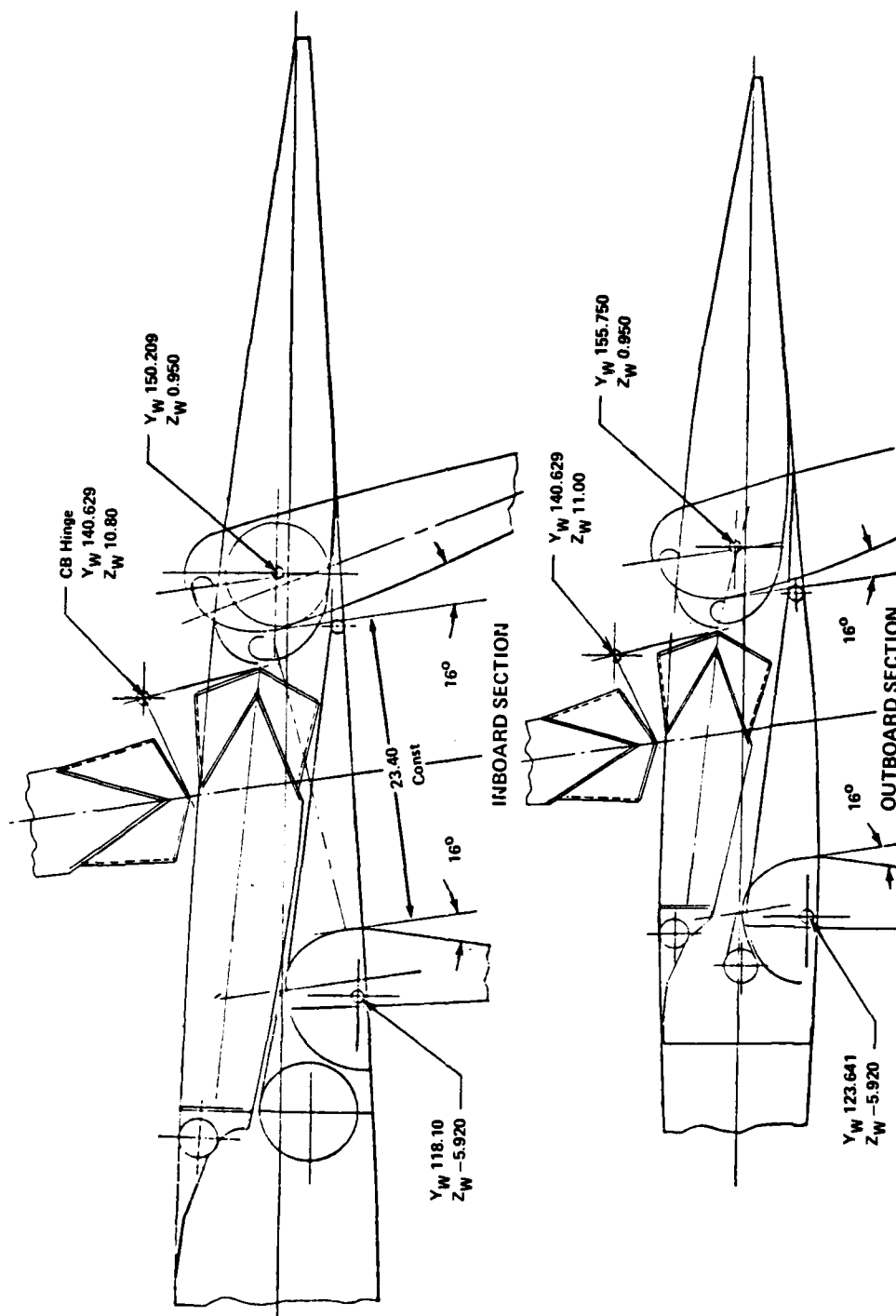


COL 20944A

Figure 4-31 Summary of Expected Test Mission Performance

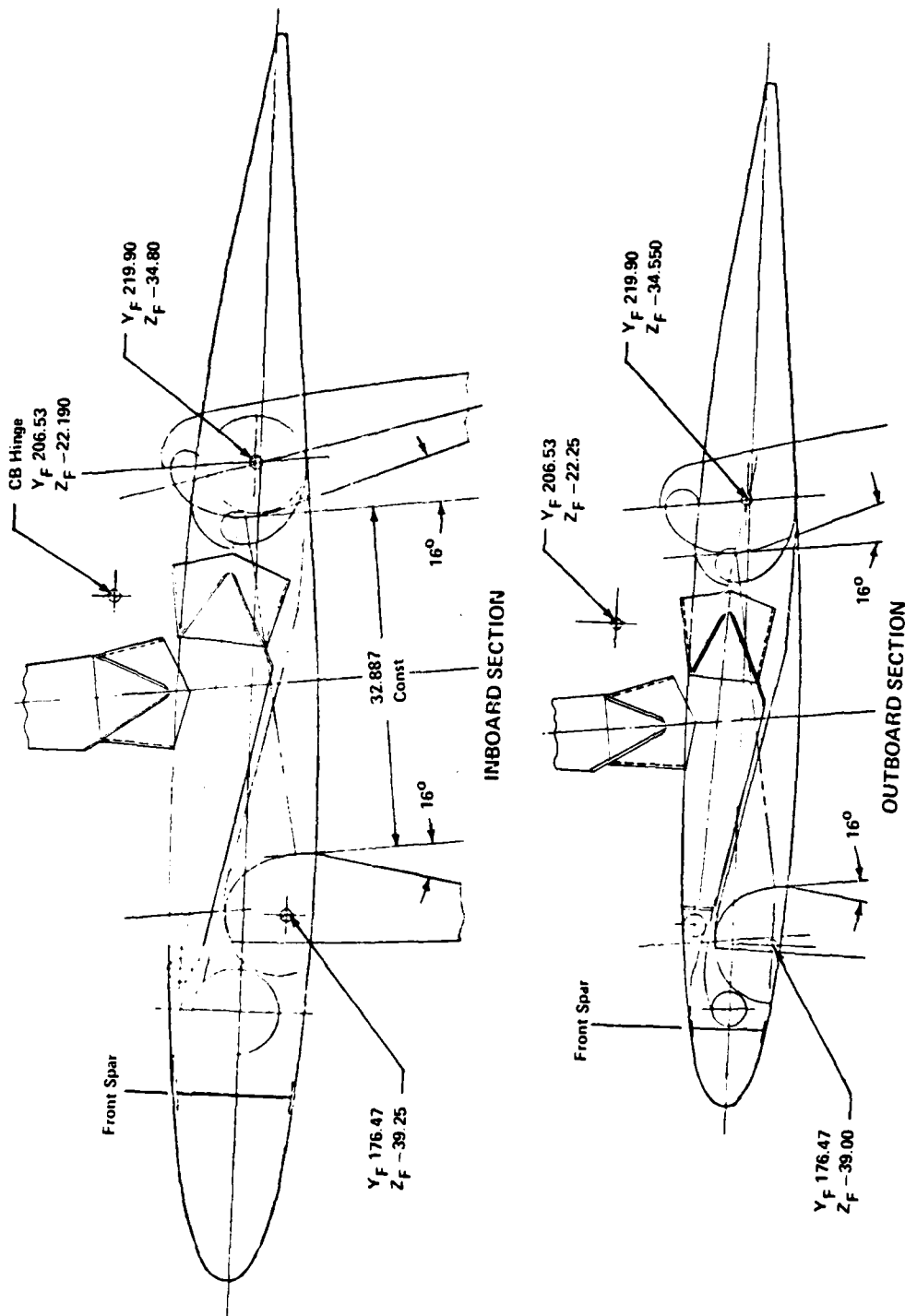


**Figure 4-32 Rectangular Augmenters**



COL 22300

Figure 4-33. Wing Augmenter Cross-Sections



COL 22301

Figure 4-34. Canard Augmenter Cross-Sections



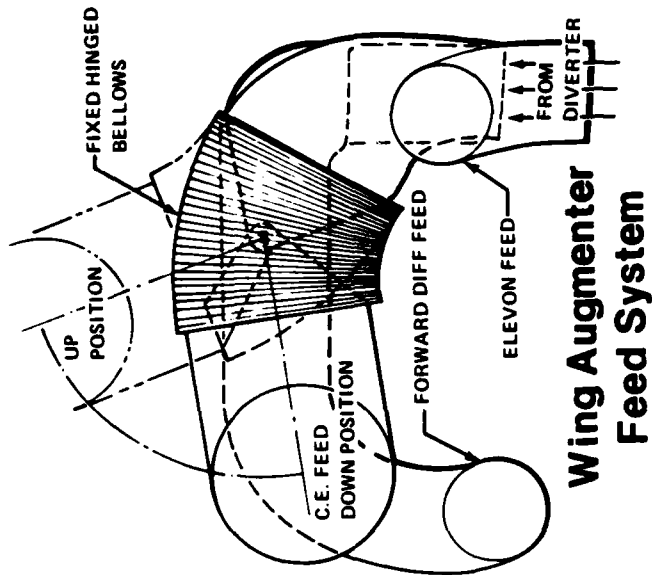
PARAMETER	XFV-12C	TPA 175
$A_2/A_0$	13.800	13.600
$A_0$ TOTAL	153.70 IN. <sup>2</sup>	153.38 IN. <sup>2</sup>
$A_0$ DISTRIBUTION	18-60-18	15.5-63-15.5
$A_2$	2121.21 IN. <sup>2</sup>	2086 IN. <sup>2</sup>
SPAN	64.50 IN.	70.00 IN.
$A_2$ LOCAL	32.887 IN.	29.80 IN.
L/D	1.242	1.240
$R_0/t$	8.00	8.00
SPIRAL-K	1.60	DIFF 1.80 ELEV 1.20
DUCT AREA:	--	--
DIFFUSER	55.332 IN. <sup>2</sup>	90.00 IN. <sup>2</sup>
C.B.	184.44 IN. <sup>2</sup>	165.0 IN. <sup>2</sup>
ELEVATOR	55.332 IN. <sup>2</sup>	63.62 IN. <sup>2</sup>

Forward Augmenter

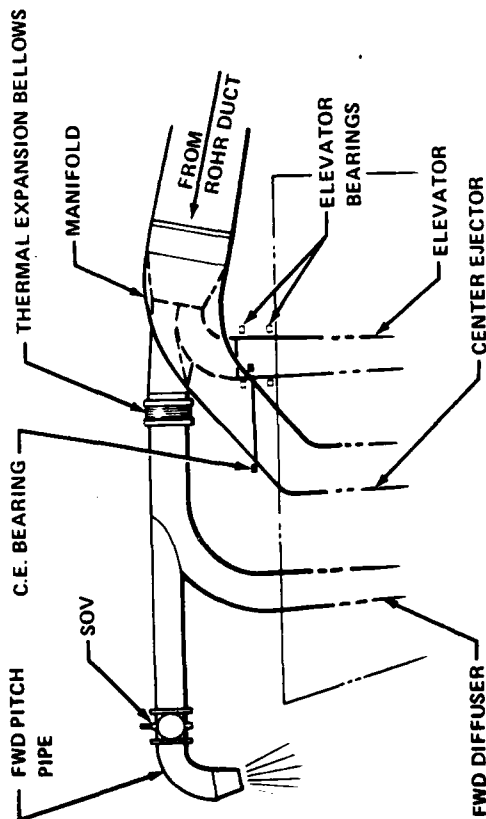
PARAMETER	XFV-12C	CONTRACT
$A_2/A_0$	20.50	22.304
$A_0$ TOTAL	136.30 IN. <sup>2</sup>	121.37 IN. <sup>2</sup>
$A_0$ DISTRIBUTION	18-60-18	16.6-58.3-19.4
$A_2$	2794 IN. <sup>2</sup>	2707 IN. <sup>2</sup>
SPAN	118.428	108.80 IN.
$A_2$ LOCAL	23.59 IN.	25.20 IN.
L/D	1.69	1.25
$R_0/t$	12.00	DIFF 10.39 ELEV 12.075
SPIRAL-K	1.30	1.30
DUCT AREA:	--	--
• DIFFUSER	49.07 IN. <sup>2</sup>	50.27 IN. <sup>2</sup>
• C.B.	163.56 IN. <sup>2</sup>	140.6 IN. <sup>2</sup>
• ELEVON	49.07 IN. <sup>2</sup>	50.64 IN. <sup>2</sup>

Aft Augmenter

Table 4-4. Xfv-12C Augmenter Parameters



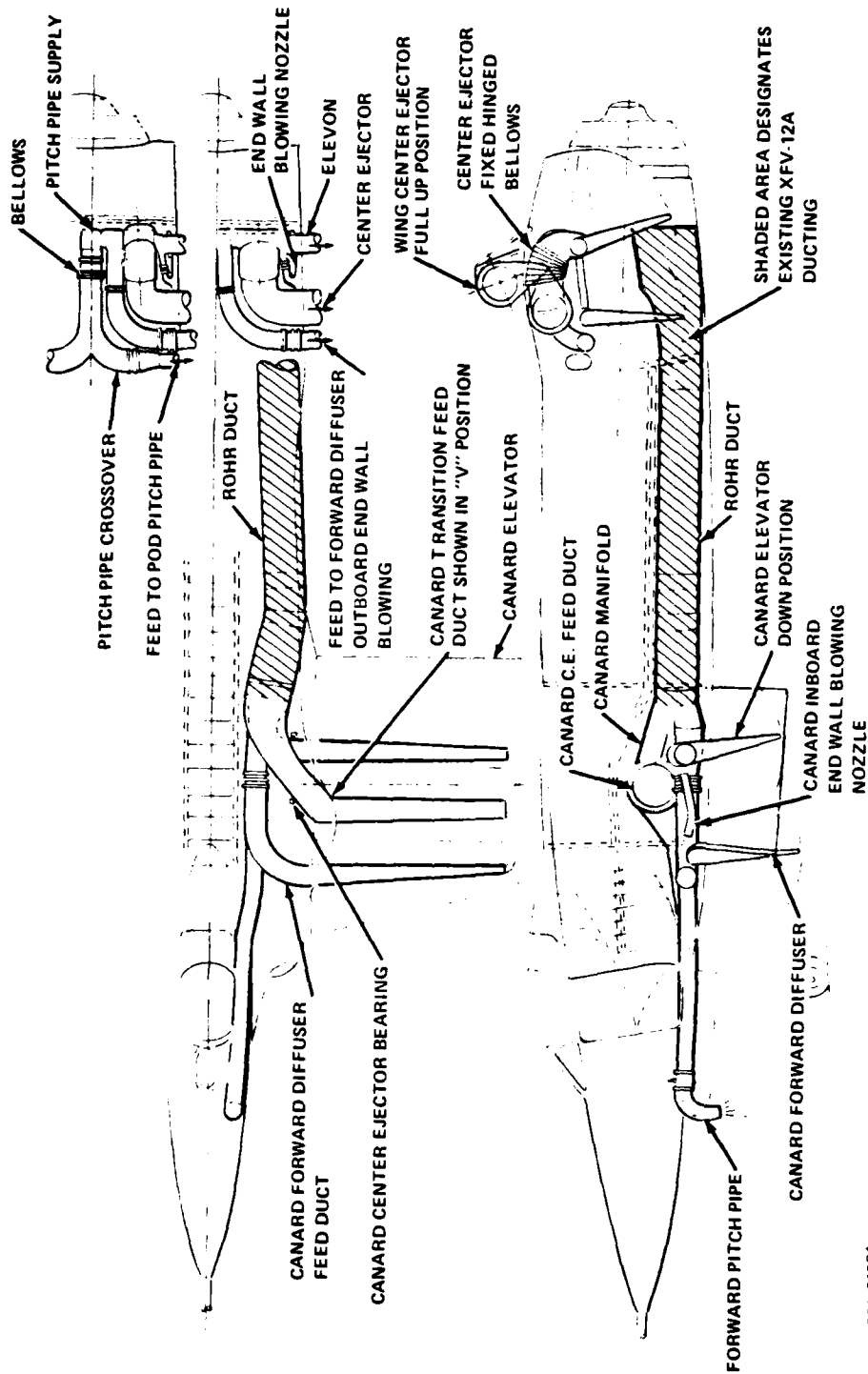
### Wing Augmenter Feed System



### Canard Augmenter Feed System

Figure 4-35 Ducting System

COL 21523



COL 21524

Figure 4-36. Ducting System

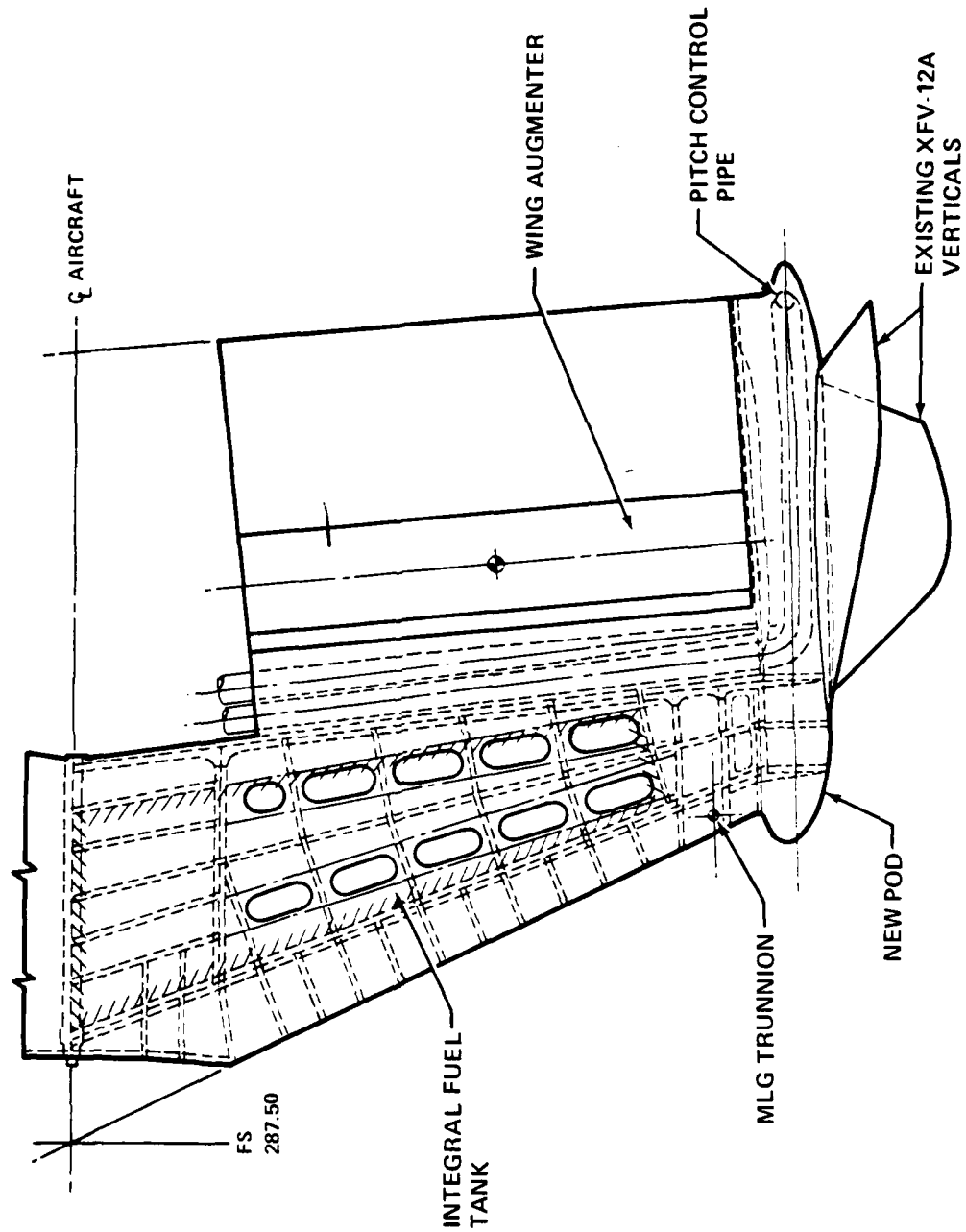


Figure 4-37 Wing Structure

COL 21375

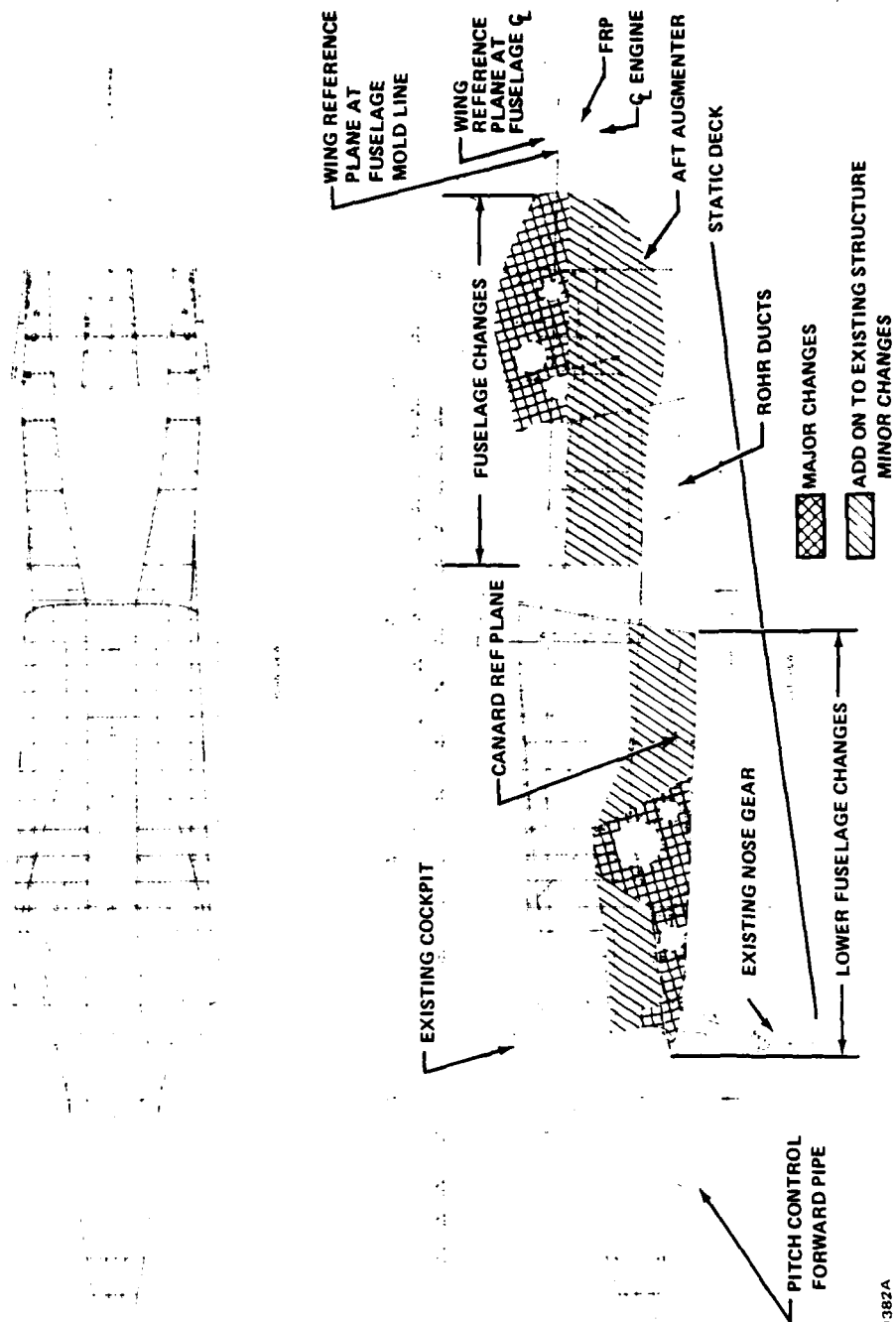
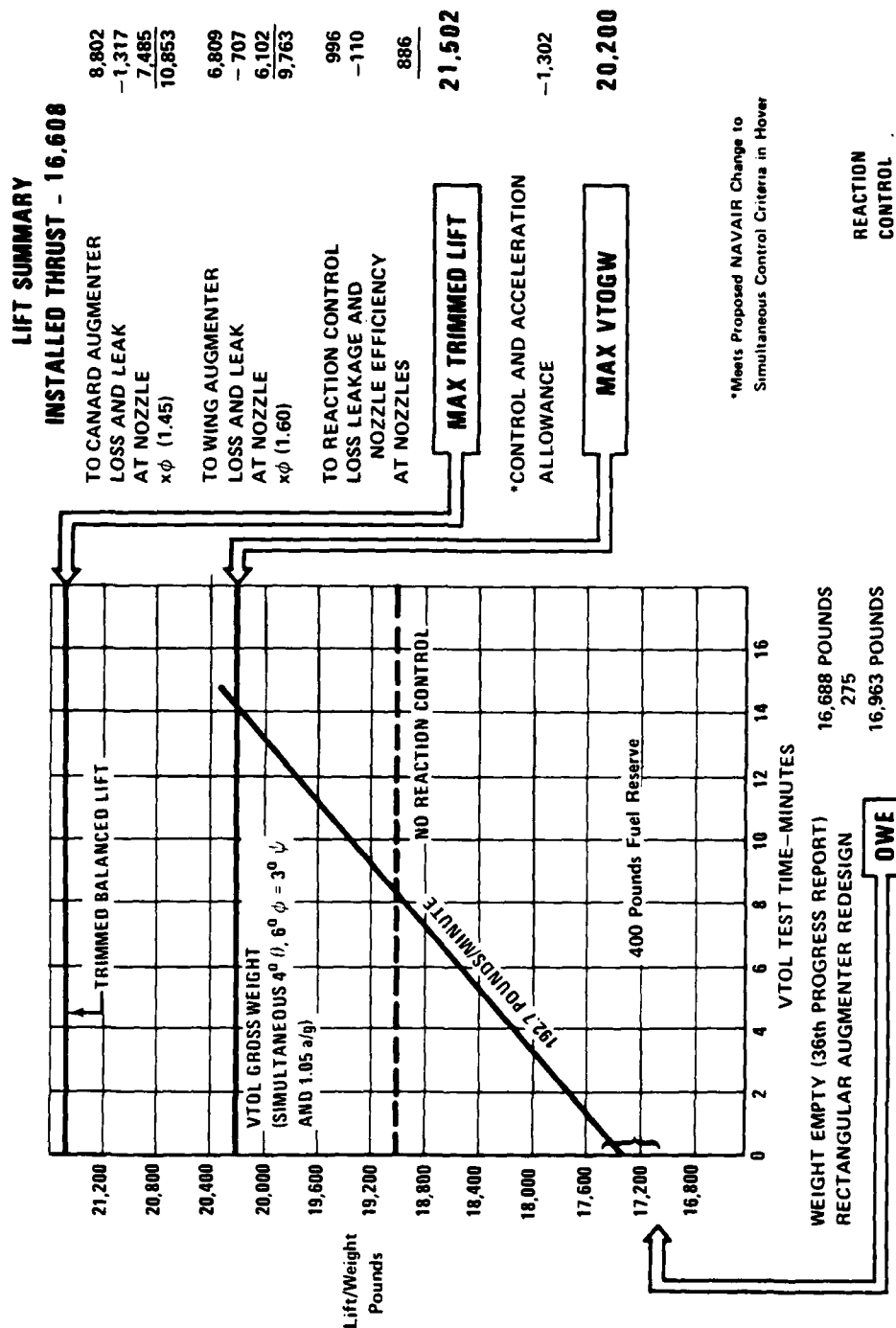


Figure 4-38 Fuselage Structure

COL 21382A





COL 21512B

Figure 4-39 Summary of Expected Test Mission Performance - XFV-12C



#### 4.5 SUMMARY

Detailed studies have shown that high performance thrust augmenters can be incorporated into a supersonic aircraft configuration with mission performance comparable with existing fleet aircraft. An empirical, analytical, and design data base has been generated that can evaluate the sensitivities of configurations and provide explicit guidelines to the designers.

High performance Coanda shapes can be incorporated into thin airfoil shapes necessary for supersonic flight. Design criteria have been established which provides the designer the necessary information to establish coanda/flap shapes that will support augmentation values ( $\emptyset$ ) in excess of 1.60.

Centerbody nozzle configurations can be integrated into the wing augmenters that will provide augmentation values over a range of 1.46 to 1.64.

The capability to package rectangular augmenters in a viable demonstrator configuration exists as shown by either study - the XFV-12B or the XFV-12C. Technical concerns exist for both configurations; however, the XFV-12B configuration is more representative of an operational configuration. The level of performance during transition from vertical flight to conventional flight is the primary concern for this configuration and should be demonstrated prior to development. The XFV-12B configuration has the highest vertical lift capability along with excellent ground effects, reingestion, and control characteristics and provides the pilot the greatest peripheral vision during vertical flight. The XFV-12C configuration's transition performance capability has been demonstrated by comparison; however, the level of vertical lift capability in ground effect is unknown and should be demonstrated prior to development.



## 5.0 MODELING

### 5.1 GENERAL

In order to compensate for the deficiencies of any experiment and the limitations of any analysis, the ejector development effort was carried out using both these tools. Numerical simulation was used to study the development of the jets from proposed centerbody nozzles and to predict the ideal pressure distributions on the ejector shroud. Scale model tests were used to verify predicted performance trends and to provide data for checking and improving the analytical methods. However, since the ejector and the analysis were being developed simultaneously, discrepancies between calculation and measurement were studied critically, in order to identify practical limits on ejector performance, as well as theoretical deficiencies.

Both the numerical and experimental models employed in the XfV-12A development program are presented here. In this section, the analytical methods used for predicting the entrainment of the turbulent jets and the pressure distribution on the ejector flaps are described. The ejector scaling parameters and the experimental apparatus and test procedures are also presented.

### 5.2 NUMERICAL MODELS

In order to compute the thrust augmentation without solving the full Navier-Stokes equations, some approximations must be made. The classical approach utilizes streamwise integration of the governing equations to determine the augmentation as a function of the jet mixing rate. The solution is obtained by iterating on the inlet velocity until the exhaust pressure matches the ambient pressure outside the ejector. This approach formed the basis of the method used for analyzing the development of the jets from various nozzles. However, it was necessary to devise an approach based on airfoil theory in order to calculate the surface pressure distribution on the airfoil flap. Both methods of analysis will be described in this section.

#### 5.2.1 JET MIXING ANALYSIS

In order to predict the jet flow fields which develop from the complex nozzles being studied, it is necessary to determine the solution for a turbulent, three-dimensional velocity and pressure field. Considerable savings in computer storage and running time were achieved by utilizing a procedure developed by Patankar and Spalding (1972), Reference (7) to reduce solution of the original boundary value problem to an initial value problem which may be solved by streamwise marching procedures. Since there is a primary direction of flow (through the ejector), the streamwise velocity component is considered to be driven by a mean pressure  $\bar{p}(x)$ , which is decoupled from the perturbation pressures,  $p'(x,y,z)$  in the



transverse planes. In addition, the gradients of the normal stresses are neglected. Under these assumptions, the governing equations in Cartesian coordinates become

#### Equation of State

$$\rho = \frac{\bar{P}}{RT}$$

#### Continuity

$$\frac{\partial}{\partial X} (\rho U) + \frac{\partial}{\partial Y} (\rho V) + \frac{\partial}{\partial Z} (\rho W) = 0$$

#### Momentum

$$\begin{aligned} \frac{\partial}{\partial X} (\rho U^2) + \frac{\partial}{\partial Y} (\rho UV) + \frac{\partial}{\partial Z} (\rho UW) &= \frac{\partial \tau_{YX}}{\partial Y} + \frac{\partial \tau_{ZX}}{\partial Z} - \frac{\partial \bar{P}}{\partial X} \\ \frac{\partial}{\partial X} (\rho UV) + \frac{\partial}{\partial Y} (\rho V^2) + \frac{\partial}{\partial Z} (\rho VW) &= \frac{\partial \tau_{YY}}{\partial Y} + \frac{\partial \tau_{ZY}}{\partial Z} - \frac{\partial \bar{P}}{\partial Y} \\ \frac{\partial}{\partial X} (\rho UW) + \frac{\partial}{\partial Y} (\rho VW) + \frac{\partial}{\partial Z} (\rho W^2) &= \frac{\partial \tau_{YZ}}{\partial Y} + \frac{\partial \tau_{ZZ}}{\partial Z} - \frac{\partial \bar{P}}{\partial Z} \end{aligned}$$

#### Energy

$$\frac{\partial}{\partial X} (\rho UH) + \frac{\partial}{\partial Y} (\rho VH) + \frac{\partial}{\partial Z} (\rho WH) = \frac{\partial}{\partial Y} \left( \frac{\mu_t}{Pr} \frac{\partial H}{\partial Y} \right) + \frac{\partial}{\partial Z} \left( \frac{\mu_t}{Pr} \frac{\partial H}{\partial Z} \right)$$

Here,  $U, V, W$ , are the time averaged velocity components and the  $\tau_{ij}$  are the turbulent shear stresses.

The turbulent stresses were related to the mean velocity gradient according to the usual eddy viscosity assumption (Schlichting 1968), Reference (8). The eddy viscosity was calculated using the turbulence kinetic energy model of Launder and Spalding (1974), Reference (9). According to this model, the eddy viscosity is assumed to be a function of the turbulence kinetic energy,  $k$ , and its rate of dissipation,  $\epsilon$ . Dimensional analysis gives

$$\mu_t = C_\mu \frac{\rho k^2}{\epsilon}$$

in which  $C_\mu$  is a constant. The transport equations for  $k$  and  $\epsilon$  are

$$\frac{\partial (\rho U k)}{\partial X} + \frac{\partial (\rho V k)}{\partial Y} + \frac{\partial (\rho W k)}{\partial Z} = \frac{\partial}{\partial Y} \left( \frac{\mu_t}{\sigma_k} \frac{\partial k}{\partial Y} \right) + \frac{\partial}{\partial Z} \left( \frac{\mu_t}{\sigma_k} \frac{\partial k}{\partial Z} \right) + \mu_t \left[ \frac{\partial U}{\partial Y} \right]^2 + \frac{\partial U}{\partial Z} \left[ \frac{\partial U}{\partial Y} \right]^2 - \rho \epsilon$$

$$\frac{\partial (\rho U \epsilon)}{\partial X} + \frac{\partial (\rho V \epsilon)}{\partial Y} + \frac{\partial (\rho W \epsilon)}{\partial Z} = \frac{\partial}{\partial Y} \left( \frac{\mu_t}{\sigma_\epsilon} \frac{\partial \epsilon}{\partial Y} \right) + \frac{\partial}{\partial Z} \left( \frac{\mu_t}{\sigma_\epsilon} \frac{\partial \epsilon}{\partial Z} \right) + c_1 \mu_t \left[ \frac{\partial U}{\partial Y} \right]^2 + \frac{\partial U}{\partial Z} \left[ \frac{\partial U}{\partial Y} \right]^2 - c_2 \rho \epsilon \left( \frac{\epsilon}{k} \right)$$



The values of the constants,  $C_\mu$ ,  $\sigma_k$ ,  $\sigma_\epsilon$ ,  $C_1$ ,  $C_2$ , suggested by Launder and Spalding were also used here.

These equations were put in finite difference form by integrating them over a control volume surrounding a typical grid point. A more complete description of this procedure and an illustration of its use has been given by DeJooode and Patankar (1978), Reference (10).

Since these equations are solved by streamwise integration, initial values of all the flow variables must be specified in order to start the calculation. The initial jet velocity was calculated from the isentropic velocity at the specified pressure ratio. It was assumed that the internal, viscous losses were the same for each nozzle, so that the same velocity coefficient,  $C_v = 0.925$  was used in each case. Because most of the nozzles to be studied employ some jet deflection to generate hypermixing vortices, the initial, calculated jet velocity vector is inclined to the ejector axis. Thus, the predictions of ejector thrust augmentation due to increased mixing are balanced against the tilt loss in the primary jet thrust. The angularity of the Coanda jets and secondary entrained flow is similarly treated.

The initial value of the turbulence kinetic energy is expressed as a fraction of the mean flow energy,

$$k = C_k U_j^2$$

and the initial dissipation rate is assumed to be proportional to the rate of energy addition by the jet

$$\epsilon = C_\epsilon U_j^3 / t$$

in which  $U_j$  and  $t$  are the initial values of the jet velocity and width. The values of  $C_k$  and  $C_\epsilon$  were determined from available data. As reported by Tennekes and Lumley (1972), Reference (11), measurements in many jet and wake flows indicate that the turbulence energy is correlated with the turbulent stress,

$$k = \overline{u'v'} / 0.4$$

In self preserving flows, the turbulent stress is proportional to the mean velocity. The maximum stress is given by

$$\overline{u'v'} = U_j^2 / R_T e^{\frac{1}{2}}$$

in which  $R_T$  is an empirical constant which depends on the type of flow; for plane jets,  $R_T = 26$ . Combining these relations yields  $C_k = 0.06$ . Similarly, the dissipation in self preserving flows is given by

$$\epsilon = U_j^3 / t R_T e^{\frac{1}{2}}$$



which yields  $C_e = 0.02$ . Additional details regarding the initial conditions subroutine have been given by Mefferd and Bevilaqua (1978) Reference (12).

The computational time required to obtain a solution for a typical ejector configuration is on the order of 15 minutes. However, it originally took more than 20 man-hours to set up the finite difference grid and specify all the values of the velocity and turbulence components at each grid point. In order to reduce this time and eliminate the arbitrariness in the grid specification, a computer code was developed as part of the XFV-12A program to generate this information from the basic ejector geometry and specified grid spacing rules. The interactive capabilities of the CYBER 176 computer and the Tektronic 4014 graphics terminal can be utilized to modify the grid, if desired. The grid generated for a typical multi-lobe nozzle is shown in Figure 5-1. The high grid density required in the wall jets is apparent. Because the nozzle is periodic along the ejector span, symmetry planes are used as computational boundaries. Details of this code and a step-by-step procedure for its use are given by Long (1981), Reference (13). Use of this code has reduced the set-up time to less than an hour.

The thrust augmentation ratio,  $\phi$ , is evaluated from the calculated momentum flux at the ejector exit. The iteration procedure is converged to within  $\Delta\phi = \pm 0.02$ . Greater accuracy could have been achieved at some cost in computer running time, but differences in augmentation of this magnitude were comparable to the experimental error.

#### 5.2.2 EJECTOR POTENTIAL FLOW ANALYSIS

The increase in thrust that results from the turbulent mixing of the primary jet and secondary streams appears as a reaction force on the ejector shroud. The reaction force is the integral of the surface pressure distribution on the shroud. In order to evaluate the measured pressure distribution it is necessary to compute the ideal pressure distributions. A method for calculating these distributions will be described in this section.

The shroud can be described as "flying" in the velocity field of the flow entrained by the jet, thus, it experiences a force analogous to the lift developed on a wing fixed in a moving stream. The circulation generated around each section of the ejector shroud can be calculated by solving a system of equations which specify that the shroud must be a streamline of the flow induced by the entrainment of the jets. For this calculation, the strengths of the sinks which represent each jet are considered to be known. These strengths can be determined from the turbulent mixing of the jets computed in the viscous solution previously discussed, or from experimental data.

A potential flow solution for the ejector wing has been obtained by replacing the shroud elements and jets with equivalent flow singularities. The flow is assumed to be irrotational, incompressible and attached. Since the flow satisfies Laplace's equation, the flow

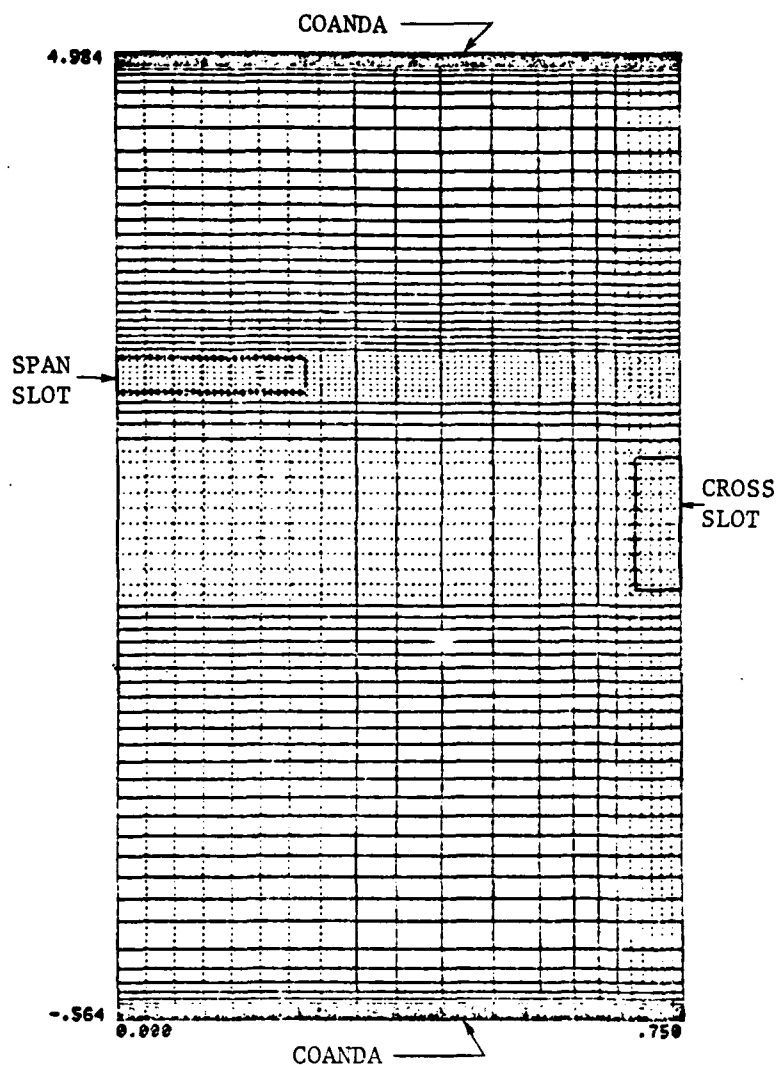


Figure 5-1 Computational Grid for Cross-Slot - Span Slot Centerbody Configuration

velocities at any field point may be obtained by superimposing the induced velocity due to all the flow singularities. The tangential and normal components of the resultant velocity at the panel control points may be expressed as follows:

$$V_{tj} = \sum A_{sj1} \sigma_1 + \sum A_{vj1} \gamma_1$$

$$V_{nj} = \sum B_{sj1} \sigma_1 + \sum B_{vj1} \gamma_1$$

where  $\sigma$  and  $\gamma$  are the source and vortex strengths respectively and  $A_s$ ,  $A_v$ ,  $B_s$ ,  $B_v$  are the influence coefficients which depend only upon panel geometry.



The shroud surfaces are shown in Figure 5-2 to be represented by a series of curved parabolic panels. The continuous distribution of flow singularity densities corresponding to an exact distribution is approximated by piecewise linear distributions of both source and vortex densities on each curved panel. The sink strengths and distributions are used to simulate jet entrainment. Vortex densities are the only unknowns in this potential flow formulation and these can be determined by appropriate boundary conditions on the ejector wing elements.

Application of the Newman boundary condition, that is, specifying the normal velocity at each control point of the panel elements, results in a system of linear equations in the unknown vortex strengths,  $\gamma$ . Having determined the singularity strengths by solving these equations, the panel velocities, pressures and off body velocities can then be obtained. Details of this inviscid solution for an ejector wing were presented by Bevilaqua and DeJooe (1978), Reference (1), for the static case, and by Bevilaqua, Woan, and Schum (1981), Reference (14), for the case of an ejector in forward flight.

### 5.3 EJECTOR SCALING LAWS

Although numerical simulation facilitates the development of some ejector components, the complexity of the ejector flow field requires that complementary testing be performed during the development process. There are some advantages to performing these tests with full size components and hot gas jets but, for reasons of cost and convenience, small scale models driven by cold air jets were used. While such models can only approximate the performance of full size ejectors, the approximation can be quite close if the appropriate scaling laws are satisfied. The purpose of this section is to discuss the requirements for ejector scaling and to show that analysis and scale model testing can be used to design full size ejectors.

In order to set up a meaningful test, the fundamental parameters on which the thrust augmenting force depends must be identified. If it is assumed that this force is a function of the jet thrust, the ejector duct geometry, and the physical properties of the fluid, dimensional analysis yields for the scaling law

$$F/T = f (Re, M, L/W, \delta_F)$$

in which the force coefficient,  $F/T$ , is the ratio of the augmenting force to the jet thrust,  $Re$  and  $M$  are the jet Reynolds number and Mach number, and  $L/W$  and  $\delta$  give the length to width ratio and diffuser half angle of the ejector duct. The force coefficient also depends on the surface roughness and ambient turbulence level, but these parameters should be controlled to insure that their effect is small. Temperature effects are usually assumed to be implicit in the variation of the Mach and Reynolds numbers; however, there is an additional effect of temperature on the turbulent mixing which will be discussed separately.



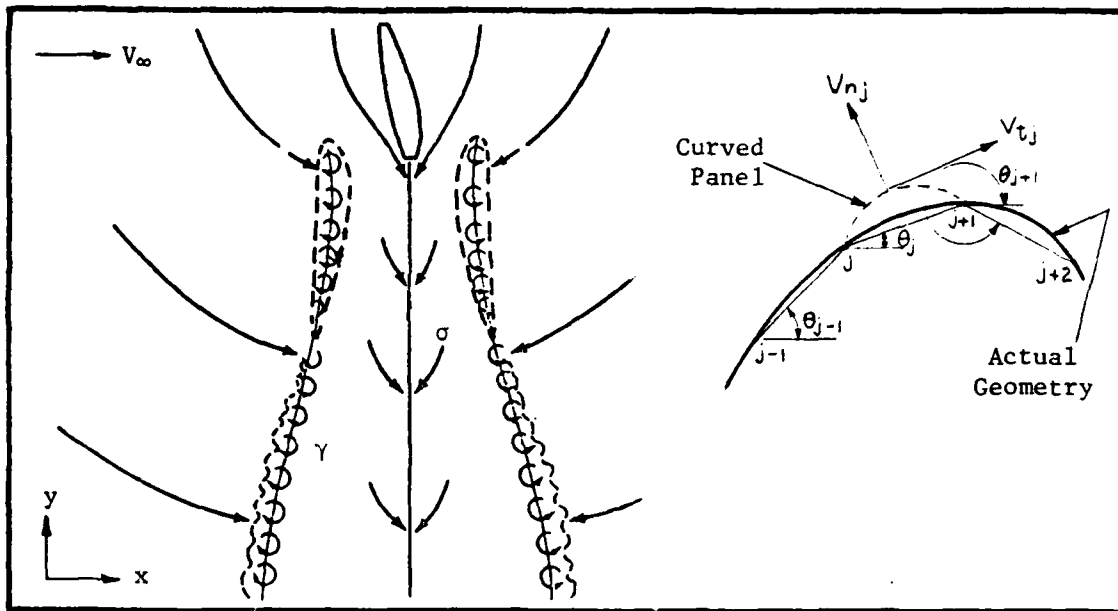


Figure 5-2 Mathematical Model of the Ejector Wing

The geometry of a scale model can be made to duplicate the full size prototype, but it is not possible to simultaneously match the Mach and Reynolds numbers of the prototype. For example, if the Mach numbers are matched, then the change in scale means the model Reynolds number will be smaller. Similarly, if the Reynolds numbers are matched by increasing the model velocity, then the model Mach number will be larger. However, because the velocity of the prototype jet is large ( $M > 1$ ), the Reynolds number is also large ( $Re \approx 10^6$ ); consequently, the flow is turbulent and the effects of viscosity are small. In this case, changes in the Reynolds number only affect the very smallest scales of the turbulence, which do not interact directly with the main flow. According to this principle of asymptotic invariance, the Reynolds number is not a relevant parameter if its value is large.

Therefore, if the Mach numbers are matched and the Reynolds numbers are large, scale model tests can be used to determine the variation of ejector thrust with nozzle geometry and diffuser angle for a given ejector configuration. On the other hand, the angle at which the flow separates, and other phenomena related to the exact details of the viscous stresses, are dependent on the Reynolds number. Thus, unless the Reynolds number is matched, model values of the separation angle cannot always be used to predict full scale separation angles. However, separation will occur at a smaller angle on the scale model, so that assuming that the prototype separates at the same angle as the model will be conservative.



As previously noted, the first order effects of temperature on the physical properties of the jet (density, viscosity, and compressibility) are implicit in scaling the Mach and Reynolds numbers. In particular, the variation of Reynolds number with temperature is shown in Figure 5-3. The effect of reducing the jet temperature by 1000°F, as in the present case, does not change the order of magnitude of the Reynolds number or the turbulent character of the flow. On the other hand, the Mach number

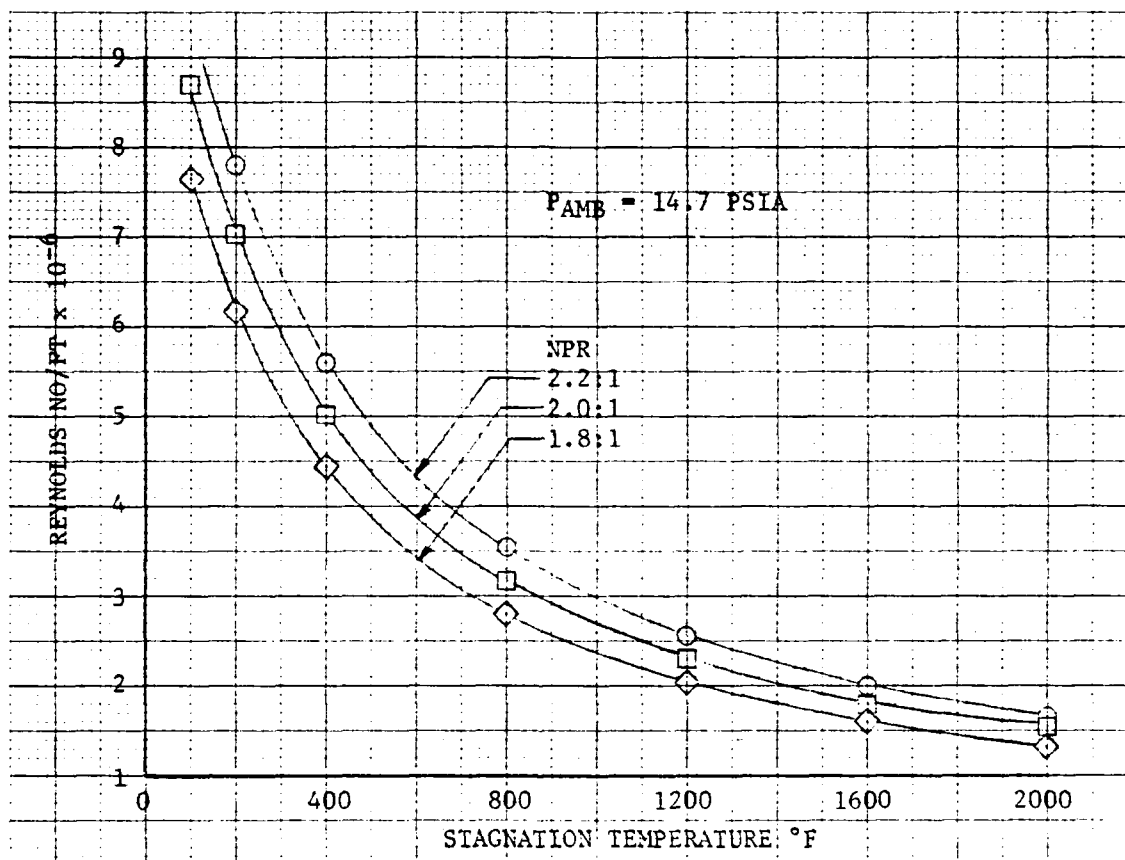


Figure 5-3 Reynolds No. Variation With Temperature

( $M \equiv v/a$ ) is independent of temperature, since both the jet velocity and the speed of sound,  $a$ , have the same dependence on temperature:

$$\text{jet velocity} \quad V = \left[ \frac{2\gamma}{\gamma-1} RT_0 \left( 1 - \left( \frac{P}{P_0} \right)^{\frac{\gamma-1}{\gamma}} \right) \right]^{\frac{1}{2}}$$

$$\text{speed of sound} \quad a = (\gamma RT_0)^{\frac{1}{2}}$$

The jet thrust is also independent of temperature since the velocity increase is balanced by a decrease in density.

The effect of temperature on the rate of turbulent mixing is not as straightforward. For small density differences, the mixing rate is



proportional to the velocity difference between the two streams. But, if the density difference is large, the mixing rate is proportional to the momentum difference. Thus, a small temperature difference will probably increase the mixing rate ( $\Delta V \sim T_0^{1/2}$ ) while a large temperature change will probably decrease mixing ( $\Delta V \sim T_0^{-1/2}$ ), although this has not been proven.

The net effect of the 1000°F temperature decrease used for these scale model tests was calculated with the jet mixing program to be a .03 increase in augmentation. This is almost within the accuracy of the calculation procedure; however, the available data seems to support this result. This is shown in Figure 5-4. Although all the data except that

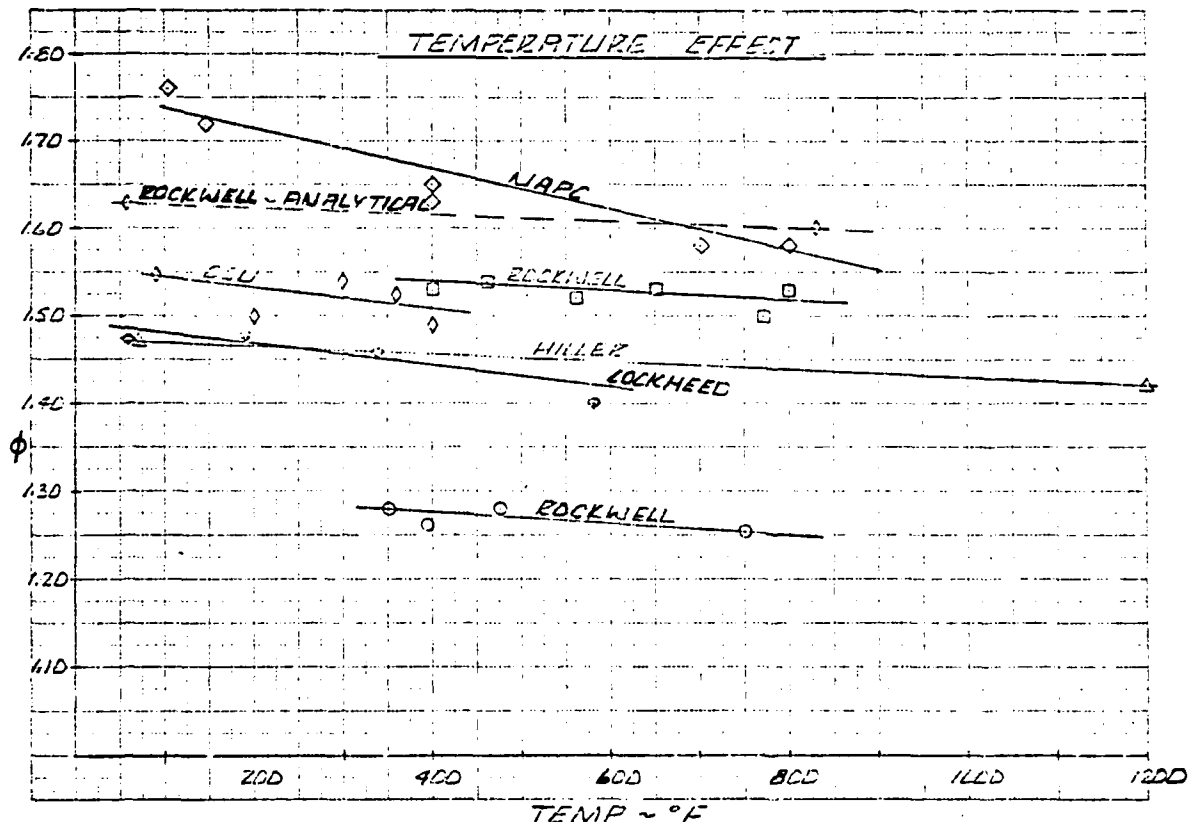


Figure 5-4 Temperature Effect

of Lockheed also included a scale or configuration change, the trend is consistent. Thus, a small increase in performance may be expected as a result of using cold jets in the model.

Full size ejectors built by Lockheed, Boeing, and DeHavilland aircraft companies produced less augmentation than the laboratory models from which they were developed. However, there were differences between the model and full size ejectors in construction, jet temperature, and various ejector parameters, so that these results are inconclusive regarding scale effects. Full size ejectors tested by Rockwell International have



generally performed as well as the laboratory models and, in one case for which the geometric scaling was nearly exact, the same performance was obtained (Mefferd, Alden and Bevilaqua, 1979), Reference (22). These ejectors are shown in Figure 5-5. Thus, it is felt that scale model testing can be used, with some caution in designing the test and interpreting the results, for the development of aircraft ejectors.

#### 5.4 APPARATUS

All scale model augments and isolated centerbody nozzle testing was conducted at Rockwell International's NAAD Columbus Thermodynamic Laboratory. During this scale model test program, two test stands, designated as Rig numbers 1 and 5 were utilized. The two rigs are similar in design and are basically load test stands capable of measuring lift forces to 1000 pounds, drag loads to 200 pounds, and side forces up to 2000 pounds. It should be noted that Rig No. 1 was a 2-D stand capable of measuring only lift and drag components. However, considering the nature of the hardware under evaluation in this phase of testing, a 2-D stand was found to be adequate to satisfy test requirements.

Each test stand is basically a floating frame, attached to a fixed outer frame through load cells to measure the two or three orthogonal forces. Tension is maintained on the load cells with cable suspended preloads. Air is supplied to the augment models from plant air or from the Thermodynamic Laboratory's compressor through four individually controlled lines. The air supply system is equipped with particle filters and dryers. Excessive variations in supply air temperature are controlled with the use of a cooling tower.

Each supply has a venturi meter with the necessary instrumentation attached to calculate mass flows using standard venturi meter equations. The four lines are fed to the diffuser, centerbody, elevon, and endwall blowers (BLCS) through four flexible two inch hoses. These flexible lines prevent excessive tare when bringing the lines across the metric part of the load stand. Tares in the lift direction are typically one to two pounds, and repeatable, and are accounted for in the data reduction program. Appropriate valving is incorporated in the plumbing so the venturis may be used with any test rig, although not at the same time. Figures 5-6, 5-7, and 5-8 are sketches of the air supply system and test stand No. 1 details, while Figure 5-9 is an overall view photograph of test stand No. 1 with a typical model installed.

Load cells, pressure transducers and thermocouples are connected at appropriate test points on the load stand, model, and air supply system to monitor forces, pressures, and temperatures. These transducers are periodically calibrated using standard laboratory practice with calibration equipment traceable to the National Bureau of Standards.

The Thermo Lab's data system is capable of monitoring 48 channels of transducer analog output data and incorporates all signal conditioning and amplification prior to signal processing by an IBM 1800 computer. The data system also has the capability of performing an electrical test of the transducer's bridge integrity by use of a resistance calibration test

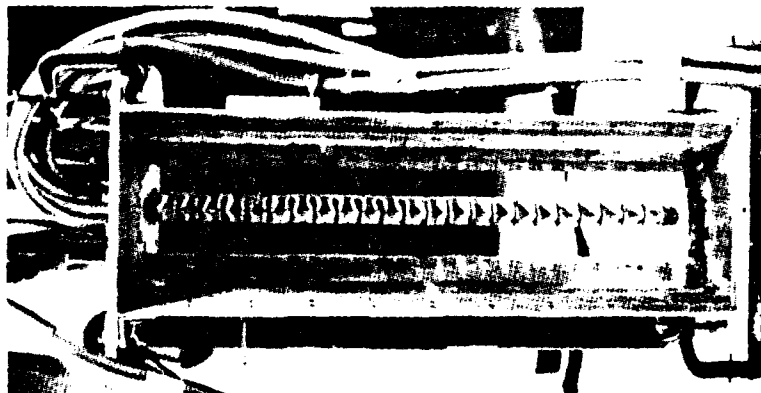
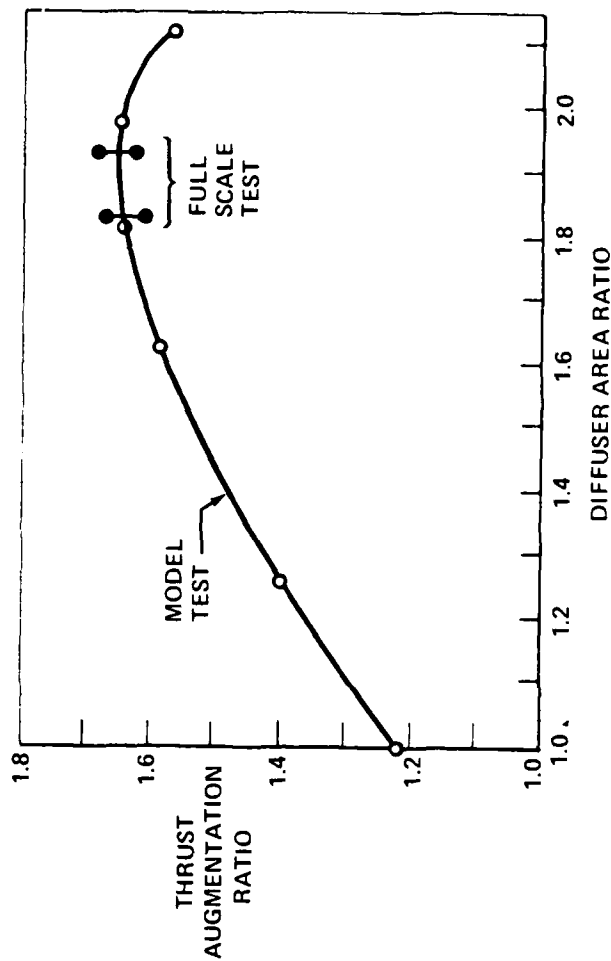


Figure 5-5. Scale and Full Size Ejectors

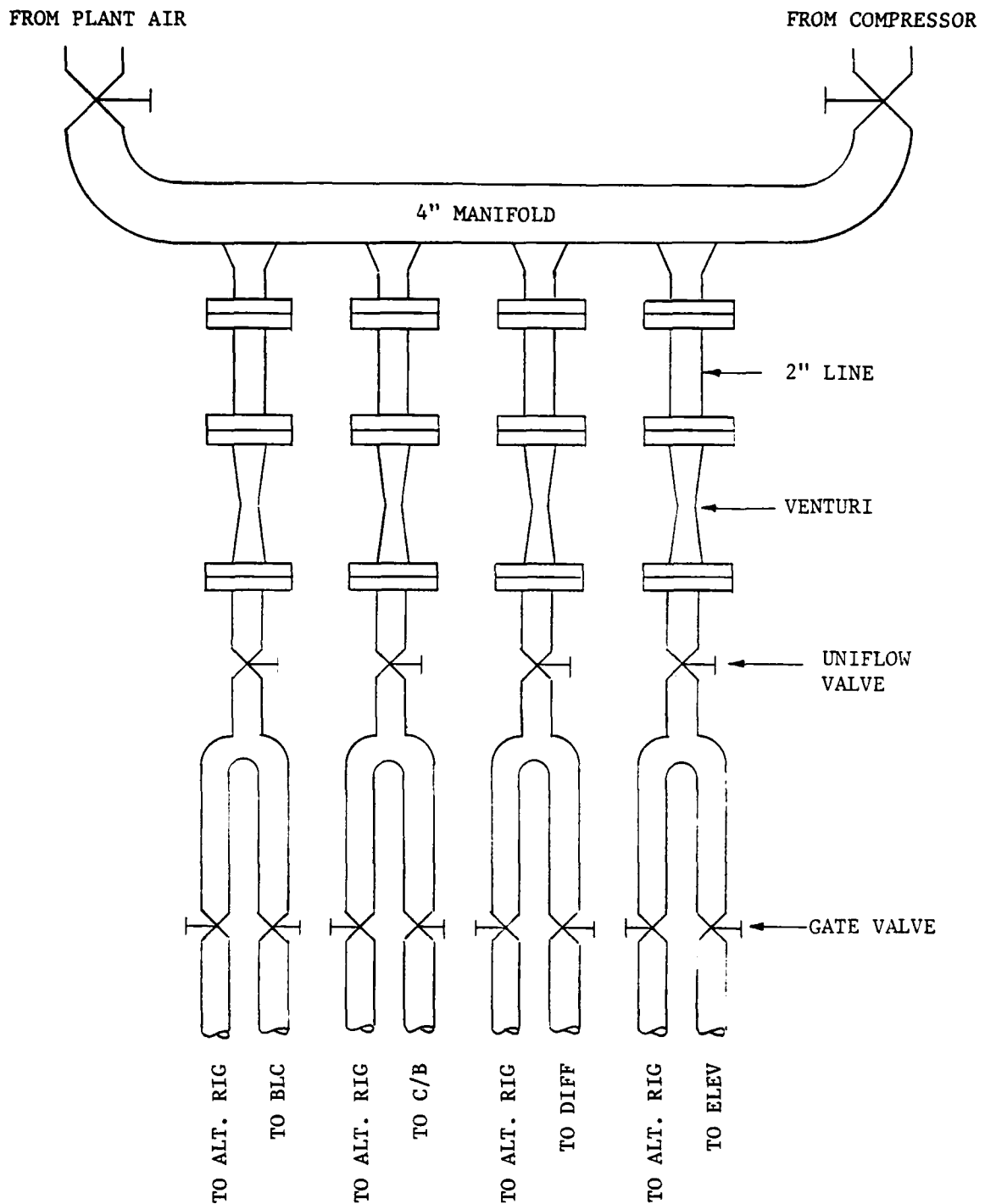


Figure 5-6. Air Supply System

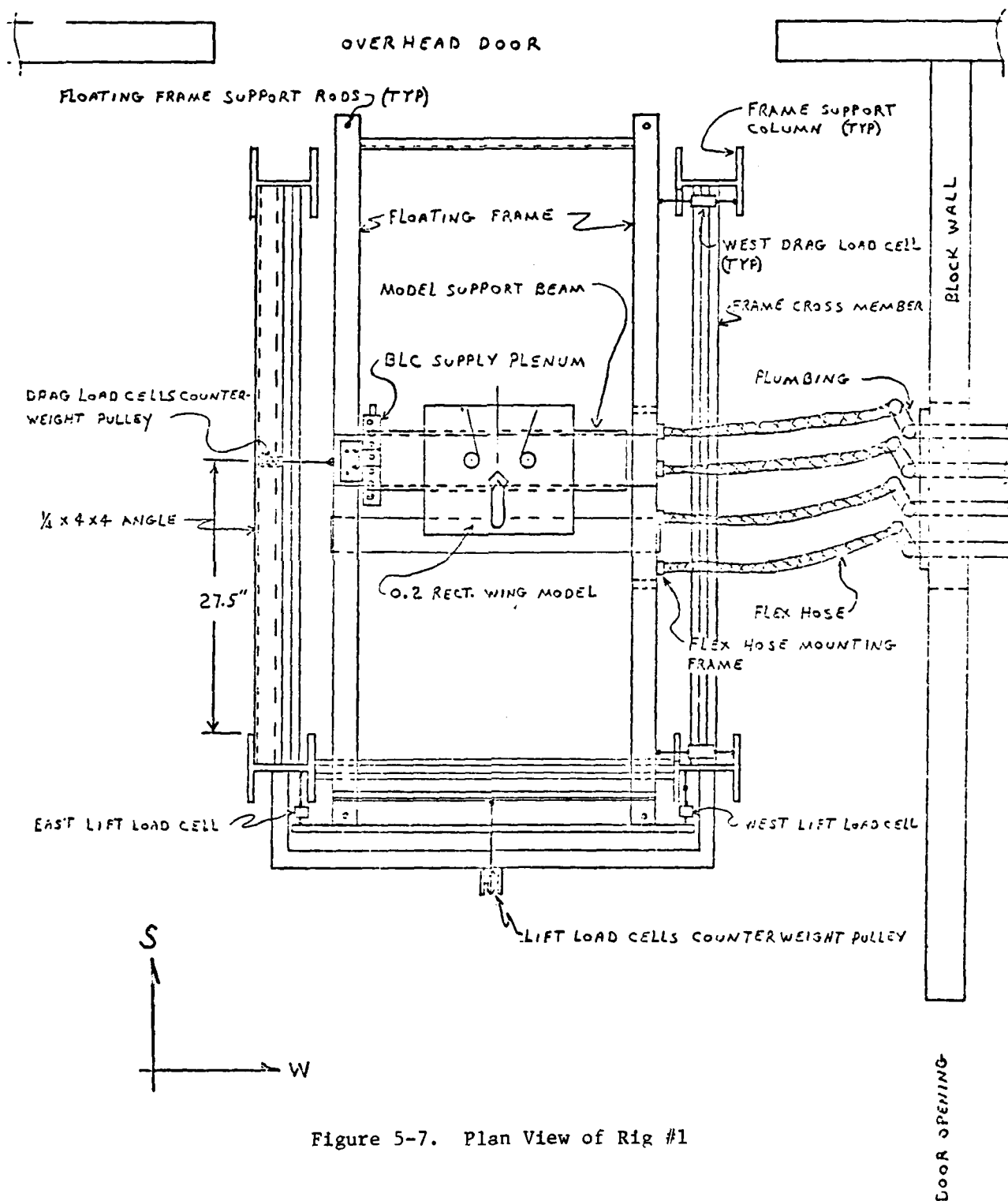


Figure 5-7. Plan View of Rig #1

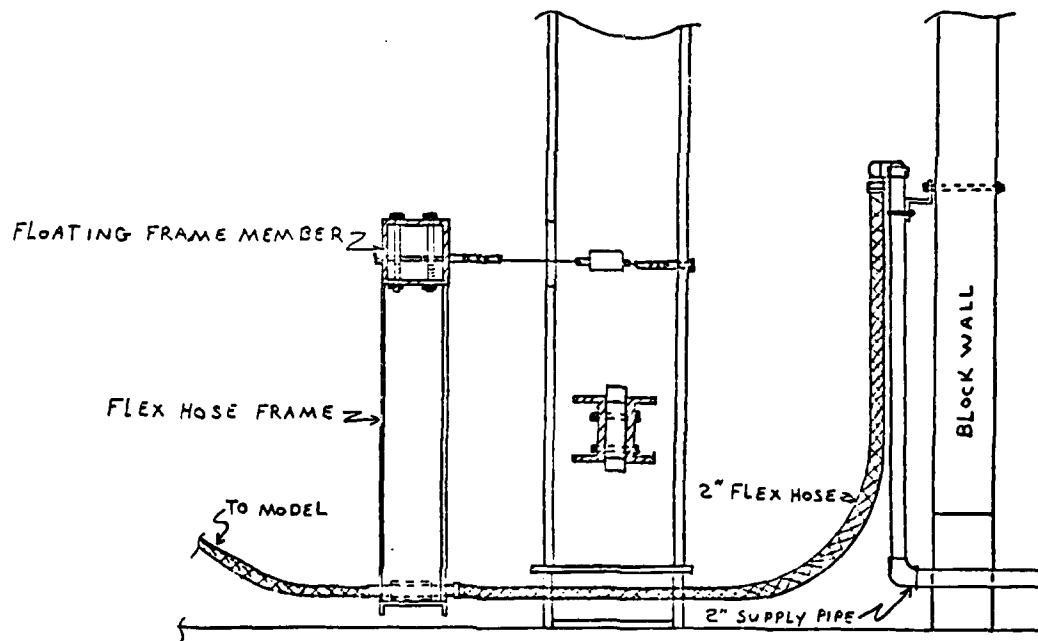
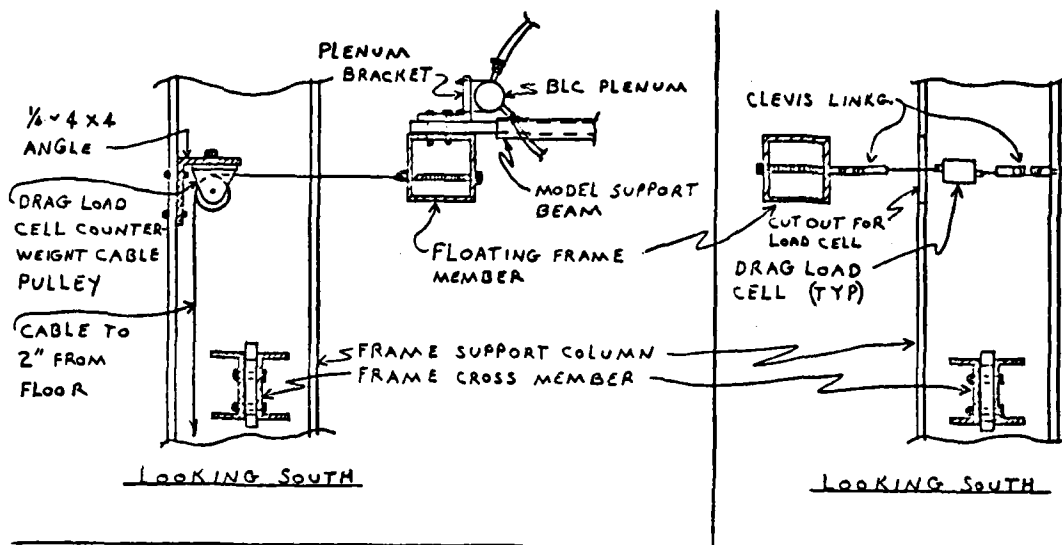


Figure 5-8. Section Blowups of Modifications to Rig #1



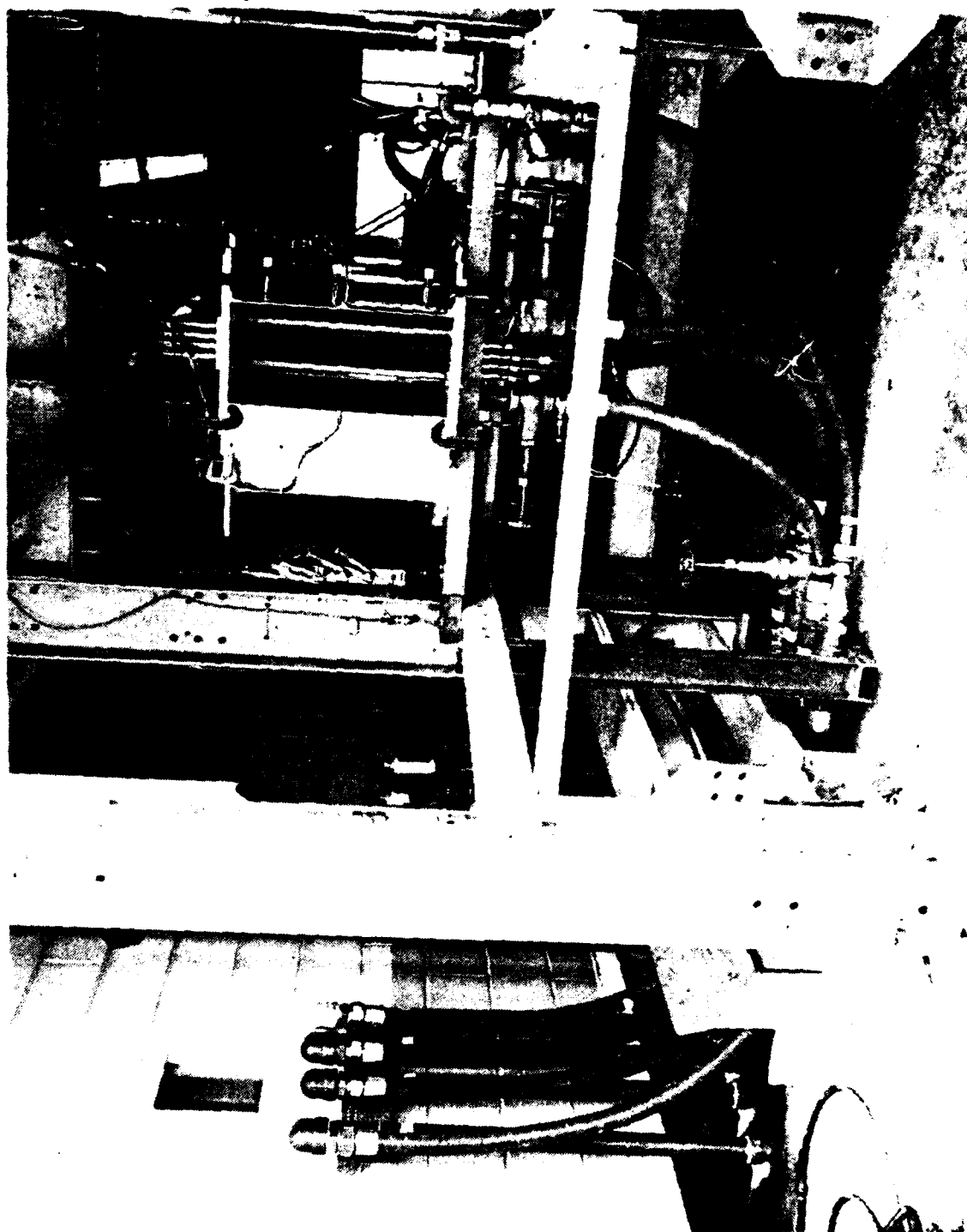


Figure 5-9. Overall View of Test Stand No. 1



(R-CAL). This was routinely done by the computer prior to each test run, and any drift in transducer excitation or signal amplification is automatically compensated for. Also prior to each test run the load cells were checked by using calibrated lead weights, and this data recorded by the computer and stored with the data for each test run.

Data acquisition and reduction is handled by an IBM 1800 computer that contains a 48 channel multiplexer and a 14 bit plus sign analog to digital converter. The computer has 32 kilowords of core storage, approximately 500 kilowords of disk storage, and a four microsecond cycle time.

Input/output devices consist of a 30 character/minute keyboard printer, a 260 card/min card reader-punch, and a 240 line/minute line printer. Two analog output channels of ten bit resolution are available for plotting data on line. Seven (possible 24) levels of process interrupt control are provided to control the various functions of the processor. Two 16 bit digital output (electronic contact operated) words are available for control of external devices. One 16 bit digital input word in conjunction with an external 16 channel multiplexer is used for digital input data.

Data reduction is handled by appropriate user written computer programs. Conversion constants for all transducers are contained in the software and utilized to convert transducer electrical outputs to equivalent engineering units. Appropriate equations are programmed to calculate augmentor airflow parameters such as isentropic thrust, flow coefficients, velocity, Reynolds number, and etc. Selected parameters are calculated and punched to cards for additional data analysis by the Corporate Computing Systems TSO and CDC, which are IBM 370 and CDC Cyber 176 computers, respectively.

During the course of this test program, numerous airflow surveys, in and around the augmentor, were made with a 3-axis, computer controlled, survey rake. Both pitot-static probes and a 5-port flow angularity probe (United Sensor Mod DC-125-24-F-22-CD) were used to collect survey data. Computer programs were available to reduce pressure and position data to thrust, mass flow, velocity profile distortion, flow angularity, and etc. This type of data reduction was done on both the IBM 1800 computer as well as the Corporate Computer Systems.

Further information concerning the Thermodynamics Laboratory complex can be found in the facilities section of this document.

## 5.5 AUGMENTER MODELS

The augmentor models used during this test program were rectangular, 0.2 scale representations of a midspan cut of the full scale wing hardware. Rectangular models allow much quicker changes to model geometry and are considered satisfactory for evaluating the relative merits of one centerbody versus another. A cross section of a typical model is shown in Figure 5-10 along with annotations of augmentor dimensional parameters. The basic model consists of a forward and aft Coanda-flap surfaces, both with log spiral Coanda surfaces, and a centerbody nozzle. Flaps of various configurations were attached to the Coanda surfaces, and endwall



plates extending to the flap trailing edges were used to complete the closeout of the shroud. A wing leading edge simulation was attached to the diffuser of a length representing 0.2 scale of the full size wing.

The augments plenums, Coandas, flaps, endwalls, and endwall blowers were fabricated in accordance with References (15) and (16). Two sets of Coandas were used on Rig No. 1 during this program and were referred to as "old Coandas" and "new Coandas." The new Coandas differ in the log spiral shape which is defined by the initial radius ( $R_0$ ) and spiral "K" factor. In addition, the new Coandas had corner blowers incorporated at each end of each Coanda nozzle to provide additional control of adverse airflow in the augments corners.

Both Coanda shapes had the same spiral factor ( $K = 1.3$ ), but the initial radius ( $R_0$ ) was changed to diffuser  $R_0 = .483$  inches and elevon  $R_0 = .4156$  inches. These  $R_0$ 's gave  $R_0/t$  values of 10.39 and 12.075, respectively, for the diffuser and elevon, and reflect the aircraft values for a midspan cut, while the "old Coandas" had an  $R_0/t = 8.7$  for diffuser and elevon, which more nearly represented aircraft values at the outboard end of the nozzles.

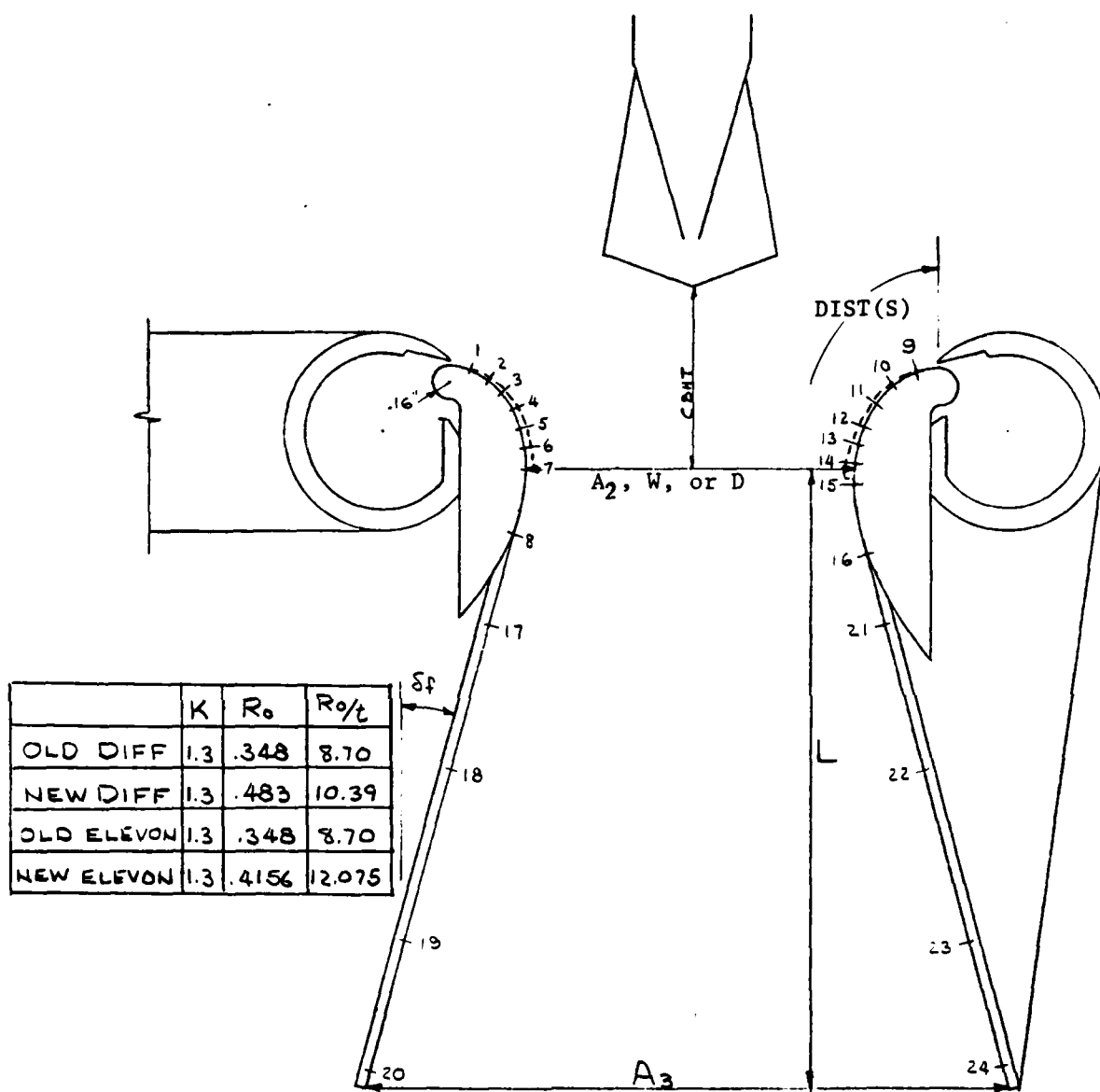
Centerbody performance testing using the "old Coandas" was done with the 7°, 15°, 22.5°, and 28° hypermixing nozzles, as well as with the 14 element asymmetric, 14 element asymmetric mods 1 and 2, and 18 element asymmetric. All subsequent asymmetrics and mods as well as all symmetric centerbody nozzles were tested using the "new Coandas." All the hypermixing centerbodies plus the 14 element asymmetric mod 2 were also retested with the "new Coandas" for a comparison data base.

Details of the Coanda nozzle internal construction can be seen in Figure 5-11. The Coanda surface is integral with the internal radius surface and attached to the plenum tube which also forms the nozzle lip. The attachment is made utilizing a slotted hole which allows nozzle gap adjustments.

Air was supplied to the plenum through a feed pipe which has a row of holes the full length of the nozzle, exiting air into the plenum in a direction opposite to the nozzle exit. Spanwise pressure distribution was accomplished by enlarging or plugging selected holes as required. The ratio of plenum volume to nozzle exit area was sufficient to uniformly choke the nozzle with a minimum of spanwise flow.

The inboard ends of the plenum tubes were fabricated with two grooves on the outside diameter; one groove provided sealing utilizing an O-ring and the other was a recess for set screws which held the nozzle to an adapter fitted to the inboard endwall. This arrangement allowed the rotation of the nozzles within the adapter, thereby permitting variations in Coanda turning angle, that is flow angle from nozzle exit to throat.

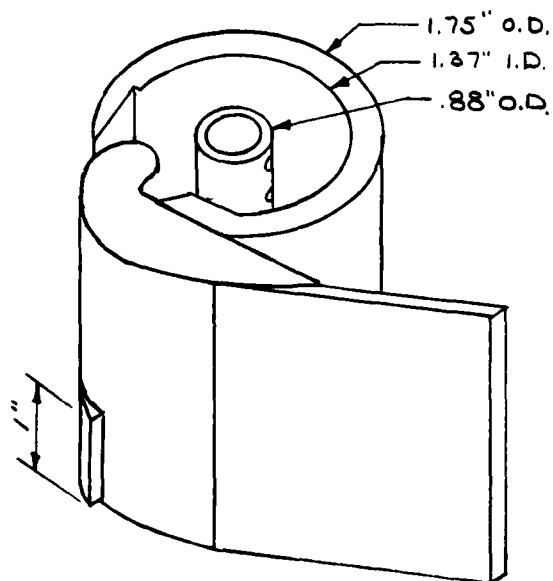
The corner blowers (dedicated nozzles) shown in Figure 5-11, located at each end of each Coanda nozzle were supplied with air from the same plenum as the primary nozzle. Convergence to the nozzle exit was provided to ensure a uniform exit pressure profile.



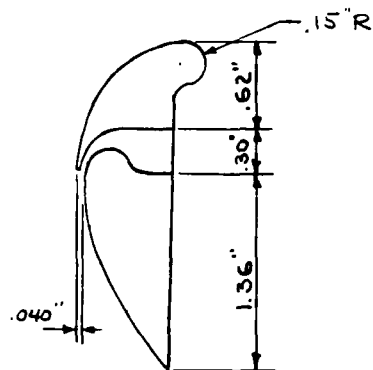
P <sub>s</sub> TAP No & CoANDA SURFACE DISTANCE NOZZLE EXIT-TO-TAP																	
	TAP No	1	2	3	4	5	6	7	8	9	10	11	12	13	14	15	16
RIG 1	DIST	.17	.37	.59	.73	.91	1.09	1.28	1.88	.24	.48	.77	.94	1.14	1.31	1.50	2.13
RIG 5	DIST	.25	.43	.60	.77	.96	1.13	1.34	1.92	.18	.42	.67	.90	1.10	1.26	1.46	2.12

TAP LOCATIONS TESTS 278, 294, 304

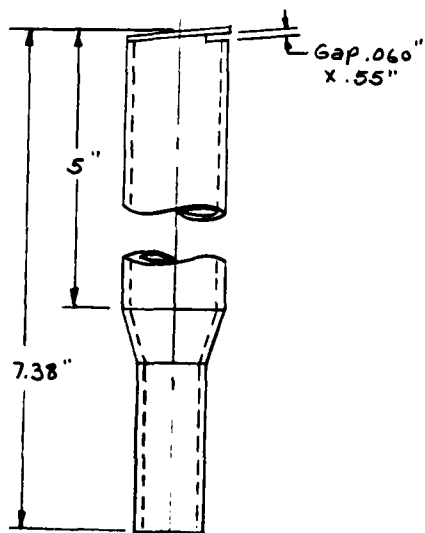
Figure 5-10. Augmenter Geometry



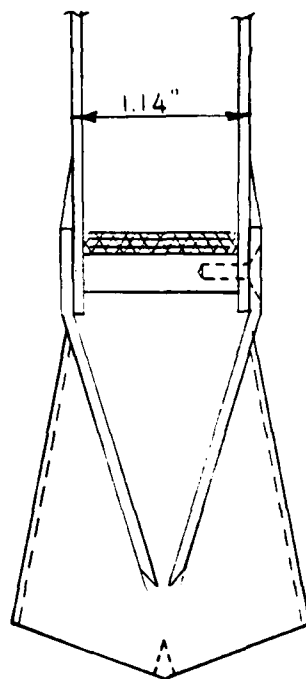
COANDA NOZZLE - FLAP



CORNER BLOWER



NICKEL BLOWER



CENTERBODY NOZZLE

Figure 5-11. Augmenter Model Construction Details



Figure 5-10 shows locations of static taps on the Coanda surfaces which were located at midspan of the nozzle. Pressure taps 1 through 16 were on the actual Coanda surfaces while taps 17 through 24 were on the flaps. The table in Figure 5-10 provides tap locations as distance on the surface from the nozzle exit. Location of taps 17 through 24 varied with the particular flap used, and this information may be obtained from Figures 5-12, 5-13, and 5-14 for each individual flap.

Starting with a 16 April 1981 date, additional surface static pressure taps were added to the model on test stand No. 5. These taps were added to the Coanda-flap surfaces as well as to the upper surface of the wing leading edge simulation. A new test number (307) was assigned to the Phi runs of the rig 5 model to mark this major change. Figure 5-15 shows the locations of both the original and added static pressure taps.

The method of attaching centerbody nozzles to the centerbody plenum is shown in Figure 5-11. This type of construction resulted in cost and time savings as nozzle changes could be made by fabricating only the nozzle element section and utilizing a common plenum. This type of centerbody nozzle construction also resulted in time savings with regard to obtaining uniform nozzle pressure distributions, in that the screening, used to distribute airflow uniformly along the span of the nozzle, remained with the plenum and did not require changing when nozzle elements were changed, so long as the nozzle exit areas were approximately the same.

The effect of internal screening of a nozzle on the jet turbulence intensity was studied using a hot film anemometer. It was determined, the screening had little effect. Figure 5-16 presents the turbulence intensity profiles for three nozzle screening configurations and Figure 5-17 presents a  $\phi$  versus  $A_3/A_2$  comparison of two screening configurations.

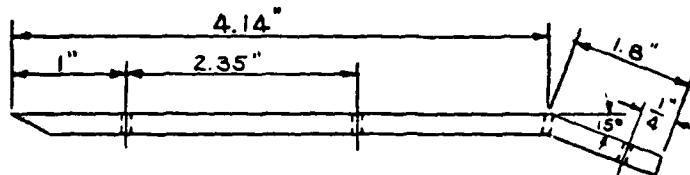
Boundary layer control devices (BLCS) were incorporated in the endwalls located at or slightly below the augmentor throat line (see Figure 5-18) in the endwalls to provide control of airflow separation on these surfaces. The BLCS consisted of three or four (depending on throat dimension) rotatable slot nozzles exiting air parallel to the endwalls at a nozzle pressure ratio comparable to that of the other augmentor nozzles.

The amount of air used in the BLCS was typically four to five percent of the total exit area ( $A_0$ ) of the augmentor model. Figure 5-11 shows a sketch of a typical endwall "nickel blower" nozzle.

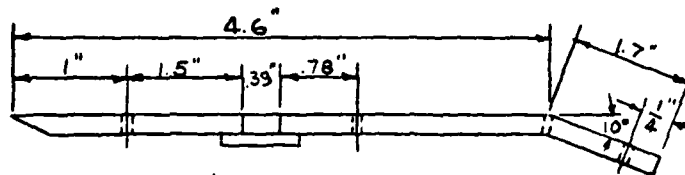
The inboard and outboard endwalls (see Figure 5-19) were fabricated in three sections which allowed the flexibility of making augmentor throat variations without a major change to the model. Spaces resulting between the sections were easily filled with spacer blocks and smoothed with epoxy compounds. A similar arrangement was utilized to provide movement of the centerbody so that centerbody height sensitivities could be studied.



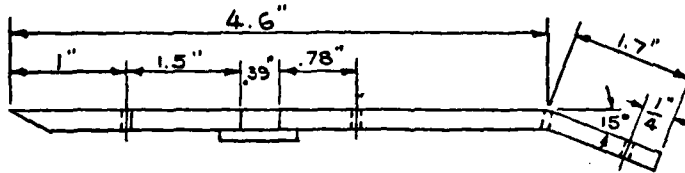
15° 5.94" FLAPERON (356-01042-191)



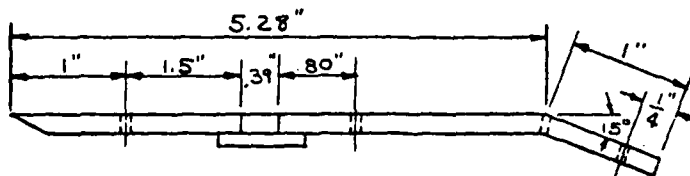
10° 6.3" FLAPERON (356-01042-251)



15° 6.3" FLAPERON (356-01042-261)



15° 6.3" FLAPERON (356-01042-271)



12.3" STRAIGHT FLAP DIFFUSER (ELEVON)

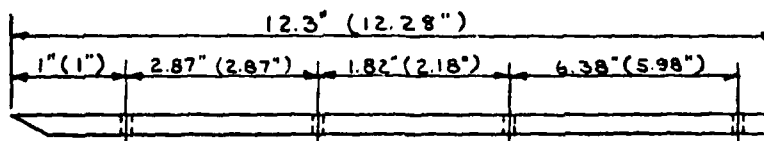
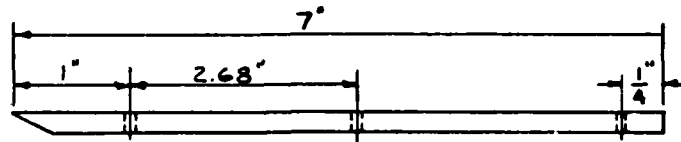


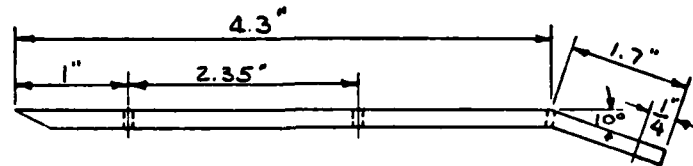
Figure 5-12. Model Flap Pressure Tap Locations



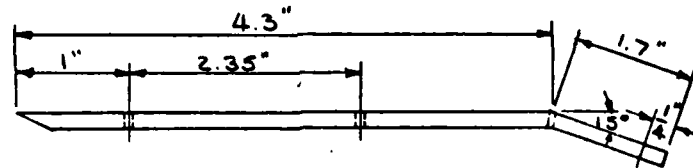
7" STRT FLAP (356-01042-063)



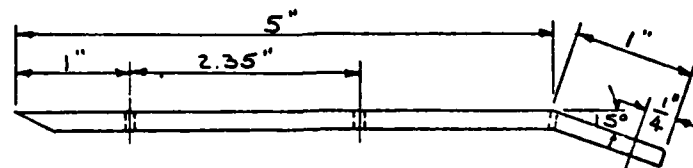
10° 6" FLAPERON (356-01042-151)



15° 6" FLAPERON (356-01042-161)



15° 6" FLAPERON (356-01042-171)



15° 7" FLAPERON (356-01042-181)

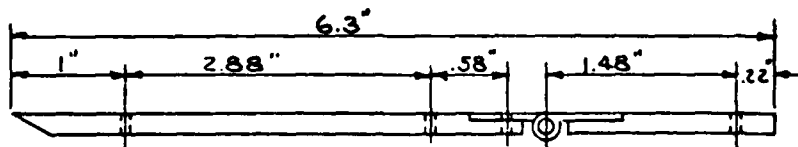


Figure 5-13. Model Flap Pressure Tap Locations

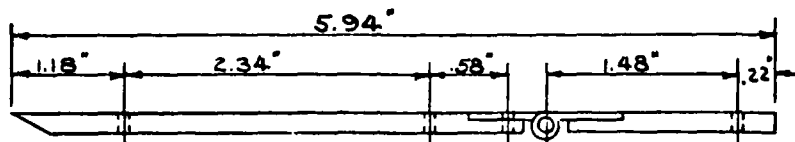




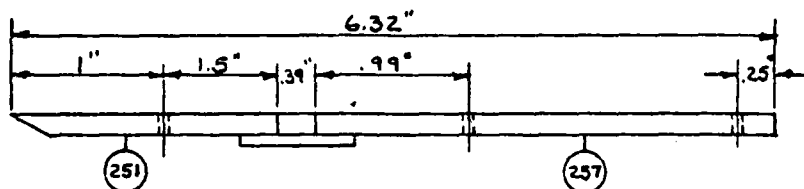
## 6.3" HINGED FLAP (356-01042-201)



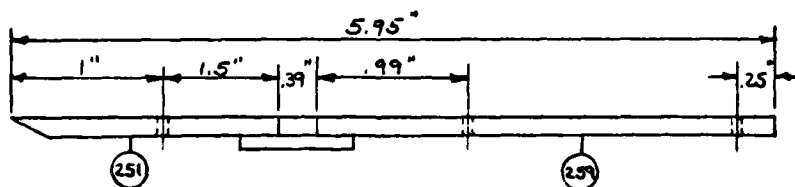
## 5.94" HINGED FLAP (356-01042-301)



## 6.32" STRAIGHT FLAP (356-01042-251/257)



## 5.95" STRAIGHT FLAP (356-01042-251/259)



## 9.5" STRAIGHT FLAP DIFFUSER (ELEVON)

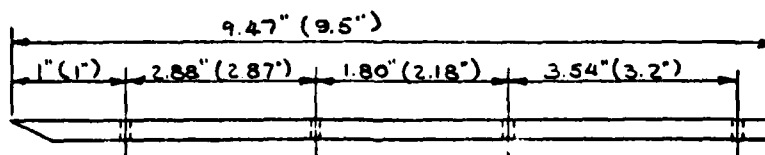
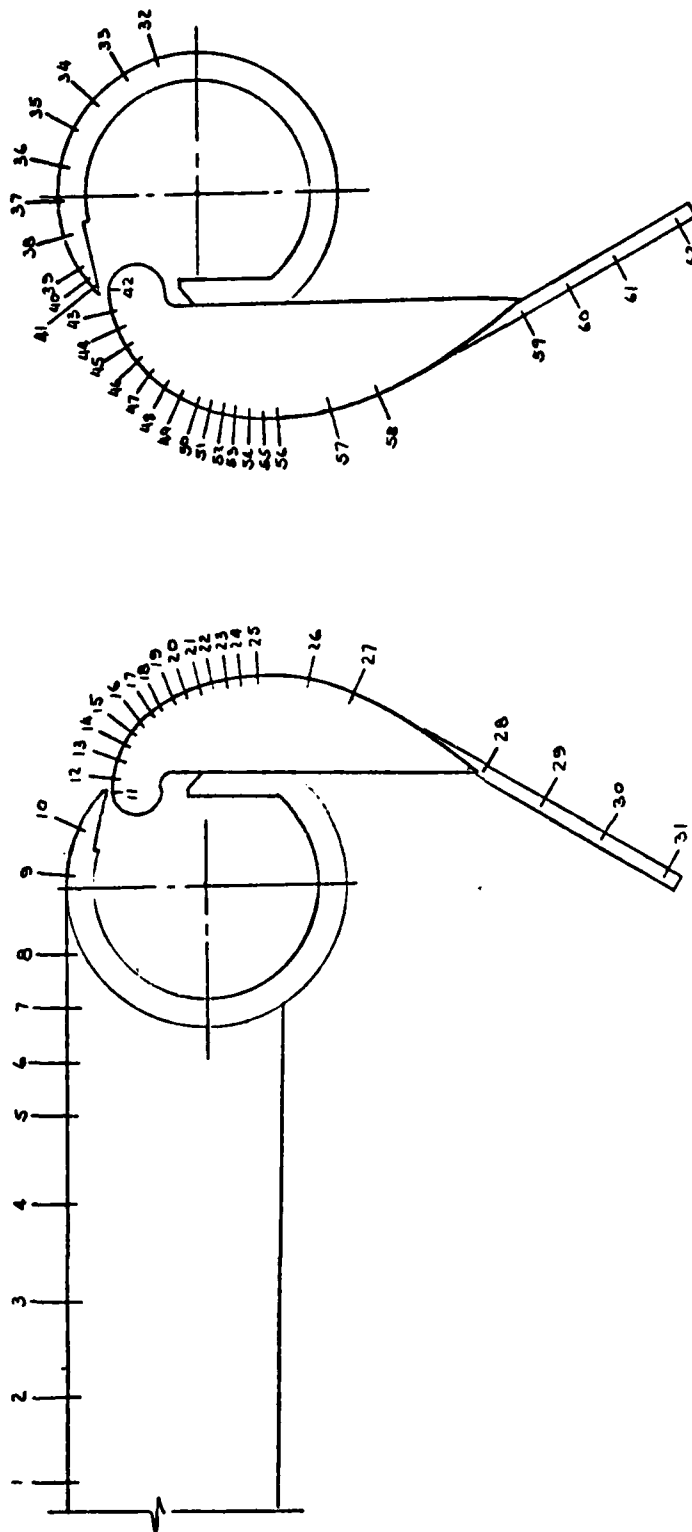


Figure 5-14. Model Flap Pressure Tap Locations



REF No VS SCV MODULE No/PORT No VS DIST FROM NOZZ EXIT																																		
REF No	1	2	3	4	5	6	7	8	9	10	11	12	13	14	15	16	17	18	19	20	21	22	23	24	25	26	27	28	29	30	31			
MODULE/ PORT No	1/37	1/36	1/35	1/34	1/33	1/32	1/31	1/30	2/3	2/4	2/5	2/6	2/7	2/8	2/9	2/10	2/11	2/12	2/13	2/14	2/15	2/16	2/17	2/18	2/19	2/20	2/21	1/2	1/3	1/4	1/5			
DIST	6.70	5.49	4.49	3.47	2.47	1.48	1.69	1.17	.63	.28	.04	.14	.25	.36	.43	.53	.61	.68	.78	.88	.96	1.06	1.15	1.26	1.34	1.47	1.95							
REF No	32	33	34	35	36	37	38	39	40	41	42	43	44	45	46	47	48	49	50	51	52	53	54	55	56	57	58	59	60	61	62			
MODULE/ PORT No	1/29	1/28	1/27	1/26	1/25	1/24	2/23	2/22	2/21	2/20	2/19	2/18	2/17	2/16	2/15	2/14	2/13	2/12	2/11	2/10	2/9	2/8	2/7	2/6	2/5	2/4	2/3	2/2	1/7	1/8	1/9			
DIST	1.94	1.76	1.44	1.21	.96	.73	.49	.25	.16	.09	.04	.10	.18	.32	.43	.55	.68	.80	.91	1.00	1.11	1.17	1.27	1.36	1.46	1.76	2.13							

Figure 5-15. Surface Static Press Tap Location ~ Rig 5, Test 307



EFFECT OF INTERNAL SCREENING

ON JET TURBULENCE INTENSITY

SCBT15-1 CENTERBODY ~ NOZZLE VEL  $\approx$  900 fps

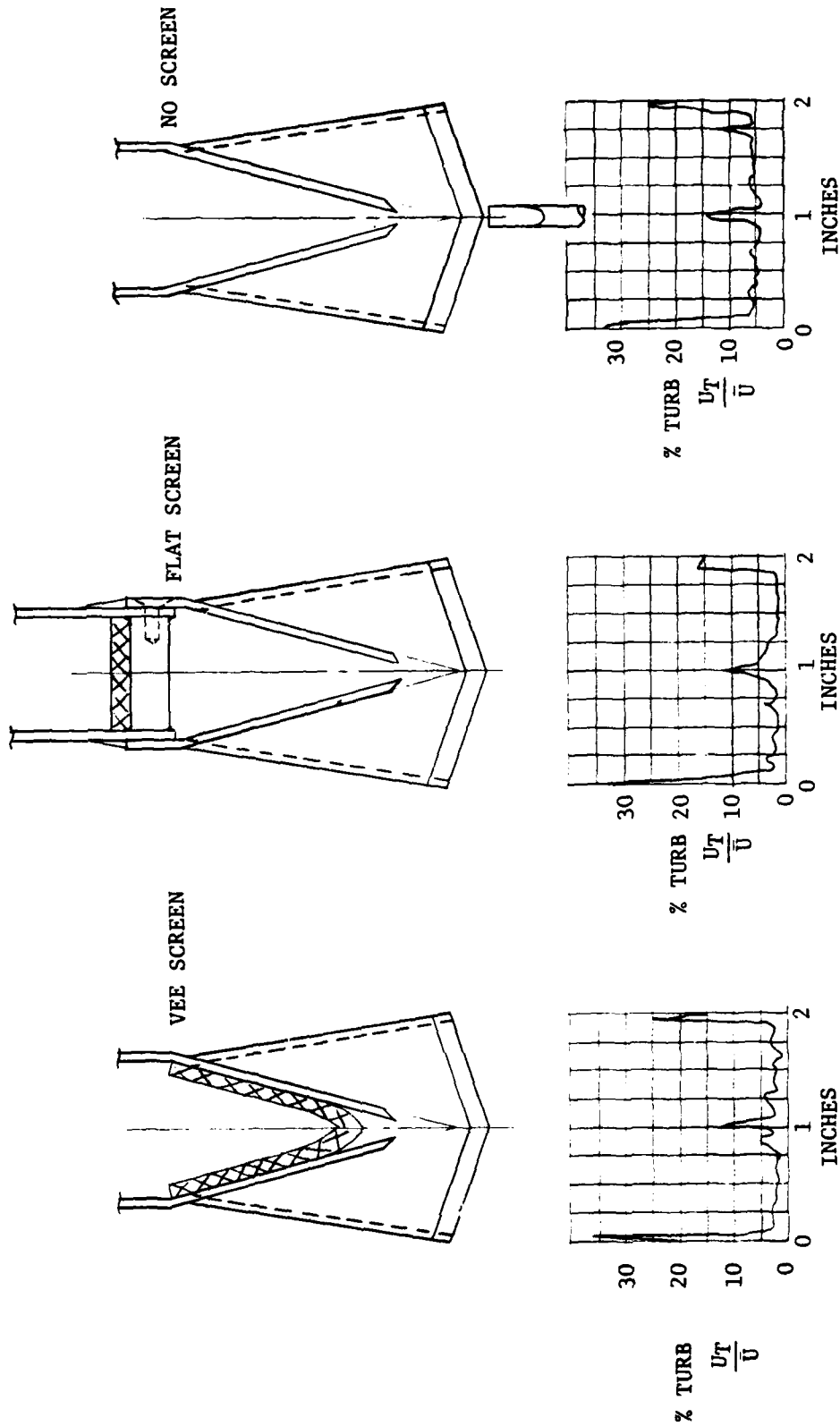
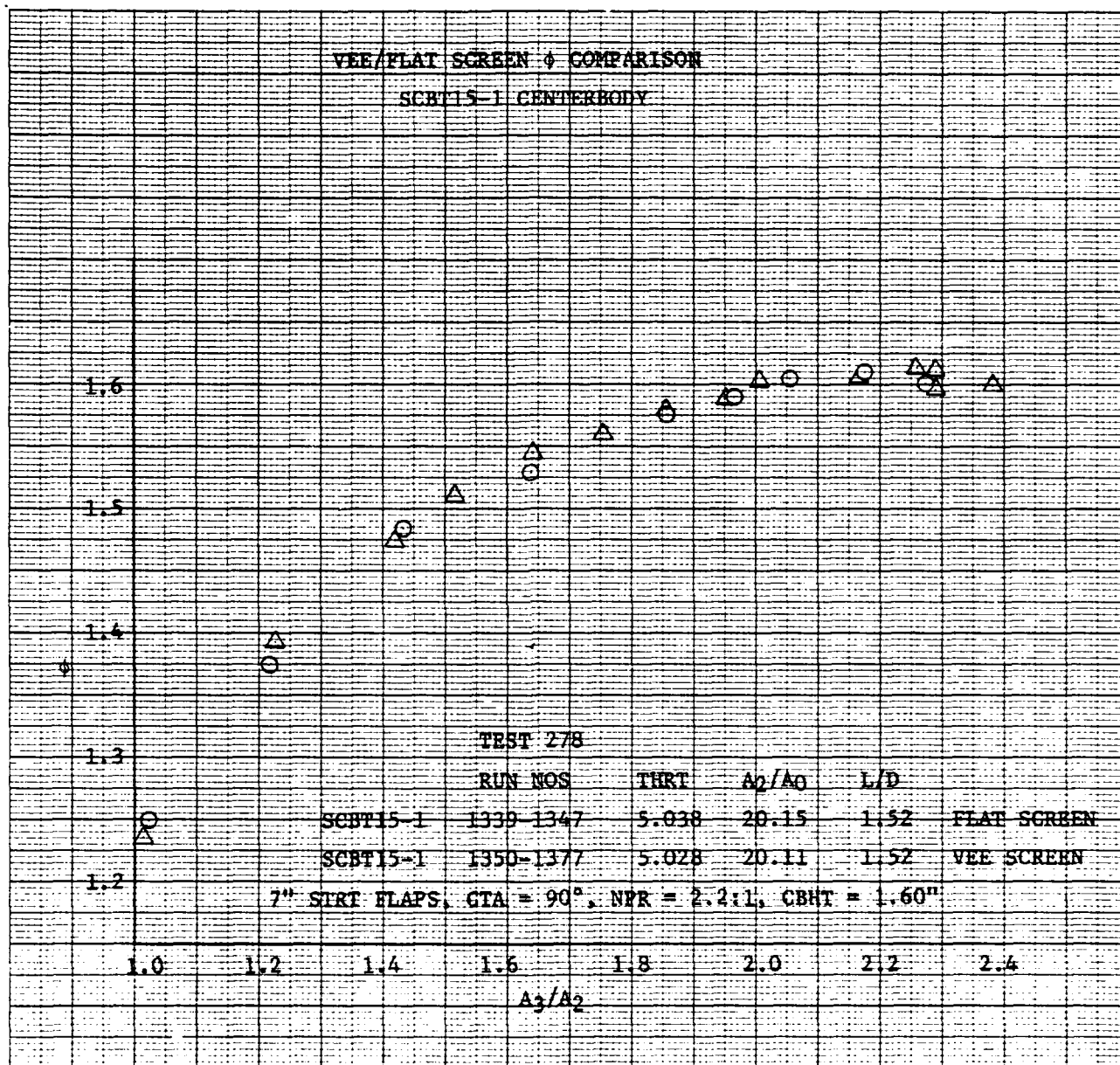
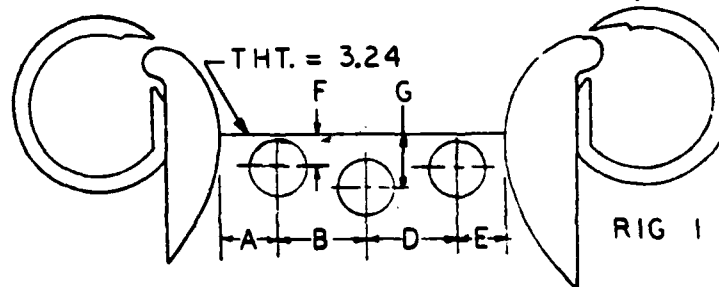
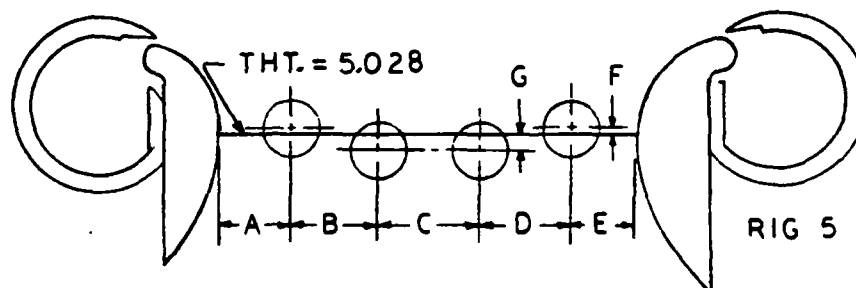
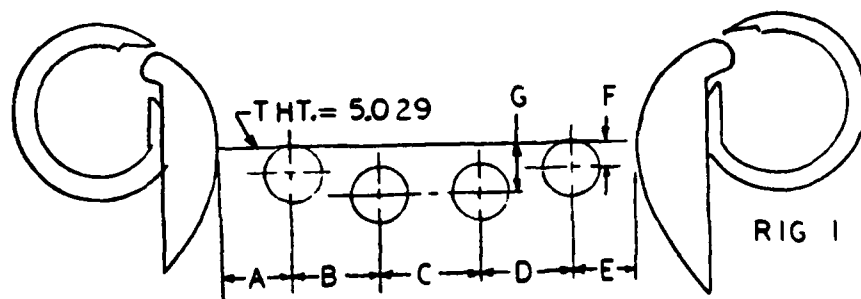


Figure 5-16.

Figure 5-17 Vee/Flat Screen  $\phi$  Comparison SCBT15-1 Centerbody



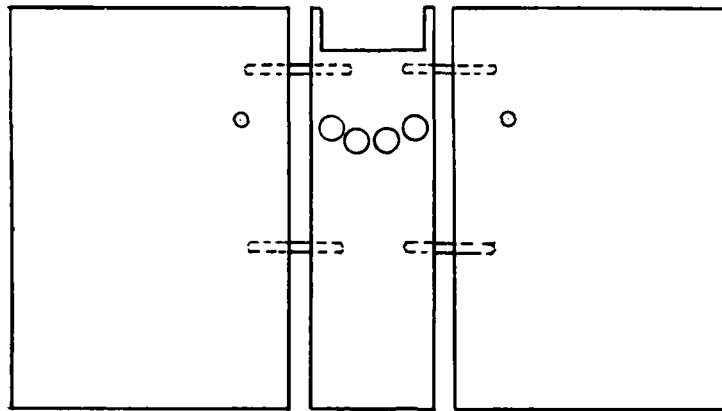
## ENDWALL BLOWER LOCATIONS



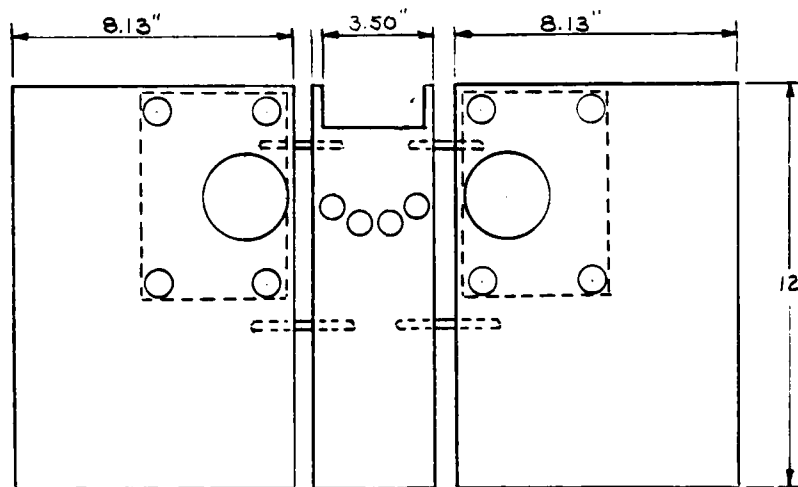
	A	B	C	D	E	F	G
RIG 1 IB	1.05	.98	.98	.97	1.05	.36	.59
RIG 1 OB	1.10	.98	.98	.97	1.00	.35	.55
RIG 5 IB	1.26	.79	.95	.80	1.22	.19	.35
RIG 5 OB	1.25	.90	.90	.75	1.22	.19	.35
RIG 1 IB/OB	.75	.87	—	.87	.75	.50	.75

NOTE: 1. SKETCH NOT TO SCALE.  
 2. DIMS. A & E WILL VARY WITH THE THROAT. DIMS. SHOWN ARE FOR THROATS INDICATED.

Figure 5-18 Endwall Blower Locations



OUTBOARD ENDWALL



INBOARD ENDWALL

Figure 5-19 Augmenter Endwall Construction Details



## 5.6 INSTRUMENTATION ACCURACY

Since the measured  $\phi$  is defined by the equation  $\phi = L/\dot{m}V$  where

Lift = Measured load stand thrust  
 $\dot{m}$  = Measured venturi mass flow  
V = Nozzle exit velocity based on nozzle pressure ratio.

The fractional error in  $\phi$  may be defined as

$$\frac{\Delta\phi}{\phi} = \sqrt{\left(\frac{\Delta L}{L}\right)^2 + \left(\frac{\Delta\dot{m}}{\dot{m}}\right)^2 + \left(\frac{\Delta V}{V}\right)^2}$$

Load Cell Error - The lift load cells are calibrated using dead weights which are calibrated on a HOMS scale having a calibration accuracy of  $\pm .11$  percent. The lift load cells mounted in the test stand gave an average error of .224 percent based on 31 separate test runs. Tolerance on hose tare corrections was found to be .006 percent. The total expected probable error in lift measurements was calculated to be .25 percent.

Venturi Meter - The Venturi meters used during this test program have a basic accuracy ( $C_D$ ) of  $\pm 1.0$  percent based on calibrations supplied by the Mechanical Engineering Department of The Ohio State University.

Pressure Transducers - The three pressure transducers used in determining  $\phi$  were an upstream and  $\Delta P$  transducer on the Venturi meter used to calculate mass flow, and a transducer to determine nozzle pressure ratio which is utilized to calculate jet velocity. The working standard to calibrate transducers has a basic accuracy of  $\pm .06$  percent. The transducers have accuracy limits of

- . Hysteresis  $\pm .10$  Percent Full Scale
- . Non-Linearity  $\pm .25$  Percent Full Scale
- . Repeatability  $\pm .050$  Percent Full Scale
- . Temperature on Span  $\pm .005$  Percent
- . Temperature on Zero  $\pm .005$  Percent



The readout accuracy of pressures through the data system to the computer are estimated to be .061 percent.

Combining the above accuracy limits gives a total probable error in pressure measurements of  $\pm .28$  percent.

$$\frac{\Delta P}{P} = \sqrt{(.0006)^2 + (.0010)^2 + (.0025)^2 + (.0005)^2 + (.00005)^2 + (.00005)^2 + (.00061)^2} = .0028$$

Velocity - The equation for jet velocity used in the data reduction programs was:

$$Vel = \sqrt{\frac{\gamma \cdot R \cdot Temp \cdot 2 \left(1 - NPR \frac{1-\gamma}{\gamma}\right)}{\gamma-1}}$$

where  $\gamma = 1.4$ ,  $R = 1716$ ,  $Temp = \text{Air Temp in } ^\circ R$ ,  $NPR = \text{nozzle pressure ratio}$ . Assuming an error in pressure measurement of .28 percent, an error in jet velocity of .117 percent can be expected.

Mass Flow - The equation for mass flow used in the data reduction programs is:

$$\dot{m} = \frac{Y_a \cdot \pi \cdot D_v^2 \cdot C_D \sqrt{2 g^2 \cdot (P_{up}/(Temp \cdot R)) \cdot \Delta P}}{4 \sqrt{1 - A_v^4}}$$

$$\text{where } Y_a = \left[ \frac{\left( \left( \frac{PR}{Y} \right)^2 \left( \frac{Y}{Y-1} \right) \left( 1 - PR \frac{Y-1}{Y} \right) (1 - A_v^4) \right)}{(1 - PR) (1 - (A_v^4 \cdot PR^{2/\gamma}))} \right]^{1/2}$$

$D_v$  = Venturi throat dia. inches  
 $C_D$  = Venturi flow coefficient =  $.99 \pm 1\%$   
 $g$  =  $32.2 \text{ ft/sec}^2$   
 $P_{up}$  = Vent upstream pressure  
 $Temp$  = Vent Air Temp  $^\circ R$

$R$  =  $1716 \text{ ft}^2/\text{sec}^2 \text{ } ^\circ R \left( 53.35 \left( \frac{\text{ft} \cdot \text{lbs}_f}{^\circ R \text{ lbs}_m} \right) \times 32.2 \left( \frac{\text{lbs}_m \cdot \text{ft}}{\text{lbs}_f \text{ sec}^2} \right) \right)$

$\Delta P$  = Venturi upstream press - Venturi throat press  
 $A_v$  = Venturi throat dia./Venturi upstream dia.  
 $PR$  = Venturi throat press/Venturi upstream press

Assuming an error of .28 percent in the upstream and  $\Delta P$  pressure measurements and a one percent error in Venturi flow coefficient, a probable error in mass flow measurements of 1.29 percent can be expected.

Combining the above errors in lift, velocity, and mass flow:

$$\frac{\Delta \phi}{\phi} = \sqrt{(.0023)^2 + (.00117)^2 + (.0129)^2} = .0132$$

An expected probable error in  $\phi$  due to instrumentation errors is therefore approximately 1.3 percent. It will be noted that in calculation of





velocity and mass flow no error was assumed to be made in measurement of temperature. Examining the equations for  $\dot{m}$  and Velocity it can be seen that the product of these two equations will result in temperature effects cancelling.

## 5.7 TEST PROCEDURES AND METHODS

### 5.7.1 Short Time Repeatability

To determine the possible variation in augmentor performance over a short period of time and the possible error encountered by taking lift and pressure data at an instantaneous time slice, a series of runs were made comparing results where ten data samples were taken and averaged and compared to results of a single sample data point. Figure No. 5-20 is a comparison plot of single sample/data point versus ten samples/per data point at one sec  $\Delta$  between samples. Results show that  $\phi$  at any given time is comparable to  $\phi$  over a period of ten secs.

This sampling/average technique was further tested by increasing the time between samples from one sec. to ten sec. to spread the data acquisition per data point over a period of 100 secs. The lower plot on Figure No. 5-20 shows the results of one sample/sec. versus one sample/ten sec for a ten sample data point. Comparing the standard deviation for these two runs at 2.2:1 NPR shows the one sample/sec. data point and one sample/ten sec data point have standard deviations of .0026 and .0019, respectively. Based on these studies, the one sample per second - ten sample data point technique was incorporated as a permanent part of the data acquisition program, starting on April 8, 1980.

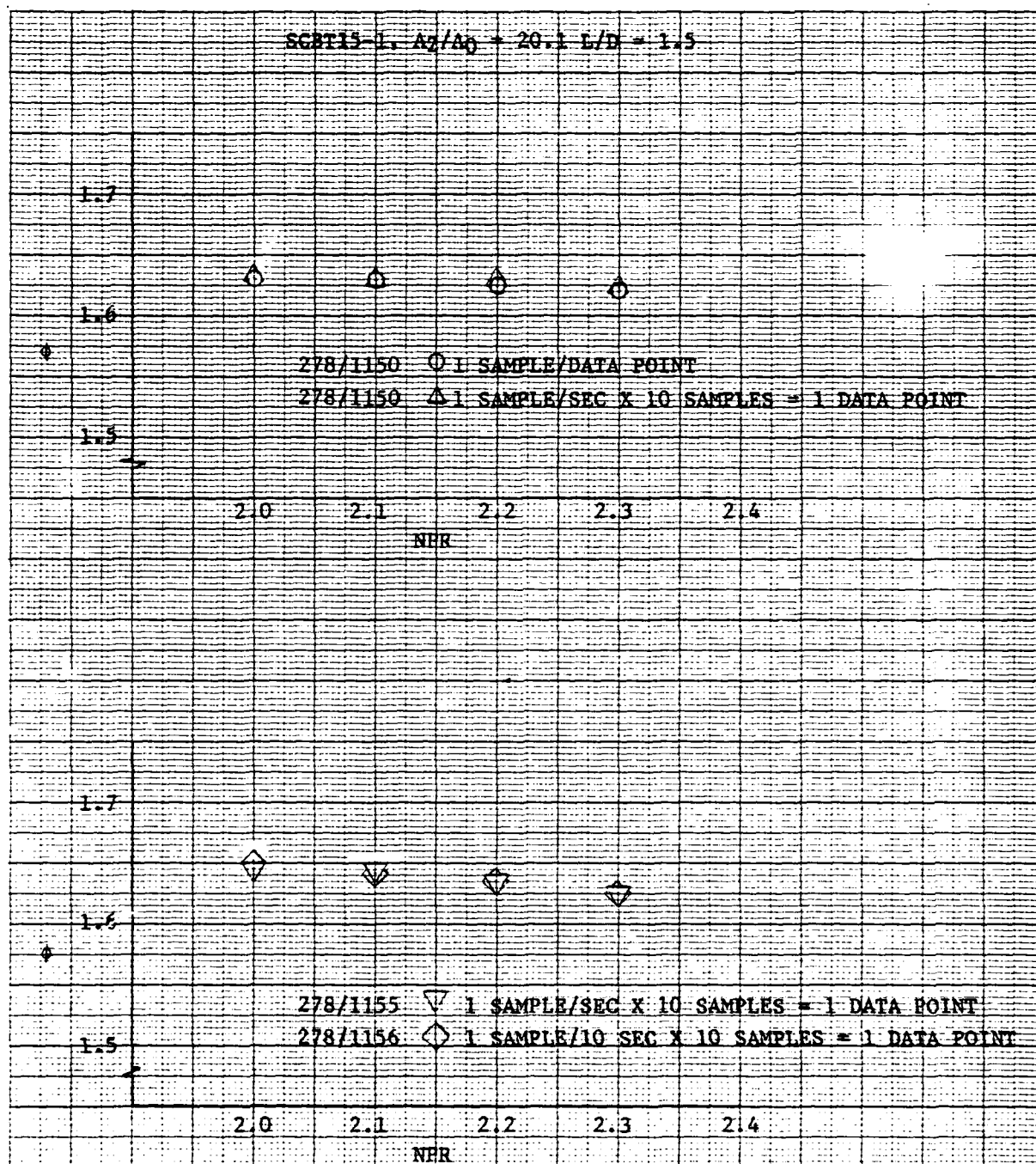
### 5.7.2 Long Time Repeatability

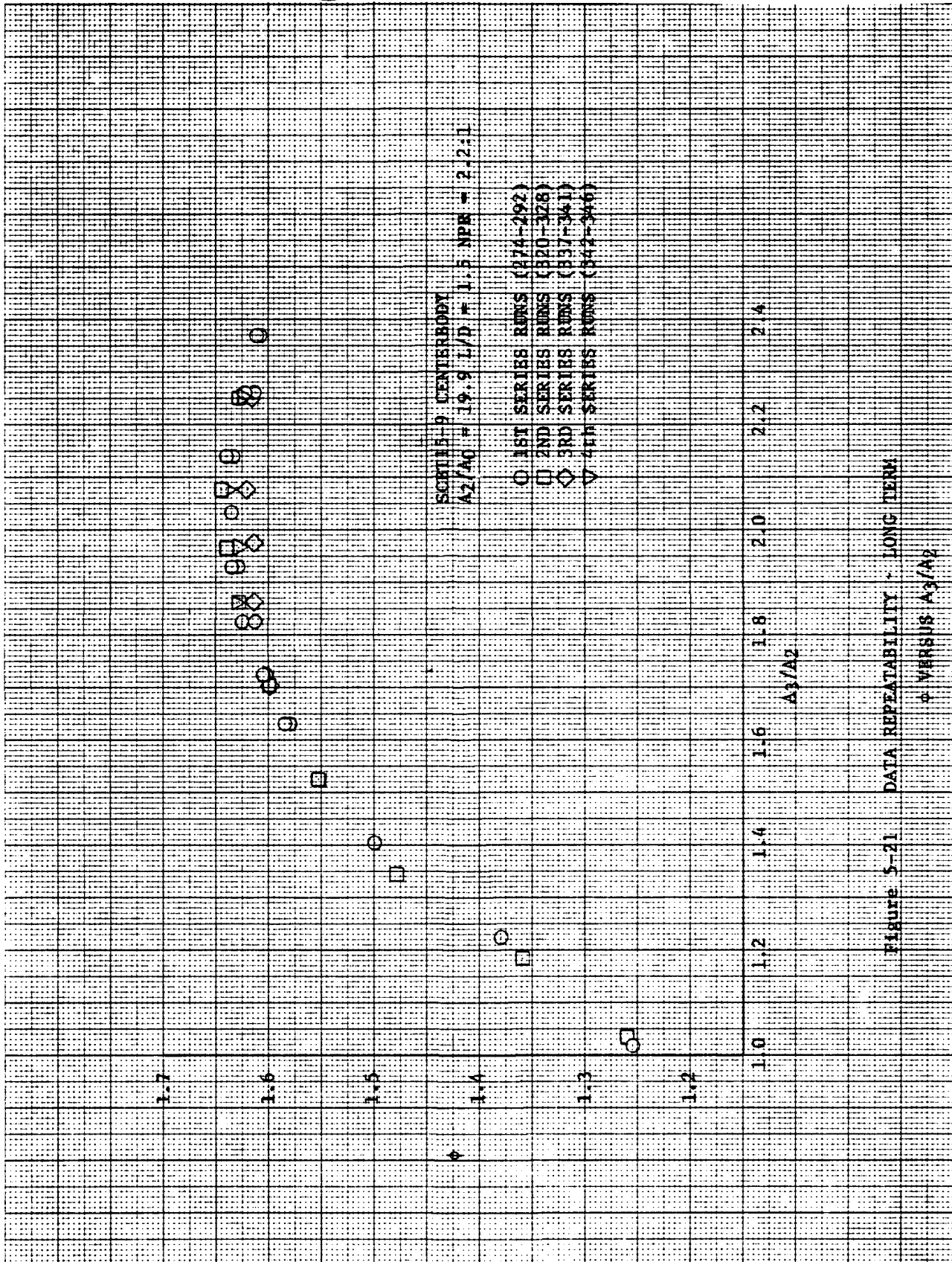
During a series of test runs where changes to the model's flaps and endwalls were being made, it was thought prudent to restore the model to a baseline configuration periodically to check the repeatability of the model's performance. Figure 5-21 shows a  $\phi$  versus  $A_3/A_2$  comparison of four run series over a two week period, where the maximum scatter in  $\phi$  performance was approximately  $\pm .013$ . This sort of repeatability check was made periodically throughout the program, wherever an opportunity presented itself. On occasion, a centerbody that had previously been tested, was reinstalled in the model to obtain additional data, and this gave the opportunity to make a check run to insure no undetected sources of error had developed in the model or instrumentation.

### 5.7.3 Rig 1 to Rig 5 Data Comparison/Repeatability

During the nozzle development program, a second test Rig (No. 5) was brought into use and an augmentor shroud fabricated to the same specifications as the augmentor on Rig No. 1.

In order to test centerbodies on both rigs and have confidence that the data could be accurately compared, test runs were made on Rig 1 with a centerbody/shroud configuration that had previously been tested on Rig

Figure 5-20 Data Repeatability - Short Term  $\phi$  Versus NPR

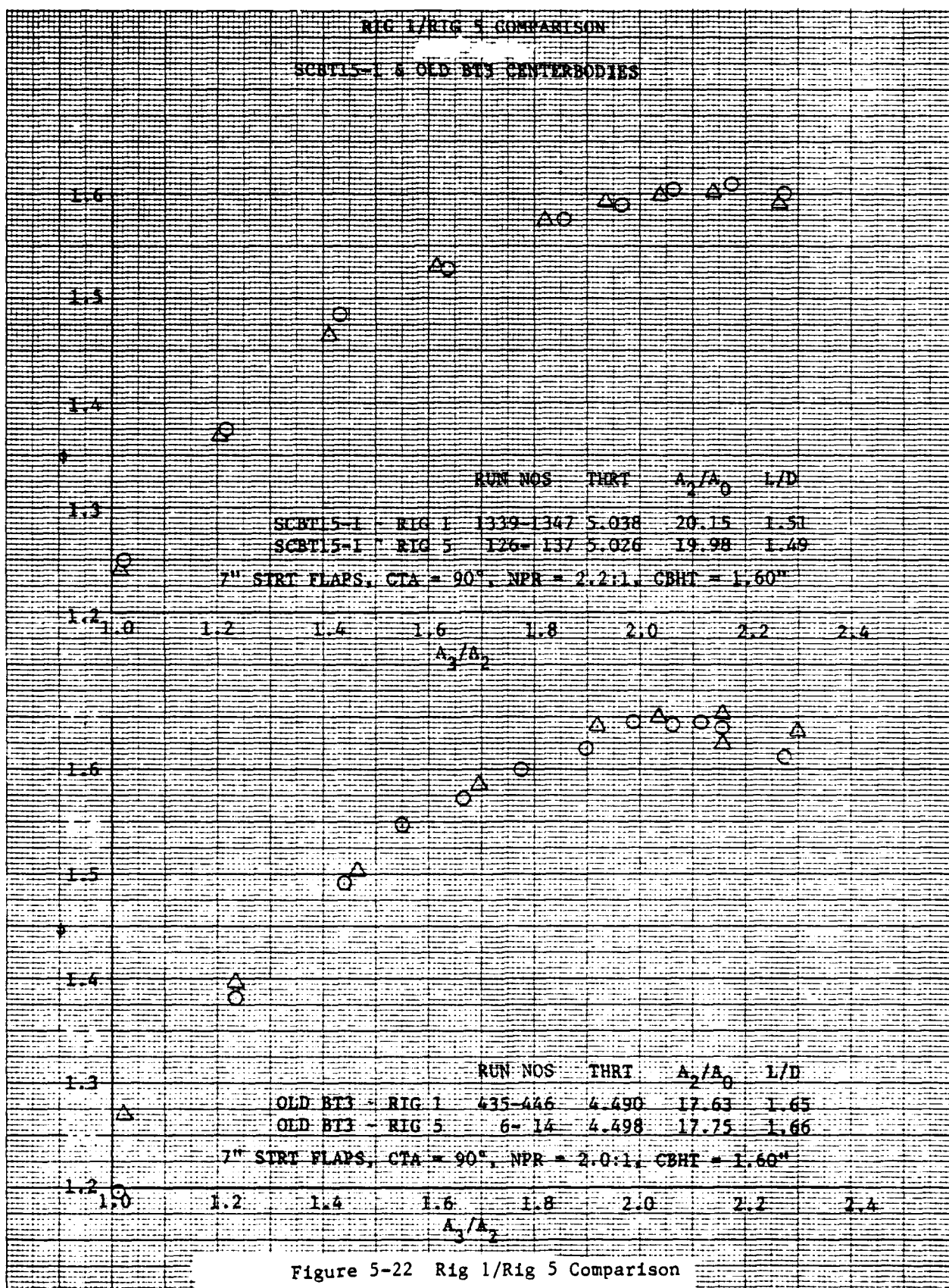




No. 5. Figure 5-22 shows a comparison plot of the  $\phi$ 's obtained for two centerbody nozzles on Rigs 1 and 5. Results were quite comparable and allowed centerbodies to be tested on either rig without possible rig or shroud differences clouding the data.

#### 5.8 SUMMARY

Analytical methods for predicting the entrainment of the turbulent jets and pressure distributions on the ejector flap have been described. Consideration of physical laws, mathematical analysis, and experimental data have been presented to show that scale model ejectors, powered by cold air jets, can be used to aid in the development of full size ejectors, powered by hot exhaust gases. Experimental apparatus and test procedures devised to ensure accurate and repeatable data are also described.





Rockwell International

NR81H-50

(THIS PAGE INTENTIONALLY LEFT BLANK)



## 6.0 COANDA DEVELOPMENT

6.1 INTRODUCTION

As a result of the XfV-12A wing diagnostic test program discussed in Section 2.3.6 of this report, several flow deficiencies associated with the wing Coanda-flap components were identified. As discussed previously in Section 3.1, an improvement rationale was selected for each of the major augmentor components. For the Coanda-flap surfaces, this approach entailed utilizing both model scale and full scale component isolated testing in combination with aircraft design and packaging studies. Based on these investigations, Coanda selection criteria were developed which identified candidate configurations satisfying both performance and design criteria. These candidate configurations were then evaluated on a full scale segment model simulating aircraft feed characteristics. Due to the unique flexibility of this model, additional studies evaluating the candidate configuration's sensitivity to inlet Mach number, feed duct position, internal Coanda shapes, and various internal flow turning devices were also performed. Finally, the optimum external Coanda shape in combination with other selected geometric modifications were incorporated and evaluated on the L/H XfV-12A wing aft Coanda-flap component (elevon).

This data when compared to comparable data obtained from the baseline XfV-12A elevon provided an indication of the relative improvement and Coanda flow quality and performance which resulted from the Coanda development effort.

6.2 SCALE COANDA EVALUATION

During the course of augmentor development work, a number of Coanda shapes were evaluated to identify a shape which would maximize augmentor performance and at the same time be compatible with aircraft packaging constraints. A number of factors must be considered when selecting a specific shape, to minimize losses and prevent jet separation from the surface while the jet is being turned. It has been determined empirically, for the nozzle pressure ratios currently being tested, a radius of curvature ( $R_0$ ) at the nozzle exit must be at least approximately eight times the nozzle gap ( $t$ ) to prevent separation at the nozzle. In addition, to prevent jet separation downstream of the nozzle exit, while the Coanda surface is operated in an augmentor, a "rule of thumb" has been observed that the local radius of curvature should be at least four times the local jet width ( $R_0 \geq 4$ ). Also the radius of curvature at the point where the Coanda surface joins the straight flap should be as large as possible to prevent a sudden diffusion loss as the jet passes the point where the radius changes from some value (however large) to a radius of infinity for the straight flap.

Another consideration while turning the jet is the running length, where a long running length ( $s$ ) would maximize the distance for entrainment of the co-flowing stream, but would also increase the surface friction losses.



Packaging considerations provide another constraint on the Coanda shape in that the desirable larger radii ( $R_1$  and  $R_0$ ) result in thicker nozzles which are difficult to enclose in a relatively thin supersonic wing section. A convenient shape easily definable mathematically, allows specifying  $R_0$  at the nozzle exit and provides for a gradually increasing radius of curvature is the log spiral shape. Figure 6-1 presents the log spiral and the equations which define its shape and some of its characteristics. Also shown is this log spiral integrated into a Coanda nozzle where it can be seen which spiral parameters are determined by the maximum allowable space available for packaging the nozzle. The dimension Y will increase in proportion to  $R_{90}^\circ$  which in turn increases with an increase in  $R_0$  and a decrease in the spiral K factor. In the present forward and aft flap design, the tangent point of the flap with the log spiral occurs at  $\theta = 106^\circ$  and it is desirable to have this parameter ( $R_{\theta=106^\circ}$ ) as large as possible.

The internal radius of curvature ( $R_1$ ) should also be as large as possible for two reasons: (1) to provide as gradual as possible convergence towards the nozzle exit so as not to distort the pressure profile at the exit, and (2) to provide as gradual a change as possible between  $R_1$  and  $R_0$  at the nozzle exit to prevent the sudden diffusion loss associated with a sudden change in radius of curvature mentioned above. However, large  $R_1$ 's also demand that the X dimension increase, which in turn drives the total surface thickness upward.

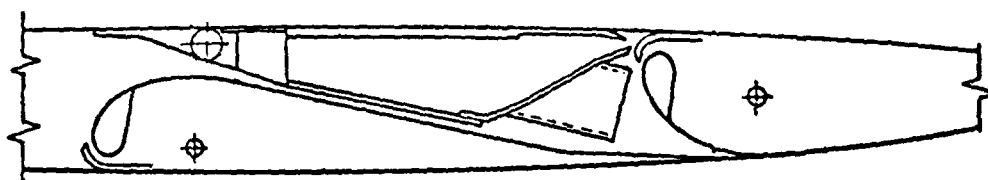
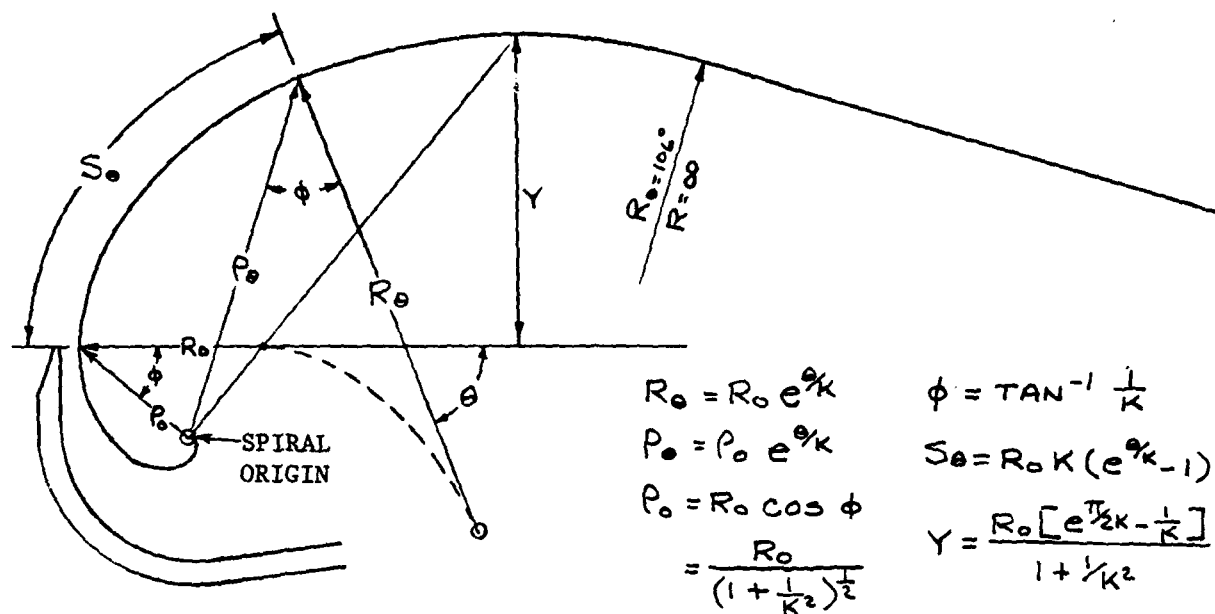
A number of 0.2 scale log spiral Coanda shapes were evaluated in free air to determine the performance characteristics of Coanda nozzles that might be acceptable. Table 6-1 presents the nozzles tested and some of their physical parameters.

Performance characteristics measured for these nozzles were: jet spreading, nozzle efficiency in the form of thrust coefficient ( $C_T$ ), and Coanda Turning Efficiency (CTE), which is a measure of the pressure remaining in the jet after being turned. The performance characteristics were measured at Coanda turning angles (CTA) of  $30^\circ$ ,  $60^\circ$ ,  $90^\circ$ , and  $120^\circ$  at nozzle pressure ratios (NPR) from 1.5:1 to 3.25:1. References (17) and (18) document the results of these tests in detail and some of the results are presented here. Table 6-2 lists the spiral shapes tested and compares their performance.

The entrainment index (I) discussed in Reference (17) is essentially the product of local jet width (w) normalized to nozzle gap (t) and local peak jet velocity ( $V_p$ ) normalized to nozzle avg. exit velocity ( $V_0$ ). Some observations of the flow quality of these Coanda surfaces are listed below according to Coanda spiral number.

- |       |   |
|-------|---|
| No. 1 | Marginally acceptable - lower than average $C_T$ and I - Large $R_1/t$ gives thick nozzle.  |
| No. 2 | Good performance - Highest entrainment index (I) and better than average $C_T$ - However, large jet width to local radius ratio ( $W_{90}/R_{90}$ ) - likely to separate when operated in an augmentor. |





COANDA SURFACE PACKAGING

Figure 6-1. Coanda Spiral-Definition & Packaging



Table 6-1 Physical Parameters of Nozzles Tested

No.	K	$R_0$	t	$R_0/t$	$R_1/t$	$R_{90}$	Y	$S_{90}/t$
1	1.17	.518	.063	8.20	7.90	1.983	.890	27.1
2	1.20	.520	.065	8.00	5.40	1.925	.880	25.9
3	1.20	.520	.055	9.40	6.40	1.925	.880	30.7
4	1.30	.640	.073	8.79	6.87	2.143	1.037	26.7
5	1.50	.590	.063	9.37	7.94	1.681	.890	26.0
6	1.80	.440	.071	6.20	2.50	1.053	.618	15.5
7	1.80	.440	.071	6.20	7.00	1.053	.618	15.5
8	1.80	.682	.075	9.10	2.50	1.632	.958	22.8
9		.675	.077	8.80	3.50	.675	.675	13.8

Table 6-2 Spiral Shapes Tested

No.	K	$R_0/t$	$R_1/t$	$W_{90}$	$W_{90}/R_{90}$	$C_v$	$I = \frac{V_p}{V_o} \frac{W}{T}$
1	1.17	8.20	7.90	.46	.23	.81	4.18
2	1.20	8.00	5.40	.82	.43	.84	6.53
3	1.20	9.40	6.40	.53	.28	.85	4.77
4	1.30	8.79	6.87	.57	.27	.83	4.73
5	1.50	9.37	7.94	.38	.23	.76	4.00
6	1.80	6.20	2.50	.54	.51	.83	4.81
7	1.80	6.20	7.00	.43	.41	.88	3.71
8	1.80	9.10	2.50	.46	.28	.80	4.28
9	$\infty$	8.80	3.50	.38	.56	.87	3.84

- No. 3      Good performance - Higher than average  $C_v$  and  $I$  -  
Longest running length ( $S_{90}/t$ ) - Safe  $W_{90}/R_{90}$ .
- No. 4      Good  $C_v$  and  $I$  - largest  $R_0 = 90$  - fairly long running  
length - safe  $W_{90}/R_{90}$ .
- No. 5      Lowest  $C_v$ , lower than Average  $I$ , lowest jet spreading.
- No. 6      Good  $C_v$ , however,  $R_0/t$  small -  $W_{90}/R_{90}$  high -  
separates at  $NPR > 2.0:1$ .
- No. 7      Good  $C_v$ , however,  $R_0/t$  small -  $W_{90}/R_{90}$  high -  
separates at  $NPR > 2.5:1$ .
- No. 8      Lower than average  $C_v$  - separates at  $CTA < 60^\circ$  at  
 $NPR > 2.5:1$ .
- No. 9      Good  $C_v$  - low entrainment index - separates at  
 $CTA < 60^\circ$  at  $NPR > 2.5:1$ .



Based on the above measurements and observations, a selection criteria was developed, which is discussed in detail in Reference (19) and summarized in paragraph 4.2 of this document, which allows a designer to select a log spiral compatible with packaging and nozzle pressure ratio requirements.

The Coanda shape tests discussed up to this point were all done at a model scale of approximately 0.2 to acquire as large a data base as possible in a short period of time. Configurations identified as potentially acceptable were then evaluated at full scale and the results of this testing is in the External Coanda Shape Evaluation portion of the Coanda segment model discussion (6.4.7).

### 6.3 INTERNAL RADIUS EVALUATION

In addition to the external Coanda shape testing discussed above, an isolated 20-inch span Coanda segment model was tested in an effort to identify the effect of variations in Coanda nozzle radius of approach and/or the nozzle lip convergence angle on Coanda component performance. Component lift and Coanda jet growth profiles were primarily utilized to quantify the performance levels of the configuration tested. The testing was conducted in two major phases. The objective of the initial phase was to isolate candidate configurations for values of radius of approach between  $R_1/t = 2$  and  $R_1/t = 5$ . This range was selected based on past trade studies which indicate that acceptable values of  $R_1/t$  lie within this range from both a component performance and a design-packaging compatibility viewpoint. Additional information concerning the effect of nozzle lip convergence angle was also obtained during this phase of testing. All testing during Phase I was conducted in the Columbus Thermodynamics Lab. The second test phase was conducted at the Wright-Patterson Air Force Base Propulsion Labs. Higher values of compressor pressure and flow were available at this facility allowing a more adequate simulation of the pressure environment the component would be exposed to when installed in a thrust augments. The primary objective of Phase II was to evaluate the suitability of the internal radius ratio of 3.0 ( $R_1/t = 3.0$ ) for aircraft hardware application.

#### 6.3.1 Phase I

A great deal of isolated Coanda component testing had been conducted with an internal radius ratio of 4.0 ( $R_1/t = 4.0$ ). While this radius of approach was found to be acceptable, design-packaging studies indicated slight improvements in hardware packaging were available through reductions in internal radius ratio. However, previous test experience indicated that radius ratios of approximately 2.0 ( $R_1/t = 2.0$ ) could induce external Coanda jet flow separation. The purpose of this test was to identify the minimum internal radius which developed acceptable external Coanda flow quality while maximizing design-packaging benefits.

The model utilized in this test series was a 2-D isolated Coanda segment model with a 20-inch span. A  $K = 1.3$   $R_0/t = 8.7$  external log spiral shape, and a nozzle exit height ( $t$ ) of .3 inch (see Figures 6-2 and 6-3) were used for the evaluation of the internal radius ratios.

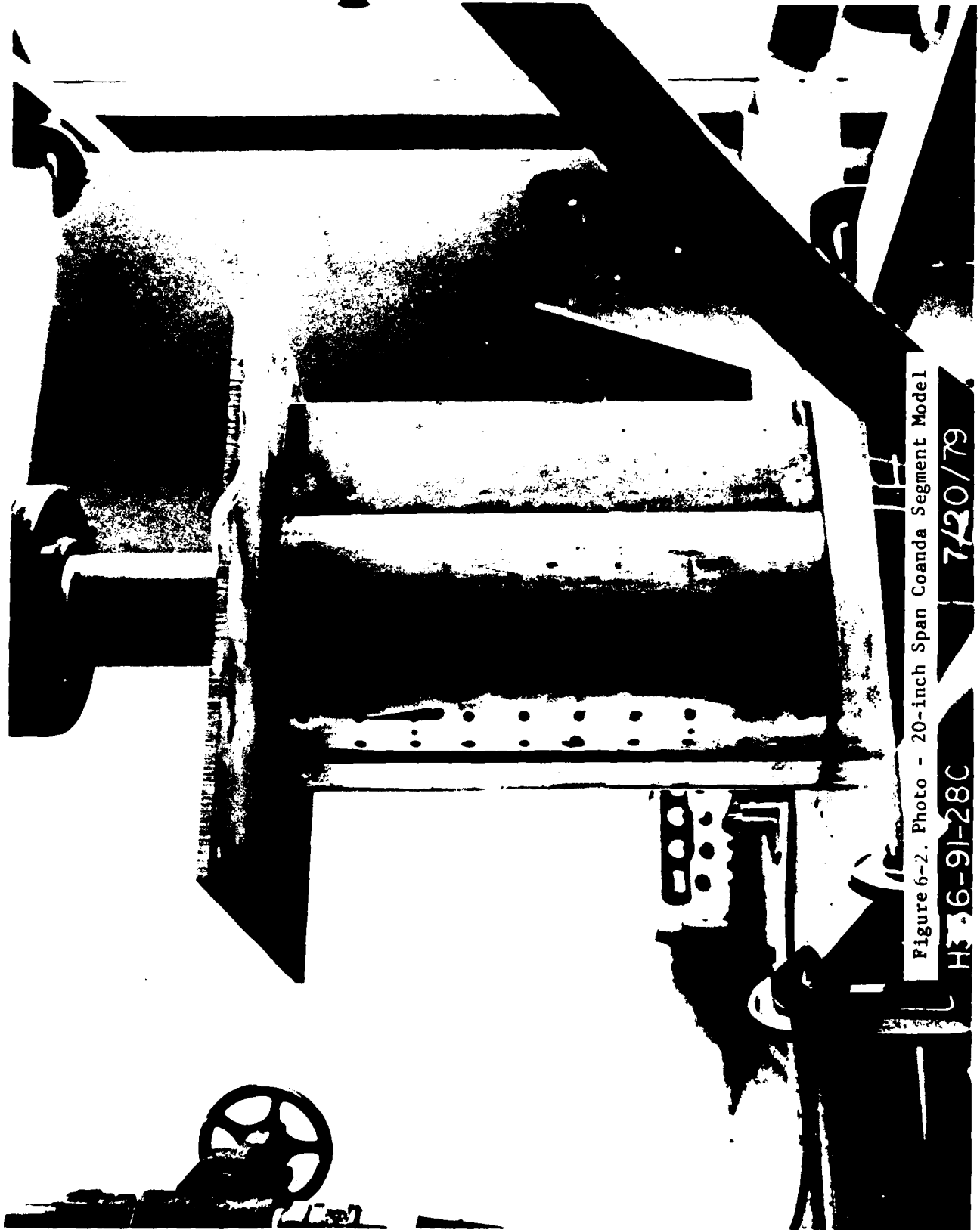


Figure 6-2. Photo - 20-inch Span Coanda Segment Model

7/20/79

H 16-91-28C

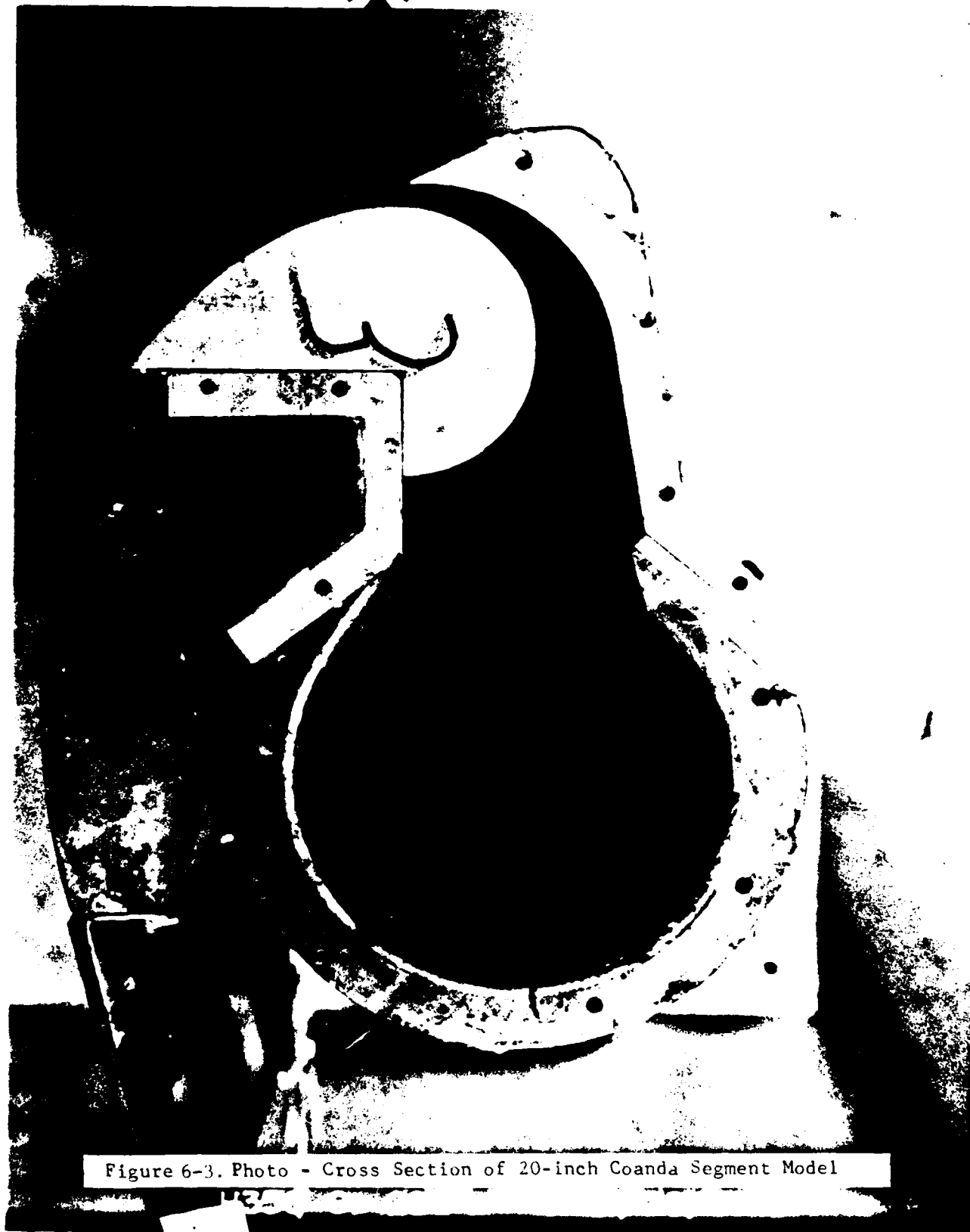


Figure 6-3. Photo - Cross Section of 20-inch Coanda Segment Model



During this phase of testing, three internal radius ratios were tested ( $R_1/t = 2, 3$  and  $5$ ) with  $0^\circ$  nozzle lip convergence angle. To isolate the effect of increasing nozzle lip convergence angle, the  $R_1/t = 2.0$  configuration was also tested with a  $10^\circ$  nozzle lip convergence. A sketch of the model with internal radius ratios from  $2.0$  to  $5.0$  installed is presented in Figure 6-4 along with the variation in upstream Mach number for each of the radius ratios pictured.

It should be noted that while an internal radius ratio of four is pictured in Figure 6-4, this radius ratio was not evaluated during this test series. A radius ratio of  $4.0$  was evaluated extensively during the Coanda segment model test program (see Reference (20)). The relative performance indicators utilized during this test series are listed below:

- Coanda jet growth total pressure profiles at nozzle exit,  $3t$ ,  $5t$ ,  $7t$ ,  $9t$ ,  $15t$ , and  $26t$  downstream of nozzle exit.
- Internal and external Coanda surface pressure taps located on the internal radius at  $90^\circ$ ,  $60^\circ$ ,  $30^\circ$  and  $.5$  s/t upstream nozzle exit, and  $5$ ,  $10$ ,  $19$  and  $26$  s/t downstream of nozzle exit on the external Coanda shape.
- Nozzle flow coefficient ( $C_D$ ) and component velocity coefficient ( $C_V$ ) versus nozzle pressure ratio.

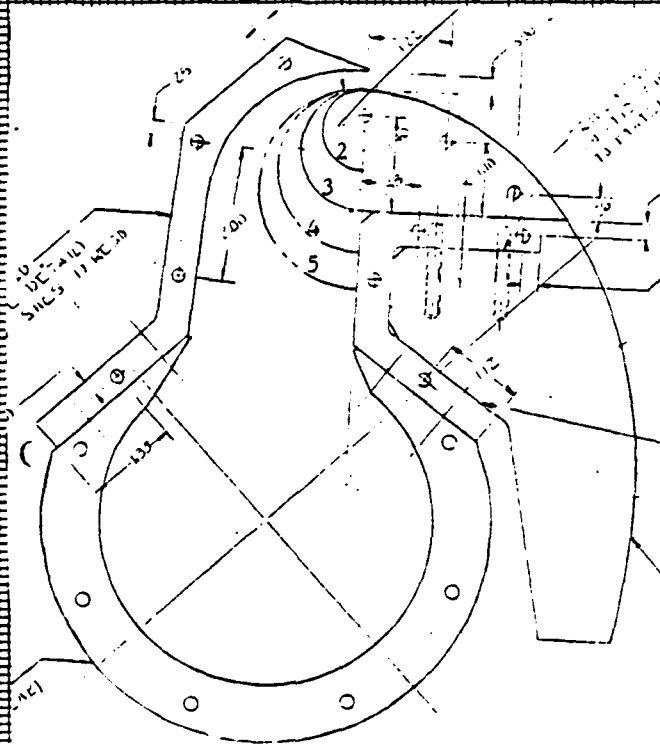
Comparisons of data of this type have typically been utilized to evaluate relative Coanda flow quality and performance during the previous model and full scale isolated Coanda component evaluation test programs and has been found satisfactory in isolating problems which may exist between individual components. Careful analysis of the data obtained during this test series resulted in the following conclusions (see Figures 6-5 to 6-7).

- No significant variations in turning efficiency (CTE) or relative jet growth can be inferred from the data presented in Figures 6-5 and 6-6. The small differences indicated in these comparisons are well within the data scatter for measurements of this type.
- Coanda surface pressure distributions indicate that none of the configurations tested exhibited any external Coanda flow separation up to the maximum nozzle pressure ratio tested,  $NPR \leq 2.5$ , (see Figure 6-7).

Figures 6-8 to 6-10 present data comparisons developed for variations in the nozzle lip convergence angles of  $0^\circ$  and  $10^\circ$  of lip tilt for the  $R_1/t = 2.0$  internal radius configuration. There is some indication that increasing the nozzle lip convergence angle may result in a slight reduction in external Coanda jet entrainment. This can be inferred from the small improvement in turning efficiency (CTE) shown in Figure 6-8 followed by a slight reduction in Coanda jet growth versus s/t presented in Figure 6-9. However, further study is necessary before any definite correlation between nozzle lip convergence angle and component entrainment can be developed. The small decrease in entrainment noted is more than



$R_1/t$  Model



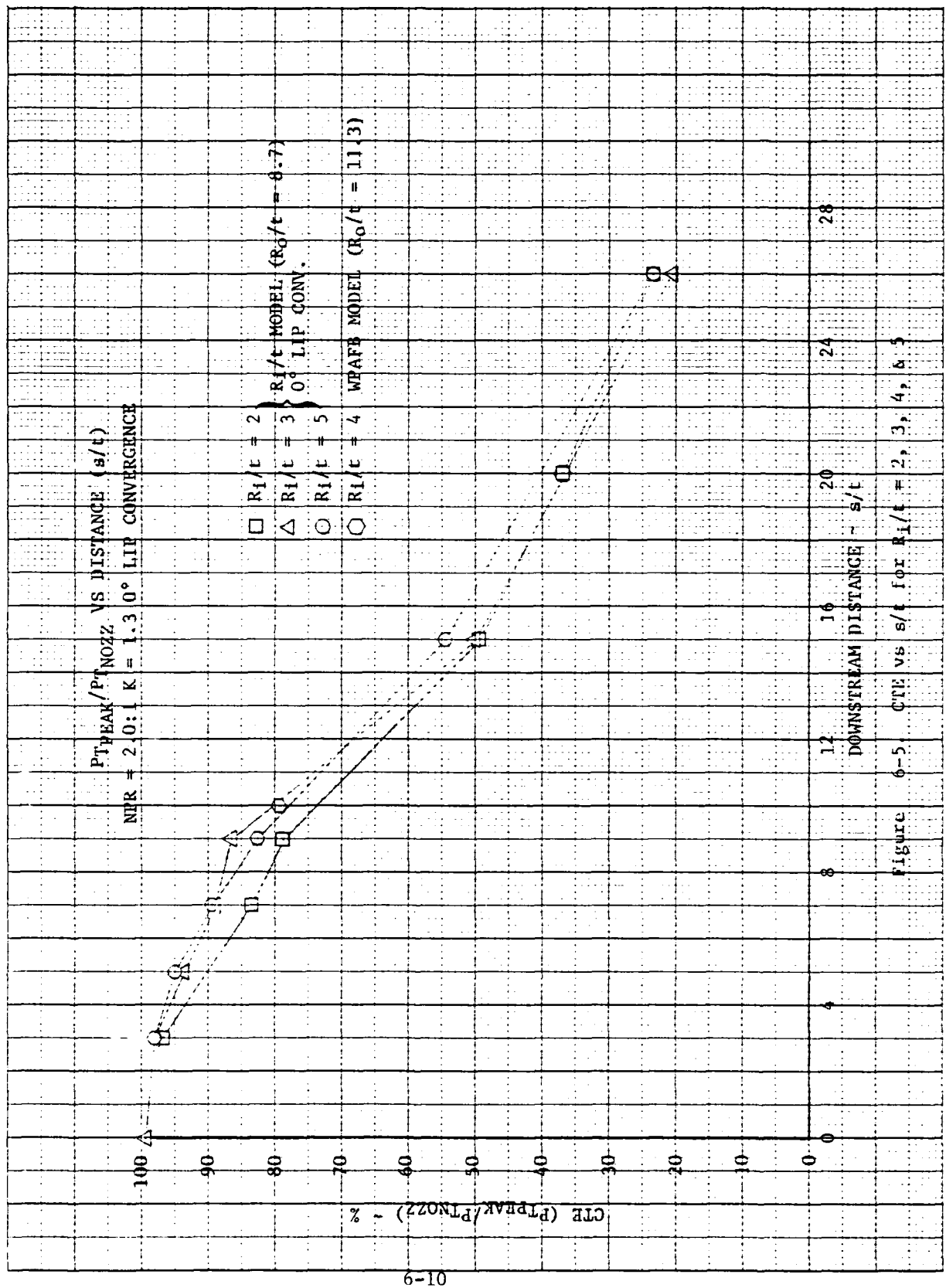
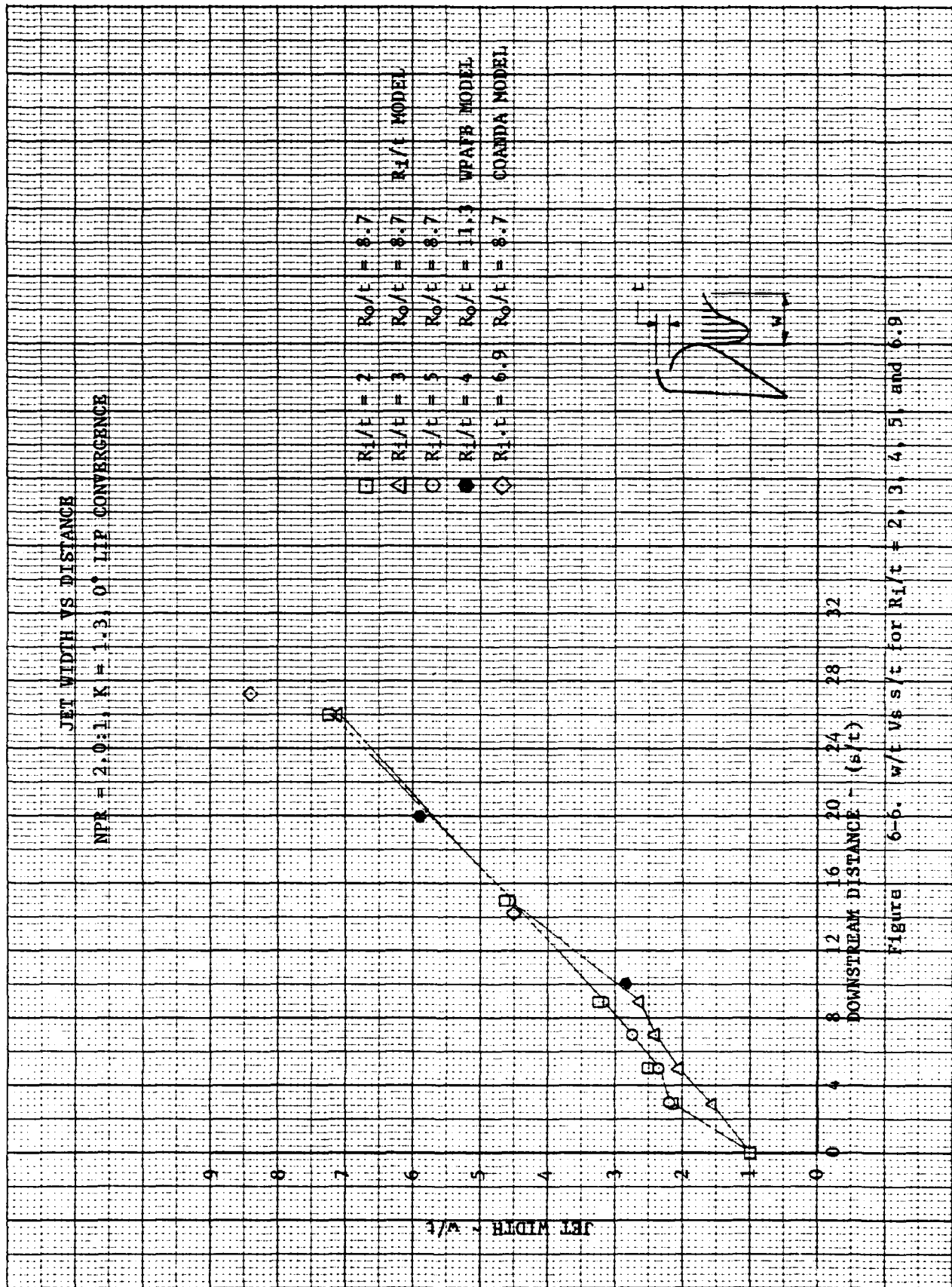


Figure 6-5. CTE vs s/t for  $R_1/t = 2, 3, 4, 5$





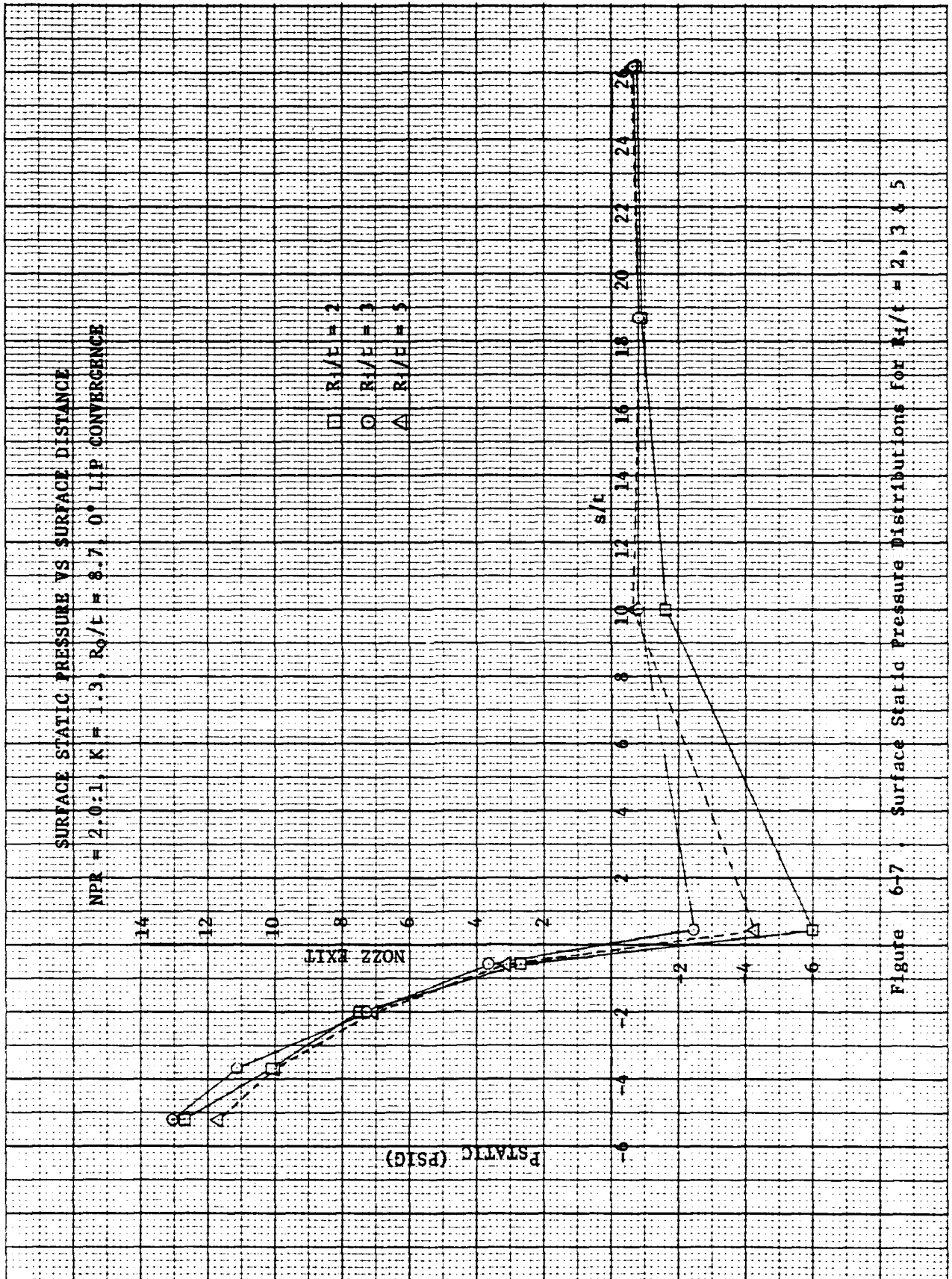


Figure 6-7 Surface Static Pressure Distributions for  $R_1/t = 2, 3, 5$



Rockwell International

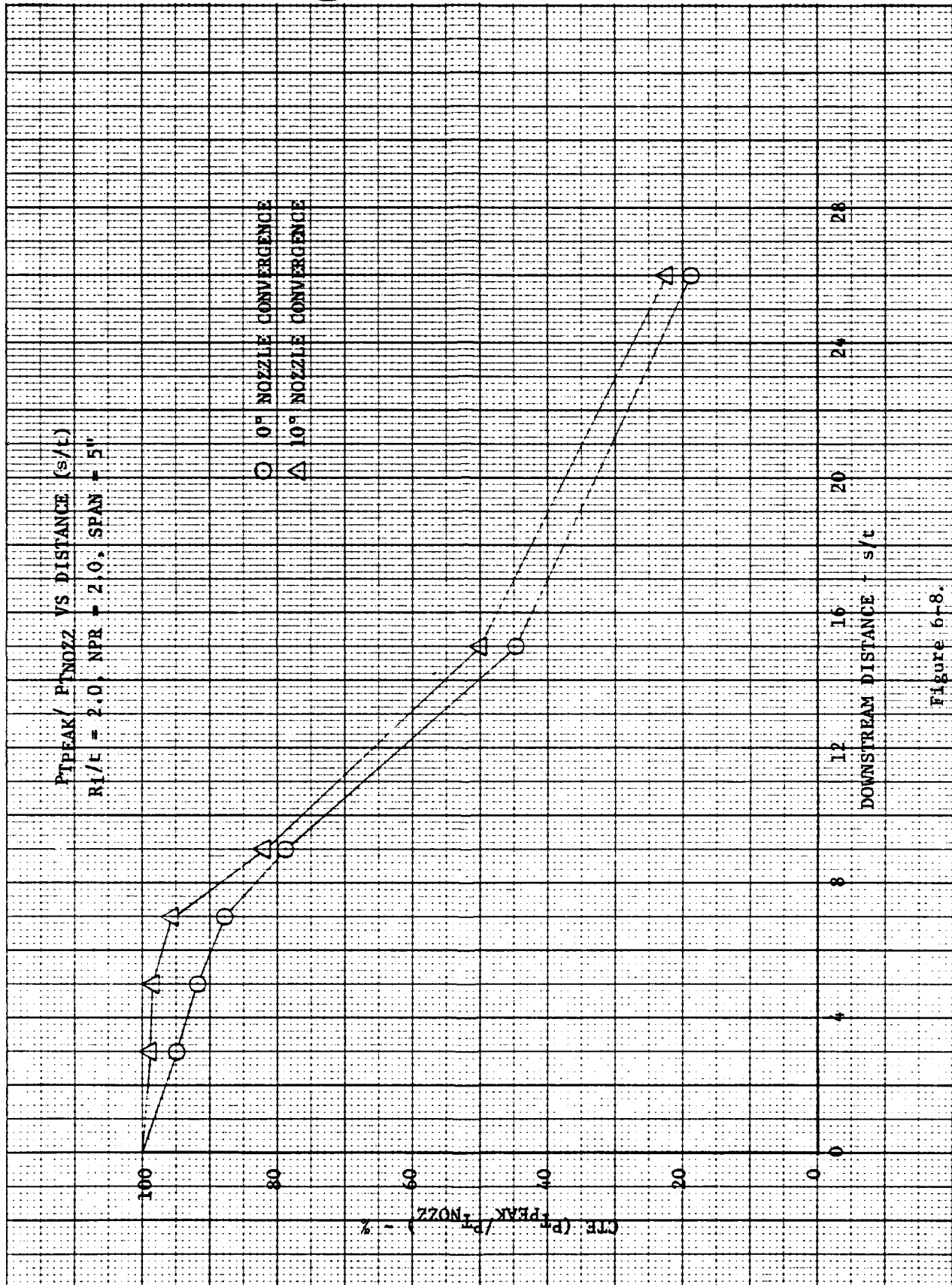
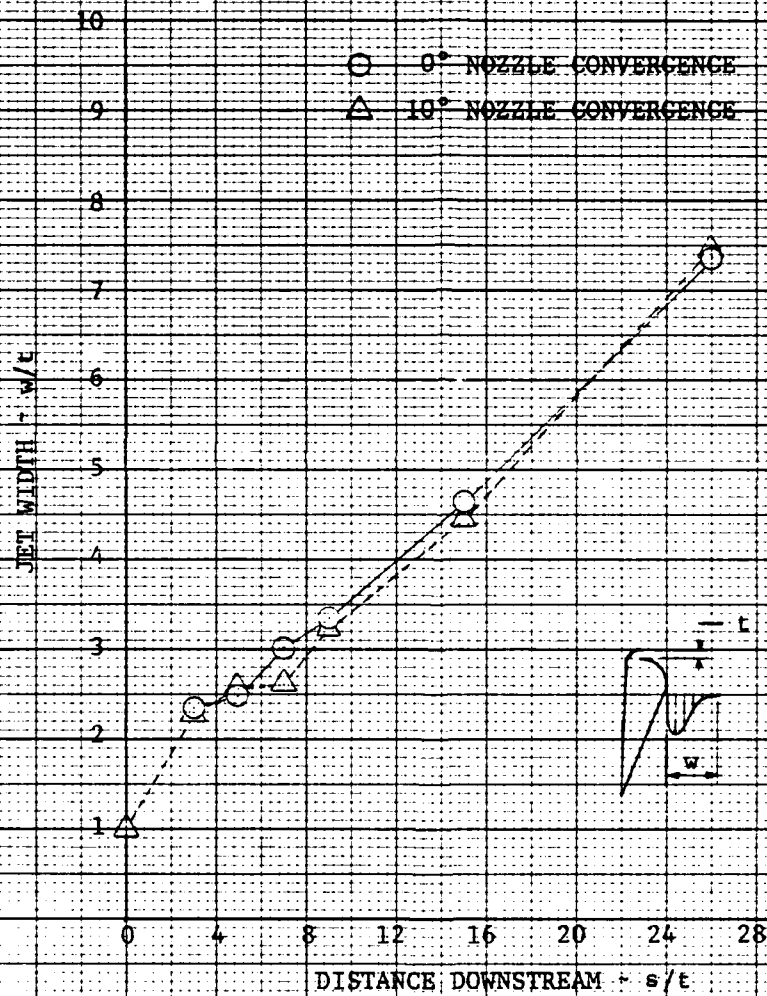


Figure 6-8.



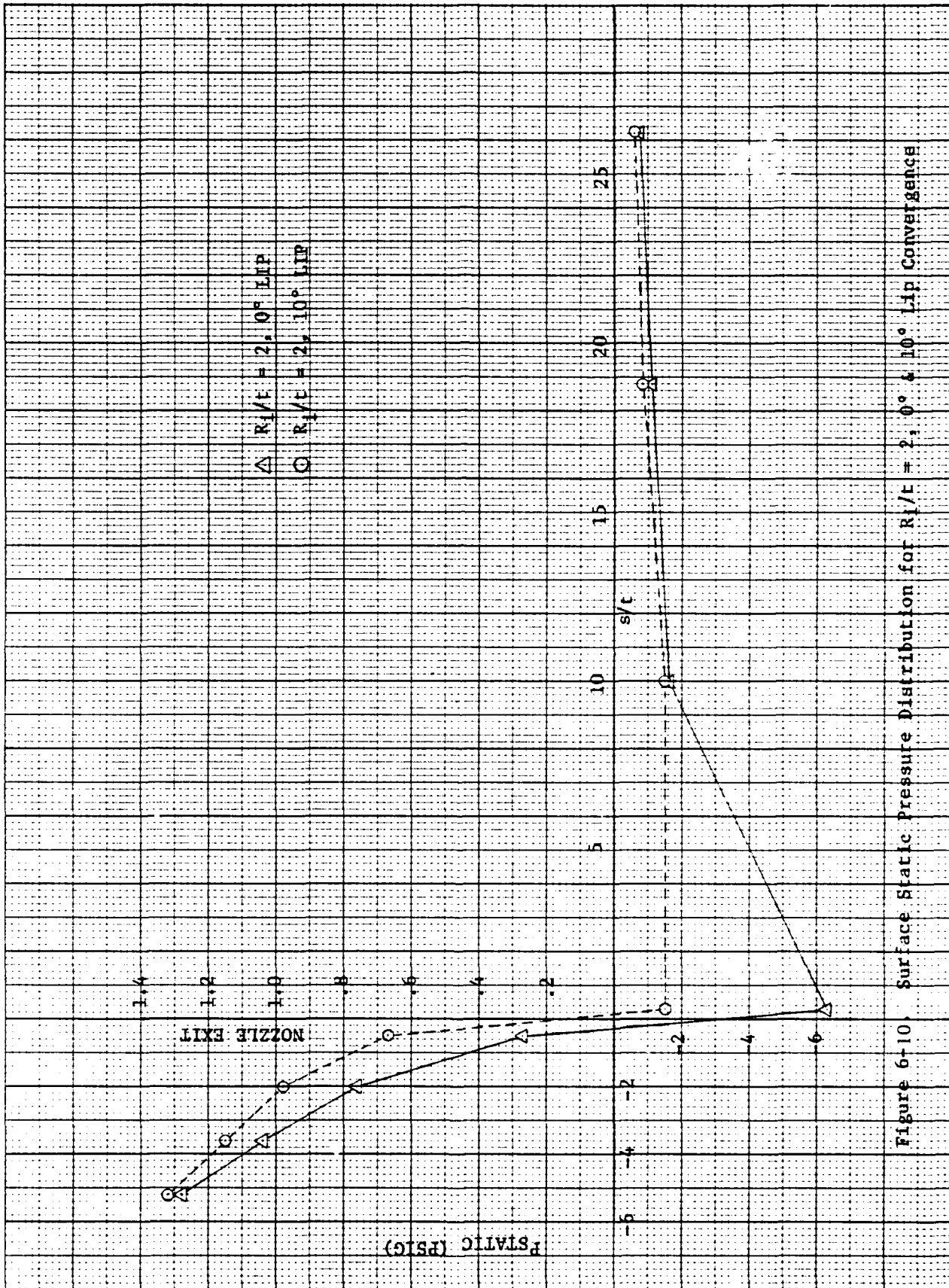
Rockwell International

Figure 6-9 .  $w/t$  Vs  $s/t$ ,  $R_1/t = 2$ , 0° & 10° Convergence



Rockwell International

40 1320

K-2 10 T NCH Rev H  
FEL RCO U.S.A.Figure 6-10. Surface Static Pressure Distribution for  $R_1/T = 2, 0^\circ \text{ \& \ } 10^\circ \text{ Lip Convergence}$



offset by the benefits obtained by slight degrees of nozzle lip convergence preventing the Coanda nozzles from distorting under pressure to a non-converging or converging-diverging (C-D) nozzle shape. The decrements in nozzle performance which may result from off-design C-D nozzles could be significantly larger than the performance decrease caused by slightly converging the nozzle as measured in this test. It is also possible that the slight decrease in entrainment noted may well be within test data measurement tolerances and be nothing more than data scatter.

In an effort to more fully simulate "in augments" flow conditions during isolated Coanda testing, it was necessary to test the isolated flap at nozzle pressure ratios somewhat higher than their typical "in augments" pressure levels. It was discovered that running isolated components at NPR's 25 to 30 percent greater than their normal operating level will approximate the pressure environment they will experience when installed in an augments shroud. Based on this information, additional tests were conducted in the internal radius variation test series at nozzle pressure ratios of approximately 3.0 ( $\text{NPR} \approx 3.0$ ). Phase I test data and concurrent design and packaging studies indicated that an internal radius ratio of 3.0 ( $R_1/t = 3.0$ ) could provide the desired hardware packaging benefits while providing some margin of safety to assure acceptable flow quality and component performance. It should be noted that while the internal radius ratio of 2.0 ( $R_1/t = 2.0$ ) appears satisfactory based on the data obtained during the initial test series, previous experience indicated that radius ratios in this range were responsible for unacceptable Coanda flow quality and performance (see References (17), (18), and (19)). Based on this data base the  $R_1/t = 2.0$  was not utilized in future designs.

#### 6.3.2 Phase II

In an effort to more fully evaluate an internal radius ratio of 3.0 ( $R_1/t = 3.0$ ) and to further investigate the effect of nozzle lip convergence angle on component flow quality and performance, the  $R_1/t$  Coanda segment model utilized in the Phase I test series was installed in the isolated component test facility at Wright-Patterson Air Force Base (See Figures 6-11 and 6-12). A full description of this facility is presented in Section 10.0 of this document. It was necessary to conduct this phase of testing at the WPAFB facility in order to achieve model nozzle pressure ratios of approximately 3.0, providing a more realistic simulation of the flow conditions the components experience when installed in an augments.

Measurements performed and data obtained in order to quantify the models performance and flow quality included:

1. Model lift, nozzle mass flow, and nozzle pressure ratio (NPR) to be used to compute nozzle flow coefficient ( $C_D$ ) and component velocity coefficient ( $C_V$ ).
2. At four spanwise locations (2, 5, 7, 5 and 10 inches from inboard endwall) total pressure jet growth profiles were recorded at the nozzle exit plane and 3, 7, 9, 15 and 26 nozzle diameters ( $s/t$ 's) downstream of nozzle exit.



Figure 6-11 Photo - Test Hardware Installed at WPAFB Facility

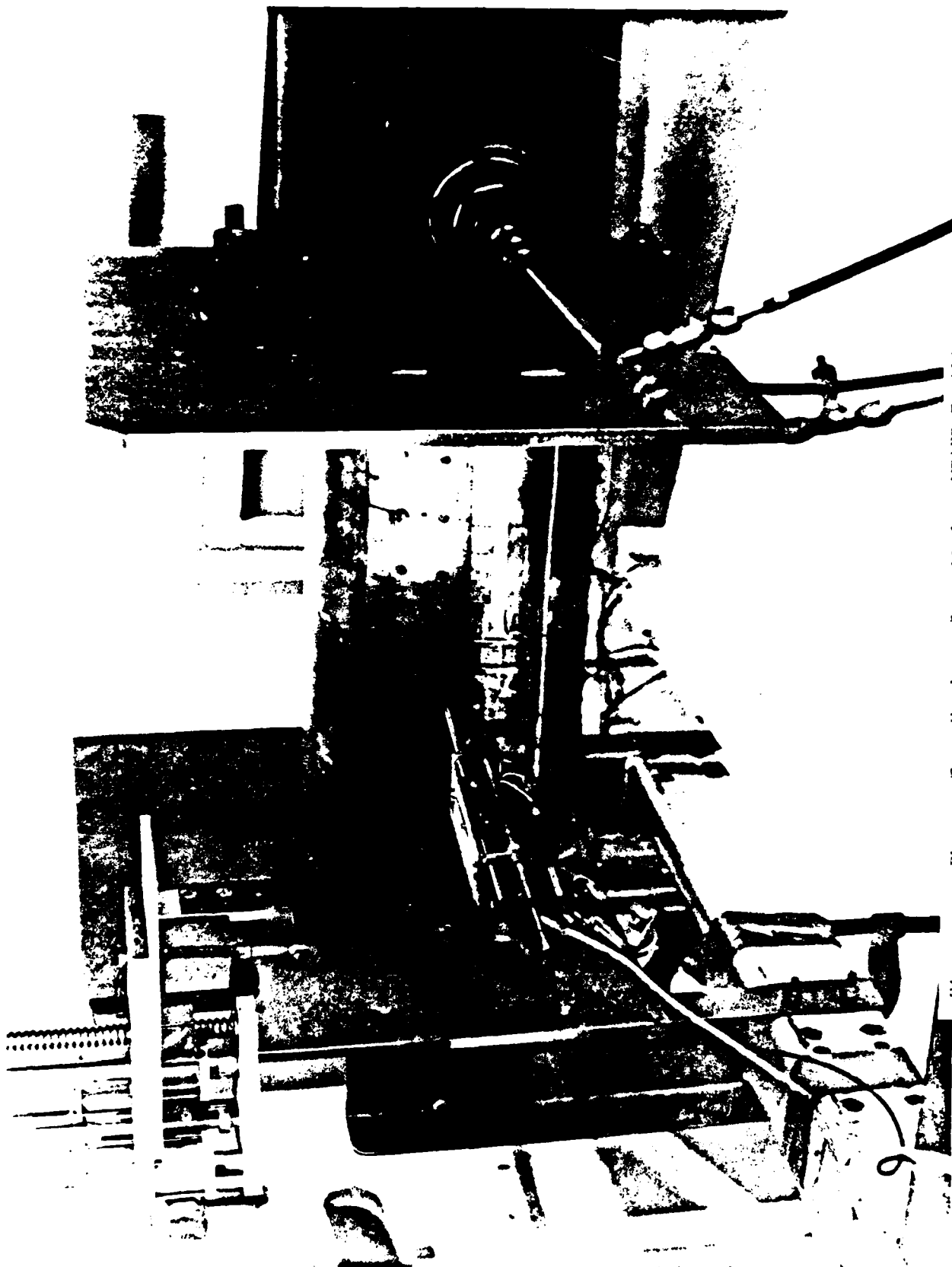


Figure 6-12 Photo - Test Hardware Installed at WPAFB Facility





3. Coanda surface pressure taps were located midspan on both the internal and external Coanda surfaces as shown in Figure 6-4. This data was used to detect the presence of external Coanda flow separations.

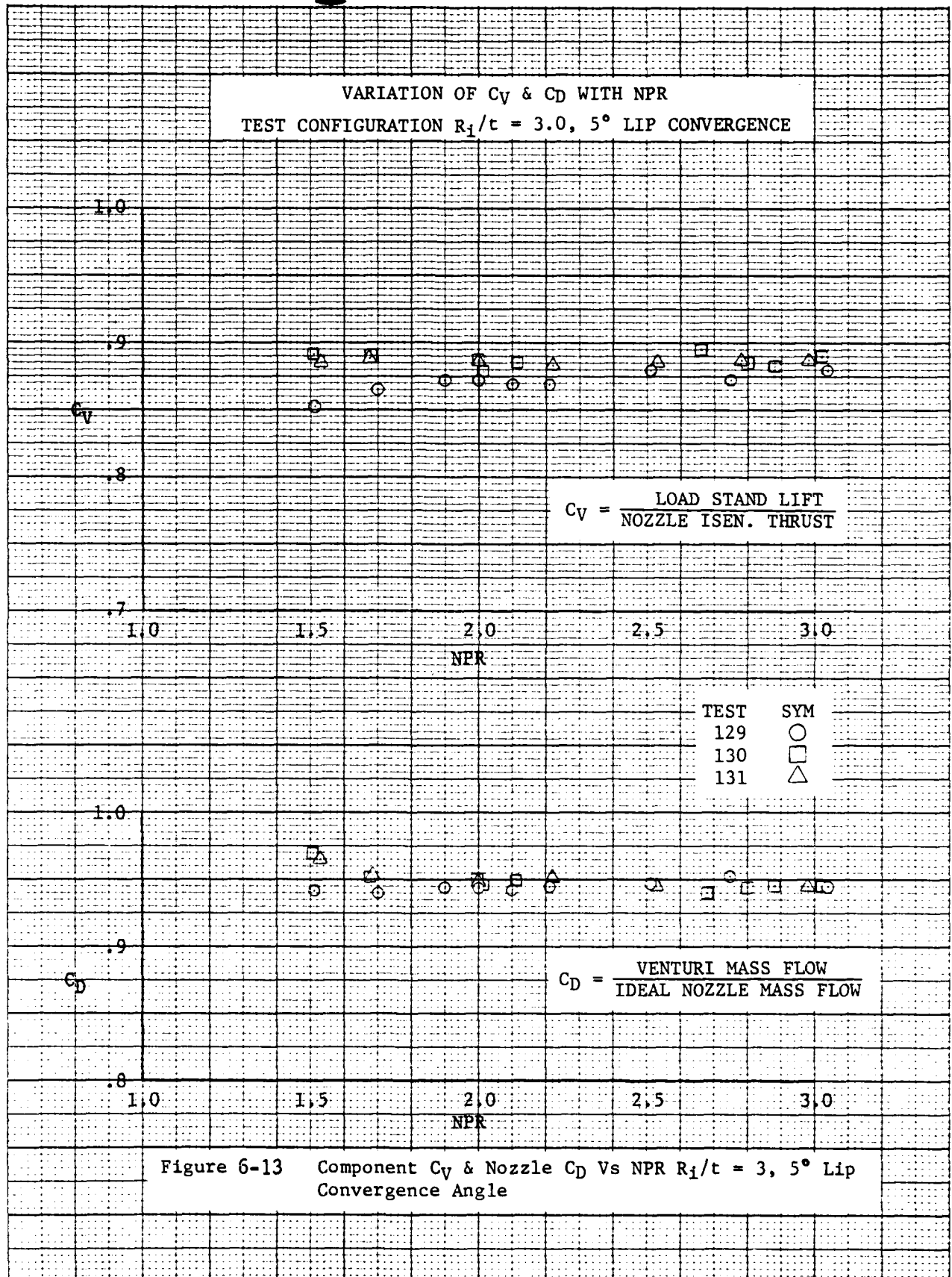
The initial configuration evaluated was the internal radius ratio of 3.0 ( $R_1/t = 3.0$ ) with  $5^\circ$  of nozzle lip convergence. Isolated component performance for this configuration is shown in Figure 6-13. Generally, this configuration produced acceptable external flow quality and levels of performance through the entire pressure range tested. There was no indication of external Coanda flow separation and nominally the flow quality appeared to be comparable to its  $R_1/t = 4.0$  counterpart reported in Reference (20). Unfortunately, direct comparisons of relative isolated component performance are not possible for the  $R_1/t = 3.0$  and the  $R_1/t = 4.0$  configurations. The  $R_1/t = 3.0$  configuration was evaluated on the 20-inch span Coanda section model described in this report while the  $R_0/t = 4.0$  investigation was conducted utilizing the 50-inch span Coanda segment model described in Reference (20). Obviously, comparisons of total component performance would be unrealistic due to the numerous geometric differences in the respective test hardware.

Investigation of nozzle lip convergence angle is of interest because of the tendency of the full scale aircraft nozzle to exhibit varying degrees of nozzle lip expansion proportional to NPR and gas temperature. This expansion can result in distortions in the Coanda nozzle shape which are severe enough to form non-converging or C-D type nozzles. Since these expansions are random and proportional to NPR and gas temperature, it is unlikely that the NPR (Mach number) and degree of C-D would match. In fact, when the character of C-D nozzles are not matched to their NPR, their performance will be off design and a simple convergent nozzle will often exhibit superior levels of performance. Additionally, the potential gains in nozzle performance possible through the use of C-D nozzles are quite small at  $NPR \approx 3.0$ . Finally, the degree of complexity and tolerances required to match a C-D nozzles characteristics is beyond the practical scope of our current hardware fabrication techniques. Matching the degree of expansion to the nozzle C-D versus NPR characteristics would be extremely difficult. Therefore, it would appear that it is quite desirable to prevent the nozzle from expanding during test since current materials and fabrication methods do not allow complete elimination of nozzle expansion. Some method must be identified which will eliminate the possibility of forming a C-D channel when the nozzle expands.

In order to prevent the nozzle from distorting to some non-optimum shape, a small degree of additional nozzle lip convergence (lip tilt) can be built into the nozzle exit approach geometry. The lip tilt will be reduced during operation - the amount of reduction being proportional to operating NPR and gas temperature. Theoretically it is possible to match the degree of nozzle lip expansion and nozzle lip tilt so that at the typical normal operating pressure ratio the nozzle would distort to the optimum nozzle shape and area. Unfortunately, the hardware tolerances required to accomplish this option are not possible with current fabrication techniques. It is also difficult to define the aircraft's



46 1320

10 X 10 TO 1 INCH 2.5 IN DIA. HP  
KLEIN & L. CO. MADE IN U.S.A.



nominal operating pressure ratio. This value is dependent on ambient conditions and engine power settings. To assure that the nozzle remains convergent in nature through the entire nozzle pressure ratio range, slightly more nozzle lip convergence than is required is built into the nozzle approach geometry. In order to identify if Coanda component performance and flow quality are sensitive to this nozzle lip convergence angle, the  $R_1/t = 3.0$  configuration was tested at  $5^\circ$  and  $10^\circ$  lip convergence angles. For these two lip configurations, the following parameters were measured: velocity coefficient ( $C_v$ ), flow coefficient ( $C_D$ ), turning efficiency (CTE), jet spreading, and Coanda surface static pressures. Over a range of nozzle pressure ratios (1.5:1 to 3.0:1) and at several span stations, there was no evidence in the data (see Reference (21)) to indicate that increasing the nozzle lip coverage angle from  $5^\circ$  to  $10^\circ$  produces notable differences in total component performance or external coanda jet entrainment.

It should be noted that during the Phase I test series, a slight reduction in external Coanda jet entrainment was detected when the nozzle lip convergence angle was increased from  $0^\circ$  to  $10^\circ$  lip tilt angle. Initially, the results of the two test phases may appear conflicting. However, it is possible that a slight reduction in entrainment may result from any increase in lip convergence angle above the nominal  $0^\circ$  lip tilt or that the decrease in entrainment noted is so small that it may be within the typical test measurement tolerances. It is obvious that the numerous benefits resulting from small degrees of nozzle lip convergence more than offset the slight decrease in entrainment noted during the initial test phase. In general, allowing the nozzle to distort to a non-converging approach geometry could result in a substantial reduction in isolated component performance. Therefore, it was concluded that a nozzle lip convergence angle of  $5^\circ$  to  $10^\circ$  be incorporated in the Coanda component hardware.

#### 6.4 COANDA SEGMENT MODEL

##### 6.4.1 Introduction

Analysis of data obtained during the XFV-12A wing diagnostic test program identified several flow deficiencies associated with the wing aft Coanda jet. In an effort to isolate these deficiencies and define solutions, a series of investigations utilizing a part span mockup of the elevon were conducted. This model designated the Coanda segment model was designed with provisions allowing variations in hardware geometry, and airflow feed conditions. Selected changes which provided notable improvement in Coanda flow quality and performance were then incorporated and evaluated on the L/H wing elevon as discussed in Section 9.0 of this report. A complete description of the Coanda segment model test program can be found in Reference (20).

##### 6.4.2 Test Program

The test program was conducted at Wright-Patterson Air Force Base (WPAFB) Aeronautical propulsion Laboratory (APL), Dayton, Ohio. A full



description of the WPAFB test facility is presented in the facilities section of this report. These tests were conducted in three basic phases (see Figure 6-14) and included variations in the following variables.

#### Flow Variations

- Nozzle Pressure Ratio
- Internal Feed Duct Mach Number

#### Model Variations

- Feed Duct Location Relative to Coanda Nozzle Exit Plane
- External Coanda Shapes
- Internal Coanda Shapes
- Internal Flow Turning Devices

The effects of variations in the variables on total component performance were isolated through direct measurements of model loads, nozzle airflow, and pressure characteristics. A traversing pressure rake was employed for measurements of pressure profiles at various s/t's along the Coanda surface. Various flow visualization techniques were employed to determine component flow quality and isolate the degree of spanwise flow angularity.

#### 6.4.3 Model

The model tested shown in Figure 6-15 simulates the XFV-12A lefthand wing elevon inboard section (initial 50 inches of span) and is completely defined in Reference (20). In order to simulate aircraft feed conditions on the model, an S-shaped feed duct similar to its aircraft counterpart was fabricated and attached directly to the model mounting plate, Figure 6-15. The basic model design allowed for a high degree of flexibility providing for variations in feed duct location relative to nozzle exit plane, as shown in the sketch on Figure 6-16. A manually adjusted dump door, Figure 6-17, was located at the outboard end of the model to provide variations in inlet Mach number.

Three different Coanda shapes were installed during the test program. A sketch presenting geometric comparisons of the three shapes is presented in Figure 6-18. Following pressurization of each Coanda shape, plaster castings at 8, 24, and 42 inches from the inboard endwall were made to verify that the shape contours were within specified design tolerances.

Direct hardware modifications were accomplished to evaluate internal radius ratios of 3.0 and 4.0.

#### 6.4.4 Baseline Performance

Prior to any attempt to optimize the overall performance of the XFV-12A's elevon utilizing the Coanda segment model, it was imperative that the Coanda segment model in its baseline configuration simulate the performance and flow characteristics of the existing wing elevon. The primary purpose



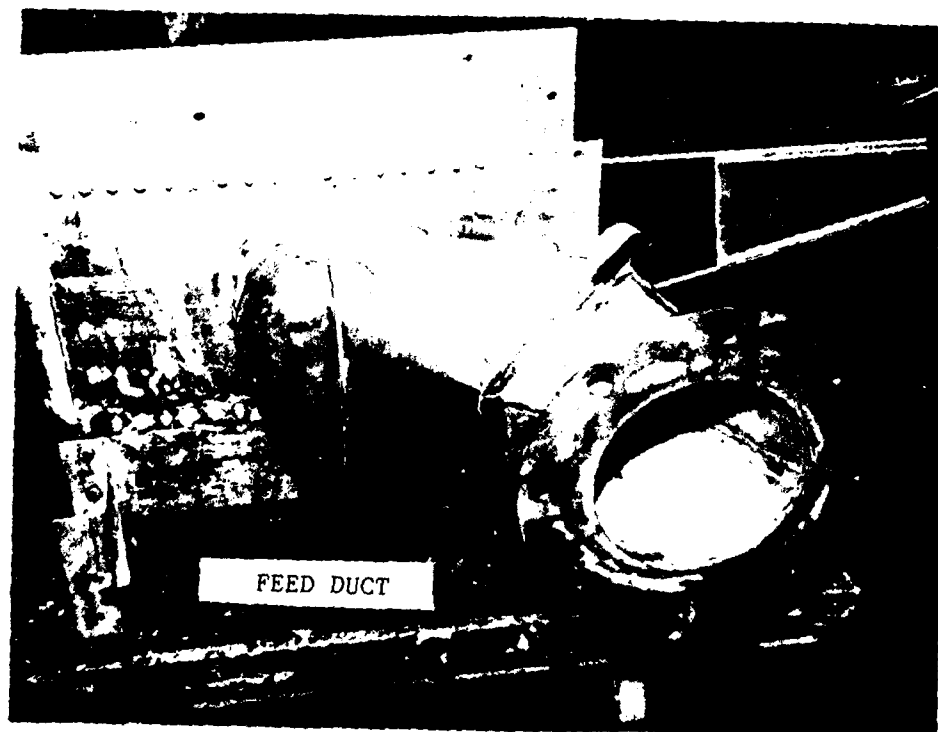
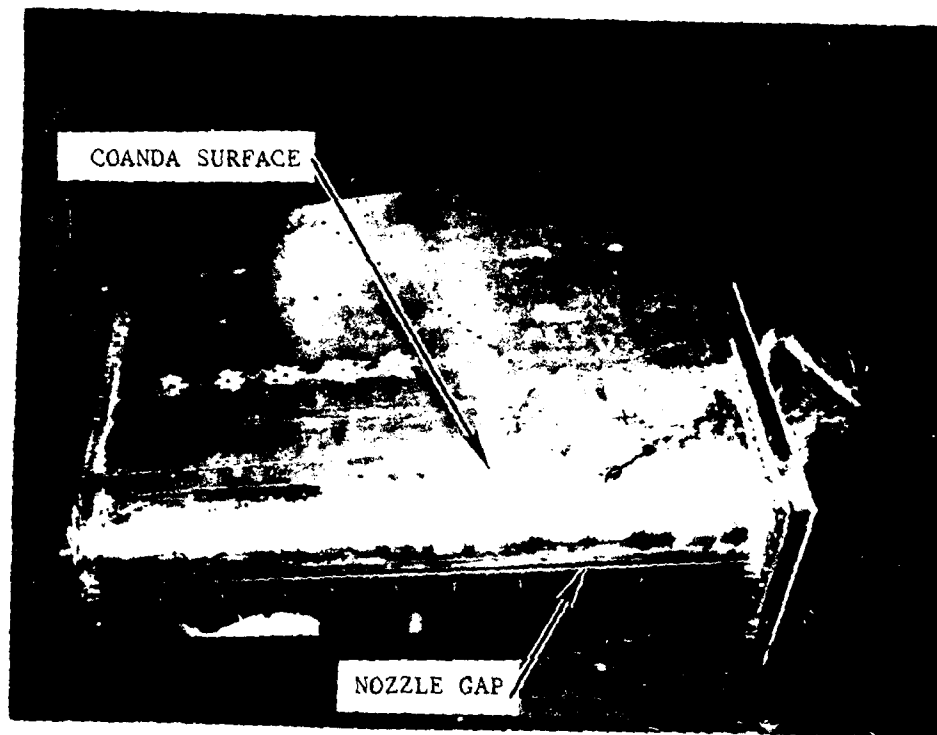


FIGURE 6-15 FULL SCALE ELEVON COANDA SEGMENT MODEL

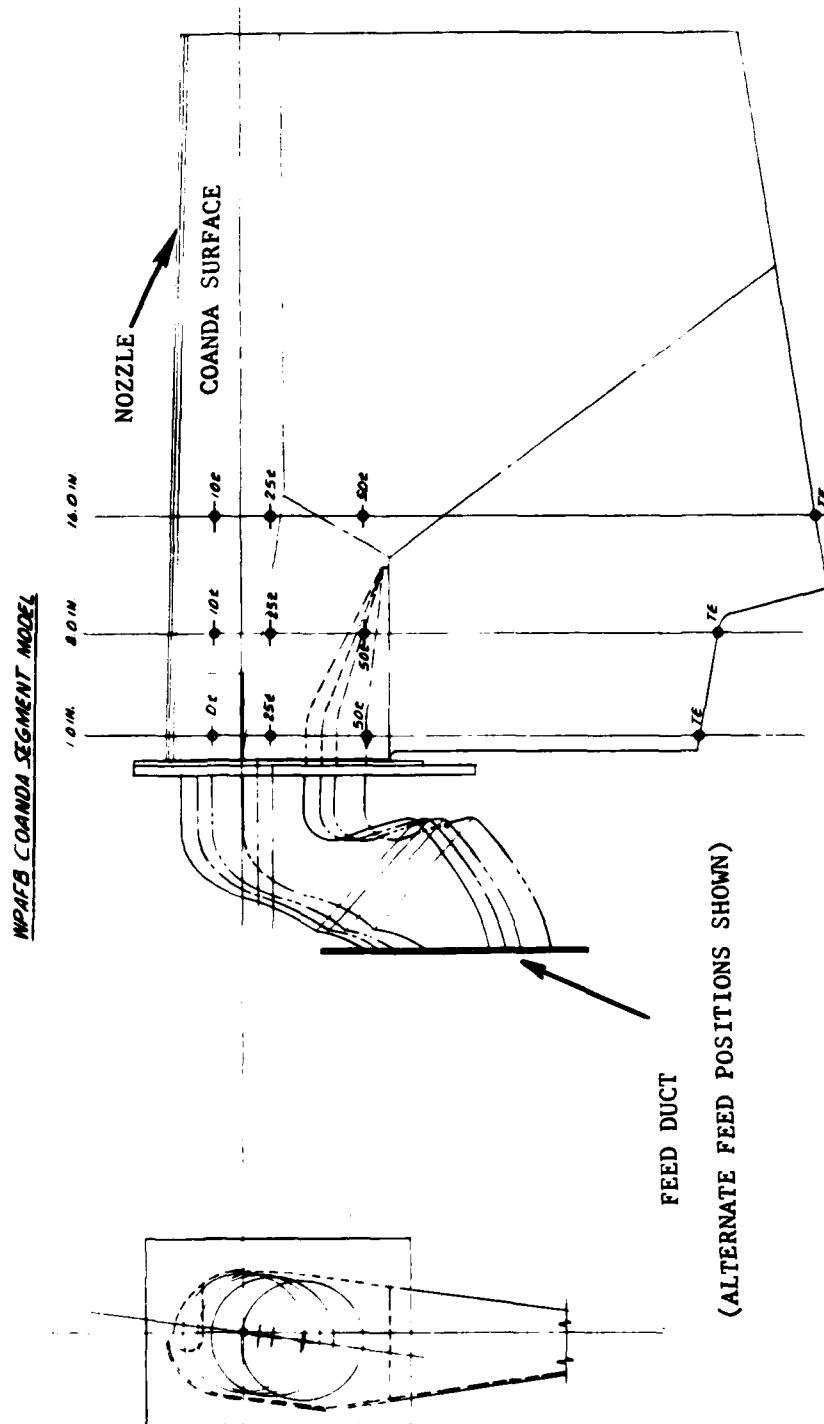


FIGURE 6-16 FEED DUCT POSITIONS

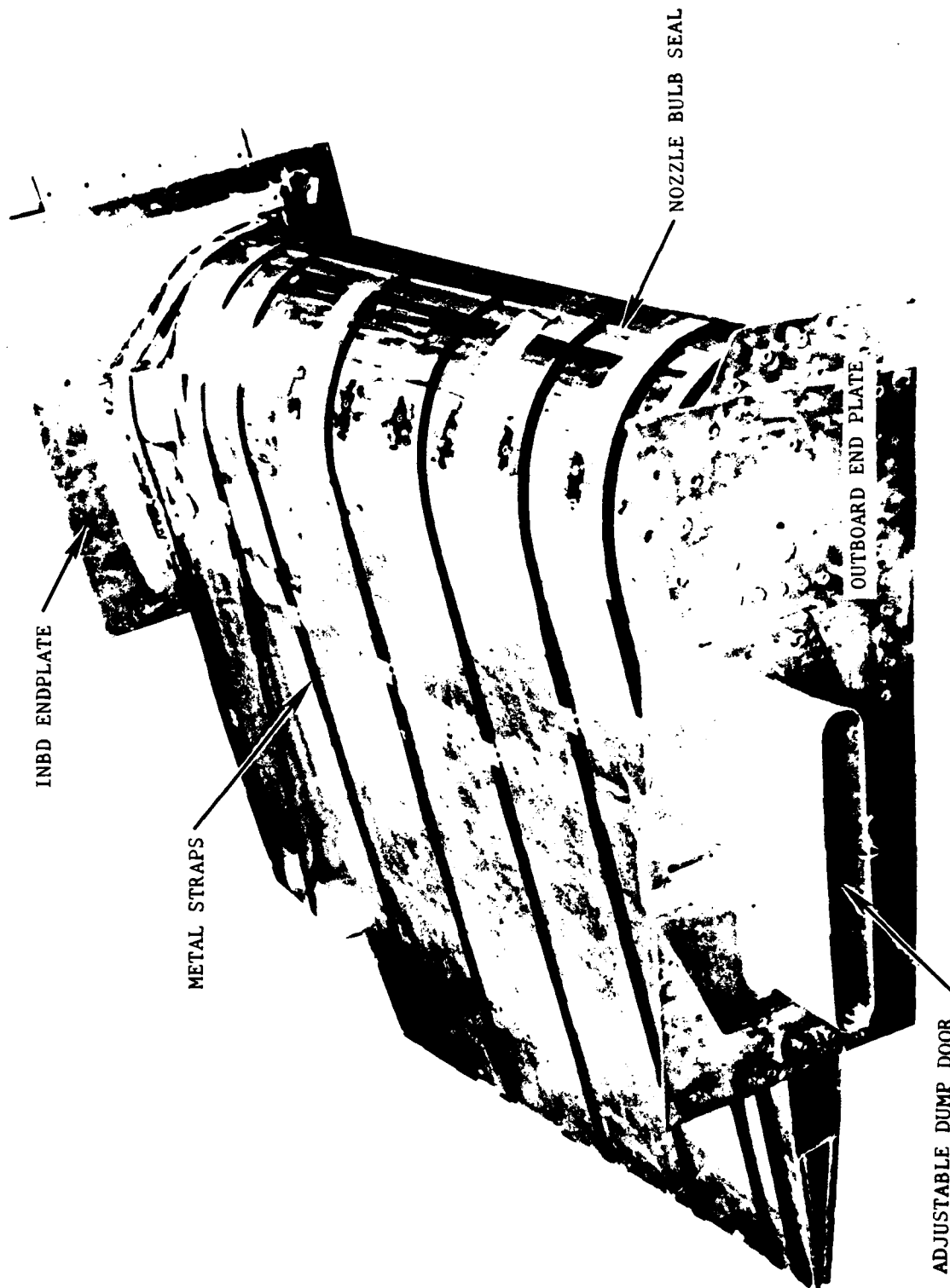


FIGURE 6-17. DUMP DOOR



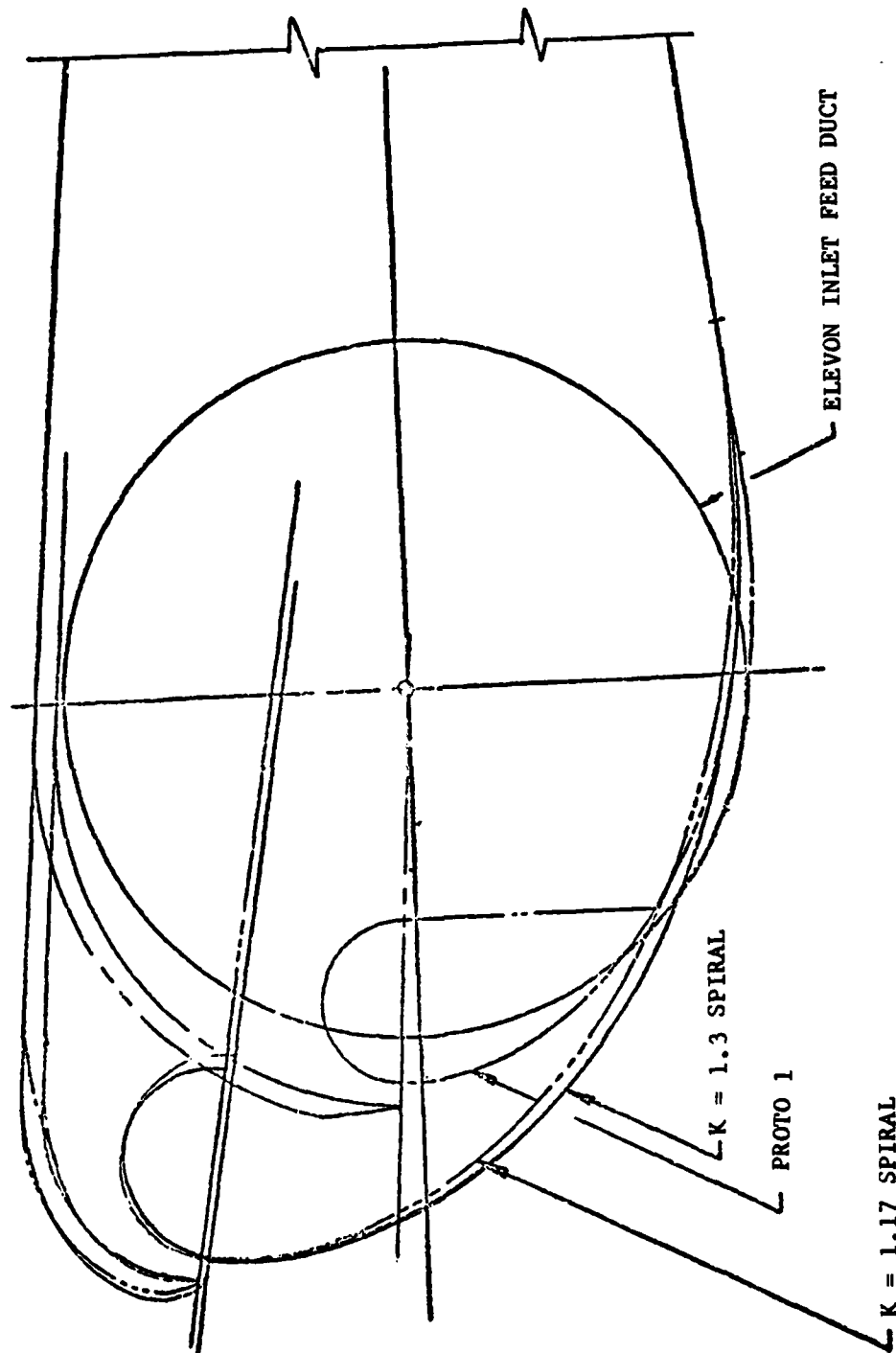


FIGURE 6-18. COANDA SHAPE COMPARISON



of the initial test series was to establish the performance characteristics of the baseline configuration to assure simulation of the Proto 1 elevon. Comparison of this data, Reference (20), indicates the performance similarity.

As presented in Figure 6-19, the spanwise nozzle total pressure distribution for the Coanda segment model and the XFV-12A elevon are very similar in nature. Both exhibit high pressure peaks in the inboard corner, followed by a flow defect outboard of the interface turning vane, and finally flat profiles from approximately ten inches outboard.

Flow visualization studies conducted on both components indicated that both exhibited similar flow characteristics; i.e., a high degree of spanwise flow angularity in the inboard region of each component. Figures 6-20 and 6-21 present flow visualization photographs which are representative of these tests.

Based on the foregoing information as well as analysis of pressure profile data, it can be concluded that the segment model successfully represented the XFV-12A aft flap.

#### 6.4.5 Location of Feed Duct

Variations in the location of the feed duct relative to the Coanda nozzle exit plane were evaluated for sensitivities of Coanda flow quality and performance. Basic variations of one, two, and four inches were conducted as shown in the sketch, Figure 6-16. Test data indicated that relocating the Coanda feed duct one and two inches below the Coanda nozzle exit plane significantly improves component flow quality. At the two inch position, however, a notable drop in the nozzle exit total pressure was observed from the inboard endwall to the outboard end of the interface turning vane as shown in Figure 6-22. Inspection of the model hardware indicated that when the feed duct was located at the two inch position, the interface turning vane was actually blocking flow from the inboard region of the Coanda nozzle exit. As shown in Figure 6-23, removing the turning vane vastly improved the pressure distribution in this region. While the interface turning vane proved useful when the feed duct was located in the baseline position, it is not required and is in fact harmful when the feed duct is located in the two inch position. Moving the feed duct to the four inch position failed to produce any further notable improvement in Coanda flow quality. Variations in  $C_v$  and  $C_D$  as a function of feed duct location are presented in Figure 6-24. Additional confirmation of the improved flow quality with the relocated feed duct (without turning vane) was the jet pressure profile development along the surface, Figure 6-25.

#### 6.4.6 Effect of Inlet Mach Number

Opening the dump door at the outboard end of the model produced a variation in feed duct mass flow and Mach number at constant nozzle pressure ratios. The objective of this procedure was to vary Mach number to simulate variations in feed duct area. As shown in Figure 6-26, reducing the feed duct Mach number from  $M = .235$  representative of the

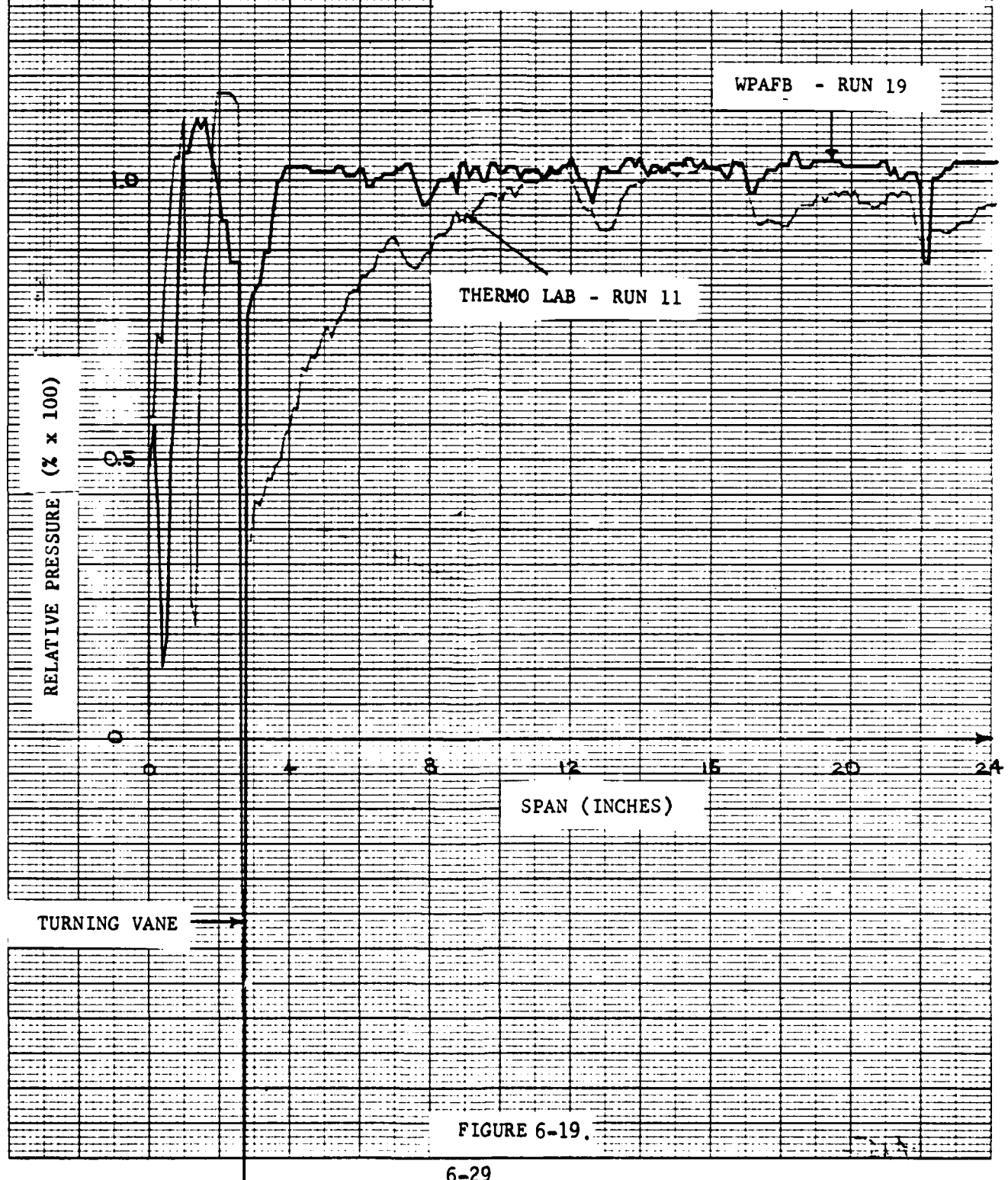


Rockwell International

NOZZLE TOTAL PRESSURE DISTRIBUTION COMPARISON

WPAFB - RUN 19 - BASELINE CONFIGURATION

THERMO LAB - RUN 11 - AIRCRAFT SIMULATION

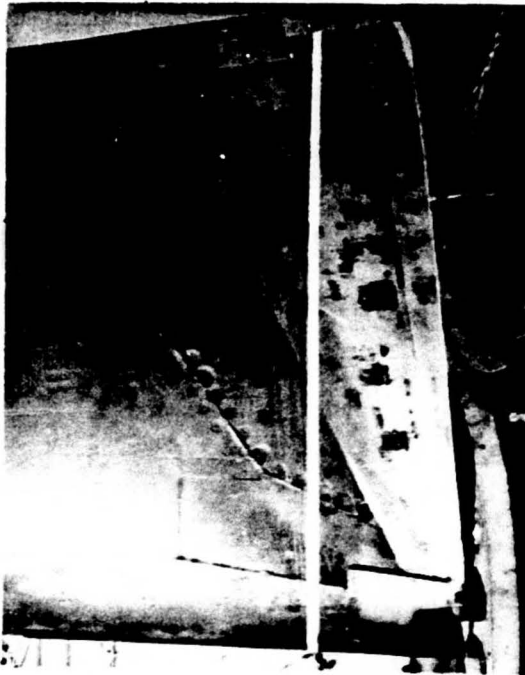




(A) INBOARD CORNER



(B) 6 IN. OUTBOARD



(C) 8 IN. OUTBOARD



(D) 14 IN. OUTBOARD

FIGURE 6-20. FLOW VISUALIZATION. ELEVON  
IN THERMO LAB.



FIGURE 6-21 FLOW VISUALIZATION. COANDA  
SEGMENT MODEL. RUN 34



Rockwell International

NOZZLE TOTAL PRESSURE DISTRIBUTION VS. SPAN

RUN 19 - BASELINE CONFIGURATION

RUN 32 - FEED DUCT 1 INCH BELOW COANDA PLANE

RUN 37 - FEED DUCT 2 INCHES BELOW COANDA PLANE

RUN 46 - FEED DUCT 4 INCHES BELOW COANDA PLANE

NOMINAL PRESSURE RATIO = 2.05

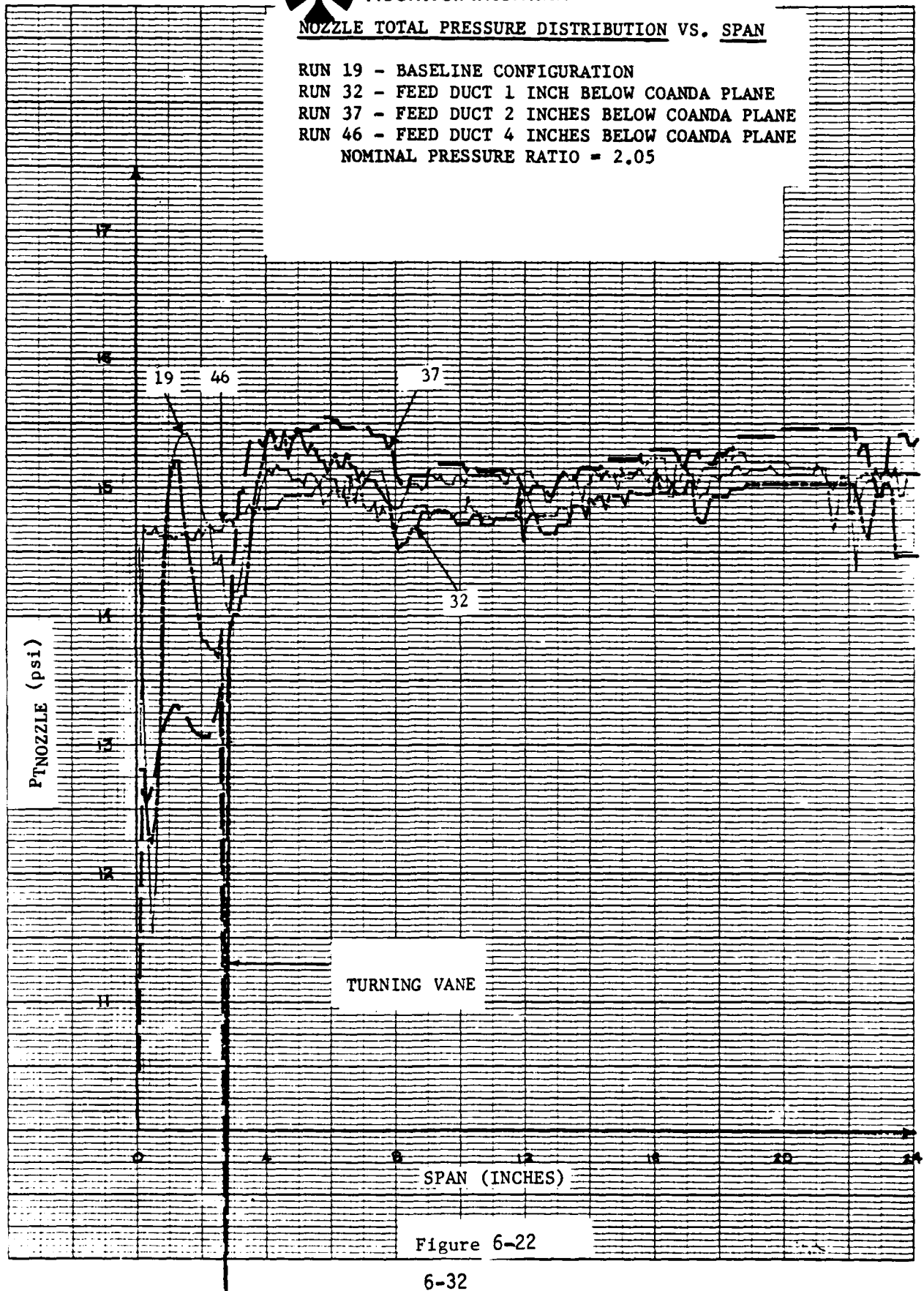


Figure 6-22

NOZZLE TOTAL PRESSURE DISTRIBUTION VS. SPAN

RUN 37 - TURNING VANE PRESENT

RUN 41 - TURNING VANE REMOVED

NOMINAL PRESSURE RATIO = 2.05

DUMP DOOR CLOSED

FEED DUCT 2 INCHES BELOW COANDA PLANE



Figure 6-23



## FLOW AND VELOCITY COEFFICIENTS

- RUN 19 - BASELINE CONFIGURATION
- RUN 32 - FEED DUCT 1 INCH BELOW COANDA PLANE
- △ RUN 37 - FEED DUCT 2 INCHES BELOW COANDA PLANE
- RUN 46 - FEED DUCT 4 INCHES BELOW COANDA PLANE

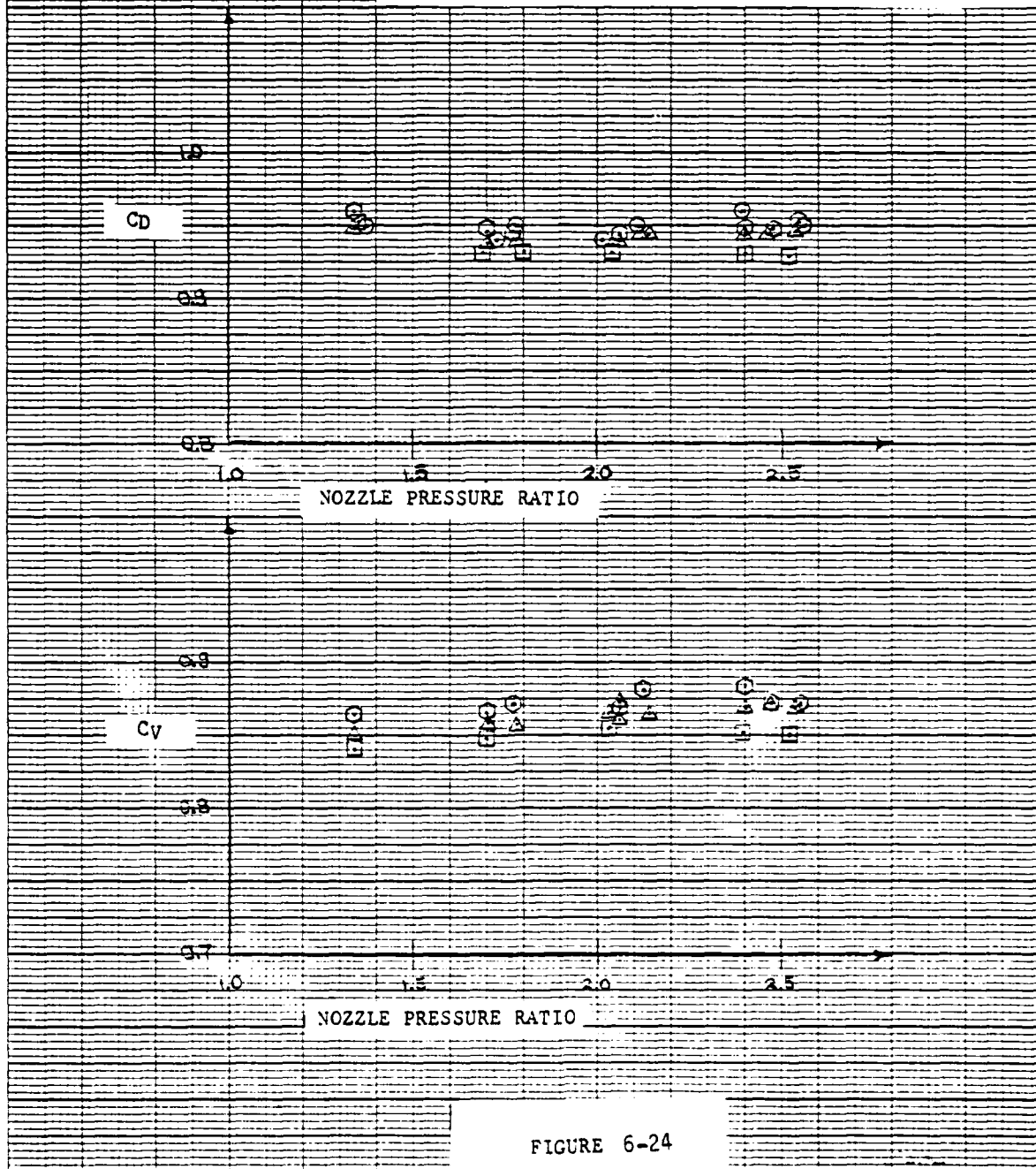


FIGURE 6-24





A COMPARISON PLOT OF THE FOUR DIFFERENT  
FEED DUCT CONFIGURATIONS AT THE 16 INCH  
SPAN STATION

- RUN 23 - BASELINE CONFIGURATION
- RUN 35 - FEED DUCT 1 INCH BELOW COANDA PLANE
- △ RUN 39 - FEED DUCT 2 INCHES BELOW COANDA PLANE
- RUN 42 - FEED DUCT 2 INCHES BELOW COANDA PLANE
- RUN 48 - FEED DUCT 4 INCHES BELOW COANDA PLANE

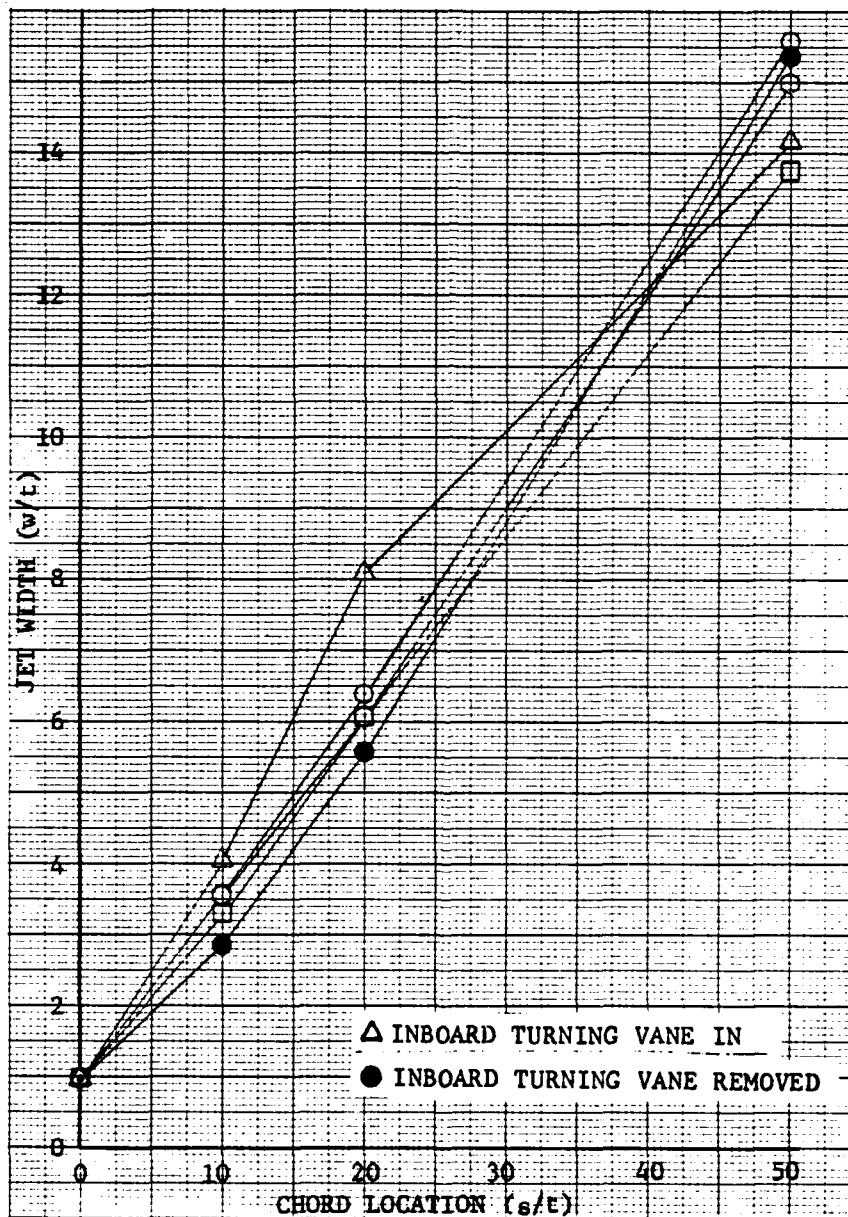


Figure 6-25 Jet Width Vs Chord 16" Span Station



Rockwell International

NOZZLE TOTAL PRESSURE DISTRIBUTION VS. SPAN

A COMPARISON OF INLET MACH NUMBERS

RUN 19 - INLET  $M_N = 0.135$ RUN 22 - INLET  $M_N = 0.235$ 

NOMINAL PRESSURE RATIO = 2.05

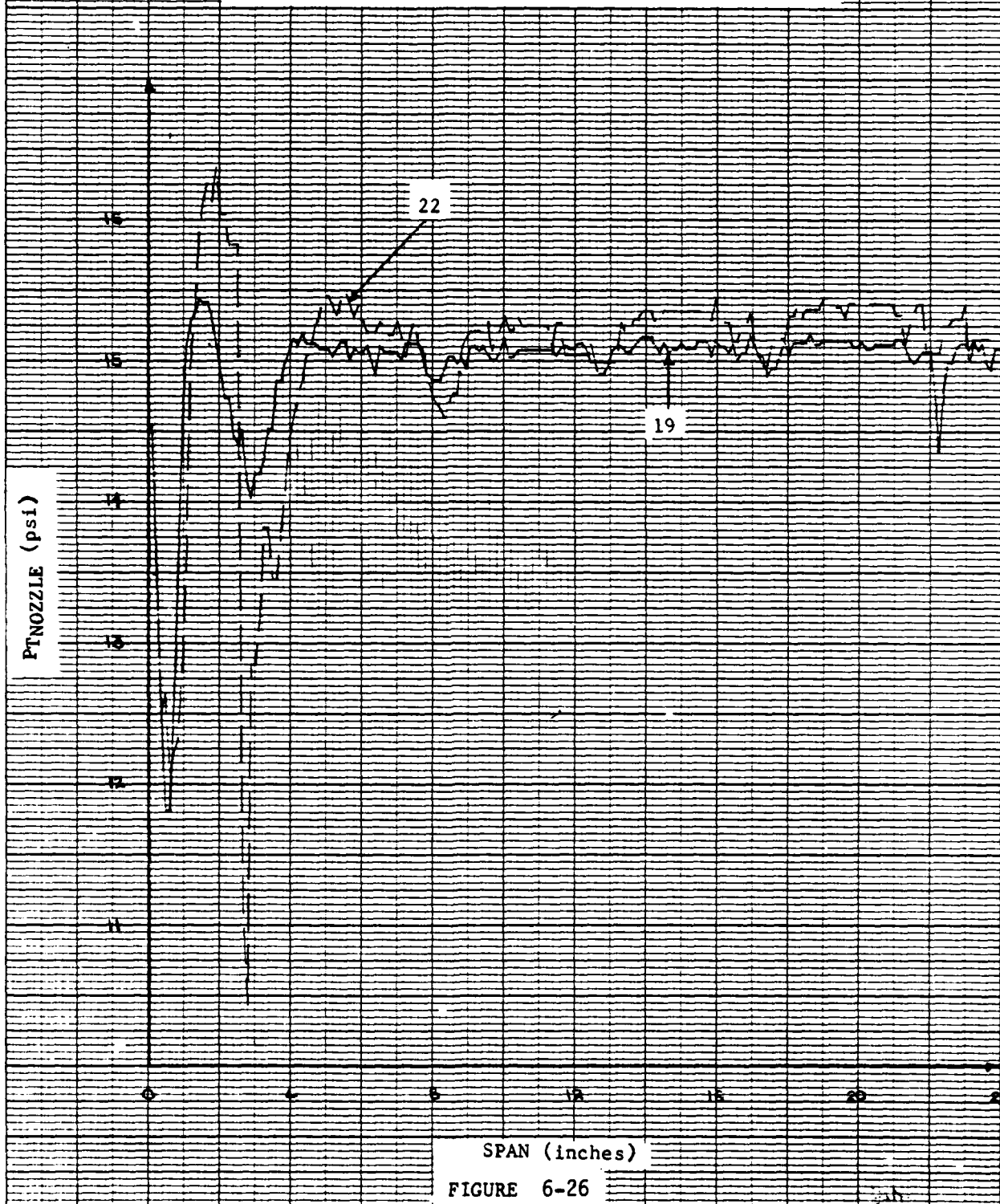


FIGURE 6-26



XFV-12A elevon to  $M = .135$  failed to produce any notable improvement in spanwise nozzle total pressure distribution. In fact, no improvement in any of the Coanda evaluation parameters was noted during the Mach number variation test series. Based on this information, it was concluded that no improvement in flow quality could be expected by simply increasing the feed duct area, i.e., reducing feed duct Mach number.

#### 6.4.7 External Coanda Shape Evaluation

Phase II testing of the segment model was conducted to evaluate full scale performance of Coanda shapes established by model scale tests as having potentially improved performance. Also, an attempt was made to improve the flow quality at the inboard end which was found to have a large spanwise component on Proto 1. Reference (18) documents previous tests of these Coanda shapes on a scale model, and some data are included here for comparison purposes.

The models tested were full scale tapered sections of the inboard 50 inches of the L/H wing elevon. The gap settings were chosen to give about the same  $R_0/t$  (10.5 - 11.5). The  $R_1/t$  was set at a nominal value of four. Comparison of the Coanda shapes were conducted by utilizing the following four performance criteria:

1. Flow and velocity coefficients
2. Jet growth
3. Turning efficiency
4. Nozzle pressure distribution

Figure 6-27 is a comparison plot of the flow ( $C_D$ ) and velocity ( $C_V$ ) coefficients obtained for the three Coanda shapes. Little differences in flow coefficients were noted for the three Coandas which is to be expected since flow coefficients are primarily dependent on internal nozzle design.

The velocity coefficient plot indicated about two percent better performance of the  $K = 1.3$  spiral over the  $K = 1.17$  spiral and a similar increment between the Proto 1 and  $K = 1.3$  spiral. The velocity coefficients for the  $K = 1.7$  and  $K = 1.3$  spirals compare favorably with the values obtained on scale models reported in Reference (18). Isolated points are plotted on Figure 6-27 as solid symbols.

The jet growth, an indication of entrainment, was measured for the three Coanda shapes and the results are compared in Figure 6-28. This comparison was conducted at span station 16 to avoid the jet disturbing effects of the auxiliary corner blower. Little difference was noted in the jet growth characteristics for the three Coanda shapes. Very good correlation with scale model data was obtained. Scale model test data (Reference (18)) is plotted in Figure 6-28 as solid symbols.

The Coanda Turning Efficiency (CTE) as defined ( $PT_{peak}/PT_{nozzle}$ ) is a measure of the pressure remaining in the jet after being turned by the Coanda some given distance. A comparison plot of the Proto 1 simulation

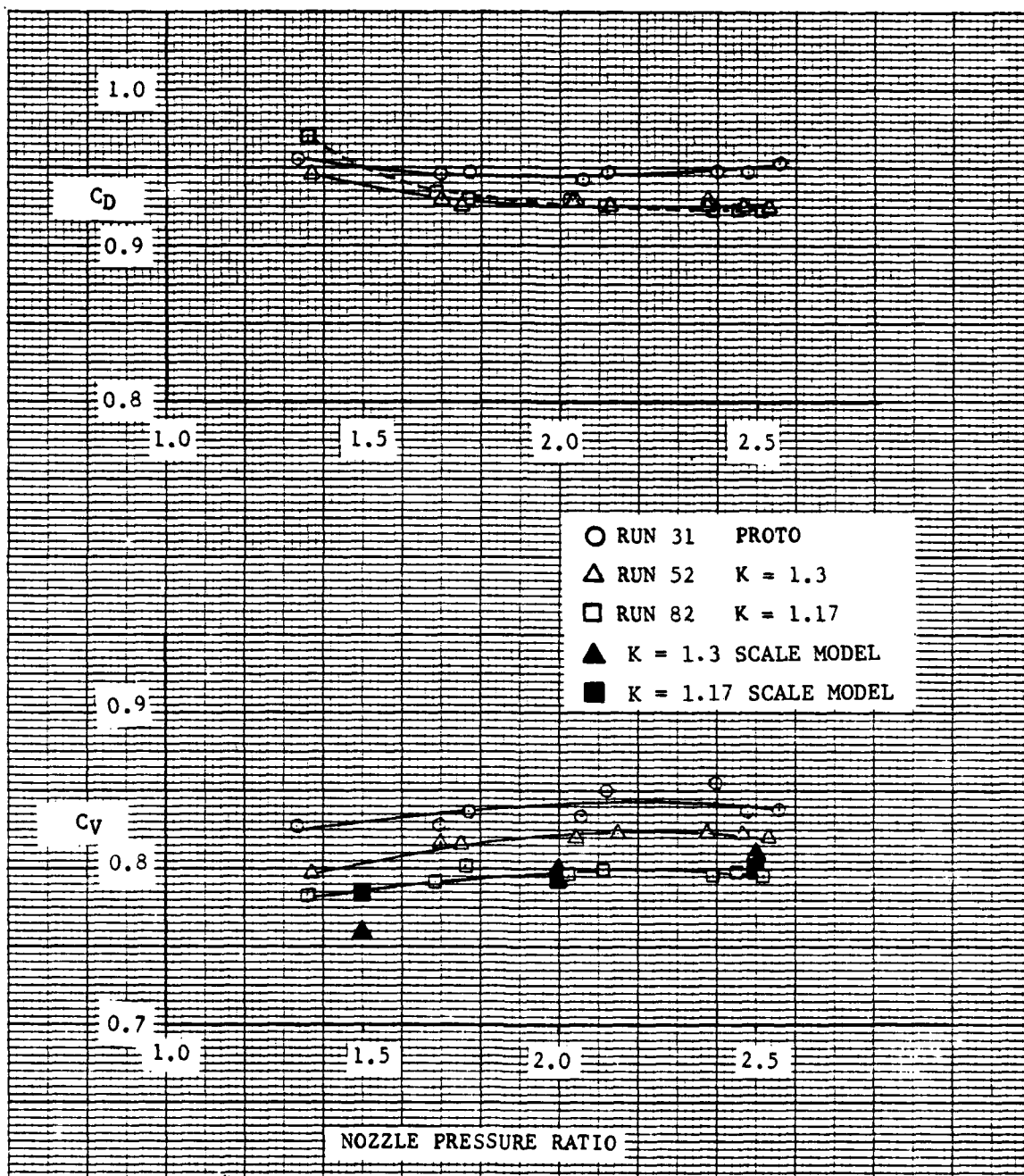
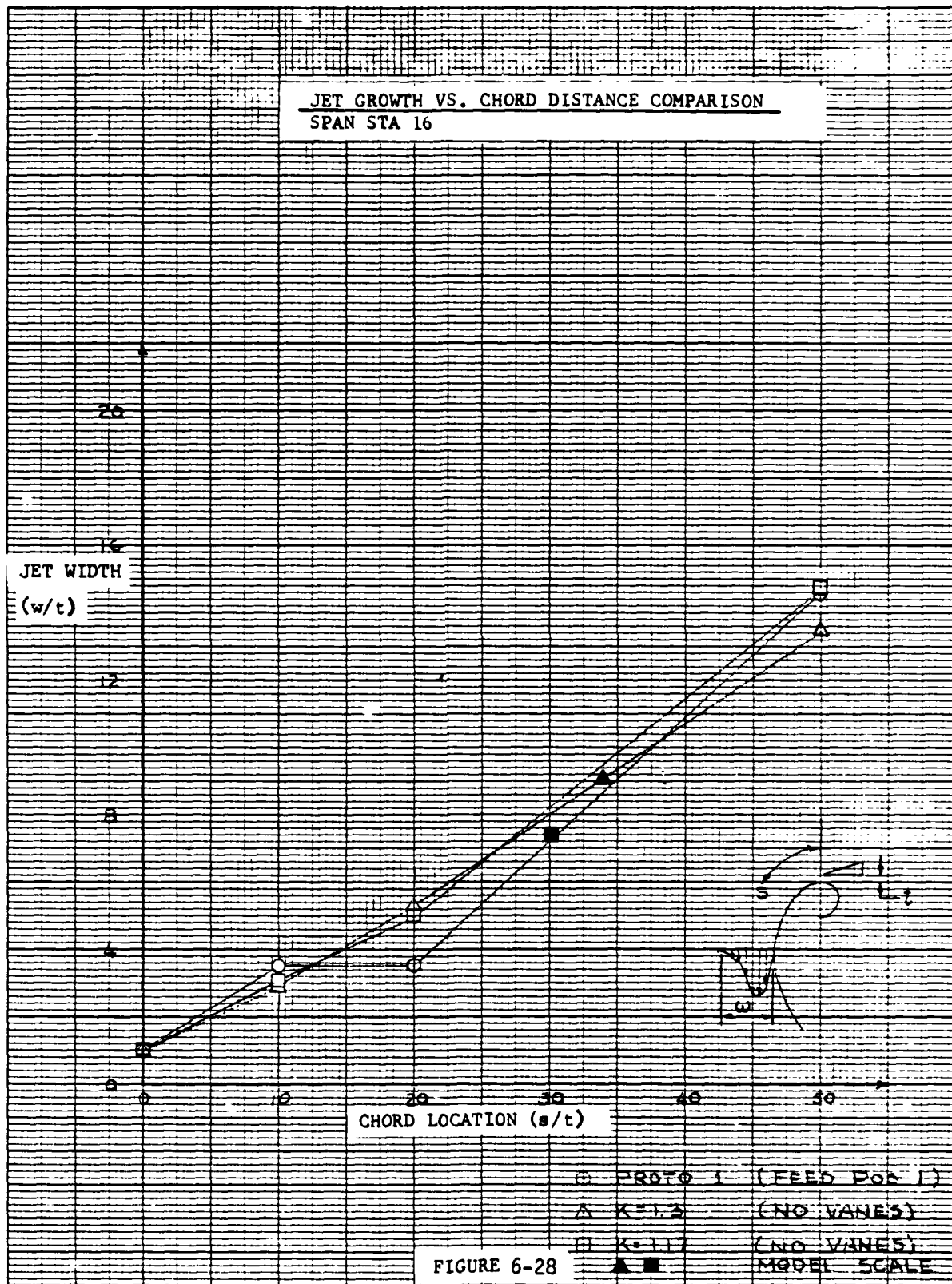


Figure 6-27 Flow and Velocity Coefficients Comparison  
WPAFB Coanda Segment Model





and the  $K = 1.17$  Coanda with three vanes in the dedicated nozzle is presented in Figure 6-29. At ten nozzle gaps ( $10t$ ) from the nozzle the  $K = 1.17$  Coanda is clearly better at all span stations and at  $50t$  from the nozzle the benefits of the vanes in the auxiliary corner blower are very much evident for the first five inches of span. Figure 6-30 is a similar plot comparing the Proto 1 simulation to the  $K = 1.3$  Coanda with a single turning vane in the auxiliary blower. Similar results were observed; i.e., at  $10t$  the  $K = 1.3$  spiral was better at all span stations and at  $50t$  very much better CTE of the inboard five inches.

Attempts were also made during this phase of testing to improve the nozzle pressure distribution, especially at the inboard end. Figure 6-31 shows improvements made to the main nozzle pressure distribution by the addition of vanes in the auxiliary corner blower (examples of corner blower vane installation may be seen in Figures 6-32, 6-33, and 6-34). This primary nozzle pressure distribution improvement is probably related to creation of a more favorable airflow at the inlet duct by the vane installation in the corner blowers. Improvements to the primary nozzle pressure distribution were also realized by the addition of a turning vane in the primary nozzle. Figure 6-35 presents a comparison plot of  $P_{T_1}$  versus span for the  $K = 1.17$  Coanda with and without the vane. The installation of the primary nozzle turning vane may be seen in Figure 6-36.

#### 6.4.8 Phase III - Internal Radius Evaluation

6.4.8.1 General - Phase III testing was conducted to identify the effect of reducing the internal Coanda nozzle radius of approach on the external Coanda flow quality and performance. Design studies which were conducted in parallel with this test program indicated that some improvements in augmentor packaging could result from reductions of the internal Coanda radius ratio ( $R_1/t$ ). Up to this point in the test program the internal radius of approach had been held constant at a value of  $R_1/t = 4.0$ . Previous test data evaluating variations in internal radius ratio indicated that reductions in internal radius to values below  $R_1/t = 3.0$  could result in distortions in the Coanda nozzle pressure profile which often produced external Coanda flow separation. Since further evaluation of radius ratios less than 3.0 would be counterproductive, an internal radius ratio of 3.0 was installed in the external Coanda  $K = 1.17$  log spiral configuration. See Figure 6-37 for comparison of shapes.

6.4.8.2 Turning Efficiency and Jet Growth - Turning efficiency and jet growth are presented in Figure 6-38 and 6-39. Data obtained from testing this configuration are compared with its  $R_1/t = 4.0$  counterpart in Figure 6-40, external Coanda jet total pressure decay, and Figure 6-41, Coanda total pressure profile jet growth. Flow visualization for the two radii is presented in Figure 6-42. Results of these comparisons indicate only a slight variation in external Coanda flow quality was produced by reducing the internal radius ratio from 4.0 to 3.0.

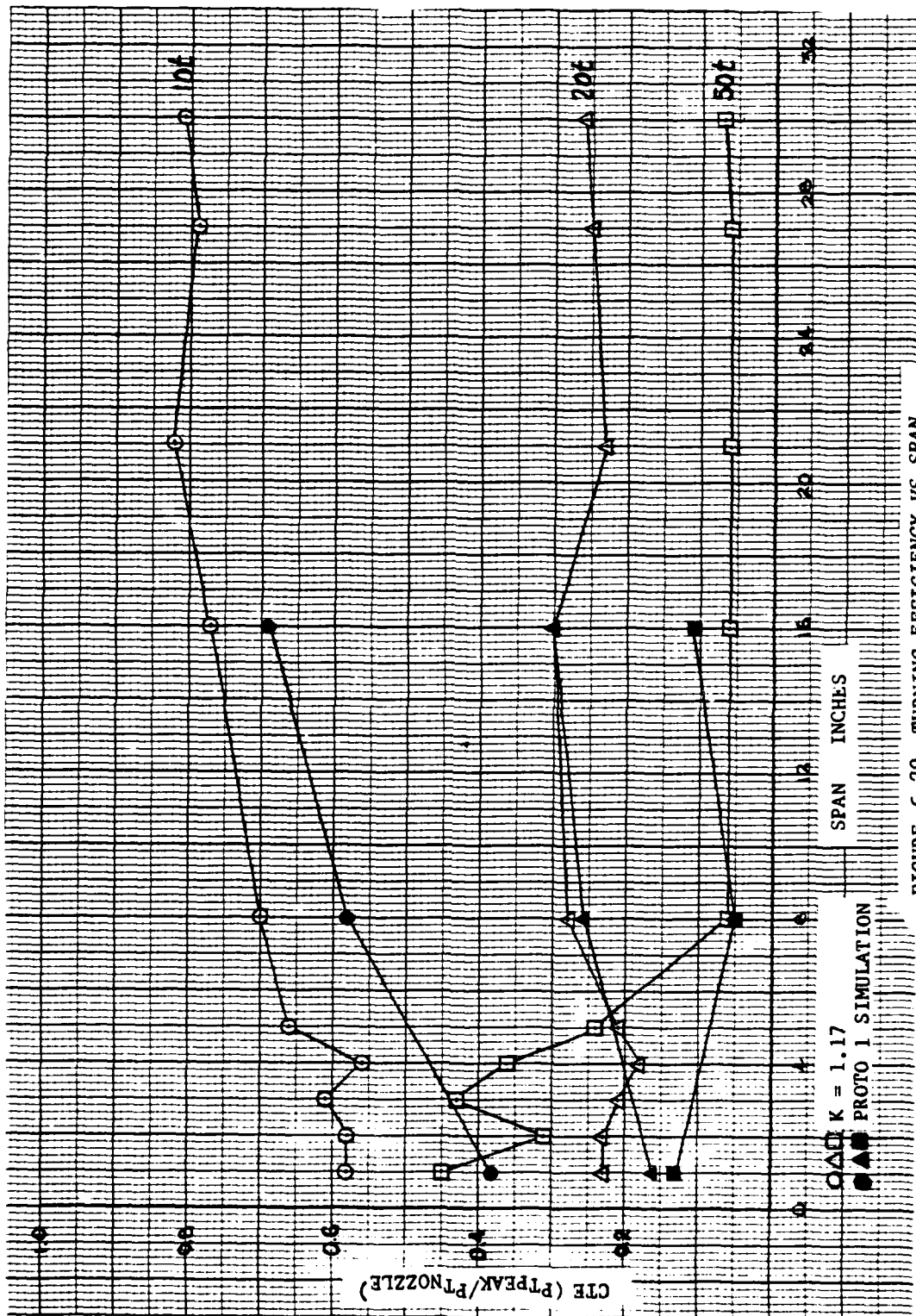


FIGURE 6-29 TURNING EFFICIENCY VS SPAN  
 $K = 1.17$  AND PROTO 1 SIMULATION

6-41

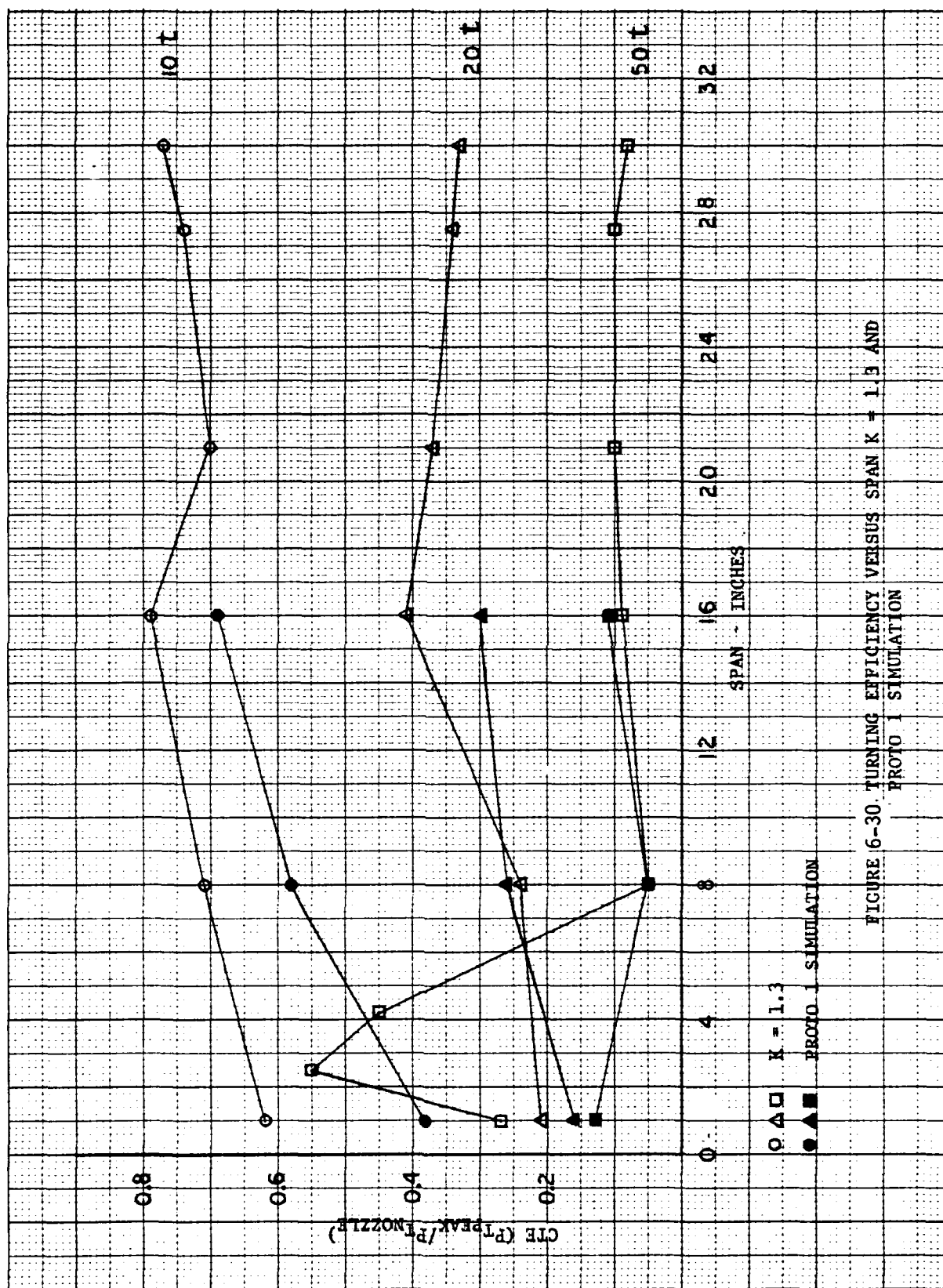


FIGURE 6-30. TURNING EFFICIENCY VERSUS SPAN  $K = 1.3$  AND  
PROTO 1 SIMULATION





— RUN 52 - NO VANES  
- - - RUN 66 - ONE VANE  
- · - RUN 78 - TWO VANES

$K = 1.3$

DUMP DOOR CLOSED

NOMINAL PRESSURE RATIO = 2.05

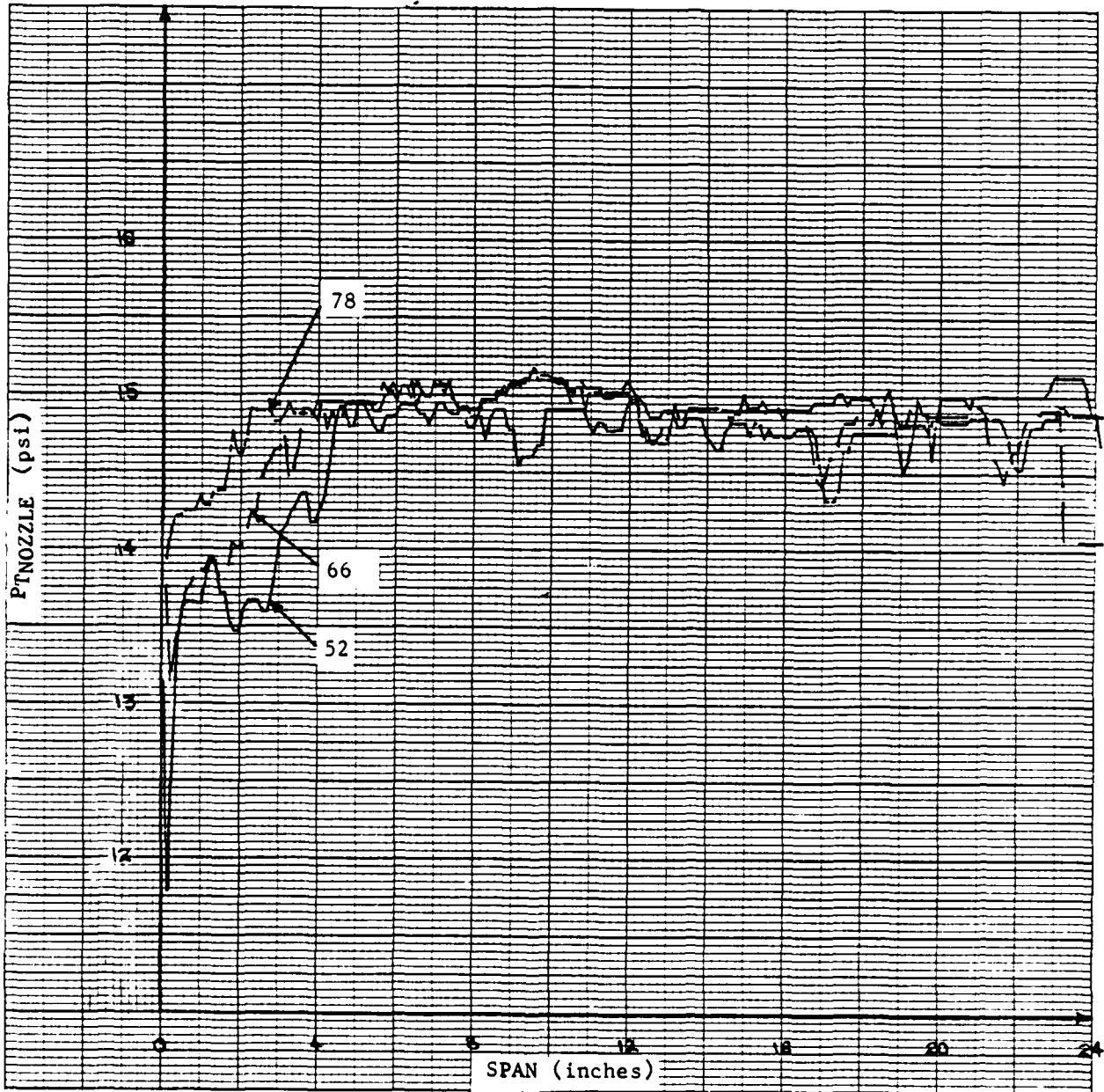


Figure 6-31 Nozzle Total Pressure Distribution Versus Span

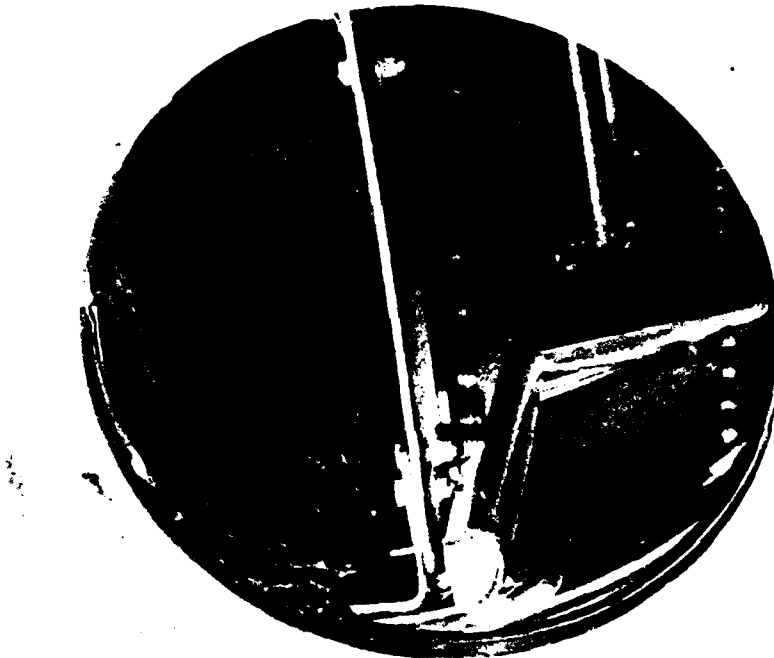


FIGURE 6-32. DEDICATED NOZZLE VANES

SINGLE VANE



FIGURE 6-33. DEDICATED NOZZLE VANES

DOUBLE VANE

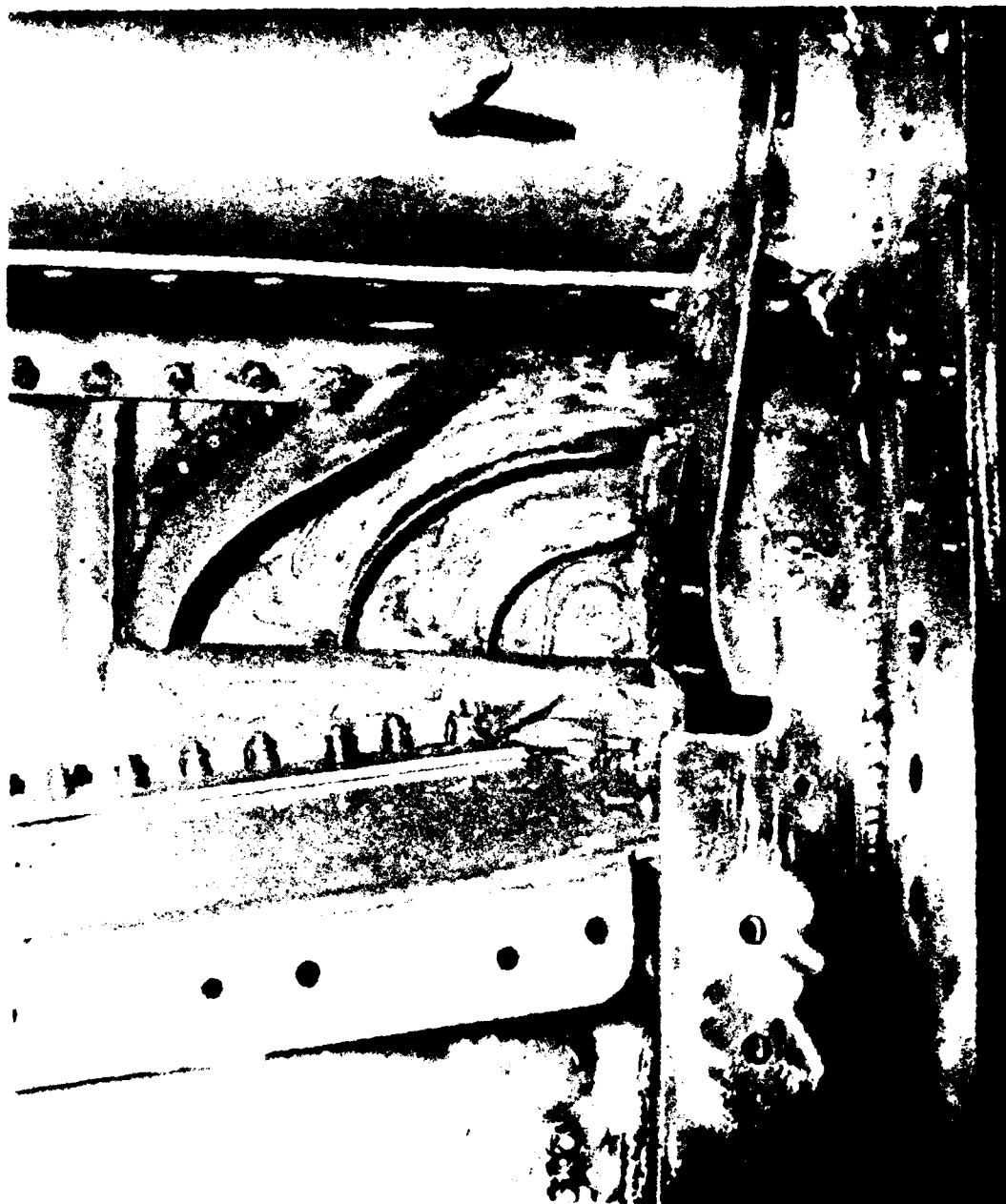


FIGURE 6-34 DEDICATED NOZZLE VANES

3 VANE CASCADE



RUN 82 - BASELINE CONFIGURATION  
RUN 90 - TURNING VANE IN PRIMARY  
NOZZLE

NOMINAL PRESSURE RATIO = 2.05

K = 1.17

DUMP DOOR CLOSED

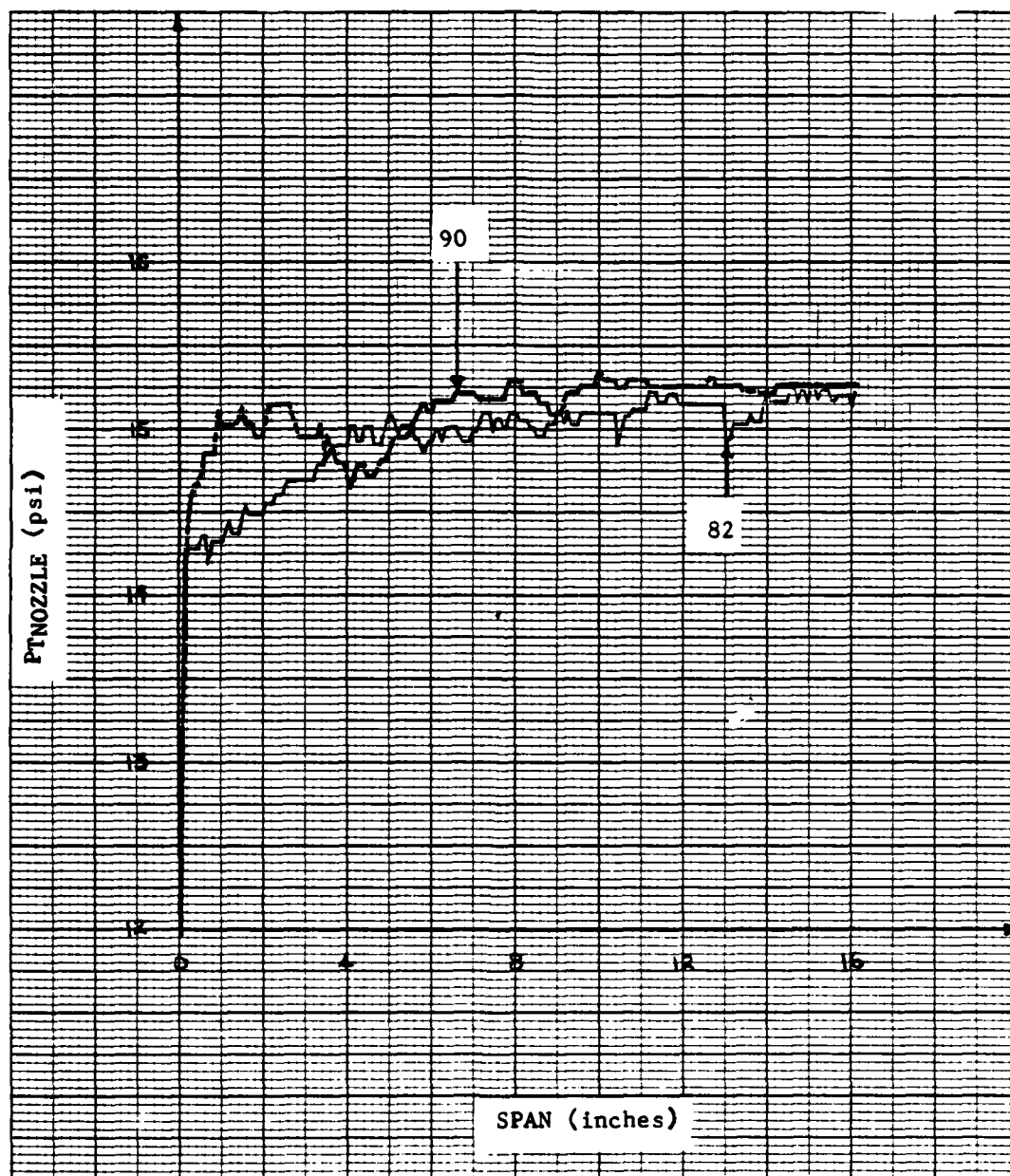


Figure 6-35 Nozzle Total Pressure Distribution Versus Span



FIGURE 6-36 . PRIMARY NOZZLE VANE

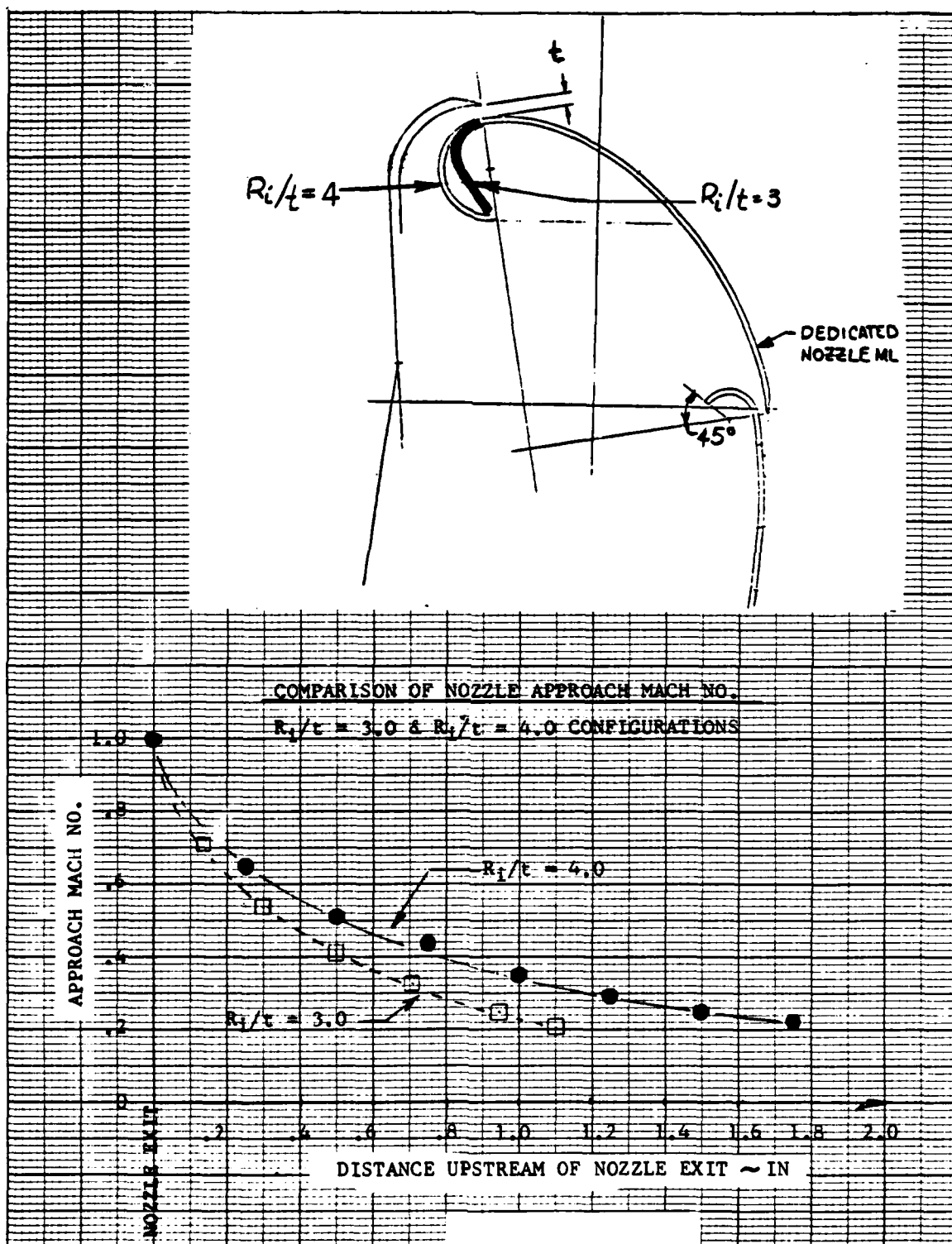
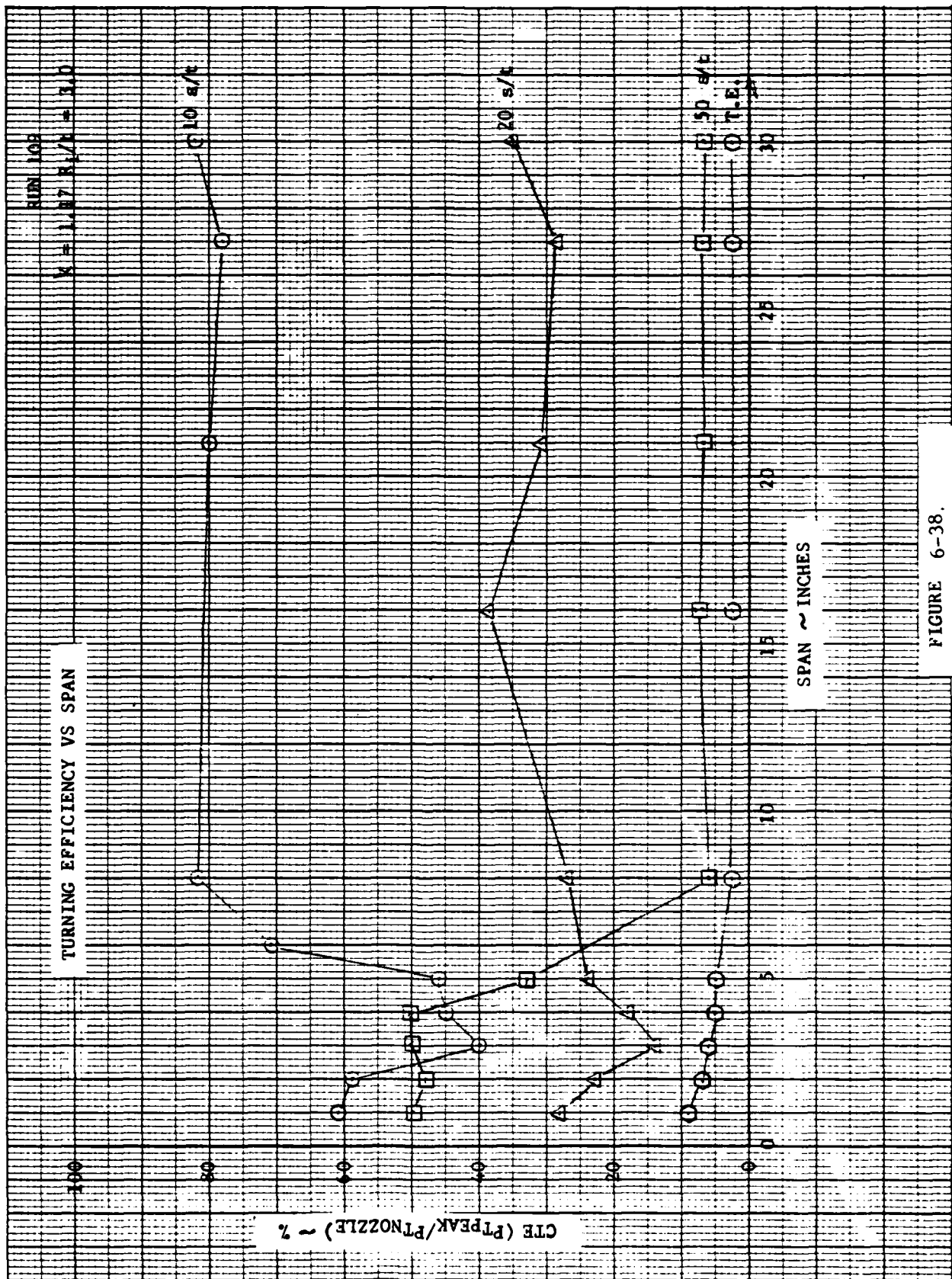
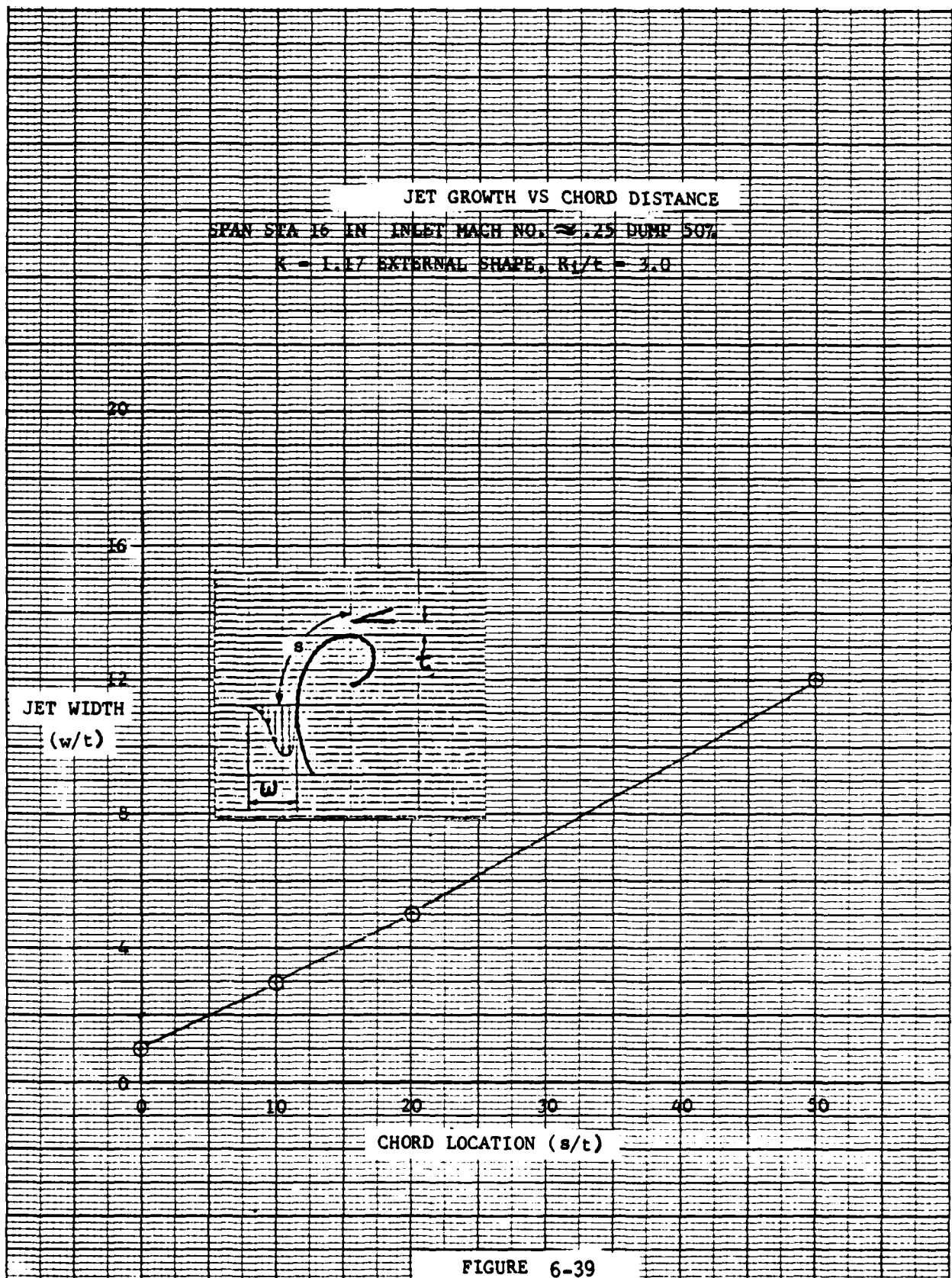


Figure 6-37 Sketch of Internal Radius Variations



**FIGURE 6-38.**





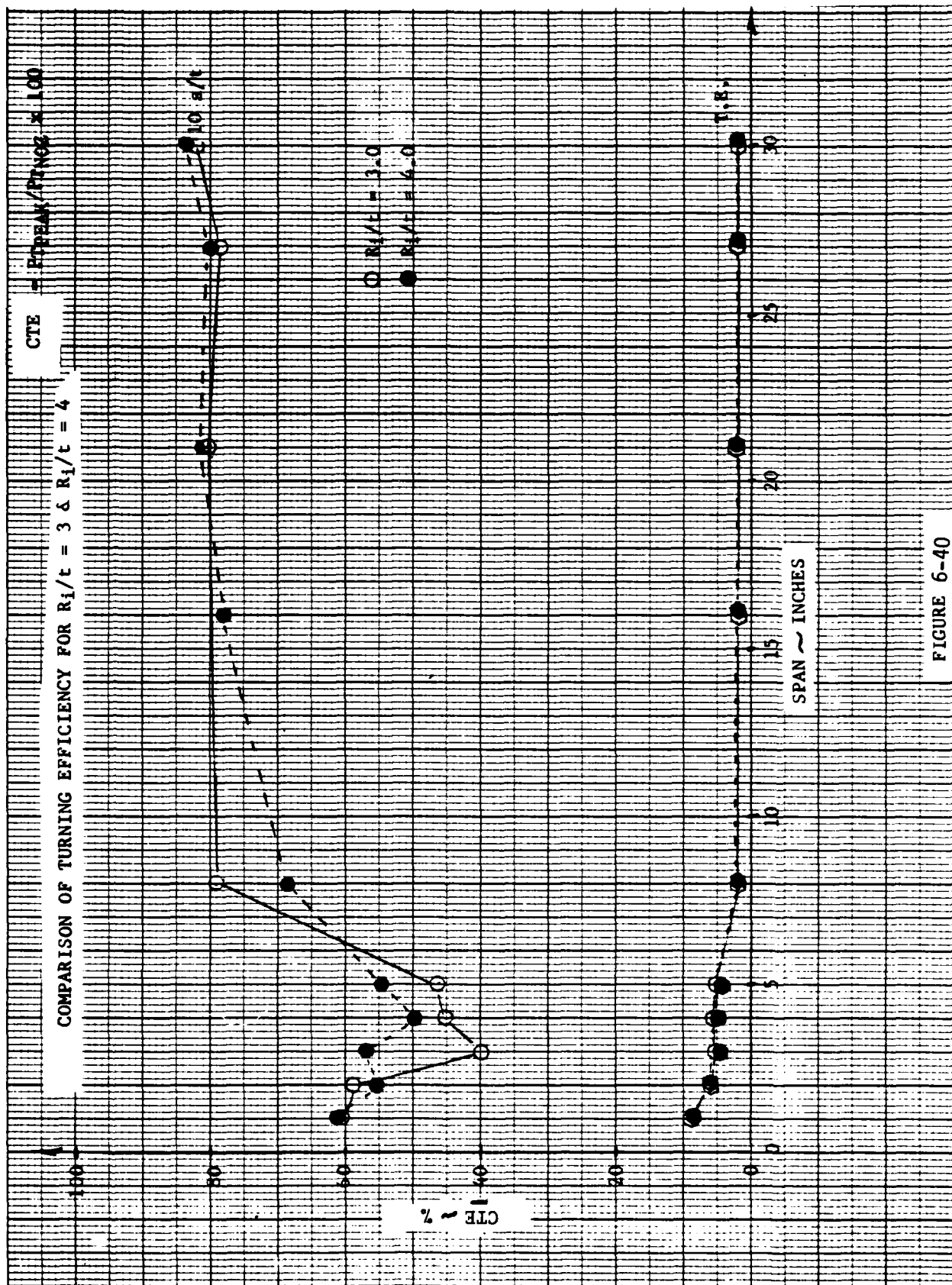


FIGURE 6-40

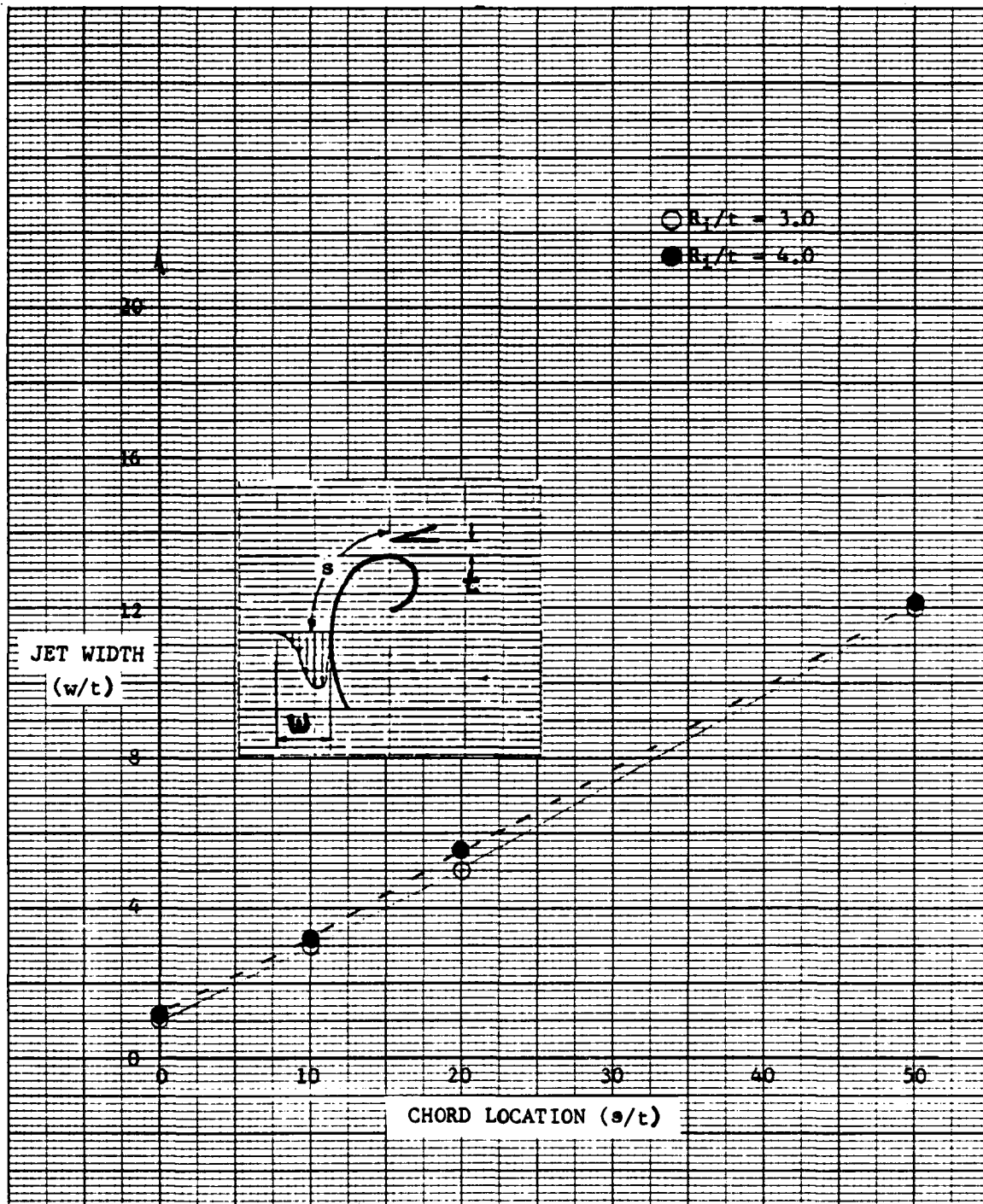
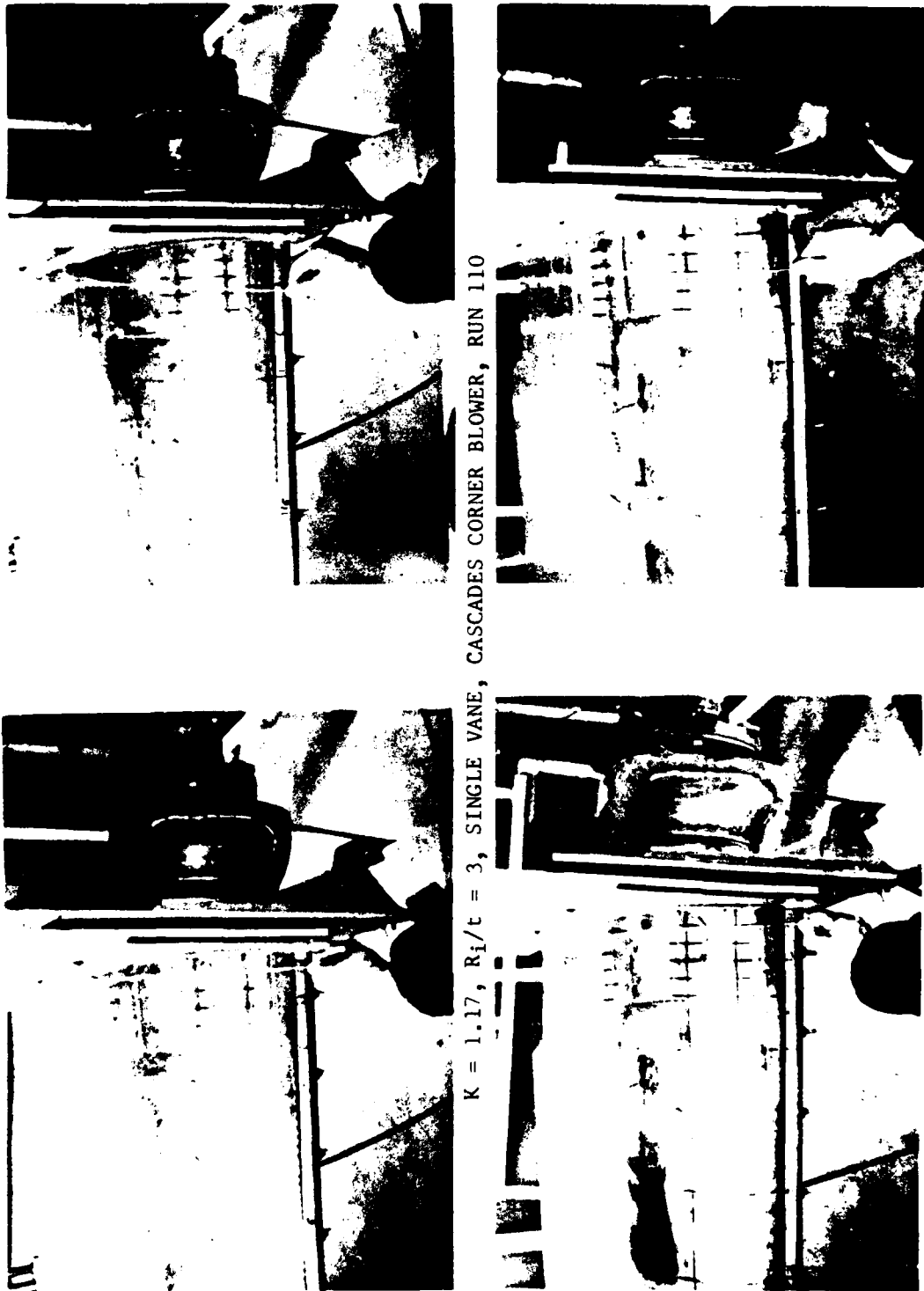


Figure 6-41 Jet Growth Comparison -  $R_1/t = 3.0$   
and  $R_1/t = 4.0$  Configuration



$K = 1.17, R_1/t = 3$ , SINGLE VANE, CASCADES CORNER BLOWER, RUN 110

$K = 1.17, R_1/t = 4$ , SINGLE VANE, CASCADES CORNER BLOWER, RUN 95

FIGURE 6-42 FLOW VISUALIZATION



**6.4.8.3 Flow and Velocity Coefficients** - Although no external Coanda flow separations were noted as a result of the reduction in internal radius ratio, slight reductions in nozzle flow coefficient were noted for the  $R_1/t = 3.0$  configuration while velocity component coefficients were approximately the same for the two configurations (see Figure 6-43). It is believed that the slight reduction in flow coefficient is the result of the smaller internal radius distorting the nozzle exit pressure profile from the classical "top hat" mean profile normally measured on the larger internal radius configuration. Previous experience with distorted nozzle exit pressure profiles indicates that profiles of this type are often more prone to external Coanda flow separation and should be avoided.

#### **6.4.9 Summary**

Results of these tests satisfied the test objectives in providing definition for the improvement of the XFV-12A elevon. Specific conclusions are summarized below:

- 1 The WPAFB test facility is satisfactory for evaluation of flow characteristics and incremental performance changes of augmentor component models.
2. The elevon segment model is a valid simulation of the full scale elevon for investigation of flow problems and evaluation of solutions.
3. Relocating the elevon feed duct below the Coanda nozzle plane improves inboard flow characteristics.
4. Minimal improvement of elevon flow characteristics is realized by increasing feed inlet flow area.
5. The external Coanda shape defined by  $K = 1.3$  resulted in the highest turning efficiency in the region immediately downstream of the nozzle when compared with the  $K = 1.17$  and Proto 1 shapes. The velocity coefficient for the  $K = 1.3$  shape was superior to the one for  $K = 1.17$  and comparable to Proto 1.
6. The addition of properly placed vanes in the inboard end of the primary nozzle and in the dedicated nozzle improved inboard primary nozzle pressure distribution and inboard flow quality.
7. Results of tests with a reduced internal Coanda nozzle radius were largely inconclusive. However, the slight reduction in flow coefficient obtained for the smaller radius is of sufficient concern to defer adoption.

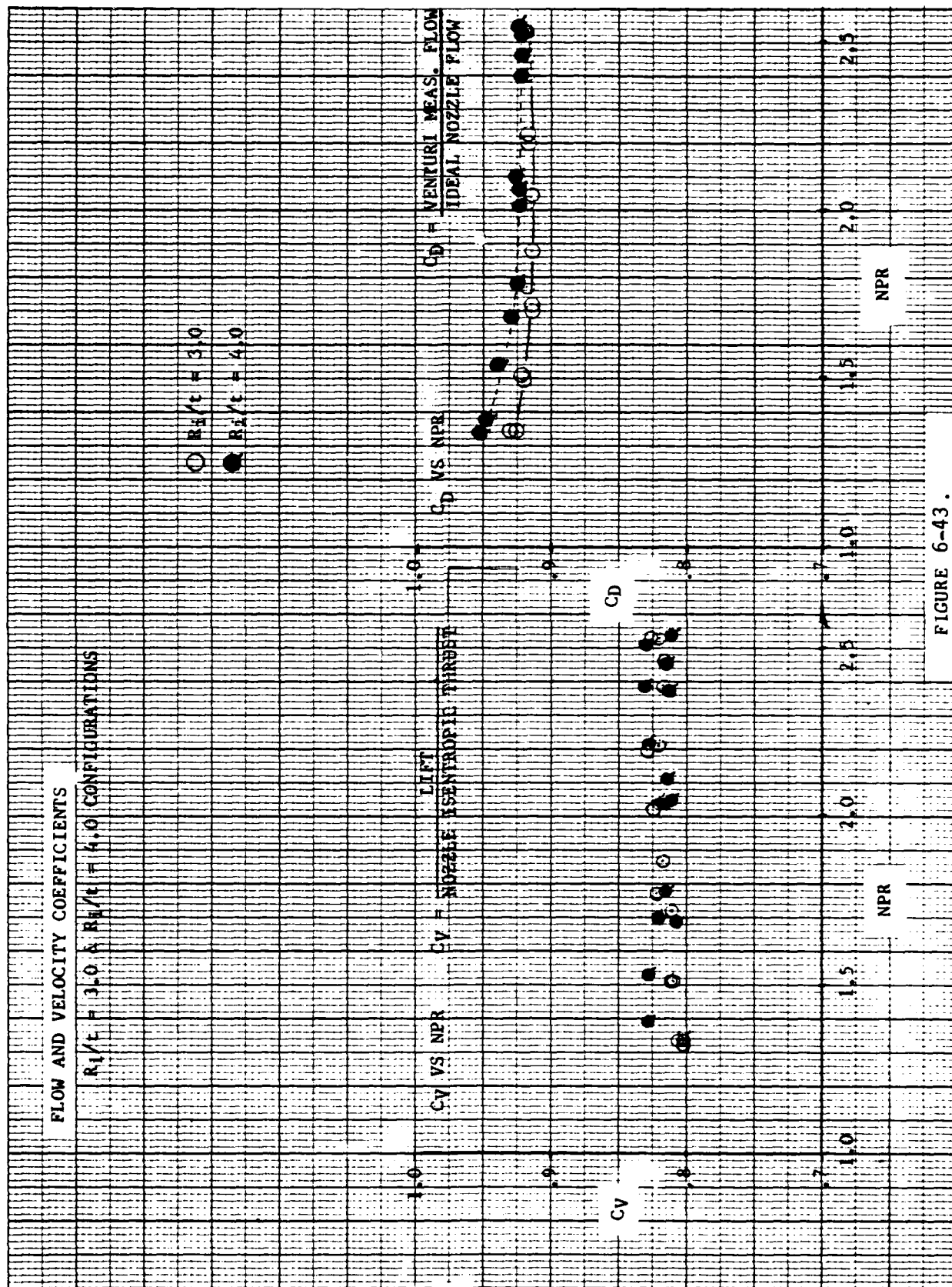


FIGURE 6-43.



## 7.0 CENTERBODY NOZZLE DEVELOPMENT

### 7.1 GENERAL

The process of ejector thrust augmentation is driven by the primary jet entrainment, which pumps the secondary stream through the ejector. Thus, increasing the jet entrainment rate will increase the thrust augmentation. The purpose of this section is to summarize the research performed in order to develop a nozzle for increasing the entrainment of the central jet in the XFV-12A wing augmenter. First, use of the jet mixing analysis for optimization of the basic hypermixing nozzle will be described. This will be followed by a description of progress in the development of an asymmetric cross slot nozzle. Finally, a study of the symmetric cross slot nozzle will be presented. It is shown that the use of a cross slot nozzle and a corresponding increase of ejector inlet ratio increases the thrust augmentation of the wing ejector from 1.46 to 1.64.

### 7.2 HYPERMIXING NOZZLES

Significant increases in thrust augmentation have been achieved with the hypermixing nozzle (Reference (23) and (24)) shown in Figure 7-1. The alternating jet segments at the exit of the nozzle serve to introduce a row of streamwise vortices into the jet. These vortices enhance the turbulent entrainment, and thus pump additional fluid through the ejector. The rate of entrainment depends on the strength and spacing of the vortices which are functions of the initial deflection and size of the jet segments.

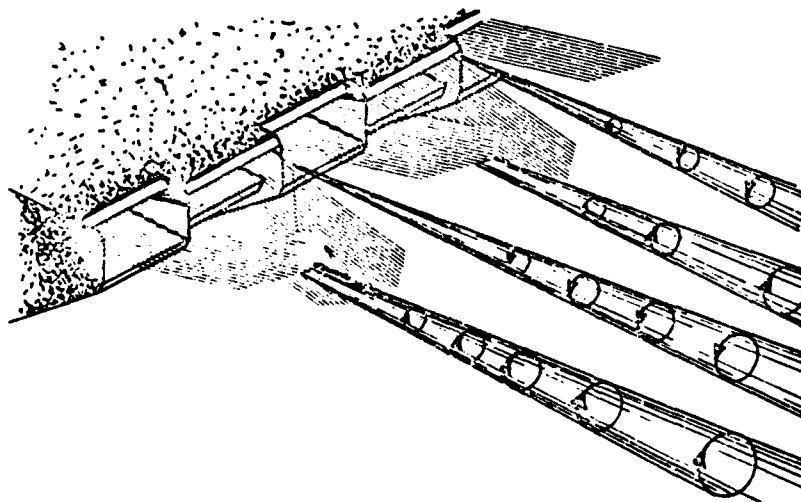


Figure 7-1 Hypermixing Nozzle Exit



The combination of these parameters which gives the best performance depends on the ejector inlet area ratio and lengths, as well as the nozzle location. On the basis of the limited data available, a nozzle with an initial deflection angle of  $7^\circ$  and a segment aspect ratio of 12.5 was chosen for the XfV-12A configuration tested at NASA Langley. As part of the present aircraft development program, the jet mixing analysis previously described was used to evaluate the possibility of improving performance by redesigning the hypermixing nozzle. The ejector section at the wing root was chosen for analysis.

The computed effect of varying the jet parameters is shown in Figure 7-2.

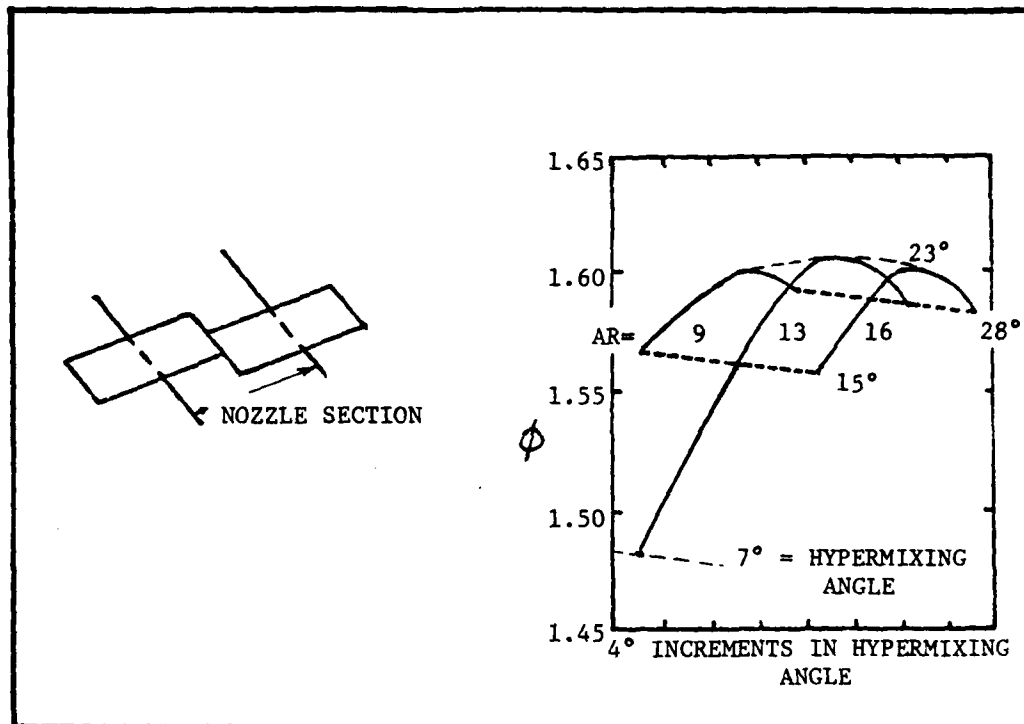


Figure 7-2 Effect of Jet Parameter Variations on Thrust Augmentation

Changes in the deflection angle are seen to have greater effect on the augmentation than the aspect ratio. In Figure 7-3, the jet deflection angle is held constant at  $23^\circ$ , and the aspect ratio is varied over the range from  $AR = 3$  to  $AR = 24$ . The computed velocity distributions are as shown. In the figures, the hypermixing jet runs along the span in the foreground with a Coanda jet behind it; the other Coanda jet has been removed to permit a clear view of the hypermixing jet. At low aspect ratios, the vortices are close together so that they soon merge and cancel each other. As seen in the velocity distribution for the  $AR = 3$  case, this limits the spreading of the jet, which then limits the augmentation.



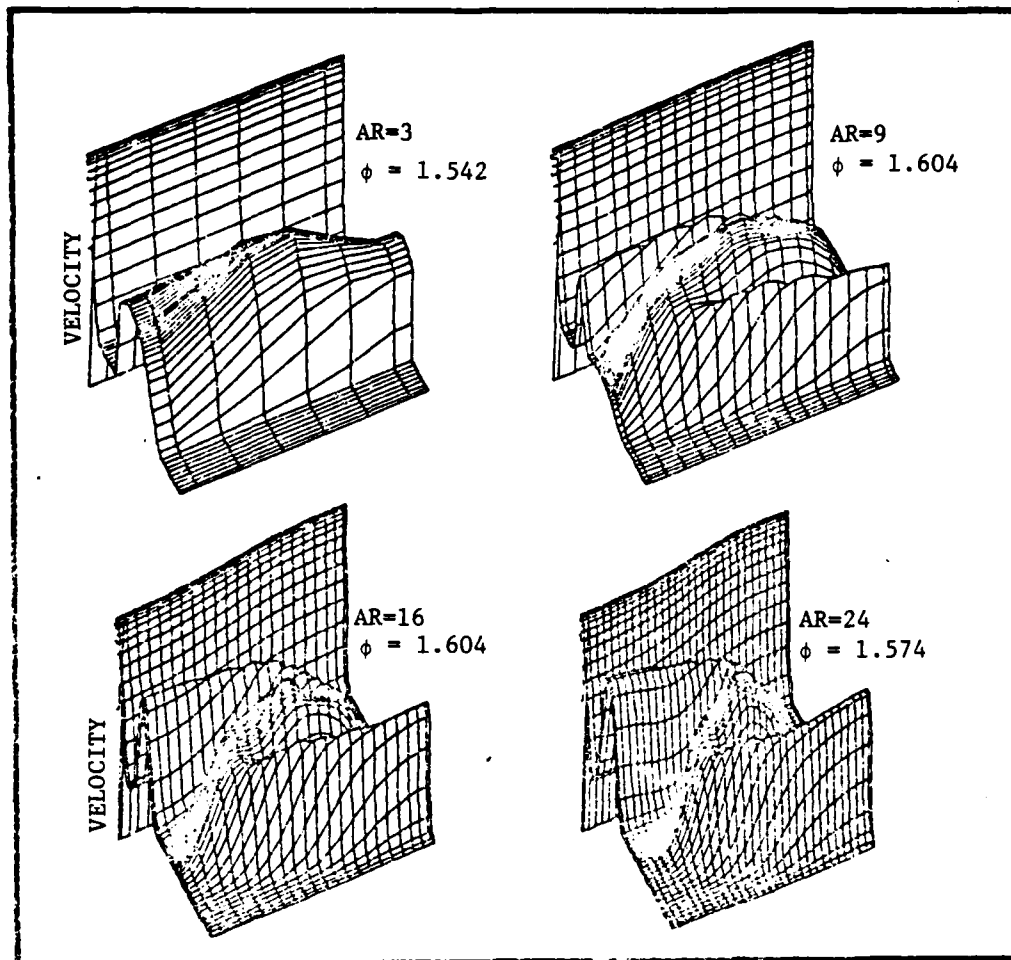


Figure 7-3 Computed Effect of Hypermixing Aspect Ratio on the Jet Mixing

As the aspect ratio is increased, the interference between vortices is reduced, so that the mixing and augmentation also increase. In the limit, as the aspect ratio becomes too large, the number of vortices is reduced to the point that the mixing and augmentation decrease. This can be seen in the velocity distributions, which are normalized with respect to the vortex spacing. For the  $AR = 24$  case, the hypermixing effect does not extend to the ends of the segment shown.

The computed effect of aspect ratio on augmentation is shown for these jets in Figure 7-4. The thrust augmentation has a relatively broad peak for aspect ratios between 10 and 15. This is consistent with the measurements of Salter (Reference (25), who found little change in



the entrainment of hypermixing jets over this range. Because the aspect ratio of the baseline aircraft nozzle is near the middle of this range, no additional effort was directed towards optimizing this parameter.



Figure 7-4 Effect of Hypermixing Nozzle Aspect Ratio On Thrust Augmentation, Deflection =  $23^\circ$

As seen in Figure 7-2, a significant increase in augmentation was predicted for an increase in the hypermixing angle from  $7^\circ$  to  $23^\circ$ . In order to test this prediction a set of four nozzles were built and tested in a mid-span section model of the XFV-12A wing. In Figure 7-5, the augmentation measured at a diffuser area ratio of two is compared to the computed thrust increments. Although the augmentation did reach a maximum at approximately the same angle as predicted, the measured thrust increment was not as large. The measured and calculated velocity distributions at the ejector exit, shown in Figure 7-6, were qualitatively similar. However, there were quantitative differences which also indicated that the analysis could be improved.

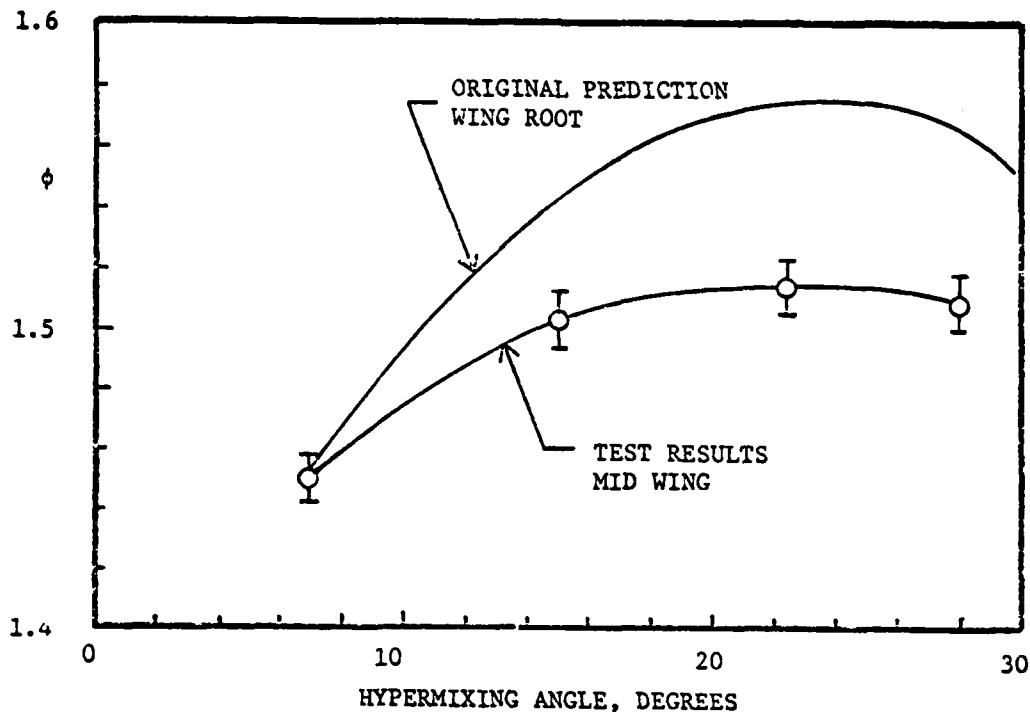


Figure 7-5 Comparison of Computed and Measured Effect of Hypermixing Angle

#### 7.2.1 Analytical Improvements

Because data was not available, initial values of the secondary flow angularity and turbulence constants had to be assumed. In order to improve the specification of initial conditions, these parameters were measured for each of the four nozzles. The magnitude and direction of the secondary flow was measured with a five-port pitot-static probe at the positions shown in Figure 7-7. A vector diagram of the data measured at the center of a segment of the 15° nozzle is shown in Figure 7-8. Typical data is presented in Figure 7-9. The data from these nozzles were then generalized to improve the inlet angularity subroutine used in the jet mixing analysis.

Because it is difficult to measure turbulence parameters in supersonic jet flows, the effect of the turbulence constants on the jet mixing was studied parametrically. In Figure 7-10, the measured and computed profiles at the center and end of a jet segment are compared for the original values of these constants. Better agreement was obtained by increasing the kinetic energy by a factor of four, as shown in Figure 7-11, or by decreasing the dissipation constant by a factor of 1/16, as shown in Figure 7-12. Since the eddy viscosity is proportional to  $k^2/\epsilon$ , these changes were equivalent to increasing the eddy viscosity by a factor of 16.

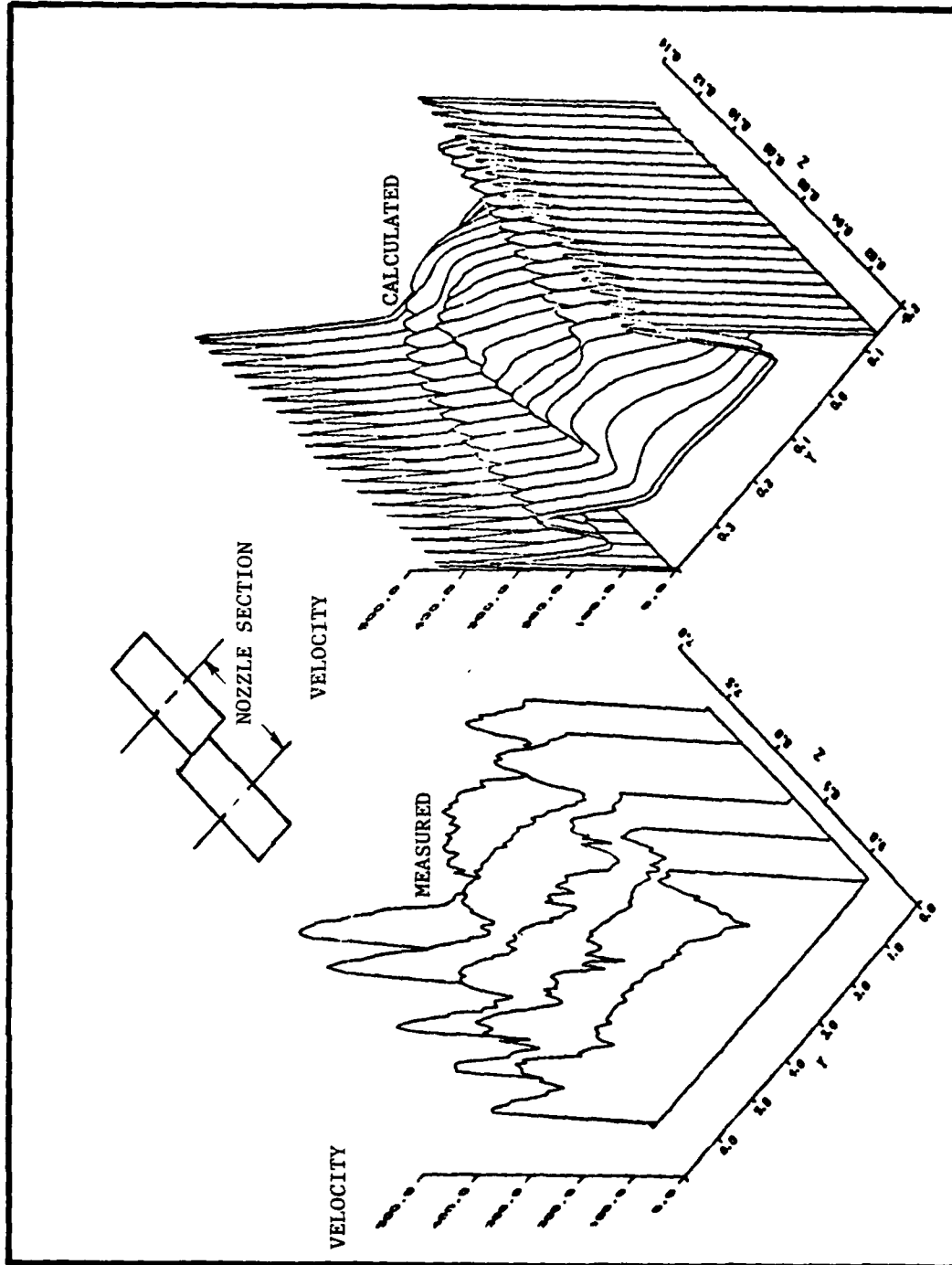


Figure 7-6 Comparison of Hypermixing Velocity Distributions at Ejector Exit

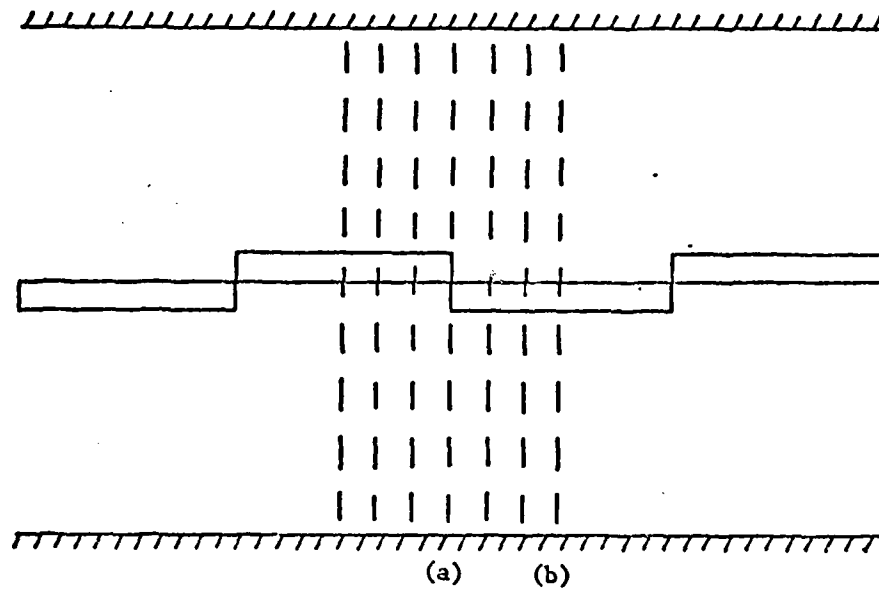


Figure 7-7 Hypermixing Nozzle Survey Stations

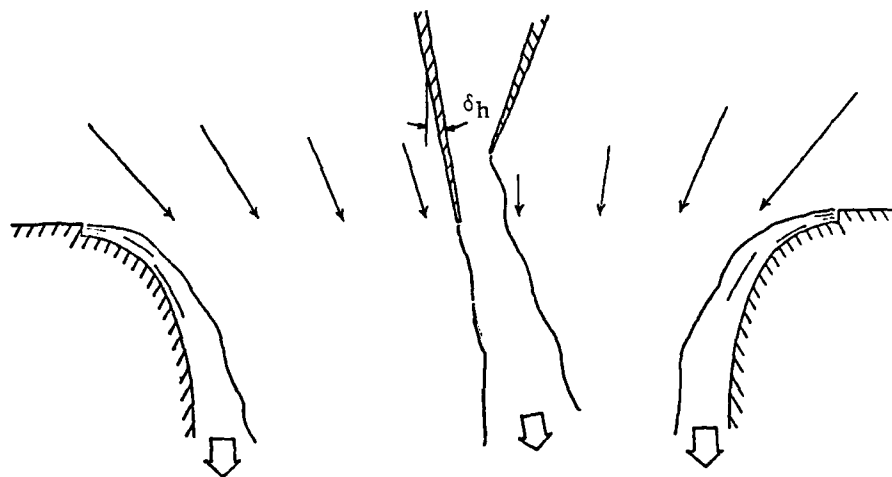


Figure 7-8 Measured Inlet Velocities

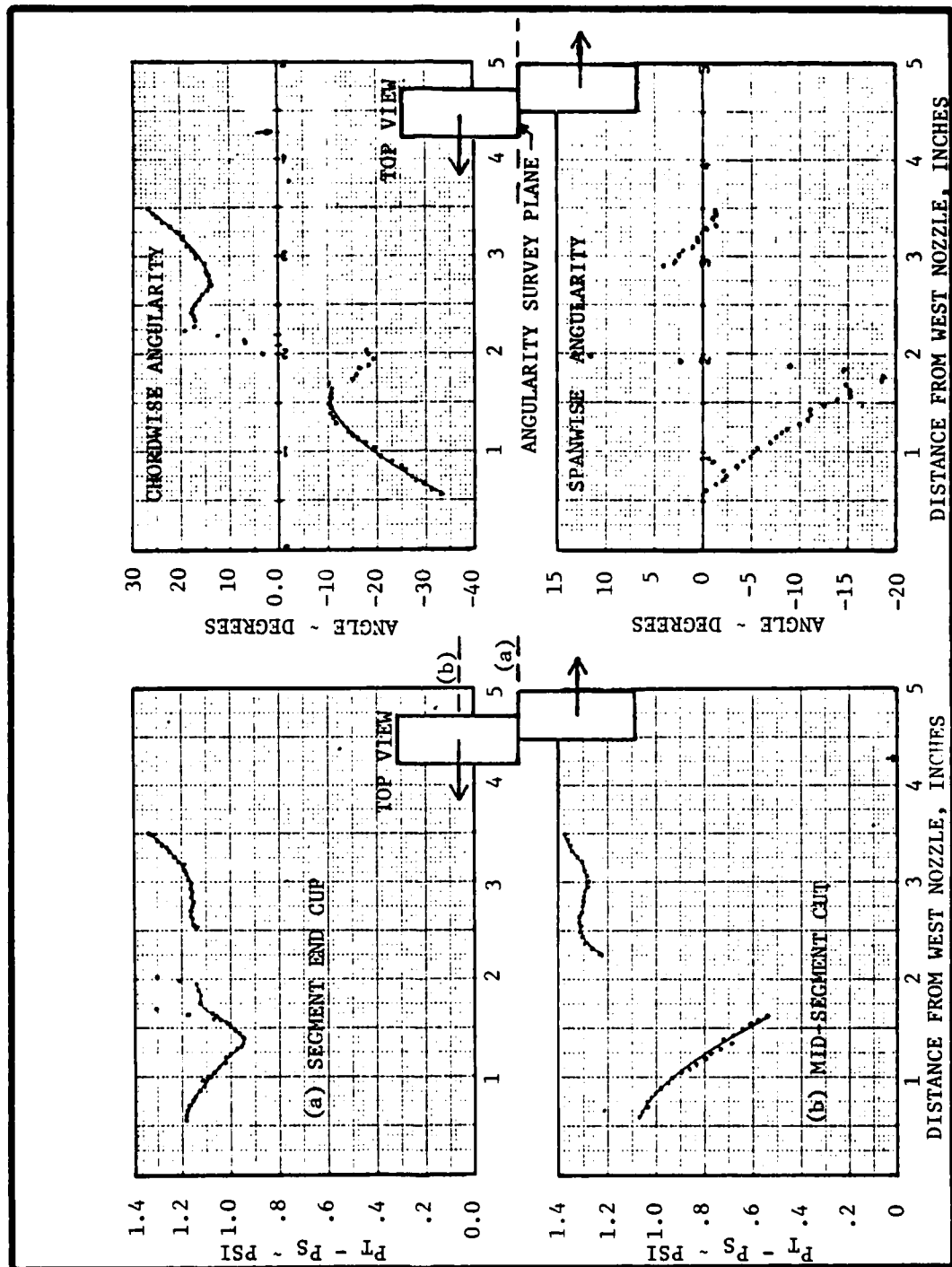


Figure 7-9. Dynamic Pressures and Angularity of Inlet Secondary Flow, 15° Hypermixing  
Angle and  $A_2/A_0 = 15.2$

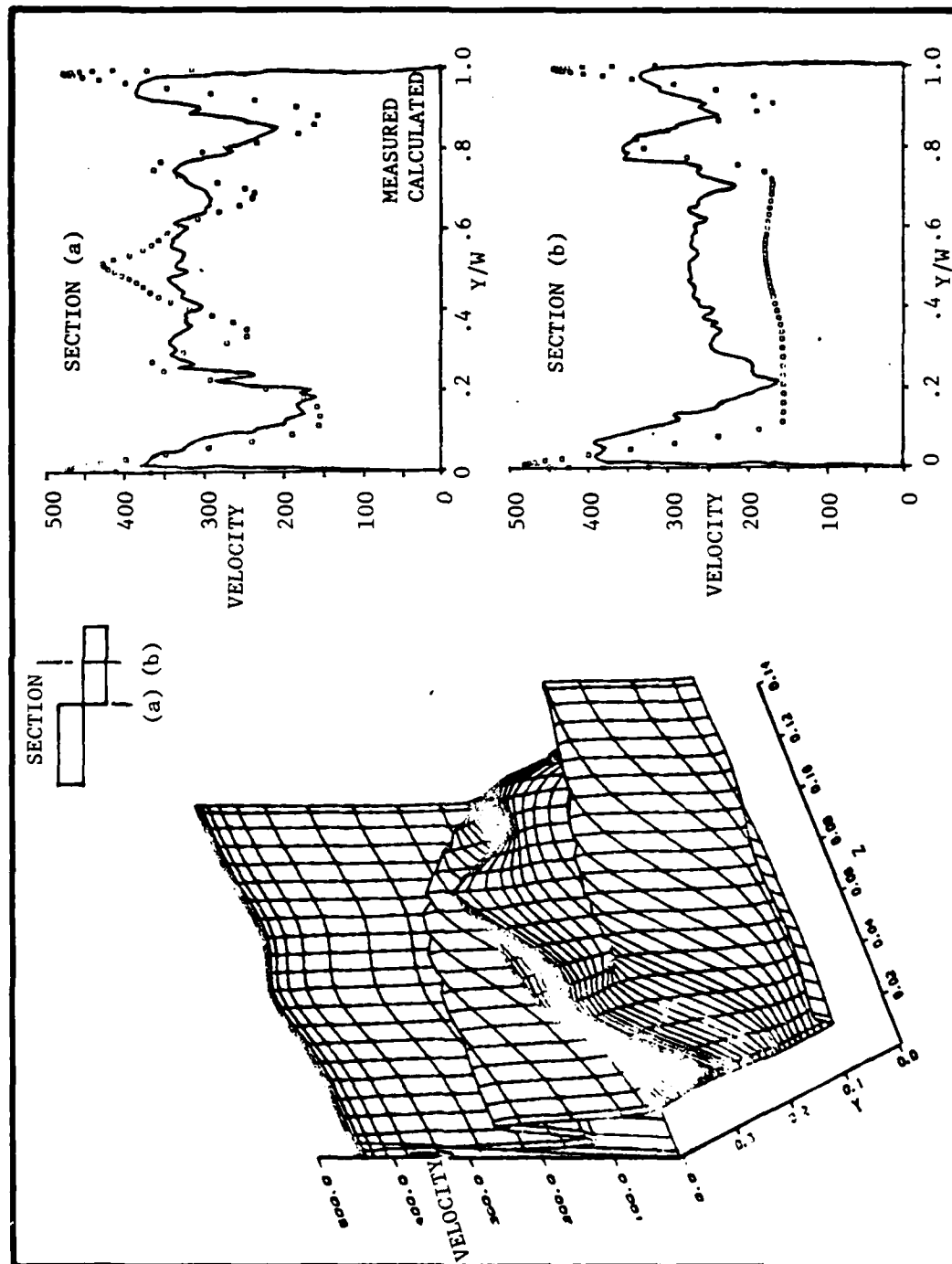


Figure 7-10 22.5° Hypermixing Jet Velocity Distribution with Original Values of  $C_k$  and  $C_\epsilon$

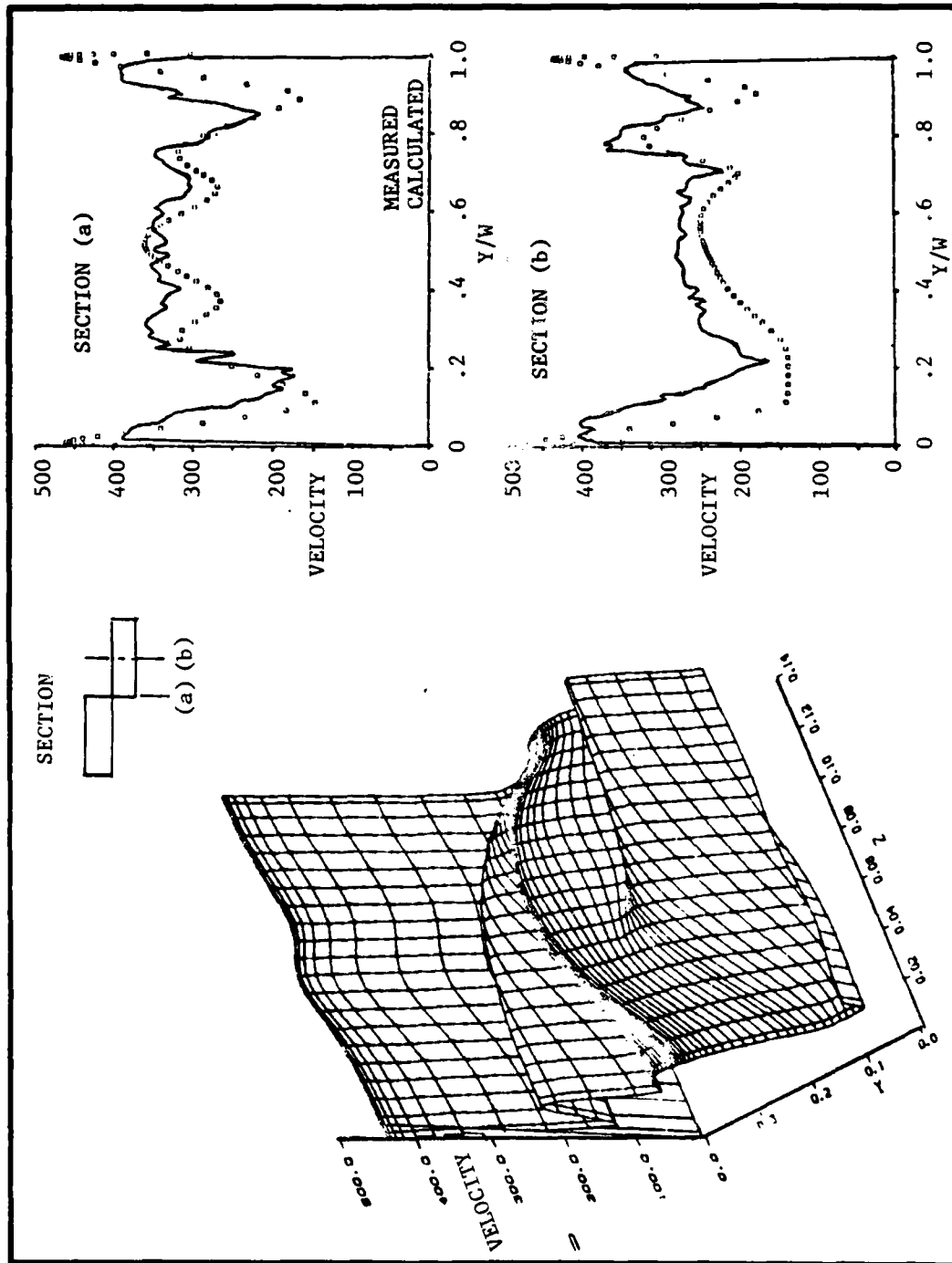


Figure 7-11 22.5° Hypermixing Jet Velocity Distribution with  $C_k = 4. \times C_{k, \text{ref.}}$



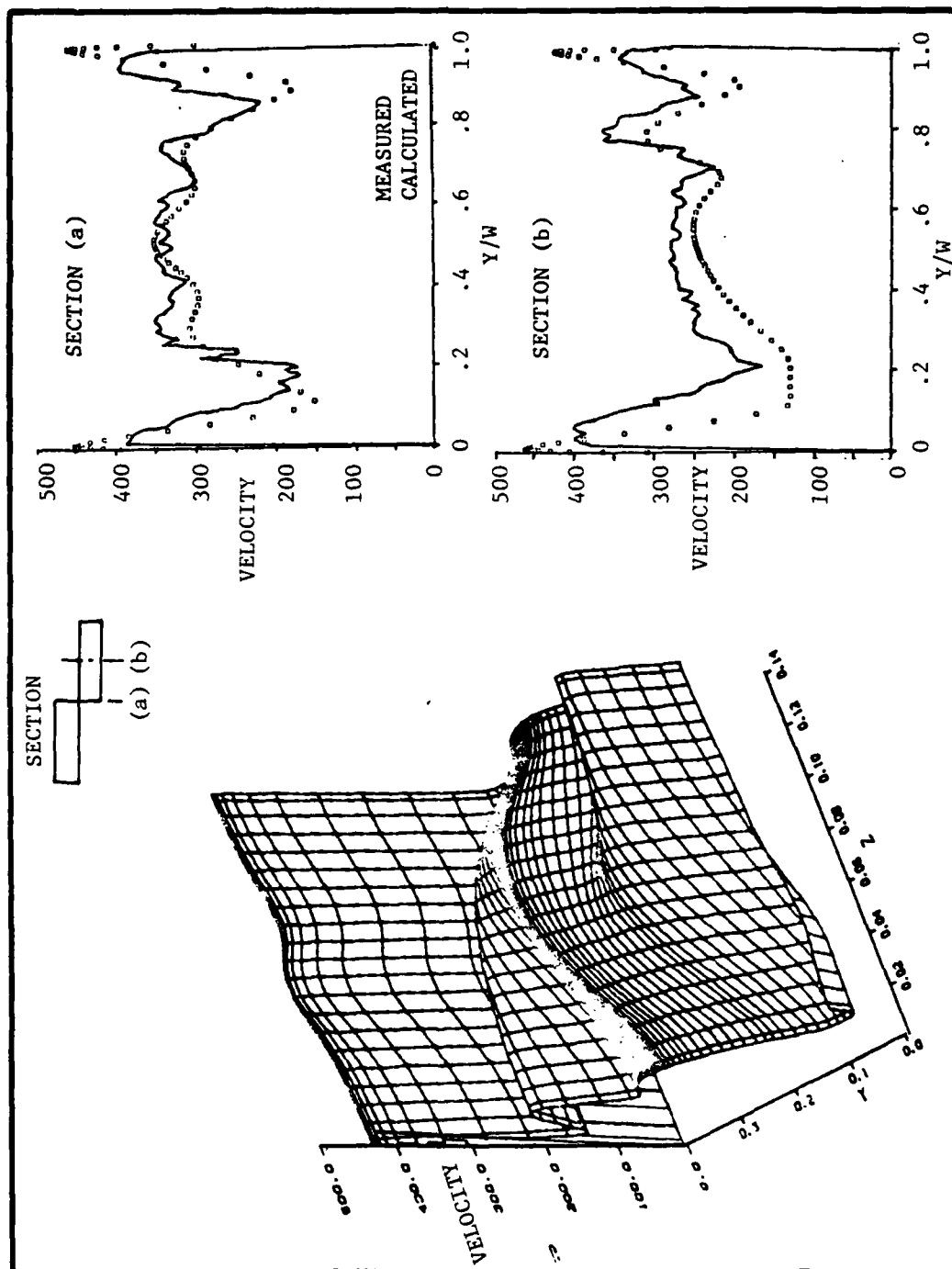


Figure 7-12 22.5° Hypermixing Jet Velocity Distribution with  $C_\epsilon = C_{\epsilon,ref}/16$



It thus became necessary to measure the turbulence intensity in the jets in order to determine the correct values of the turbulence constants. Measurements made with hot film and kulite probes both indicated that a value of  $C_k = 0.04$  was appropriate. The corresponding value of the dissipation constant was found to be  $C_\epsilon = 0.003$ . These values are typical of channel flows.

Figure 7-13 shows a comparison of the measured augmentation with the increments computed using these values of the constants and the improved angularity subroutine. Good agreement was obtained up to approximately  $20^\circ$ . It was felt that the difference at larger angles was due to violating the basic small angle assumption of the analysis, and to neglecting the effect of swirl on the turbulence production. In order to

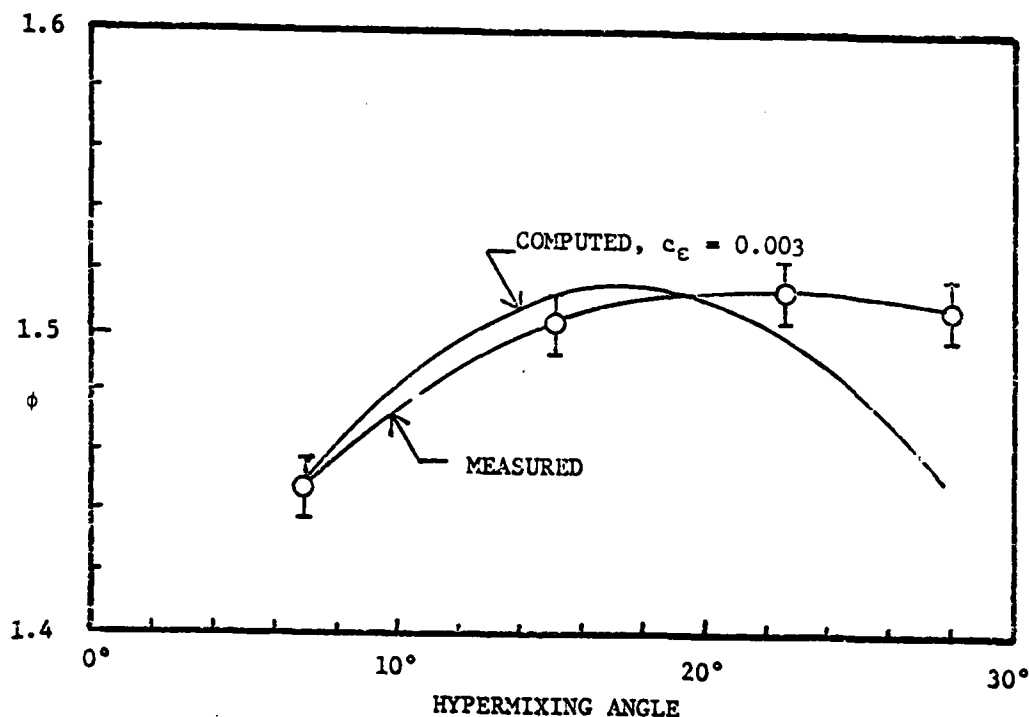


Figure 7-13 Comparison of Measured and Computed Augmentation

improve the calculations, it was decided to include the neglected swirl terms in the turbulence equations. In these equations, the term representing the generation rate of turbulent kinetic energy can be written in general form as:

$$G = -\rho \overline{u'_i u'_j} \frac{\partial u_i}{\partial x_j}$$



If the eddy viscosity model

$$-\rho \overline{u'_i u'_j} = \mu_t \left( \frac{\partial U_i}{\partial x_j} + \frac{\partial U_j}{\partial x_i} \right)$$

is used along with the cartesian coordinates notation,  $U_1 = U$ ,  $U_2 = V$ ,  $U_3 = W$ ,  $x_1 = x$ ,  $x_2 = y$ , and  $x_3 = z$ , then  $G$  is

$$G = \mu_t \left[ \left( \frac{\partial U}{\partial y} \right)^2 + \left( \frac{\partial U}{\partial z} \right)^2 \right] + \mu_t \left( \frac{\partial W}{\partial y} + \frac{\partial V}{\partial z} \right)^2 + 2\mu_t \left[ \left( \frac{\partial V}{\partial y} \right)^2 + \left( \frac{\partial W}{\partial z} \right)^2 \right]$$

If it is assumed that  $U \gg V, W$  and  $\frac{\partial}{\partial y}, \frac{\partial}{\partial z} \gg \frac{\partial}{\partial x}$  the original form of

the production term is obtained. The effect of including all the production terms is shown in Figure 7-14. The increase in augmentation is greatest at the largest angles, but the increase is not sufficient to significantly improve the predictions in this region. Thus, it was concluded that the applicability of the jet mixing analysis is limited to angles less than about  $20^\circ$ . Since the measured augmentation was found to have a maximum at small angles, this is not likely to be a serious limitation.

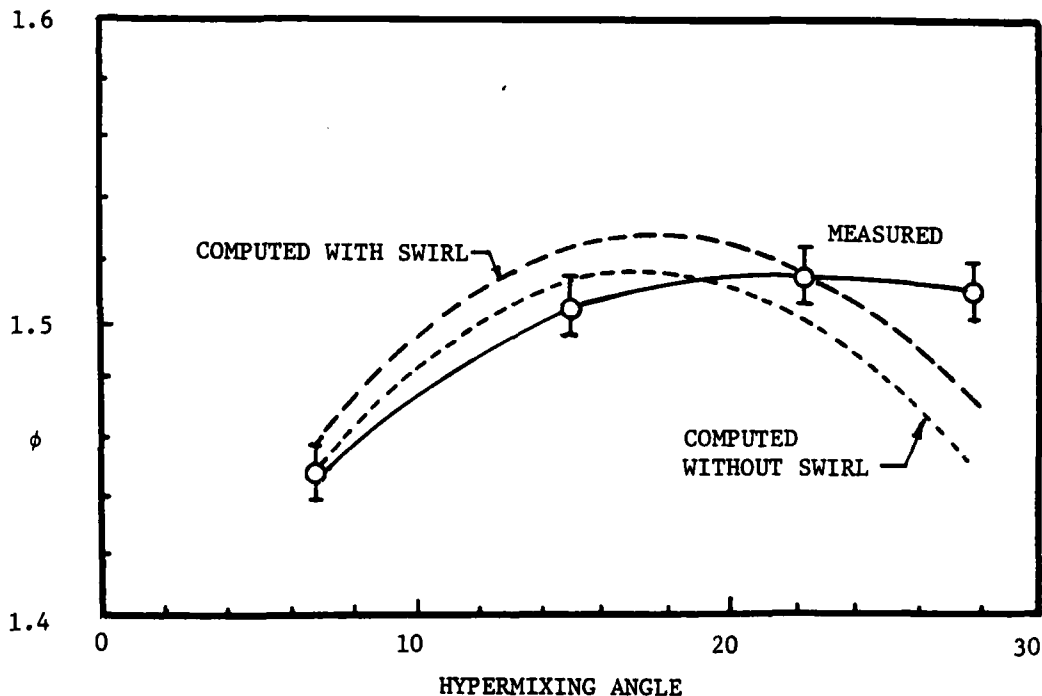


Figure 7-14 Effect of Swirl on Analytical Prediction



### 7.3 ASYMMETRIC NOZZLES

#### 7.3.1 Introduction

The asymmetric cruciform centerbody nozzle design was developed in an effort to capitalize on the generally superior entrainment characteristics of the symmetric cross slot nozzle configuration while maintaining packaging limits imposed by typical supersonic airfoil contours. This design combines a series of aft facing spanwise slot nozzles with an alternating series of cross slots on the forward side. The aft facing span slots provide a flat surface contour for the airfoils upper surface close-out while the cross slot is hidden in the airfoil cross section (see Figure 7-15).

This basic nozzle design offers several packaging advantages over the hypermixing nozzle concept. These advantages include elimination of an upper surface close-out system and the removal of discontinuities from the upper surface of the airfoil. In an effort to develop an asymmetric centerbody nozzle, which would be compatible with the XFV-12A aircraft design constraints while optimizing augmentor performance, a series of asymmetric centerbody designs were evaluated.

Typically, during this series, nozzles were conceptually defined utilizing both the available experimental data base and analytical trade studies. Based on this information, if a performance gain was anticipated, the nozzle was then designed and fabricated. Initial experimental evaluation entailed measuring the isolated thrust efficiency ( $C_T$ ) of the nozzle design. Isolated nozzle efficiency ( $C_T$ ) is an indication of the nozzles isolated thrust performance and is defined as the ratio of the nozzles measured thrust to its potential ideal thrust level. Utilizing the level of  $C_T$  as a reference, it is possible to correct the measured augmentation ratio for the observed efficiency differences between nozzles. The value of this correction is that it points out the relative gain or loss in mixing (entrainment) due to a nozzle configuration change without biasing the nozzles performance for actual differences in internal and external losses or differences in workmanship during fabrication. This method allowed for direct comparisons with performance predictions made utilizing the 3D TKE analytical technique which assumes that the value of a nozzle thrust efficiency ( $C_T$ ) is a constant.

Following the isolated performance evaluation, each centerbody nozzle was then installed in the augmentor model for a series of performance evaluations. Traversing pressure surveys were utilized to examine the nozzles mixing characteristics and isolate the augmenters relative flow quality.

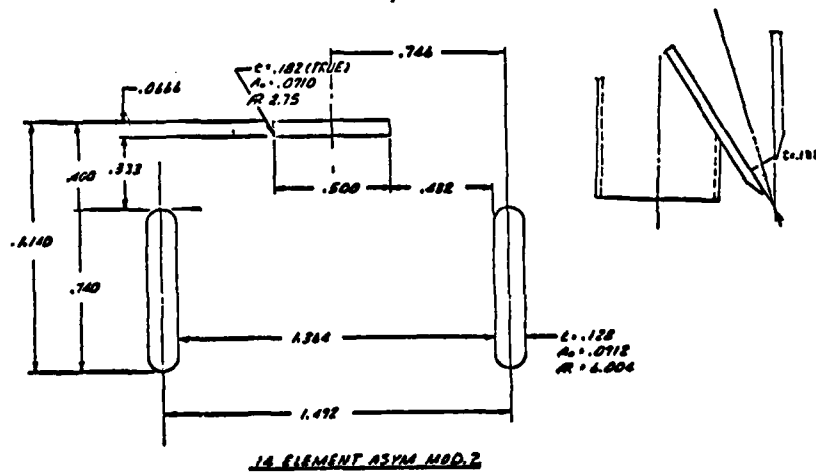
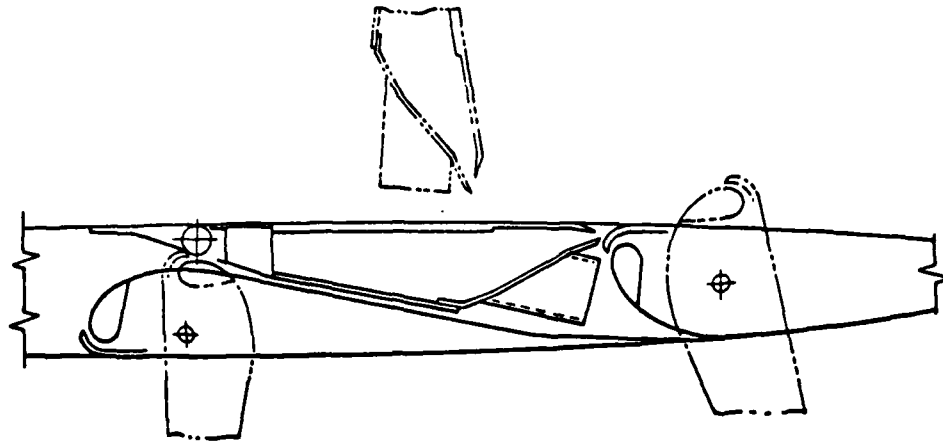


Figure 7-15 Asymmetric Centerbody Packaging Concept



The nozzles relative performance level was defined utilizing a mix of analytical and experimental analysis techniques. Direct comparisons of experimental data both isolated and in augments were employed. Measured in augments performance levels were corrected for differences in isolated nozzle thrust efficiency. This corrected data was compared to analytical performance estimates to identify potential differences in a nozzles entrainment characteristics. The remainder of this section will discuss a number of the asymmetric nozzle designs along with pertinent results and conclusions.

### 7.3.2 14 Element Asymmetric Centerbody Nozzle

The initial centerbody in this test series was designated as the 14 element asymmetric (see Figure 7-16). The basic design of this nozzle was based on information which had been developed during previous augments test programs; however, its specific geometric parameters were defined by current aircraft packaging constraints. Utilizing the 3D TKE program, analytical trade studies evaluating the performance of the baseline 14 element asymmetric centerbody compared to the 15° hypermixing centerbody were conducted. While this analytical method had been used extensively to evaluate hypermixing nozzle configurations, this was the first attempt to evaluate asymmetric style nozzles. Based on available information concerning the inlet conditions for this style nozzle, an increment of  $+0.03\Delta\phi$  was computed for the asymmetric design as compared to the 15° hypermixing configuration. Subsequent to this initial computation, a series of experimental inlet surveys were conducted on an asymmetric style nozzle. The information was then utilized to update the inlet condition modeling in the 3D TKE technique. Additional analytical trade studies utilizing the improved inlet condition modeling indicated a performance decrement of approximately  $.03\Delta\phi$  associated with the asymmetric style nozzle.

Previous experimental trends indicated that asymmetric style nozzles were capable of producing higher levels of performance than comparable hypermixing nozzle designs. Based on this information, and in an effort to optimize the performance potential of the asymmetric design, the nozzle development effort continued. Isolated testing of the 14 element asymmetric nozzle indicated that its nozzle efficiency ( $C_T$ ) was approximately  $.03\Delta C_T$  higher than the 15° hypermixing design (see Figure 7-17).

Baseline in augments performance for this centerbody at the 3.24 inch throat configuration,  $A_2/A_0 = 15.2$ , is presented in Figure 7-18. Initially, the demonstrated performance was disappointing. However, examination of the pressure survey data Test 280, Run 8 obtained during this test series indicated that both the centerbody span slot and cross

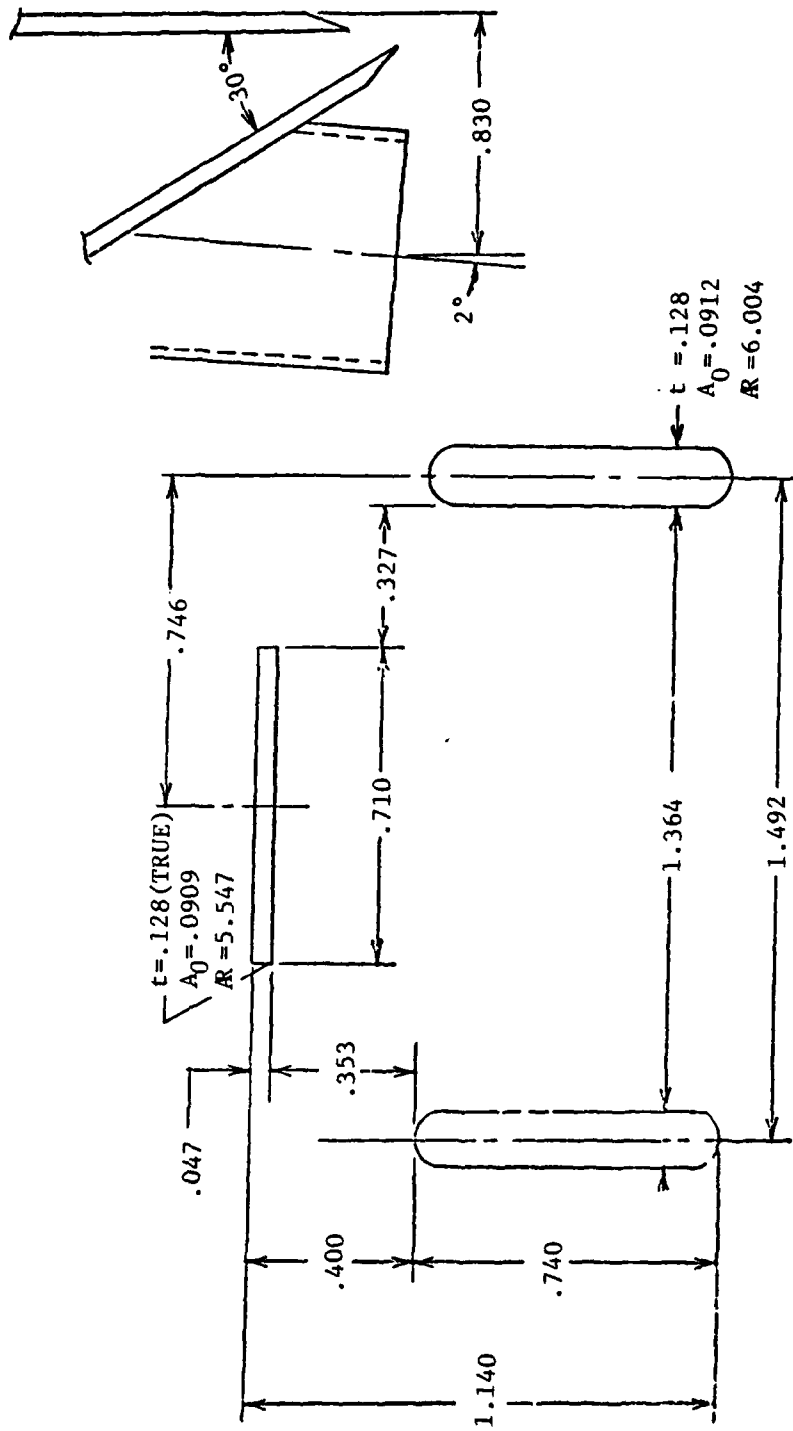
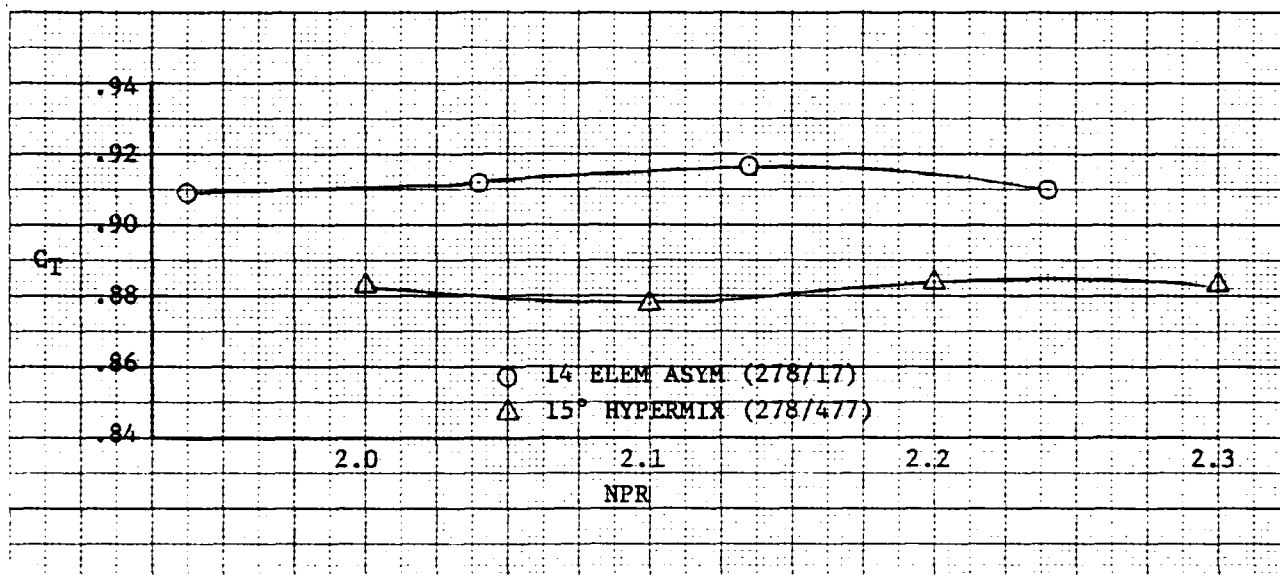
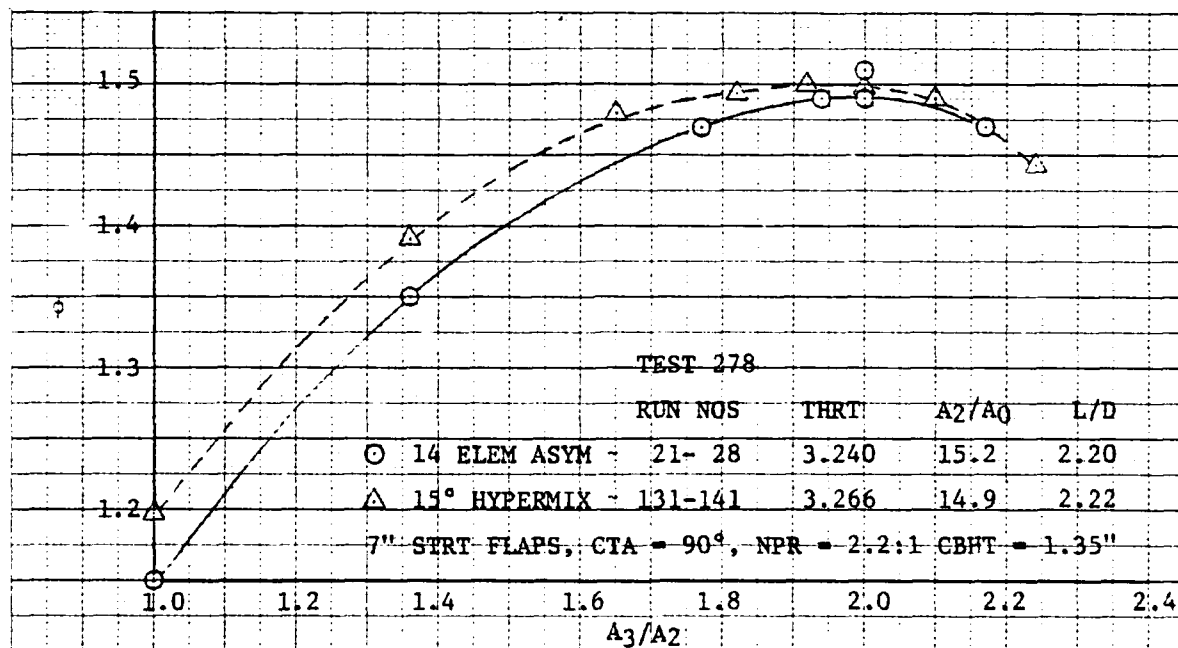


Figure 7-16 14 Element Asymmetric Nozzle

Figure 7-17 Isolated Centerbody Nozzle Efficiency ( $C_T$ )Figure 7-18 14 Element Asymmetric Versus 15° Hypermixing Centerbody Nozzle  $A_3/A_2$  Comparison





slot nozzles were strongly merged with the Coanda jets. Past experimental experience indicated that this type of flow condition typically limited a nozzles entrainment potential. Follow-on analytical trade studies were conducted utilizing the 3D TKE program with inputs modified in a manner to rotate the centerbody jet producing premature merging of the centerbody and Coanda jets. The program indicated a large decrement in potential performance could be expected from the highly merged jet flow condition. Additional analytical studies indicated that enlarging the augmenter throat from 3.24 inches to 4.42 inches (increasing the  $A_2/A_0$  from 15.2 to 20.2) would "unmerge" the nozzle jets and produce a performance increment of  $+0.06 \Delta\phi$ .

Figure 7-19 presents the experimental performance of the 14 element asymmetric for a range of augmenter throat widths. The increment in performance obtained by enlarging the throat was approximately  $+0.04 \Delta\phi$ . Pressure survey data indicated that the enlarged throat widths did substantially reduce the merging of the centerbody-Coanda jets possibly accounting for the increased levels of performance.

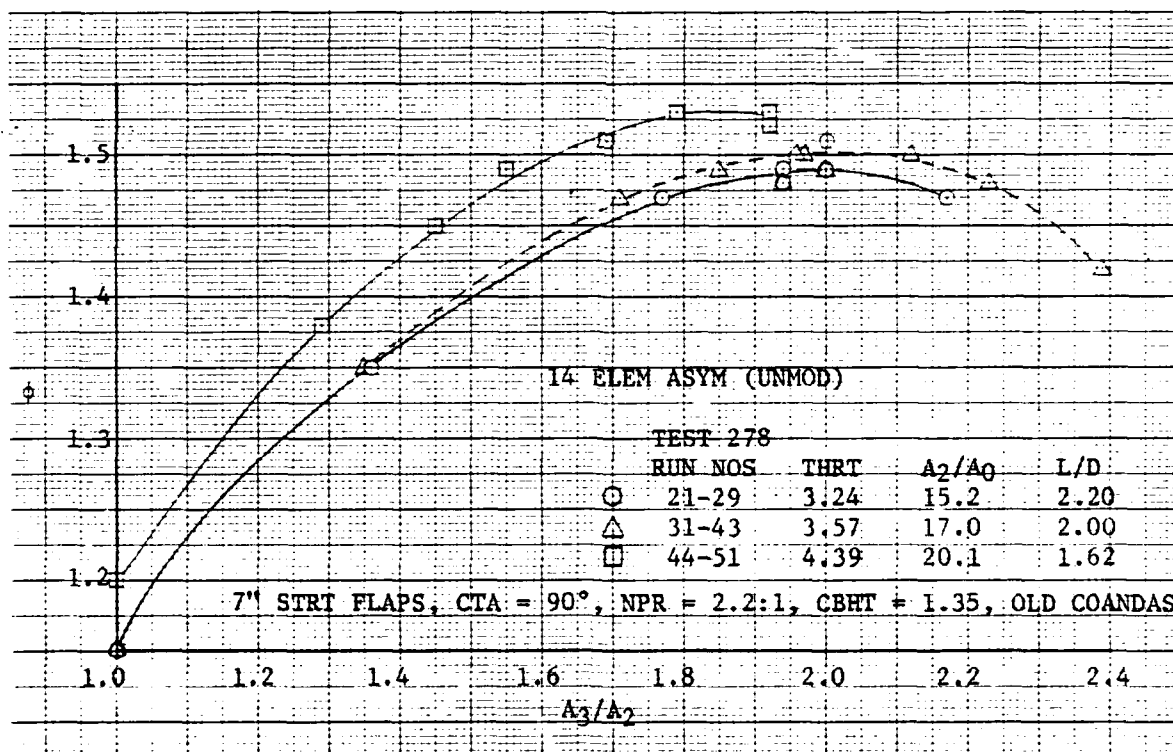


Figure 7-19 14 Element Asymmetric Throat Width Comparison



To determine if the centerbody and Coanda jets could be "unmerged" by other means, a modification to three midspan cross slot elements was made to reduce the relative launch angle between the two jets from  $32^\circ$  to  $25.5^\circ$ . A sketch of this nozzle configuration, designated 14 element asymmetric mod 1, is presented in Figure 7-20. Survey data indicated that the jets did unmerge, however, the region of  $\Delta P_T = 0$  moved from between the centerbody jets to the forward side between the diffuser jet and cross slot jet. No improvement in entrainment or overall performance was noted (see Figure 7-21).

#### 7.3.3 14 Element Mod 2 Asymmetric Nozzle

In an attempt to improve the jet spreading (entrainment) characteristics of the span slot nozzles while minimizing any adverse interaction between the cross slot and span slot nozzles, the aspect ratio (AR) of these nozzles was reduced from 5.55 to 2.75 (see Figures 7-16 and 7-22). Analytical studies utilizing the 3D TKE program predicted a performance increment of  $+0.03 \Delta \phi$  would be associated with the reduced AR design. This increase was apparently the result of stronger span slot tip vortices produced by the reduction of their aspect ratio.

Isolated centerbody nozzle performance tests indicated that the 14 element mod 2 (reduced AR span slot) nozzle efficiency ( $C_T$ ) was similar to the 14 element baseline asymmetric (see Figure 7-23). Apparently, modifications necessary to reduce the span slot AR had little effect on the isolated performance of the centerbody.

Figure 7-24 presents in-augmenter performance comparisons displaying a performance increment of approximately  $+0.03 \Delta \phi$  demonstrated by the 14 element mod 2 (reduced span slot AR) nozzle. Comparisons of traversing pressure surveys obtained at the augmenter exit indicated that the reduced AR span slot did exhibit superior entrainment characteristics. This improved entrainment was evidenced by increased jet spreading in the chordwise Coanda jet direction while spanwise spreading characteristics were similar.

The reduced AR span slot nozzles do, in fact, appear to increase the entrainment characteristics of the asymmetric nozzle design without notable reductions in isolated nozzle efficiency resulting in an overall improvement in measured augmentation ratio.

#### 7.3.4 14 Element Mod 3 Asymmetric Nozzle

It was hypothesized that two span slots in close proximity may produce a set of co-rotating vortices resulting in increased levels of entrainment. A further modification to this centerbody was made by replacing the single span slots with a twin slot configuration as shown in the sketch of Figure 7-25. This centerbody nozzle design was designated 14 element asymmetric mod 3. Analytical trade studies utilizing the 3D TKE program indicated that the twin span slot configuration could provide a modest performance improvement ( $\approx 0.01 \Delta \phi$ ) over its single span slot counterpart.

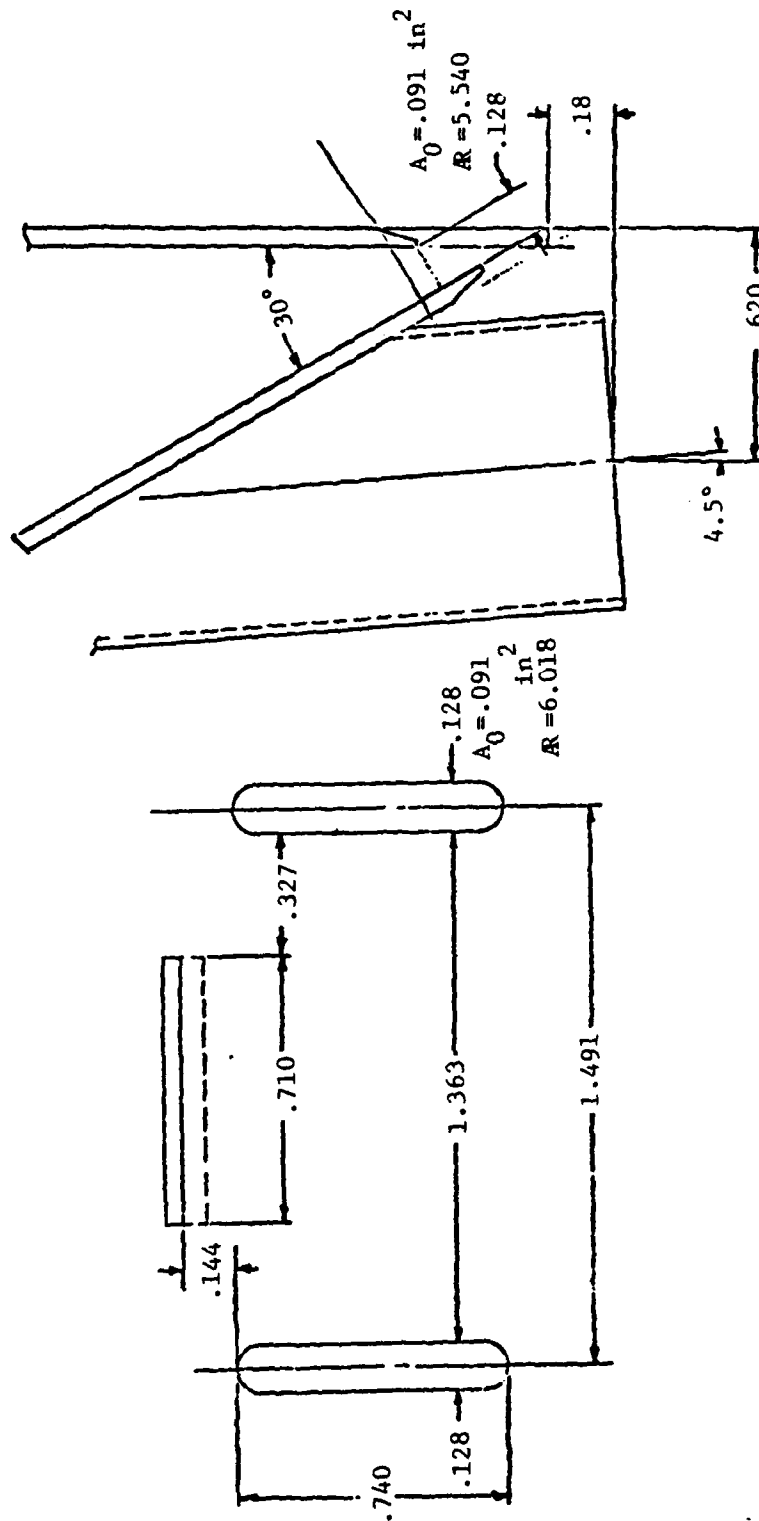


Figure 7-20 14 Element Asymmetric Mod No. 1

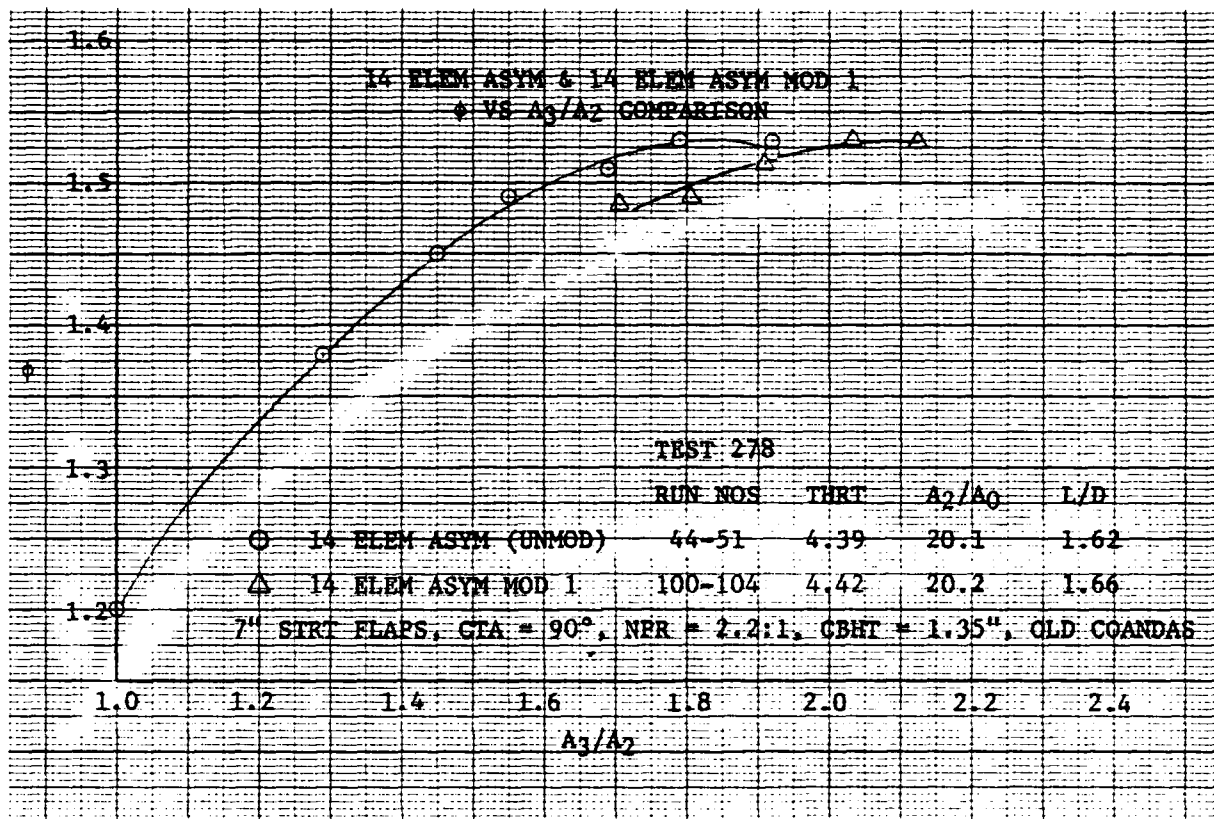


Figure 7-21 14 Element Asymmetric and 14 Element Asymmetric Mod No. 1 Comparison



NR81H-50

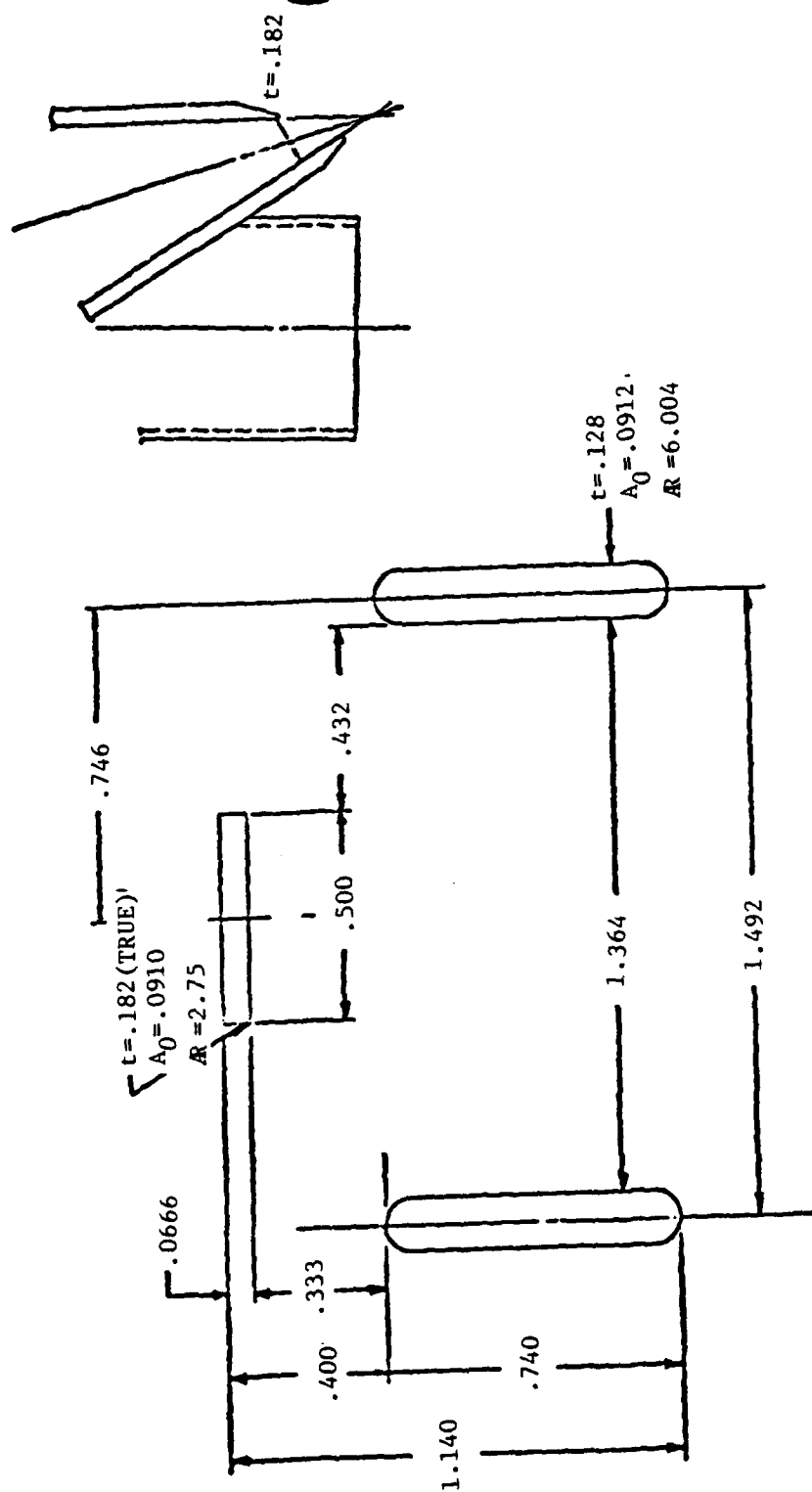


Figure 7-22 14 Element Asymmetric Mod No. 2

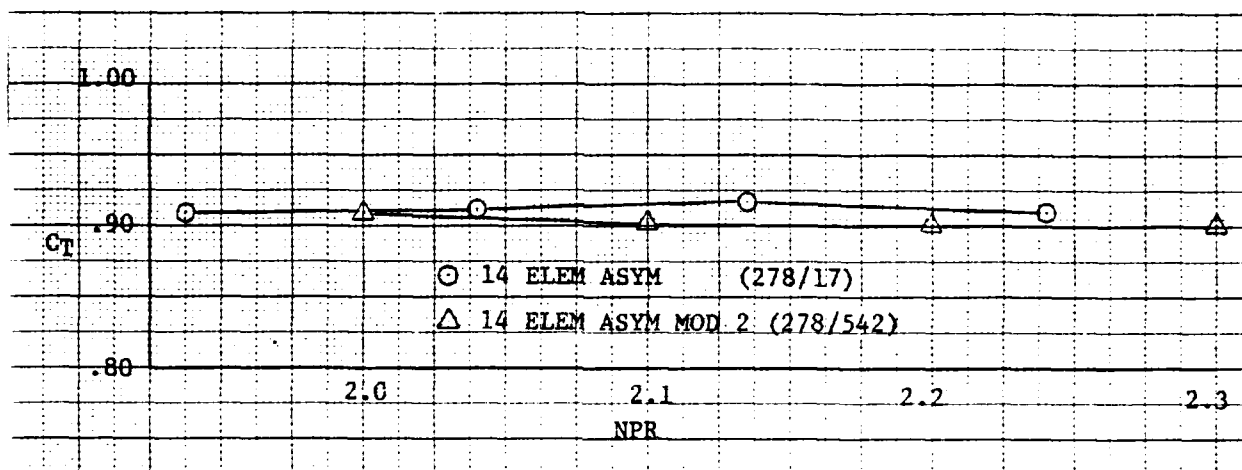


Figure 7-23 Isolated Nozzle Efficiency

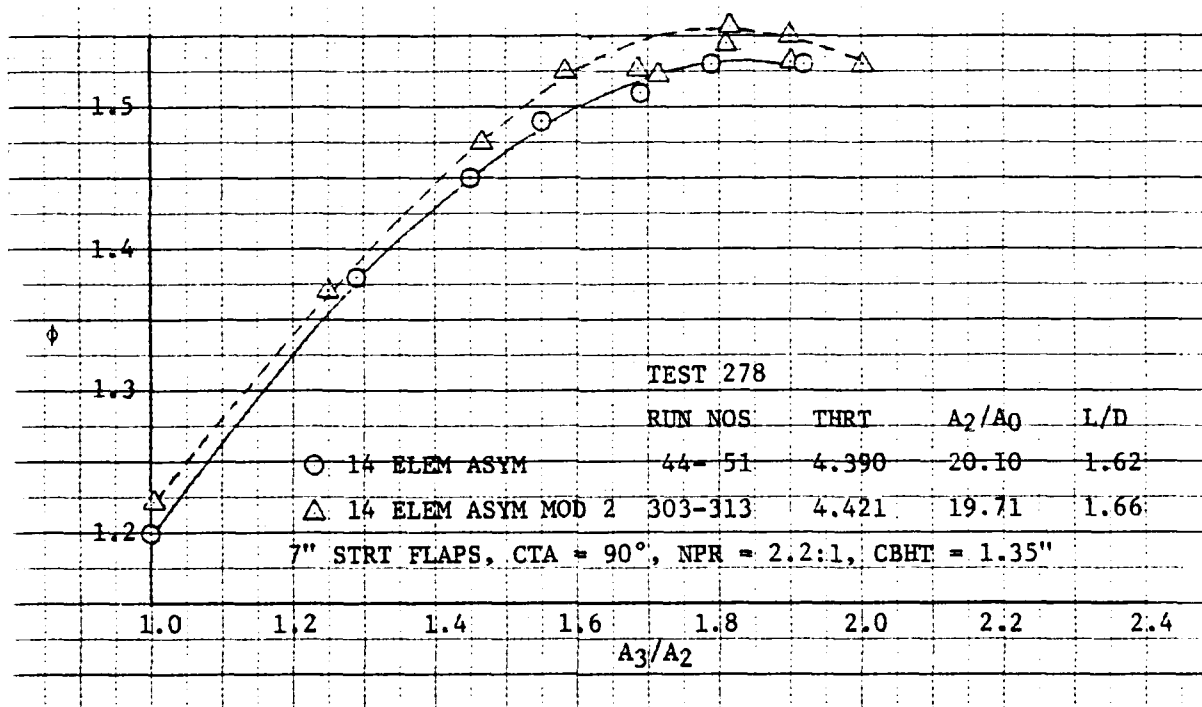


Figure 7-24 14 Element Asymmetric and 14 Element Asymmetric Mod No. 2 Comparison

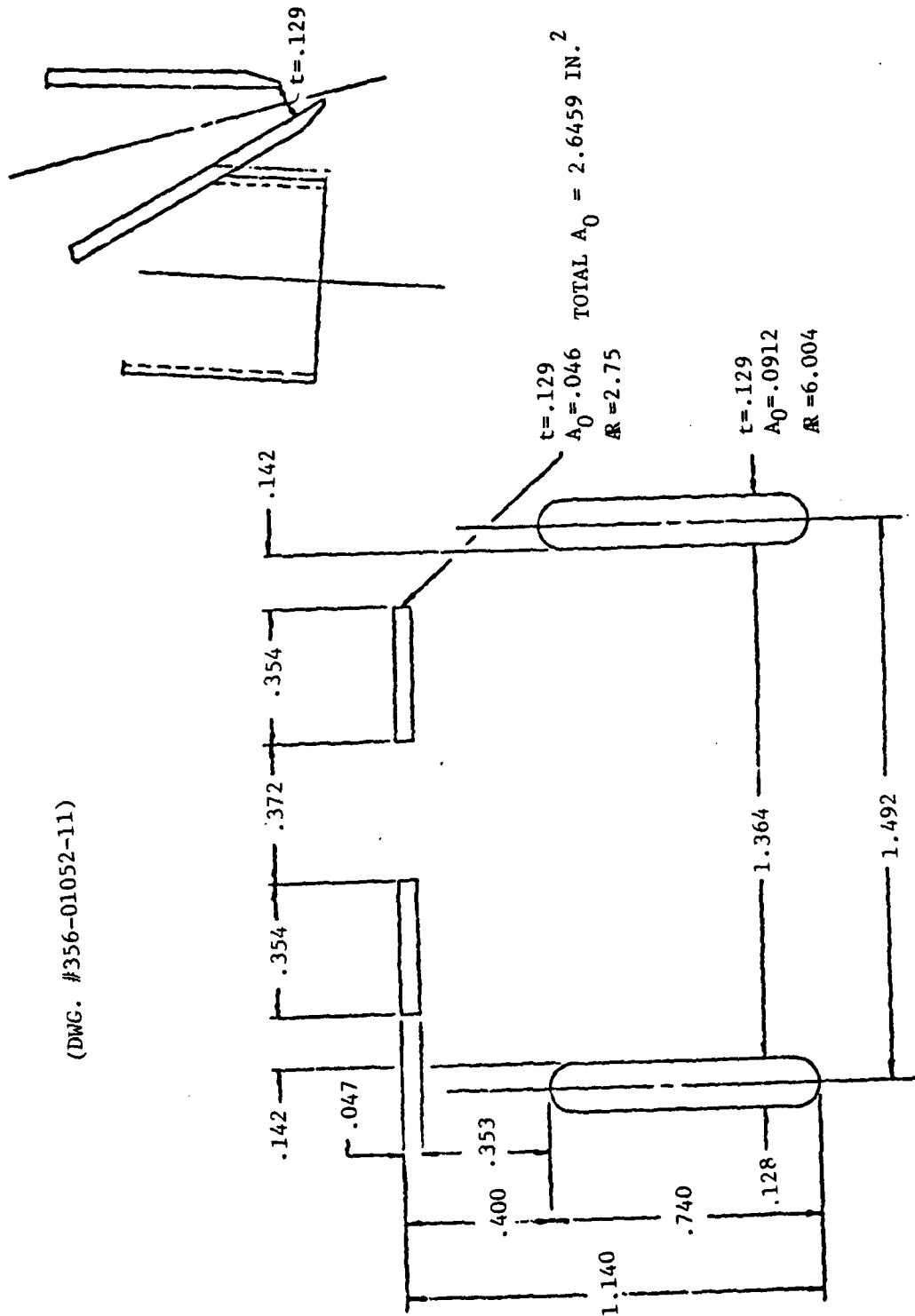


Figure 7-25 14 Element Asymmetric Mod No. 3



Isolated performance investigations of the 14 element mod 3 (twin span slot) design indicated that this nozzle's thrust efficiency,  $C_T$ , was significantly lower than the mod 2 (single span slot) configuration (see Figure 7-26). The in-augmenter performance of the mod 3 design is presented in Figure 7-27. While the nozzle's overall measured performance is about  $.025 \Delta\phi$  less than the mod 2 design, it should be noted that this performance deficiency can easily be attributed to the mod 3 nozzle's isolated performance. The measured decrement in  $C_T$  for the mod 3 nozzle would account for approximately  $-.05 \Delta\phi$  decrement in total augmenter performance assuming this nozzle's entrainment was comparable to the mod 2 (single span slot) design. Apparently, the increased levels of entrainment produced by the twin span slot design offset a large portion of the  $C_T$  decrement resulting in the measured penalty in augmentation compared to its single span slot counterpart. The decrement in isolated performance,  $C_T$ , may be attributable to increased skin friction drag produced by the twin span slots additional internal nozzle perimeter or may be, in part, due to flaws in workmanship resulting from nozzle modification.

It appears that while the twin span slot design may produce additional levels of mixing (entrainment) as indicated by the 3D TKE analysis, these increased levels of mixing are inadequate to offset the large penalty in nozzle efficiency associated with this design.

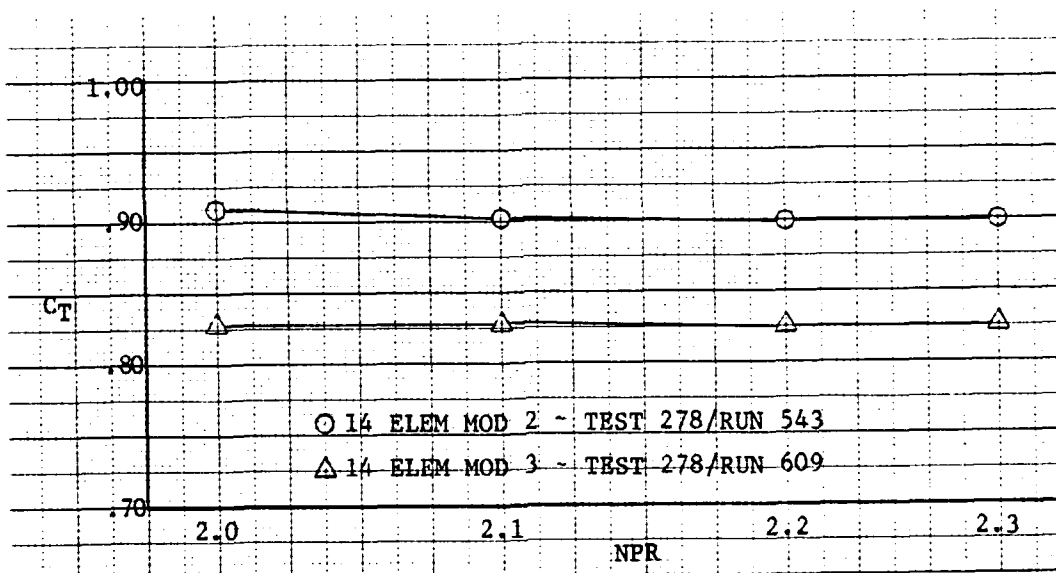


Figure 7-26 Isolated Nozzle Efficiency ( $C_T$ )



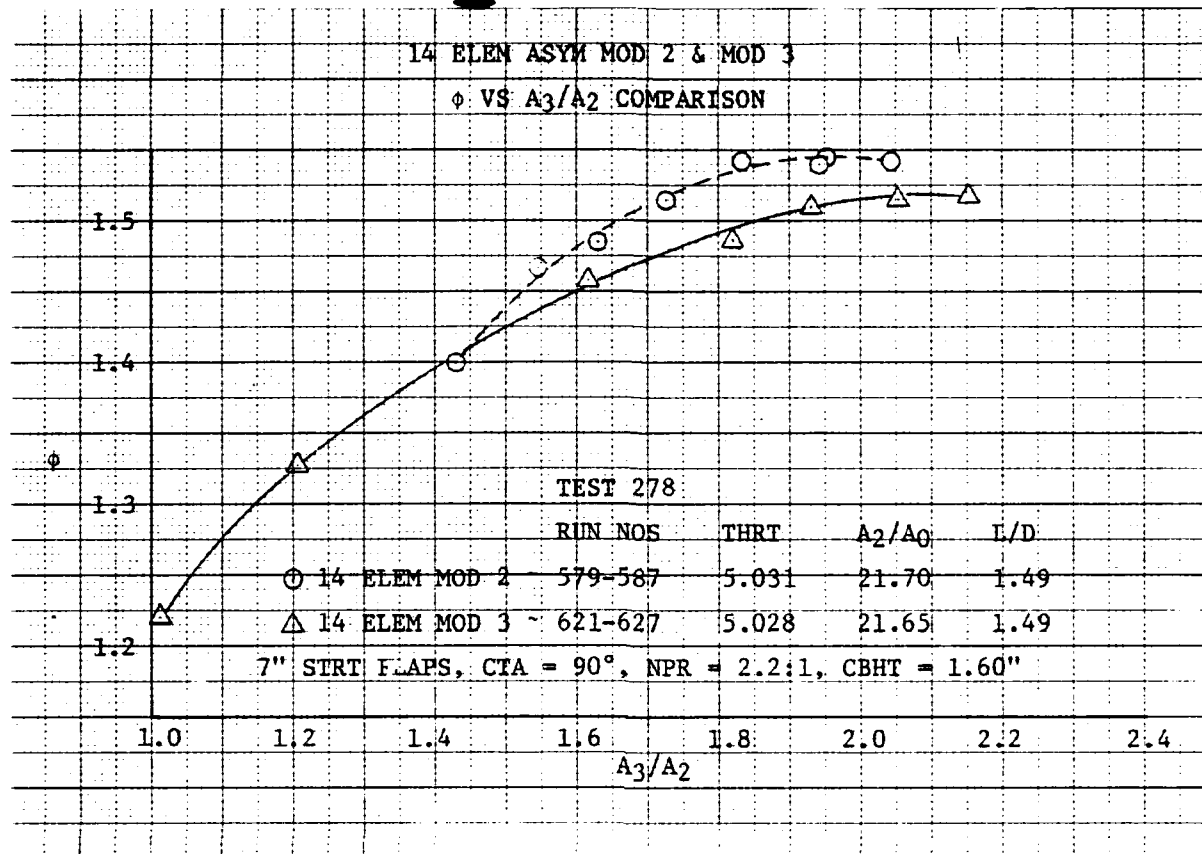


Figure 7-27 14 Element Asymmetric Mod 2 and Mod 3 Comparison

### 7.3.5 18 Element Asymmetric

In an effort to determine if the number of cross slot elements had an effect on centerbody performance, an 18 element asymmetric centerbody nozzle was designed and fabricated (see Figure 7-28). Geometrically, this nozzle was similar in design to the 14 element mod 2 asymmetric. That is, a series of race track cross slots alternating in combination with a series of single span slot nozzles. Exit area flow split and relative nozzle launch angles were all similar to the 14 element mod 2 centerbody configuration.

Analytical studies utilizing the 3D TKE technique indicated a performance increment of approximately  $+0.04 \Delta\phi$  could be expected from increasing the number of cross slot nozzle from 14 to 18. Again, during the analytical trade study, isolated nozzle thrust efficiency was assumed to be the same for both the 14 element and 18 element designs. Apparently, the predicted performance increase was the result of improved mixing (entrainment) characteristics due to the increased number of cross slot nozzles.

Figure 7-29 presents a comparison of the measured values of nozzle efficiency ( $C_T$ ) for the 14 element and 18 element designs. The decrement of approximately  $-0.04$  to  $.05 \Delta C_T$  can be attributed to the

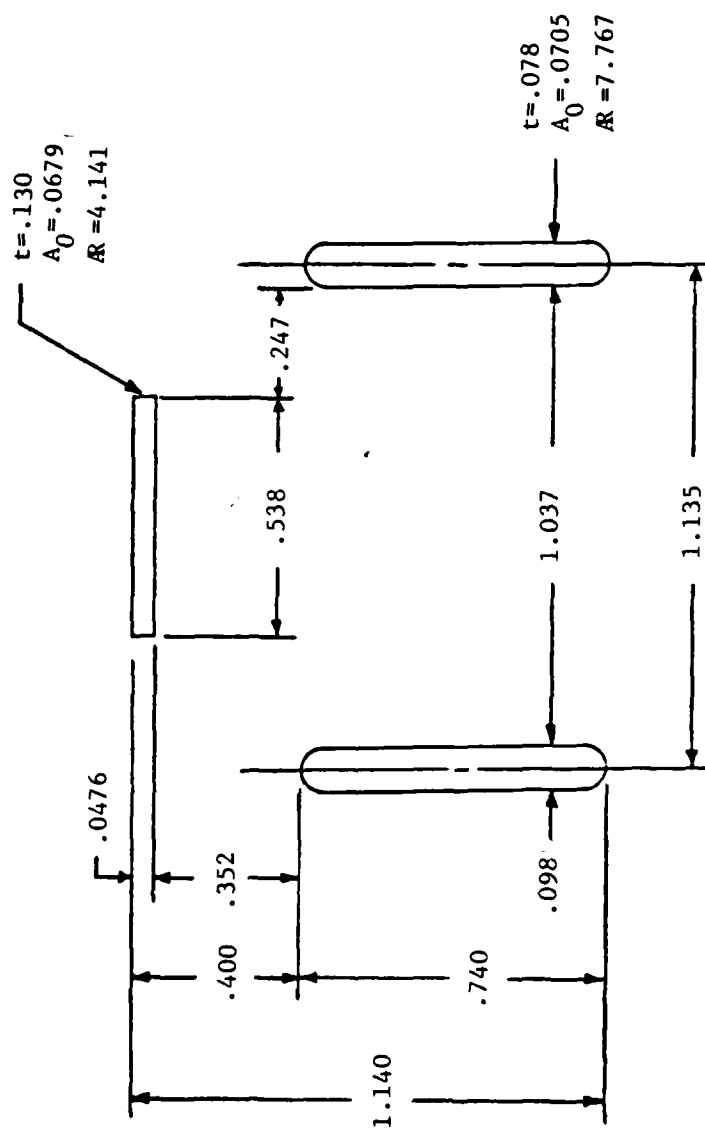


Figure 7-28 18 Element Asymmetric Nozzle

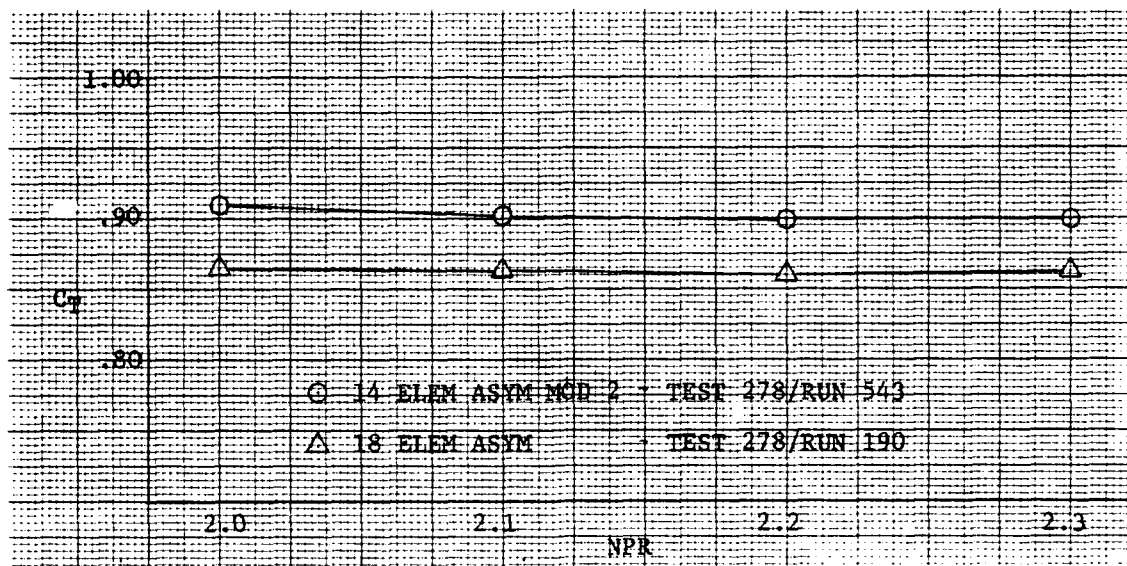


Figure 7-29 14 Element Mod 2 and 18 Element Asymmetric Comparison  
Isolated Nozzle Efficiency ( $C_T$ )

increased nozzle perimeter resulting in additional losses in nozzle efficiency due to increased skin friction and nozzle boundary layer growth. A comparison of in-augmenter performance of  $\phi$  versus  $A_3/A_2$  presented in Figure 7-30 shows a loss in performance of  $-.04 \Delta\phi$  for the 18 element design compared to its 14 element counterpart. Correcting the 18 element's augmentation deficiency for its measured decrement in isolated nozzle efficiency accounts for approximately .045 of the  $\Delta\phi$  loss. The loss in nozzle efficiency due to the addition of cross slot elements appears to offset any potential improvement in mixing entrainment produced by the additional cross slot elements.

#### 7.4 SYMMETRIC CENTERBODY NOZZLE

##### 7.4.1 Introduction

An improvement in augmentation over hypermixing of about .04 was obtained with the initial tests of the asymmetric nozzles. Further improvements may have been obtained through a test/analysis optimization program. However, it was uncertain how long such a program would take or how much improvement could be obtained. Therefore, it was decided to experimentally determine the maximum that could be gained by utilizing full width cross slot nozzles. In Reference (26) such a nozzle was shown to produce performance gains.

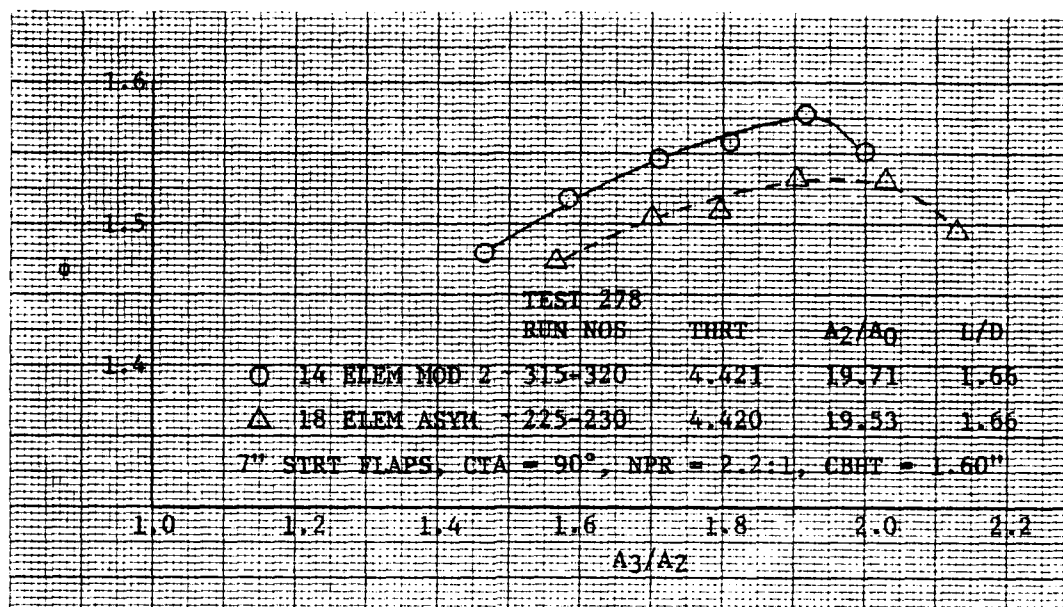


Figure 7-30 14 Element Mod 2 Asymmetric and 18 Element Asymmetric  $\phi$  Versus  $A_3/A_2$  Comparison

The nozzle used in Reference (26) was adapted for testing in the XfV-12A wing augmentor. A sketch of the nozzle is shown in Figure 7-31 and the results of the test are presented in Figure 7-32. This result was very encouraging and indicated a potential for the symmetric nozzles. However, the BT-3 nozzle was too wide for packaging within the XfV-12A. Therefore, a reduced width nozzle was design, fabricated, and tested. A sketch of this nozzle is shown in Figure 7-33 and the test results shown in Figure 7-32 were very disappointing. A decrement in augmentation ratio of approximately .07 was obtained.

In order to improve the performance of the reduced width nozzle and yet maintain a packageable design, a program was initiated to develop a high performance symmetric cross slot nozzle.

The nozzle development program consisted of a systematic series of tests to determine ejector performance and flow characteristics as a function of nozzle geometric parameters. The length of time required between nozzle design and test necessitated defining a matrix of nozzles designed to study cross slot width, span slot and cross slot aspect ratios, span slot/cross slot flow split, bowtie ratio and initial jet flow angularity. A parallel study was conducted in which the jet mixing analysis computer code was utilized. Correlation between test and analysis would lead to a

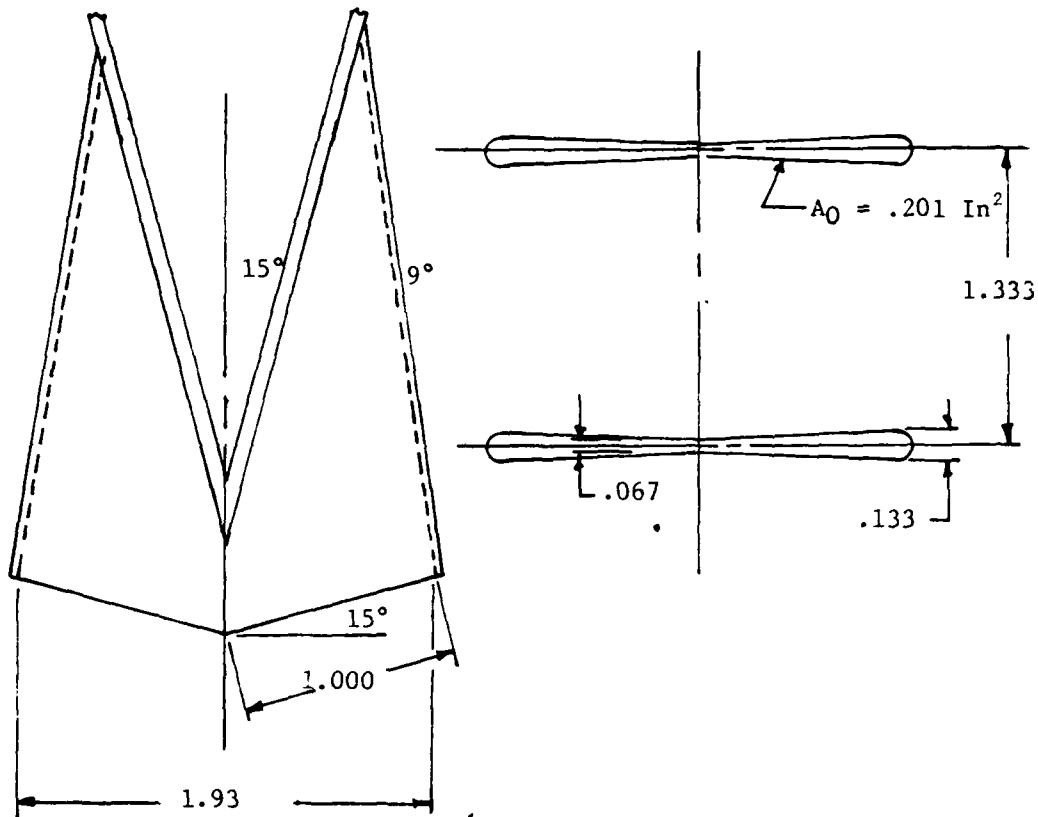


Figure 7-31 Symmetric Cross-Slot Nozzle (BT-3)

better understanding of the complex interactions between nozzle geometry and ejector flow characteristics along with the capability to define a packageable high performance symmetric cross slot nozzle.

#### 7.4.2 Bowtie Ratio Effects

The cross-slot nozzle bowtie ratio (BTR) is defined as the ratio of the nozzle thickness at the tip to the nozzle thickness at the centerline. The purpose of increasing BTR is to increase entrainment by placing more primary flow into the vortex structure at the cross-slot tip.

The effect of increased BTR on ejector performance was obtained both analytically and experimentally. Experiments were conducted on centerbody nozzles with BTR's of 1, 2, and 3. All nozzle and ejector parameters were held constant except BTR.

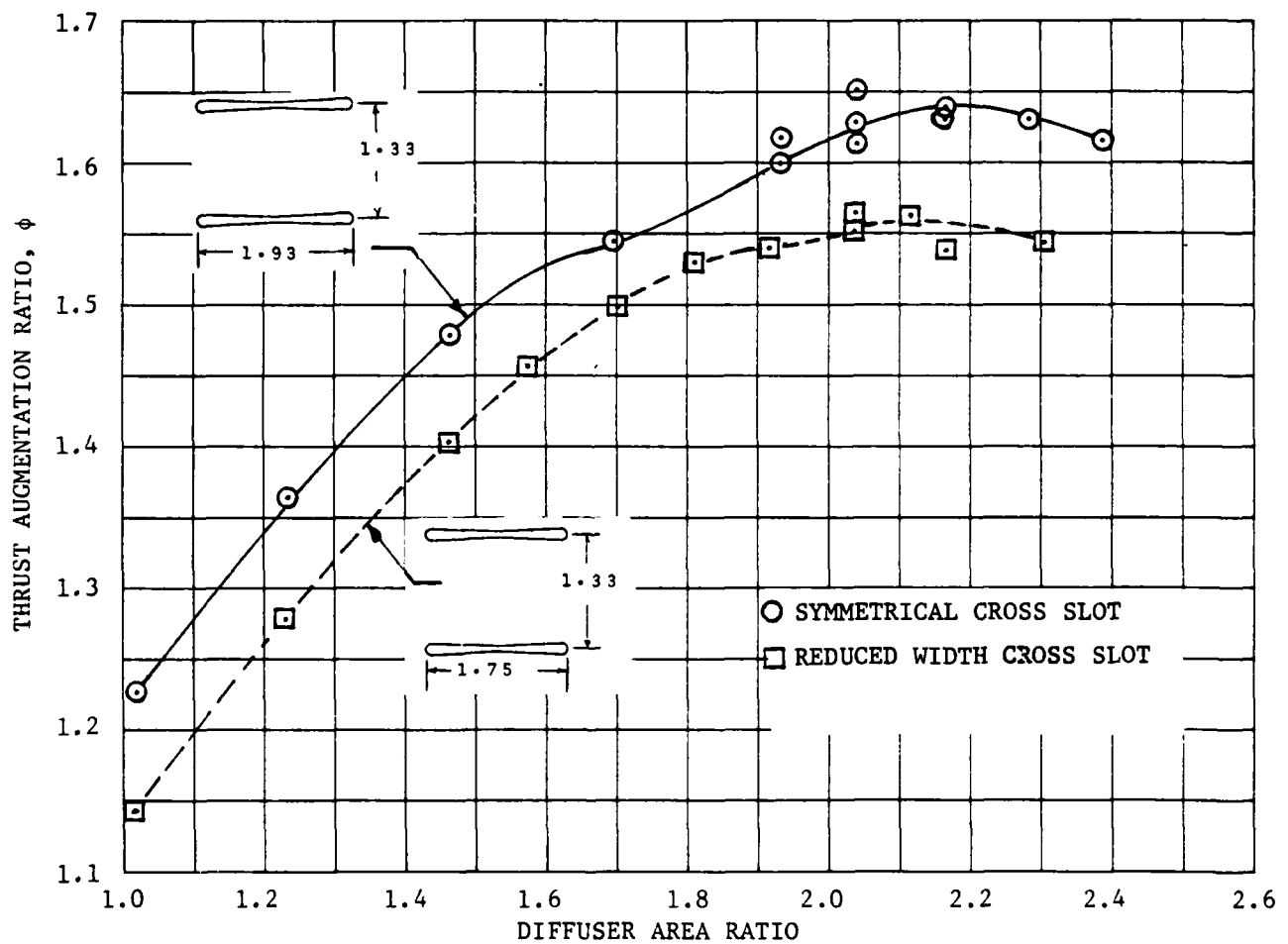


Figure 7-32 Symmetric Cross-Slot Nozzle Thrust Augmentation Versus Diffuser Area Ratio

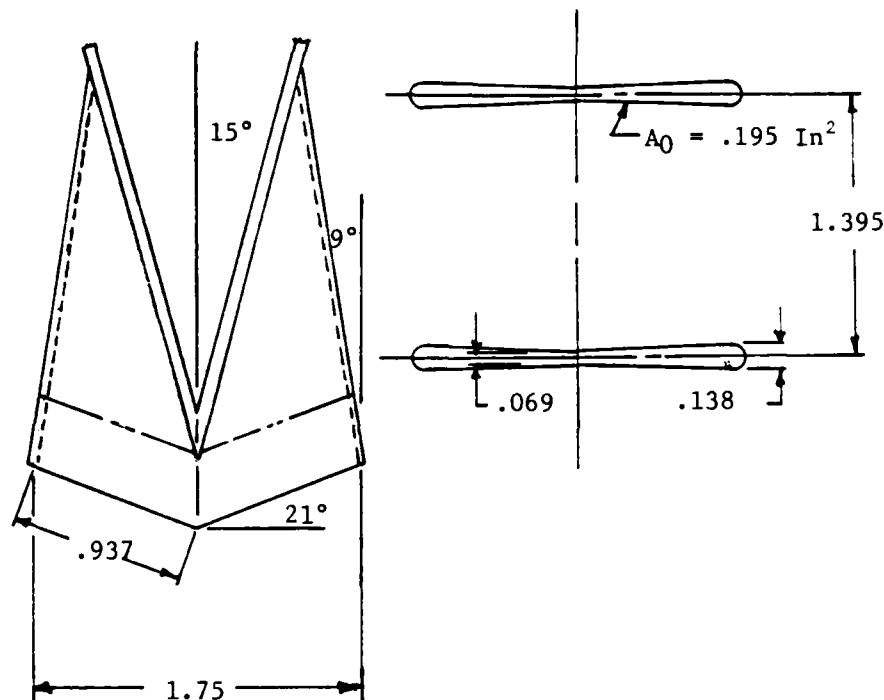


Figure 7-33 Reduced Width Symmetric Cross Slot Nozzle

Analytically, a linear jet angle distribution was assumed for the cross-slot nozzle and was the same for all BTR's. Figure 7-34 presents a typical comparison of the measured and assumed distributions for one nozzle lobe. The nozzle thrust coefficient was assumed to be 0.925.

A comparison of the experimental and analytical ejector performance results are shown in Figure 7-35 as  $\Delta \phi$  versus BTR for a pressure ratio = 2.2 and a diffuser area ratio of 2.0. The experimental results have been adjusted for  $C_T$  effects i.e., corrected by the experimentally determined  $C_T$ 's shown in Figure 7-36.

The analytical development of the jets for BTR = 1, 2, and 3 are shown in Figures 7-37, 7-38, and 7-39, respectively. The axial velocity profiles at three streamwise stations corresponding to the ejector throat, a point approximately midway through the diffuser and the ejector exit, are shown on the left. The convection velocities in the transverse planes at the throat and midway through the diffuser are shown on the right. The exit plane is not shown because the transverse velocities have virtually decayed by that station. The spanwise axis runs from left to right along the base of each profile, while the chordwise axis runs from bottom to top along the side. Note that the spanwise scale on the axial plots have been elongated to show detail. In the transverse planes, each velocity vector is centered on a grid point; the surface of the axial velocity profiles is

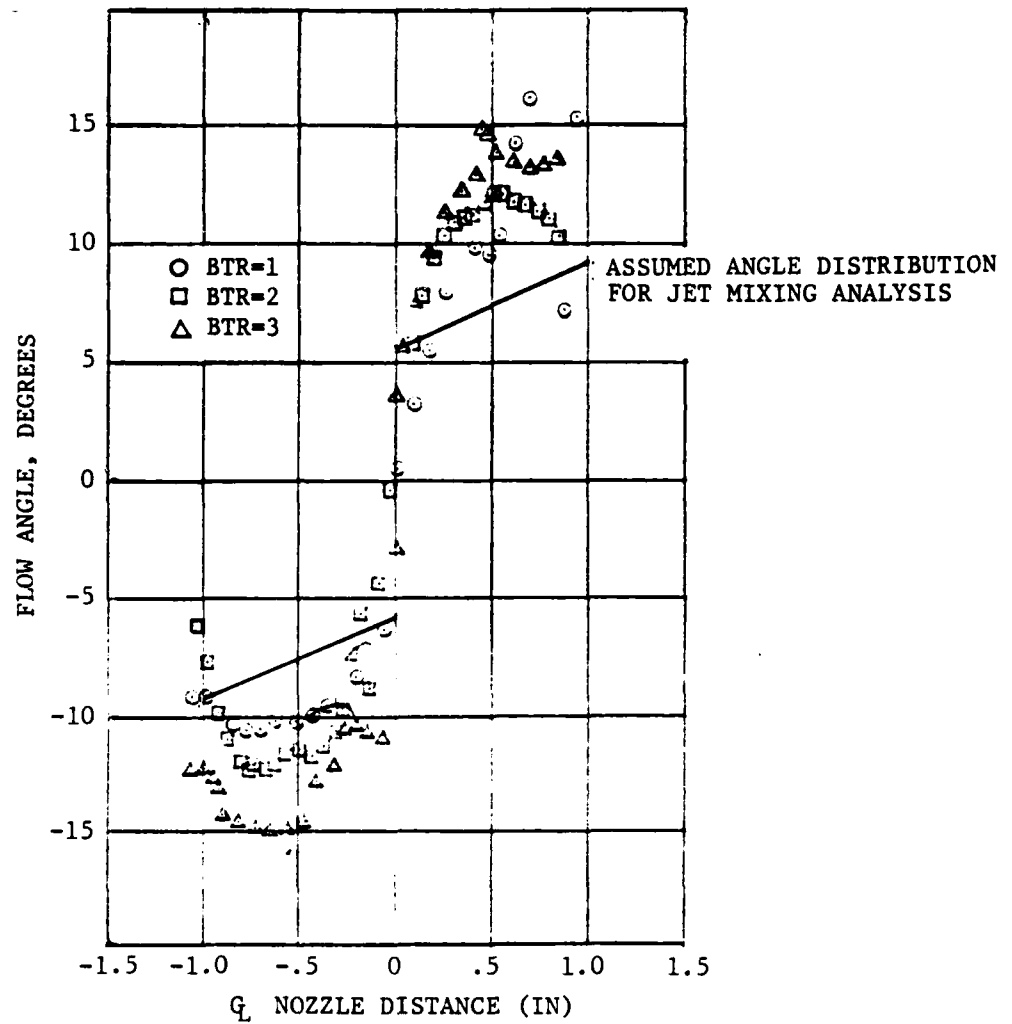


Figure 7-34 Variation of Jet Flow Angle for Various Nozzle Bowtie Ratios

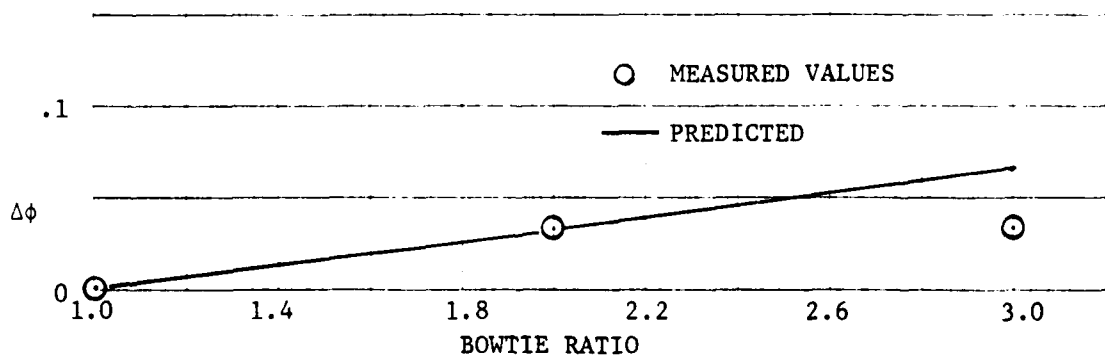


Figure 7-35 Effect of Bowtie Ratio On Thrust Augmentation



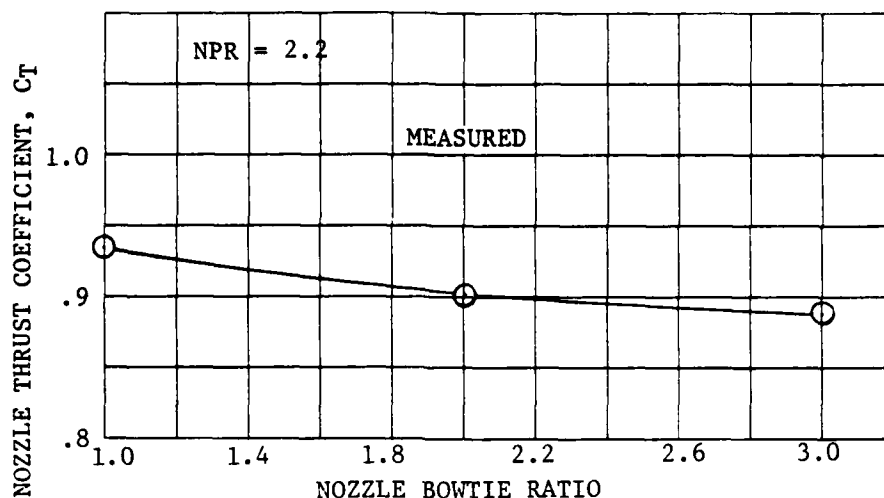


Figure 7-36 Effect of Nozzle Bowtie Ratio on Nozzle Thrust Coefficient

defined by lines passing over these points. The near Coanda jet in the axial velocity profiles has been omitted for clarity. The left hand symmetry plane runs through the center of a span slot and the right hand symmetry plane runs through the center of a cross slot.

One side of the vortex pair which develops at the ends of each cross slot are visible in the transverse planes. The mixing action of these vortices increases the entrainment in this region, which causes the jet to develop the "dog bone" shaped cross section shown schematically in Figure 7-40. The influence of the increased BTR is seen in the transverse plane at the throat and by the increased spanwise spreading of the cross slot at the exit.

The experimentally obtained axial velocity plots at the throat are shown in Figure 7-41 and the exit axial velocity plots are shown in Figure 7-42.

It is concluded that increases in BTR result in enhancement of the "Dog Bone" vortices and hence increased entrainment and augmentation. However, the experimental results showed a degradation in nozzle thrust coefficient with increased BTR, which negated the benefits of increased mixing. However, it may be possible to design an increased BTR nozzle with a high  $C_t$ .

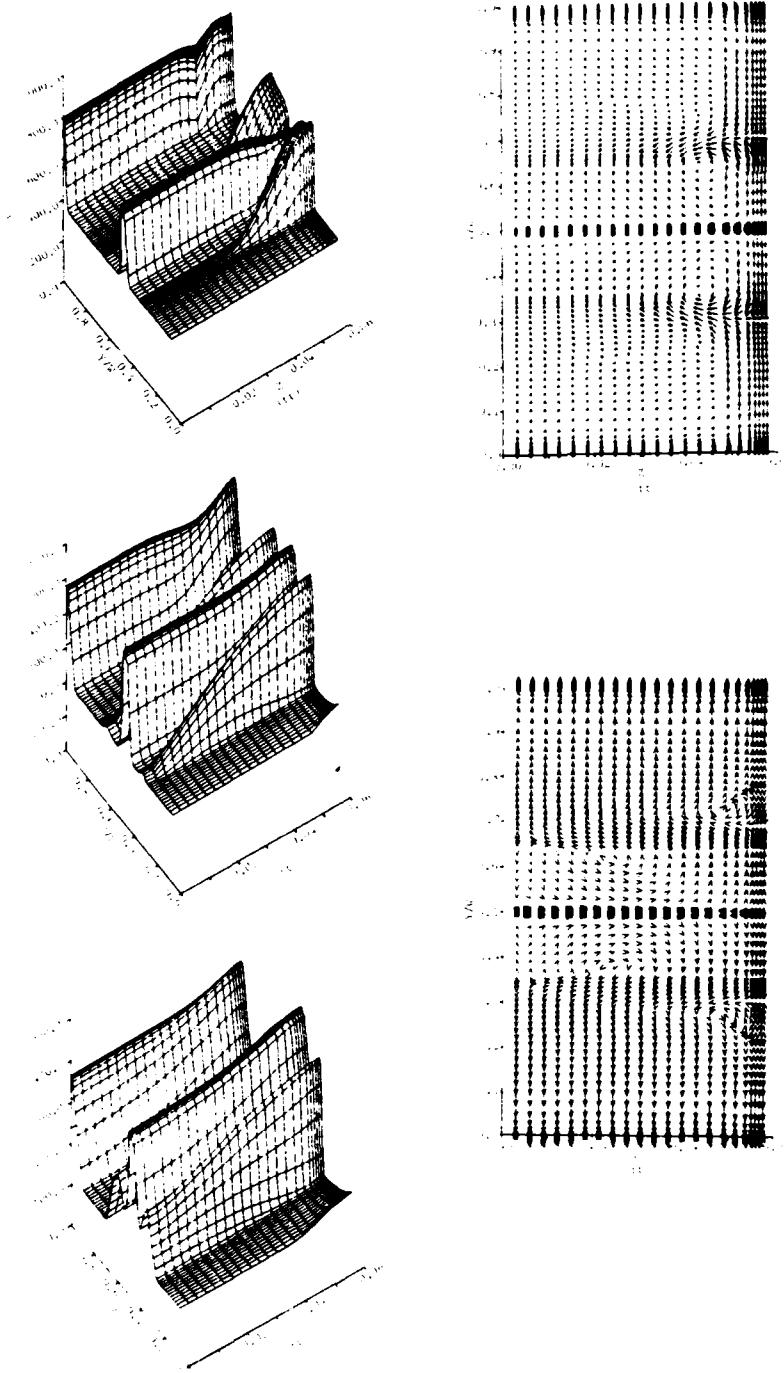


Figure 7-37 Bowtie Ratio 1 Nozzle  
(Study Baseline)

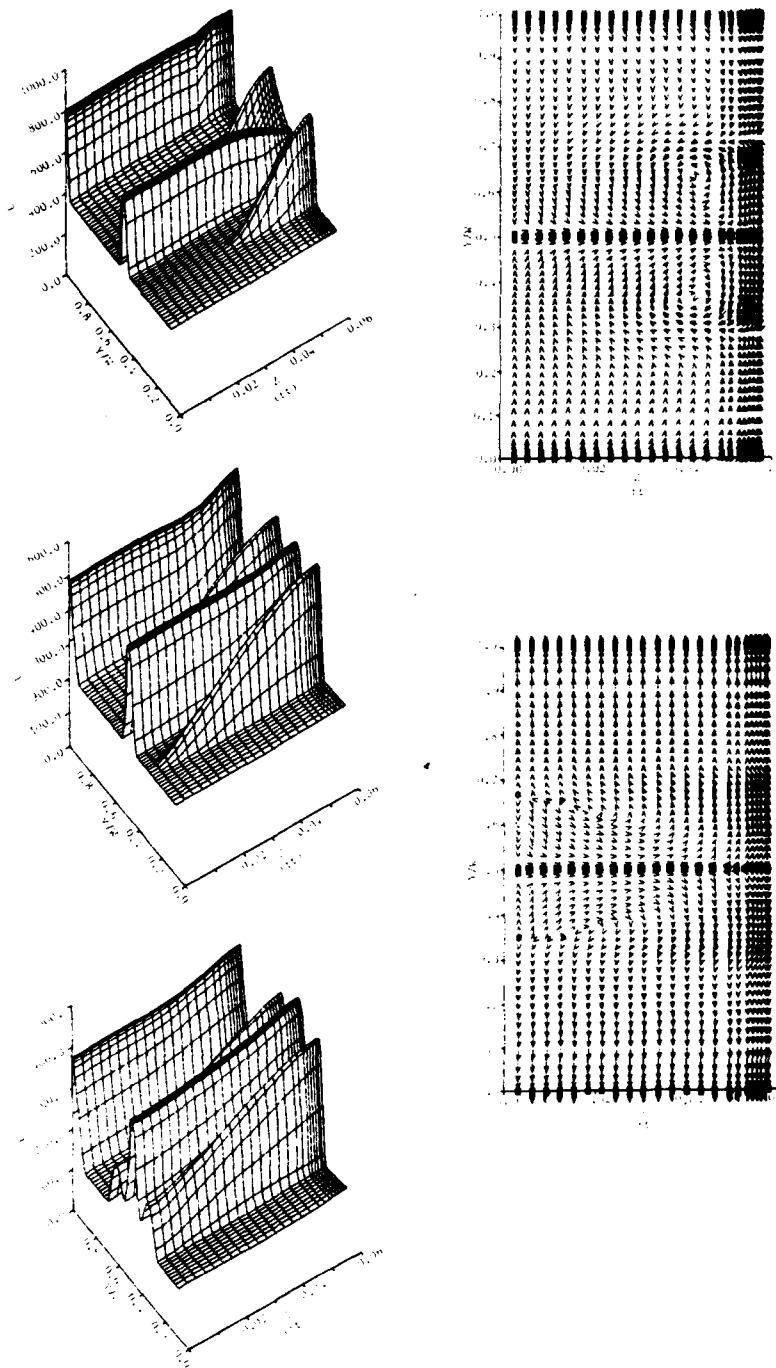


Figure 7-38 Bowtie Ratio 2 Nozzle

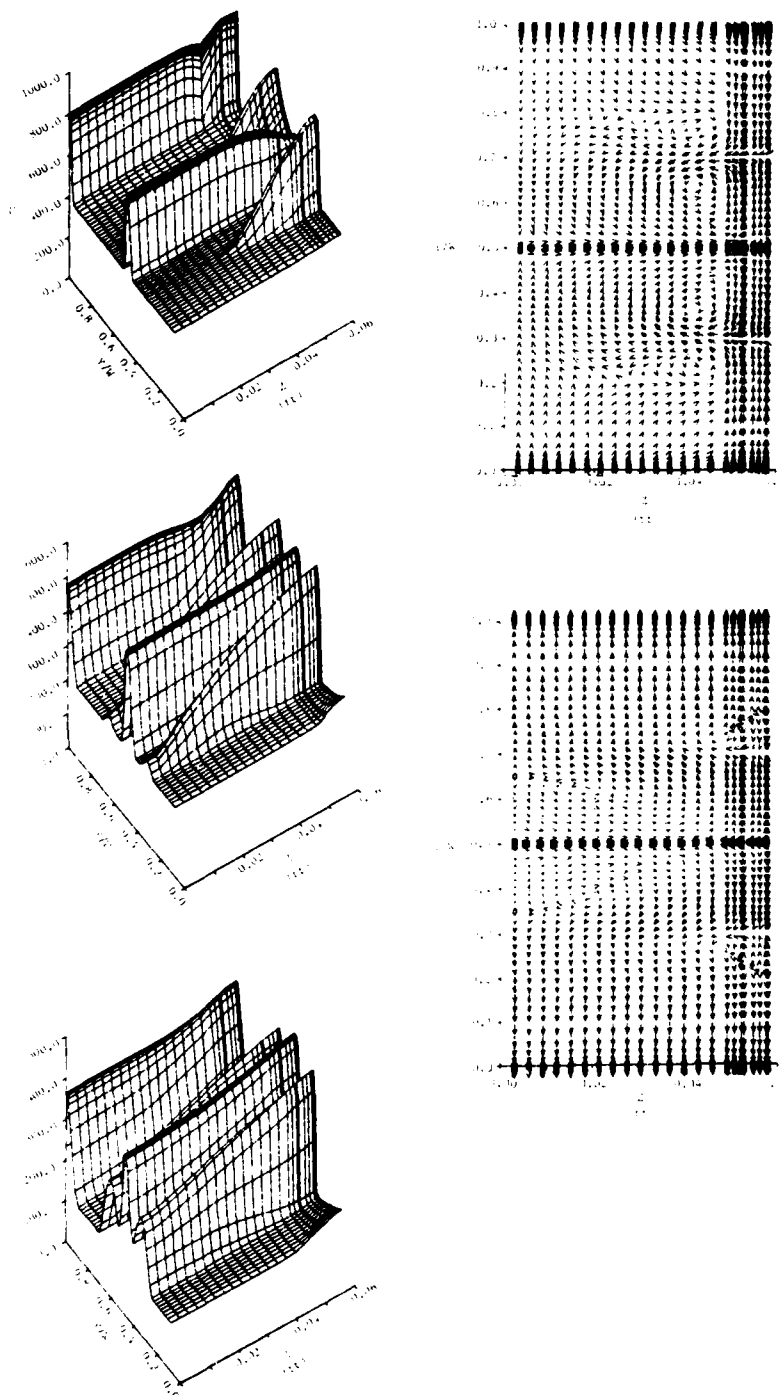


Figure 7-39 Bowtie Ratio 3 Nozzle

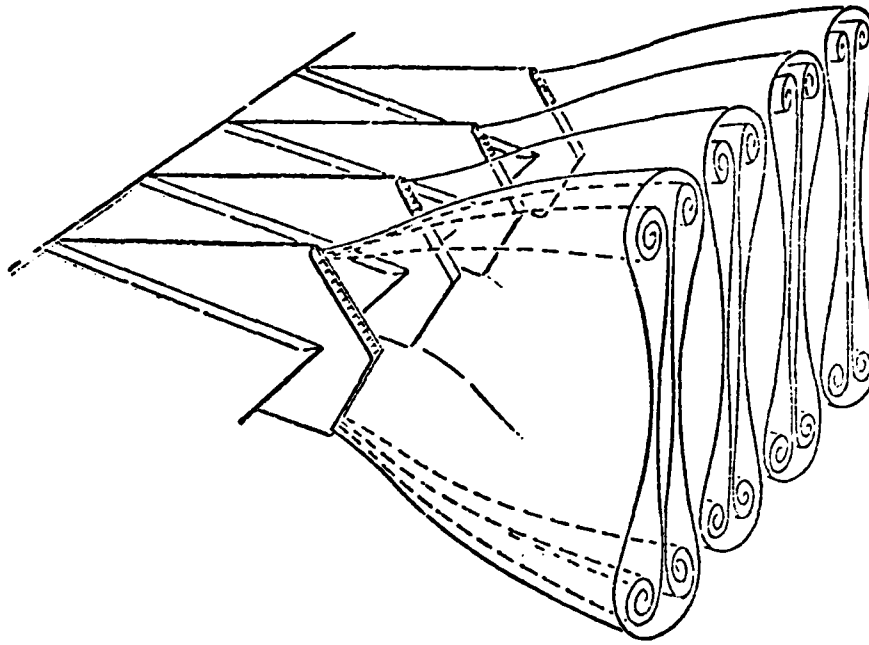


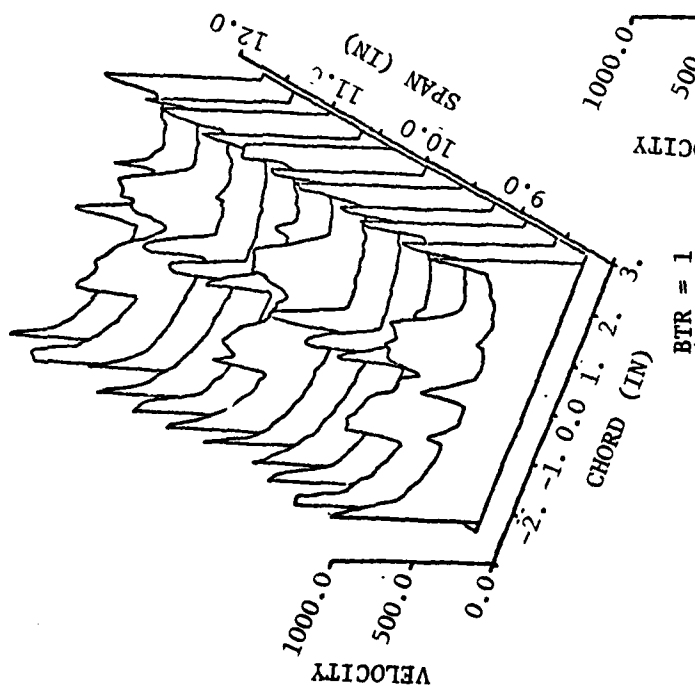
Figure 7-40 Simulation of Vortex Structure  
Produced By Cross Slot Nozzle

#### 7.4.3 Span Slot Aspect Ratio Effects

The increase in aspect ratio (length/thickness) of a slot nozzle in free air is known to produce increased entrainment. Therefore, an experimental and analytical study was conducted to determine the effect of span slot aspect ratio on ejector performance.

The effect of span slot aspect ratio variations on ejector performance is shown in Figure 7-43. The results show that reducing span slot aspect ratio actually increased the augmentation ratio, which is contrary to expectations based on free-air data.

Integration of the computed exit velocity profiles shown in Figures 7-44, 7-45, 7-46, and 7-47 reveals a three percent increase in massflow ratio when span slot aspect ratio is reduced from 17.8 to 12. It is concluded, that the larger aspect ratio span slots interfere with the development of the cross-slot jets and thereby reduce the entrainment of the cross-slots.



7-40

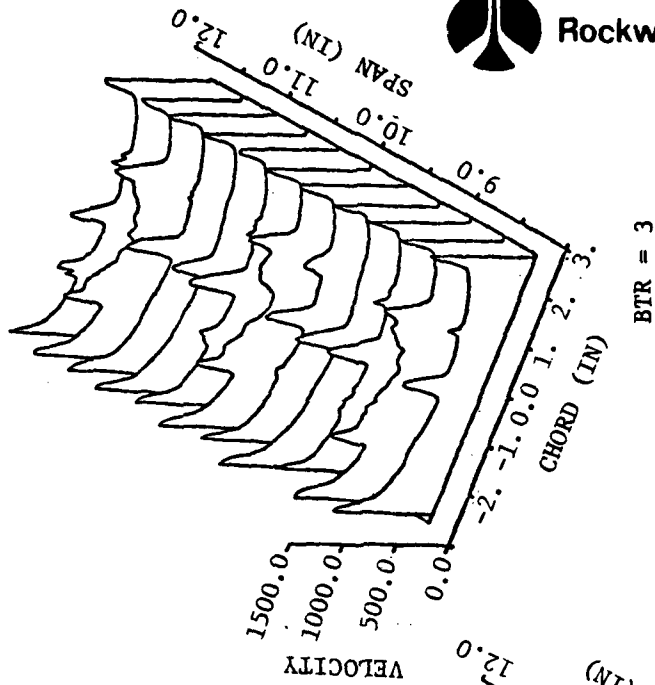
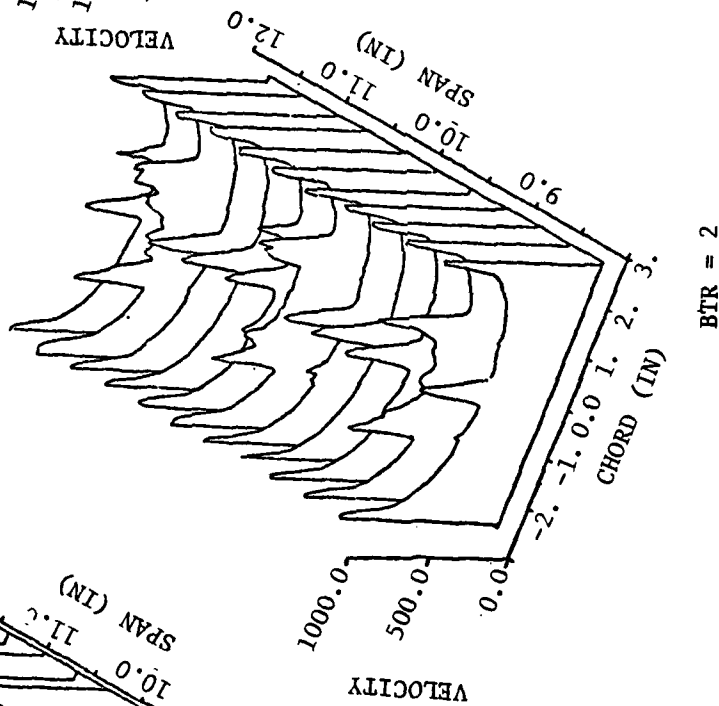


Figure 7-41 . Axial Velocity Profiles at Augmenter Throat



Rockwell International

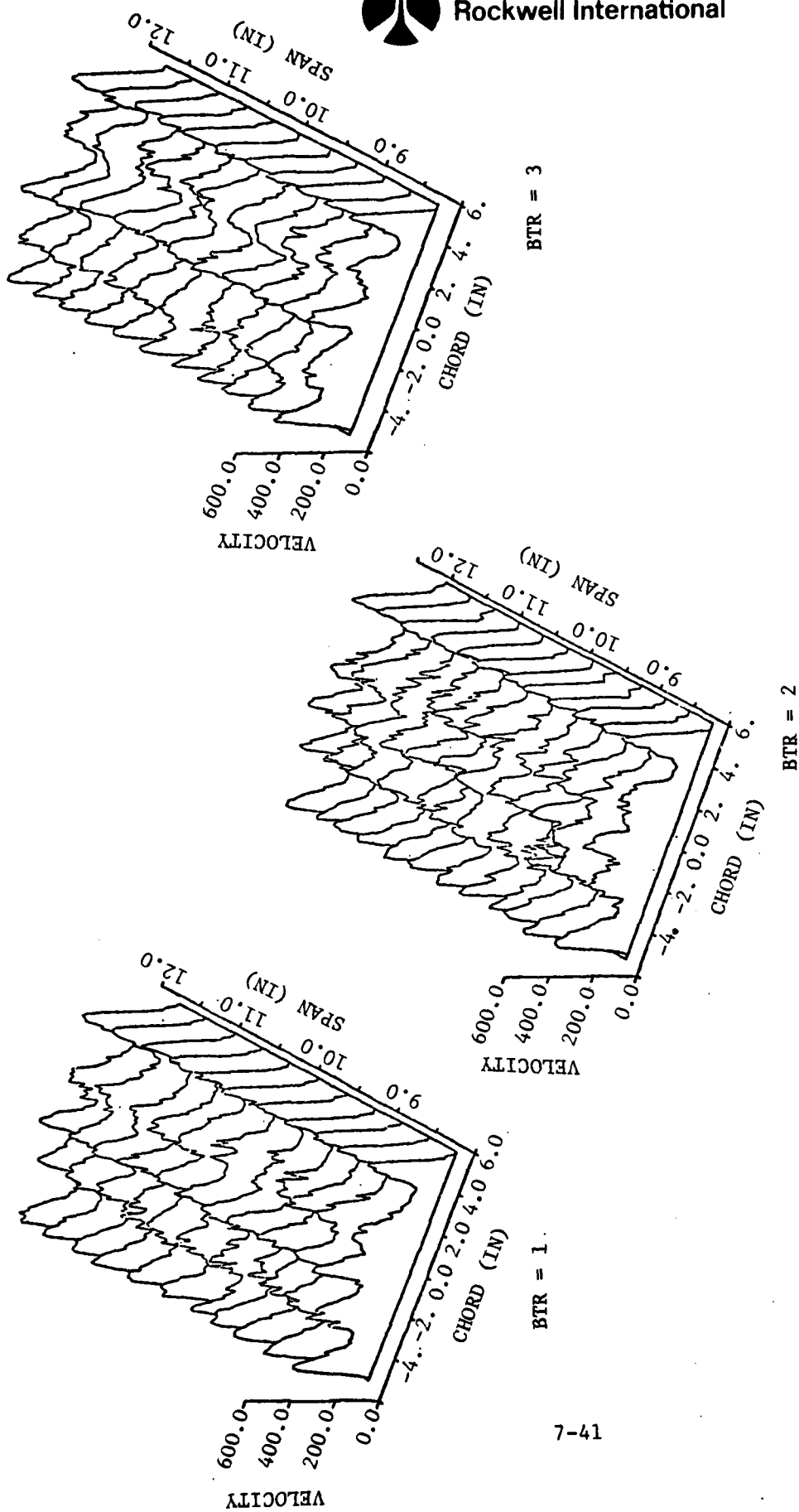


Figure 7-42. Axial Velocity Profiles at Augmenter Exit

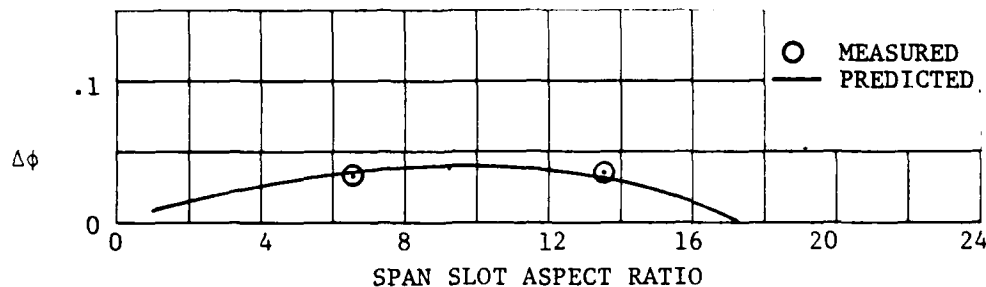


Figure 7-43 Effect of Span Slot Aspect Ratio On Thrust Augmentation

Therefore, the reduction of span slot aspect ratio results in an increase of entrainment by the cross-slots, that is greater than the loss due to reduced span slot aspect ratio.

#### 7.4.4 Cross-Slot Aspect Ratio

The cross-slot jets play the dominant role in inducing flow through the ejector. Increased entrainment can be obtained by increasing the aspect ratio of the cross-slot jet. Therefore, an analytical study was conducted to determine the effect of cross-slot jet aspect ratio on ejector performance.

The jet mixing analysis code was used during the study. The baseline nozzle had a BTR=1 and 36 percent of the flow in the span slot. The diffuser area ratio was 2, and the initial jet angle was invariant with cross-slot aspect ratio. The cross-slot area remained constant as aspect ratio was varied. Details of this study can be found in Reference (27).

Figure 7-48 presents the predicted variation of incremental augmentation ratio with cross-slot aspect ratio. As expected, the results show a significant increase in augmentation as the aspect ratio is increased from 25 to 50. The variation of local exit massflow and total massflow is shown in Figure 7-49. The exit velocity profile shape factor,  $\beta$ , is shown in Figure 7-50. It can be seen that the increased aspect ratio has increased entrainment and produced flatter exit velocity profiles.

#### 7.4.5 Effect of Span Slot/Cross-Slot Flow Split

An important nozzle design parameter is the division of total centerbody primary flow between the cross-slots and the span slots. Therefore, an analytical study was conducted to determine the optimum flow split for a fixed centerbody primary area and a fixed shroud geometry. Results of the study were verified by experimental data.



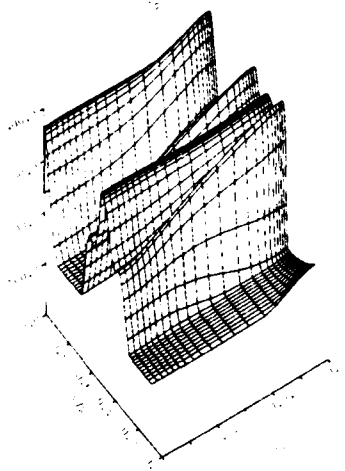
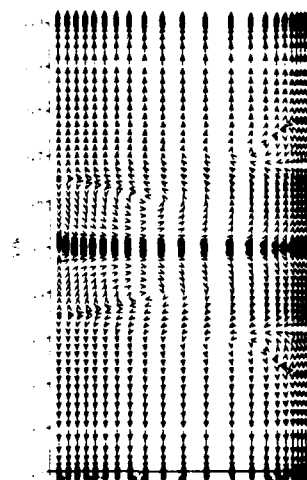
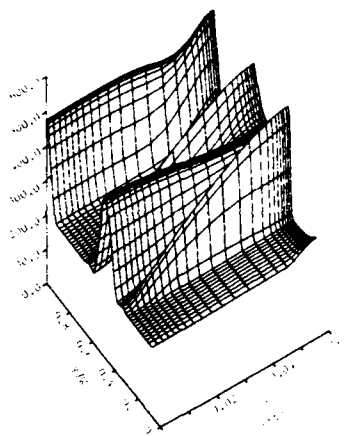
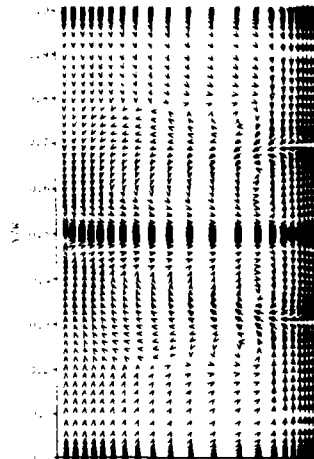
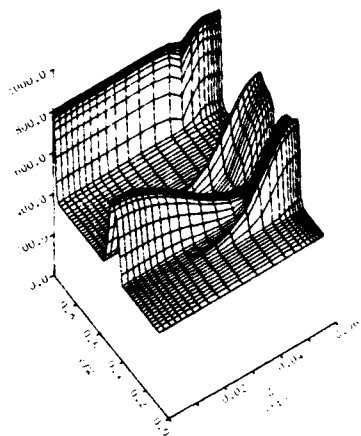


Figure 7-44 Span Slot Aspect Ratio 1  
Nozzle

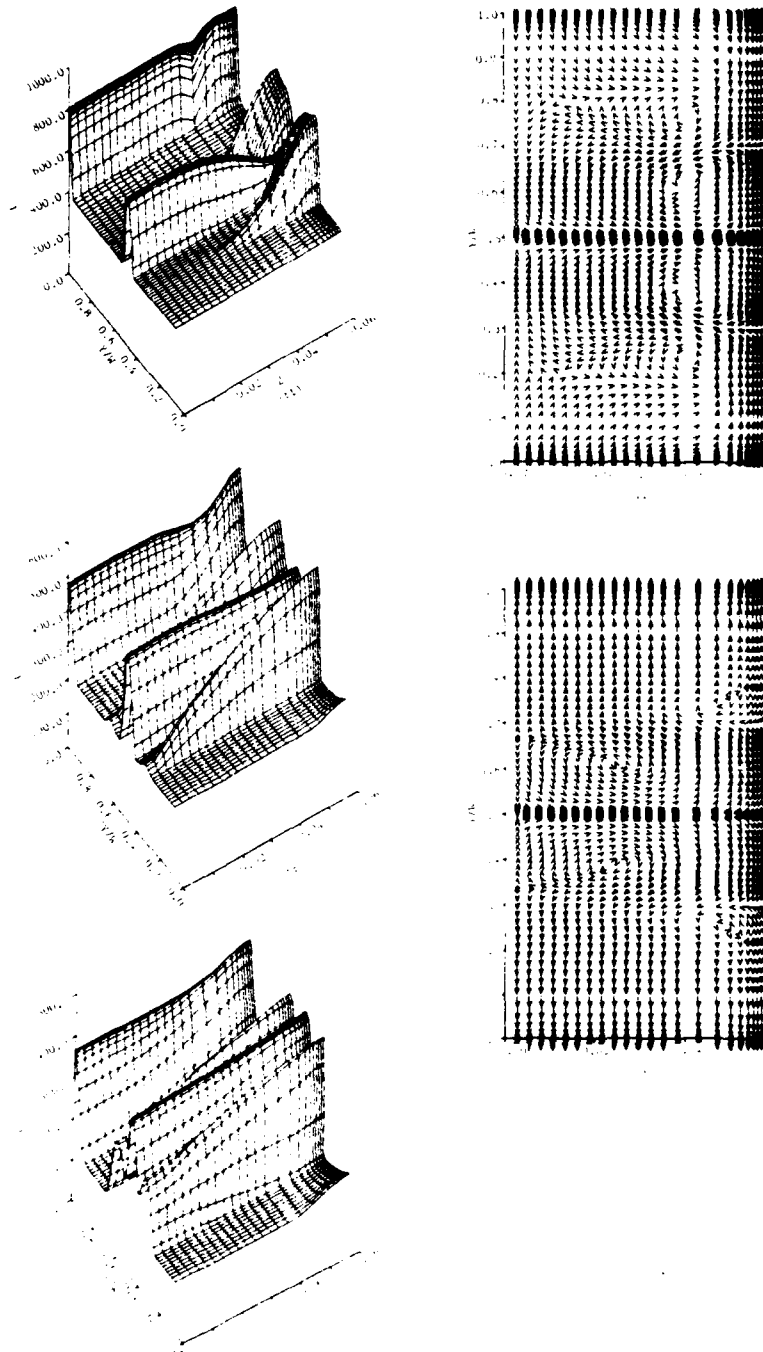


Figure 7-45 Span Slot Aspect Ratio 9  
Nozzle



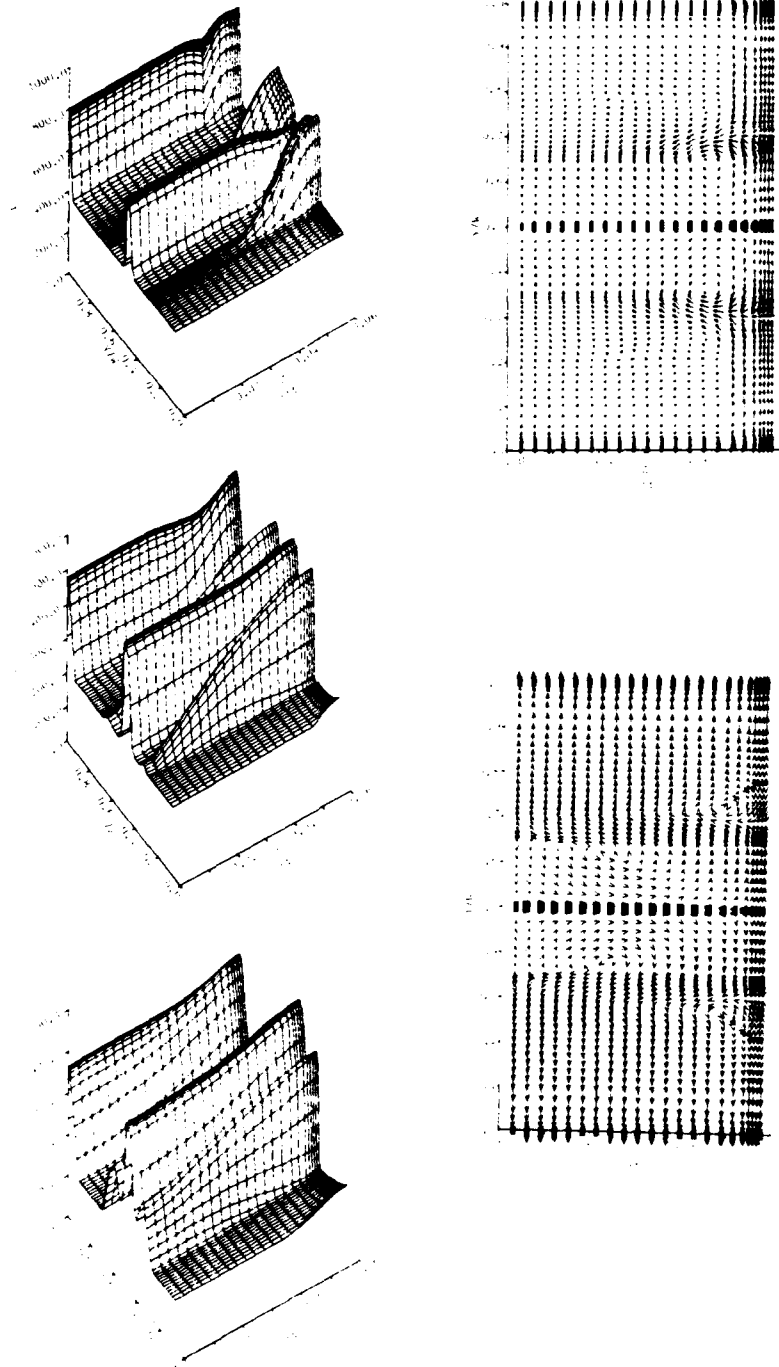


Figure 7-47 Span Slot Aspect Ratio 17.5  
Nozzle

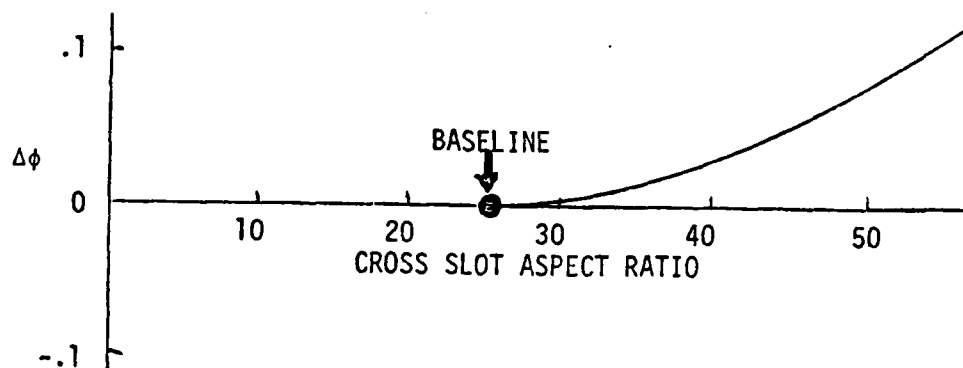


Figure 7-48 Effect of Cross Slot Aspect Ratio on Thrust Augmentation

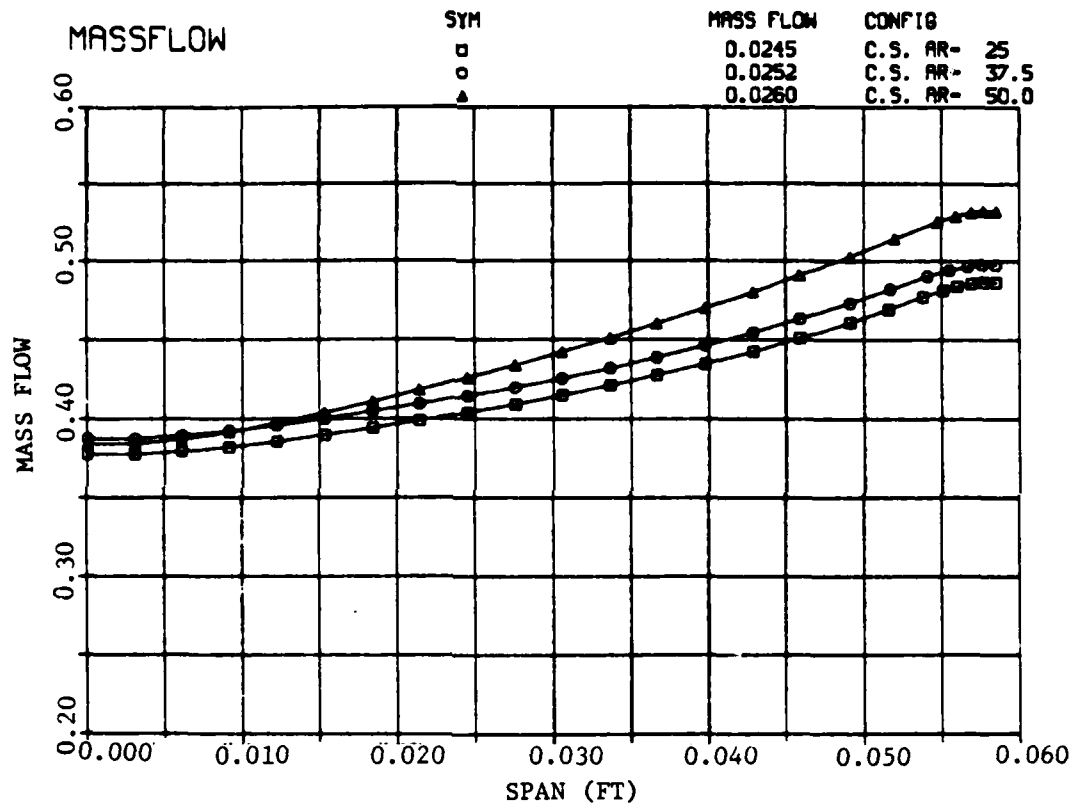


Figure 7-49 Spanwise Variation of Exit Massflow

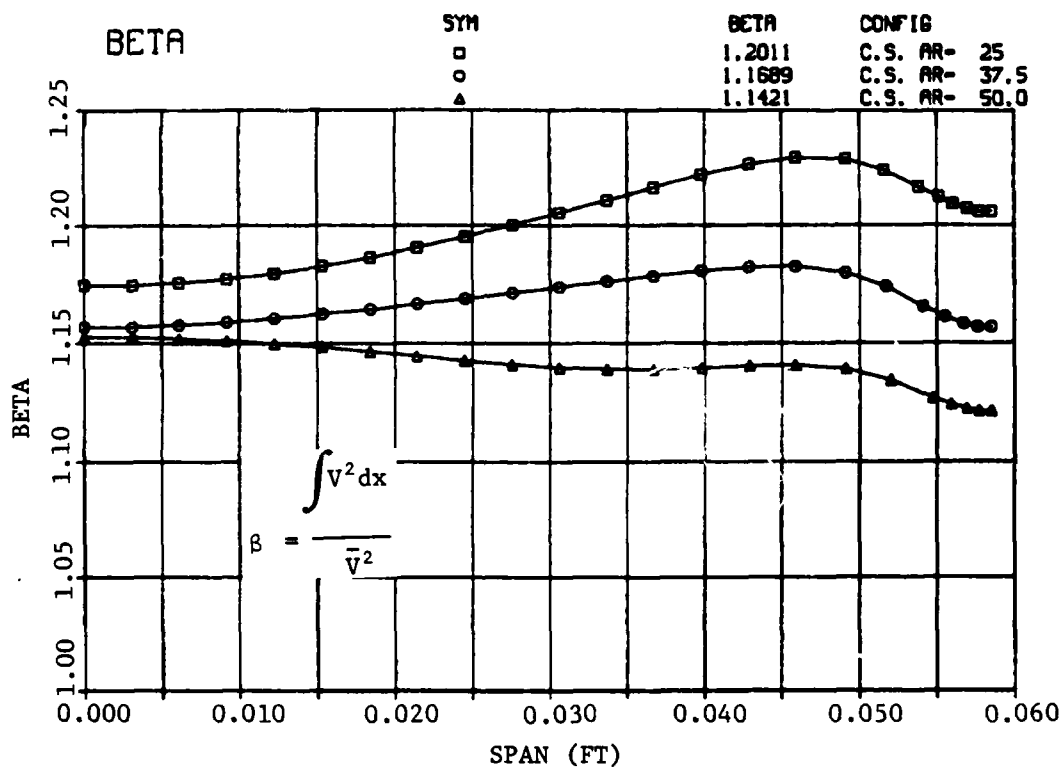


Figure 7-50 Spanwise Variation of Exit Velocity Profile Shape Factor,  $\beta$



The flow split is defined as the ratio of the total span slot flow area to the total centerbody flow area. A 100 percent flow split would indicate an all span slot configuration, while zero percent flow split would be all cross-slot. The flow split was obtained by varying the cross-slot or span slot thickness while maintaining a constant nozzle length.

The variation of incremental augmentation ratio with flow split is shown in Figure 7-51. As expected, the plane slot nozzle is the worst case; however, unexpectedly the augmentation increases as flow split is changed to an all cross-slot configuration.

The jet development for flow splits of 0%, 60%, and 80% are shown in Figures 7-52, 7-53, and 7-54, respectively. The 36 percent flow split was shown previously in Figure 7-37. Referring to the exit axial velocity plots, it can be seen that the span slots apparently impede the development of the cross-slot jets and hence limit the entrainment potential.

The variation of total massflow at the ejector exit is shown in Figure 7-55 for flow splits of 0%, 36%, and 60%. The corresponding velocity profile shape factors,  $\beta$ , are shown in Figure 7-56.

Verification of the flow split trend was obtained experimentally by designing and testing a nozzle with 65 percent of the flow to the span slot. The incremental augmentation is shown in Figure 7-51 and compares favorably with the predictions. However, it should be noted that the experimental results were obtained for BTR = 2 nozzles, whereas, the analysis was conducted with BTR = 1.0 nozzles. This difference is not believed to have an effect on the trends.

A comparison of the exit axial velocity profiles for the 65 percent and 36 percent flow split nozzles are shown in Figure 7-57. These experimental plots show clearly the influence the span slot has on the development of the cross-slot jet.

Further experimental verification of the effect of flow split was obtained by designing and testing an all cross-slot nozzle. The nozzle was designed to have a bowtie ratio = 1. The all cross-slot nozzle results shown in Figure 7-51 indicate that it is slightly better than the baseline nozzle (BTR = 1). A comparison of the exit axial velocity profiles for zero percent and 36 percent flow split nozzles are shown in Figure 7-58. This result is in qualitative agreement with the analysis.

It is concluded from both experiment and analysis that flow splits between zero percent and 50 percent have little effect on thrust augmentation.



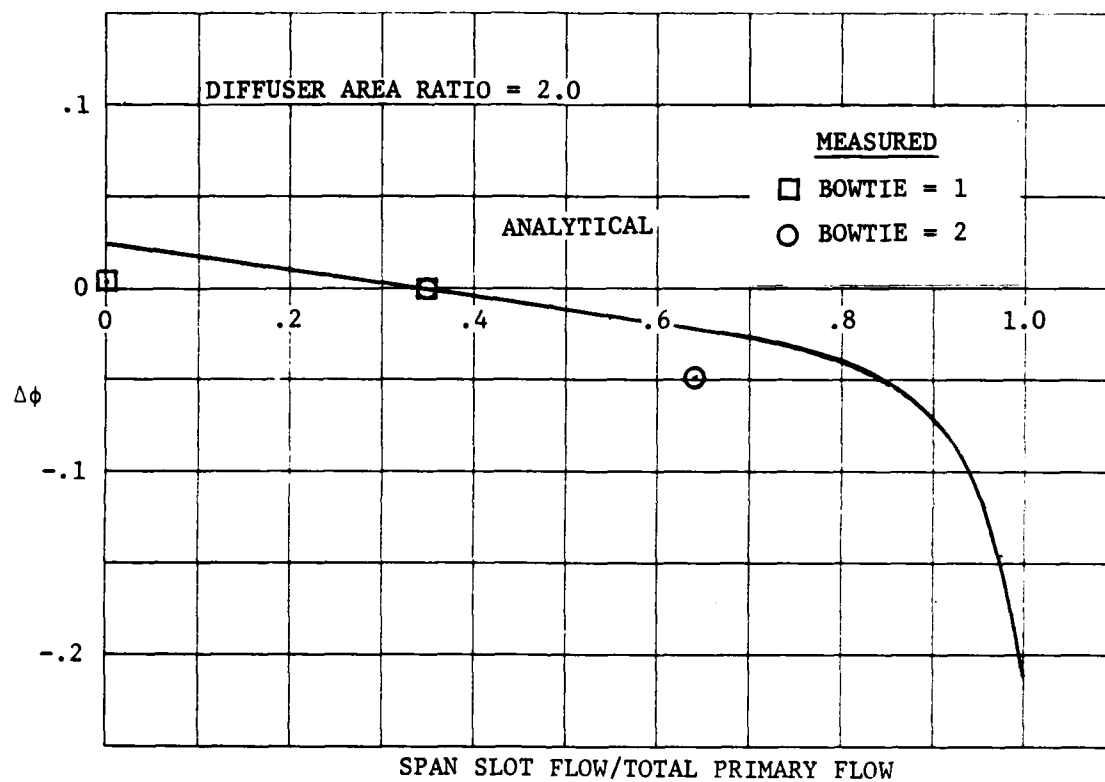


Figure 7-51 Effect of Flow Split On Thrust Augmentation

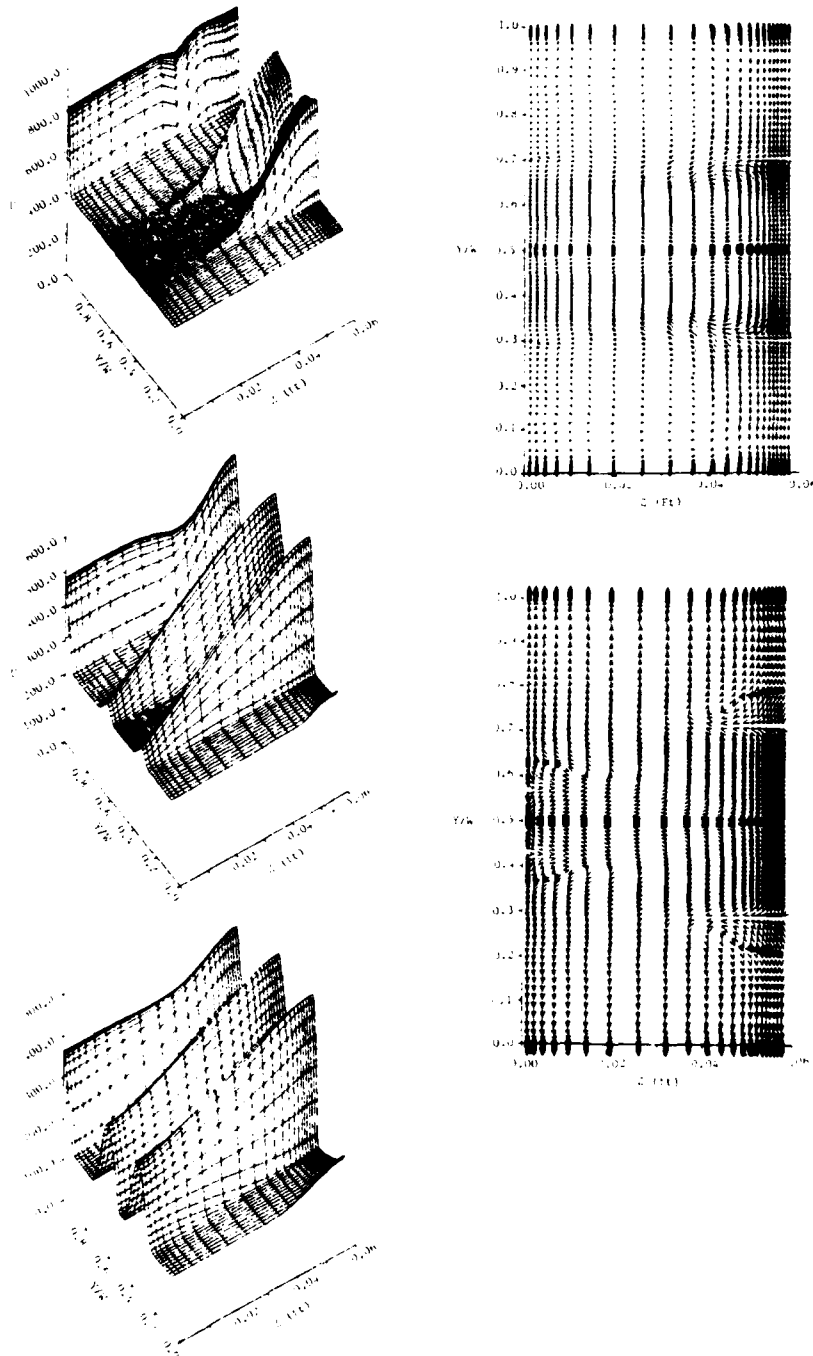


Figure 7-52 0% Flow Split Nozzle

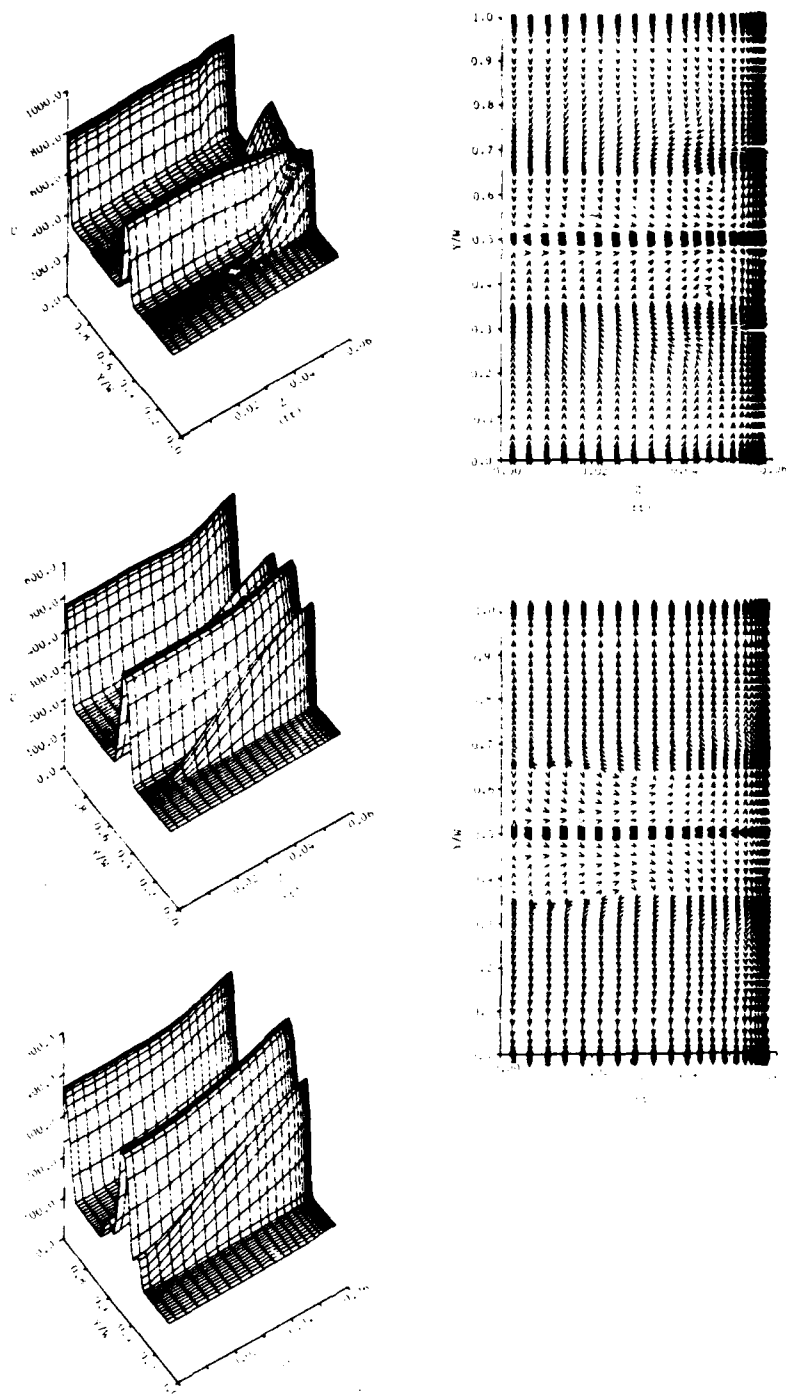


Figure 7-53 60% Flow Split Nozzle

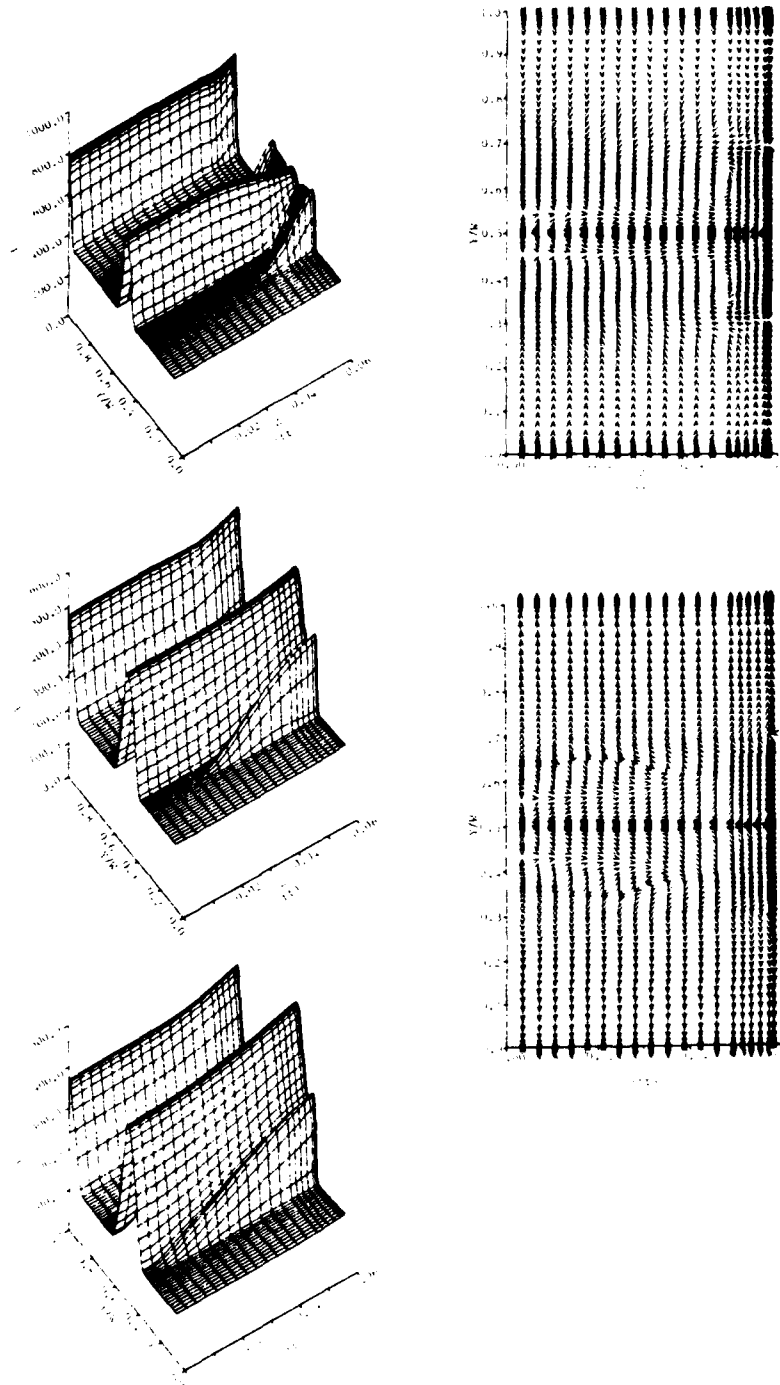


Figure 7-54 80% Flow Split Nozzle

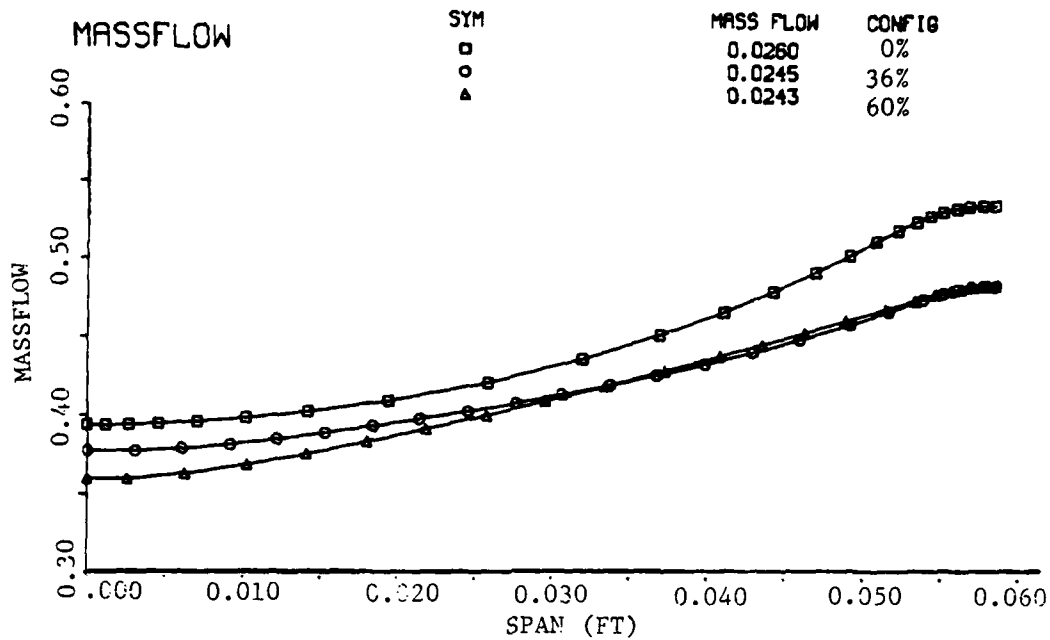


Figure 7-55 Effect of Flow Split on Spanwise Variation of Exit Massflow

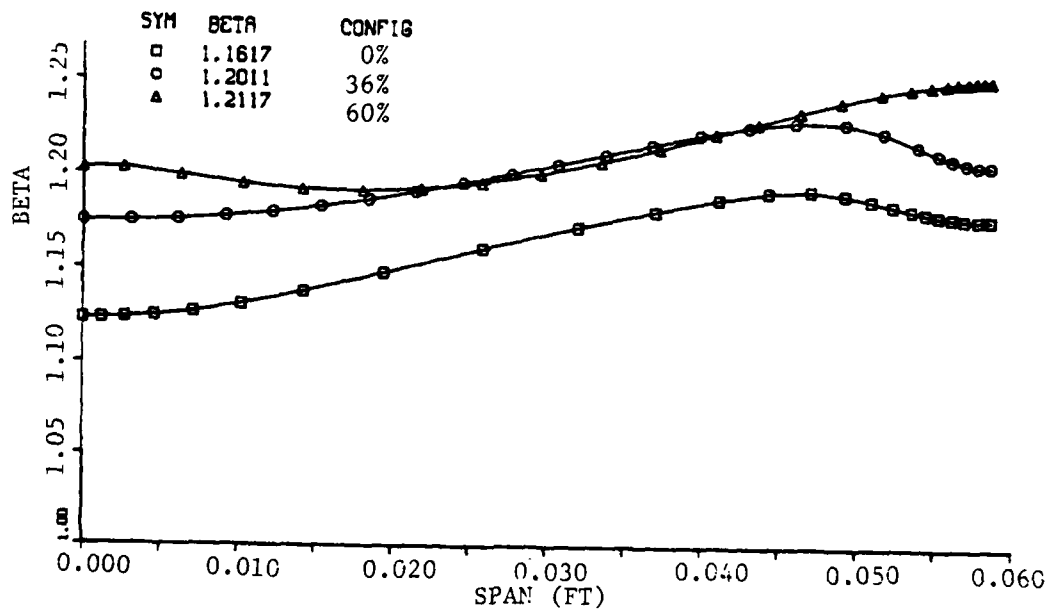


Figure 7-56 Effect of Flow Split On Spanwise Variation of Exit Velocity Profile Shape Factor

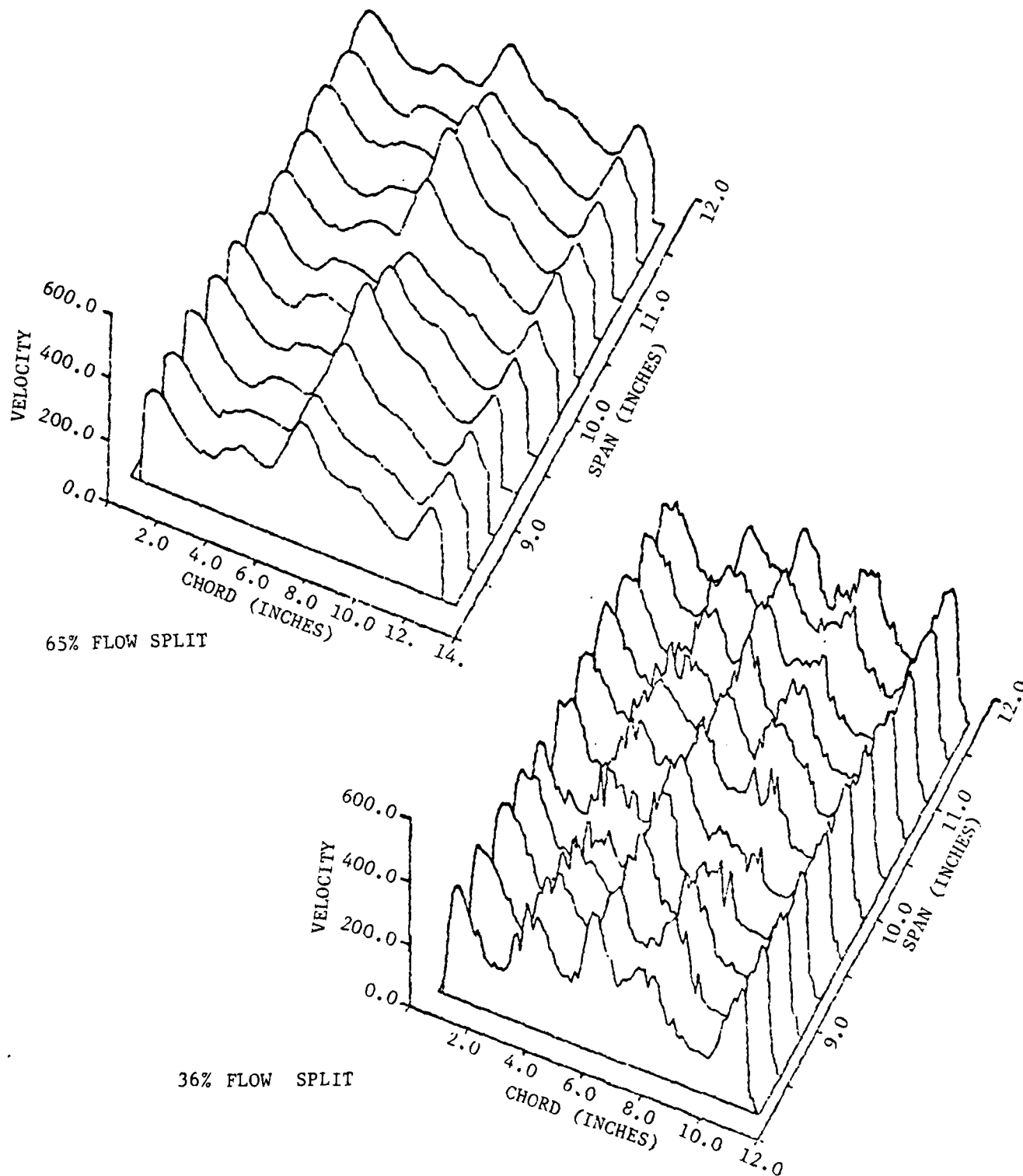


Figure 7-57 Comparison of Exit Axial Velocity Profiles for 36 Percent and 65 Percent Flow Split Nozzles

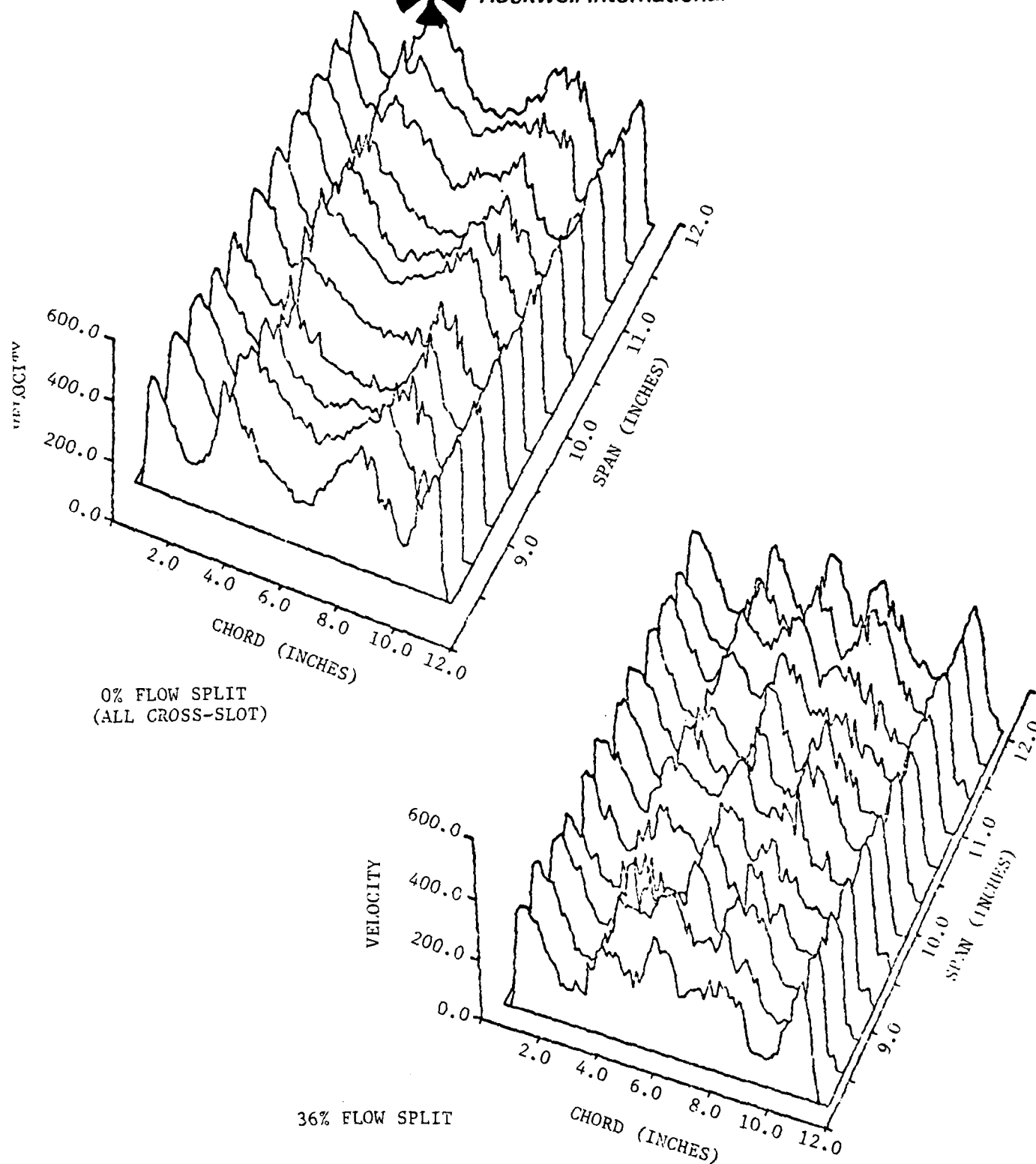


Figure 7-58 Comparison of Exit Axial Velocity Profiles for 0 Percent and 36 Percent Flow Split Nozzles



#### 7.4.6 Effect of Number of Elements

The effect of increasing the number of nozzle elements within a fixed span was evaluated analytically. The study was conducted at diffuser area ratio = 2, BTR = 1, 36 percent flow split and fixed total nozzle area. The configurations evaluated were obtained by fixing the cross-slot width and the span slot thickness and varying the cross-slot thickness and span slot length proportionately.

Figure 7-59 shows that increasing the number of elements results in significant increases in augmentation. This is a consequence of the increased cross-slot aspect ratio and reduced span slot aspect ratio as shown in Figure 7-60. These results are consistent with those previously presented for aspect ratio.

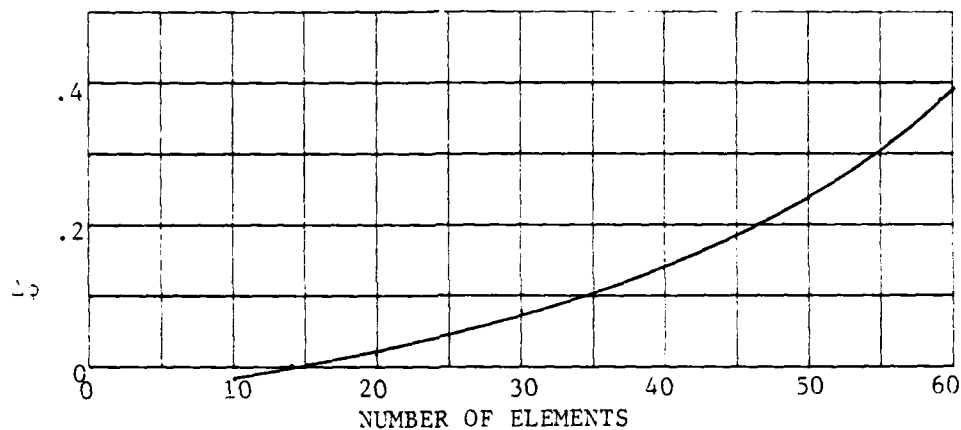


Figure 7-59 Variation of Thrust Augmentation With Number of Elements ( $C_T$  = Constant)

The analytical results were obtained using the same nozzle thrust coefficient for all configurations. However, experimental results for asymmetric nozzles presented in Reference (28) show a reduction in thrust coefficient as the number of elements is increased. Adjusting the analytical values shown in Figure 7-59 for  $C_T$  effects produces the results of Figure 7-61. Therefore, it is concluded that increased mixing obtained by increasing the number of elements would be partially compensated by a loss in thrust coefficient.



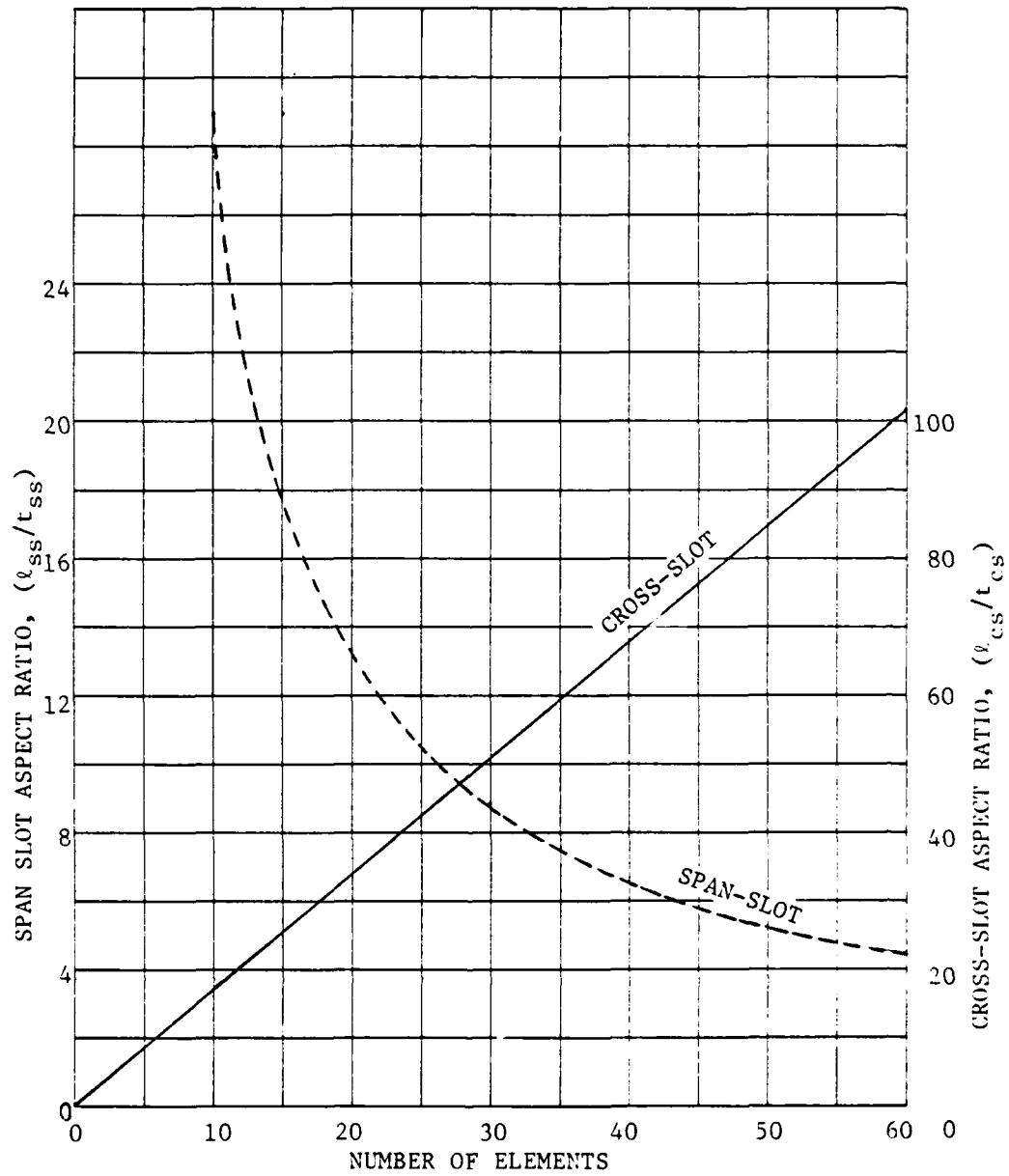


Figure 7-60 Variation of Nozzle Aspect Ratio With Element Spacing

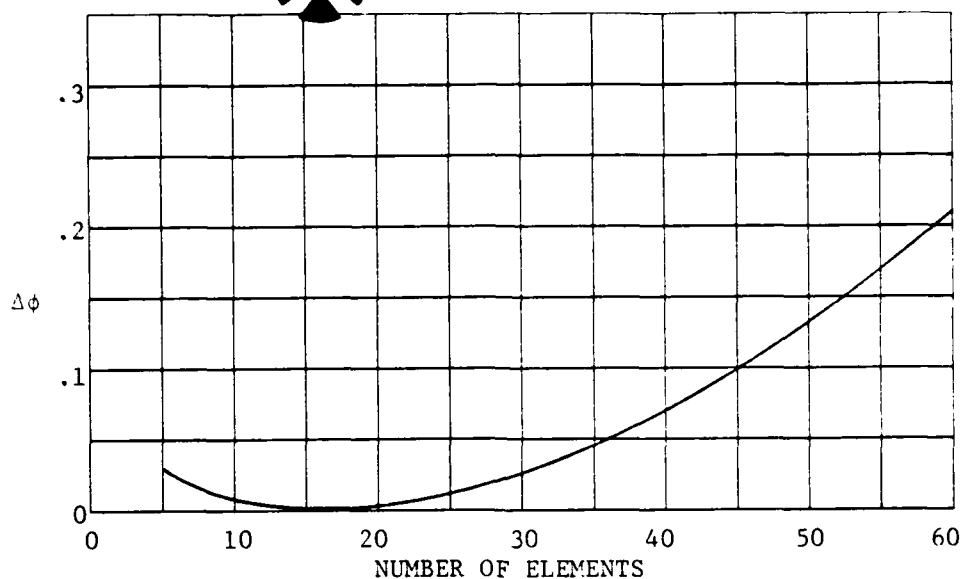


Figure 7-61 Variation of Thrust Augmentation With Number of Elements  
(Adjusted for  $C_T$  Effects)

#### 7.4.7 Jet Angle Study

The hypermixing nozzle studies, both test and analysis, had identified that the initial jet flow angle was a primary factor in ejector performance. The flow angles generated by the hypermixing nozzles were directly related to the angle of the slots and were easily known, a priori, for both tests and analysis. Correlation and/or nozzle design was therefore rather straightforward. However, the cross slot nozzles presented a problem in that the relationship between flow angle and geometry was not usually known. Therefore, an experimental test matrix was defined for the purpose of determining the dependence of flow angle on nozzle geometry. A parallel analytical study was conducted (using the jet mixing analysis) to determine the effect of jet flow angle on augmentation ratio. Correlation of the two studies resulted in a capability to define the nozzle geometry required to obtain the desired augmentation ratio. The results of these studies are presented in this section.

Figure 7-62 presents the test matrix to determine the effects of cross slot nozzle angles on the jet flow angles. This matrix was designed to study the effects of launch angle at constant wedge and the effect of wedge angle at constant launch angle. Four centerbodies were designed and tested. Free air surveys were made using a five-port flow direction probe.

The results of the tests are shown in Figure 7-63 where measured flow angles are shown plotted versus non-dimensional distance from the center of the cross slot. Comparison of Figure 7-63a, 7-63b, and 7-63c shows that the mean jet flow angle increases with wedge angle. Launch angle (Figure 7-63a, 7-63c, and 7-63d) has an effect on the angle distribution over the last 20 percent of cross slot nozzle width.

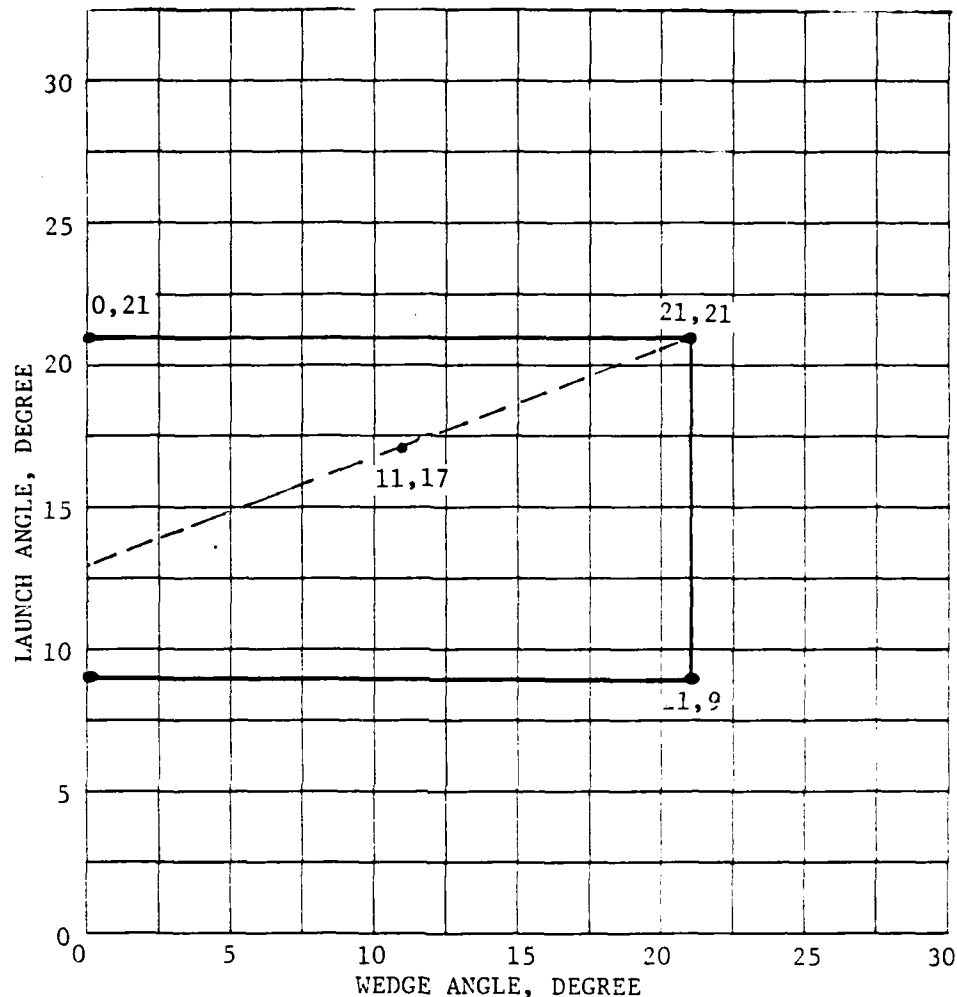


Figure 7-62 Nozzle Test Matrix for Jet Angle Study

The effect of cross-slot nozzle flow angle on ejector performance was obtained using the jet mixing analysis computer code. The analysis was conducted utilizing the .2 scale rectangular wing model geometry at an exit area ratio of 2.0. Analytical solutions were obtained for assumed angle distributions which varied linearly across the nozzle and for constant angle distributions. A comparison of a linear and a constant angle distribution is shown in Figure 7-64.

The computed augmentation ratios are shown in Figure 7-65 as a function of average flow angle. The results indicate that augmentation is a function of both angle distribution and magnitude. The peak augmentation for both types of distributions appears to occur at about  $Q_{avg} = 18^\circ$ .

The computed development of the jets for angle distributions of (0,0), (0,28), and (21,21) are shown in Figures 7-66, 7-67, and 7-68, respectively.

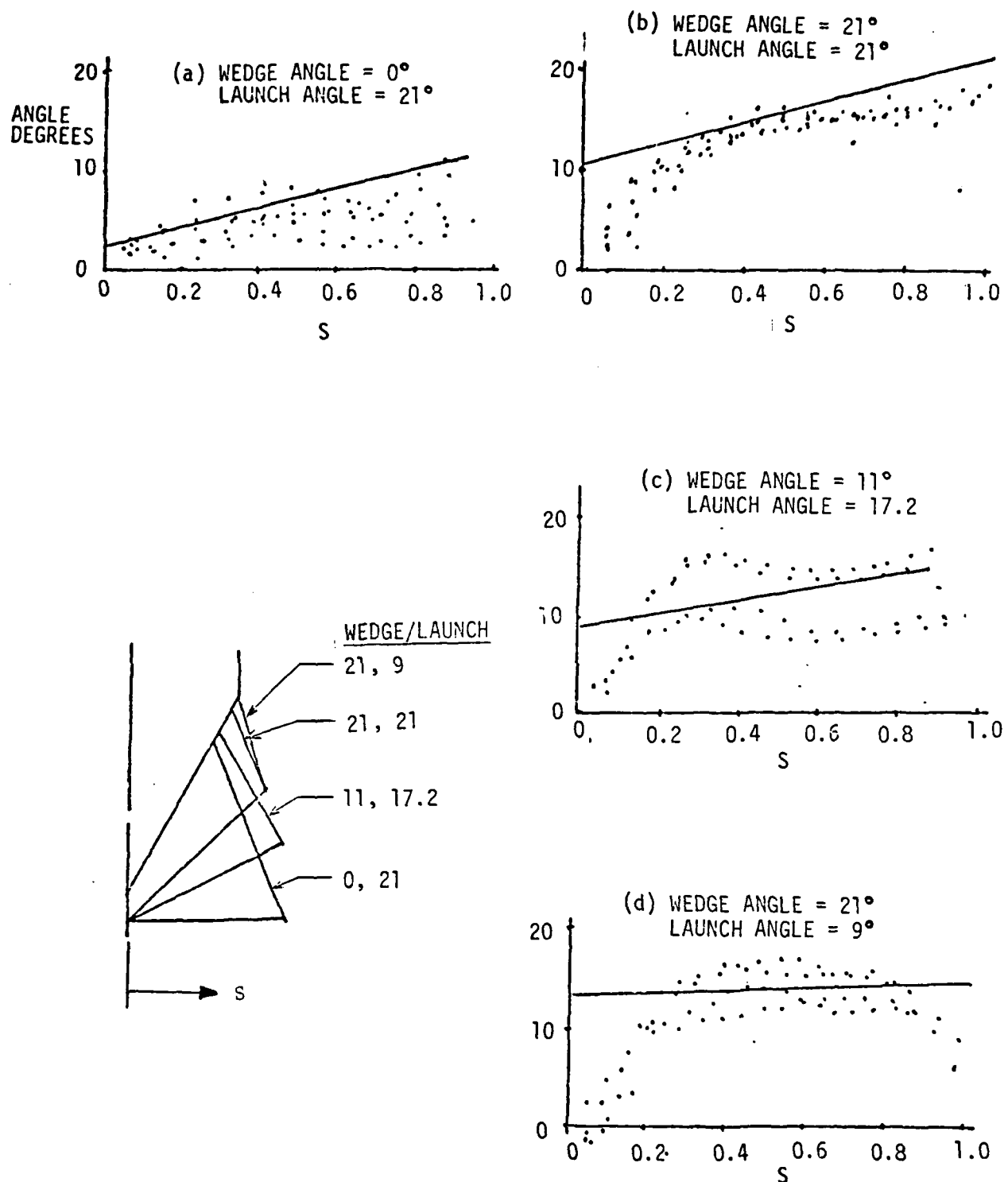


Figure 7-63 Measured Cross-Slot Nozzle Exit Flow Angles

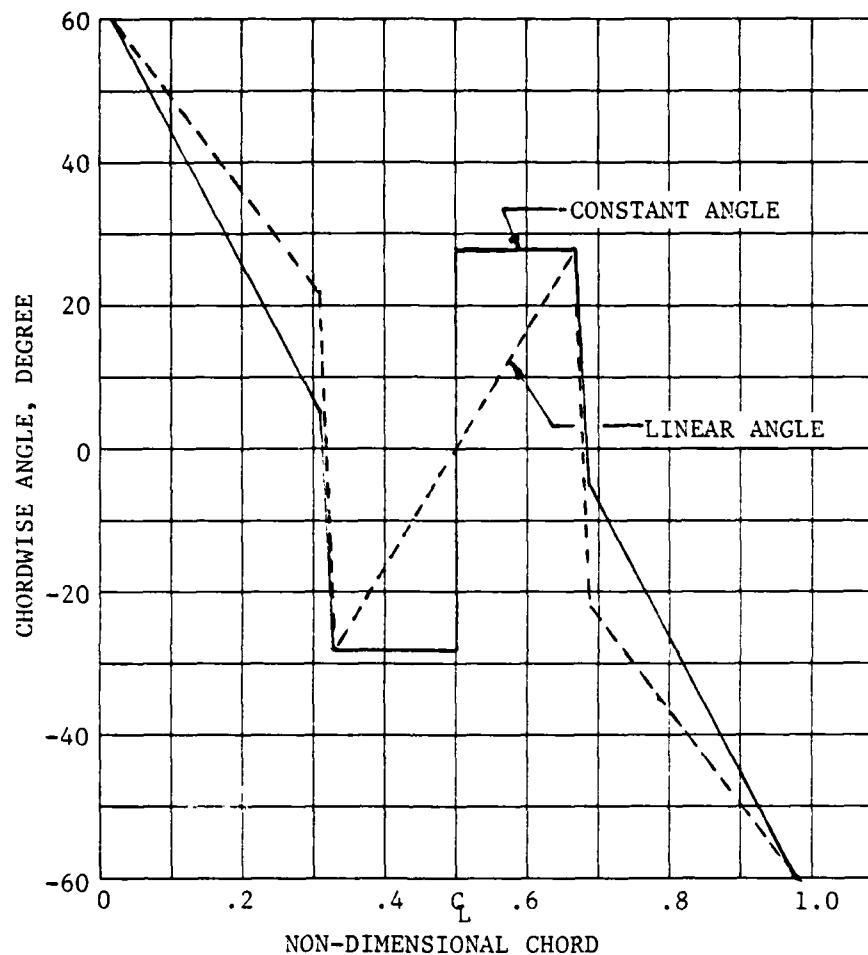


Figure 7-64 Assumed Angle Distribution at Initial Data Plane

Comparison of the axial velocity plots at the ejector exit show that increased vortex strength due to jet angle has increased the mixing (spreading) of the cross slot jets. Furthermore, the linear angle distribution configuration promoted greater mixing as is apparent from the elimination of the secondary velocity region between the span slot and the cross slot.

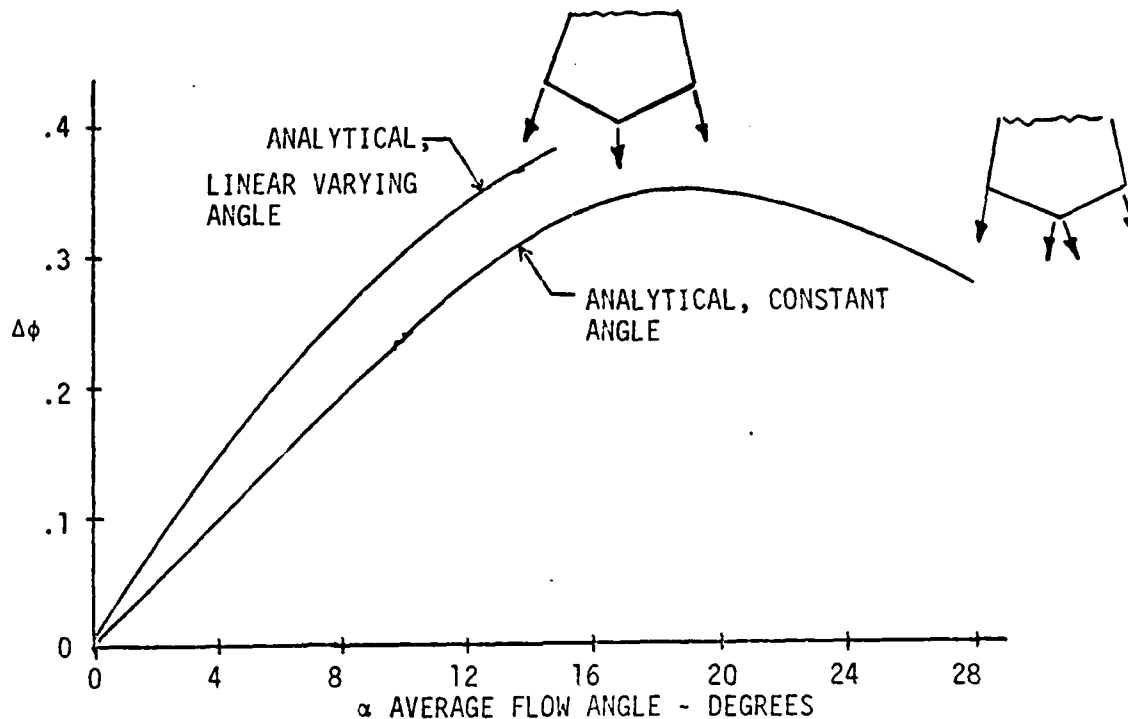


Figure 7-65 Effect of Constant and Linearly Varying Cross-Slot Jet Flow Angles on Thrust Augmentation

The results of the combined experimental/analytical jet angle study were utilized to design a nozzle capable of a linear jet angle variation. A sketch of the nozzle is shown in Figure 7-69 and the nozzle is defined in Reference (29). The nozzle had a BTR = 1, flow split = 36 percent, and linear angle variation from zero degrees to 37.2 degrees at the tip.

Free-air measurements of the nozzle flow angularity is shown in Figure 7-70. A nearly linear angle variation was obtained and indicates the capability to design a nozzle based on desired flow characteristics.

The performance of this nozzle is compared in Figure 7-71 with a nozzle having a nearly constant jet angle. The analytical results showed that the linear angle nozzle should have produced an augmentation level of about .05 greater than obtained experimentally. The results obtained with this nozzle and several others led to a more detailed study of the shroud surface pressures. The pressures indicated the possibility of local separation on the Coanda surfaces for nozzle configurations capable of thrust augmentation levels above 1.63. Therefore, separation effects make it difficult to determine relative nozzle performance. These effects are discussed in more detail in the shroud section.

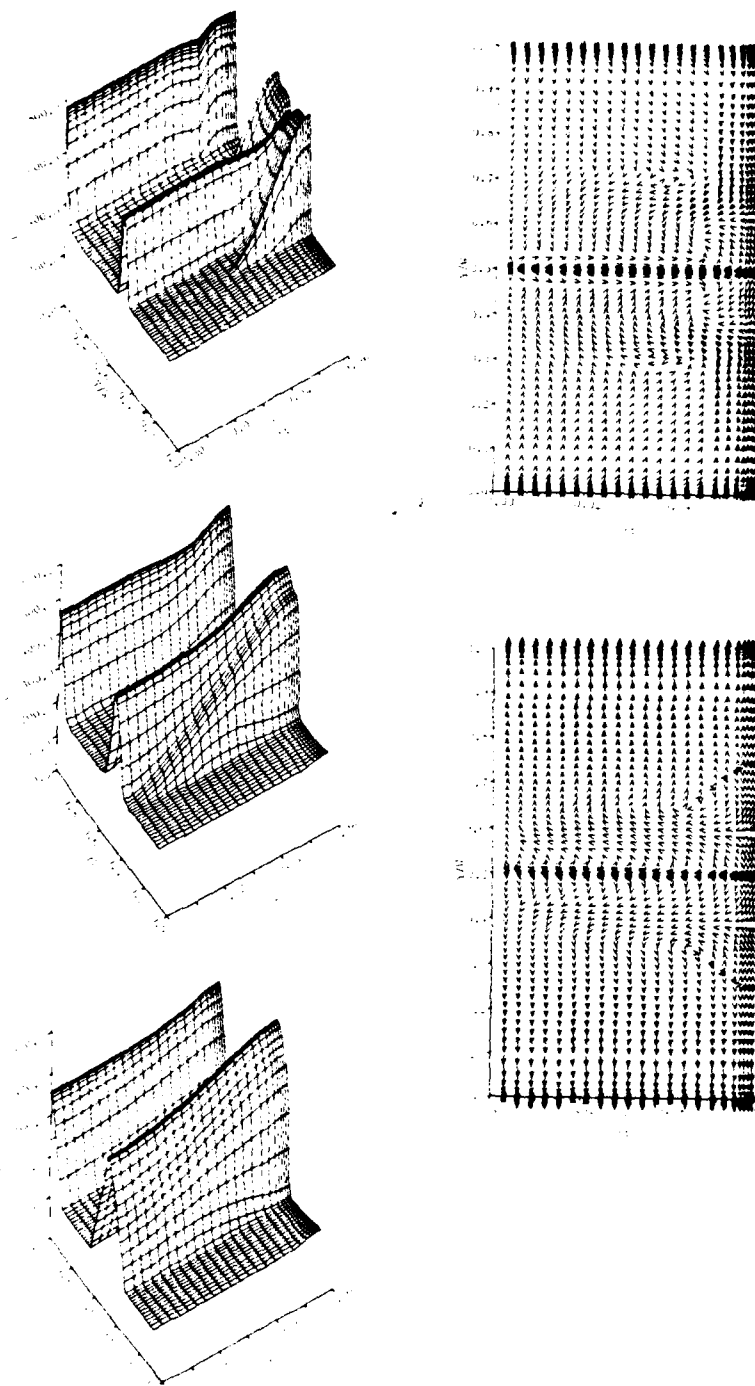


Figure 7-66 Zero Degree Jet Angle Nozzle

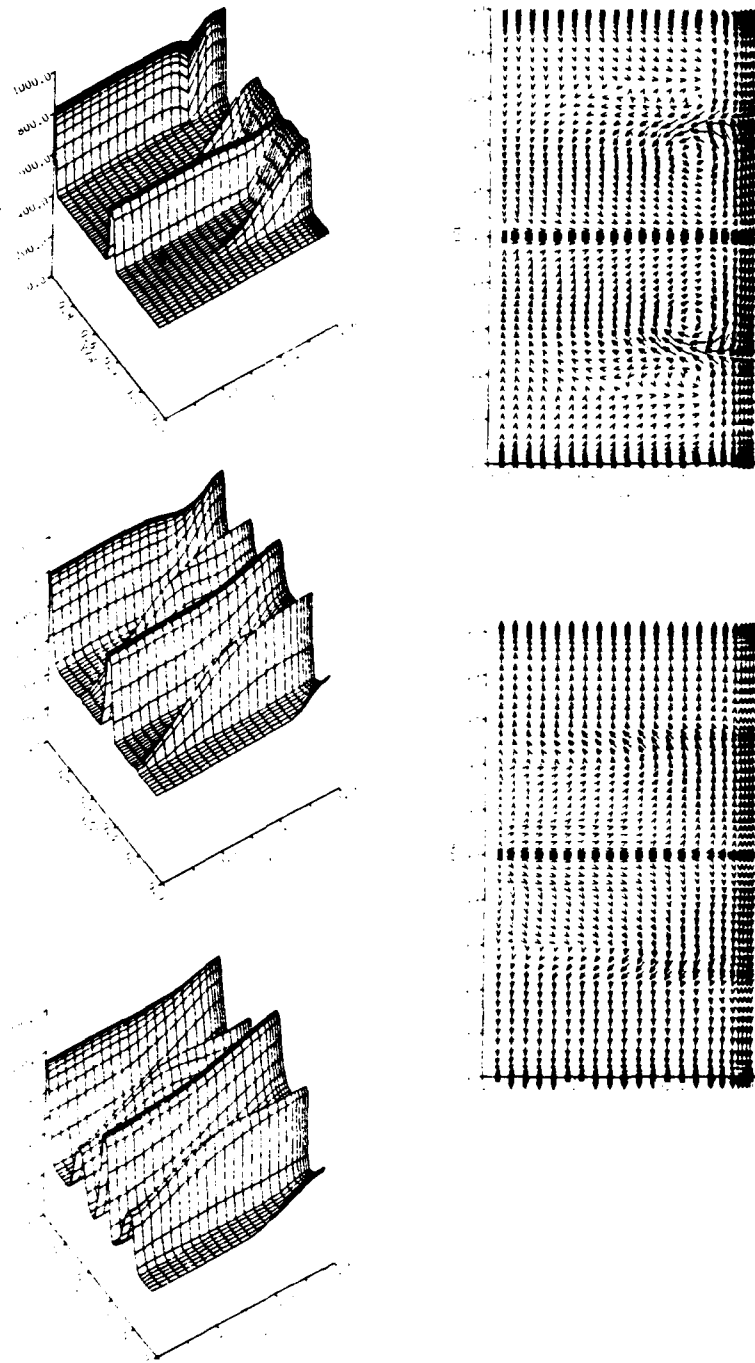


Figure 7-67 Linear Jet Angle  
(0 to 28 Degrees) Nozzle



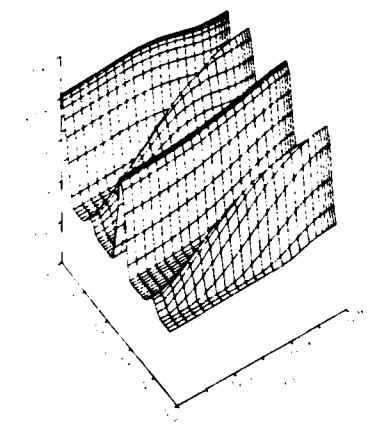
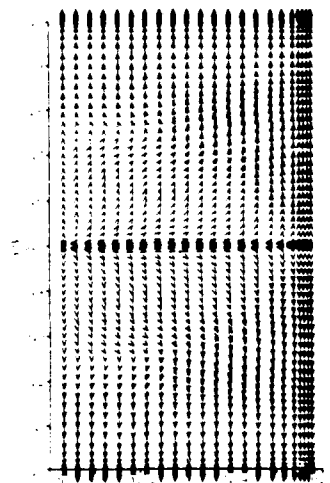
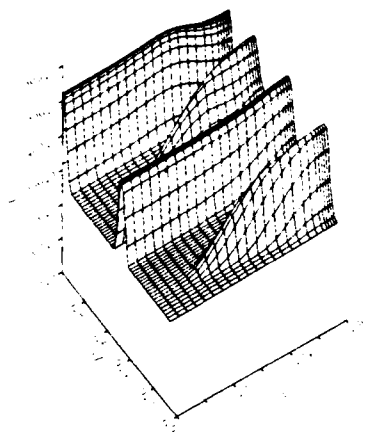
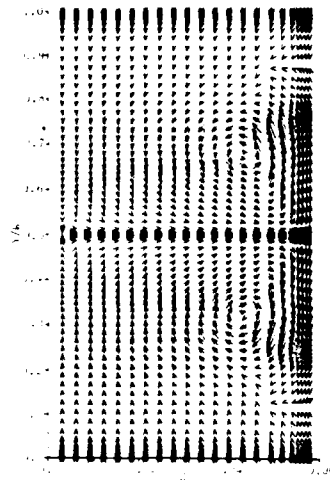
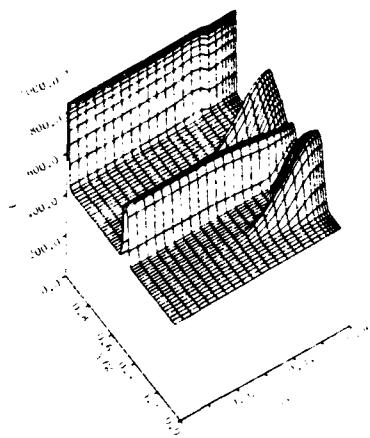


Figure 7-68 Constant Jet Angle  
(21 Degrees) Nozzle

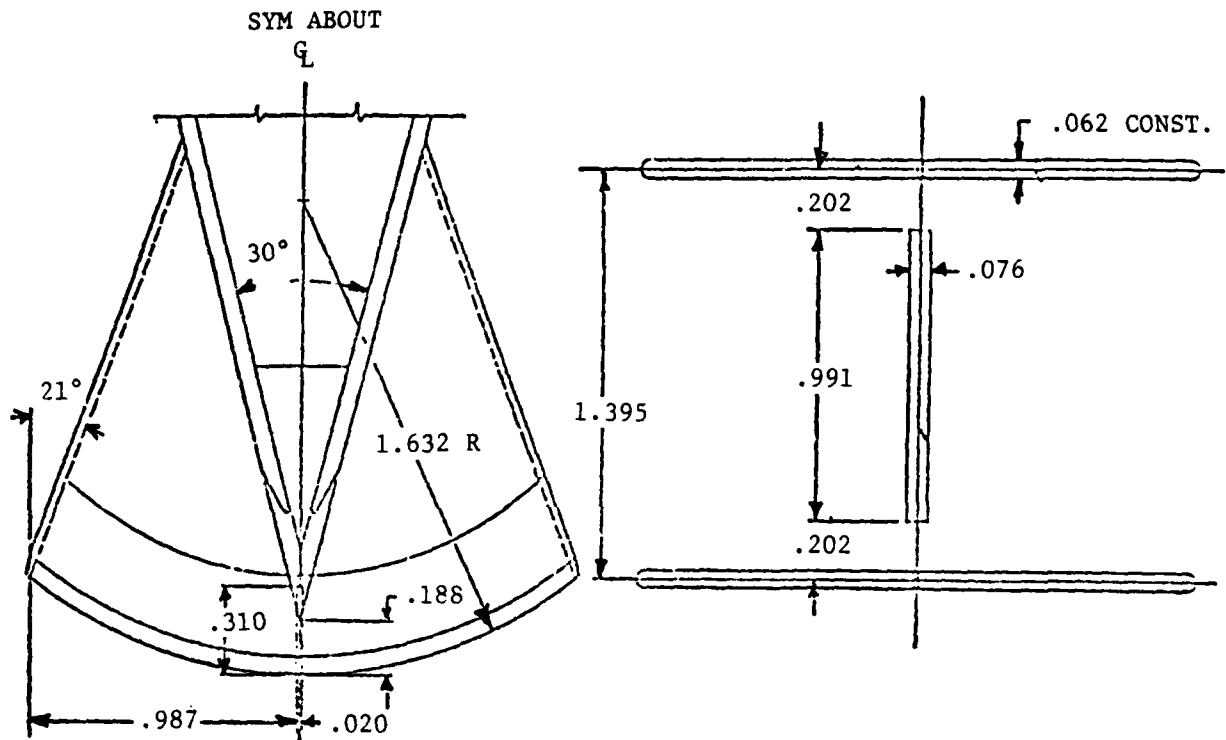


Figure 7-69 Cross Slot-Span Slot Nozzle with a Linearly Varying Exit Profile

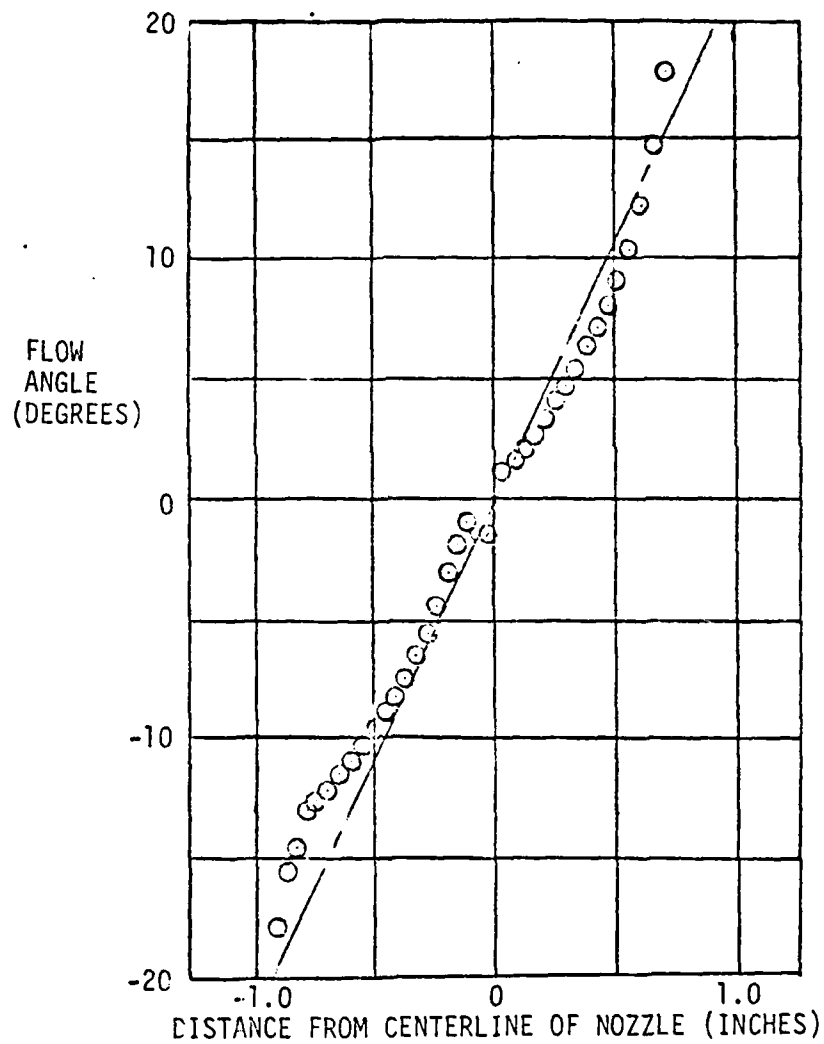


Figure 7-70 Measured Flow Angles for Linearly Varying Slot Nozzle Configuration

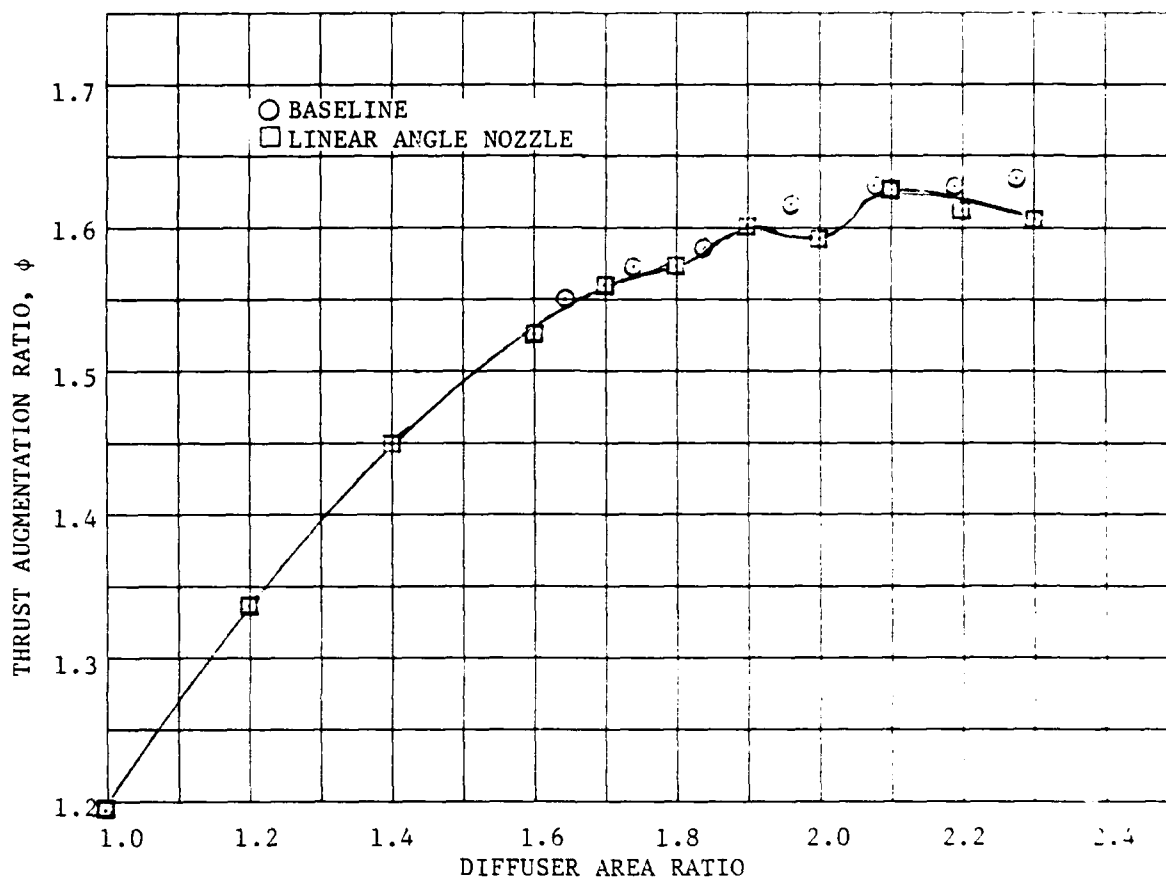


Figure 7-71 Effect of Linear Jet Angle Distribution on Thrust Augmentation

#### 7.5 SUMMARY

The improved version of the jet mixing program has been shown to be a useful tool for analyzing the performance of centerbody nozzles. Test and analysis have shown that the thrust augmentation of the XfV-12A wing can be increased from 1.46 to 1.51 by increasing the hypermixing jet angle from 7° to 22.5°. Similar development of an asymmetric centerbody configuration resulted in a peak  $\phi$  of 1.55. A symmetric cross slot centerbody with optimized bowtie ratio, cross slot flow split and aspect ratio, and cross slot exit flow angularity gave a peak  $\phi$  of 1.64. Pressure distributions on the Coanda surfaces suggested that  $\phi$  was limited to this value by the appearance of separation bubbles. This effect should be further studied.



## 8.0 SHROUD STUDY

8.1 GENERAL

Ejector thrust augmentation involves no more than a novel application of the familiar circulation theorem of aerodynamic lift. An isolated jet induces an essentially lateral flow, as seen in Figure 8-1. The pressure and velocity of the secondary flow approaching an ejector is altered by the presence of the shroud. A circulation which redirects the secondary flow through the ejector is generated around each of the ejector flaps. The

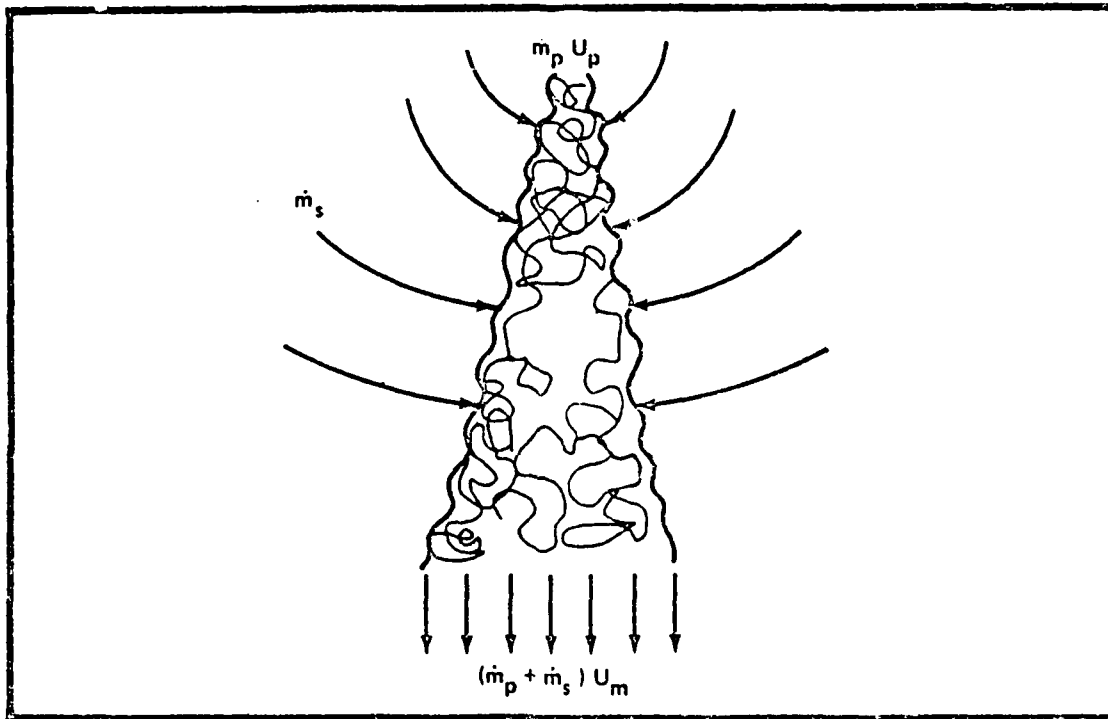


Figure 8-1 Streamlines of the Flow Induced by a Free Jet

flaps are thus considered to be "flying" in the entrained velocity field of the jet, Figure 8-2, and they experience a force related to the lift developed on a wing fixed in a moving stream. The thrust augmentation ratio can therefore be defined as the ratio of the primary jet thrust plus the axial force on the flaps to the isentropic thrust of the primary mass:

$$\phi = \frac{T + F}{\dot{m}V}$$

The theoretical augmentation can be increased by changing the shape and location of the shroud. But, in addition, the forces generated on the shroud due to the augmented thrust must be carried as a pressure loading around the shroud surface. Flow separation from the shroud will result in

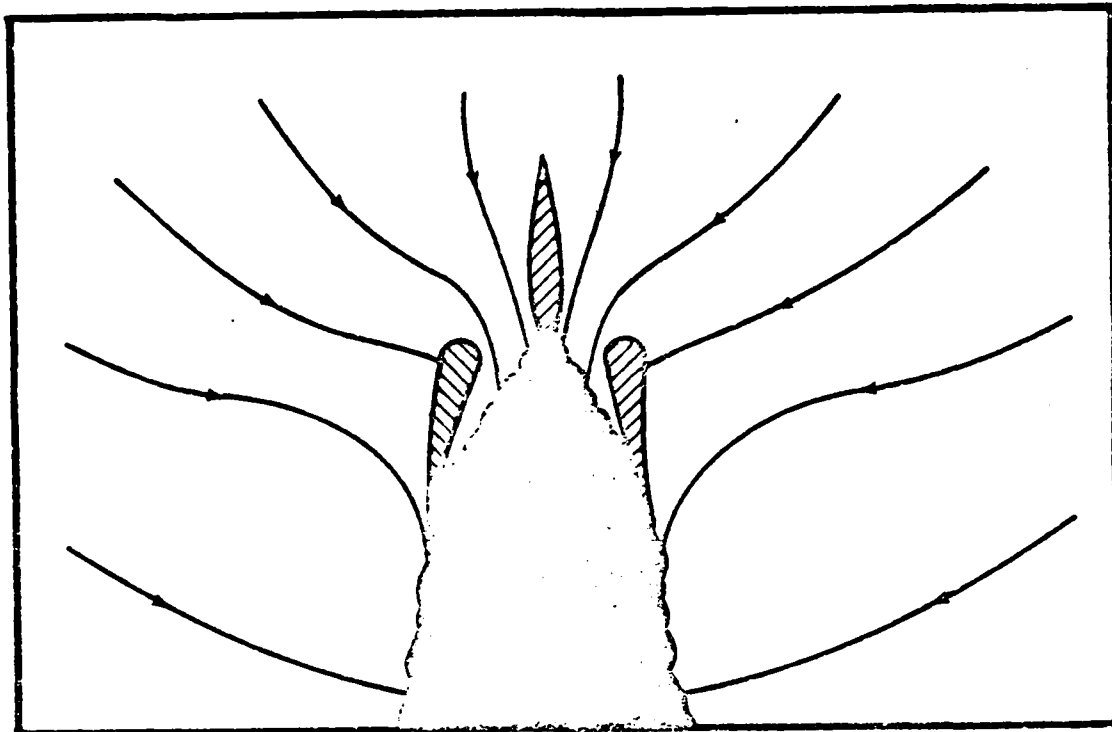


Figure 8-2 Entrainment by the Primary Jet Induces a Secondary Flow

a loss in performance for the augmentor. Therefore, it is important that consideration be given to understanding the shroud as an ejector component. This section presents experimental and analytical results of the effects of shroud related parameters such as flap length, flap asymmetries, flaperons, etc., on ejector performance.

#### 8.2 EFFECT OF FLAP LENGTH

A series of experimental runs were conducted to determine the effect of flap length on ejector performance. The tests were conducted utilizing the .2 scale model on test rig no. 5. The series consisted of runs in which the length of the seven-inch straight flaps was increased to 9.5 inches and 12.3 inches, respectively. This resulted in  $L/W$ 's of 1.5 (baseline), 2.0, and 2.5. The effect of increased flap lengths on thrust augmentation ( $\phi$ ) is shown in Figure 8-3. It is seen that  $\phi$  is independent of increased flap lengths for diffuser area ratios (DAR's) less than 1.6. However, for DAR's greater than 1.6, it is seen that increasing flap length increases  $\phi$  for a given DAR and increases the value of DAR at which maximum  $\phi$  occurs. These results are consistent with those reported in Reference (30).

The effect of flap length on the distribution of the aft flap Coanda surface pressures is shown in Figure 8-4. In general, it is seen that

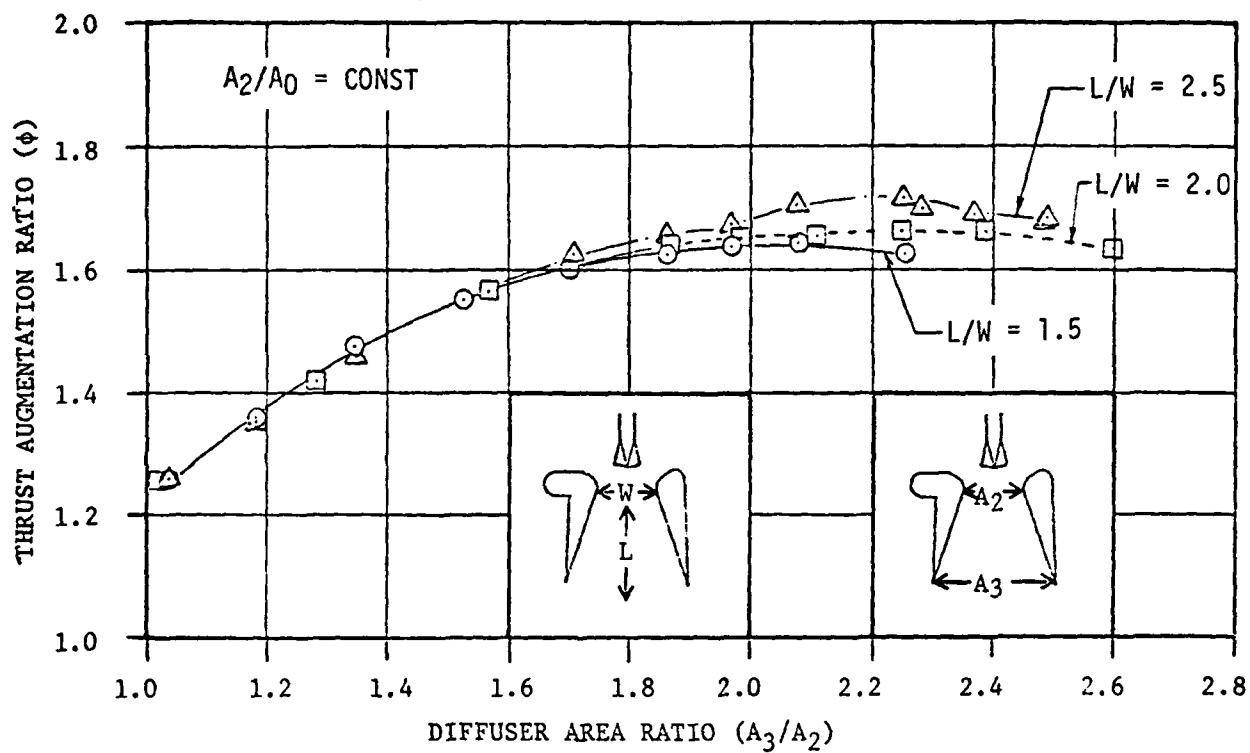


Figure 8-3 Effect of Flap Length on Thrust Augmentation Ratio

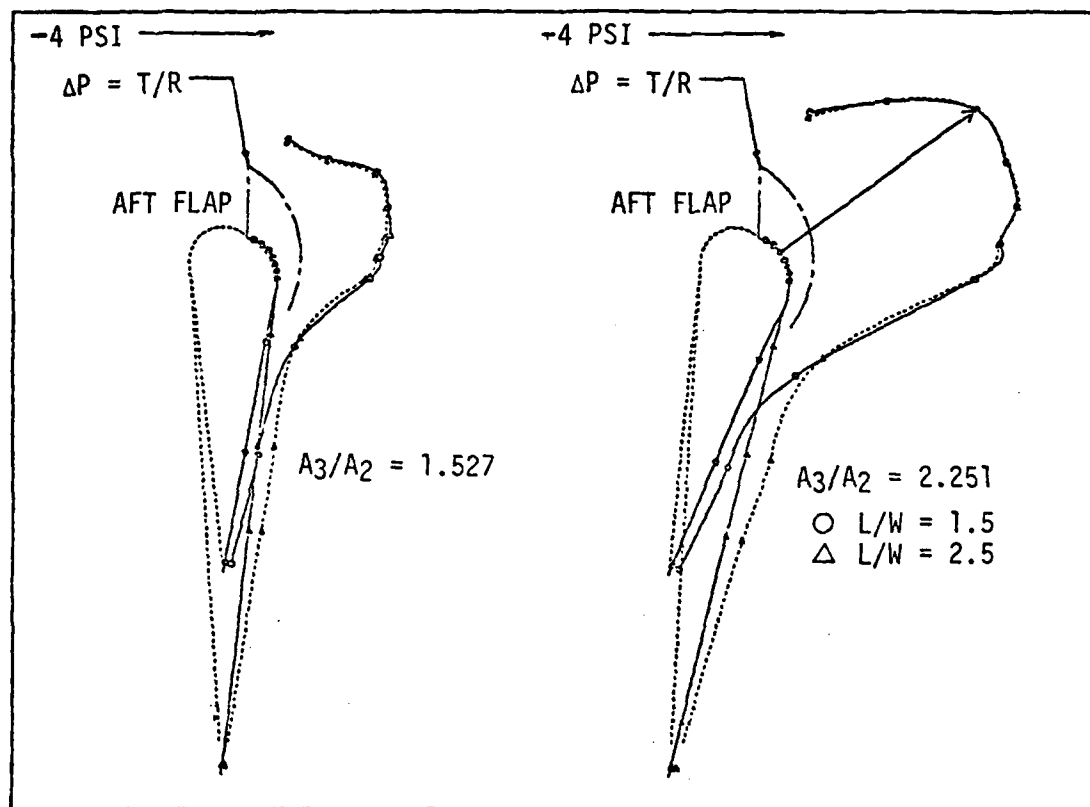


Figure 8-4 Effect of Flap Length on Surface Pressure Distribution





Rockwell International

increased flap length has little effect on either the magnitude of pressure or its distribution around the Coanda surfaces. The same trend was observed for the forward flap.

In order to increase understanding of flap length effects, augmentor exit surveys were obtained at diffuser area ratios of 1.183 and 1.965. The data from these surveys were integrated to obtain momentum, mass flow, thrust and a velocity profile factor ( $\beta$ ). The effect of flap length on exit mass flow is presented in Figure 8-5. The velocity profile factor is shown in Figure 8-6.

The independence of  $\phi$  with flap length for area ratios less than 1.6 is due to at least two cancelling effects. First, for a given DAR, increased flap length would result in reduced flap angle, i.e., the flaps are flying at a lower angle of attack. Therefore, the velocities induced by the flaps at the throat are lower. However, the throat velocity data indicate no effect due to flap length. Hence, it is likely that increased mixing cancels the effect of angle.

At diffuser area ratios greater than 1.6, the baseline configuration is stalled. Stall is a condition in which the resultant force continues to increase, but the force vector for each shroud is tilted downward. A sketch of this condition is shown in Figure 8-7. When augmentation is limited by this phenomenon, the secondary mass flow, i.e., throat velocity, continues to increase past the point of maximum thrust.

At large diffuser area ratios, the increases in  $\phi$  at constant diffuser area ratio with increased L/w is due to a reduced flap angle which tilts the resultant force vector upwards. Secondly, the jets are brought closer together resulting in a lower velocity profile shape factor. This latter result is seen in Figure 8-6

### 8.3 FLAP LENGTH ASYMMETRIES

The integration of an ejector into the wing of an aircraft requires compromises in both wing and ejector geometry. The XfV-12A required tapered ejectors. However, design studies showed that a nearly rectangular ejector could be designed for the XfV-12C configuration. Even though the ejector could be nearly rectangular, it would require asymmetries in flap length. Therefore, a test program was initiated to assess the effects of different fore and aft flap lengths on ejector performance. Unfortunately, only one asymmetric flap length test series was completed prior to program termination.

The results of a test in which the aft flap length was 1.78 inches longer (model scale) than the forward flap is shown in Figure 8-8. The DAR for the asymmetric flap configuration has been defined in two different ways and the data have been presented accordingly. It is seen that a 25 per cent increase in aft flap length had no effect on peak  $\phi$ . Furthermore, using the symmetric definition of exit area yielded a better correlation than using the asymmetric definition. The data obtained for this series also indicated no effect of flap length asymmetries on thrust angle.

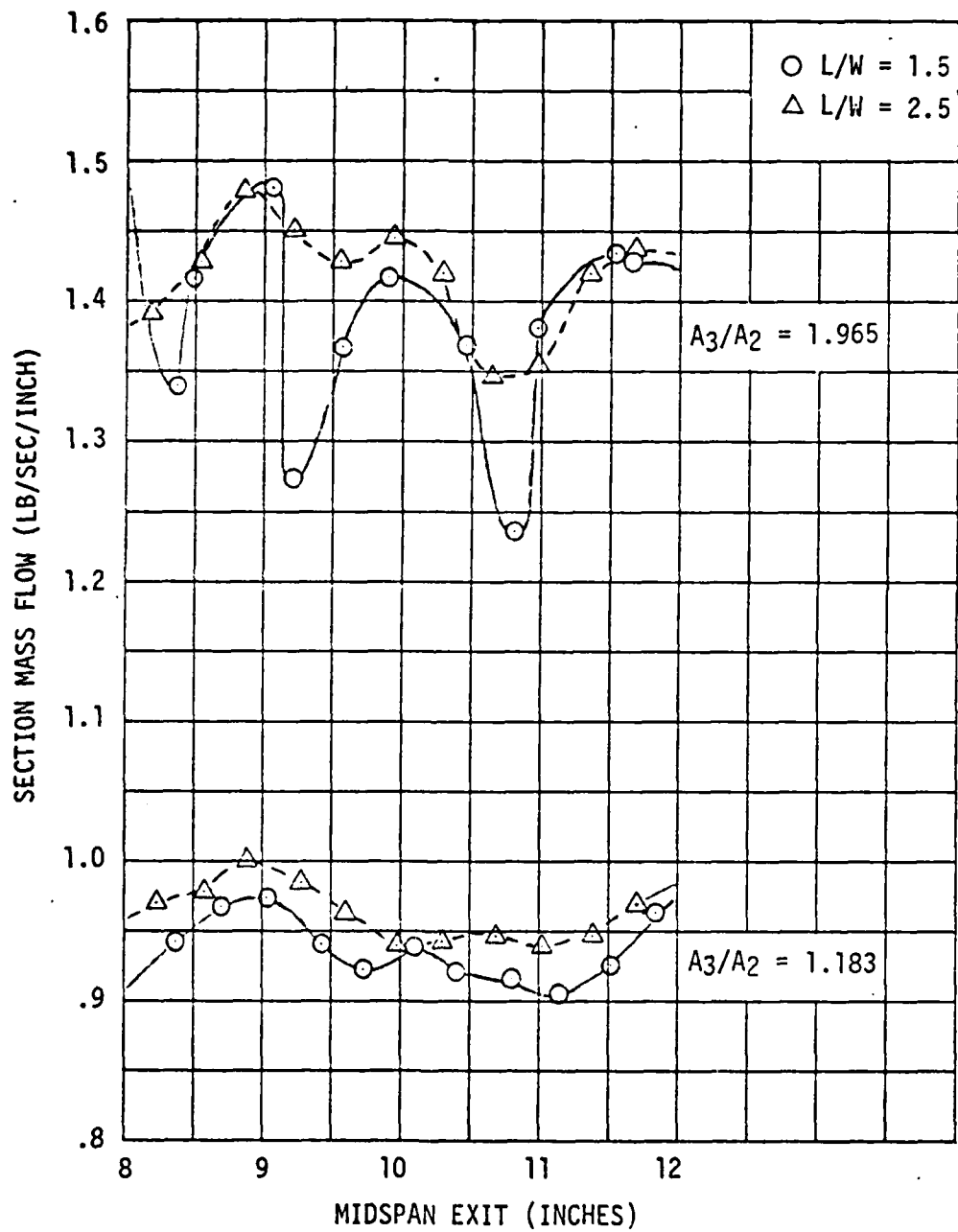


Figure 8-5 Effect of Flap Length on Section Mass Flow

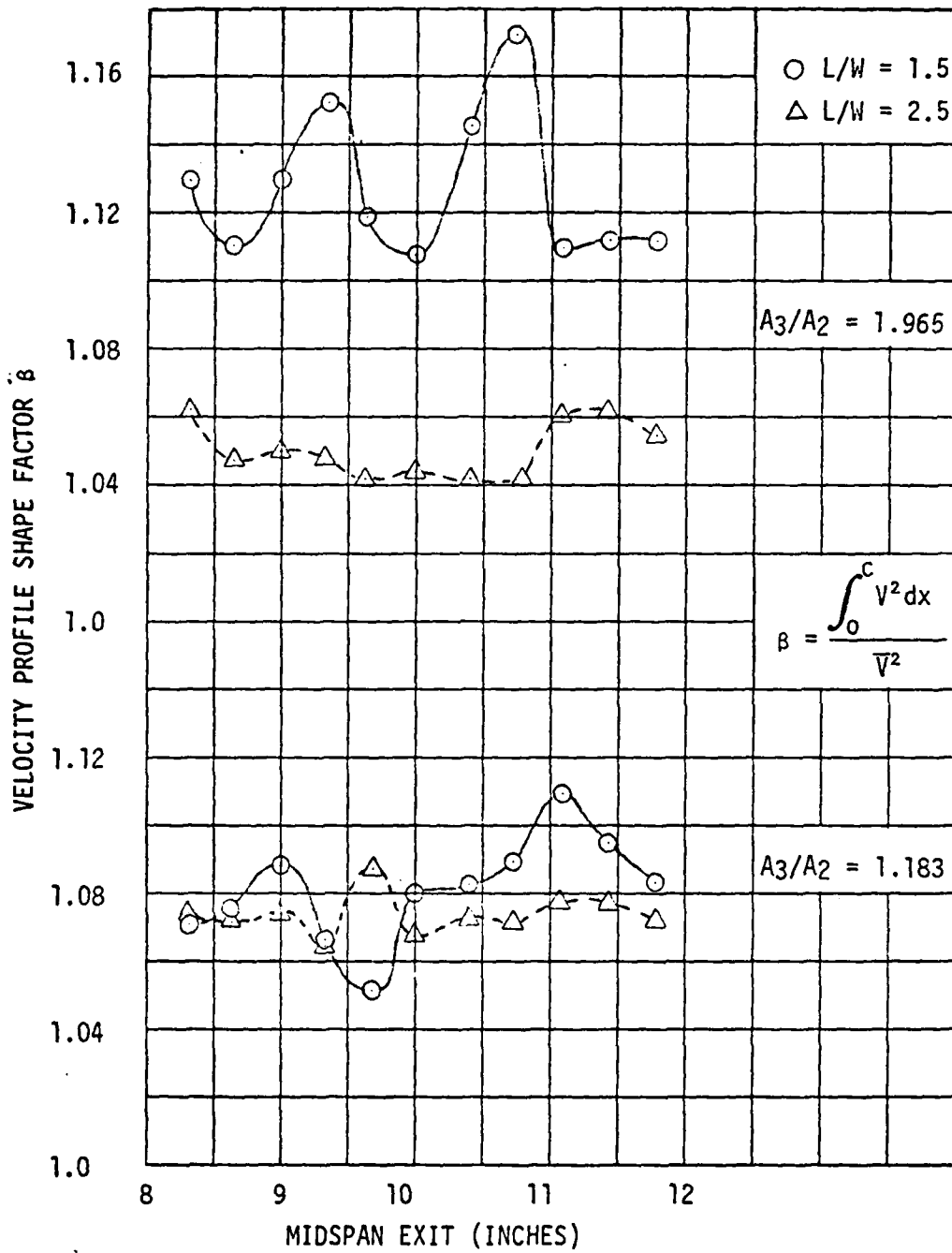


Figure 8-6 Effect of Flap Length On Velocity Profile Shape Factor

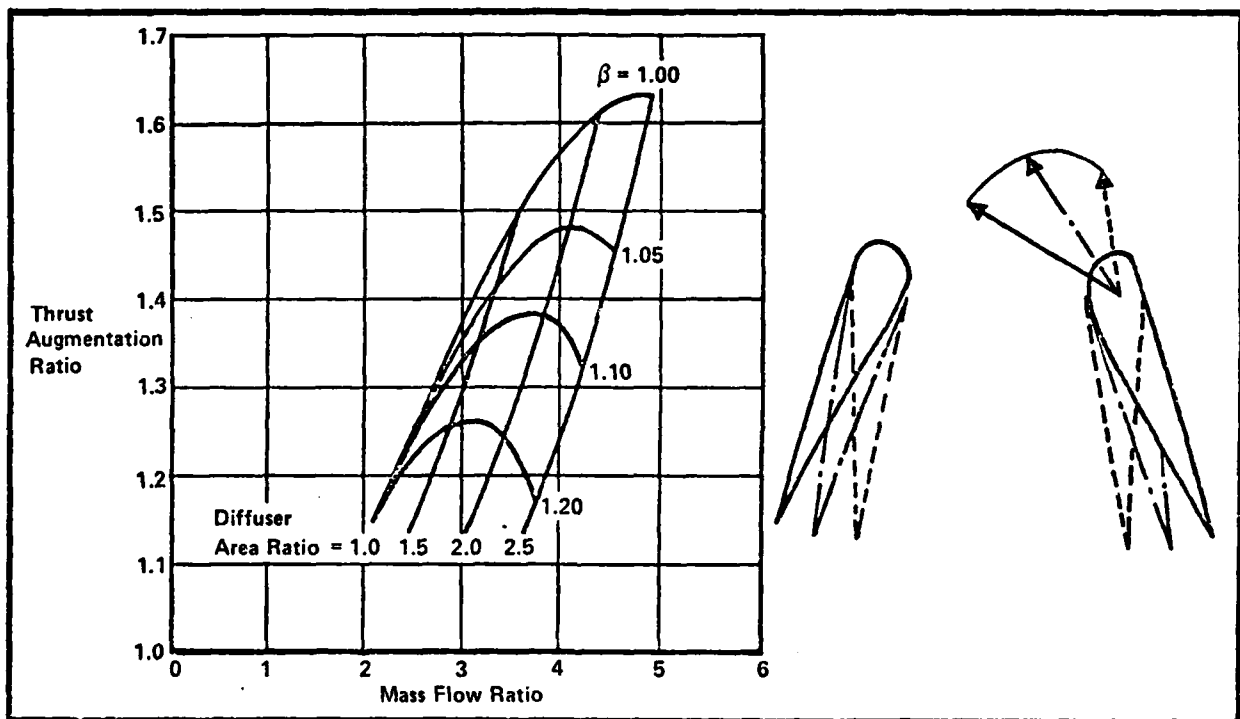
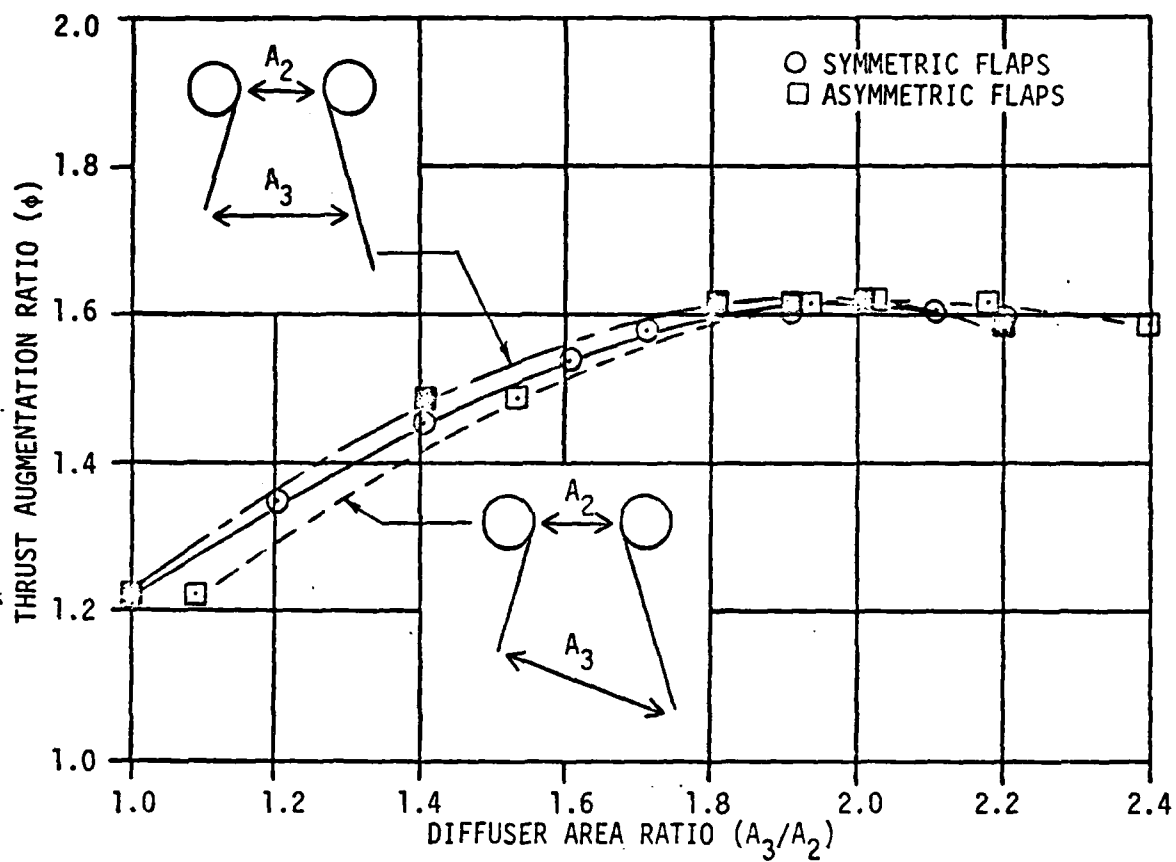


Figure 8-7 Inclination of the Thrust Vector Limits the Thrust Augmentation

Figure 8-8 Effect of Asymmetric Flap Length on  $\phi$



#### 8.4 LOCAL SEPARATION EFFECTS (BUBBLES)

Careful study of the thrust augmentation ( $\phi$ ) variation with diffuser area ratio (DAR) shown in Figure 8-9 shows a characteristic that has been typical for all of the high performing symmetric cross-slot (CS) nozzles. Namely, a break in  $\phi$  between DAR's of 1.6 and 1.8. This characteristic is thought to be due to a local separation that first occurs on the forward flap Coanda surface and then, at a slightly higher DAR, on the aft flap.

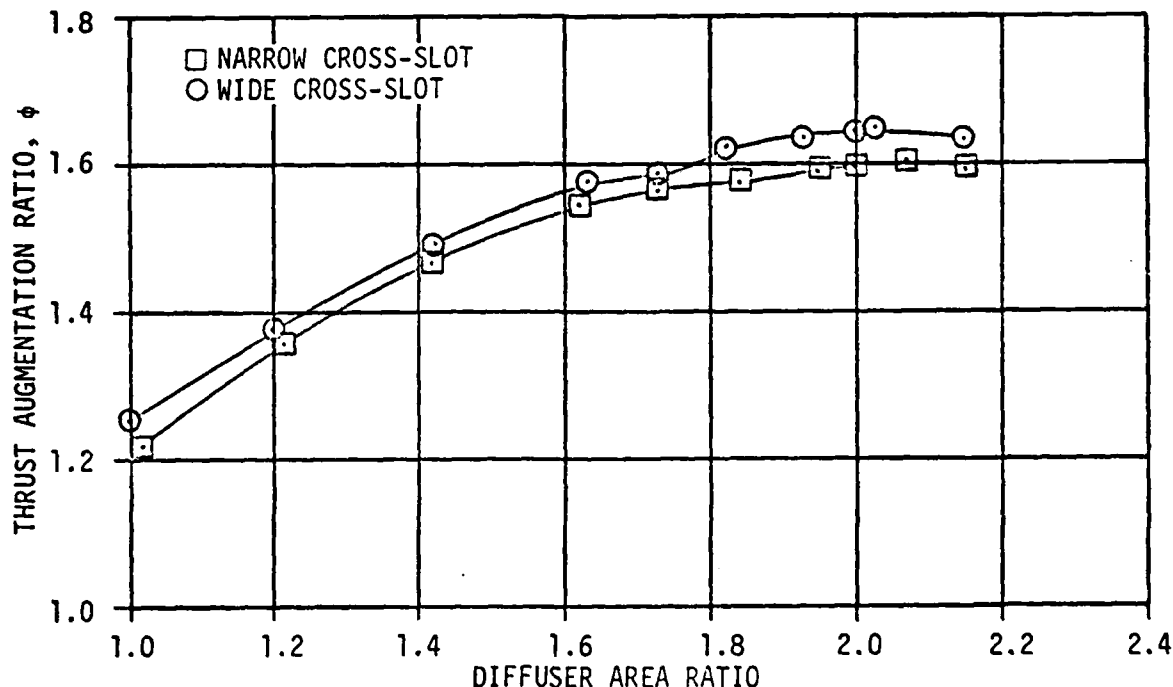


Figure 8-9 Effect of Cross-Slot Width on Thrust Augmentation Ratio

Figure 8-10 presents a comparison of the pressure distribution on the forward flap surface for both narrow and wide cross-slot nozzles. Figures 8-10a and 8-10b show that both nozzles produce the same pressure distributions, however, the wide CS nozzle produces a more negative value of pressure. The irregularities in pressure occurring at about 20 nozzle thicknesses ( $s/t$ ) around the surfaces are thought to be due to local separation. The possibility of expansion and compression waves has been ruled out because of the relatively large distance from the nozzle.

This Coanda surface pressure data has been replotted in Figure 8-11 to show the variation of surface pressure with diffuser area ratio for a given pressure tap location. At the fourth tap ( $s/t \approx 20$ ) the previously discussed irregularities can be clearly seen.

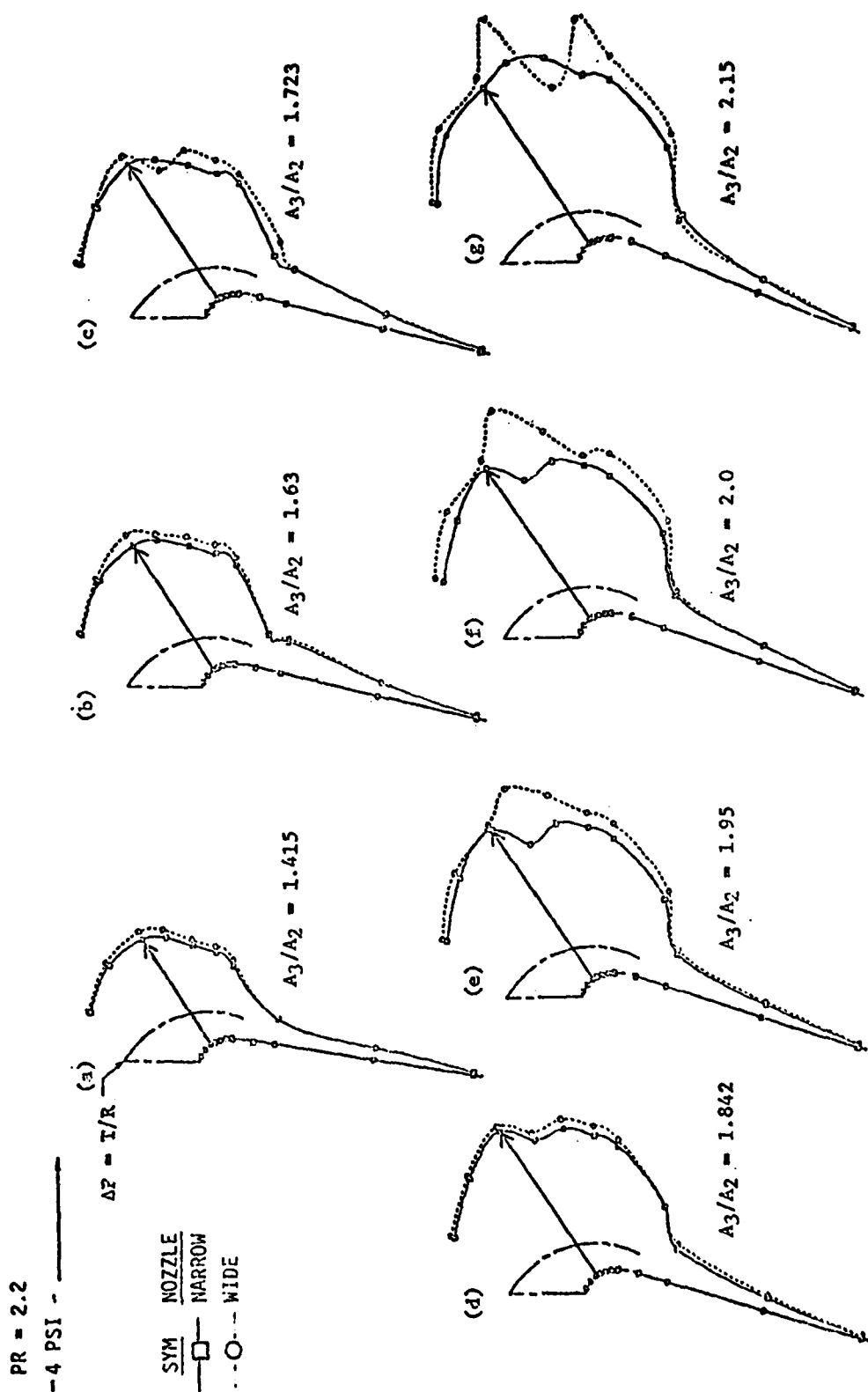


Figure 8-10 Forward Flap Surface Pressures for Narrow and Wide Nozzles

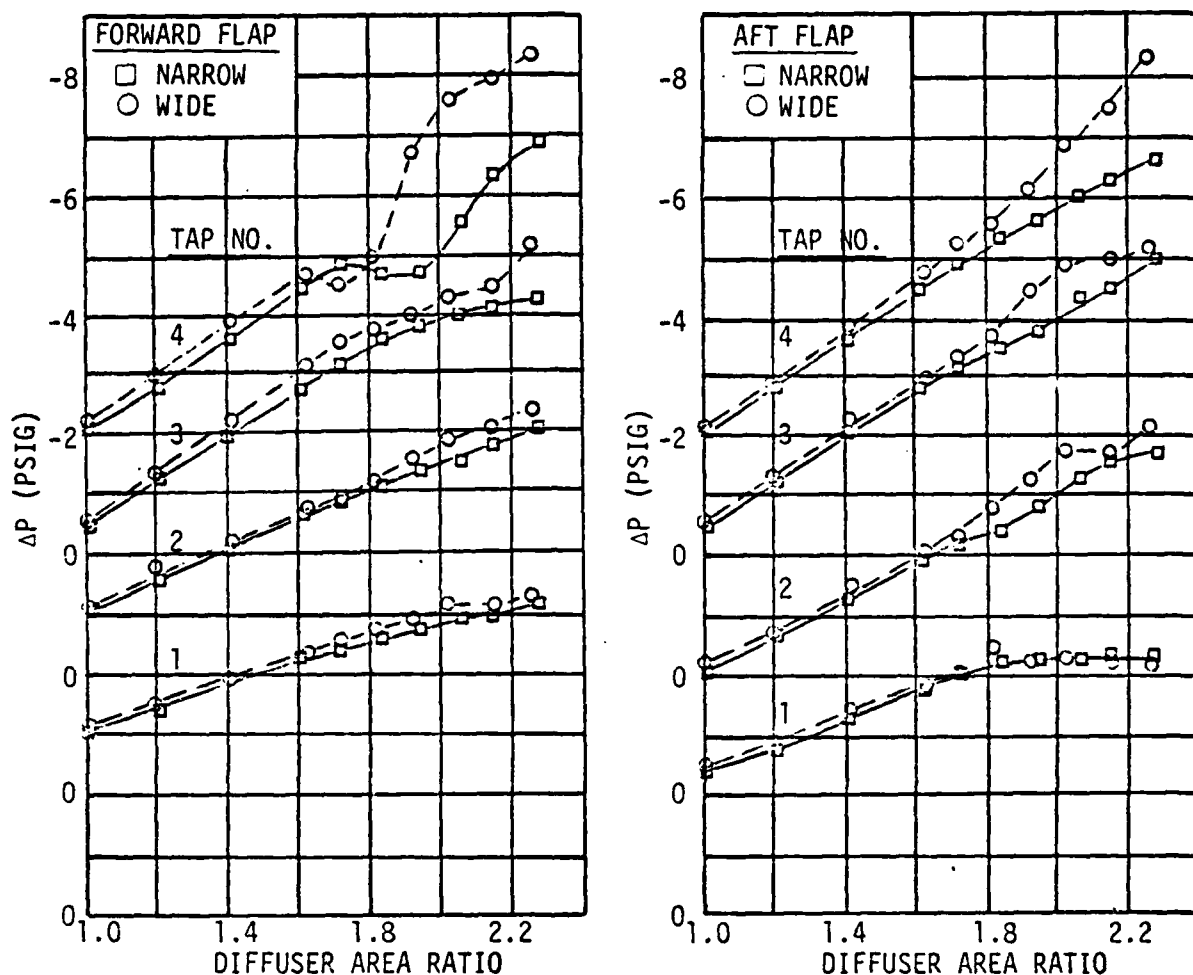


Figure 8-11 Variation of Surface Pressure with Diffuser Area Ratio

Additional data which show the possibility of local separation on the Coanda surfaces is shown in Figures 8-12. These data show the effect of artificial surface roughness (grit) on surface pressure. The pressures are plotted versus arc length (measured from nozzle exit). The grit was placed between pressure taps three and four. Figure 8-12 shows that without grit the aft flap has a very smooth pressure distribution. However, the addition of grit creates a local separation with a pressure loss downstream of the separation point. The pressure distributions on the forward flap are very similar with and without grit, i.e., local separation is indicated. The character of the aft flap pressure distribution with grit and the forward flap pressure distribution without grit are similar. The effect of grit on ejector performance is shown to be a loss in  $\phi$  of at least .04.



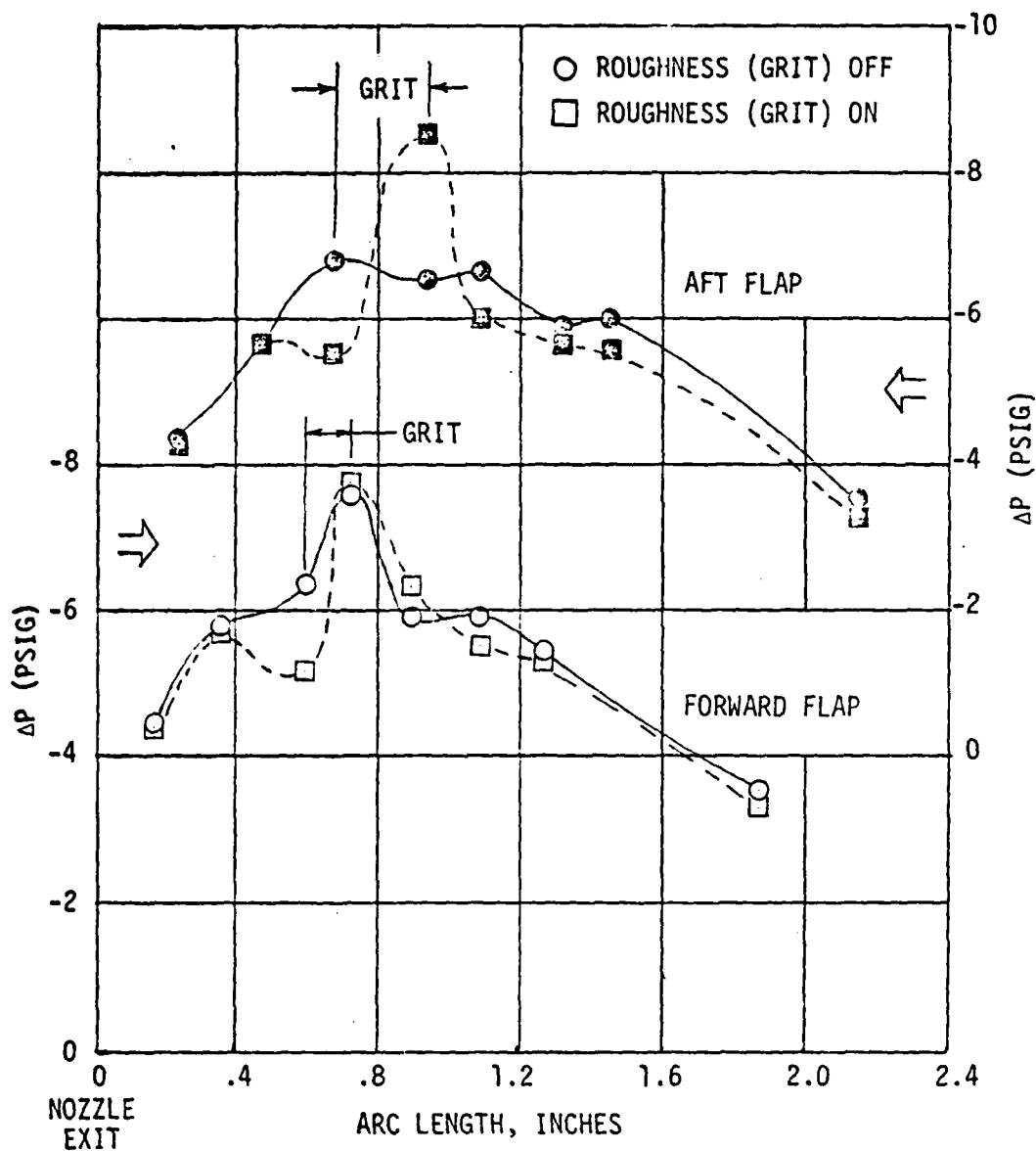


Figure 8-12 Effect of Roughness On Coanda Surface Pressures

It is concluded, based on these data, that both the forward and aft flaps experience local separation at  $s/t \approx 20$ . The indicated separation location is near the point at which the pressure gradient becomes adverse.

#### 8.5 INVISCID ANALYSIS OF SHROUD

An analysis of the shroud has been conducted using an inviscid computer code. The procedure employed was to set the secondary flow rate through the shroud by adjusting the strengths of an assumed center jet sink



distribution. The strengths were adjusted so that the throat velocity obtained from the inviscid code was equal to a desired value (obtained from experiment or the jet mixing analysis).

Figure 8-13 shows the modeling used to represent the .2 scale rectangular wing at a diffuser area ratio of 2.0. The computed streamlines are also shown. Figures 8-14 and 8-15 present a comparison of experimental and computed velocities at the ejector throat and at the inlet plane. Figure 8-16 shows a comparison of chordwise flow angles at the inlet plane. Each figure presents experimental data at a span station under a cross-slot nozzle and one under the span slot. The secondary flow is seen to be almost two-dimensional. The agreement between test and theory is excellent and shows that the inviscid code is quite useful in determining inlet flow characteristics.

A comparison of computed and experimental surface pressures are shown in Figure 8-17. The pressure due to Coanda jet turning, i.e.,  $\Delta P = \text{Thrust/Radius}$ , has been removed from the experimental data. The throat velocities obtained from the jet mixing code were used as control points.

Interestingly, the lowest pressures do not occur at the throat. It is concluded that the shroud surface pressures are composed of a part due to channel-type flow and a part due to airfoil-type flow. The superposition of the two types moves the minimum pressure away from the throat and towards the shroud leading edge.

The excellent agreement of the inviscid code with experimental data led to a request to increase the number of pressure taps on the shroud surfaces. However, detail pressures were obtained for only one centerbody nozzle configuration prior to XFV-12A program termination. A comparison of theory and experiment for that configuration is shown in Figure 8-18. The comparisons shown have the largest discrepancy at the "leading edge." The potential flow solution indicates a large adverse pressure gradient just upstream of the nozzle. It is possible that the flow could be separated in this region and be re-entrained further downstream. An analogy can be drawn between this "postulated separation" and typical airfoil leading edge separation. In the latter, leading edge separation results in a rapid increase in drag with no appreciable change in lift. Separation of this type for the ejector would be quite detrimental to performance and difficult to detect without further detailed instrumentation. Further study of ejector leading edge separation was planned.

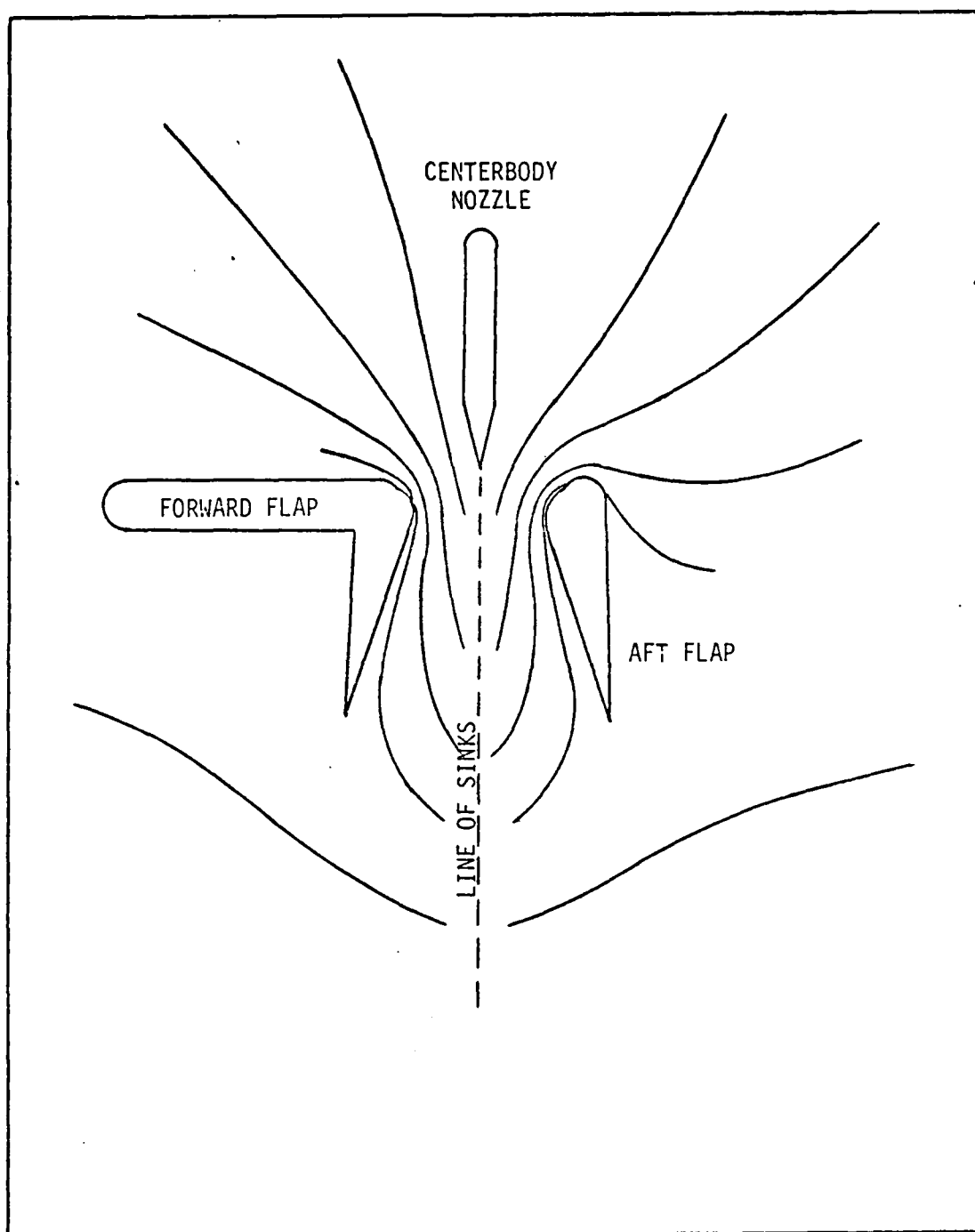


Figure 8-13 Entrainment by the Primary Jet Induces A Secondary Flow

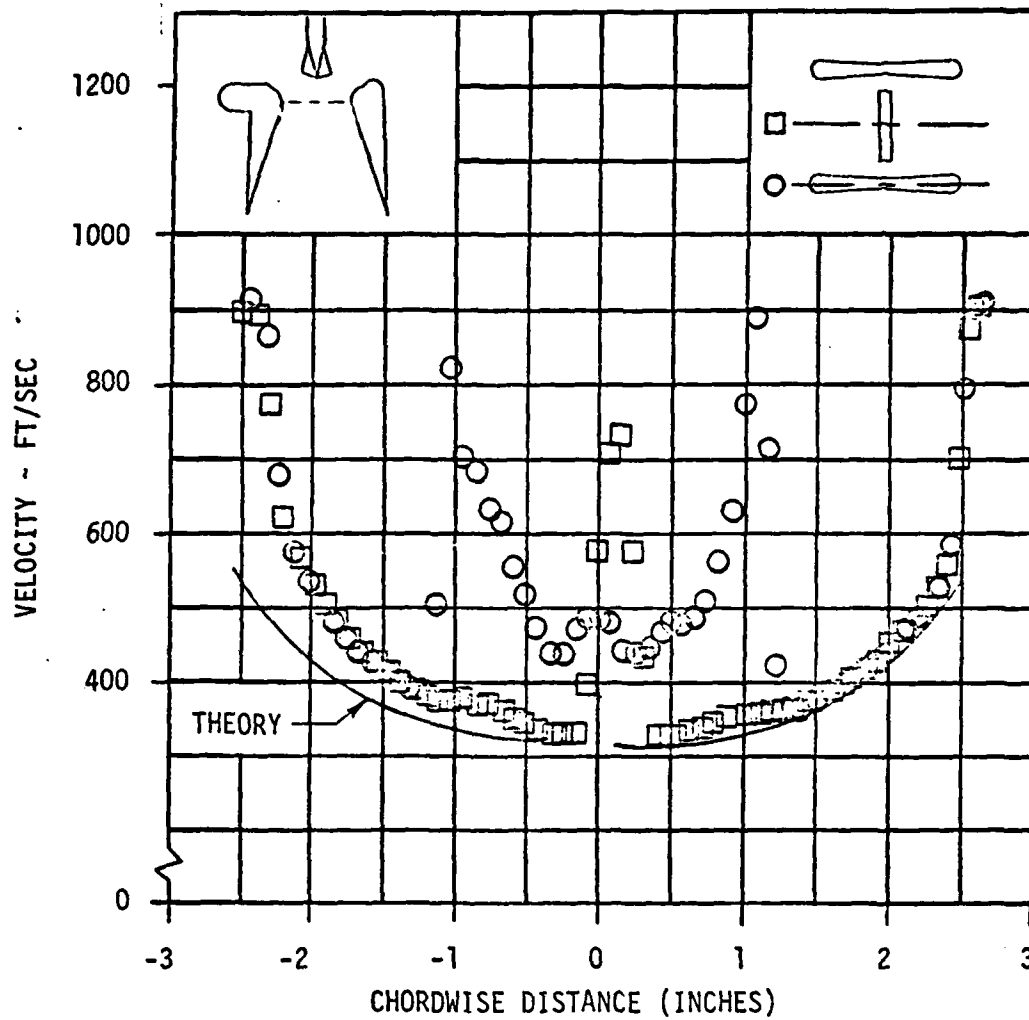


Figure 8-14 Comparison of Experimental and Theoretical Velocities at the Throat Plane

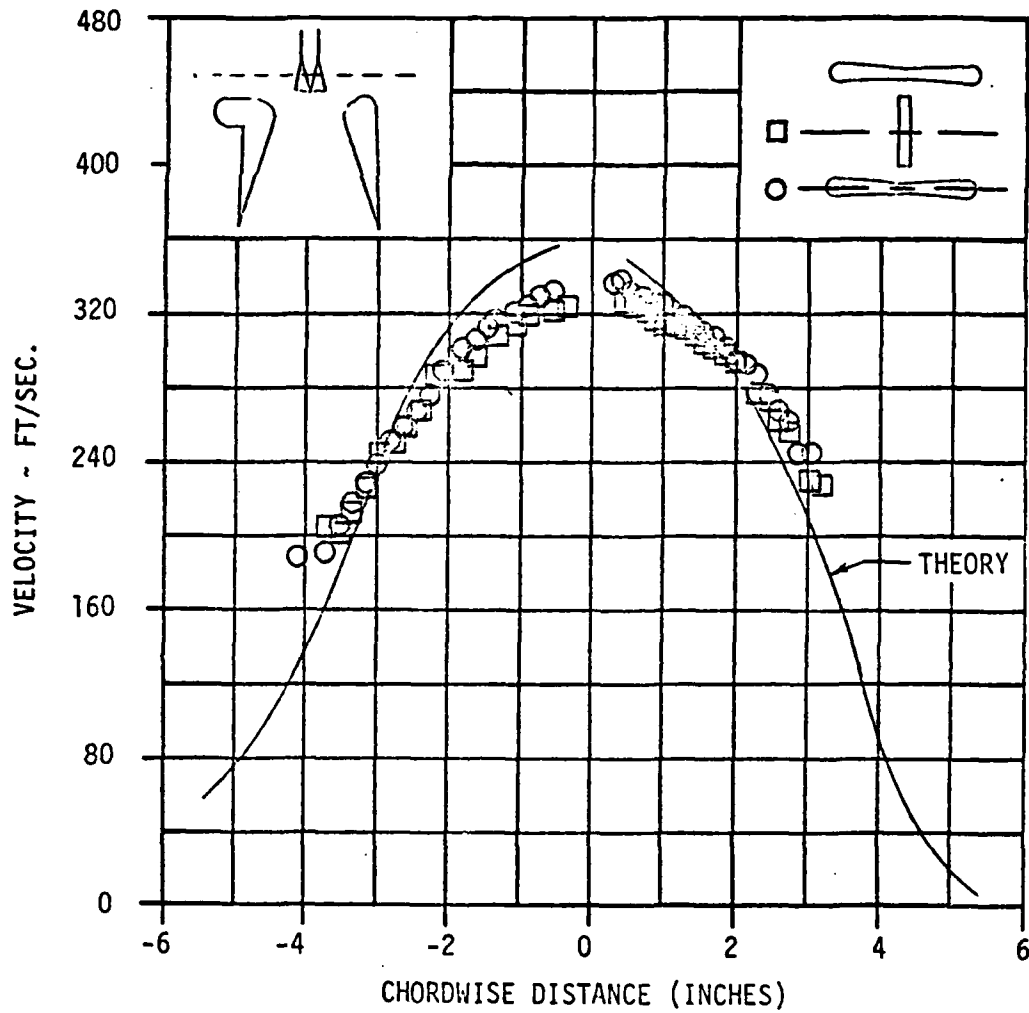


Figure 8-15 Comparison of Experimental and Theoretical Velocities At A Nozzle Plane

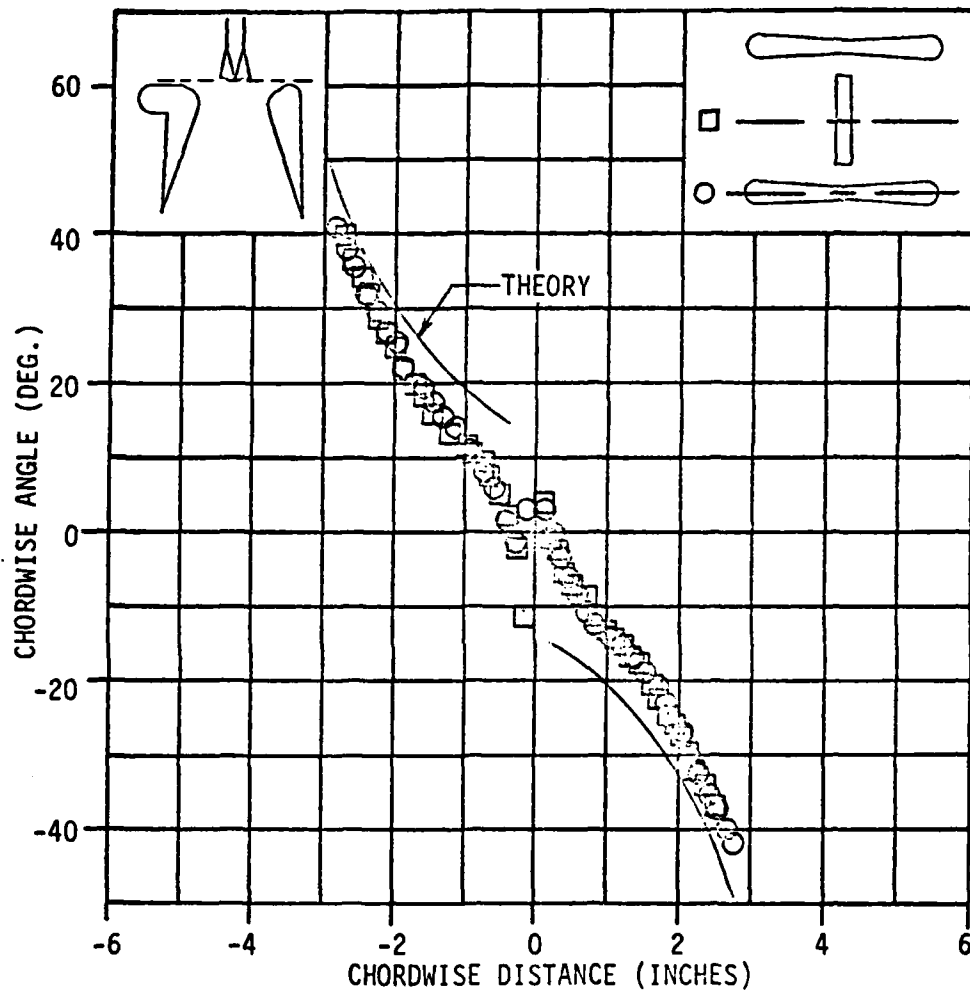


Figure 8-16 Comparison of Experimental and Theoretical Flow Angles At the Inlet Plane

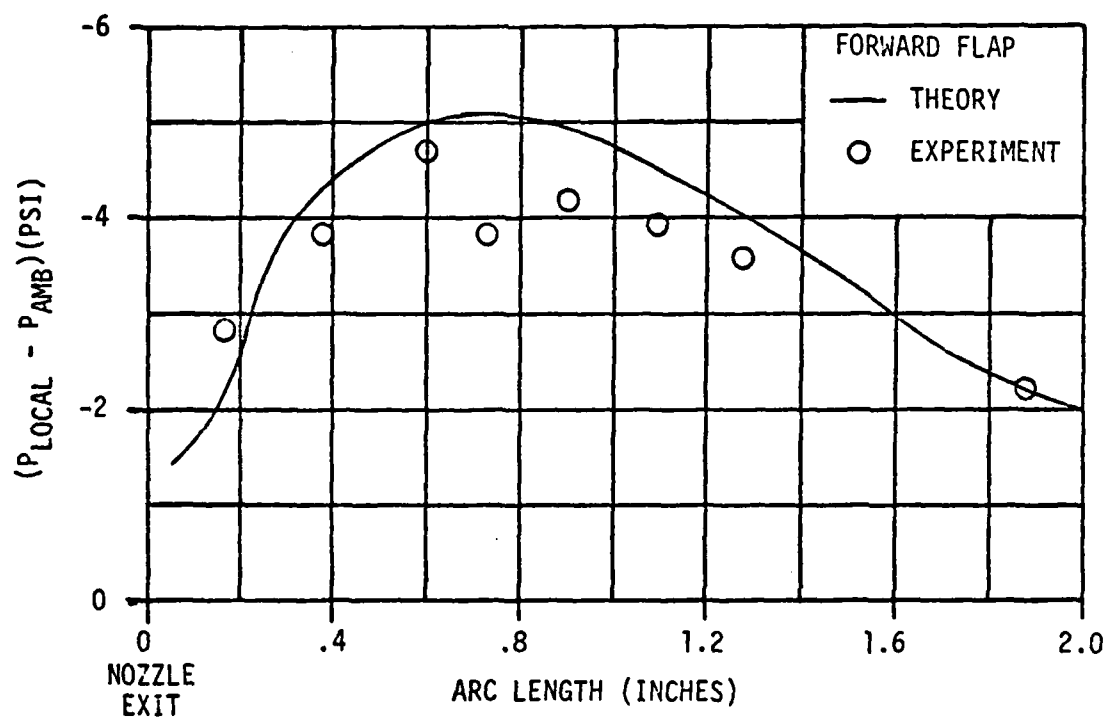
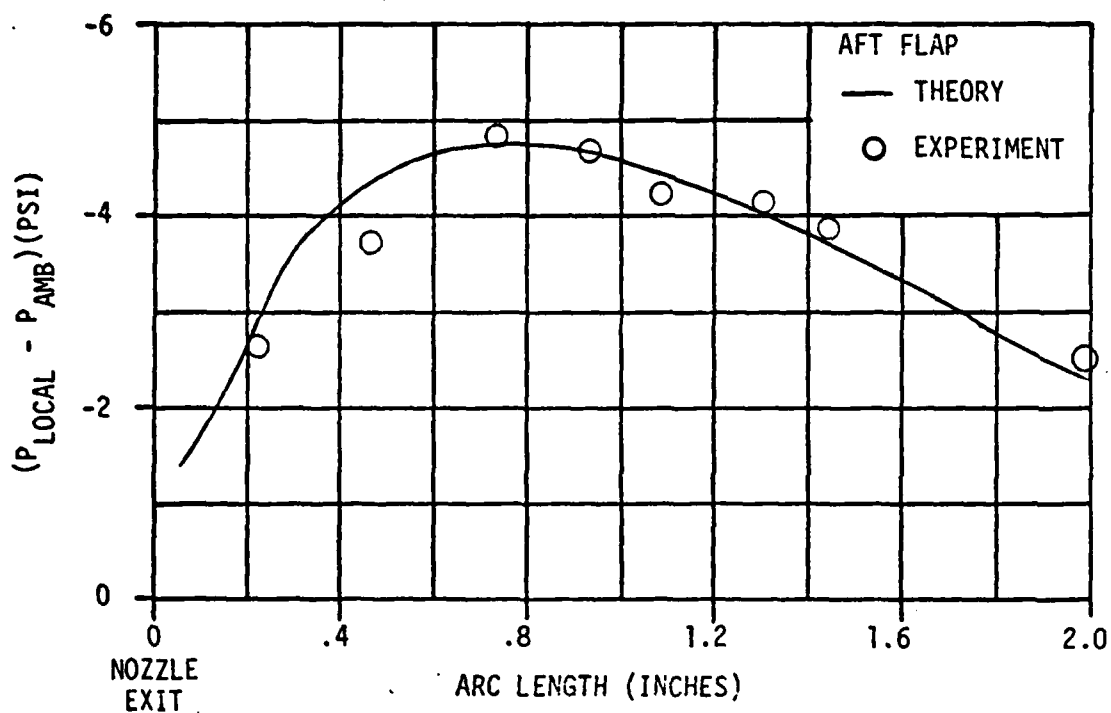


Figure 8-17 Comparison of Experimental and Theoretical Surface Pressures

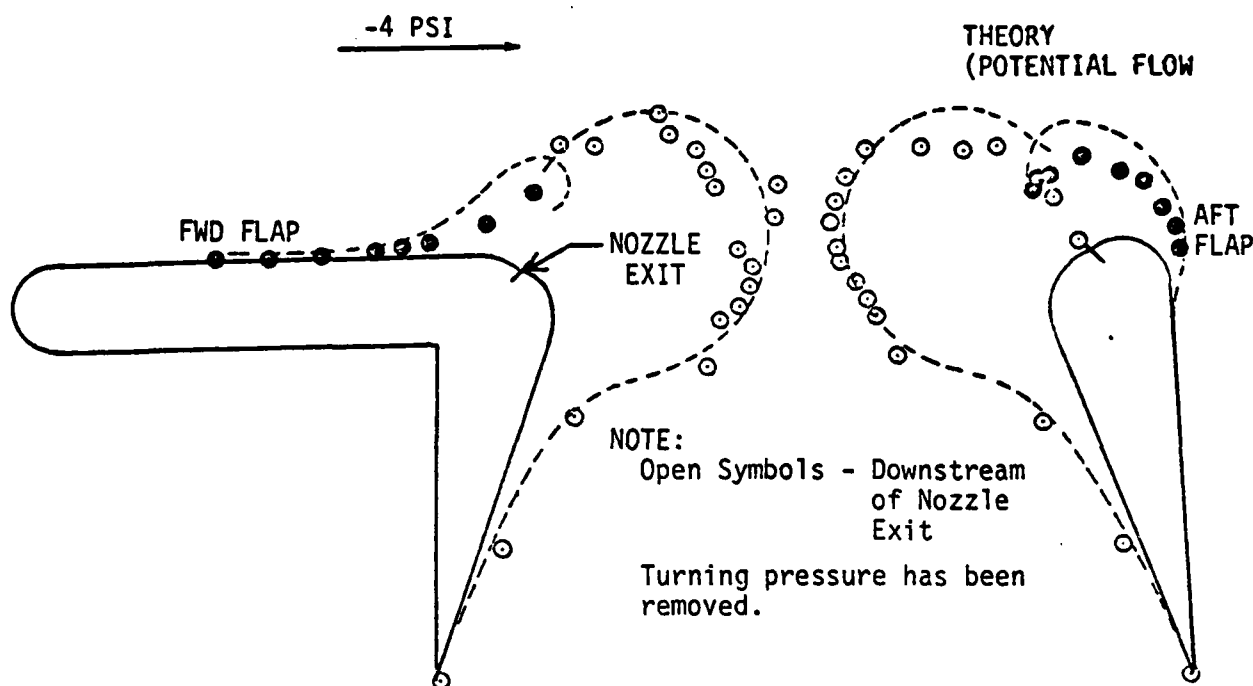


Figure 8-18 Comparison of Predicted and Experimental Shroud Pressure Distributions

#### 8.6 FLAPERONS

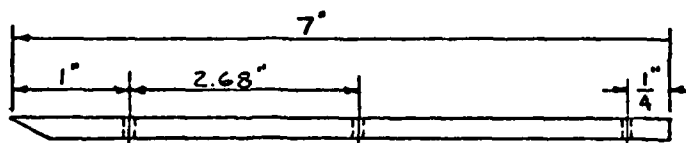
Ejector performance can be increased through improved nozzle designs (mixing) or through improved shroud geometry. The use of flap trailing edge tabs or flaperons as a means of improving external diffusion has been reported in Reference (31). The flaperons have an effect similar to that of trailing edge flaps with blowing. First, there is an increase in lift due to trailing edge camber and, secondly, lift is increased as a result of the jet flap diffusion reported in Reference (32). Therefore, a series of tests were conducted on the 0.20 rectangular ejector to study flaperon effectiveness for the XfV-12A shroud geometry.

A sketch of the flaperon configuration tested is shown in Figure 8-19. A comparison of thrust augmentation and throat velocity for the straight flap and flaperon configurations are shown in Figure 8-20 and 8-21, respectively. The results show an average increase in thrust augmentation of .04 for diffuser area ratios less than 1.8. However, there is no increase in peak augmentation. The throat velocity continues to increase past peak  $\phi$  for both configurations. The flaperon configuration was visually observed to have corner separation at the largest diffuser area ratio.





7" STRT FLAP (356-01042-063)



15° 7" FLAPERON (356-01042-181)

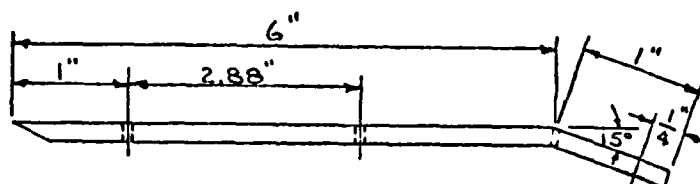


Figure 8-19 Sketch of the Flaperon Configuration

The lack of exit flow surveys and detailed pressure distributions make it difficult to determine why the flaperon configuration did not obtain a larger peak  $\phi$ . It is postulated that two separate factors contribute to the poor peak performance. First, the previously discussed leading edge separation would occur at a lower diffuser area ratio with flaperons. Secondly, the data presented in Reference (31) showed a degradation in peak  $\phi$  for a kinked flaperon versus a rounded tab.

Exit surveys and detailed leading edge pressure instrumentation would be desirable to develop a fuller understanding of flaperons.

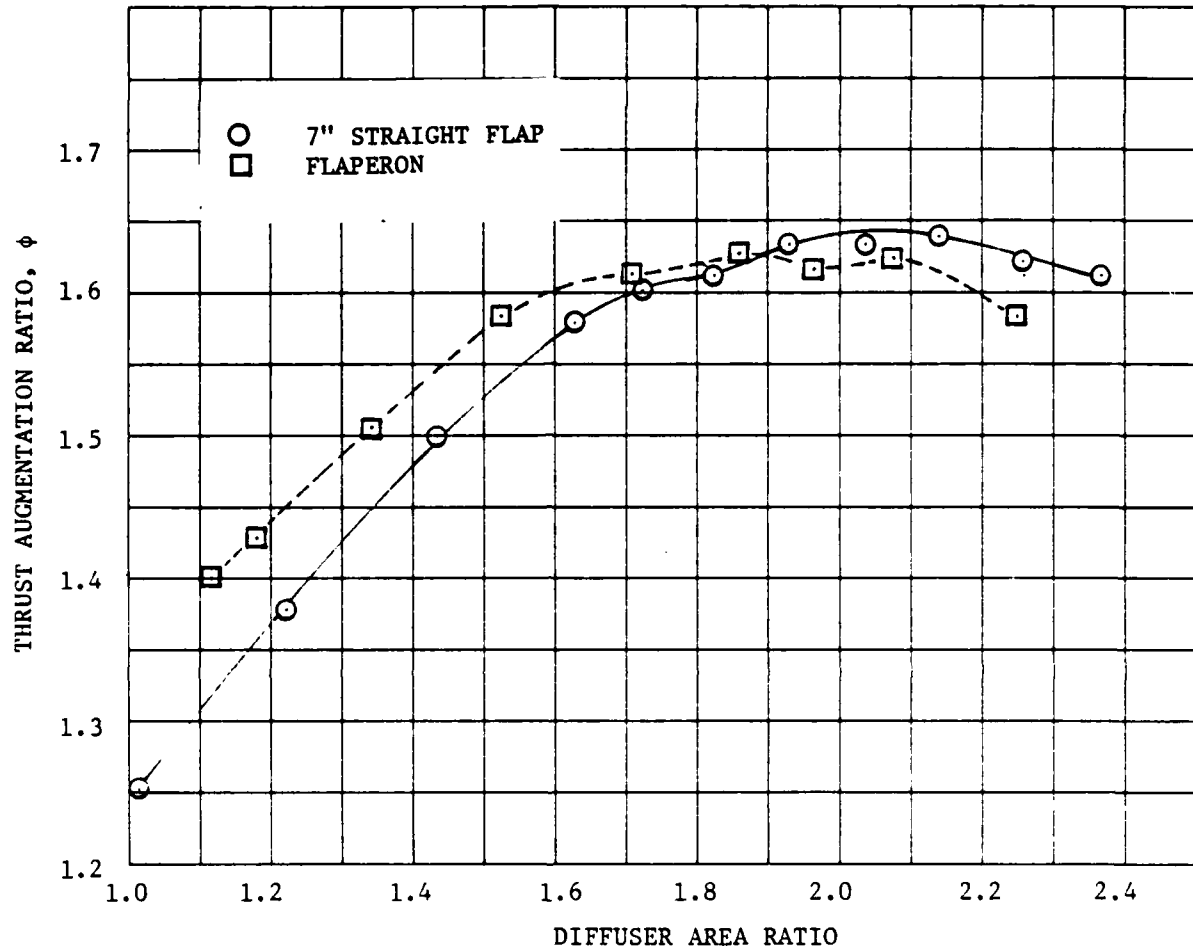


Figure 8-20 Comparison of Thrust Augmentation for the Straight Flap and Flaperon Configuration

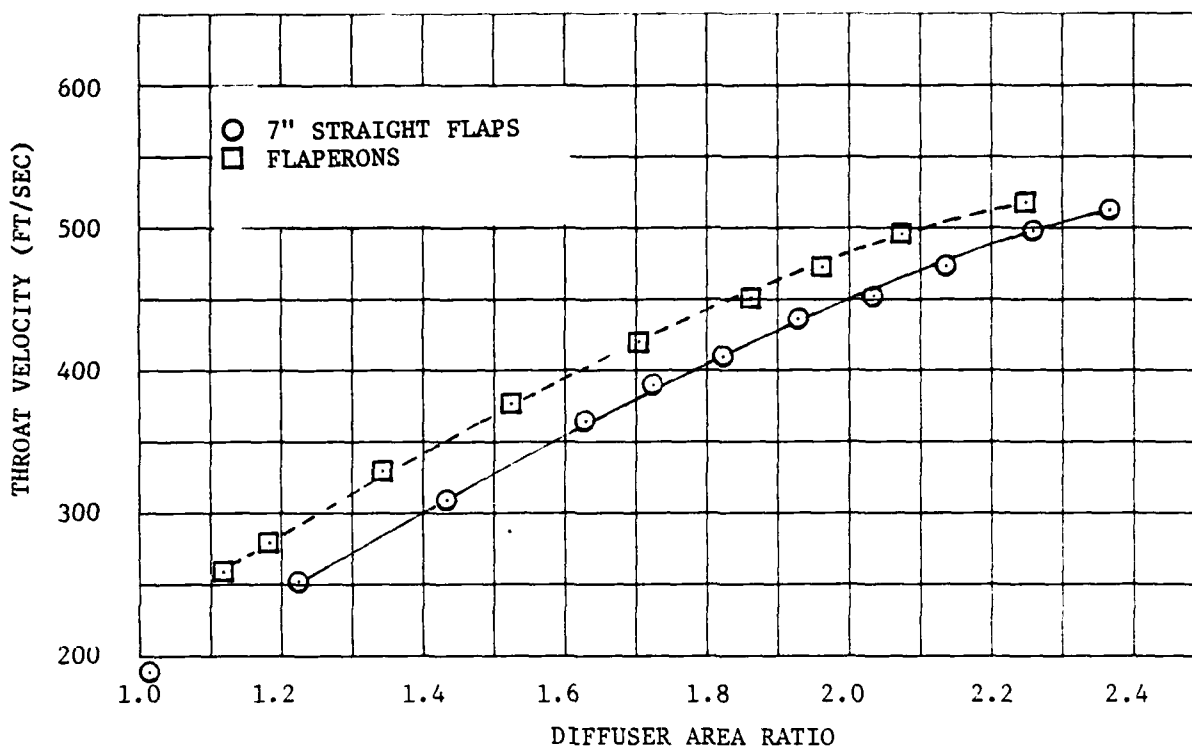


Figure 8-21 Comparison of Throat Velocity for the Straight Flap and Flaperon Configuration

#### 8.7 BOATTAIL ANGLE EFFECTS

Increases in the boattail angle of the centerbody nozzle result in increased internal plenum area and a possible reduction in internal flow losses. However, external flow separation or reduced inlet efficiency may result. Therefore, an experimental investigation was conducted to determine the effect of centerbody nozzle boattail angle on ejector performance.

Three scale model centerbodies with boattail angles of  $30^\circ$ ,  $40^\circ$ , and  $50^\circ$  were built and tested. The centerbodies were identical except for boattail angle. The results of the test are shown in Figure 8-22 as thrust augmentation versus diffuser area ratio. It can be seen that boattail angle in the range tested had no effect on thrust augmentation. Therefore, an improvement in full-scale plenum efficiency could be obtained with increased boattail angle without a performance reduction.

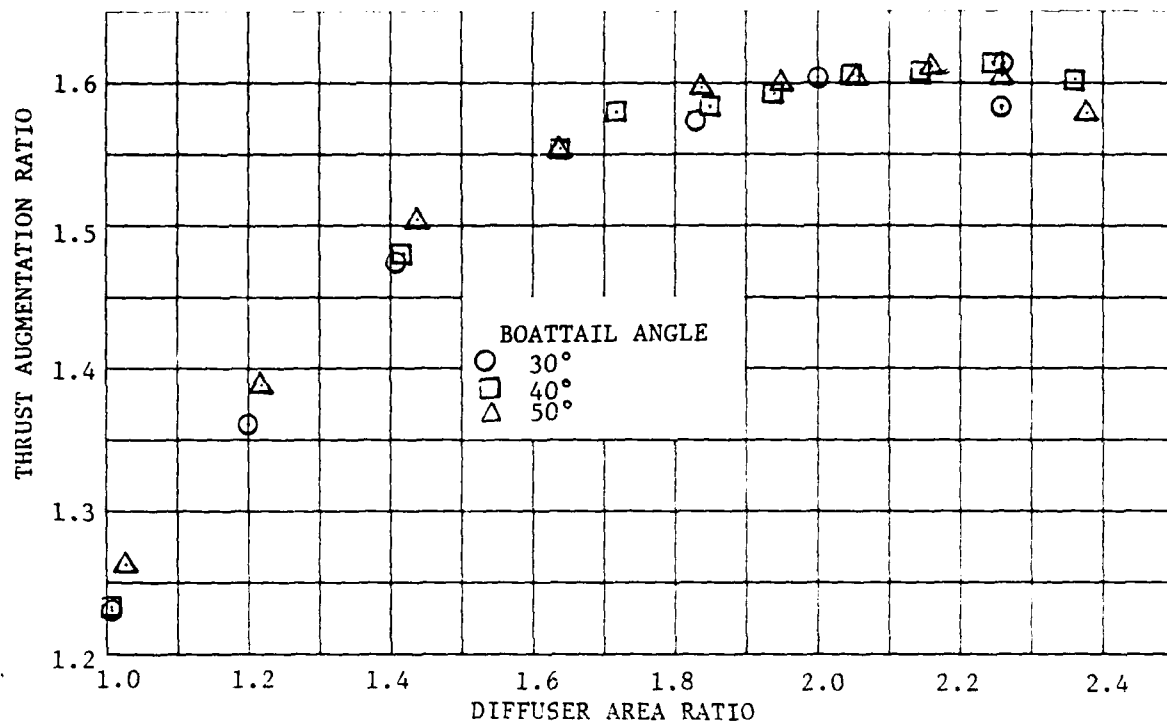


Figure 8-22 Effect of Boattail Angle on Thrust Augmentation

#### 8.8 SUMMARY

An experimental and analytical study of shroud parameter effects on ejector performance show the following: improvement in augmentation ratio with longer shrouds are the result of more effective diffuser mixing; modest asymmetries of ejector flap lengths do not degrade augmentation ratio; local areas of separation and reattachment have been identified for a XFV-12A type ejector; and flaperons are an effective method of increasing shroud circulation lift until onset of separation. In addition, a potential flow solution to predict shroud surface pressures has been developed and gives results that compare favorably with experimental data.



## 9.0 FULL SCALE COMPONENTS

9.1 INTRODUCTION

Results of the Langley hover testing of the XTV-12 indicated that the lack of expected performance of the augmenters could be traceable to deficiencies in individual augmentor components, that is, diffuser, elevon, centerbody, and endwall blowers. An evaluation and improvement program was inaugurated to identify the deficiencies of each component and incorporate whatever improvements would be considered necessary or beneficial. The improvements to be made would come from the existing augmentor data base, as well as any necessary analytical evaluations, scale or full size testing of hardware.

Results of the testing of full scale components will be the topic of discussion in this section of the report. The extent of full scale hardware testing included: evaluation of the Proto 1 existing left hand diffuser, elevon, and endwall blowers in the North American Aircraft Division Columbus plant's Thermodynamics Lab, evaluation of the Proto 1 L/H elevon at a facility at Wright-Patterson Air Force Base, evaluation of the modified improved L/H elevon at WPAFB, and evaluation of improved endwall blowers in North American Aircraft Division, Columbus plant, Thermodynamics Lab.

Additional full scale Coanda development testing was done at WPAFB on a Coanda segment model, and the results of that testing is discussed in Section 6.0 (Coanda Development) of this document. The testing facilities for both the WPAFB test site and North American Aircraft Division, Columbus plant, Thermodynamics Lab are described in Section 10.0 of this report.

9.2 PROTO 1

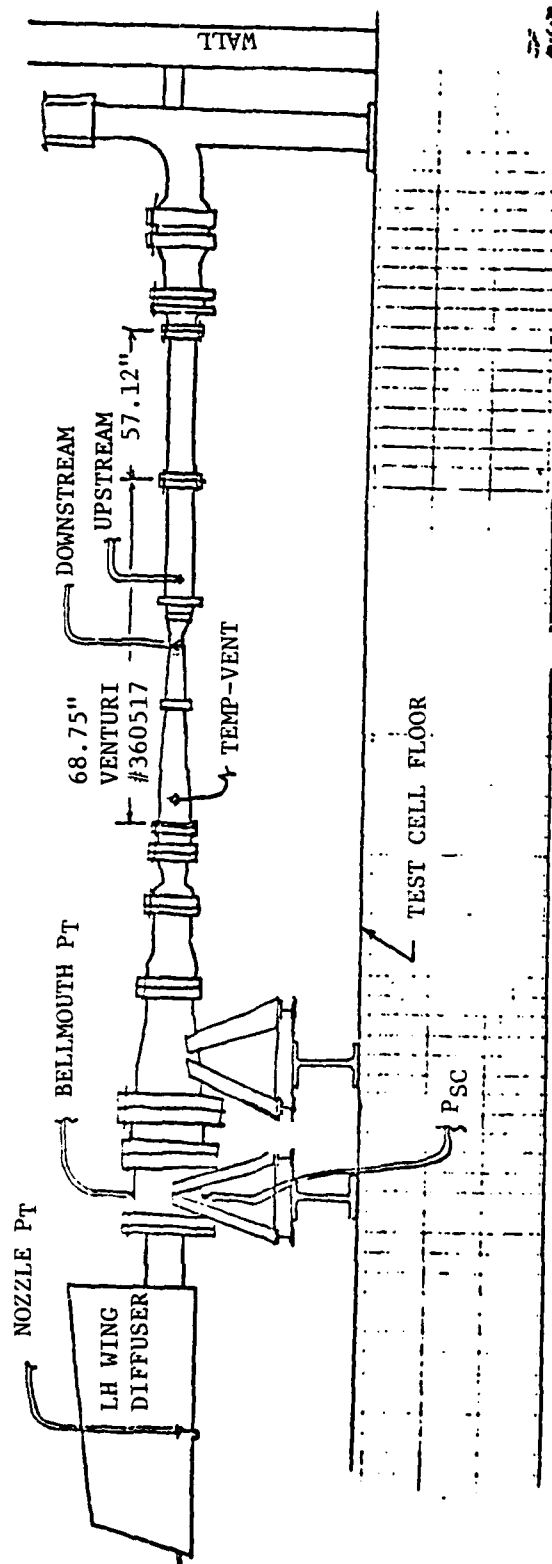
The evaluation test of the L/H Proto 1 wing components after the Langley hover testing has previously been reported in Reference (33) and will be summarized here.

9.2.1 Diffuser

The L/H wing diffuser was tested in the North American Aircraft Division, Columbus plant, Thermo Lab to obtain the following information:

- a. Nozzle coefficients
- b. Nozzle gaps actual
- c. Nozzle gap expansion
- d. Spanwise nozzle total pressure distributions
- e. Chordwise jet profiles at the nozzle and downstream
- f. Visual indications of flow quality and angularity

The Thermo Lab test set-up is sketched in Figure 9-1. The inboard and outboard endwalls in the vicinity of the diffuser were simulated by contoured aluminum sheets.



SKETCH OF XFV-12A WING COMPONENT

TEST IN THERMO LAB

Figure 9-1.



The nozzle total pressure spanwise survey, shown in Figure 9-2, exhibits the same inboard pattern seen in previous tests with the biggest deficiency inboard, immediately followed by the peak pressure.

The remainder of the survey indicates more uniform spanwise distribution than was indicated in previous tests. The spanwise nozzle pressure distributions were made at nozzle pressure ratios of 1.8, 1.6, 1.5, and 1.2 and were relatively independent of NPR.

Chordwise total pressure profiles were obtained at the nozzle, and at 10t, 20t, and 50t from the nozzle, and also at the trailing edge of the flap. These jet profiles were made at five selected span stations which were located as shown in Figure 9-3. A typical set of profiles is illustrated in Figure 9-4, and a plot of all the measurements is presented in Figure 9-5 in the form of jet peak pressure normalized with nozzle exit pressure (CTE) versus span station. At the three midspan locations, the profiles indicate satisfactory flow to the trailing edge, however, the inboard and outboard pressure profiles reflect the disturbed flow at these locations. The efficiency at 10t appears to be slightly less than had been seen in previous tests. At the outboard span station (107") the efficiencies reflect the hinged triangular panel (see Figures 9-3 and 9-7), which was inclined into the flow for these tests simulating its position on the aircraft.

Flow quality and angularity were investigated using a hand held tuft as a flow visualization aid. Figures 9-6 and 9-7 are photographs of the results. The two inboard surveys show the most outboard spanwise location where steady corner flow was obtained and the most inboard location where steady chordwise flow was obtained. The two outboard surveys likewise indicate the steady flow boundaries. Notes that the disturbed flow region outboard is approximately six inches wide.

Nozzle gap expansion under pressure with cold flow was measured using five linear potentiometers installed at five spanwise locations as shown in Figure 9-8. Results of three runs with the gages installed is presented in Figure 9-9. It can be seen that out to midspan, gap expansion approached four percent at a nozzle pressure ratio of 1.84:1. Outboard the expansion is on the order of one percent. The nozzle gap versus span was also measured without pressure and this data compared to design values is presented in Figure 9-10.

Leakage was investigated with the airflow system blocked at the upstream end of the Venturi, and a flowmeter for low flows installed. The Coanda nozzles were covered with metal plates, sealed, and then covered with tape. The corner nozzles were plugged with tapered wood plugs, sealed, and taped. Leaks on the flap surface appeared to be small. Several leaks in the interface region were identified. A leakage area of 0.46 sq. in. was determined for the diffuser and the flow measurement system. This area was used in determining the nozzle area coefficients presented in Figure 9-11. The leakage area of the wing diffuser itself was approximately 0.24 sq. in.

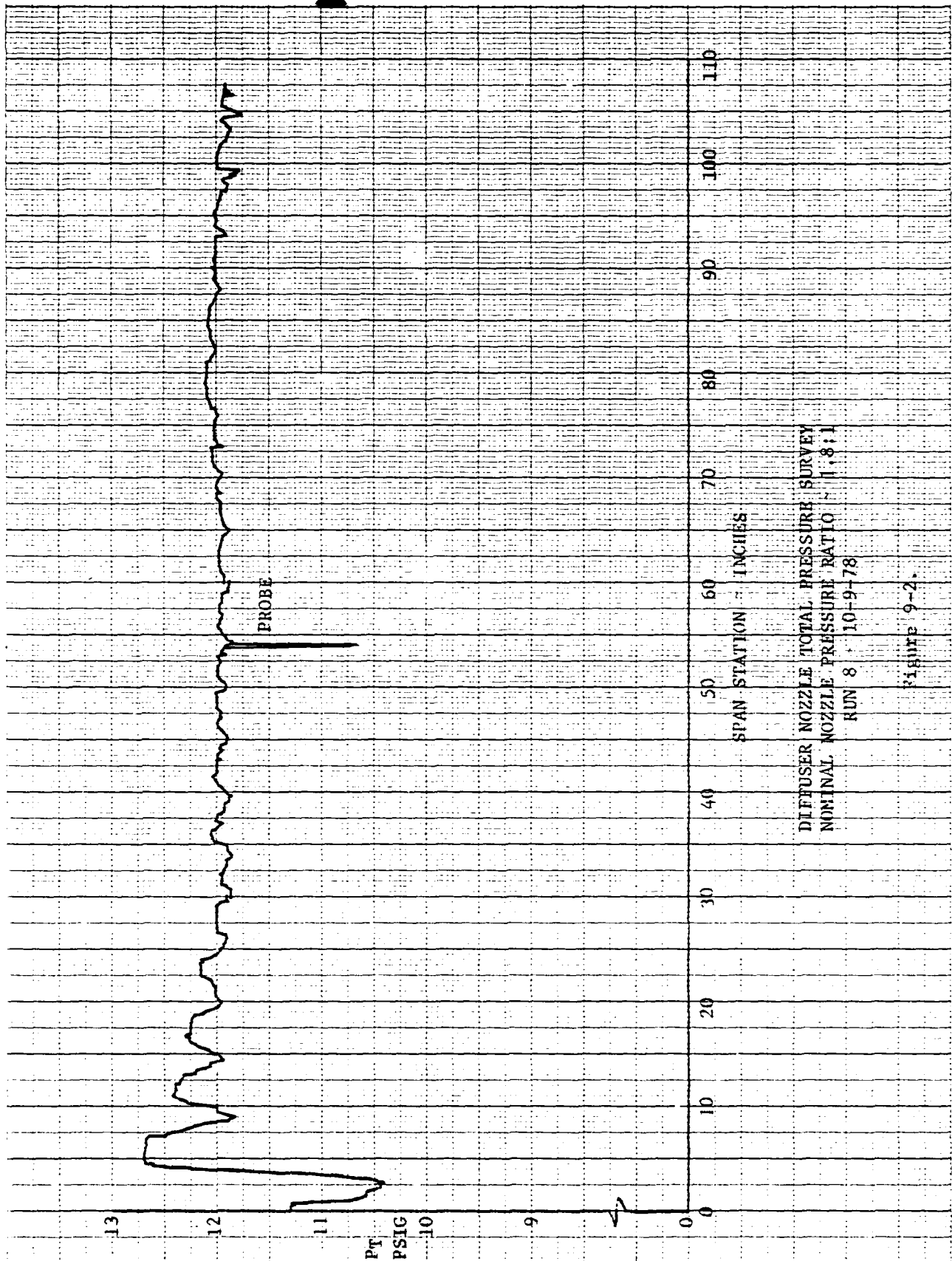


Figure 9-2.





PRESSURE PROFILE LOCATIONS  
PROTO 1 L/H WING DIFFUSER

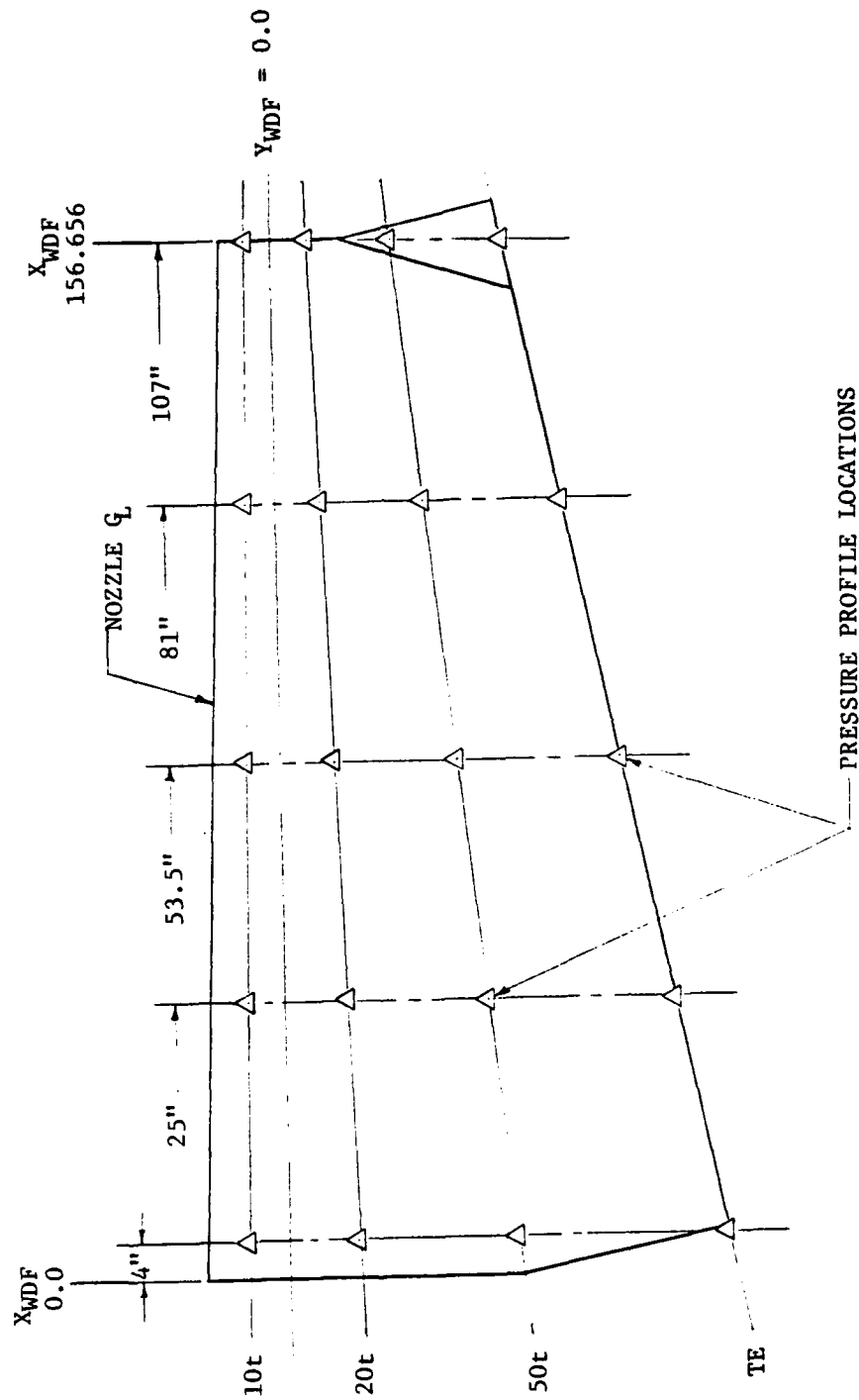


Figure 9-3.

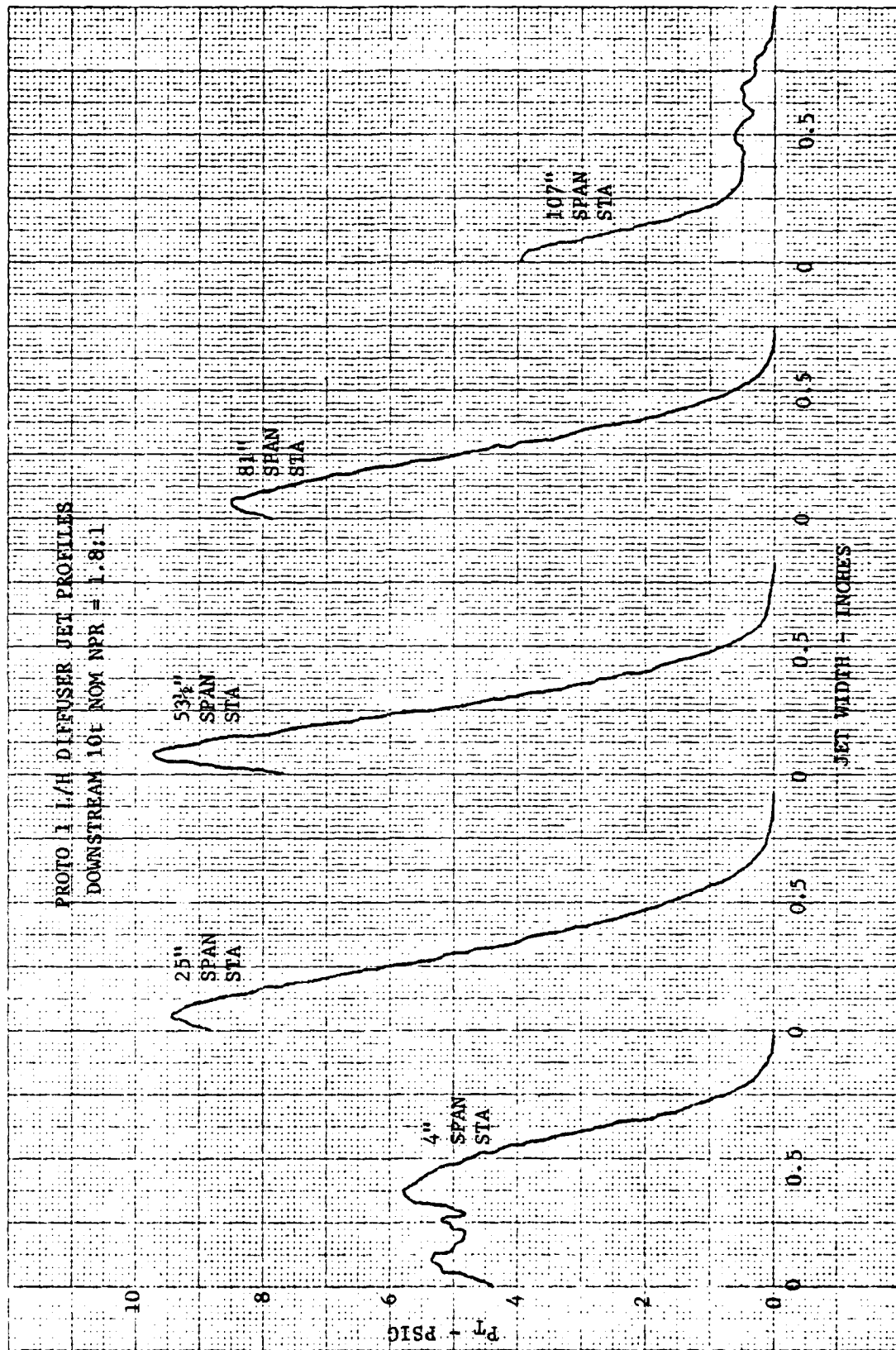


Figure 9-4.



Rockwell International

40120

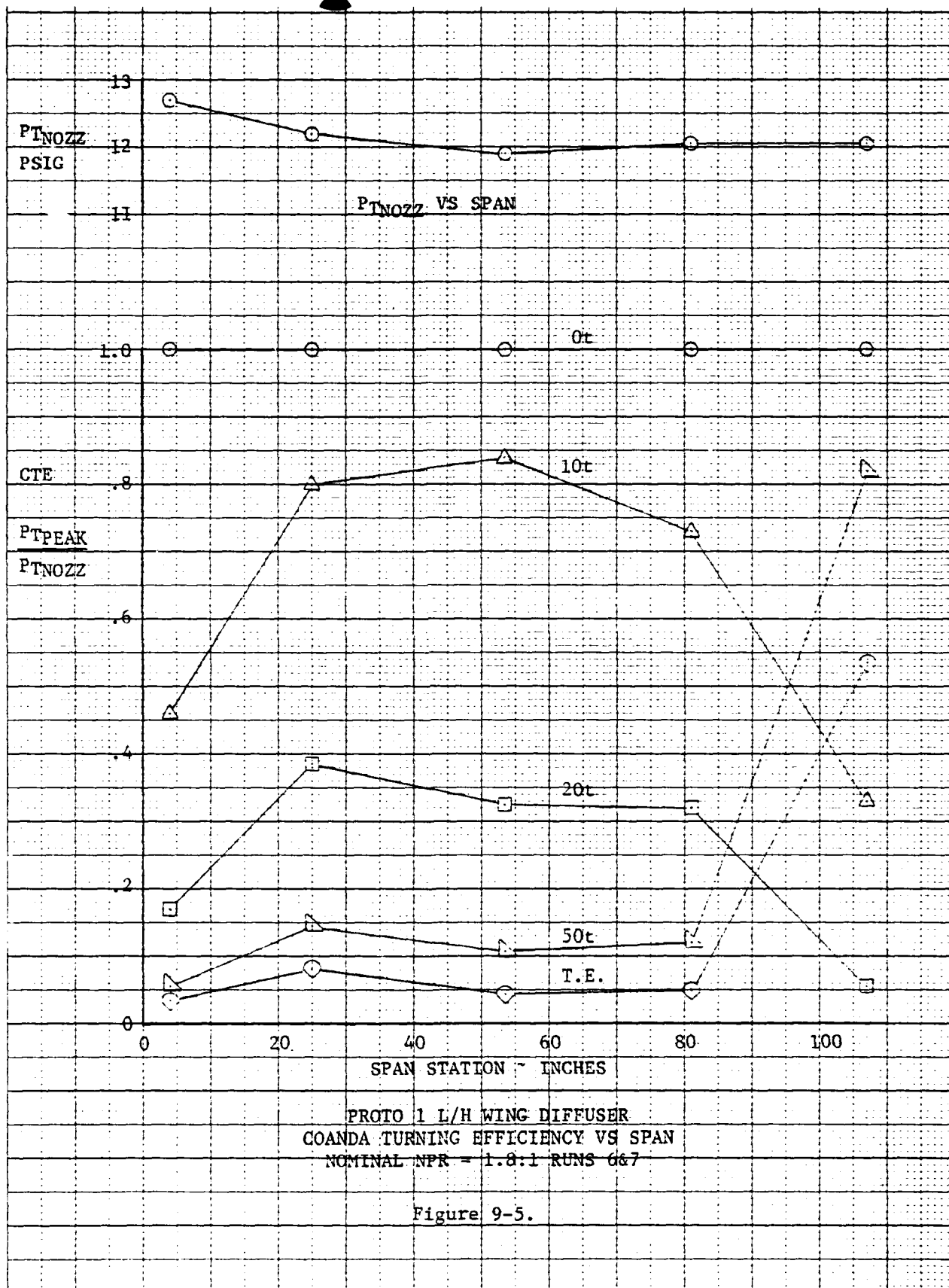
 1/2" MAX TO 1" INCH  
 1/2" MAX TO 1" INCH


Figure 9-5.



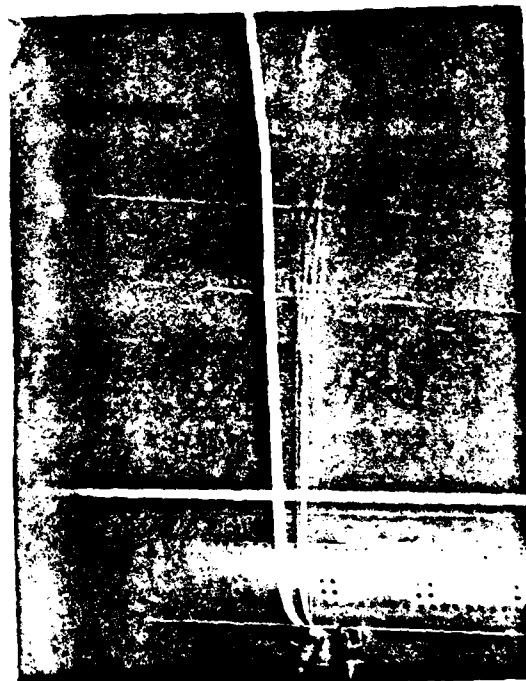
(a) Inboard Corner



(b) Near Inboard Corner

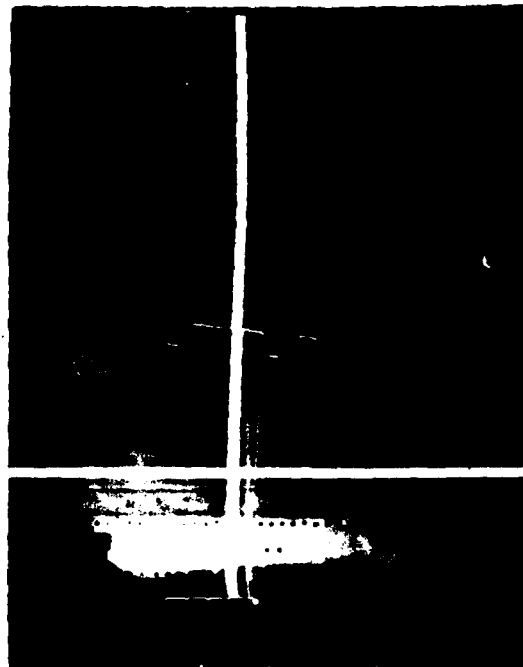


(c) 26" Outboard

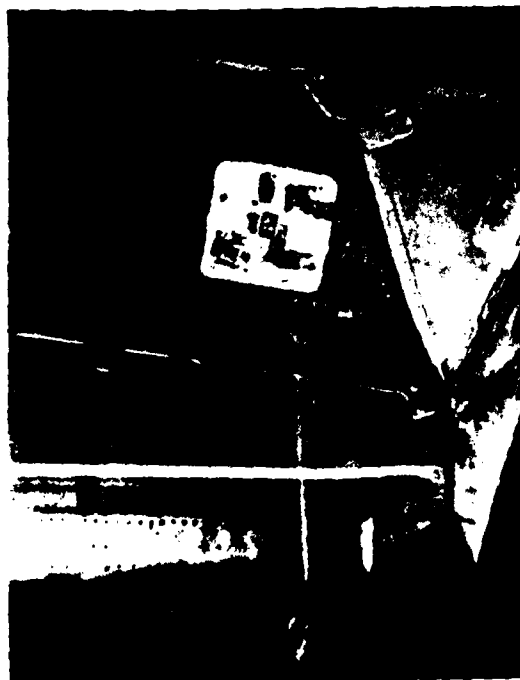


(d) 54" Outboard

Figure 9-6.  
Flow Visualization



(e) 81" Outboard



(f) 100" Outboard



(g) Outboard Corner

Figure 9-7.  
Flow Visualization

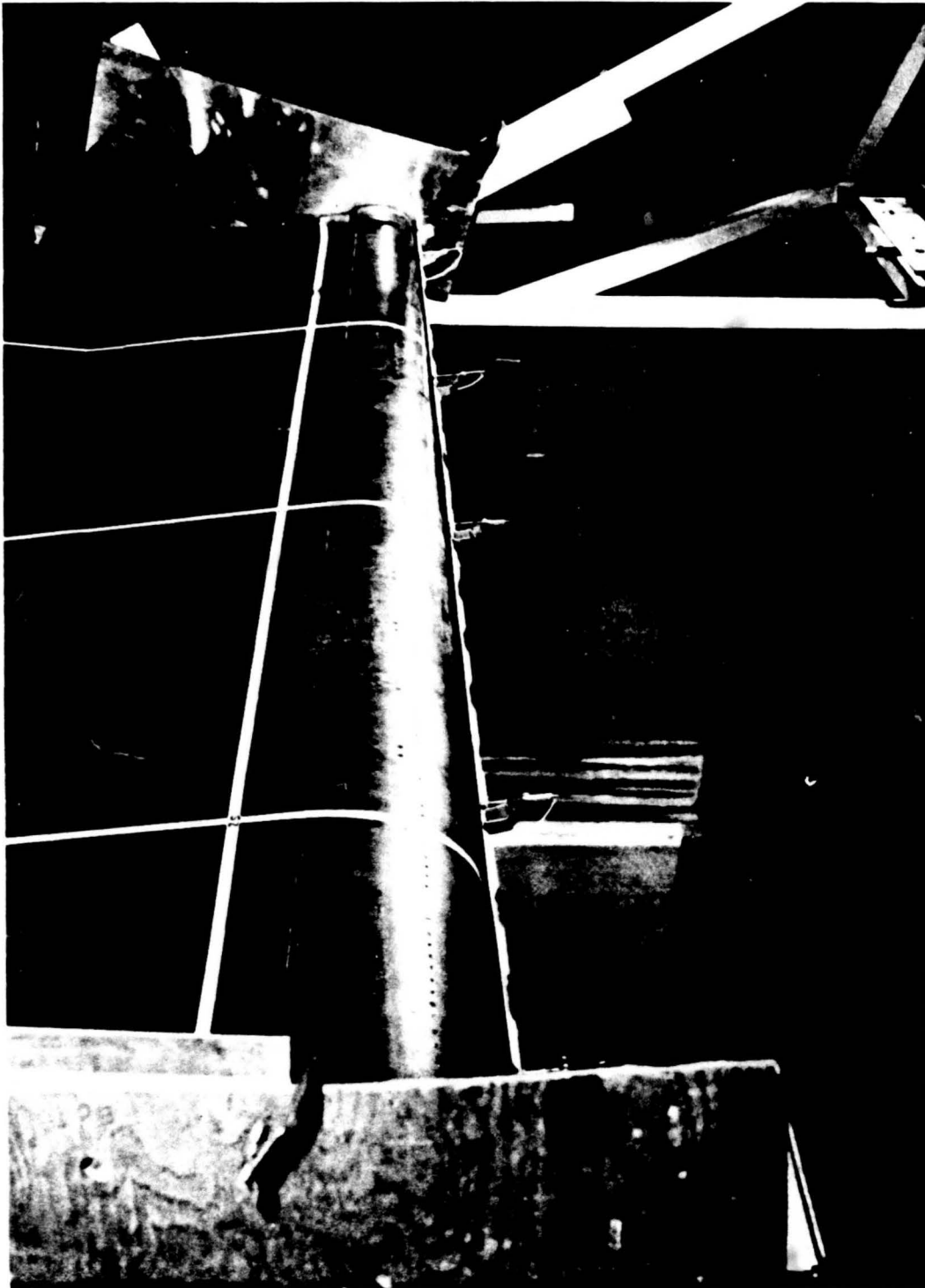
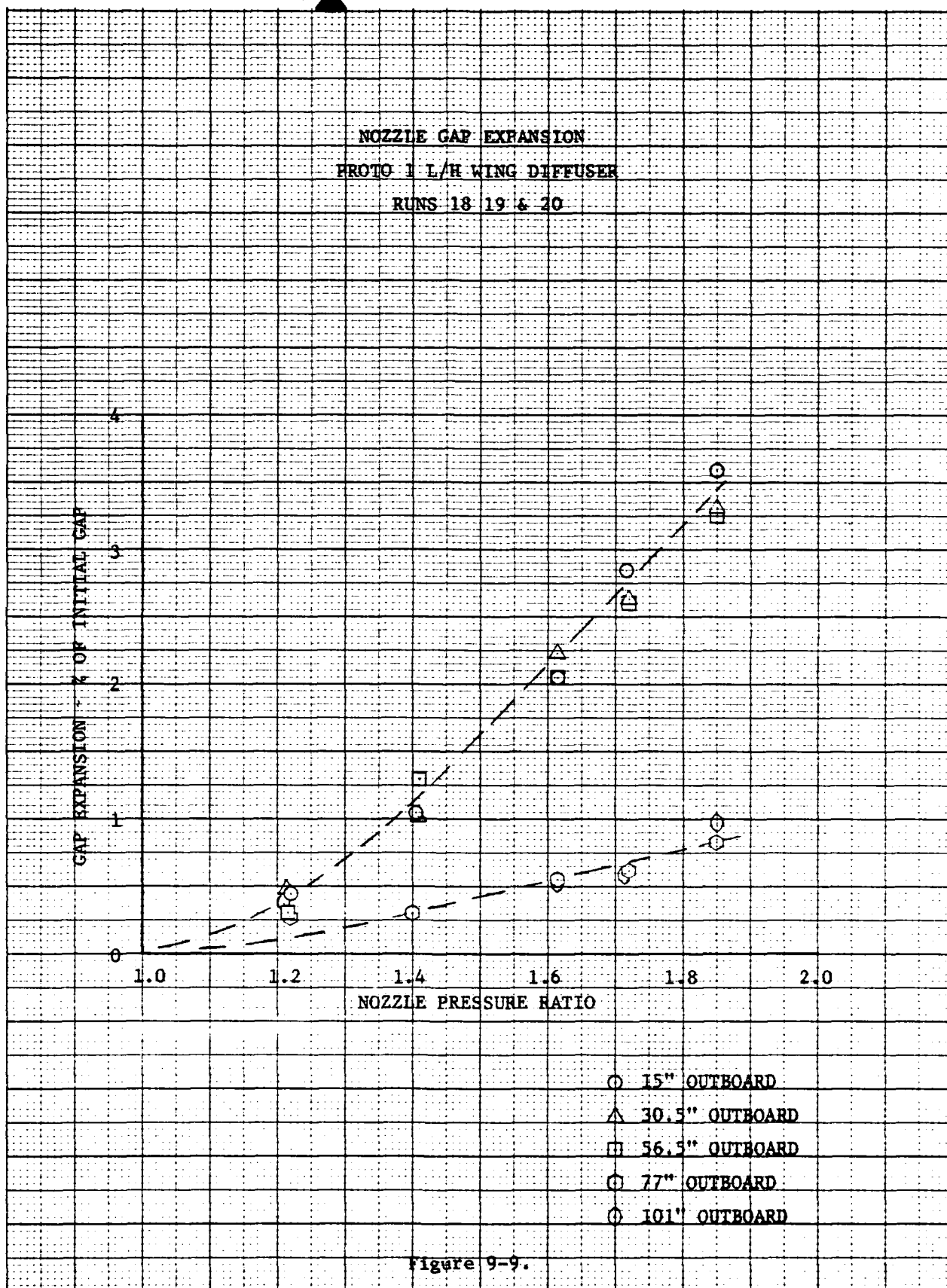


Figure 9-8. Nozzle Expansion "Pots" - Installation on Wing Diffuser



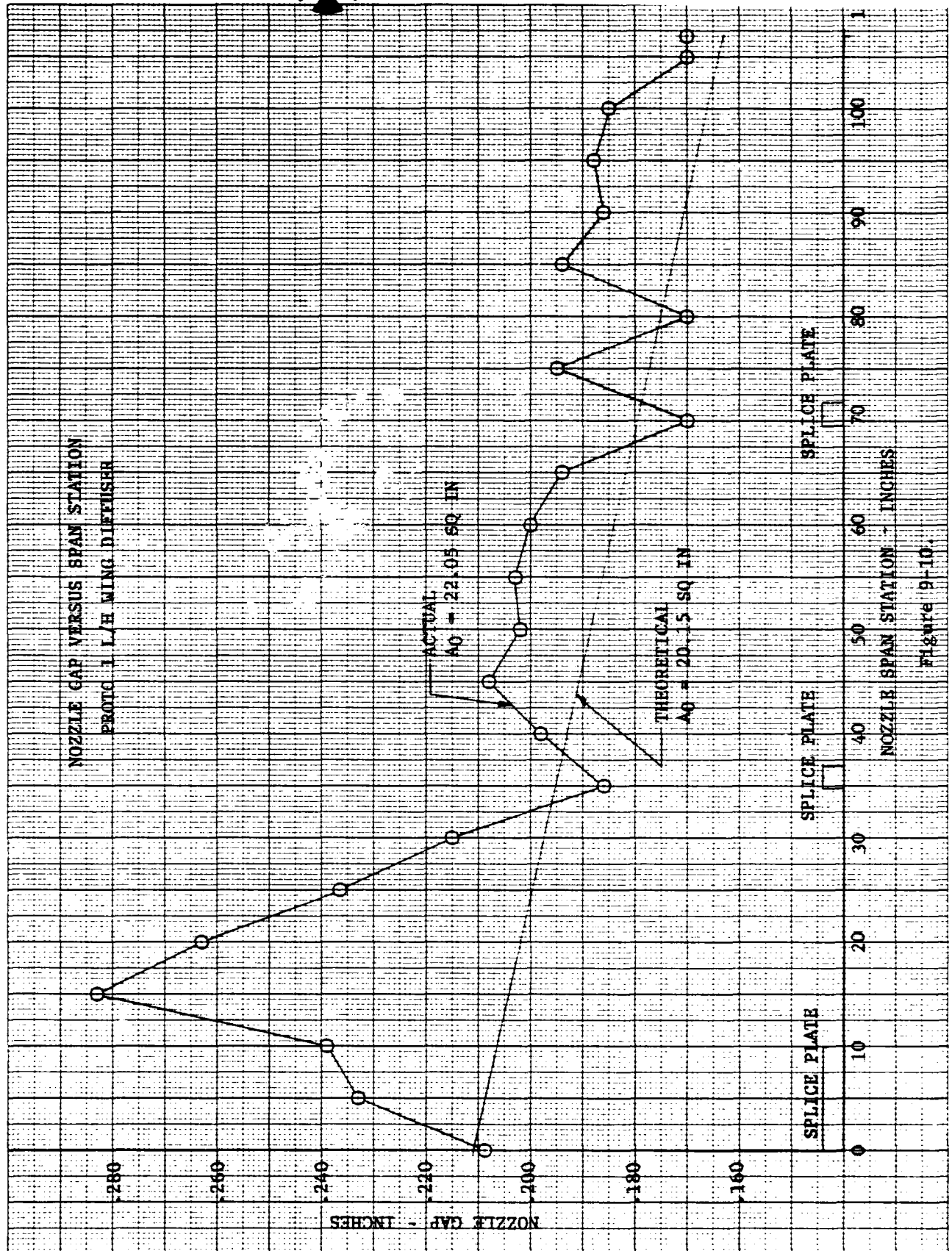
Rockwell International





Rockwell International

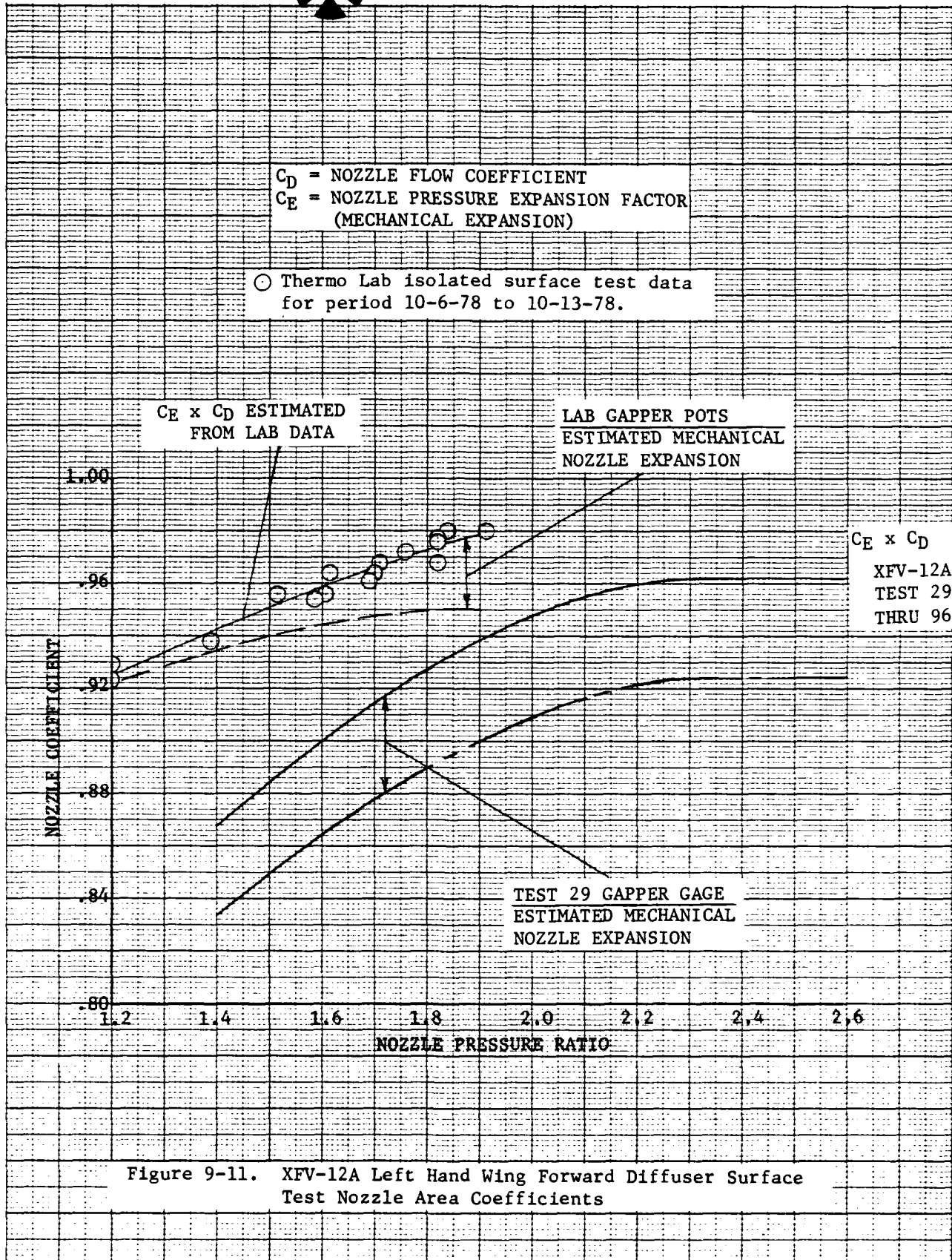
46 1510

 K-2 10 X 10 TO THE CENTIMETER 10 X 10 CM  
 KEUFFEL & ESSER CO. MADE IN U.S.A.






Rockwell International





### 9.2.2 Elevon

The Proto 1 L/H elevon was also tested in a similar manner as the diffuser utilizing the same test set-up (Figure 9-1). The inboard and outboard endwalls immediately adjacent to the elevon were simulated by flat aluminum sheets.

The nozzle total pressure spanwise survey presented in Figure 9-12 exhibits the same pattern inboard as indicated in previous tests. The lowest nozzle pressure inboard coincides with the outboard corner of the inboard corner blower, then recovers to a level approximately equal to average nozzle pressure in about eight inches. From this point outward, the pressure distribution is relatively uniform as seen in previous elevon tests. As had been found with the diffuser, the spanwise elevon nozzle pressure distribution was relatively insensitive to nozzle pressure ratio. Note that the bolt indicated in Figure 9-12 is a stray bolt which had become lodged in the nozzle, and as it did not interfere with test objectives, no attempt was made to remove it for these tests.

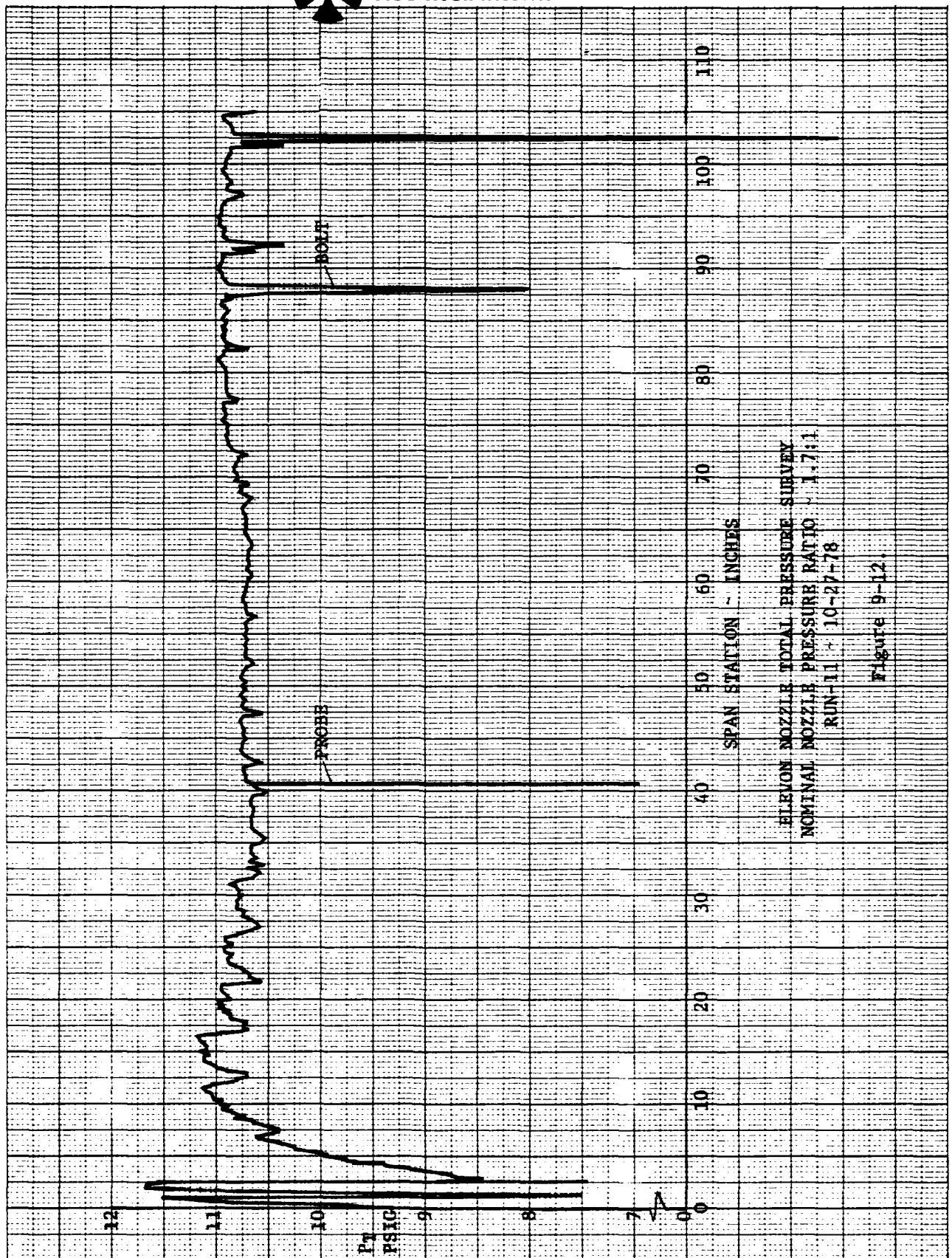
Chordwise total pressure profiles were obtained at the nozzle exit, at 10t, 20t, 50t from the nozzle, and at the trailing edge, at span stations illustrated in Figure 9-13. Figures 9-14 and 9-15 are examples of the jet profiles obtained at the nozzle and at 10t from the nozzle at a nominal nozzle pressure ratio of 1.6:1. At the nozzle the pressure distribution from surface to lip was less uniform than that noted on the diffuser, especially at the inboard corner, however, considering the complex vane geometry required to turn the flow at the inboard corner, the resulting pressure profile was perhaps as good as could be expected with this design. The results of all the jet profile measurements are summarized in Figure 9-16 in the form of turning efficiency (local peak pressure/nozzle exit pressure) versus span. The low values inboard, downstream of the nozzle exit suggest flow angularity in this region, which can also be seen in the flow visualization photographs in Figure 9-17 and 9-18.

Nozzle gap expansion under pressure was measured using the same linear potentiometers used on the diffuser (see Figure 9-8). Results of these measurements are presented in Figure 9-19 in the form of percent gap expansion with pressure relative to the unpressurized reading for several span stations. Unlike the diffuser, the gap expansion is relatively linear with nozzle pressure ratio and uniform along the span of the nozzle, reaching a value of approximately four percent expansion at the highest nozzle pressure ratio tested (1.82:1). The actual nozzle gaps measured with no pressure versus span are presented in Figure 9-20 and the results compared to the design values.

Leakage was investigated with the airflow system blocked at the upstream end of the six-inch Venturi, and air was supplied through a two-inch Venturi and in turn through the endwall blowing feed pipe. The two inch Venturi was used instead of the low-flow flowmeter used in the leakage test of the diffuser, in order to obtain a wider range of test pressure ratios. The nozzles were sealed in the same manner as the diffuser was, in that the Coanda nozzles were covered with metal plates, sealed, and



Rockwell International



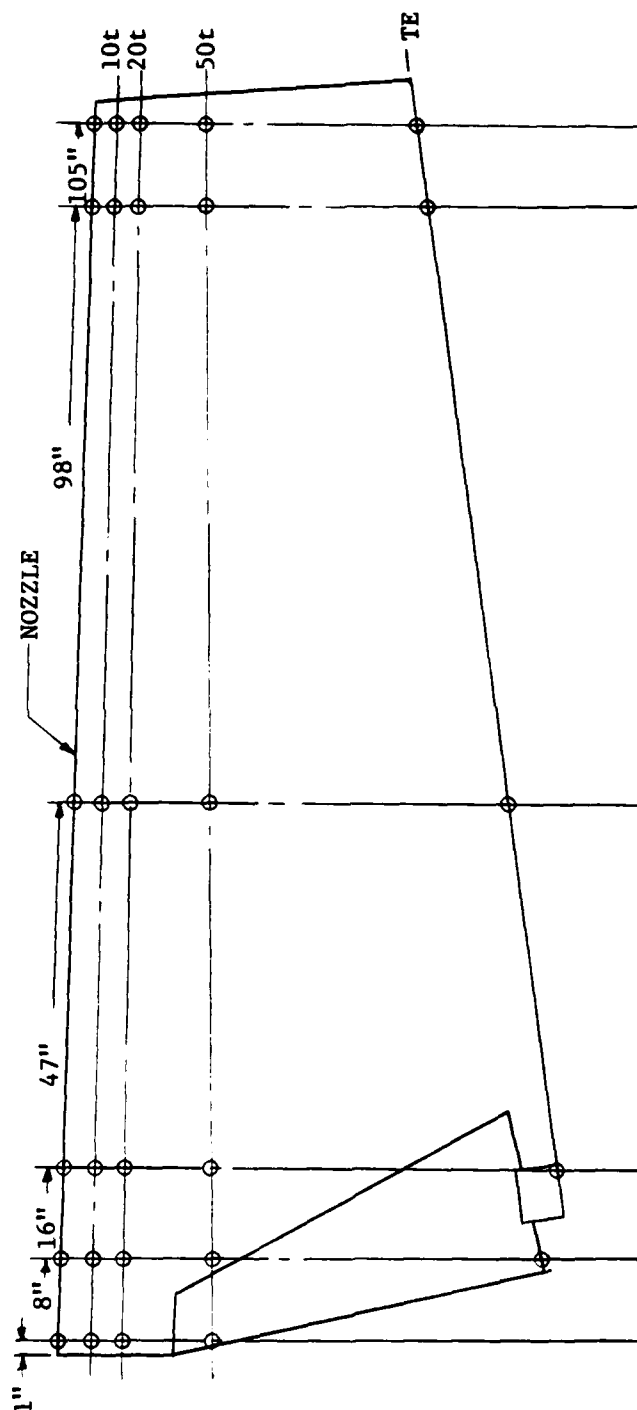


Figure 9-13. Pressure Profile Locations - Proto 1 L/H Wing Elevon

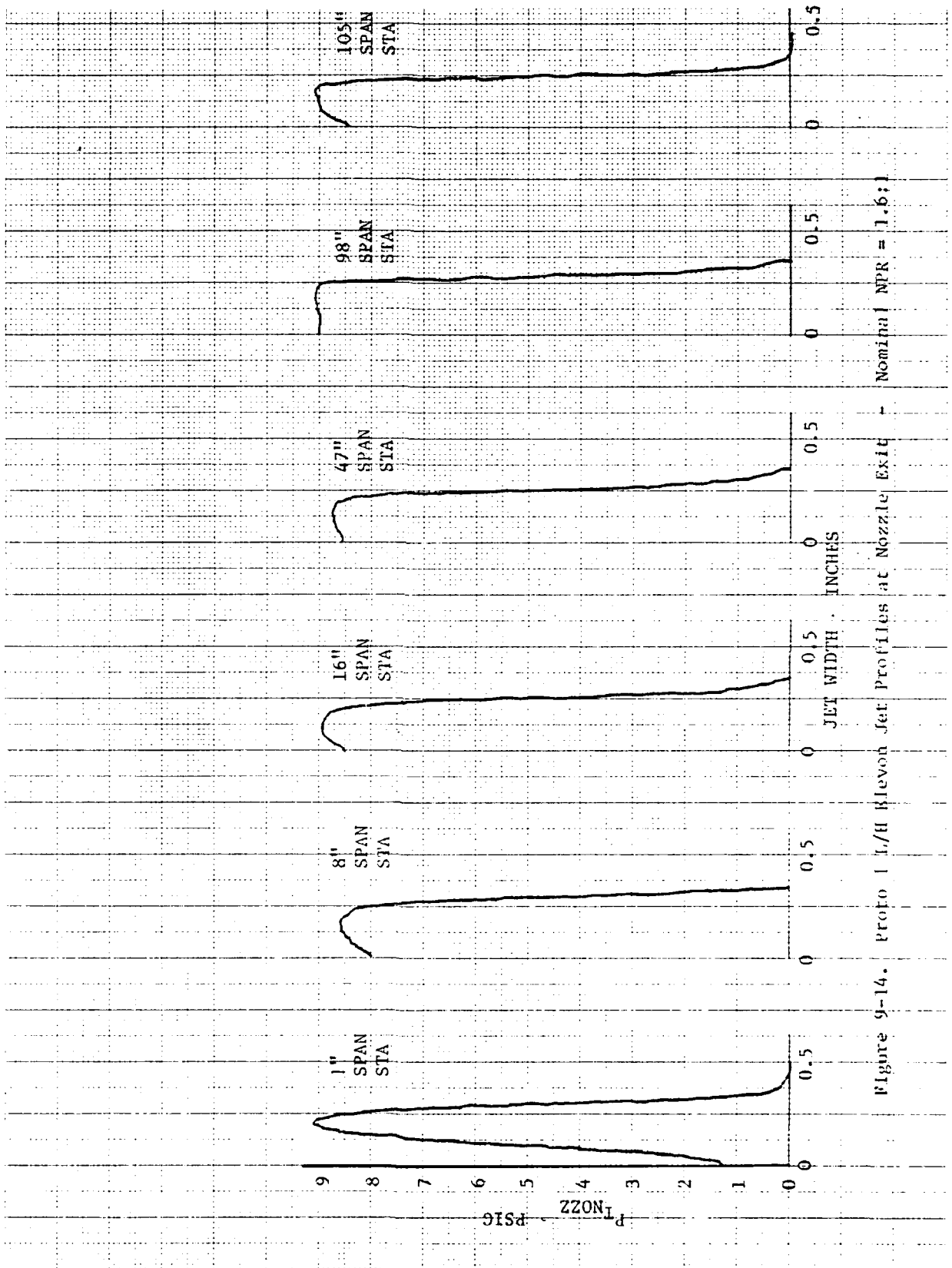


Figure 9-14. Proto 1 L/H Klevon Jet Profiles at Nozzle Exit - Nominal NPR = 1.6:1

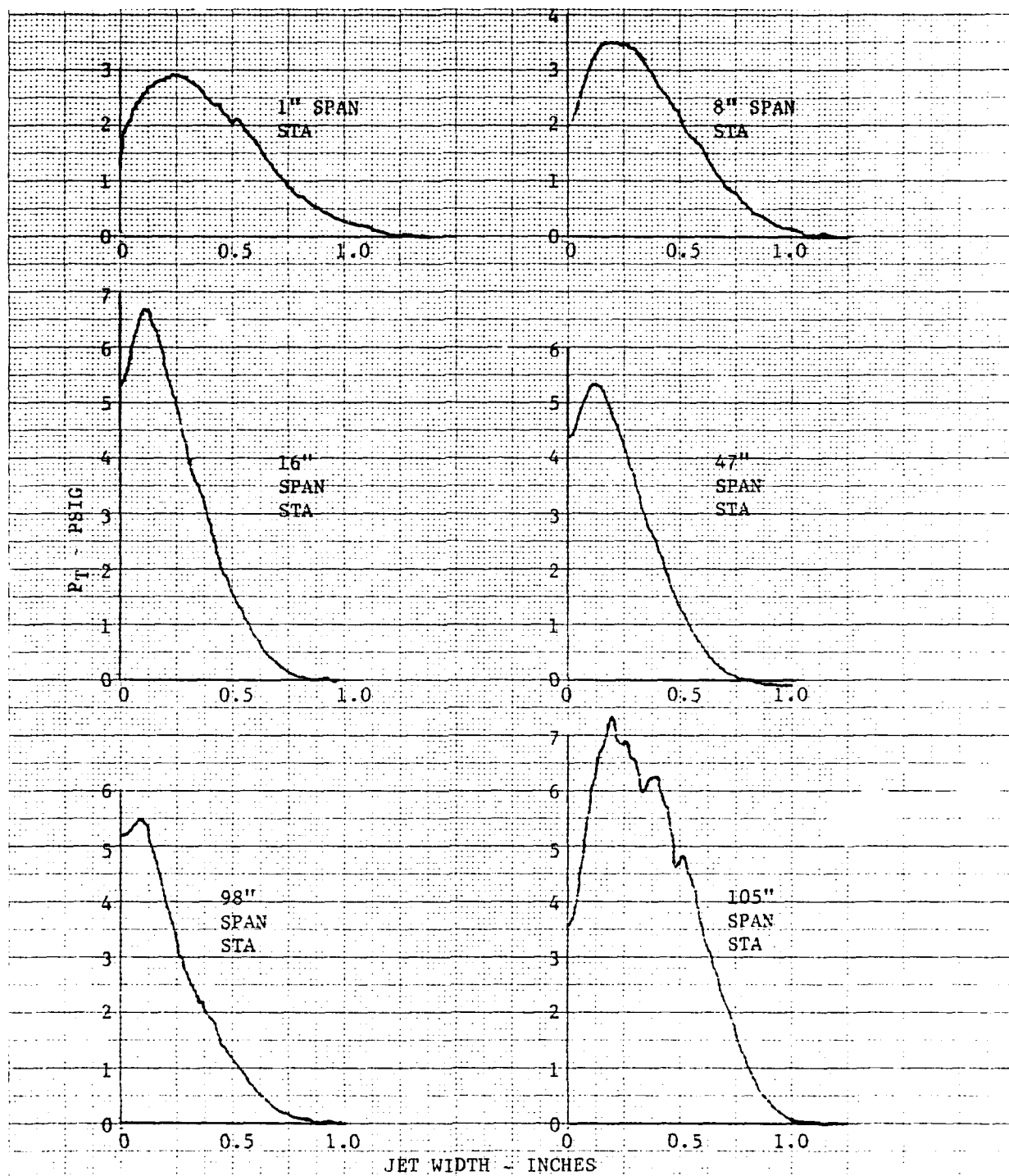


Figure 9-15. Proto 1 L/H Wing Elevon Jet Profiles Downstream 10t  
Nominal NPR 1.6:1

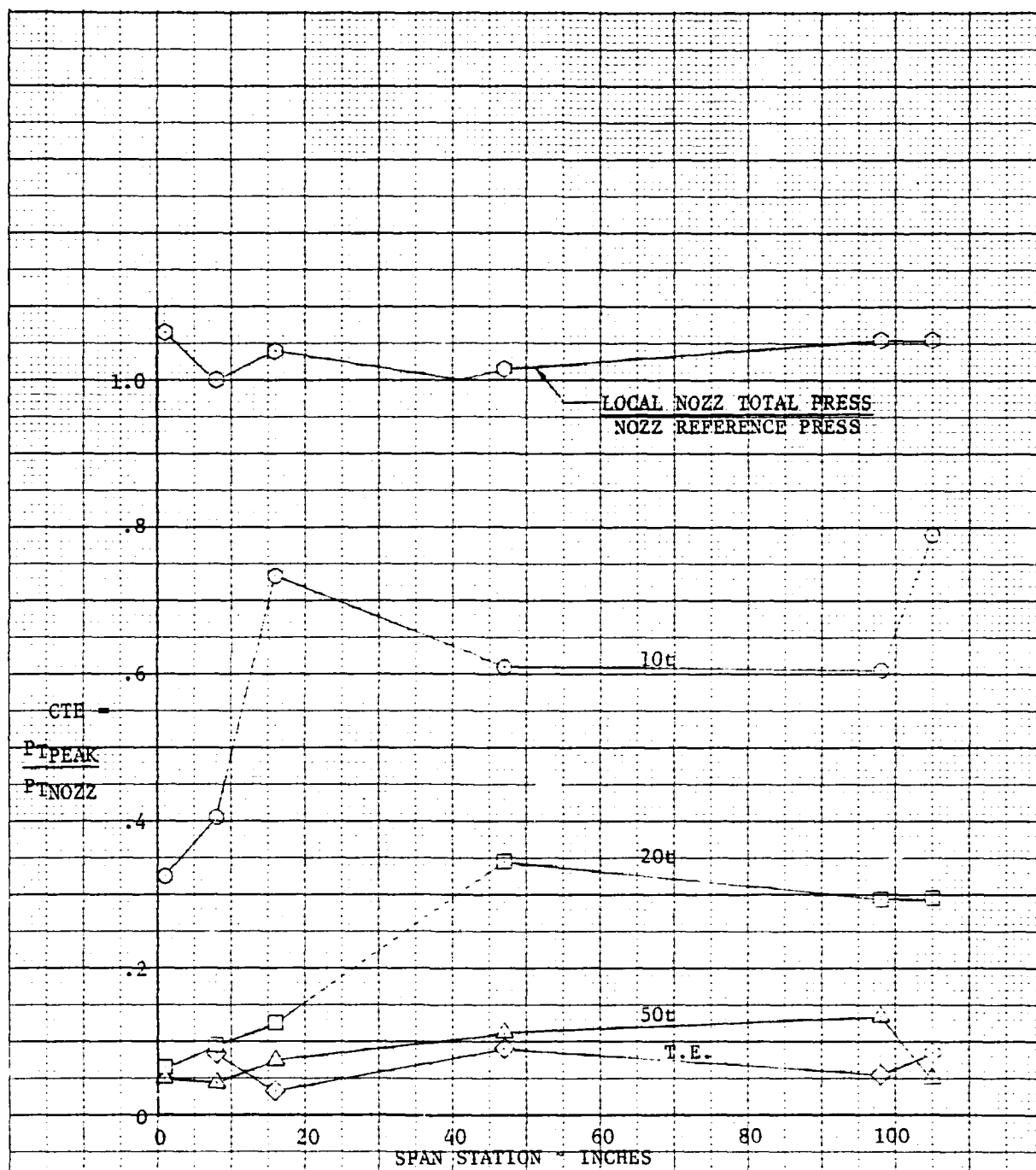


Figure 9-16. Coanda Turning Efficiency Vs Span, Proto 1 L/H Wing Elevon,  
Nominal Pressure Ratio = 1.6:1



Inboard Corner



6" Outboard



8" Outboard



14" Outboard

Figure 9-17.  
Flow Visualization





47" Outboard



98" Outboard



102" Outboard



Outboard Corner

Figure 9-18.  
Flow Visualization  
9-21

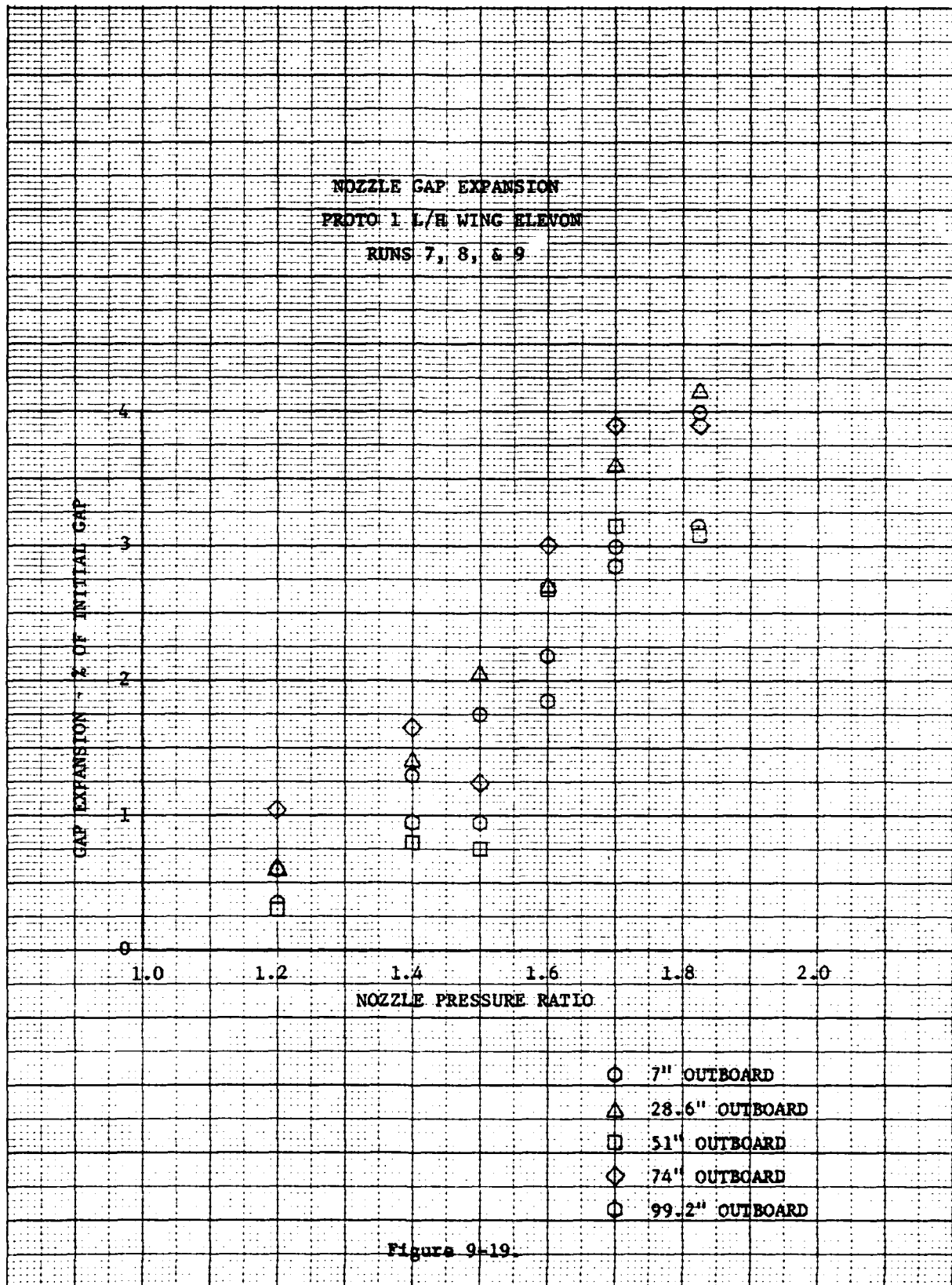
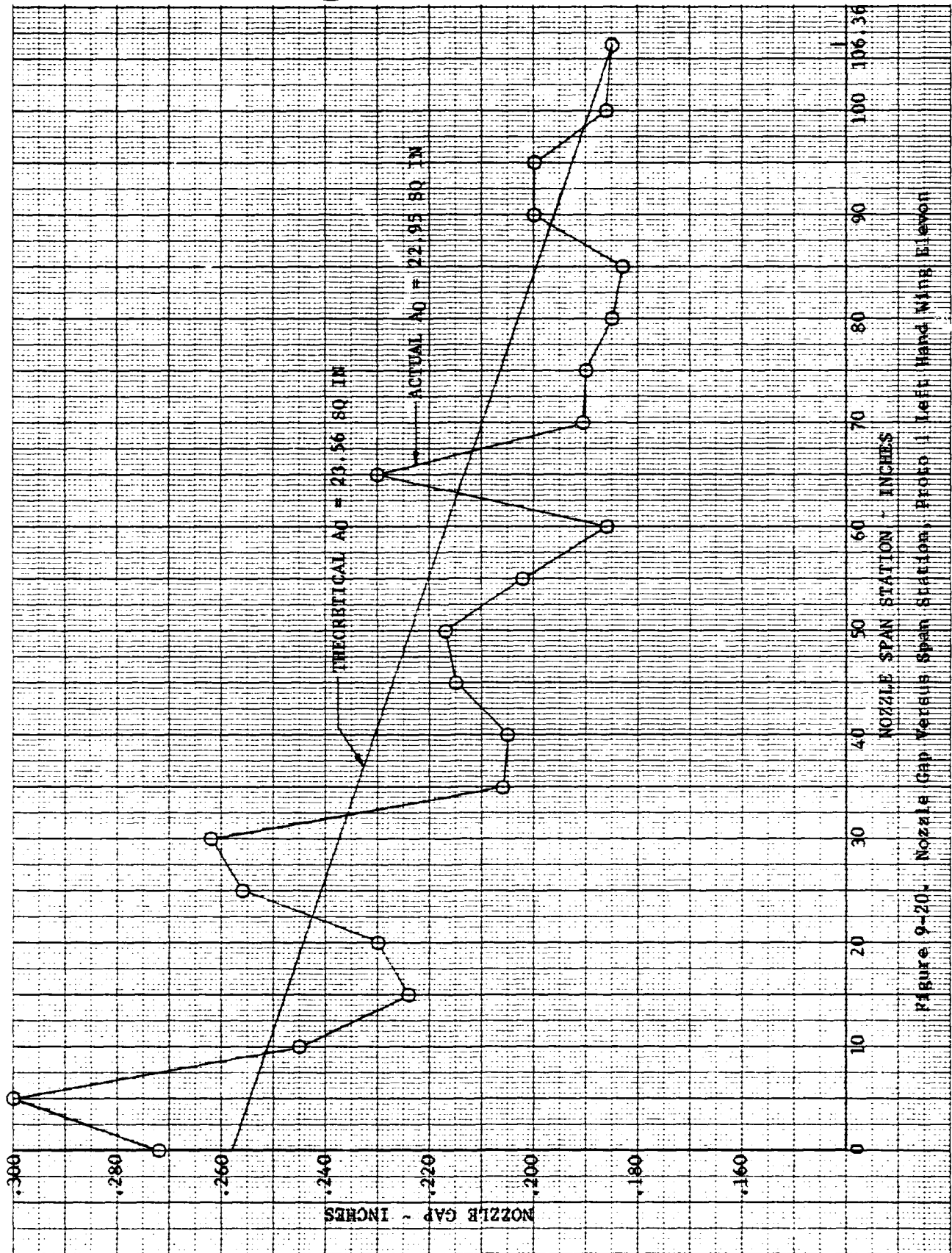


Figure 9-19.





covered with tape. Leaks on the flap surface appeared to be minor. Leakage from under the upstream edge of the inboard corner blower hood was quite apparent. With the nozzle unplugged, such leakage would tend to be less, however, any leakage flow in this region tends to act against the Coanda nozzle flow. Such flow, and the edge of the hood itself, are adverse to improving corner flow. Leakage at the inboard and outboard edges of the elevon was quite apparent.

From the measurements an equivalent leakage area of 0.75 sq. in. was determined for the elevon and the flow measurement system. This area was used in determining the nozzle area coefficients presented in Figure 9-21. The leakage area of the wing elevon itself is approximately 0.53 sq. in., twice that of the wing diffuser. The overall nozzle coefficient presented in Figure 9-21, which takes into account the combined effect of the discharge characteristics of the nozzle, leakage, and nozzle area change, is within two percent of previous lab test results. With the nozzle expansion contribution isolated, the nozzle flow coefficient is seen to be less than unity as expected at pressure ratios of interest. The typical flat characteristic of the overall coefficient with pressure ratio likewise echoes previous lab test results.

### 9.2.3 Isolated Wing Endwall Blowing Nozzle Tests

The inboard and outboard wing endwall blowing nozzles which were part of the aircraft configuration tested at NASA Langley were tested as isolated components in the Thermodynamics Laboratory in order to verify the nozzle coefficients used in the Langley performance computations and to determine areas of potential improvement. As a consequence of these initial tests, design modifications were tested. Results of these additional tests indicated that improved flow characteristics were obtained with the modified inboard and outboard nozzles. Recommendations for further improvement had been made at the time testing was suspended. Further testing was deferred when the ongoing aircraft design studies being conducted in parallel indicated that the simpler augmentor concept developed would in turn enable simpler, more efficient endwall blowing nozzles to be incorporated in the revised augmentor design. The lessons learned in these tests, however, are generic to the design of any endwall blowing system.

9.2.3.1 Outboard Endwall Blowing Tests - Initial tests were conducted with the basic design, a straight Coanda slot nozzle, and with a hood added to the basic nozzle. The hood was added in the course of the tests at NASA Langley to direct more flow aft. The results of these lab tests, both with and without the hood, indicated that flow coefficients were similar to those used at Langley, and while flow directly downstream of the nozzle was satisfactory, flow in the fore and aft corners, formed by the diffuser flap and elevon, respectively, was unsatisfactory. Based on both pressure surveys and flow visualization, flow in the elevon corner was essentially non-existent.

To improve flow in the corners, the straight nozzle was replaced by one in which the ends of the straight nozzle were canted to point to the forward and aft corners. Nozzle geometry is presented in Figure 9-22.

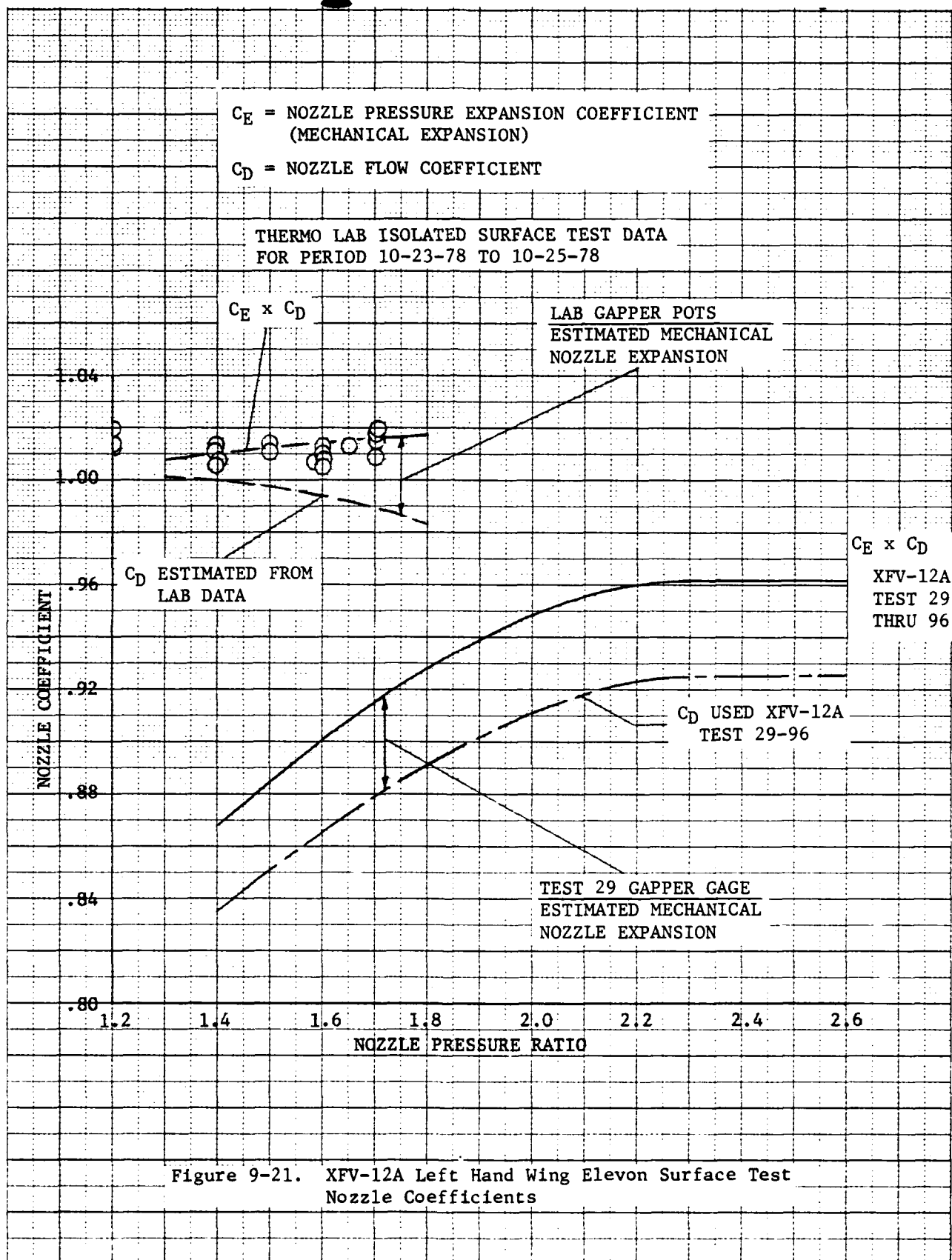


Figure 9-21. XFV-12A Left Hand Wing Elevon Surface Test  
Nozzle Coefficients



	PRIMARY	AUXILIARY SLOT	EXTENDED ELEVON
TOTAL LENGTH (IN.)	9.81	0.75	1.31
AVG GAP (IN.)	0.205	0.255	0.155
✕ TO $q_L$ ⊥	0°	52°	28°
AREA (IN. <sup>2</sup> )	2.029	0.191	0.203

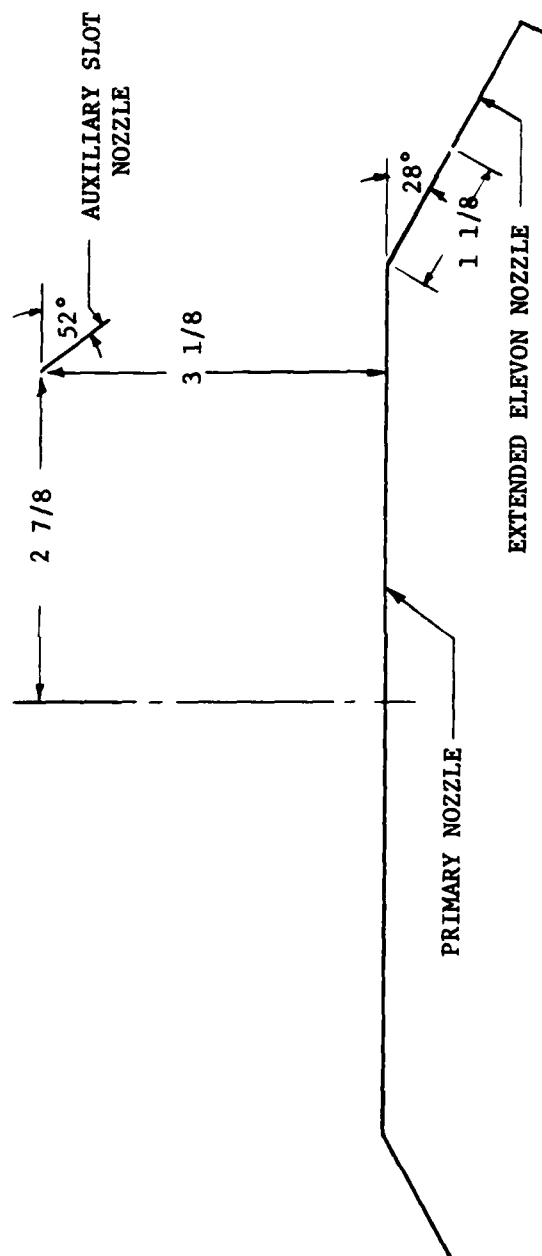


Figure 9-22. Outboard Endwall Nozzle Dimensions



Results of initial tests of the modified nozzle indicated that flow in the diffuser corner was satisfactory, but that flow in the elevon corner was not. Addition of an auxiliary slot nozzle turned more toward the elevon, located 3-1/8 inches below the primary nozzle (to minimize interference with nozzle structure) provided a small, insufficient improvement in the corner flow. With the addition of an auxiliary nozzle which effectively extended the primary nozzle into the elevon corner, satisfactory flow in the endwall-elevon corner was obtained. The simulated extended elevon corner nozzle and auxiliary slot nozzle are shown in relation to the primary nozzle in Figures 9-22 and 9-23. Pressure profiles obtained with this configuration are compared with the results of the tests of the Langley test nozzle configuration in Figure 9-24. These show the significant increase in pressure obtained in the elevon corner and the more symmetrical fore-to-aft pattern. At the conclusion of this test series, it was recommended that the primary nozzle be extended to the elevon corner and be subjected to performance verification tests with and without the auxiliary slot nozzle.

The primary design guideline resulting from these tests is the necessity for extension of the endwall nozzle to the flap/endwall corners, for in order to minimize separation, the total endwall surface must be subjected to endwall blowing.

9.2.3.2 Inboard Endwall Blowing Tests. The inboard endwall nozzle was initially tested with and without the hood that had been added at Langley to improve flow in the elevon-endwall corner. Test results indicated that the flow coefficient was similar to that used in the Langley tests. They also indicated that flow in the elevon corner with the hood installed was satisfactory at the lower end of the elevon but that a region of no flow existed immediately downstream of the augmentor throat. With the hood removed, flow in the corner was wholly unsatisfactory, as indicated by the randomly directed tufts seen in Figure 9-25. As seen also in Figure 9-25, however, with the hood installed, a separated flow region existed on the endwall downstream of the nozzle-hood intersection. Flow in the diffuser-inboard corner was similar to the elevon corner flow in that it was satisfactory at the lower end of the diffuser flap but inadequate near the throat.

In order to obtain satisfactory flow characteristics, separate nozzles, designed to direct flow into each corner, were installed in the endwall in addition to the basic nozzle. These are shown in Figure 9-26. Note in the test set-up that 2 x 4's were used to simulate the diffuser and elevon flap intersections with the endwall for this series of tests. A traversing rake was used to obtain the pressure distribution, at a fixed distance downstream of the primary nozzle exit, between the elevon and diffuser flaps. Typical of the distributions obtained are those presented in Figure 9-27, which were obtained at a distance 40, 70, and 100 throat heights downstream, 1/4 inch and 1/2 inch above the endwall surface. These distributions indicate that flow in the diffuser flap corner is unsatisfactory in the upstream region, that pressures are low on the elevon side of the endwall and that peak pressures are obtained downstream of the primary nozzle.



Figure 9-23. Simulated Extended Elevon Corner Nozzle & Auxiliary Slot Blower





THERMO LAB ISOLATED TEST  
NOMINAL NOZZLE PR = 1.9

PROFILES AT 100t

(APPROXIMATELY 21 IN. DOWNSTREAM OF NOZZLE)

DIFFUSER  
SIDE

--- LANGLEY CONFIGURATION  
--- REVISED CONFIGURATION

ELEVON  
SIDE

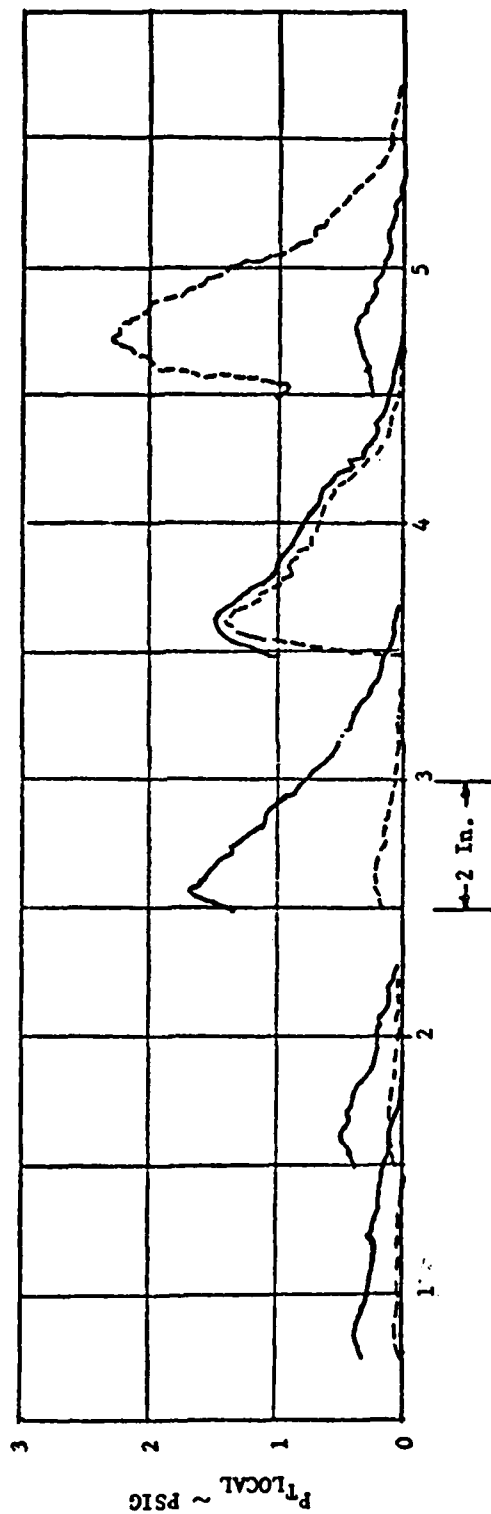
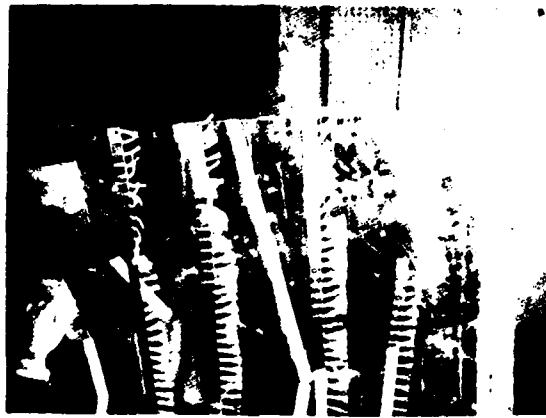


Figure 9-24.  
PRESSURE PROFILES  
OUTBOARD ENDWALL BLOWING  
XFV-12A WING



AFT CORNER WITH HOOD REMOVED



AT FORWARD CORNER



NEAR FORWARD CORNER

Figure 9-25. Inboard Endwall Flow Visualization

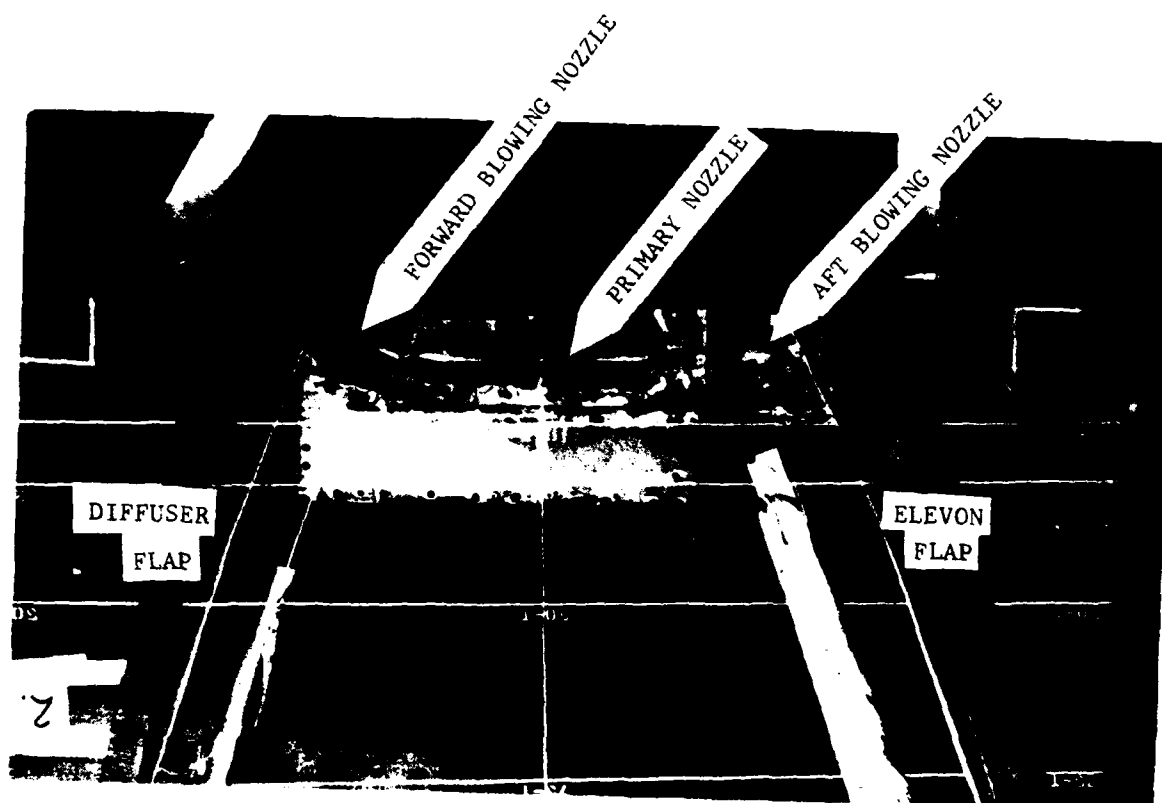
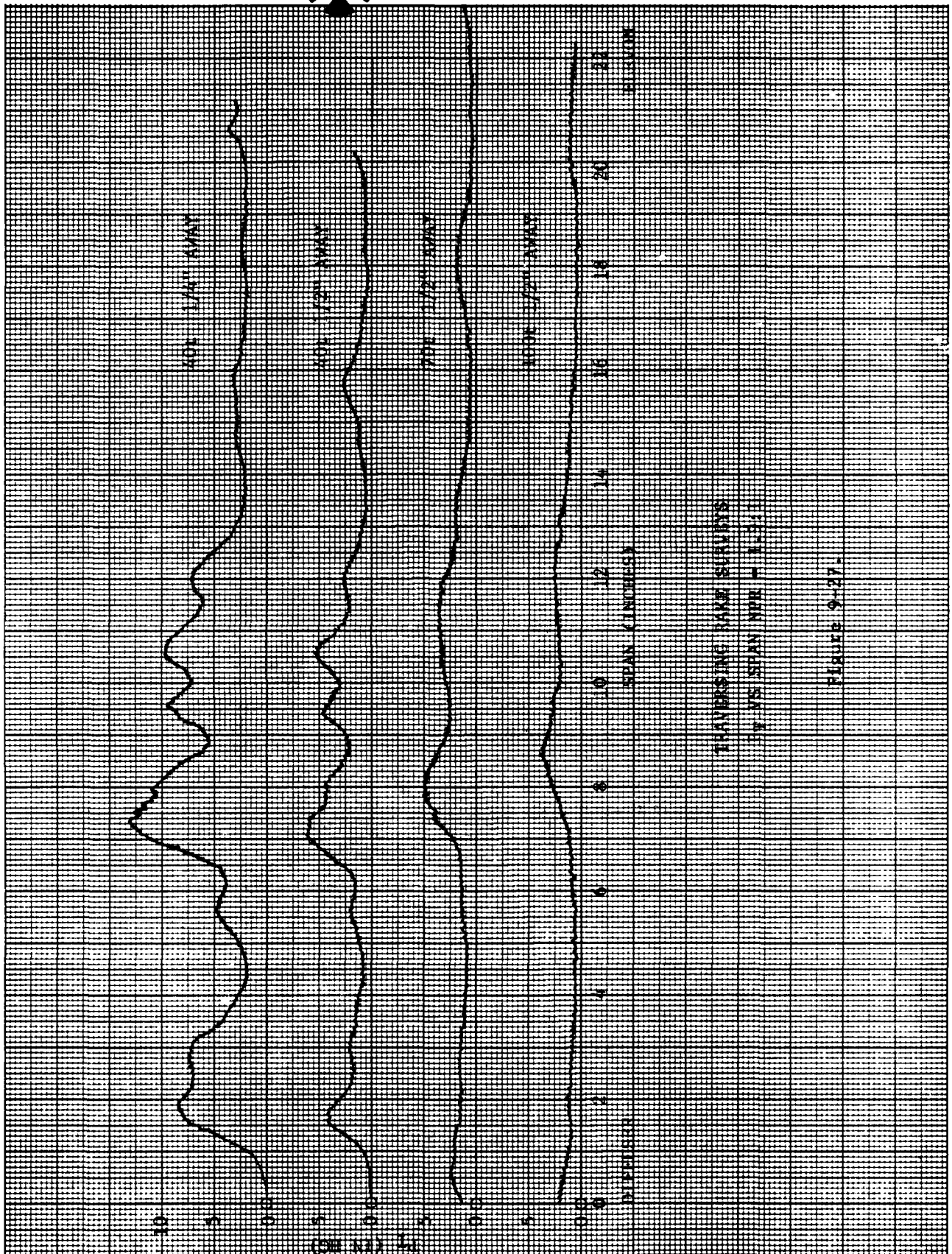


Figure 9-26. Nozzle System Close-up



Rockwell International



TRANSVERSE PEAK SURVEYS  
1" VS SPAN (INCHES) - 12.5"

Figure 9-27



In order to improve flow in the diffuser corner, it was recommended that the nozzle exit angle be increased. To improve the pressure level and distribution on the aft portion of the endwall, it was recommended that the separate aft-blowing nozzle be eliminated and that the primary nozzle be extended aft to the elevon-endwall corner. These recommendations are consistent with those for the outboard endwall.

### 9.3 IMPROVED ELEVON

Results of the Coanda segment model test which are documented in Reference (20) and summarized in Section 6 of this document indicated a number of potential improvements which could be made to the elevon, namely:

- (1) change the external Coanda shape to a log spiral with a K factor of 1.3, (2) relocate the inlet feed duct relative to the nozzle exit plane, (3) incorporate primary and dedicated nozzle vanes.

Prior to incorporating the improvements, developed during the Coanda segment model test, on the existing XfV-12A elevon, it was considered prudent to develop a baseline data base on the existing elevon at the WPAFB facility, to provide a good before and after comparison of the elevon modifications. The results of this test are documented in Reference (34) and essentially confirmed the isolated performance tests conducted at Columbus Aircraft Division's Thermo Lab, (Reference 33).

After modification of the existing wing elevon with the improvements developed during the Coanda segment model test the elevon was returned to WPAFB for evaluation of the modifications. Results of this test, which are documented in Reference (35), showed the modifications incorporated resulted in the following improvements: (1) Airflow quality at the inboard corner was significantly improved, (2) turning efficiency was improved along the entire span, (3) elimination of irregularities in the spanwise total pressure distribution, (4) expansion of the primary nozzle gap was markedly reduced.

#### 9.3.1 Test Article

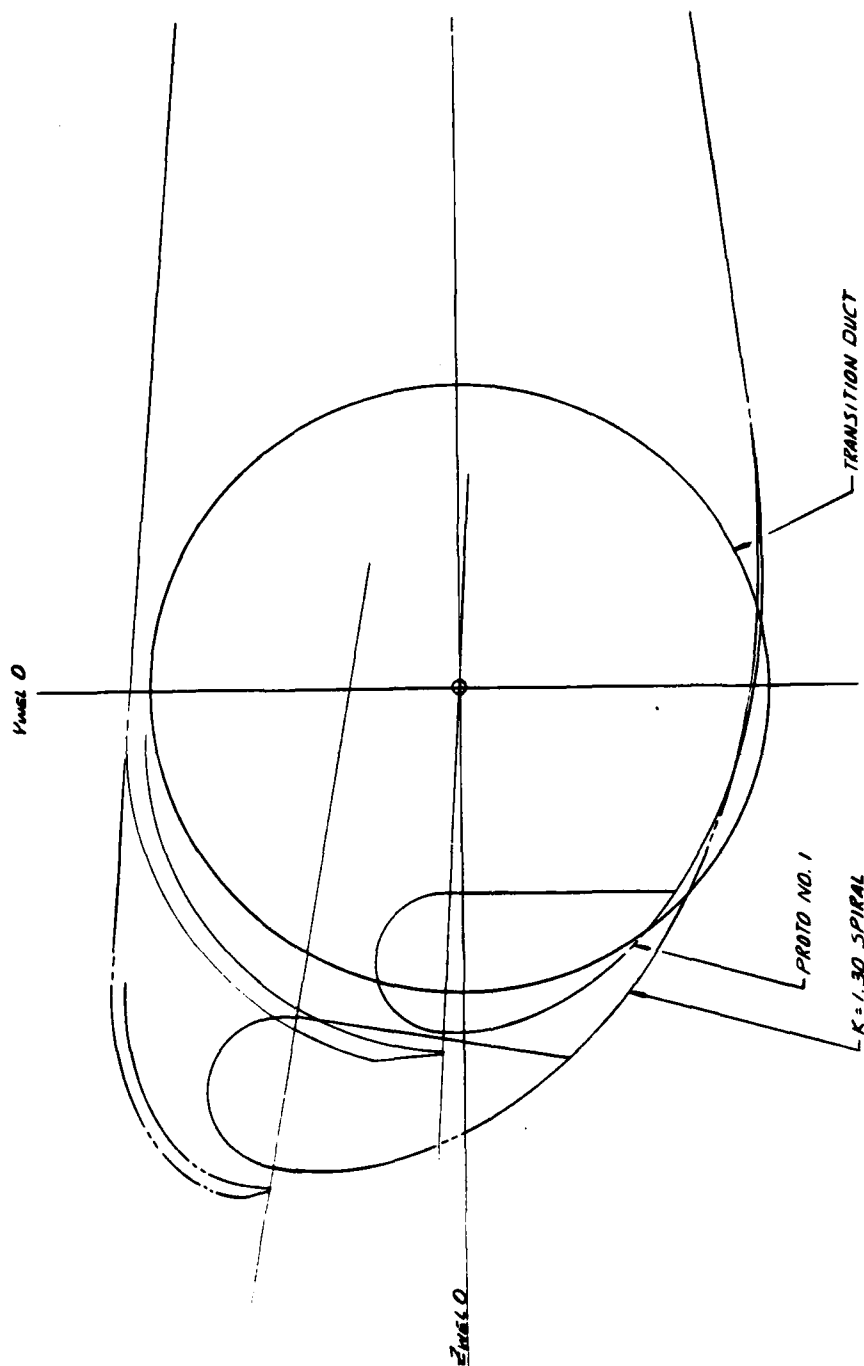
A comparison of the design parameters between the Proto 1 elevon and the modified elevon is tabulated in Table 9-1. All design changes to the elevon assembly are documented in the drawing of Reference (36) and a comparison of the Coanda shapes and feed duct location may be seen in Figure 9-28. Details of the internal nozzle vanes and an overall view of the modified elevon in the WPAFB test facility are shown in Figures 9-29 and 9-30, respectively. A listing of significant design changes incorporated are listed below:

- a. The original Coanda shape, which nearly represented a  $K=1.0$  spiral was replaced with a  $K=1.3$  log spiral.
- b. Three cascade vanes and a bullet fairing were added to the entrance of the inboard dedicated nozzle.
- c. The nozzle lip convergence angle was increased from approximately  $0^\circ$  to a nominal  $7.5^\circ$ .



Table 9-1 Design Parameters

	<u>INBOARD</u>	<u>EXISTING ELEVON</u>	<u>OUTBOARD</u>	<u>INBOARD</u>	<u>IMPROVED ELEVON</u>	<u>OUTBOARD</u>
$A_0$		23.543			23.474	
$R_o/t$	8.319		4.922	11.283		9.630
$R_i/t$	3.991		3.515	4.00		4.00
S/t Throat	27.151		16.835	34.437		29.387
S/t Exit	169.700		146.000	158.106		187.544
Feed Duct Area		50.266			50.266	
Feed Duct $M_n$		.25			.25	



Xmax 35.56

Figure 9-28. Comparison of Coanda Shapes

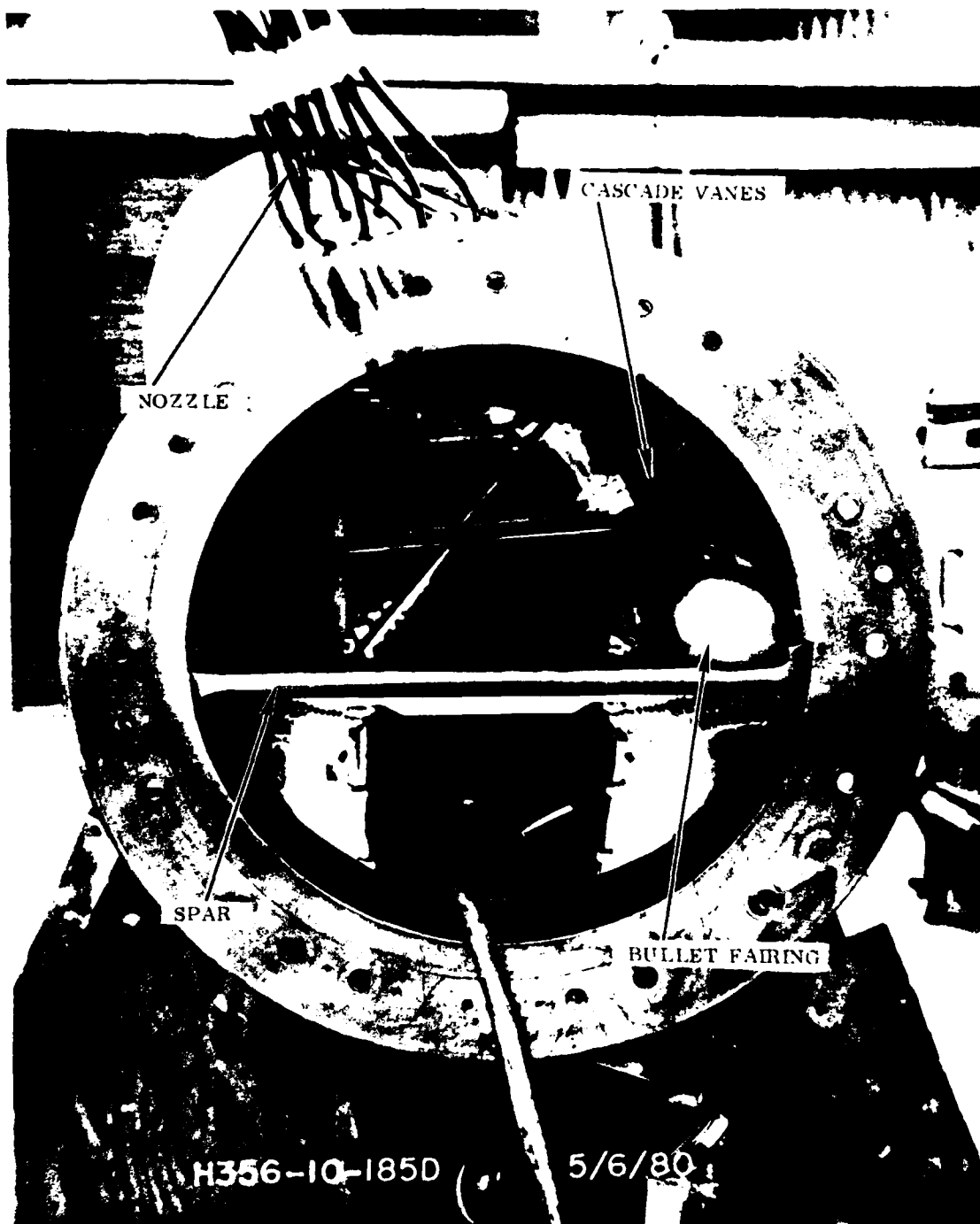


Figure 9-29. Elevon Feed





Figure 9-30. Elevon Installation in Test Stand



- d. The primary nozzle gap taper ratio (GAP O.B./GAP I.B) was changed to .5 to agree with the throat taper ratio.
- e. The nozzle internal convergence at Lt was increased to 16°.

### 9.3.2 Test Results

The improved modified elevon was evaluated by means of the following measurements and criteria:

1. Nozzle Cap Measurements
2. Primary and Dedicated Nozzle Spanwise Pressure Surveys
3. Flow and Velocity Coefficients
4. Turning Efficiency
5. Flow Visualization for Flow Angularity.

Results of nozzle gap measurements of the Proto 1 elevon and the modified elevon may be compared in Figures 9-31 and 9-32. Both sets of measurements were made after pressurization, and show considerably better gap vs. span uniformity for the modified elevon. The improved internal nozzle construction was also evident in the nozzle gap expansion vs. nozzle pressure ratio data presented in Figure 9-33. Similar improvements were noted in the dedicated nozzles..

Figures 9-34 thru 9-36 are plots of nozzle total pressure vs. span comparing results of the Proto #1 vs. improved elevon. Considerable improvement in pressure irregularities were realized, especially at the inboard and outboard ends. Similar improvements, in the pressure distributions of the dedicated nozzles, were obtained, especially on the outboard dedicated nozzle, as can be seen in Figure 9-37.

Figures 9-38 and 9-39 present the results of testing the elevons for flow ( $C_D$ ) and velocity ( $C_V$ ) coefficients. Although the plots show differences in character vs. NPR, little or no improvement was considered in these two parameters.

The Turning Efficiency (CTE) as defined,  $CTE = P_{Tpeak}/P_{Tnozzle}$ , is a measure of the pressure remaining in the jet after traveling some given distance downstream of the nozzle exit. Presented in Figures 9-40 thru 9-42 are comparison data for the two elevon configurations, at three nondimensionalized chord stations of 10t, 20t, and 50t. Improvements were noted at all three chord stations as well as along the entire span.

Flow visualization pictures for purposes of illustrating flow angularity were made at 15 PSIG for both the Proto #1 and improved elevon. Figures 9-43 and 9-44 present the improvements that were realized, especially at the inboard corner, which can be attributed to the improved turning vanes located in the inboard dedicated nozzle. To further quantify the flow angularity, oil flow techniques were used to obtain the following flow angles along the span.

NOZZ STA (IN)	10	16	26	34	Midspan
FLOW ANGLE (DEG)	7.5	7	3	2	0

[illegible]

### Figure 9-31. Nozzle Gap Measurements



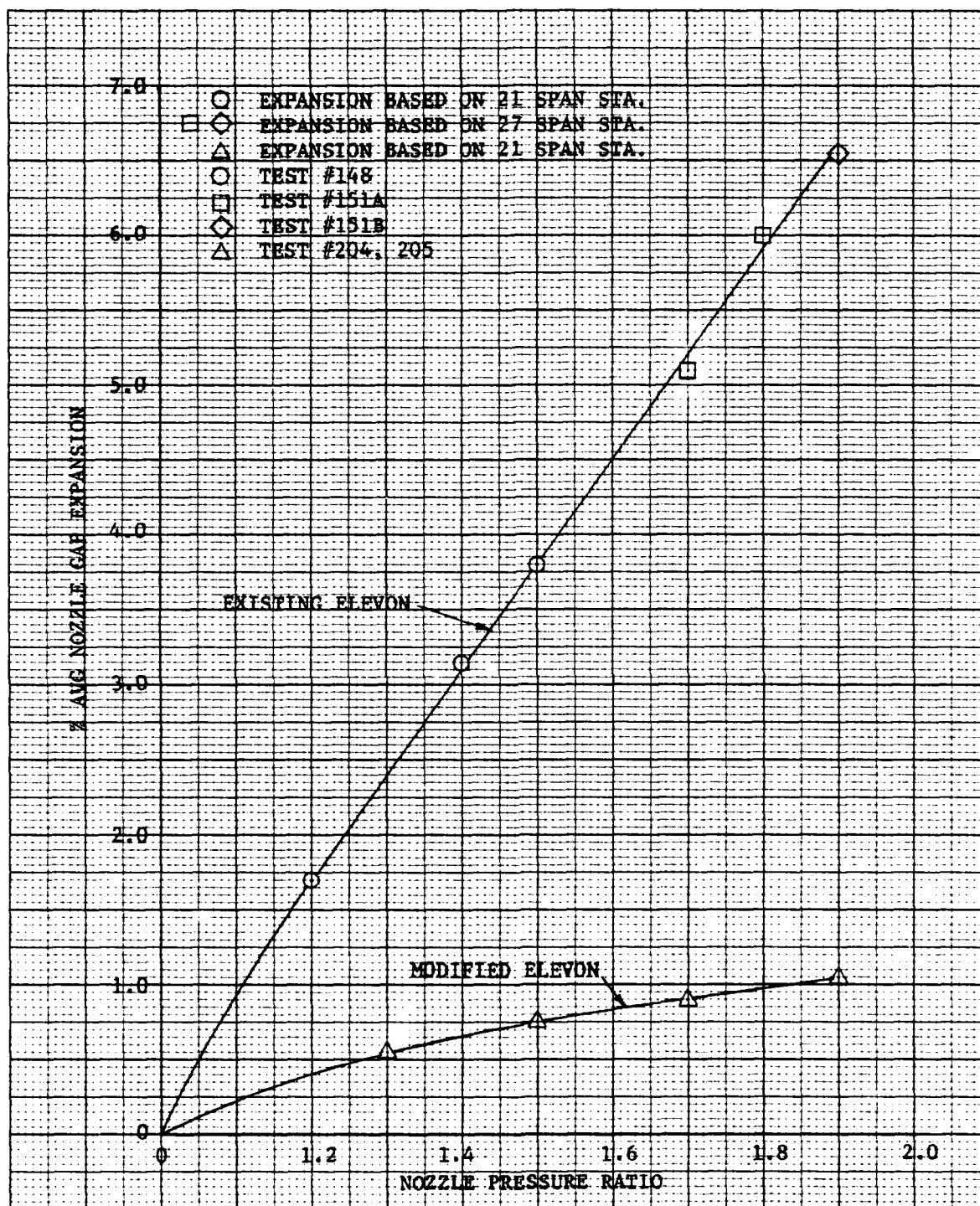


Figure 9-33. Nozzle Gap Expansion

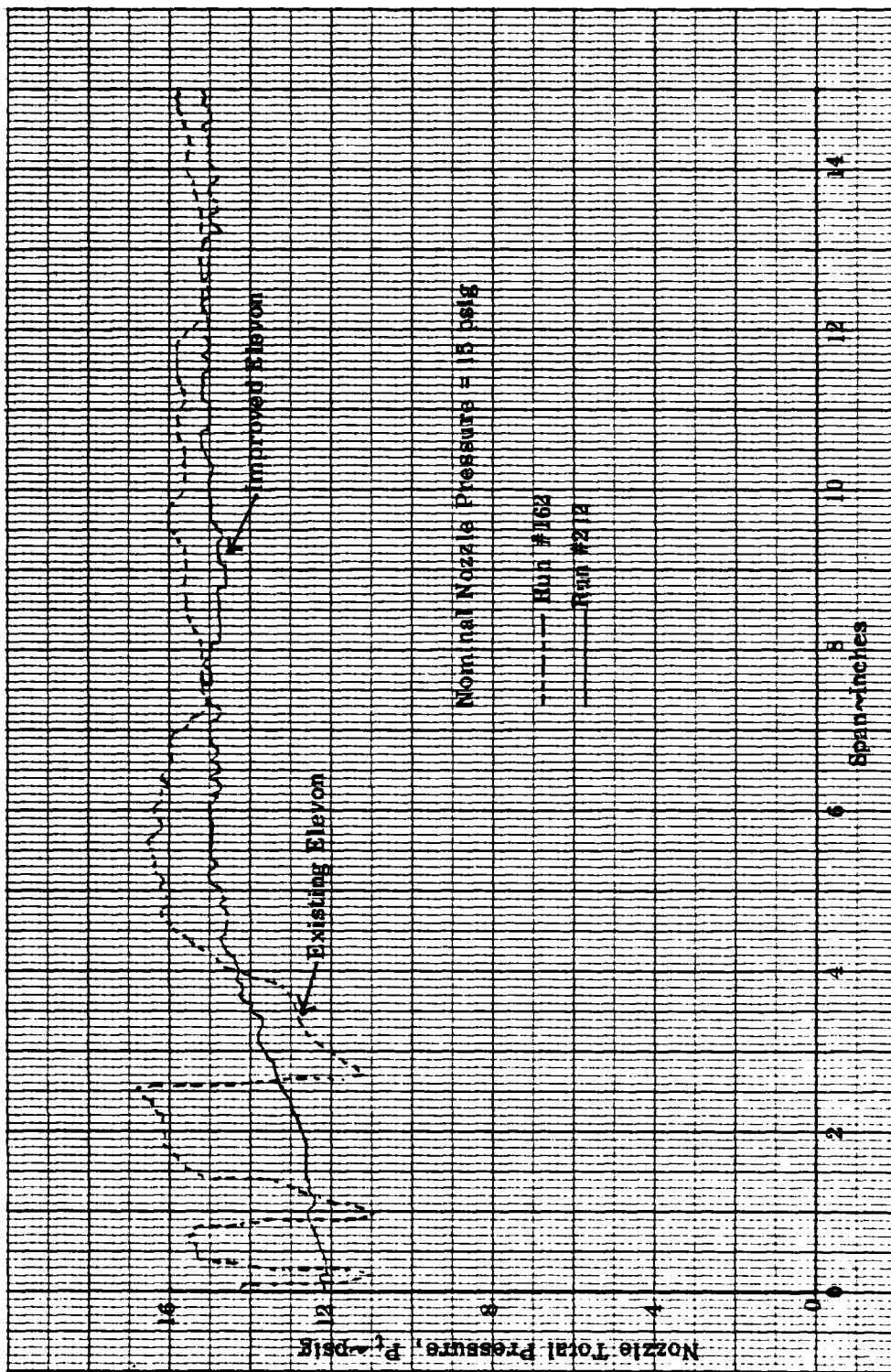


Figure 9-34. Primary Nozzle Survey Comparison - Inboard



Rockwell International

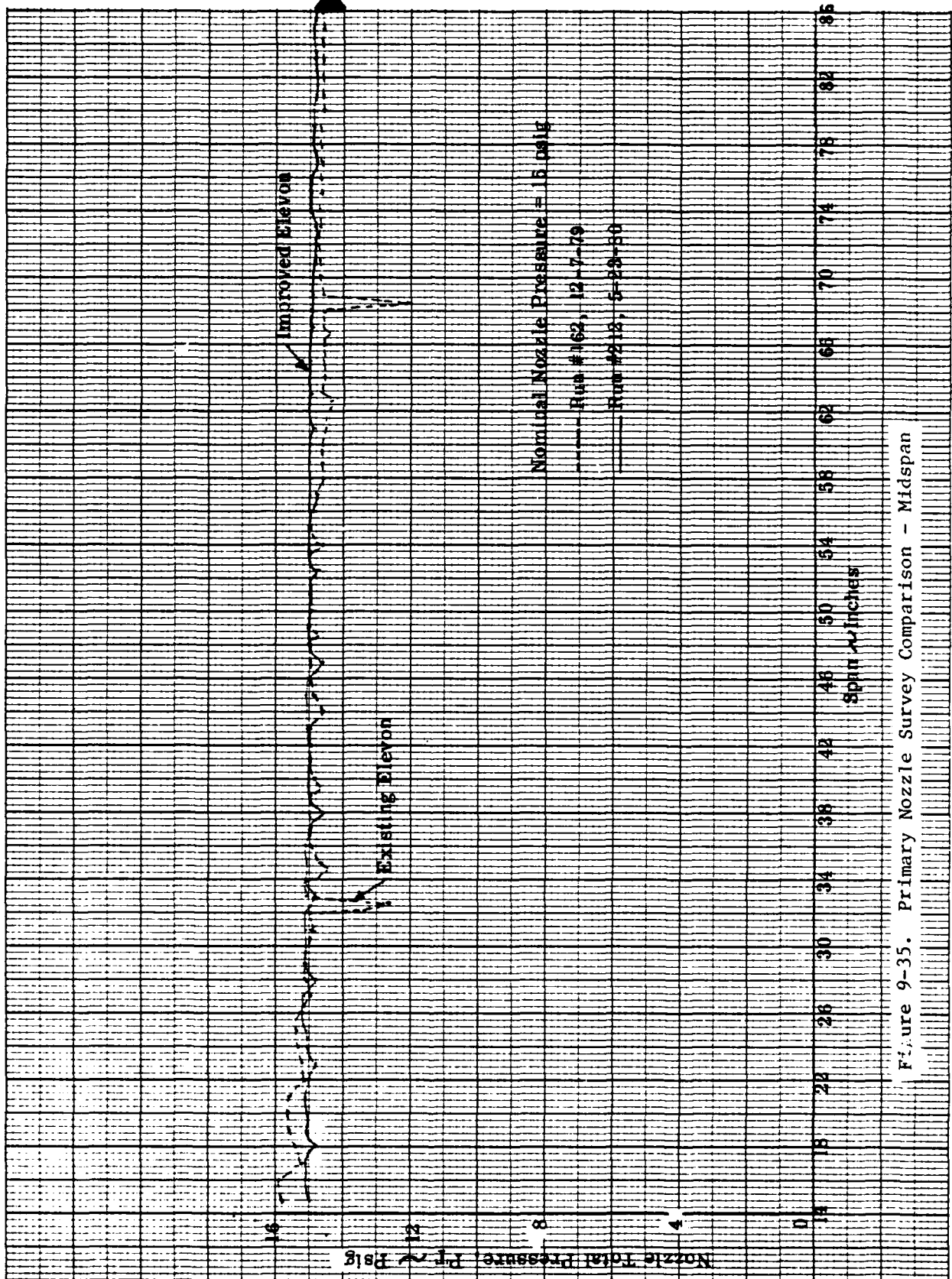


Figure 9-35. Primary Nozzle Survey Comparison - Midspan

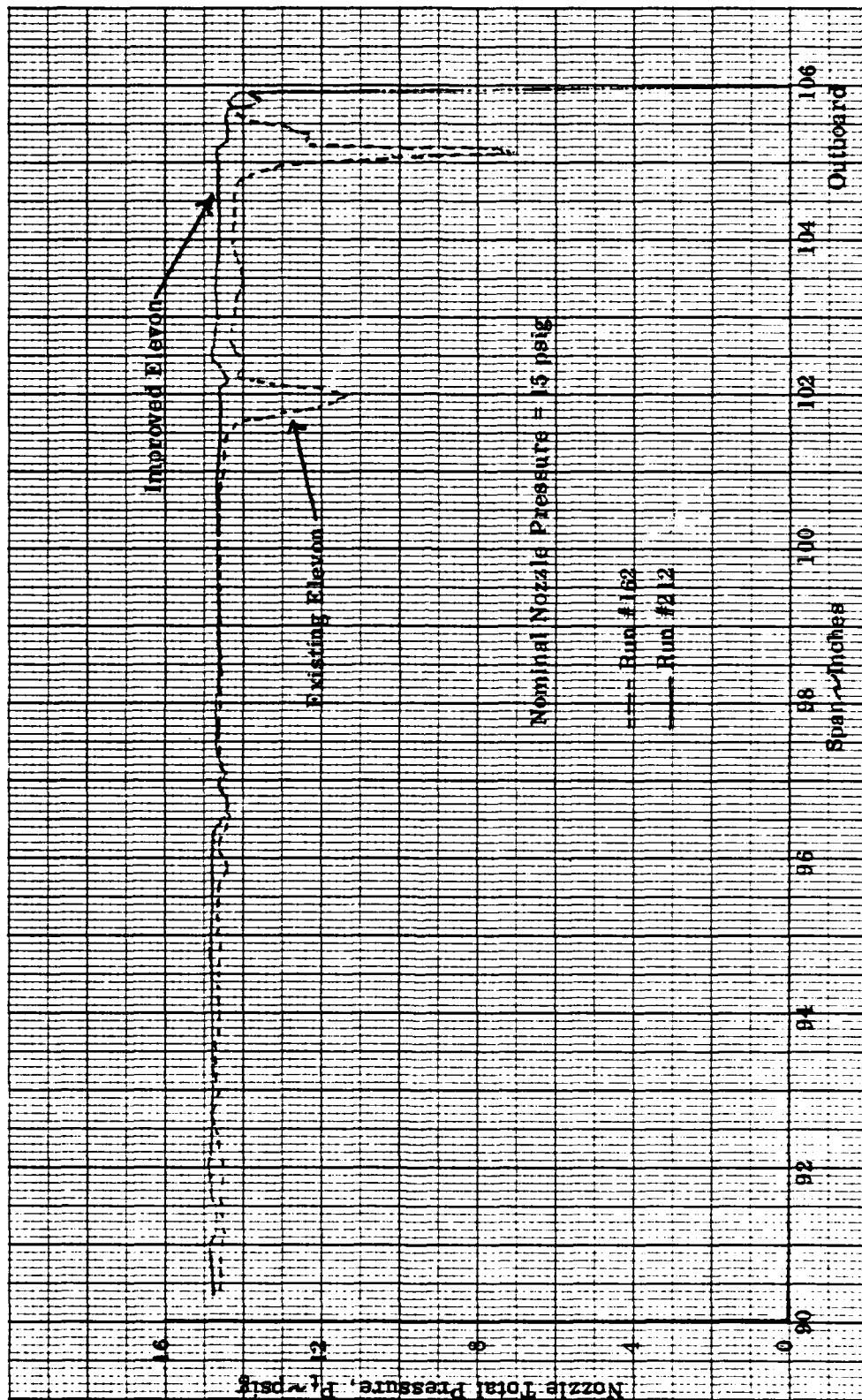


Figure 9-36. Primary Nozzle Survey Comparison - Outboard



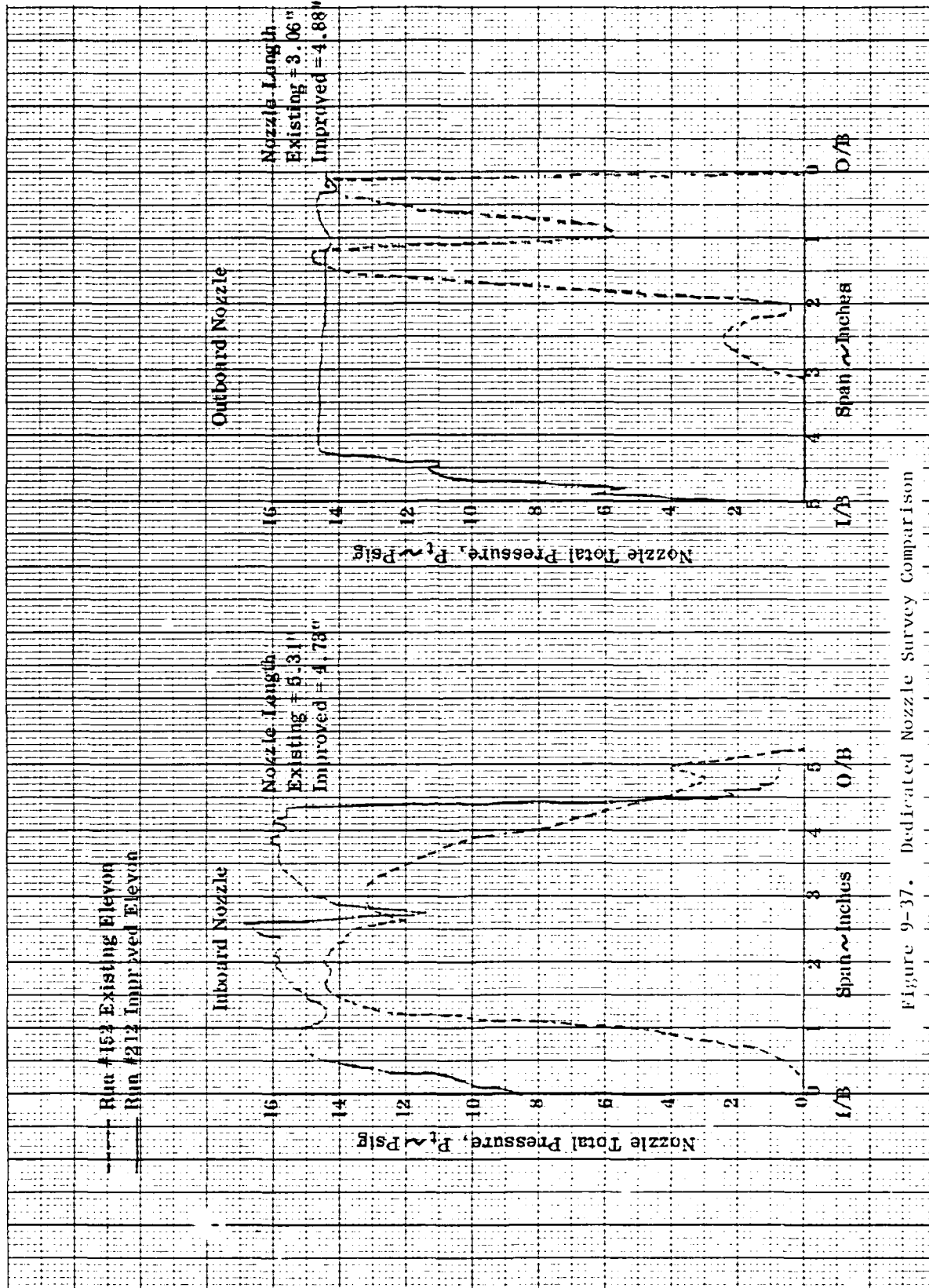
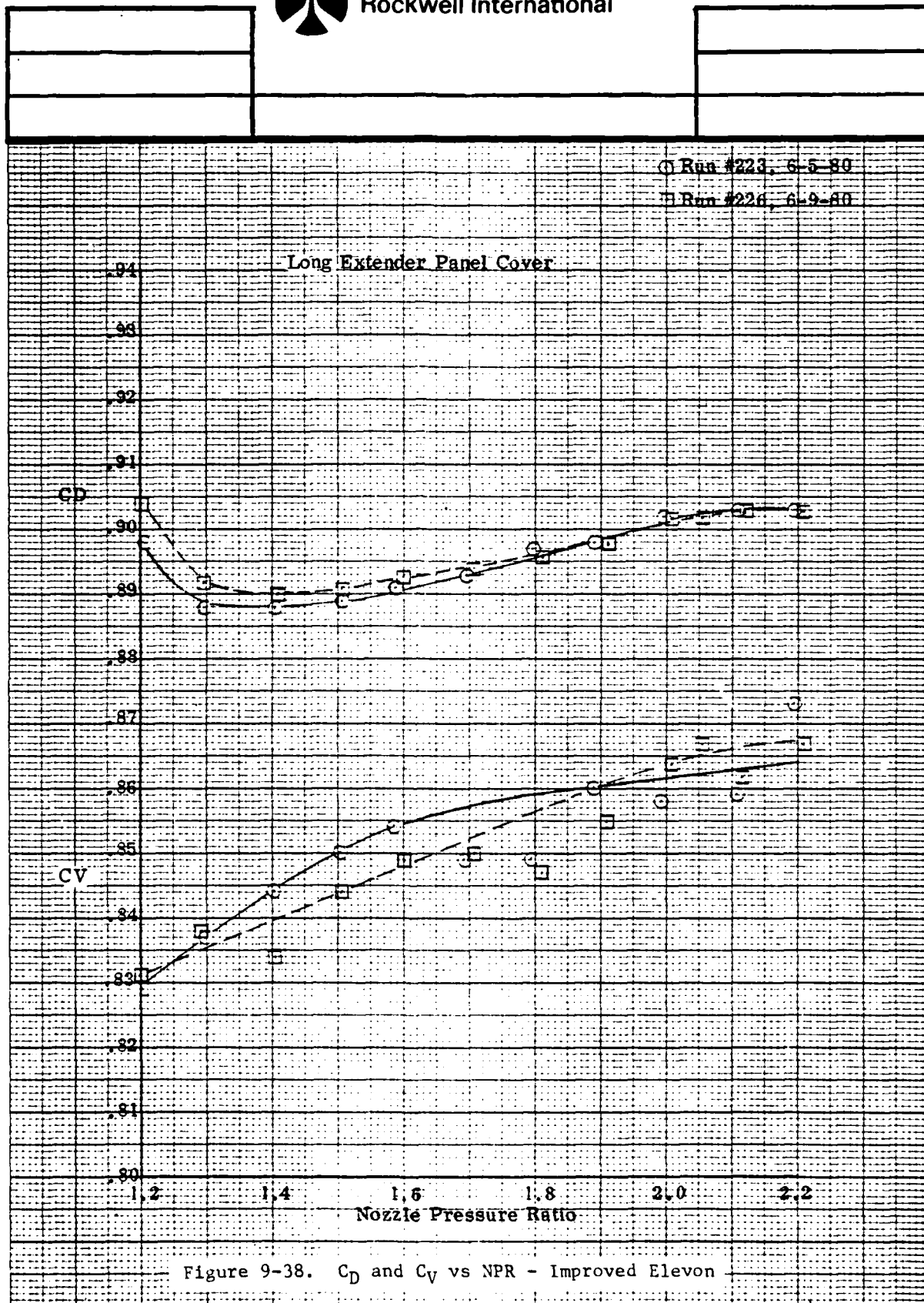
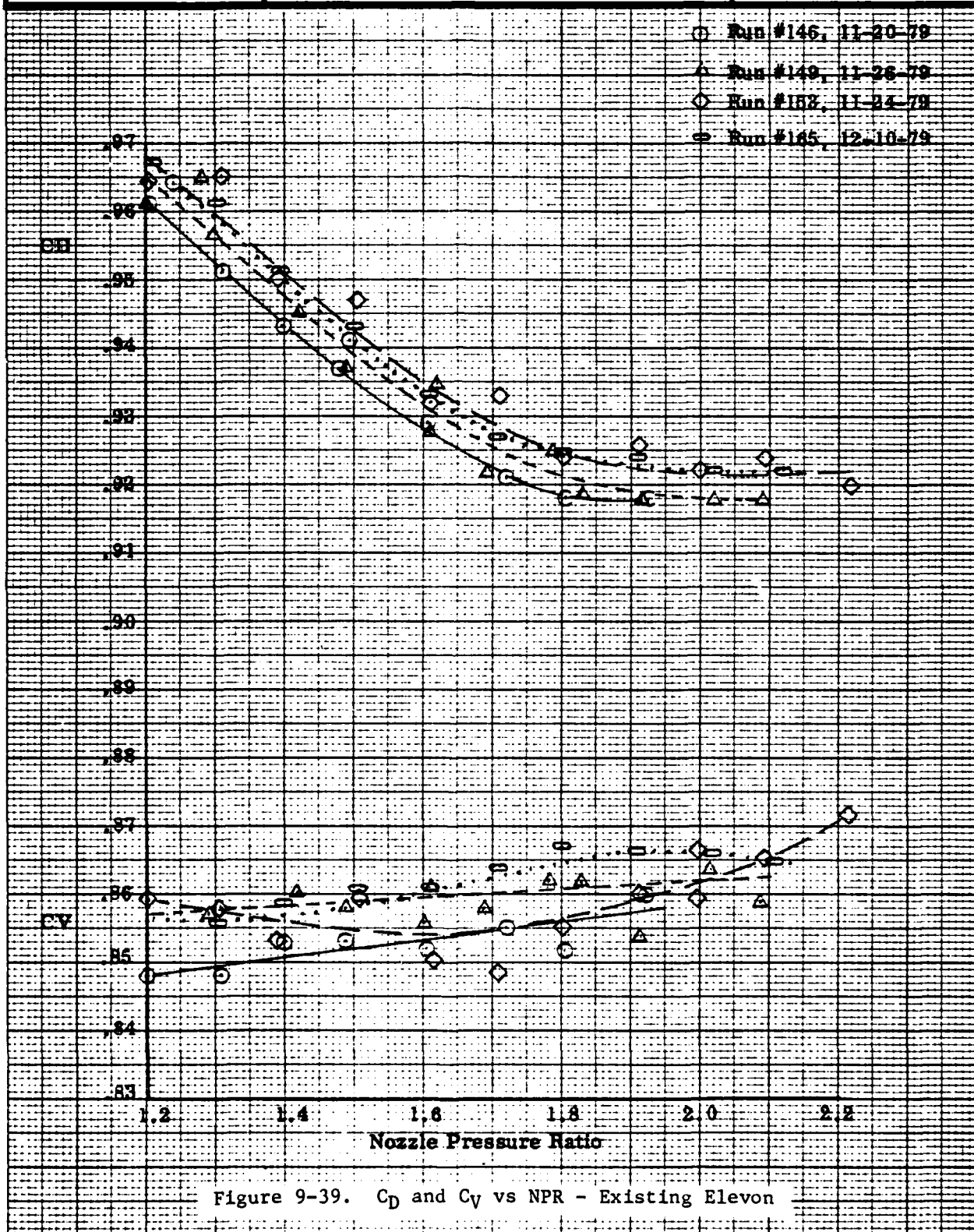


Figure 9-37. Dedicated Nozzle Survey Comparison

Figure 9-38.  $C_D$  and  $C_V$  vs NPR - Improved Elevon



Rockwell International



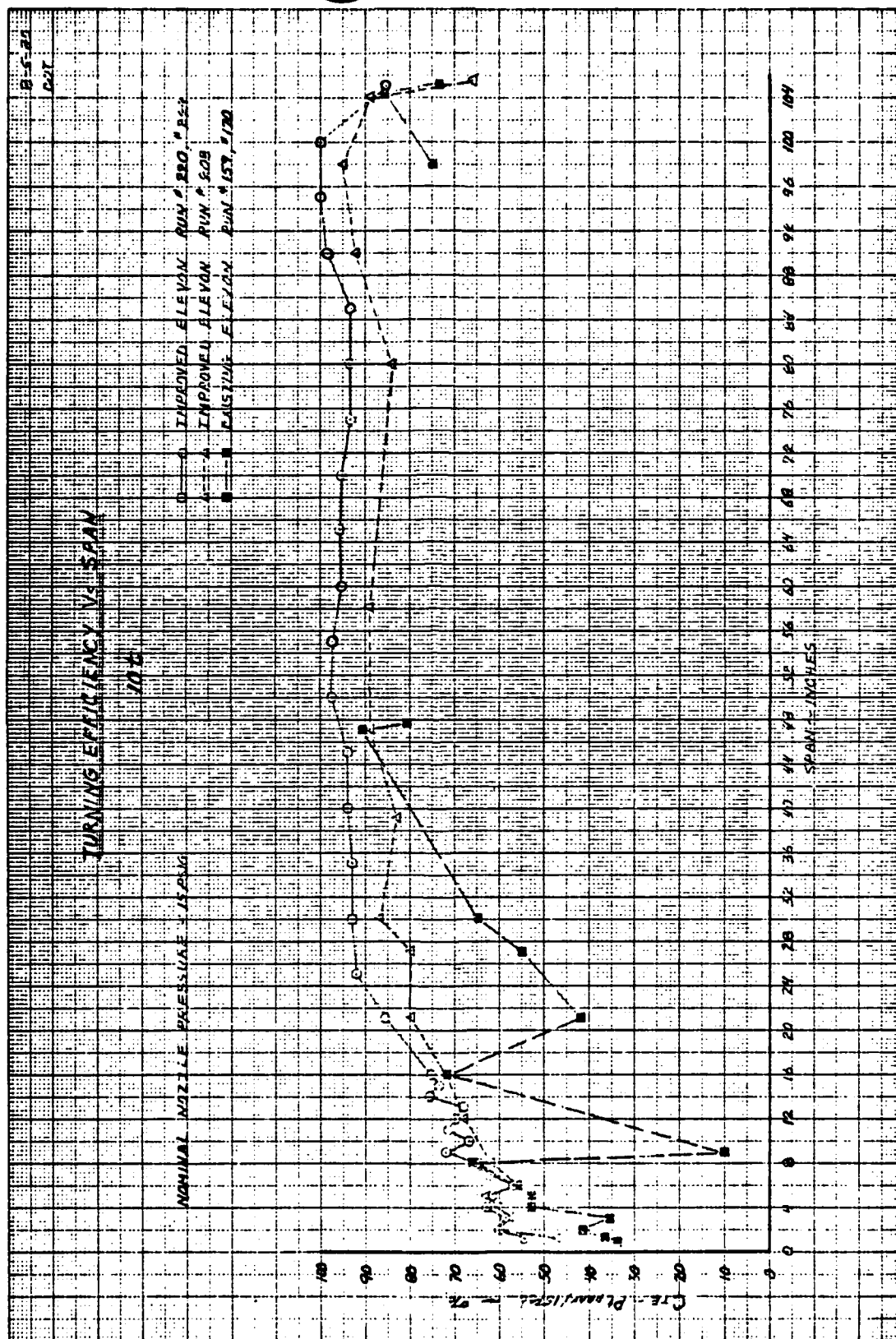


Figure 9-40. Turning Efficiency vs. Span - 10t

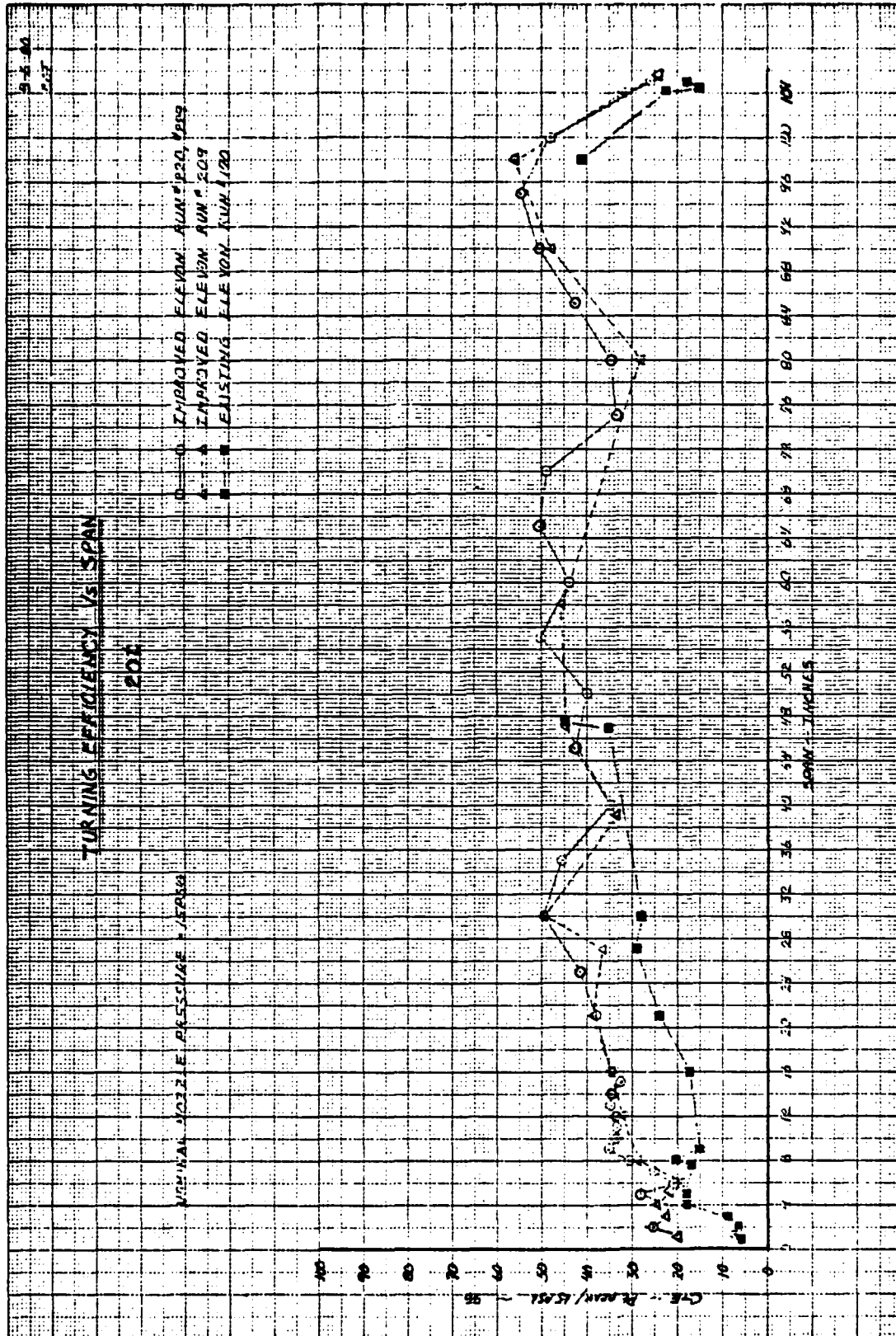


Figure 9-41. Turning Efficiency vs. Span - 20t

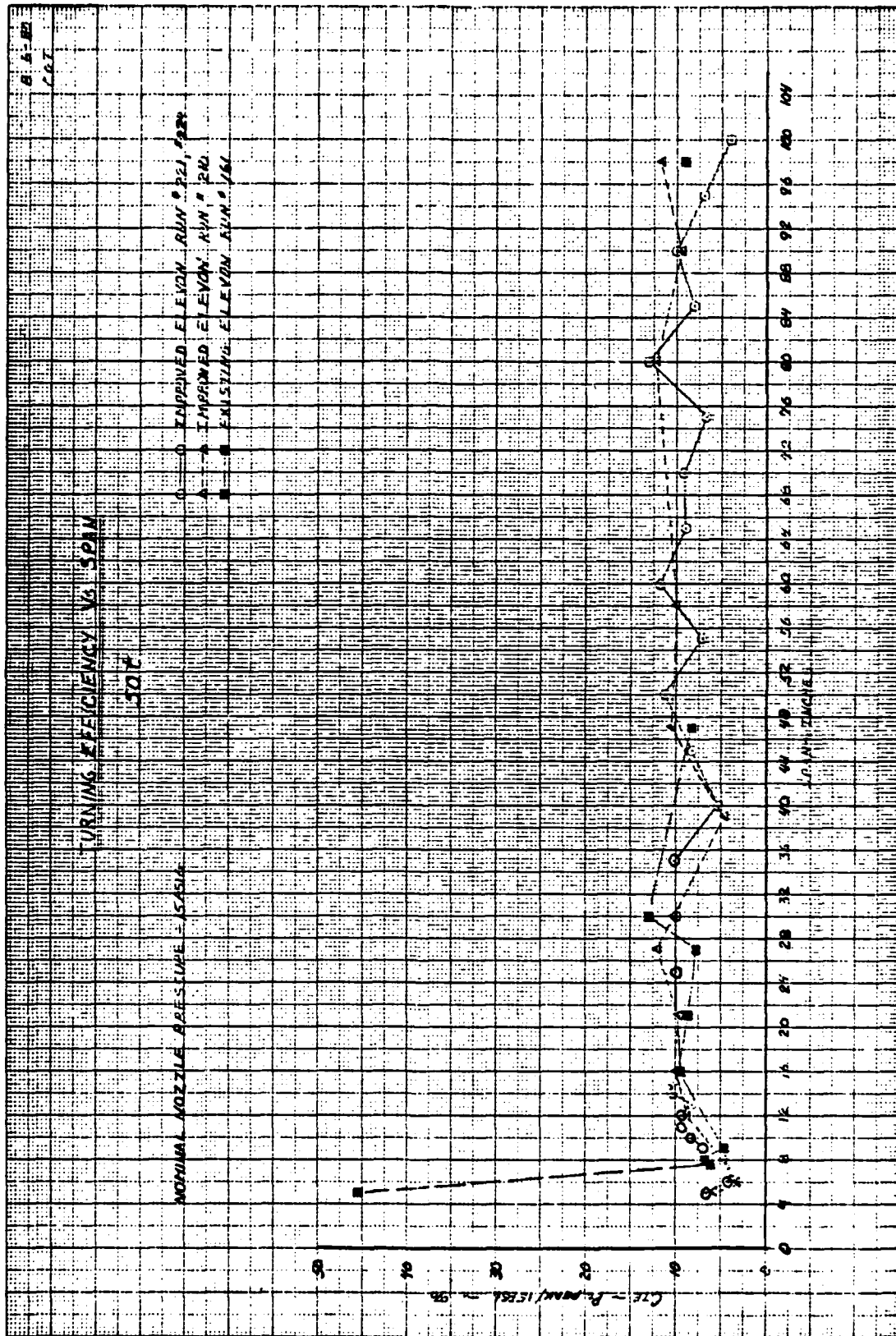


Figure 9-42. Turning Efficiency vs. Span - 50t

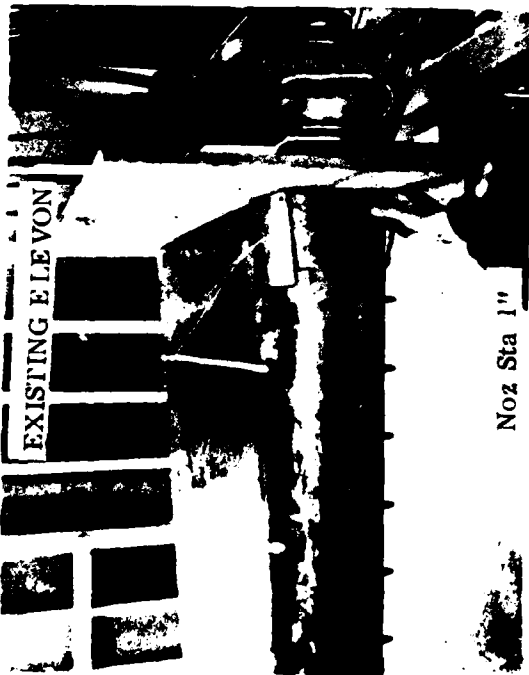
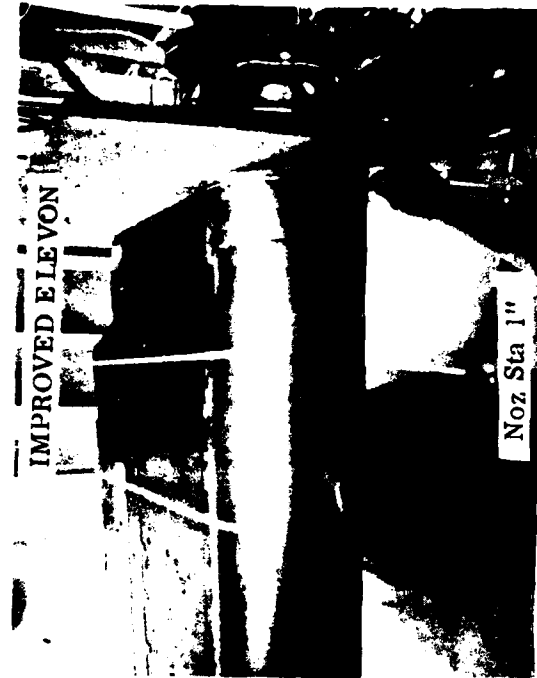


Figure 9-43. Flow Visualization Comparison at 1 and 4 Inches

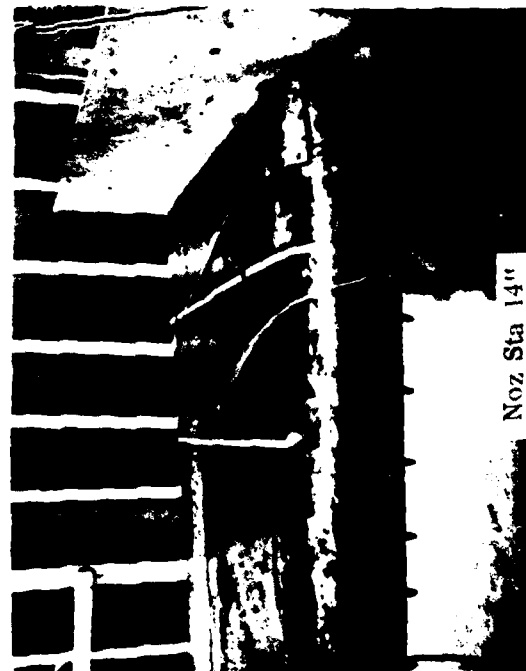


Figure 9-44. Flow Visualization Comparison at 8 and 14 Inches





Rockwell International

9.4

SUMMARY

Flow characteristics of the augmentor surfaces from the left hand wing of the Proto 1 XTV-12A were evaluated in cold flow tests. Spanwise nozzle total pressure distributions, jet profiles, nozzle coefficients and flow visualization were obtained for the wing diffuser, elevon, and inboard and outboard endwall nozzles. In addition, leakage and nozzle area growth were investigated for the diffuser and elevon. The data obtained was considered to be satisfactory for comparison with similar data of the improved augmentor surfaces.

Also presented are the improvements in overall flow quality and nozzle gap expansion control obtained on the elevon which had several design improvements made to it which included: the original Coanda shape log spiral changed from  $K = 1.0$  to  $K = 1.3$ , a three vane cascade and a bullet fairing added to the inboard dedicated nozzle, increased nozzle lip convergence from  $0^\circ$  to  $7.5^\circ$ , improved Coanda surface smoothness by eliminating splice joints, and removal of a primary nozzle turning vane which became unnecessary as a result of an improved spacing relationship between the feed and nozzle exit plane which resulted from the change in Coanda  $K$  factor.



Rockwell International

## 9.4

SUMMARY

Flow characteristics of the augmentor surfaces from the left hand wing of the Proto 1 XHV-12A were evaluated in cold flow tests. Spanwise nozzle total pressure distributions, jet profiles, nozzle coefficients and flow visualization were obtained for the wing diffuser, elevon, and inboard and outboard endwall nozzles. In addition, leakage and nozzle area growth were investigated for the diffuser and elevon. The data obtained was considered to be satisfactory for comparison with similar data of the improved augmentor surfaces.

Also presented are the improvements in overall flow quality and nozzle gap expansion control obtained on the elevon which had several design improvements made to it which included: the original Coanda shape log spiral changed from  $K = 1.0$  to  $K = 1.3$ , a three vane cascade and a bullet fairing added to the inboard dedicated nozzle, increased nozzle lip convergence from  $0^\circ$  to  $7.5^\circ$ , improved Coanda surface smoothness by eliminating splice joints, and removal of a primary nozzle turning vane which became unnecessary as a result of an improved spacing relationship between the feed and nozzle exit plane which resulted from the change in Coanda  $K$  factor.



Rockwell International

(THIS PAGE INTENTIONALLY LEFT BLANK)



## 10.0 TEST FACILITIES

10.1 GENERAL

In order to pursue the development rationale discussed in Section 3.1, it was necessary to establish test facilities capable of performing accurate performance measurements and diagnostic investigations of both model scale and full scale thrust augmenter systems and their associated components. For this purpose, three major test facilities were utilized routinely during the XTV-12A TAW technology program. Table 10-1 presents a brief outline of each facility, its utilization, and specific operating characteristics applicable to thrust augmenter research programs.

Table 10-1 Major Test Facilities

<u>TEST FACILITY</u>	<u>HARDWARE EVALUATED</u>	<u>FACILITY CHARACTERISTICS</u>
Thermodynamics Laboratory	Model Scale Augmenters Model Scale Components Full Scale Components	Compressor supplied cold flow models operating at aircraft nozzle pressure ratios (NPR's). Full scale components limited to NPR's $\leq 1.9:1$
WPAFB Test Facility	Full Scale Components Full Scale Segment Models	Compressor supplied cold flow tests performed at NPR simulating aircraft operating conditions.
Whirl Rig	Full Scale Augmenters Full Scale Components	F401 engine supplied flow simulates aircraft nozzle exit pressure and temperature characteristics

The remainder of this section will present detailed information concerning each of the facilities and their specific applications.

10.2 WHIRL RIG TEST FACILITY

Full scale augmentor and associated isolated component tests were conducted at the contractor's whirl rig test facility. This facility which is located at Rockwell International, NAAD Columbus Plant, was specially designed and fabricated for this application. The facility is basically composed of a P&WA F401 engine with inlet bellmouth and exhaust diverter, a 100-foot section of boom and ducting required to deliver a portion of the engine air flow to the item under test (see Figures 10-1 to 10-4). The facility was originally designed to allow the test article to rotate around the boom center pylon in order to demonstrate hover and control aspects of the TAW concept. Typically, however, the facility was utilized for diagnostic or performance verification tests. Investigations of this type utilized a force measuring system composed of load cells

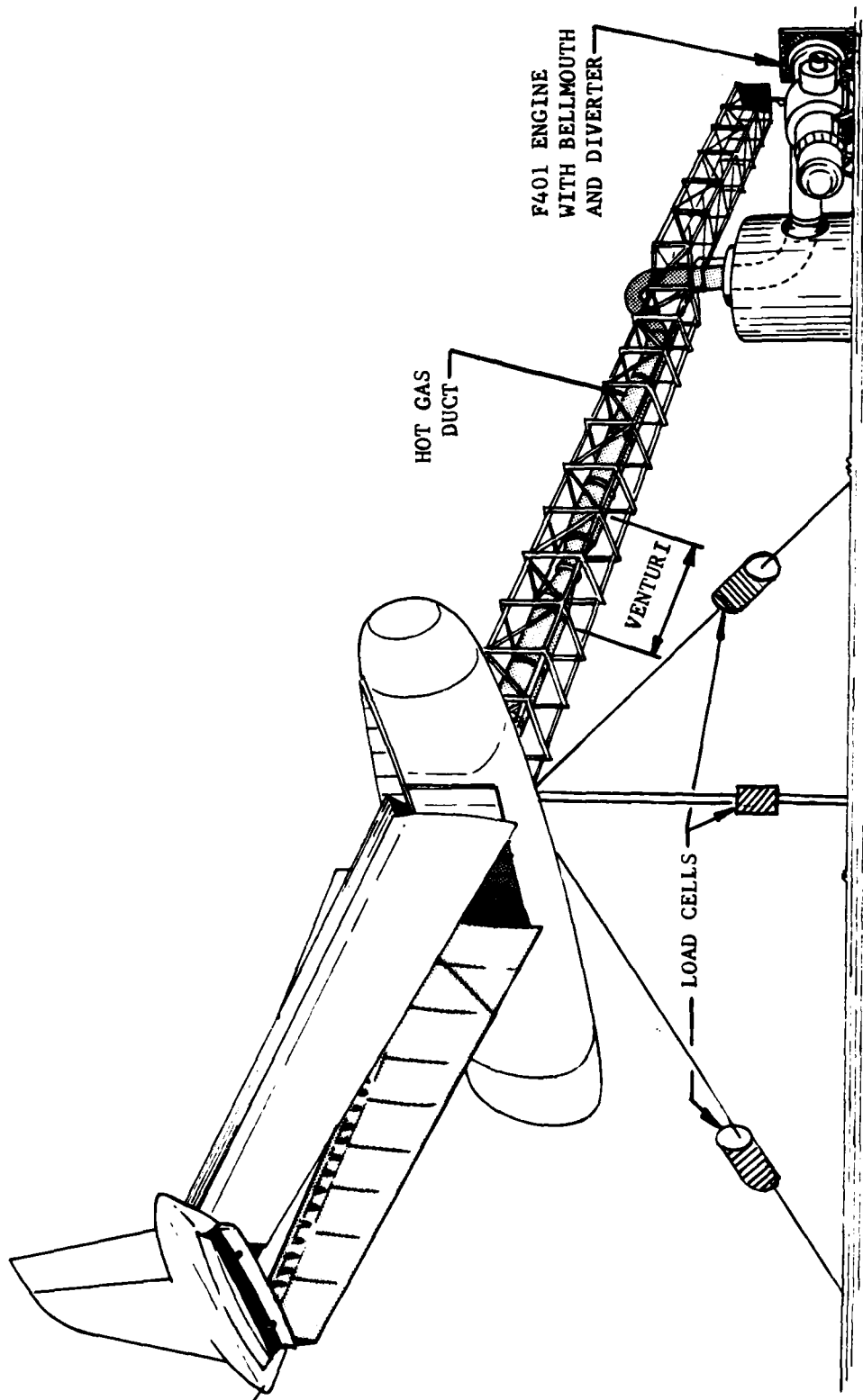


Figure 10-1. Schematic - Whirl Rig with Model Installed

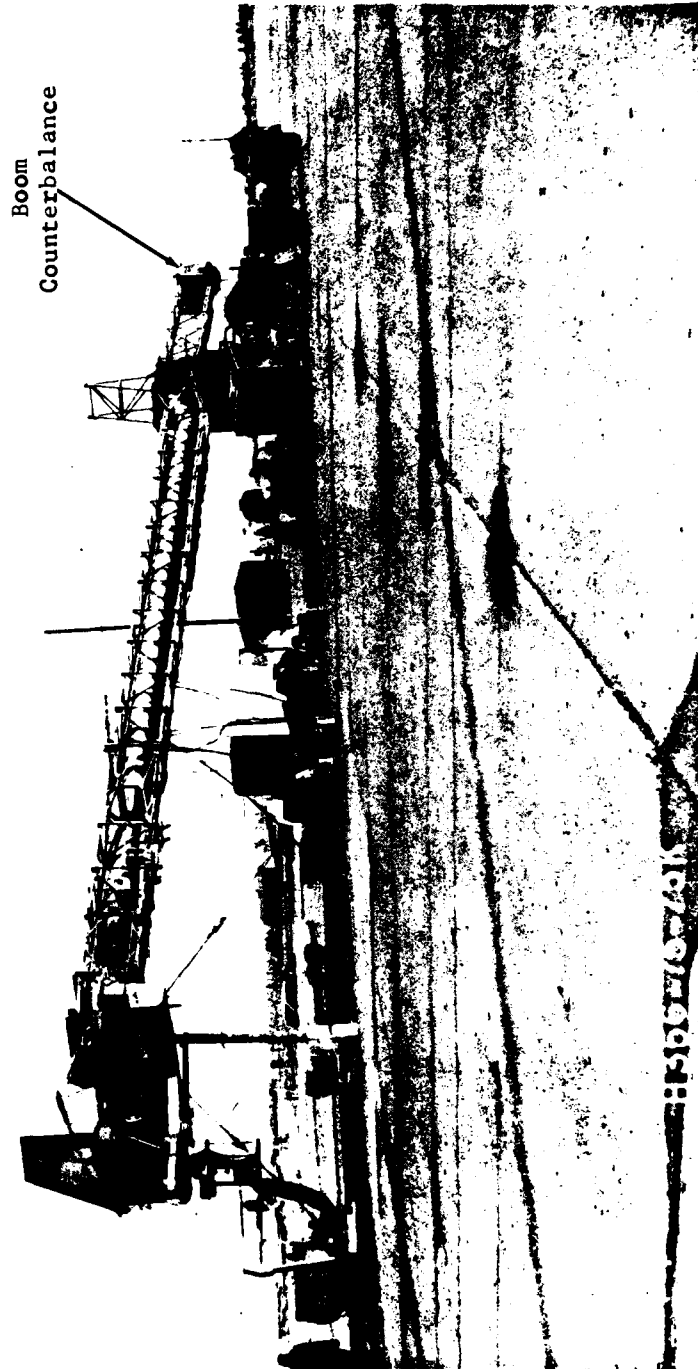


Figure 10-2. F401 Whirl Rig with Wing Model Installed

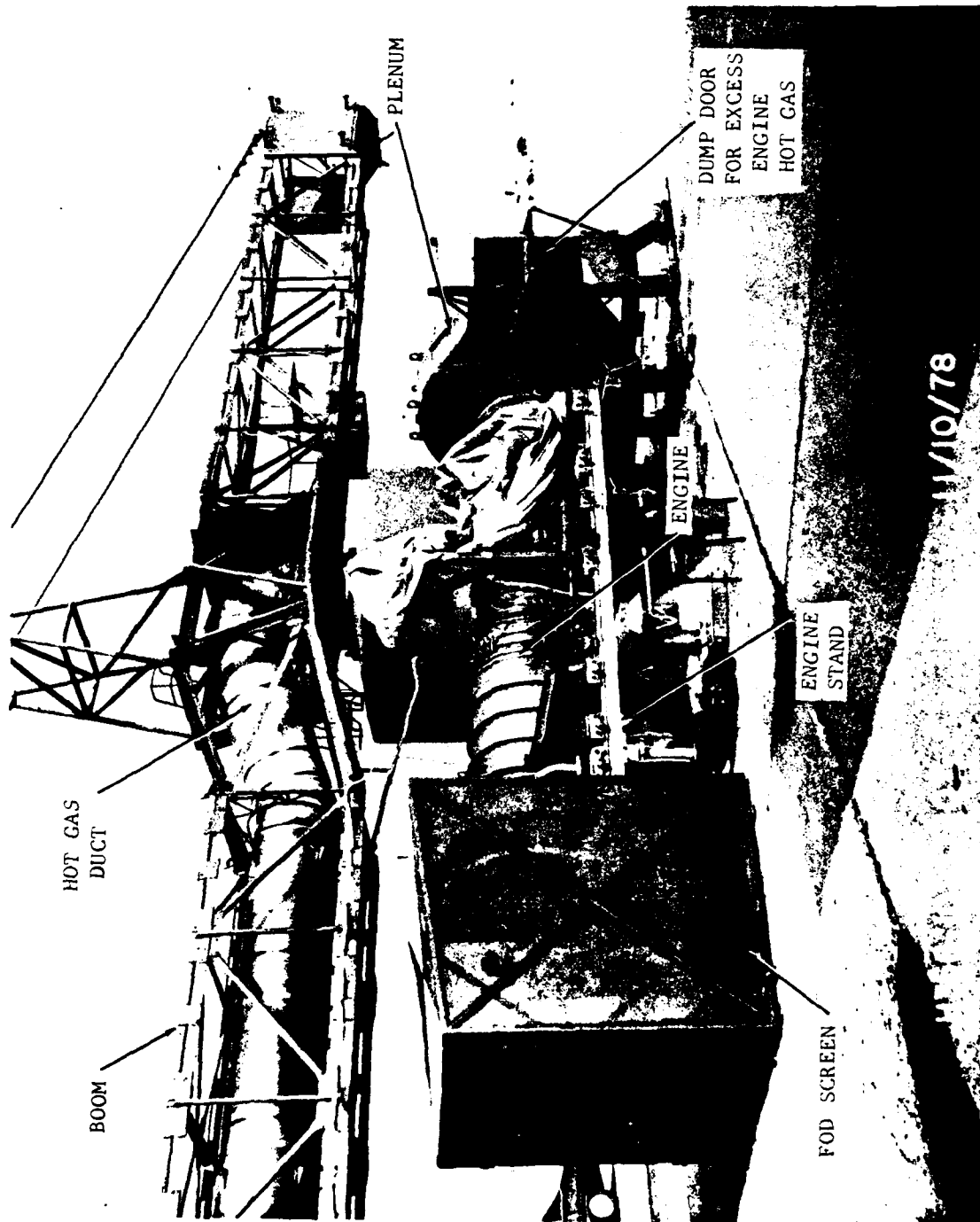


Figure 10-3. F401 Engine Installation

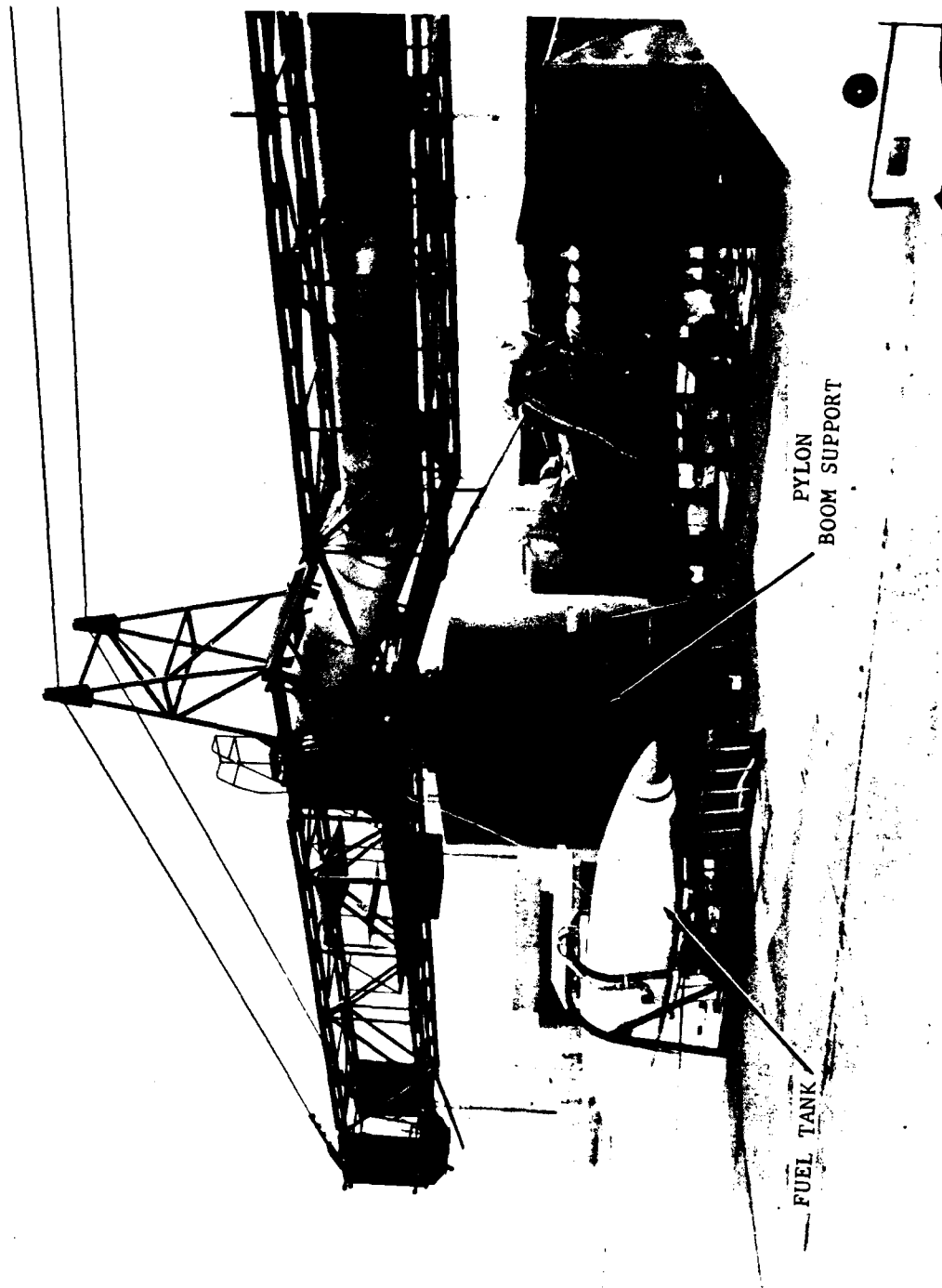


Figure 10-4. F401 Engine - Installation





located at the end of the boom to obtain test article lift and drag data. Measurements of engine airflow to the test article were obtained from a calibrated venturi located in the upstream boom structure or in the case of low flow conditions a calibrated orifice plate was substituted for the venturi. Associated instrumentation (pressure and temperature sensing devices) was located as necessary in order to determine the desired performance.

#### 10.2.1 Instrumentation and Data Acquisition

The instrumentation utilized during the whirl rig test program is essentially the same as that utilized in model scale laboratory tests. Pressure and temperature probes, load cells, traversing probes, amplifiers, and scanivalves are employed to isolate model performance characteristics. Engine operational characteristics and health are monitored utilizing fuel flow electronics, rpm signal box, vibration accelerometers, bellmouth pressure and temperature sensors, and various other diagnostic instrumentation. The major elements of the data acquisition and display system include the block house control room, instrumentation van, and test support equipment (see Figures 10-5 to 10-7).

A typical list of data requirements during a full scale augments test program is presented in Table 10-2. Subsequent to acquisition, test data is then reduced and analyzed by the engineering staff to determine the performance characteristics of the test article.

#### 10.2.2 Engine Instrumentation

An instrumented bellmouth with a conical FOD screen is attached to the engine. The engine is equipped with a P&WA instrumentation kit; however, some of the secondary fuel and oil system sensors are not connected for data acquisition. Sensors required for engine operation, trim, health monitoring and performance level determination are utilized.

Primary engine parameters such as FTIT, N1, N2, CIVV, RCVV, etc., are displayed on indicators at the engine operators console. Warning and status penalties are also provided for the engine facility power and fuel supply systems. Facility hydraulic system status and the test model surface positions are displayed at the flight control operations console. Separate DVMS are provided for each position readout. Control of the three surfaces are by individual hydraulic actuators.

Mercury and water manometers are used to set up the engine for specific test conditions and determine fan pressure ratio and airflow at the engine bellmouth. Manometers are also used to display either the venturi or orifice pressures. Pressure levels at the simulated diverter entrance and in each augments nozzle exit are also monitored. Parameters connected to the manometers are also transmitted to the telemetry receiving station. Readouts from the load cells and resolved lift and drag forces are recorded on a digital multipoint recorder at selected time intervals.

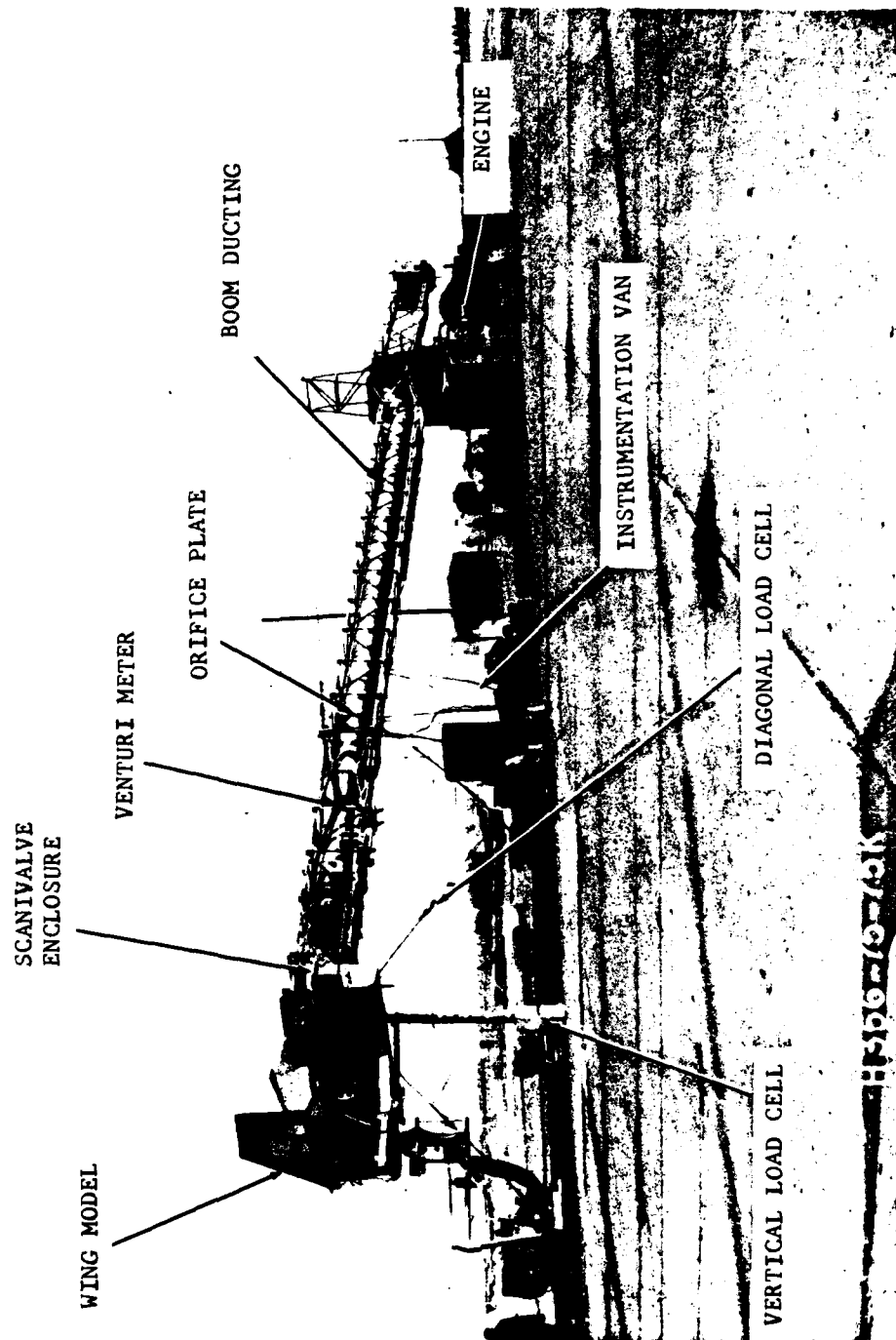


Figure 10-5. Whirl Rig - Wing Model Instrumentation Arrangement

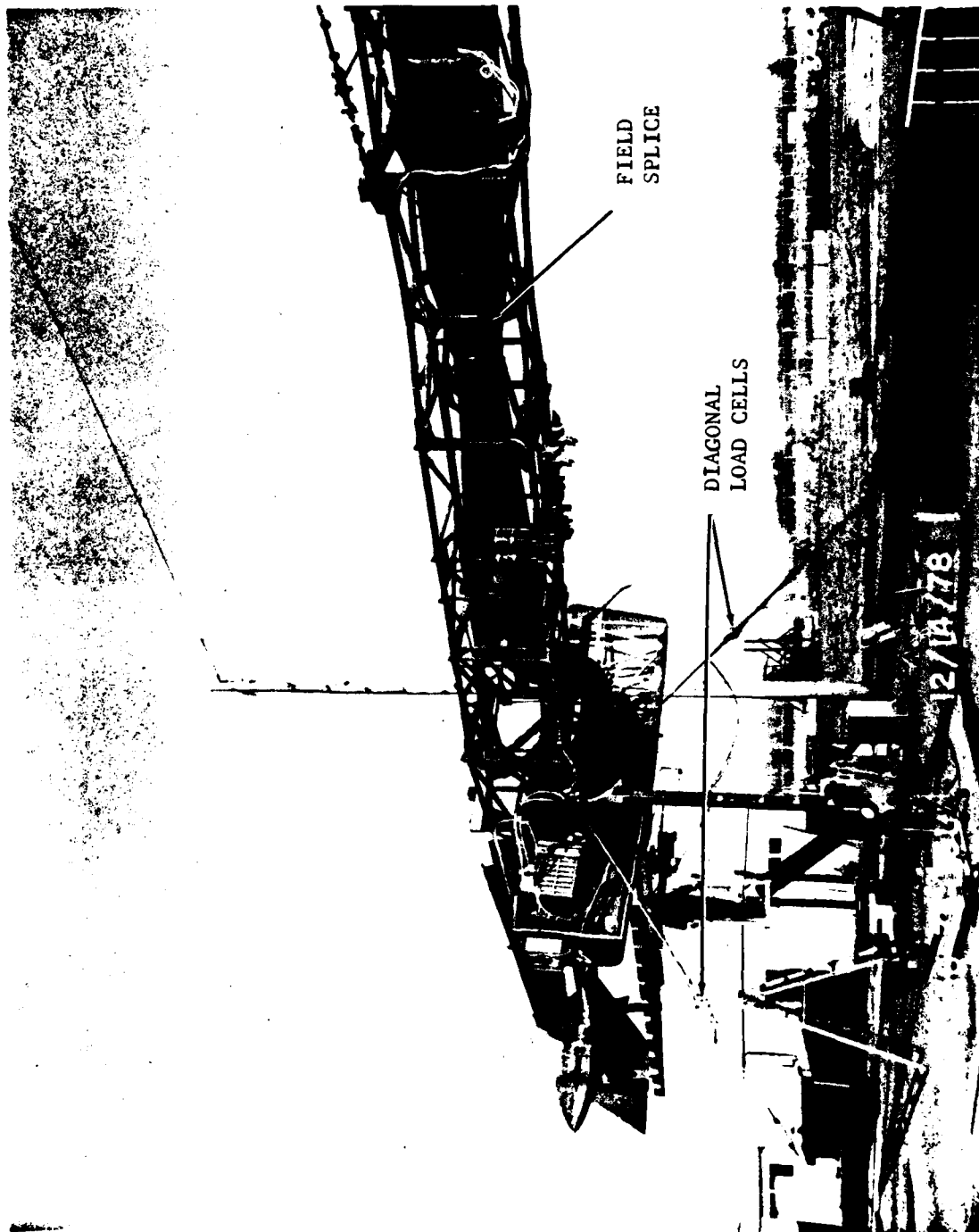


Figure 10-6. Outboard End of Boom with Model Installed

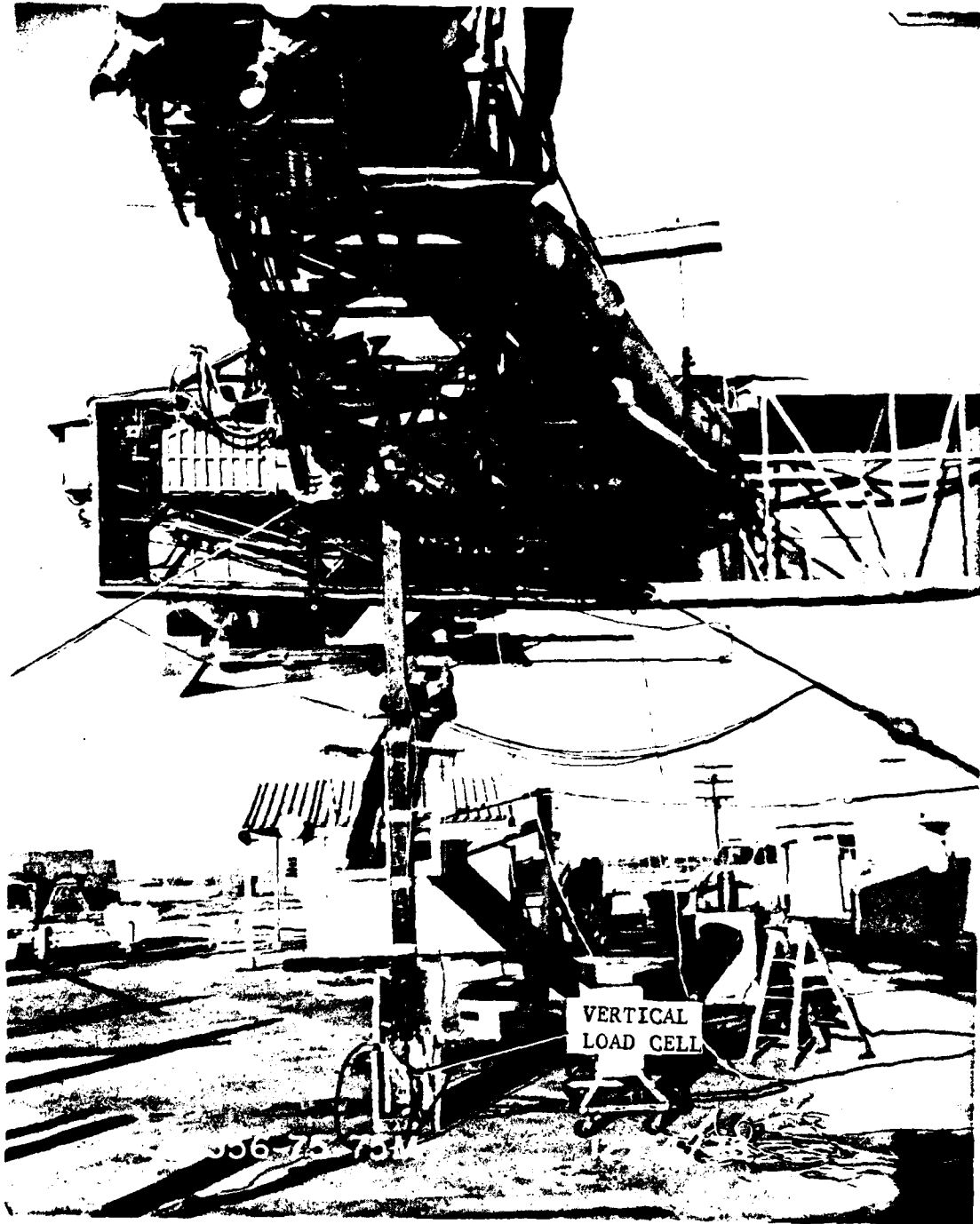


Figure 10-7. Outboard End of Boom with Model Installed



Rockwell International

Table 10-2 Whirl Rig Instrumentation Parameters

No. Parameters

Engine

Bellmouth Pressures and Temperatures	8
Control Input Positions	4
Gas Temperature and Pressures	6
Speed and Fuel Flow	3
Fuel and Oil Pressures and Temperatures	3
Vibration (Not Recorded)	3
	<u>27</u>

Boom Ducting

Venturi Static Pressures and Temperatures	4
Orifice Static Pressures	2
Boom Discharge Total Pressure	<u>1</u>
	7

Model

Interface Total Pressure and Temperatures	5
Surface Positions	3
Center Ejector Nozzle Exit Total Pressures	20
Forward Diffuser and Elevon Nozzle Exit Total Pressures	12
Augmenter Endwall Nozzle Exit Total Pressures	4
Augmenter Nozzle Expansion (5 each nozzle)	15
Center Ejector Surface Static Pressures	17
Forward Diffuser Surface Static Pressures	6
Augmenter Throat Static Pressures	10
Scanivalve Signal and Control	5
	<u>97</u>

Traversing Probe

Augmenter Exit and Throat Total and Static Pressures	6
Augmenter Total Temperatures	2
Center Ejector Jet Profile Pressures	2
Probe Span and Chord Position	<u>2</u>
	12

Facility

Loads	3
Wind Speed and Direction	<u>5</u>
	8

TOTAL 151



### 10.2.3 Instrumentation Van

The van shown in Figure 10-5 is a multipurpose test installation which is used during calibrations, pre-test checkout and actual test runs. The van is located adjacent to the whirl rig boom and contained the primary data acquisition components which are employed during aircraft testing. Transducers are housed for the model and boom parameters to eliminate the need for separate enclosures. The PCM decom and a strip chart recorder are used during pre-test checkout and surveillance of selected data channels during the test runs. Engine vibration sensor outputs are displayed on the P&WA engine vibration monitor rack. Control of the traversing probe during span and chord positioning is also accomplished from the van. The engine trim box is temporarily installed during initial checkout runs of the engine.

### 10.2.4 Model Instrumentation

Measurements obtained to isolate model performance includes the measurements taken on the model and are basically as follows: feed duct interface pressures, nozzle total pressures, nozzle expansion, surface positions, center ejector forward and aft surface static pressures and augmentor throat static pressures, mass flow rates and temperatures, lift and drag, and traversing rake surveys.

Coanda component nozzle exit total pressures are normally recorded at six span stations. Since the center ejector profiles typically show significant variation, twenty probes are employed to investigate the pressure gradients and determine average pressure levels. Probes are also installed in the inboard and outboard endwall blowing nozzles. Figures 10-8 and 10-9 show typical forward diffuser and center ejector probe placement. Each pressure is sampled at 2.5 second intervals utilizing a scanivalve. Nozzle average pressure data is used to compute component primary isentropic nozzle exit velocity.

Coanda and center ejector nozzle gap deflections are measured using a linear potentiometer attached to the nozzle and located outside the primary jet. The rod end of the potentiometer is coupled to the flap surface by a ceramic rod. Prior to installation, the potentiometers are calibrated to verify linearity over the operating range. This expansion data is used to determine individual component flow coefficients. This information is also used to isolate the effects of pressure and temperature on nozzle convergence.

A 20-inch diameter (throat) venturi is installed approximately 25 feet from the end of the boom to measure gas flow during full augmentor tests. The venturi meter discharge coefficient is determined over the test operating range using a calibrated flow nozzle prior to testing. Sharp edge orifice meters of 12.75 in. and 17.6 in. diameter are installed upstream of the venturi for component testing. This provides a differential pressure readout equivalent to that of the venturi meter at maximum flow. Total pressure and temperature probes are installed upstream of the aircraft ducting at the 32-inch duct discharge and simulated diverter entrances.

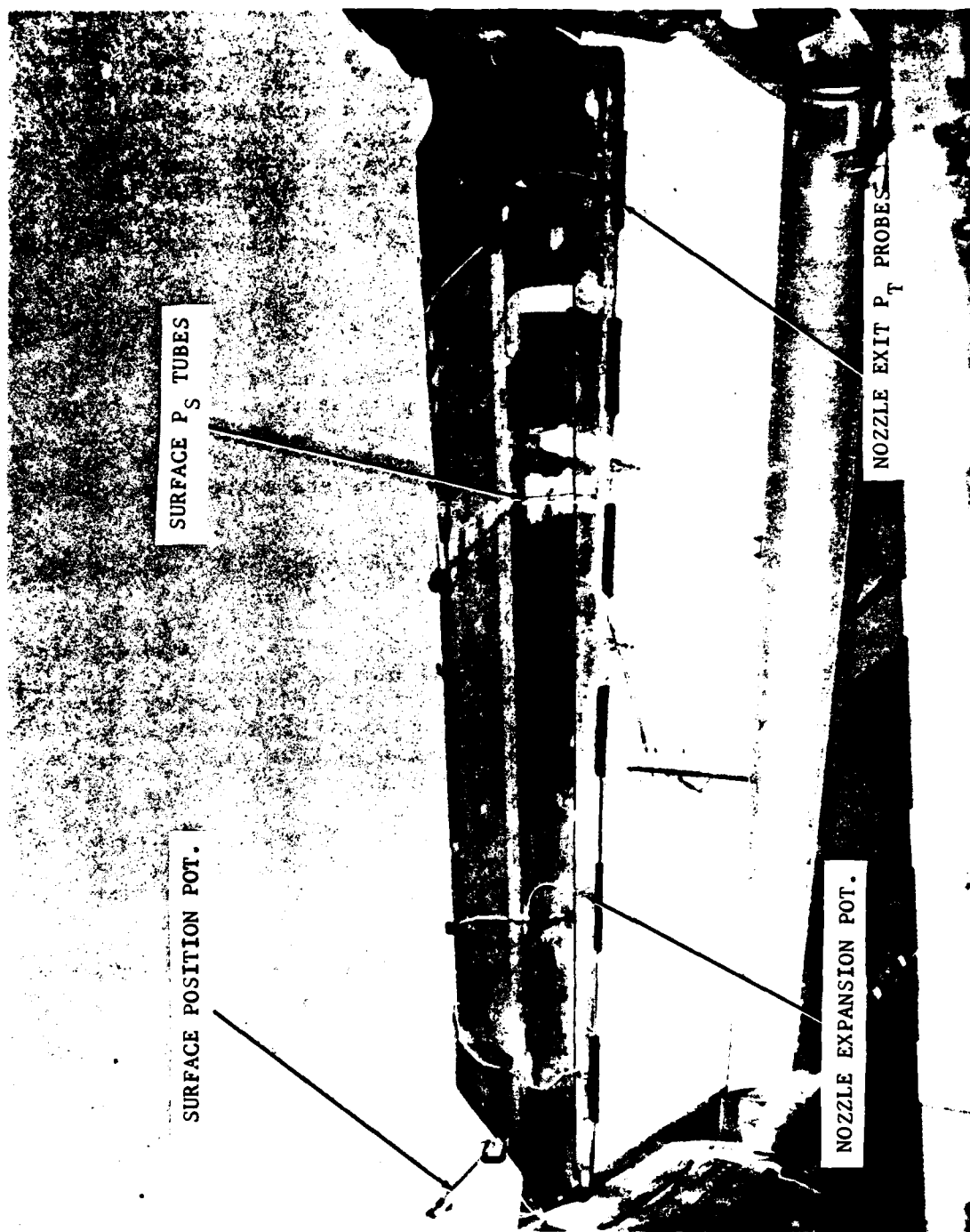


Figure 10-8. Wing Center Ejector Instrumentation

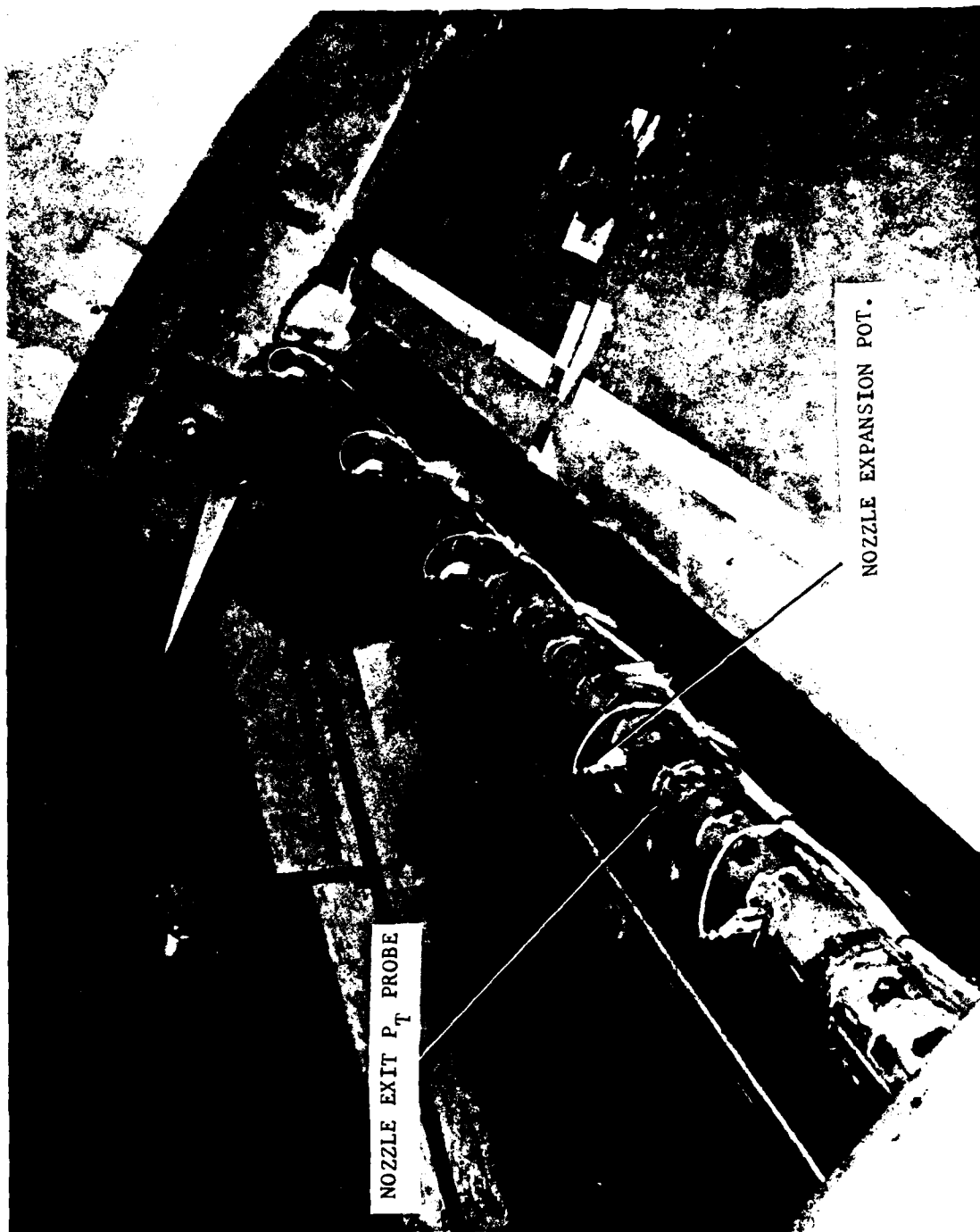


Figure 10-9. Wing Forward Diffuser Instrumentation





Rockwell International

Venturi gas temperature and throat surface temperature are recorded and appropriately used in the computation of mass flow. Leakage flow downstream of the orifice meters and venturi are determined during a special test wherein an equivalent leakage area is computed and considered in the measured net flow to the test article.

Center ejector surface static pressure tubes are often installed at mid-span on the forward and aft surface to determine down loads during full augmentor testing (see Figure 10-8). The surface taps and surface position potentiometer installation is shown in Figure 10-9. Augmentor forward and aft throat static probes (10) are located at the same aircraft test positions (see Figure 10-10). These static probes provide the data necessary to compute augmentor throat secondary velocity, an empirical parameter routinely used to quickly determine relative levels of augmentor performance.

The lift and drag forces produced by the augmentor are measured by a three-component load cell system shown in Figure 10-6 and 10-7. These forces are corrected to the estimated augmentor lift center location for evaluation of augmentation ratio and component thrust coefficient. Transducer incorporated 10,000 pound load cells previously used at Langley are installed in the system. Prior to installing the units a full range calibration is performed with a dead weight tester. Each load cell has two strain gage circuits to provide a dual signal output. One bridge is used to record by PCM or magnetic tape for use in post test data reduction. The second bridge is connected to a Digitrend 210 digital multipoint recorder located in the control room. This unit provides a digital display and printout in engineering units. Each individual load cell readout as well as a summation of lift and drag are printed out using manual select at two samples/sec.

The force measurement system consists of a vertical post held in place by diagonal tie rods. Tension preloading of the diagonal tie rods is used to produce a compression preloading of the vertical post and maintain a slack free redundant force system. Counterbalance is used to adjust the boom tare weight to the desired level.

The vertical load cell output is amplified in order to scale the 1024 PCM counts to 2000 pounds (maximum load cell change from zero balance). The diagonal load cell outputs are amplified to accommodate a load change of 4000 pounds. Even though the load cells are temperature-compensated over a range of 0 to 150°F, heater elements are wrapped around each unit to maintain a near constant temperature at 90°  $\pm$  15°F.

Utilizing the information obtained from the load cell system and the primary flow characteristics determined by the venturi, pressure and temperature instrumentation previously discussed enables the engineering personnel to compute total performance indicators such as augmentation ratio ( $\phi$ ), isolated component velocity coefficients ( $C_v$ ), and nozzle flow coefficients ( $C_p$ ).



Figure 10-10. Wing Augmenter Throat  $P_s$  Probes



Rockwell International

### 10.2.5 Traversing Probe

The traversing probe assembly is used to isolate the relative test article flow quality and determine localized augmentor performance. This assembly consists of a carriage moving along a chordwise rail supporting pitot-static pressure probes and a thermocouple temperature sensor (see Figure 10-11). The chordwise rail is mounted between fore and aft span rails and is movable along them. Both motions are motor-driven and controlled from an isolated position. Position sensors are incorporated in each motor gearbox to provide instrumentation chordwise and spanwise position information. The height of the probes is adjustable by sliding the sensors through clamping supports thus providing capability to survey various x/t locations downstream of the primary nozzle exit (see Figure 10-12). Pressure and temperature data are transmitted via telemetry and recorded on X-Y strip charts. This data is then evaluated to provide information on local thrust, mass flow, velocity, temperature and relative flow quality of the augmentor or component under test.

## 10.3 THERODYNAMICS LABORATORY

Rockwell International, NAAD-Columbus' Thermodynamics Laboratory is an environmental test facility which provides support for conducting research and development in the fields of internal fluid flow, heat transfer, and thermodynamic properties of materials and systems. This facility is located in Building 271 and has a total floor space of over 27,500 square feet. The major equipment and assets in the Thermo Lab, which provided routine support of the XFV-12A V/STOL program, included the high pressure compressor air process system, hazard proof test chambers, and data system and support instrumentation for the control and measurement of the parameters specified. Specifics of the individual test requirements and programs are discussed in the apparatus and test result sections of this report.

The high pressure compressor air process system is composed of a compressor, heater, control, and support distribution systems. A schematic layout of the system is shown in Figure 10-13. The following paragraphs provide a brief description of the major system components and their respective operating ranges.

### 10.3.1 Air Compressor

The Ingersoll Rand Compressor is a ten-stage turbo compressor operating at 9200 RPM and currently delivering airflow at 13 pounds/second at 200 psig. Figure 10-14 presents available airflow delivery in the form of compressor flow rate versus compressor discharge pressure specified and currently available levels.

### 10.3.2 Control and Distribution System

The control and distribution system is the responsibility of the laboratory operating staff. Predetermined pressure and flow requirements are set for the compressor at the main control panel. Second order or

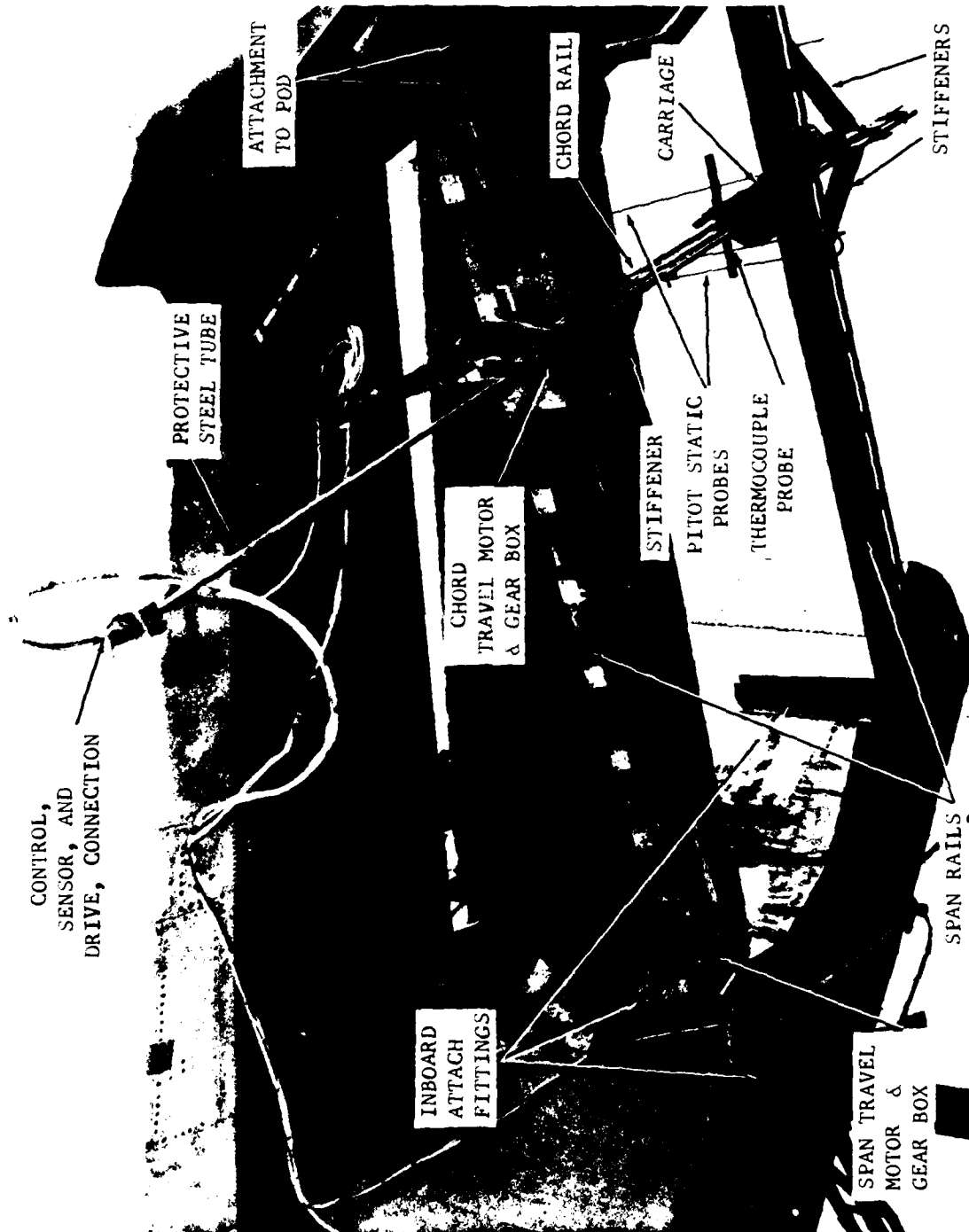


Figure 10-11. Traversing Probe - Installation

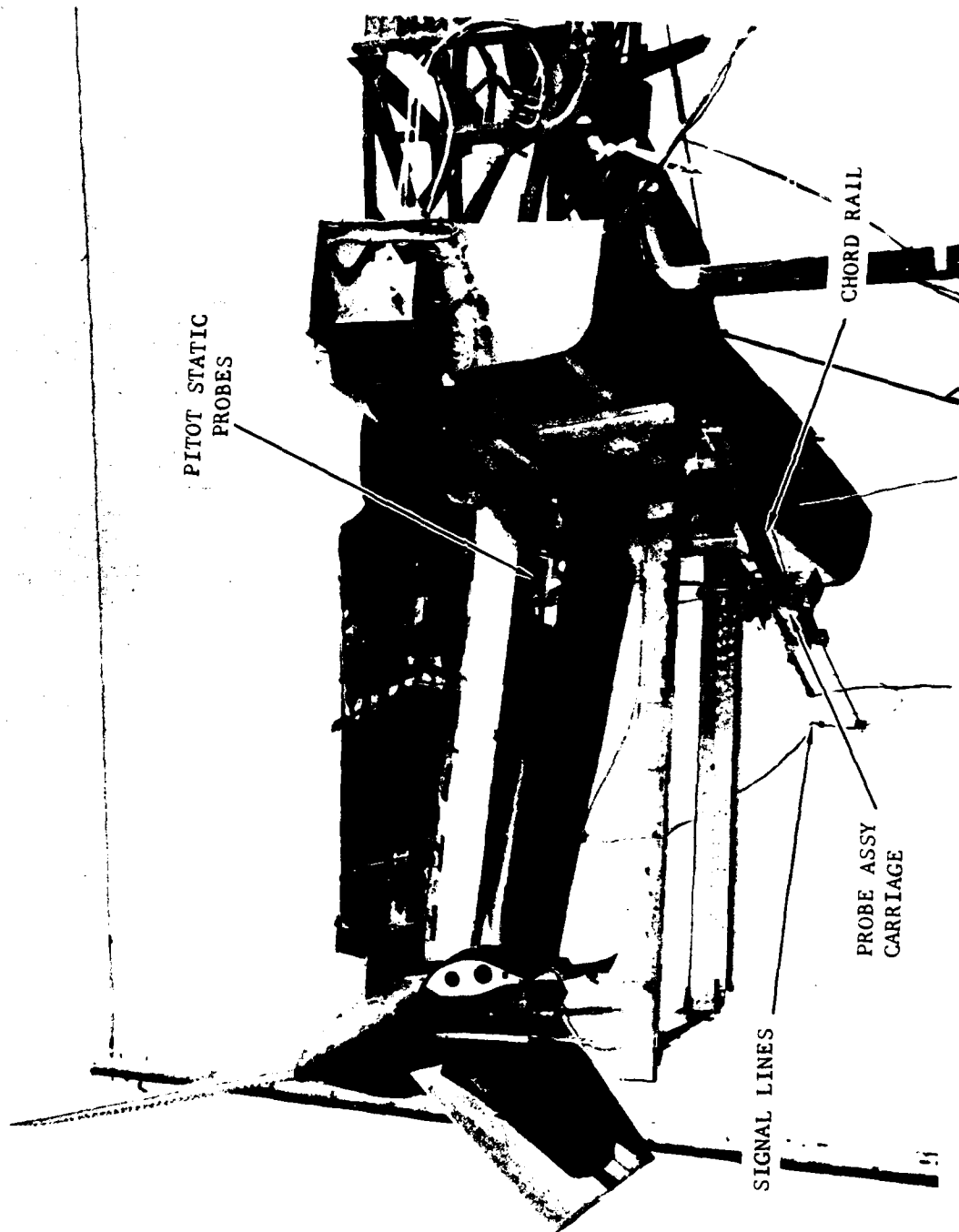
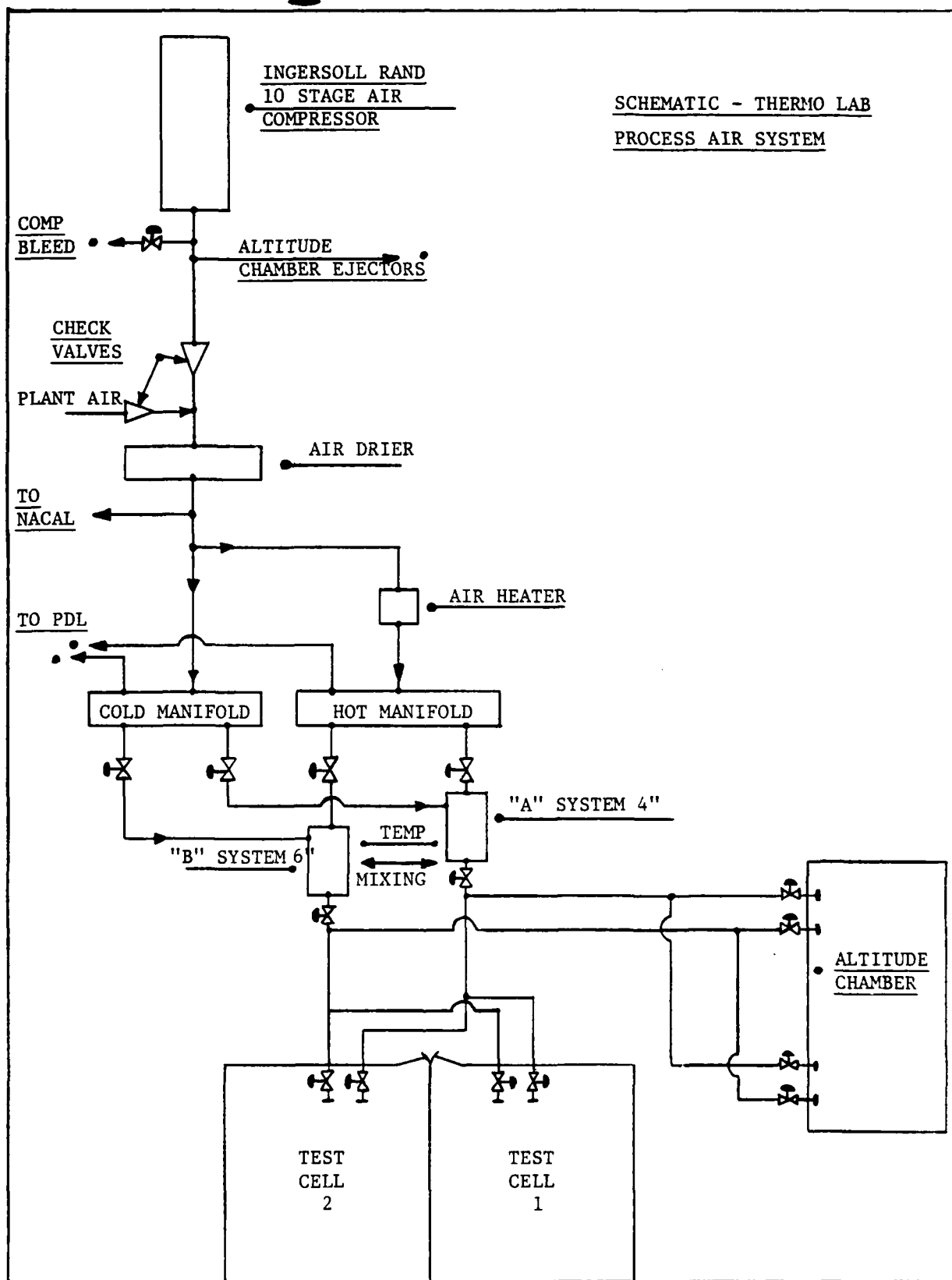
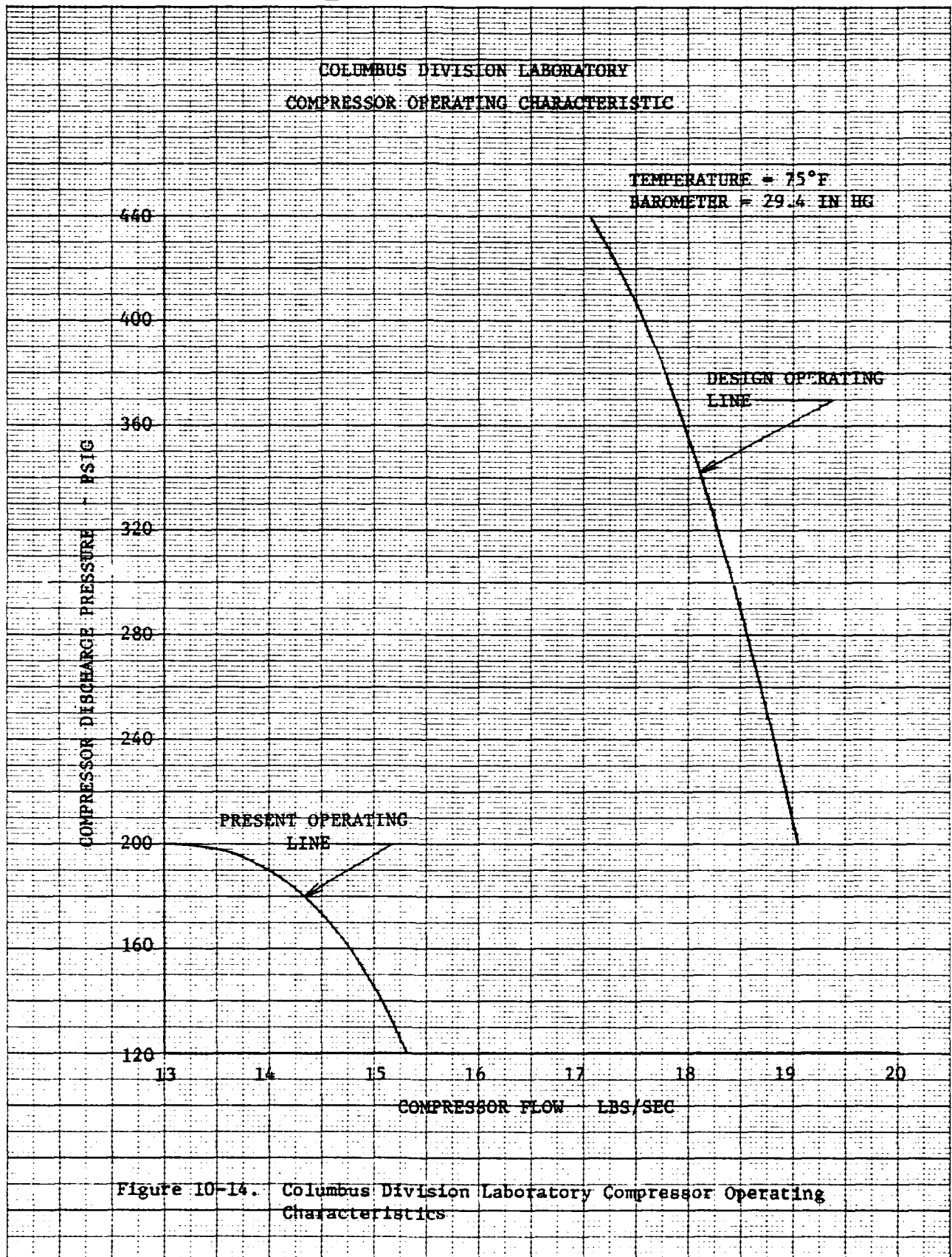


Figure 10-12. Traversing Rake Instrumentation for Center Ejector Jet Growth







close tolerance pressure variations are regulated at the test site by support personnel through a series of control valves and regulators located in the test hardware feed lines. Model pressures and flow rates are monitored by test support personnel at the specific test stand location as discussed in the test apparatus section of this report. The high pressure compressor system was utilized extensively during the model scale centerbody nozzle and augmentor shroud test programs as the primary air supply system for these models. During the full scale XFV-12A elevon diagnostic investigation, a series of tests were conducted in the Thermodynamics Laboratory hazard proof test cell number 1. This test cell is a reinforced concrete test chamber 17'W x 37'L x 14'H. The test cell was supplied primary mass flow delivered from the compressor through a four-inch line. Mass flow rates and test hardware pressures are monitored by venturi and pressure transducer instrumentation described in the full scale elevon section of this document.

#### 10.4 TEST FACILITY - WPAFB

##### 10.4.1 General

The test facility utilized in the Coanda segment model and full scale elevon test programs was located at the WPAFB Aeronautical Propulsion Laboratory, adjacent to Building 18C. The site, prior to the start of the test, shown in Figure 10-15, consisted of a concrete slab, screened-in enclosure and a 12-inch air supply line equipped with a manually operated gate valve. The air source consisted of two centrifugal compressors located in the basement of Building 18E. In order to make the existing facility suitable for testing, an air regulation and flow metering system, load stand, enclosure and operations trailer were supplied by the contractor. The modifications to the existing facility were designed to accommodate testing of either the segment model or full span aircraft elevon. The test facilities before and after installation of the enclosure are shown in Figure 10-16.

##### 10.4.2 Test Enclosure

In order to provide protection from the elements and maintain area noise levels within the WPAFB safety limits, an enclosure, 23 feet by 17 feet was assembled around the existing sheet metal roof, as shown in Figure 10-16. The interior of the enclosure was acoustically lined to attenuate the noise level to acceptable levels. Attenuation of the dump door noise was accomplished by a rectangular duct and an acoustically lined cone 18.5 feet high which directed air vertically. Farfield noise level data were acquired by WPAFB personnel during initial runs to ensure that the 95 dbA limit was not exceeded at prescribed stations in the surrounding area. Results of these tests are presented in Figure 10-17.

The four enclosure walls were constructed using 1/2 inch plywood and 2 x 4's; between studs were 3-1/2 inch fiberglass sheets. This was faced with composite material KC-5-50/150B for sound absorption. Two standard size doors, 3 feet x 7 feet, were installed in the east side of the enclosure. A rack of two acoustic panels, 11 feet by 8 feet, were





VIEW FROM PARKING LOT



VIEW FROM PATIO

FIGURE 10-15. TEST SITE UNMODIFIED

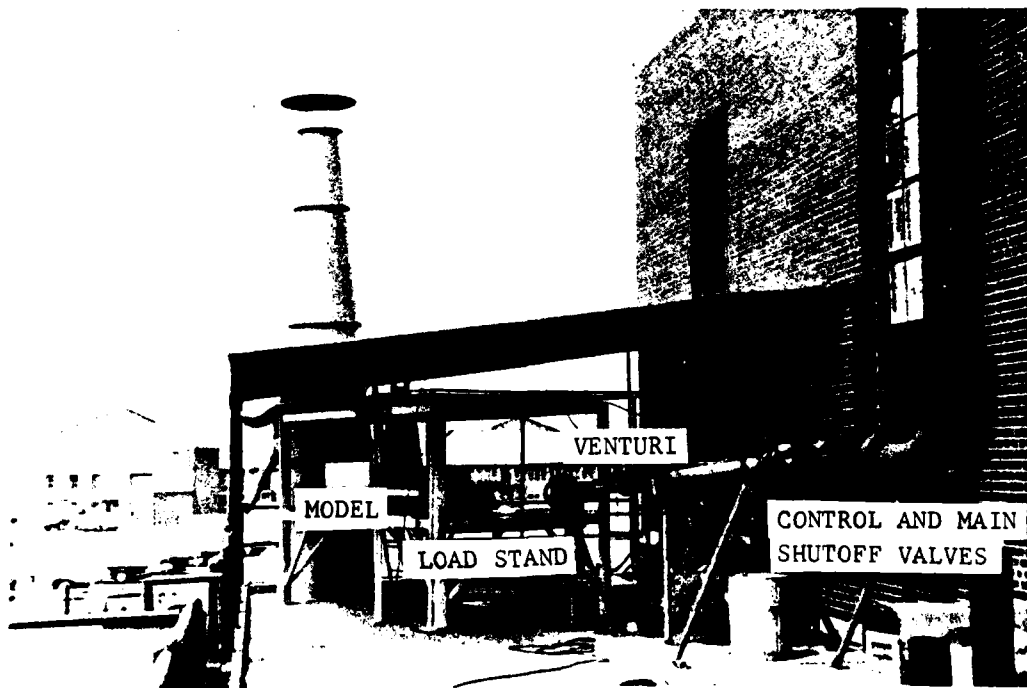
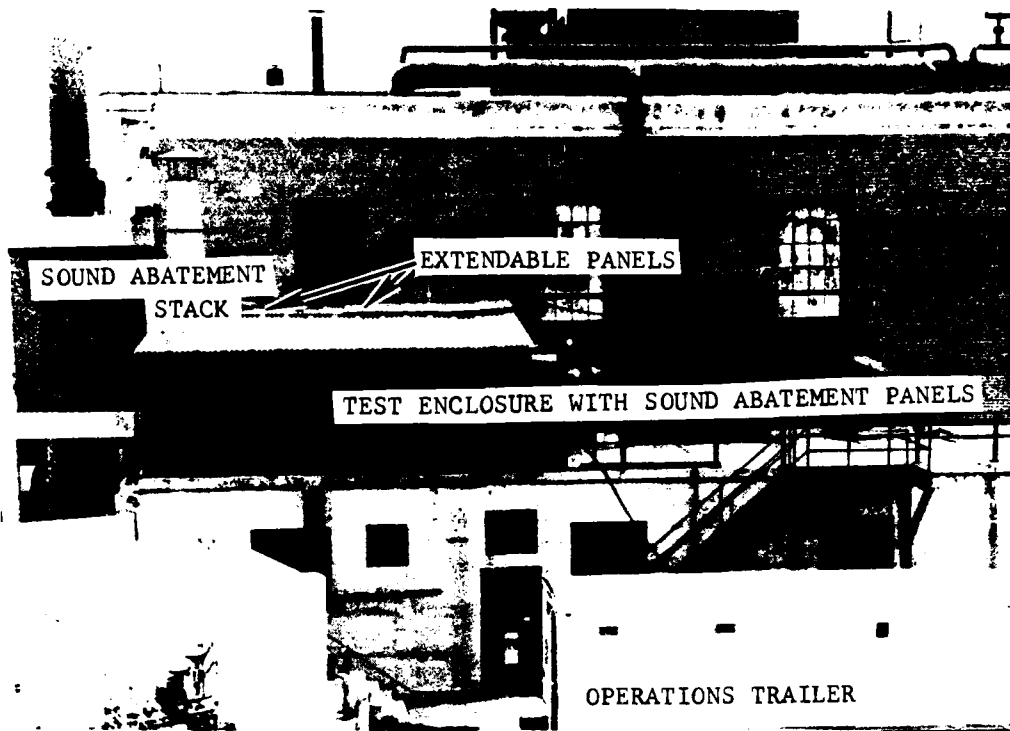
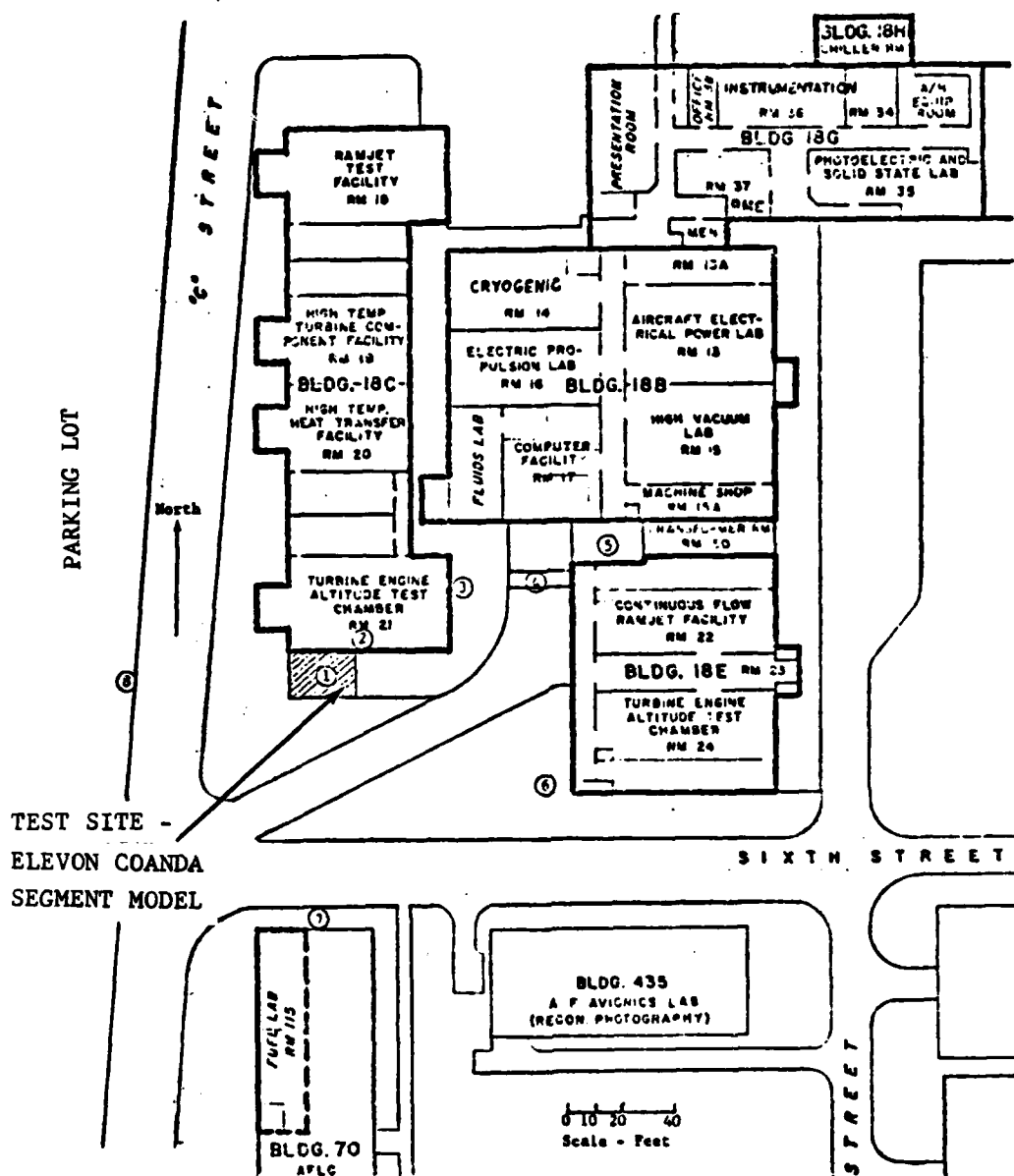


FIGURE 10-16. TEST FACILITIES



## MEASURED NOISE LEVELS

	dba		dba
(1) Inside Test Enclosure	128.0	(5) At Bldg. 18B - 18E Platform	77.5
(2) Inside Room 21	84.0	(6) Stairway Outside Room 24	81.0 (90.0)
(3) Patio Outside Room 21	79.5	(7) Lower Level at Bldg. 70	78.5 (79.5)
(4) At Bldg. 18E Door	79.5	(8) Sidewalk Across Street	77.0 (78.0)

( ) Test Enclosure Access Doors Open

FIGURE 10-17. TEST FACILITY - NOISE MEASUREMENTS



assembled and installed above the model to attenuate and prevent reflections of noise within the enclosure (off the metal roof). Nozzle efflux was exhausted through an opening in the northeast corner of the roof during Phase I testing. An additional opening in the northwest corner, nearer the model exit, was provided for Phase II and subsequent testing to reduce enclosure recirculation.

#### 10.4.3 Operations Trailer

The trailer, shown in Figure 10-16, was used as a test control station, work shop and office space. With the exception of the instrumentation sensors and X-Y plotters required for flow surveys, all recorders and signal conditioning equipment were located in the trailer.

#### 10.4.4 Instrumentation and Data

The instrumentation parameters which were recorded and monitored are listed in Table 10-3. These parameters were primarily load stand forces, air supply system and model pressures and jet survey pressures. Selected parameters were displayed as well as recorded for test control purposes. Manometers and pressure gages were located outside the test enclosure and in the vicinity of the model flow control equipment. All end sensors were located either within or just outside the enclosure. Instrumentation control, signal conditioning, power supplies, Digitrend recorder and test equipment were located in the operations trailer.

Printout data from the Digitrend were displayed in voltage levels and were acquired at a rate of two samples per second. This information was tabulated following each test in an order compatible with the data reduction program. The data reduction program was generated specifically for these tests; however, it was based primarily on modifications to portions of existing programs. Voltage levels from each input parameter were converted to engineering units and computations for nozzle pressure ratio, venturi weight flow,  $C_D$ , true lift, nozzle isentropic thrust and  $C_y$  were performed. Leakage rate and load stand interaction calibrations were incorporated as the model configuration and/or installation was changed.



Rockwell International

Table 10-3 Instrumentation Parameters

<u>PARAMETER</u>	<u>RANGE</u>	<u>SENSITIVITY</u>	<u>DIGITREND CHANNEL</u>	<u>DIRECT READOUT</u>
1. Lift Load Cell ( $L_1$ )	0-500 lb	100-lb/v	63 and 78	
2. Lift Load Cell ( $L_2$ )	0-500 lb	100 lb/v	64 and 79	
3. Side Load Cell ( $S_1$ )	0-1000 lb	100 lb/v	65	
4. Side Load Cell ( $S_2$ )	0-1000 lb	100 lb/v	66	
5. Drag Load Cell ( $D_1$ )	0-500 lb	100 lb/v	67	
6. Drag Load Cell ( $D_2$ )	0-500 lb	100 lb/v	68	
7. Drag Load Cell ( $D_3$ )	0-500 lb	100 lb/v	69	
8. Drag Load Cell ( $D_4$ )	0-500 lb	100 lb/v	70	
9. Regulator Inlet Supply Pressure	0-100 psig	10 psi/v	71	Pressure Gage
10. Upstream Venturi Pressure	0-100 psig	10 psi/v	72	Pressure Gage
11. Venturi $\Delta P$	0-25 psid	10 psi/v	73	Manometer
12. Model Interface Pressure, $P_T$	0-50 psid	10 psi/v	74	
13. Model Nozzle Midspan, $P_T$	0-25 psid	10 psi/v	75	Manometer
14. Model Interface Ref. to Midspan	0-5 psid	1 psi/v	76	
15. Rolling Probe and Gun Probe $P_T$	0-50 psid	10 psi/v	-	X-Y Plotter
16. Venturi Air Supply Temp.	0-200°F	-	80	
17. Ambient Air Temp. (Outside)	0-100°F	-	81	
18. Traversing Probe $P_T$	0-5 psid	1 psi/v	-	X-Y Plotter
19. Hose (Tare) $P_T$	0-50 psid	10 psi/v	62	
20. Air Duct Dump, $P_S$	0-5 psid	1 psi/v	77	
21. Air Dump Tube Outlet, $P_T$	0-25 psid	10 psi/v	61	
22. Barometric Pressure				



Rockwell International

## 11.0 AIRCRAFT PRESERVATION

11.1 GENERAL

At the conclusion of the NASA Langley static and dynamic tests in July 1978, the XfV-12A Prototype No. 1 aircraft was placed in storage in the large NASA flight hangar. Figure 11-1 shows the aircraft as stored. As can be seen, the storage area does not provide a benign environment. Therefore, to provide for this storage, an initial inspection was conducted including cleaning and preservation of the aircraft to inhibit deterioration. This preservation was accomplished in accordance with Contract N00019-73-C-0053, MOD P00040, Item 13, and NAVAIR Instruction 15-01-500. Subsequent inspections have been conducted periodically since February 1979 and approximately every 120 calendar days thereafter.

To implement the initial storage, a checklist was prepared using NAVAIR 15-01-500 and knowledge of detail areas of the aircraft that were subjected to unusual usage during the previous test period. This checklist was submitted to and approved by the contractor's local NAVPRO Quality representative. Table 11-1 itemizes the specific tasks inspected.

Selected items were removed from the aircraft for additional tests at the contractor's plant in Columbus, Ohio. The items included but were not limited to: YF401-PW-400 engine; left-hand canard and supply ducting; left-hand wing augmenters and supply ducting; and selected fuselage parts. All items removed are noted in the aircraft log book.

11.2 INSPECTION/PRESERVATION SUMMARY

The initial inspection/preservation was completed in February 1979 and the second inspection/preservation was completed in June 1979. Very little change from the original storage condition was noted. A general cleaning was conducted and a reapplication of preservative applied to areas which indicated suspected deterioration.

The third inspection/preservation was conducted in October 1979. Accelerated corrosion had occurred during this period. A thorough cleaning of the affected areas and preservative was reapplied.

The fourth inspection/preservation was conducted in January 1980. Because of the previous deterioration noted in the third monitoring period, a more extensive cleaning was conducted. Additional items were removed for inspection and subsequent cleaning. These items were stored as loose items with the aircraft. Preservative was reapplied to the entire aircraft.

The fifth inspection/preservation was conducted in May 1980, and the sixth inspection/preservation in September 1980. Very little change had occurred since the fourth period. The fuselage sump tank was opened and inspected during the sixth monitoring.

In February 1981, a visual inspection was conducted and a recommendation was made, and accepted, to the Navy to delay the formal inspection.

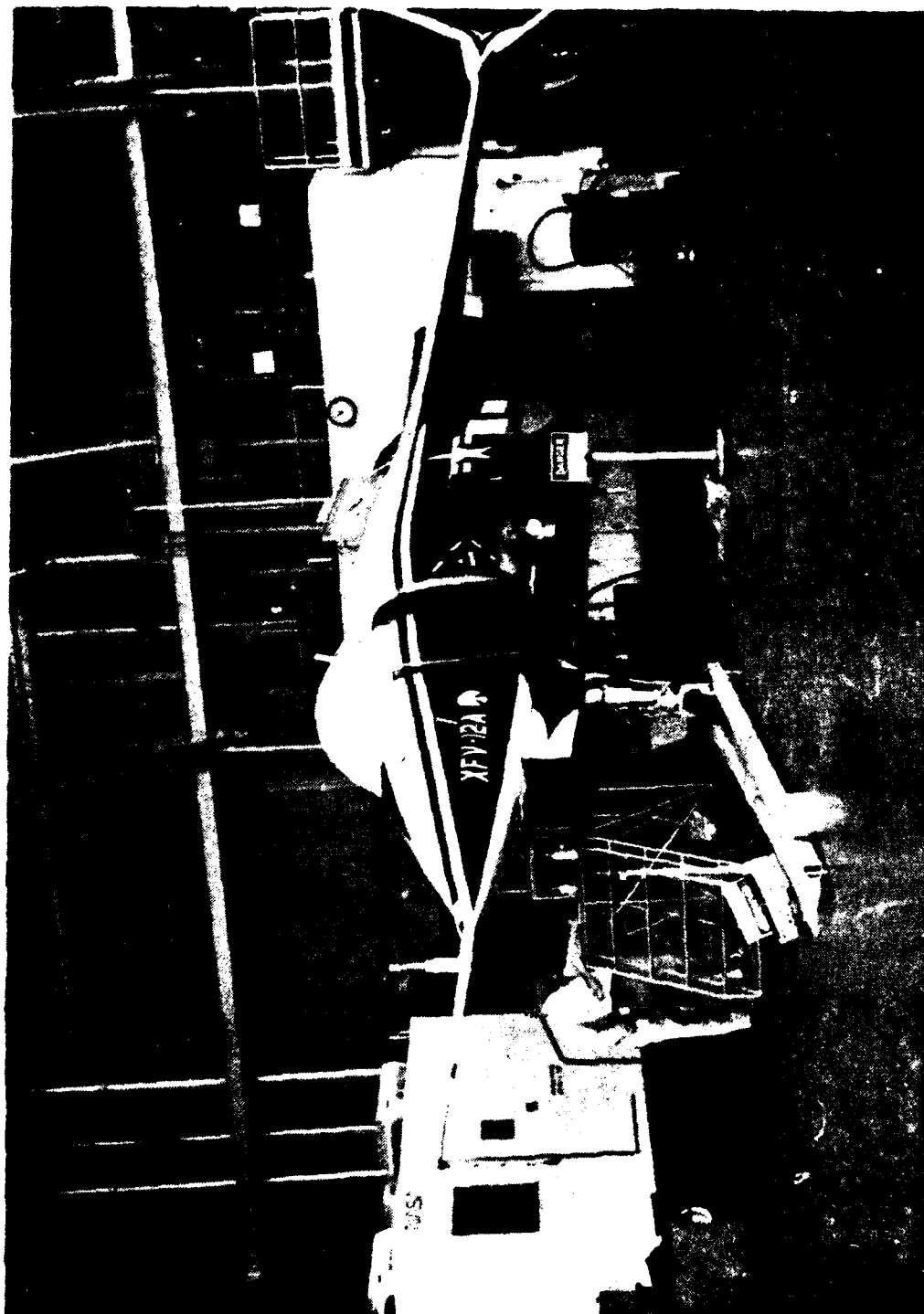


Figure 11-1 X-12A At NASA Langley - General View

11-3





Rockwell International

Table 11-1 XFV-12A - Long Term Indoor Ventilated Storage - Type A Modified (Continued)  
Ref. NAVAIR 15-01-500

SUBJECT	MECH.	INSP.	SUBJECT	MECH.	INSP.
Fuel System Lines & Fittings			Cockpit		
Hydraulic System			Quadrant		
Hydraulic Actuators			Instruments		
Service reservoirs			Rudder Pedals		
Clean; inspect for corrosion. Treat as required. Coat exposed pistons with operating hydraulic fluid.			Control Stick		
Mixer Bay			Seat		
Wing Controls					
Canard Controls					
Landing Gear					
Hydraulic Lines and Fittings			Skin Surfaces Exterior		
Clean; inspect for corrosion. Treat as Required.					
N/G Well					
Cockpit					
Mixer Bay					
Engine Bay					
Wing F/C Bay					
Canard Area					
Wing Pods					
Landing Gear			Torque Tubes and Control Rods		
Clean and lubricate; inspect for corrosion. Treat as required. Apply MIL-C-16173 Grade 2 to unpainted surfaces.					
Nose					
L/H Main					
R/H Main					
Axles			Fuel System Tanks		
Remove wheels; clean; inspect for corrosion. Treat as required					
Nose					
L/H Main					
R/H Main					



Rockwell International

All discrepancies, removals, cleaning, and applications of preservative are noted in the aircraft's inspection record.

The present condition of the aircraft is acceptable for an interim period, but if use within the next two years is contemplated, some inspection should be done on a semi-annual basis. These inspections do not assure the operational capability of the airframe or the systems, but only that corrosion effects have been minimized.



Rockwell International

NR81H-50

THIS PAGE INTENTIONALLY LEFT BLANK



Rockwell International

## 12.0 CONCLUSIONS AND RECOMMENDATIONS

During the time covered by this report, the XFV-12A program activities were directed primarily toward the development of improved augmentor performance with configurations compatible with high performance aircraft designs. This improved performance was derived from extensive and coordinated analytical and experimental efforts which provided an expanded understanding of augmentor flow parameters, component contributions, and effects of design changes for this type of ejector thrust augmentor configuration.

Program activities and objectives were highly coordinated among the Navy Project Management, the Navy Advisory Committee and the contractor. The resulting pragmatic approach produced excellent results with regard to technology development. Most of the program objectives were achieved. It is considered unfortunate that funding was terminated before these excellent results could be demonstrated with full scale hardware in order to provide a highly visible, practical, verification of this concept for high performance V/STOL aircraft.

Specific conclusions and associated recommendations with regard to future activities follow.

1. Development testing of a full size Coanda/flap surface showed that the quality of flow can be improved by relocating the nozzle away from the feed duct. This relocation, together with an optimization of the Coanda shape, eliminated the flow angularity exiting from the nozzle at the inboard end of the surface in addition to improving the nozzle total pressure distribution along the span. These changes resulted in improved surface flow and velocity coefficients.

Recommendation: Develop a design criteria, in the Laboratory, using a large scale model to produce quality flow at the inboard end of the centerbody nozzle. Based upon the above, design, fabricate, and validate full scale on the whirl rig an improved centerbody nozzle configuration.

2. Through the use of physical reasoning, mathematical analysis, and carefully controlled test techniques, scale model testing can be utilized in the development of large scale ejector systems. Experimental data have been obtained which provide substantial evidence that model scale ejectors powered by cold air jets provide a close approximation to the performance of full size ejectors powered by hot jet exhaust flows.

Recommendation: Using scale models and full scale components develop exact scaling parameters for ejectors.



3. Using a finite difference solution of Reynolds equations, which employs a two-equation turbulence model for closure, a numerical model has been developed, and successfully demonstrated by scale model tests, to accurately predict differential levels of performance related to centerbody nozzle configurations. This numerical model was developed for two-dimensional analysis and does not include performance effects related to Coanda shapes or three-dimensional inputs.

Recommendation: Incorporate Coanda jet turning phenomenon and correlate with existing experimental data base. Using this revised numerical model incorporate three-dimensional effects and validate by scale model tests.

4. Through the use of systematic testing of model scale and full size components, numerical analysis, and aircraft design studies of configuration restraints, improvement of the thrust augmentation level of the XFV-12A wing augments has been increased from the 1.26 level at Langley to 1.64 in the Laboratory.

Recommendation: Design, fabricate, and test a full scale ejector, of the configuration developed during this effort, on the whirl rig facility using the YF401 engine.

5. Aircraft design studies have integrated the improved augmenters components into a high performance ejector wing configuration that provides reduced supersonic wave drag as compared to the original XFV-12A configuration.

Recommendation: Using the ejector configuration developed under this effort, modify the XFV-12A aircraft for testing of the ejector wing concept in the NASA-Ames new 80 x 120 ft. wind tunnel.